

*NASA Conference Publication 2372*

# **Advanced High Pressure O<sub>2</sub>/H<sub>2</sub> Technology**

*Proceedings of a conference held at  
George C. Marshall Space Flight Center  
Huntsville, Alabama  
June 27-29, 1984*

---

**NASA**

---

*NASA Conference Publication 2372*

# Advanced High Pressure O<sub>2</sub>/H<sub>2</sub> Technology

*Edited by*  
S. F. Morea  
*George C. Marshall Space Flight Center*

S. T. Wu  
*The University of Alabama in Huntsville*  
*Huntsville, Alabama*

Proceedings of a conference held at  
George C. Marshall Space Flight Center  
Huntsville, Alabama  
June 27-29, 1984

**NASA**  
National Aeronautics  
and Space Administration  
Scientific and Technical  
Information Branch

1985

STEERING COMMITTEE

S. F. Morea  
Co-chairman

S. T. Wu  
Co-chairman

Members

Carl Aukerman	LeRC/NASA
Dr. Biliyar Bhat	MSFC/NASA
Carmelo Bianca	MSFC/NASA
Dr. Chris Chamis	LeRC/NASA
Fred J. Dolan	MSFC/NASA
Dr. R. L. Dreshfield	LeRC/NASA
Dr. D. P. Fleming	LeRC/NASA
L. Gross	MSFC/NASA
Dr. Gary Halford	LeRC/NASA
J. D. Hankins	MSFC/NASA
Larry Kiefling	MSFC/NASA
J. Knadler	MSFC/NASA
T. Marshall	MSFC/NASA
B. Neiberding	LeRC/NASA
Dr. Lou Povinelli	LeRC/NASA
D. Pryor	MSFC/NASA
Dr. L. A. Schutzenhofer	MSFC/NASA
H. Scibbe	LeRC/NASA
Heinz Struck	MSFC/NASA
A. Vary	LeRC/NASA
J. Wanhainen	LeRC/NASA

Administrative Staff

Mrs. Gladys Jones

Ms. Sue Weir

Mrs. Pat Corder

TABLE OF CONTENTS

FOREWORD	ix
S. F. Morea & S. T. Wu	
WELCOME ADDRESS	xi
J. Kingsbury	
BACKGROUND	xiv
S. F. Morea	
<u>I. Fatigue/Fracture/Life and Ignition/Combustion Process</u>	
OVERVIEW	1
G. Halford & C. Bianca	
A REVIEW OF FRACTURE MECHANICS LIFE TECHNOLOGY	5
J. M. Thomas	
FATIGUE LIFE EXTENSION	20
D. Matejczyk & J. Lin	
THRUST CHAMBER LIFE PREDICTION	36
H. J. Kasper & R. J. Quentmeyer	
<u>II. Manufacturing and Producibility Technology</u>	
OVERVIEW	44
R. L. Dreshfield & J. D. Hankins	
ROCKET THRUST CHAMBER THERMAL BARRIER COATINGS	49
R. J. Quentmeyer	
CERAMICS FOR ADVANCED O <sub>2</sub> /H <sub>2</sub> APPLICATION	59
H. Carpenter	
VACUUM PLASMA COATINGS FOR TURBINE BLADES	74
R. Holmes	

### III. Material Technology

OVERVIEW	91
R. L. Dreshfield & B. Bhat	
DESIGN OVERVIEW OF FIBER-REINFORCED SUPERALLOY COMPOSITES FOR THE SPACE SHUTTLE MAIN ENGINE	93
J. Lewis	
MATERIALS FOR ADVANCED ROCKET ENGINE TURBO- PUMP TURBINE BLADES	110
W. Chandler	
DEVELOPMENT OF HYDROGEN RESISTANT ALLOYS	133
W. P. McPherson	
IGNITION OF METALS IN HIGH PRESSURE OXYGEN	134
J. W. Bransford	
DEVELOPMENT AND EVALUATION OF ADVANCED LOX/GOX COMPATIBLE FLUORO-ELASTOMERS	149
J. W. Martin	
HIGH PRESSURE HYDROGEN TESTING OF SINGLE CRYSTAL SUPERALLOYS FOR ADVANCED ROCKET ENGINE TURBOPUMP TURBINE BLADE	150
R. A. Parr, W. S. Alter & M. H. Johnson	
RELATIONSHIPS BETWEEN MICROSTRUCTURE AND MICROFISSURING IN ALLOY 718	164
R. G. Thompson	
DEVELOPMENT OF NEW MATERIALS FOR TURBOPUMP BEARINGS	180
R. E. Maurer, R. A. Pallini, & S. W. Brown	

### IV. Bearing Technology

OVERVIEW	201
H. Scibbe & F. J. Dolan	

ADVANCED ROCKET ENGINE CRYOGENIC TURBOPUMP BEARING THERMAL MODEL J. C. Cody	205
HYBRID BEARINGS FOR LH <sub>2</sub> AND LO <sub>2</sub> TURBOPUMPS M. F. Butner and F. C. Lee	220
POWDER METALLURGY BEARINGS FOR ADVANCED ROCKET ENGINES J. N. Fleck, B. J. Killman & H. Munson	245
ROLLINGS CONTACT FATIGUE LIFE OF CHROMIUM ION PLATED 440C BEARING STEEL B. N. Bhat & J. H. Davis	246

#### V. Structure Dynamics

OVERVIEW C. Chamis & L. Kiefling	261
SIGNAL ANALYSIS TECHNIQUE FOR INCIPIENT FAILURE DETECTION IN TURBOMACHINERY T. Coffin	262
FLOW DYNAMIC ENVIRONMENT DATA BASE DEVELOPMENT FOR THE SSME C. V. Sandaram	277
TURBINE BLADE FRICTION DAMPING STUDY R. Dominic	289
NONLINEAR STRUCTURAL ANALYSIS FOR FIBER-REINFORCED SUPERALLOY D. A. Hopkins & C. C. Chamis	318

#### VI. Rotordynamics

OVERVIEW D. P. Fleming & L. A. Schutzenhofer	341
---	-----

EFFECTS OF BEARING DEADBAND ON BEARING LOADS AND ROTOR STABILITY J. R. Glaese & A. P. Bukley	345
PRELIMINARY RESULTS ON PASSIVE EDDY CURRENT DAMPER TECHNOLOGY FOR SSME TURBOMACHINERY R. E. Cunningham	365
DEVELOPMENT AND APPLICATION OF A UNIFIED BALANCING APPROACH WITH MULTIPLE CONSTRAINTS E. S. Zorzi, C. C. Lee & J. C. Giordano	381
ROTOR RESPONSE FOR TRANSIENT UNBALANCE CHANGES IN A NONLINEAR SIMULATION M. J. Hine, C. E. Landis & R. F. Beatty	400
DAMPING TEST VERIFICATION SETUP K. Cappel	425
DAMPING SEALS FOR TURBOMACHINERY G. L. von Pragenau	438
VIBRATION CHARACTERISTICS OF THE HPOTP OF THE SSME D. W. Childs & D. S. Moyer	452
HOUSING FLEXIBILITY EFFECTS ON ROTOR STABILITY L. B. Davis, E. A. Wolfe & R. F. Beatty	482
VII. <u>Fluid and Gas Dynamics</u>	
OVERVIEW L. Povinelli & H. Struck	508
COMPUTATIONS TO IDENTIFY REGIONS OF FLOW SEPARATIONS IN THE SSME TURNAROUND DUCT L. A. Povinelli & K. L. McLallin	511
EXPERIMENTAL EVALUATION OF AN ADVANCED SPACE SHUTTLE MAIN ENGINE HOT-GAS MANIFOLD DESIGN CONCEPT D. Pelaccio, F. F. Lepore, G. M. O'Connor G. V. R. Rao, G. H. Ratekin & S. T. Vogt	512

NUMERICAL ANALYSIS OF FLOW NON-UNIFORMITY IN THE HOT GAS MANIFOLD OF THE SSME J. Thoenes, S. J. Robertson, A. W. Ratliff & P. G. Anderson	548
FUEL AND OXIDIZER TURBINE LOSS ANALYSIS J. E. Hass	560
REDISTRIBUTION OF THE INLET TEMPERATURE PROFILE THROUGH THE SSME FUEL TURBINE J. R. Schwab	571
ANALYTICAL STUDY OF FLOW PHENOMENA IN SSME TURNAROUND DUCT GEOMETRIES K. L. McLallin	579

#### VIII. Instrumentation Technology

OVERVIEW W. Nieberding & T. Marshall	599
FIBER OPTIC RAMAN THERMOMETER FOR SPACE SHUTTLE MAIN ENGINE PREBURNER PROFILING J. A. Shirley	603
AN ADVANCED SOLID STATE PRESSURE TRANSDUCER FOR HIGH RELIABILITY SSME APPLICATION R. Johnson & D. Wamstad	618
VORTEX SHEDDING FLOWMETERS FOR LIQUIDS AT HIGH FLOW VELOCITIES J. D. Siegwarth	639
REUSABLE ROCKET ENGINE TURBOPUMP CONDITION MONITORING M. E. Hampson & S. Barkhoudarian	654
NON-INTRUSIVE SHAFT SPEED SENSOR S. Barkhoudarian, L. Wyatt & J. Maram	674

IX. Ignition/Combustion Processes

OVERVIEW	694
C. Aukerman & D. Pryor	
LIQUID ROCKET COMBUSTION COMPUTER CODE	696
DEVELOPMENT	
P. Liang	
A LASER SCHLIERIN AND ULTRAVIOLET DIAGNOSTICS	717
OF ROCKET COMBUSTION	
S. F. Fisher	
LIST OF PARTICIPANTS	732

## FOREWORD

During the development of the Space Shuttle Main Engine (SSME) it was felt by NASA that upgrading the capabilities of this engine concept was necessary in order to meet the challenge of the Space Transportation System needs of the 1990's and beyond. The MSFC was subsequently given the "lead center" role to identify technology opportunities, develop multi-year plans and to oversee the implementation of these plans with the assistance and involvement of the Lewis Research Center. Therefore, the overall objective of this program became the establishment of basic discipline technology necessary for an orderly evolution of high pressure oxygen-hydrogen stage combustion rocket engines in general and the SSME in particular, to meet the needs of earth-to-orbit space transportation for the next 20-30 years. The accomplishment of this objective is expected to contribute to the nation's space program through providing a sound technological foundation for improvement in the technical specialities of rotordynamics, structural dynamics, fluid and gas dynamics, fatigue/fracture mechanics/life, turbomachinery fluid mechanics, ignition/combustion processes, NDT/NDE inspection methods, manufacturing/producibility, materials development/evaluation, cryogenic bearings, and instrumentation.

The purpose of this conference is to present to the industry/university and government communities the initial products that are beginning to emerge from this program. Although these results address the SSME in particular, most are quite generic and should be of particular interest to engineers and academicians in the rocket propulsion field.

The content of the proceedings is organized into nine sessions, according to the nature of the NASA working groups of the SSME program. These sessions are:

- i) Fatigue/Fracture/Life and Ignition/  
Combustion Process Technology

- ii) Manufacturing and Productivity  
Technology
- iii) Material Technology
- iv) Bearing Technology
- v) Structure Dynamics Technology
- vi) Rotordynamics Technology
- vii) Fluid and Gas Dynamics Technology
- viii) Instrumentation Technology
- ix) Ignition/Combustion Processes

There are a total of forty-three papers being presented. At the beginning of each session, a summary of highlights of the session has been prepared by the session chairmen. Some of the presented papers only have abstracts included in this proceedings because the author/authors could not obtain proper clearance to release the paper in sufficient time to meet the cut off date of the publication. Every attempt will be made to publish all papers in their entirety in a NASA Conference Publication at a later date.

Finally, we wish to acknowledge the contributions from our session co-chairmen who have helped to organize each session and helped to insure the quality of the papers. Last but not least, we wish to thank the administrative staff, Ms. Sue Weir, Mrs. Gladys Jones, Mrs. Pat Corder and the Office of Public Affairs of MSFC for their professional skills in coordinating and supporting this meeting.

August, 1984  
Huntsville, AL

S. F. Morea and  
S. T. Wu Editors

## WELCOME ADDRESS

James E. Kingsbury  
Director of Science & Engineering Directorate  
NASA/MSFC  
Marshall Space Flight Center, Alabama 35812 U. S. A.

I don't believe it is necessary for me to start off by telling you about the virtues of the space program, because that would be a little like "preaching to the choir". But, we have in the last decade, with the advent of the Shuttle program embarked into an entirely new arena in space flight...- the concept of "reusable systems". One of the things found after undertaking the Shuttle program was that the state of technology, particularly in the rocket engine area, was simply inadequate to give NASA the degree of reliability and assurance felt necessary for long-term reuse of space vehicles. So some few years ago, Marshall Space Flight Center (MSFC) embarked on a technology program sponsored by the NASA Headquarters in Washington, D.C. This technology program has now been active for about 3 years, and it was thought that this would be an appropriate time to gather together those who were directly or indirectly involved and share with you the gains that have had, and are having direct impact on the Space Shuttle Main Engine.

The shuttle is a reliable vehicle at the levels that it is operating today. It is desired, however to extend those levels of performance and life by taking advantage of the technology advancements beginning to emerge out of the technology program you will hear about in the next 2-3 days. The Space Shuttle Main Engine (SSME) as part of the overall Space Shuttle, is expected to be in this nation's inventory of large liquid rocket engines for a long period of time. As such, improvements based upon the latest technology available becomes highly desirable, in spite of how well the engine has performed to date, and it has performed flawlessly.

We hope from the discussions that you hear in the next few days that you will benefit from the technology gains that have been realized. We are confident that we are making progress. We probably have learned more in some of the least understood areas in the past 3 years than we learned in the preceding 20 or 30 years. We are understanding to considerably more depth, some of the complexities associated with operating  $O_2/H_2$  high pressure engine systems. During the course of the conference, we will focus on several of these and it is our purpose to make the technologies that have been generated available to the technical community. Although these technologies certainly do have direct application to NASA's current program, the technology in many cases is also generic in nature and, therefore, would be meaningful for any development program of an  $O_2/H_2$  engine system.

One of the dangers and problems associated with technology is that the technologist learns whatever he or she learns - but it is oftentimes many months before the material is published and sometimes years before the published material finds its way into general application by people like yourselves. So our goal here this week is to reduce the transfer time by making this knowledge available to you as quickly as possible. Because significant advances have been made, the information developed to date is information that we believe should be disseminated to the academic and engineering communities, and that's our purpose here today. We are working on elements of the SSME system that give us the most significant problems with respect to either performance or life. We are not flying an engine on the Orbiter that any of us are concerned about relative to its capability to make its mission. It is designed to do certain things and it is doing them remarkably well. The concerns that we have and the interest that we have are to improve the life, reduce the cost, improve the performance thus improving the usability of the Space Shuttle. It is the focus of life and performance that you will hear most about this week. I often worry that the purpose is sometimes misunderstood or misconstrued in to thinking that we are in danger every time we launch a Shuttle

because the main engine is a marginal machine. Let me start this conference off by saying - it is not a marginal machine, it is as mature as any machine NASA has ever flown. The SSME is a fine machine. But, it does have costs associated with it in the change out of components which have limited life, and it is these costs that we feel are essential to be reduced through improved technology. This is the primary goal in this technology program. It is a comprehensive program that is scheduled to continue for a number of years and we encourage your participation as the program unfolds. I thank you for the opportunity to welcome you this morning, to greet you, and to wish you the very best and to encourage you to continue to do the work that has been started. This work is considered to be critical to NASA. In order for the Space Shuttle to be a truly operational vehicle, it must also be cost effective. In order to attain cost effectiveness, we must continue to drive costs down by improving the technologies associated with the life constraints that we currently have on the vehicle.

I know you are going to hear some exciting things in the next couple of days and I hope they will be useful to you. The conference has been arranged by MSFC under the guidance of S. F. "Sonny" Morea, the Director of the overall Advanced High Pressure  $O_2/H_2$  Technology Program, in conjunction with Dr. S. T. Wu of the University of Alabama in Huntsville (UAH), the co-sponsors of this conference. I want to extend my appreciation to these two gentlemen for what I believe will be a very fruitful conference.

## BACKGROUND

S. F. Morea  
Structures and Propulsion Laboratory  
NASA/MSFC  
Marshall Space Flight Center, Alabama 35812 U. S. A.

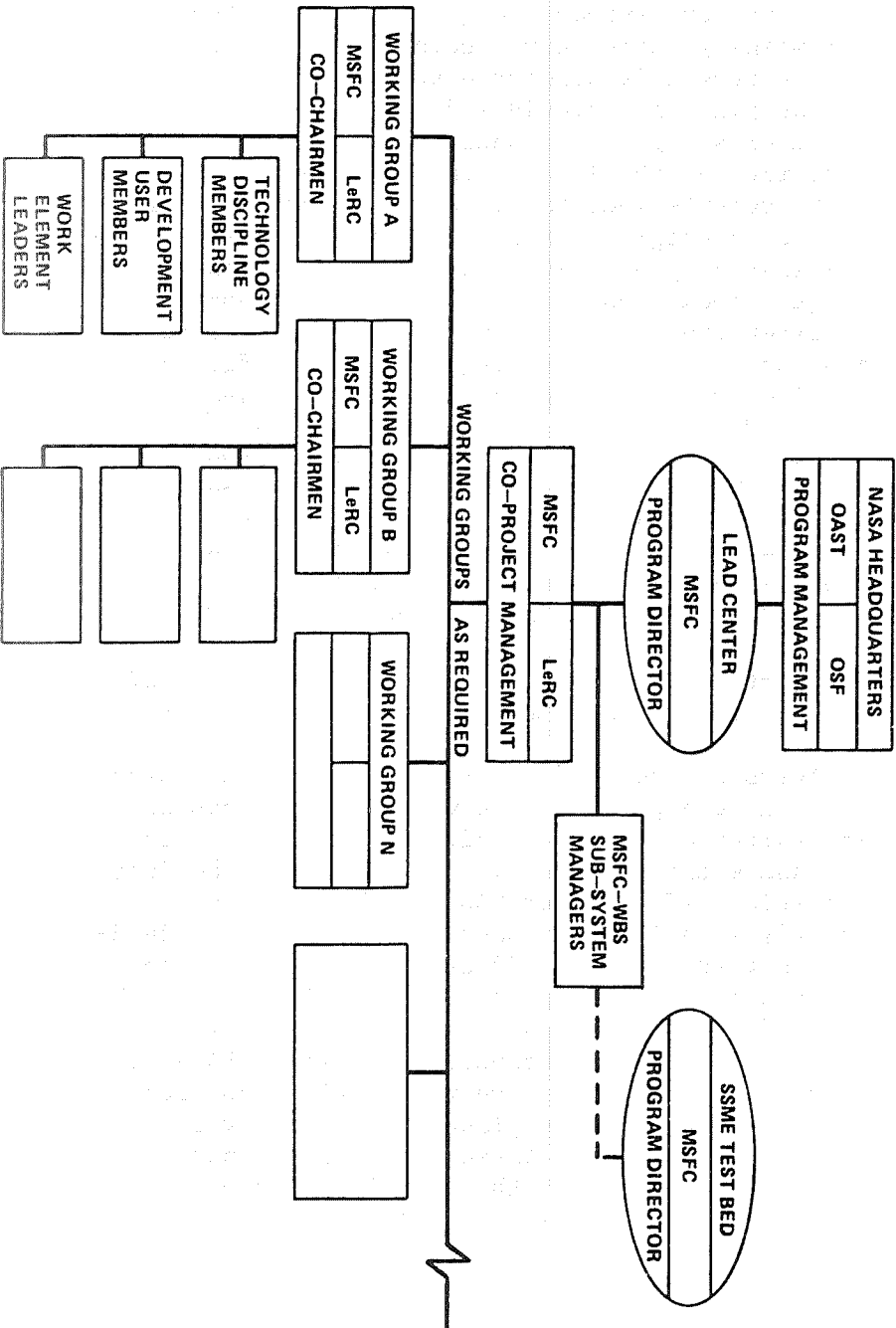
During the spring of 1980, in separate reports to the NASA, a recommendation was made by both the Aeronautics and Space Engineering Board (ASEB) as well as the Space Systems Technology Advisory Committee (SSTAC) that NASA give consideration toward funding a comprehensive technology program directed toward enhancing the usefulness of the Space Shuttle Main Engine (SSME) in order to meet the challenge of the space transportation system needs of the 1990's and beyond. The Marshall Space Flight Center (MSFC) was subsequently given the "lead center" role to identify technology opportunities, develop multi-year plans and to oversee the implementation of these plans. The planning process took approximately six (6) months followed by a procurement/contractual process that took an additional 6-12 months. One might say that effective work therefore, began on a number of work elements by January 1982. In essence, then for practical purposes we are approximately 2-2½ years into a program with an estimated life of approximately ten (10) years or more.

The objective of the program stated very simply is to establish the basic technology discipline necessary for an orderly evolution of high pressure  $O_2/H_2$  stage combustion rocket engines in general and the SSME in particular in order to meet the needs of the earth to orbit space transportation system for the next 20-30 years and perhaps longer. It will be the focal point of our liquid propulsion capability in NASA. In terms of the Space Transportation System it is essential to assure that whatever technology opportunities exist to enhance this engine, and reduce cost of Shuttle operations, that we take full advantage of those opportunities. The plan developed and modified/updated annually consists of seven (7) major thrusts. Four of these have to do with increasing

the life of the engine and consist of (1) increasing the life of the turbo machinery, (2) increasing the life of the hot flow systems, (3) increasing the life of the combustion devices and (4) increasing the life of the remaining engine components. The preponderance of the budget is allocated toward this "life" focus. The plan also provides for technology effort aimed at increasing performance. Although not as high a priority as the life extension thrusts, performance improvements inevitably become of greater significance as a program matures. Personal experience over the last 25 years with most of this nation's large liquid rocket engines support this assumption without exception. We certainly therefore need to be cognizant of that potential requirement for future SSME's. The two remaining program thrusts have to do with improved engine control analysis and health monitoring/inspection and manufacturing improvement processes. The resources approved for this program have generally increased from the two million a year level at the onset of the program growing to approximately 9 million for FY-84 and eventually projected to level off at the 10-12 million dollars per fiscal year over the next few years. Being a joint center program, part of these dollars are contracted out of MSFC and the rest of the Lewis Research Center (LERC).

In terms of the management of the program, there are some unique aspects in the way it is structured that are worthy of mention. First of all the overall program management responsibility rests with the Space Transportation Office under OAST at NASA Headquarters. It currently is a jointly funded program at NASA Headquarters in that both the Office of Aeronautics and Space Technology (OAST) and the Office of Space Flight (OSF) provide funding support. Although MSFC was given the "lead center" responsibility for NASA at the very outset, the program is very strongly supported by LeRC and is indeed jointly planned annually by the two centers. On the basis of these plans each center then administers those parts of the overall program for which they have responsibility. In the functional arrangement shown in the chart, subsystem managers tie

# ADVANCED HIGH PRESSURE O<sub>2</sub>/H<sub>2</sub> PROPULSION TECHNOLOGY MANAGEMENT PLAN FUNCTIONAL RELATIONSHIPS



the Advanced High Pressure Technology Program and the SSME Test Bed Programs together to assure that the products emerging from the technology efforts are verified as appropriate on Test Bed Systems hardware. Reporting functionally to the Project Managers are a series of ten (10) working groups. Each of these working groups have co-chairmen from MSFC and LeRC and membership consists of technologists as well as engineers representing the "needers" of the technology. Most of the working group co-chairmen are represented during this conference and you will recognize them as the session co-chairmen. This matrix working group structure serves two very important functions. it provides a mechanism whereby the technology needs of the SSME are consistently identified and communicated to the technologists. Second, it provides a mechanism to assure that the transfer of the technology products into the SSME development program occurs in a timely way. All too often in the past, technology accomplishments and products have gone unrecognized by the designer, and have taken excessively long periods of time before these products show up in designed hardware, or have not been incorporated at all. The working group matrix structure may not completely solve all of the problems of technology recognition acceptance and incorporation by the "user community", but it suggests a major long needed improvement may be accomplished in this manner. With all this said the specific purpose of this conference is to further extend the transfer of the initial products of the technology efforts of this program beyond just the SSME as we believe a significant portion of the efforts are generic in nature and hopefully of use to some of you for other applications.

OVERVIEW AND SUMMARY  
SESSION I

G. R. Halford  
Structures Division  
NASA/LeRC  
Cleveland, Ohio 44136 U. S. A.

and

C. J. Bianca  
Engineering Analysis Division  
NASA/MSFC  
Marshall Space Flight Center, Alabama 35812 U. S. A.

Overview

The first session covers the technology efforts under the FATIGUE/FRACTURE/LIFE, "F", Working Group. Co-chairmen of the Group are the authors of this overview and summary. There are presently seven major elements in the Working Group plans.

Fracture Mechanics Life Technology development for application to reusable space propulsion systems is a major portion of the effort. An extensive state-of-the-art survey of the field was recently completed (F1 Element) by Failure Analysis Associates and forms the basis of the first presentation by Dr. J. M. Thomas. A follow-on competitive Contract (F4) is planned to develop workable fracture mechanics life prediction tools for routine use by space propulsion systems designers. The F3 element deals with development of fatigue life extension procedures. The second presentation of the morning by Dr. Matejczyk of Rocketdyne brings the reader up-to-date on the results generated under this exciting program. The next three work elements, F5, F6, and F7 are contractual efforts that deal respectively with: the experimental implementation and verification of the analytic tools developed under F4; analytic modeling of retardation of cyclic crack propagation, with the goal being to understand when and how to

take advantage of decreased propagation rates and hence extend service life with confidence; development of probabilistic fracture mechanics life models in order to more realistically represent material response to service loadings. Finally, the F9 efforts are associated with the development of a variety of material durability models. Among these are: cyclic constitutive models for anisotropic blading alloys; development of fatigue crack initiation models that can accurately account for thermal-mechanical fatigue and thermal ratchetting, very high mean stresses in high cycle fatigue, cumulative damage models for the interaction of high- and low-cycle fatigue; and models that can account for the interaction of high pressure hydrogen. The F9 efforts are being handled by LeRC as Grants, In-House efforts, and in some cases as Contractual efforts.

#### Summary

The scope of the F-Working Groups activities are widespread, covering a broad range of fatigue and fracture technologies. The three specific presentations of Session I have an important, concise commonality of purpose: the utilization of fatigue and life prediction technology to provide enhanced durability of SSME materials and components. Dr. Jerrel M. Thomas' presentation on Fracture Mechanics Life Technology provided an excellent review of this important field. Emphasis was on how it applies to cyclically loaded oxygen/hydrogen propulsion components. He also covered important suggestions for reducing the inaccuracies of life prediction calculations. Improved predictions permit more effective utilization of materials to resist fracture, and thus provide enhanced durability of components.

Because of the depth and breadth of the Fracture Mechanics Life Technology program and the limited presentation time available, Dr. Thomas covered only the major highlights. The presentation took on a distinct tutorial flavor out of necessity.

Direct enhancement of durability is the desired output of the Fatigue Life Extension Program reported on by Dr. Daniel E. Matejczyk. The notion of the rejuvenation of fatigue damaged material almost has an alchemistic ring to it. However, the results of the program are clearly dispelling any such preconceived ideas. Working with SSME bill-of-materials such as MAR-M246 (Hf) (DS) and wrought Inconel 718, Matejczyk has been able to document significant workable techniques that can indeed produce healing of previously induced fatigue damage, particularly in the high cycle-to-failure regime. Various combinations of surface treatment, hot isostatic pressing, and reheat treatment have been brought to bear on the problem with attention being focused on generating a sufficiently large data base from which to draw reliable conclusions. Microstructural and fractographic interpretations are being made at every opportunity to help develop a better qualitative understanding of the damage and rejuvenation processes.

The third presentation was on Thrust Chamber Life Improvement by Harold J. Kasper. Again, as the title aptly denotes, the research results have a direct impact upon enhanced durability of an SSME component. No paper appears in the proceedings because the essence of the research has been published elsewhere (NASA CR-165585 and CR-168215). Two damage accumulation modes were described, low-cycle fatigue and cyclic-creep ratchetting. These are the dominant competing mechanisms in governing the lifetime of the thin channel walls of regeneratively cooled copper chamber liners. Cyclic-creep damage, i.e., the gradual cycle-by-cycle bulging-out and wall-thinning processes going on in the channel wall, is far more difficult to compute than low-cycle fatigue damage, and it turns out to be the most severe mechanism. Having developed a reliable procedure for assessing cyclic-creep damage, Mr. Kasper was then able to investigate a variety of coolant passage geometries and in turn deduce what geometric configurations are conducive to greater cyclic lifetimes. He found

that increasing the number of passages, while correspondingly decreasing their size, had a greater impact on enhanced durability than changes in channel cross-sectional shape.

The discussions following each presentation were informative and helped to bring out important details not included during the formal presentation.

A REVIEW OF FRACTURE MECHANICS  
LIFE TECHNOLOGY

Dr. Jerrell M. Thomas  
From a report with P. M. Besuner  
and Dr. D. O. Harris  
Failure Analysis Associates  
Palo Alto, California

Abstract

A review of current lifetime prediction technology for structural components subjected to cyclic loads was performed for NASA. The central objectives of the project were to report the current state of and recommend future development of fracture mechanics-based analytical tools for modeling and forecasting subcritical fatigue crack growth in structures. Of special interest to NASA was the ability to apply these tools to practical engineering problems and the developmental steps necessary to bring vital technologies to this stage. The authors conducted a survey of published literature and numerous discussions with experts in the field of fracture mechanics life technology. One of the key points made is that fracture mechanics analyses of crack growth often involve consideration of fatigue and fracture under extreme conditions. Therefore, inaccuracies in predicting component lifetime will be dominated by inaccuracies in environment and fatigue crack growth relations, stress intensity factor solutions, and methods used to model given loads and stresses. Suggestions made for reducing these inaccuracies include development of improved models of subcritical crack growth, research efforts aimed at better characterizing residual and assembly stresses that can be introduced during fabrication, and more widespread and uniform use of the best existing methods.

## Introduction

In the early months of 1983, Failure Analysis Associates was in the process of completing and documenting an assessment of the state of the art in fracture mechanics life technology.<sup>1</sup> This project had been undertaken for NASA in the Spring of 1982 and was focused on lifetime prediction techniques applicable to oxygen/hydrogen propulsion components. NASA wanted to know what technologies are available, how good these technologies are, how these technologies might best be enhanced, and which new technologies seemed most promising for future development. To narrow the scope of the study, some limiting decisions were made at the outset. Since oxygen/hydrogen propulsion components most often fail due to the growth of cracks or defects caused by cyclic loading, the review concentrated on fracture mechanics techniques for analyzing fatigue crack growth. Also, since the majority of the component lifetime is occupied by cracks growing at relatively slow rates, and since critical crack size most often does not have a strong influence on calculated (or observed) lifetimes, the final failure criterion was assumed not to be very influential. Such criteria therefore received secondary consideration in the review.

## Fracture Mechanics Review

Various aspects of fracture mechanics-based analyses of fatigue crack growth were extensively reviewed for the NASA study and are summarized in this paper. Such analyses compare the cyclic crack driving force with the material's response to this force. In the case of linear elastic fracture mechanics (LEFM), the driving force is measured primarily by the value of the cyclic stress intensity factor,  $\Delta K$  ( $\Delta K = K_{\max} - K_{\min}$ ), and the material response is measured by the corresponding crack growth rate,  $da/dn$ . Hence, a stress intensity factor solution -- relating the

applied loads (mechanical, thermal, or residual stress) and crack size and configuration to the value of the stress intensity factor -- is required.

#### Stress Intensity Factors

A very wide variety of stress intensity solutions are available for elastic stress analysis of cracked bodies which can be idealized as two-dimensional. Techniques for generating new solutions for two-dimensional bodies are fairly accessible and economical and can be readily provided for new stress systems and crack configurations. However, the majority of problem cracks in oxygen/hydrogen propulsion components spend most of their time as partial thickness cracks -- which are inherently three-dimensional. Although a wide variety of configurations have been treated, the current stress intensity factor solutions for three-dimensional elastic bodies are not nearly as complete as those for two-dimensional bodies. Economical numerical procedures for evaluation of K for new geometries are lacking, and the most economical techniques are not readily accessible to the technical community.

Special consideration should also be given to the appreciable additional information on crack surface opening displacements that is generated in numerical calculations of stress intensity factors, because this information can be used in the development of influence functions. Such functions could be used to economically evaluate stress intensity factors for arbitrary stresses, which would be especially useful in situations involving complex spatial stress gradients, such as arise in thermal and residual stress fields.

#### Subcritical Crack Growth

Oxygen/hydrogen propulsion components are typically subjected to cyclic loads, and the resulting fatigue crack growth is the process leading to final failure. The material's response to the applied

driving force is measured by the value of the crack growth per cycle,  $da/dn$ . Even for the simple case of constant amplitude cycling, many factors influence the crack growth rate for a given material and value of  $\Delta K$ . These include the load ratio ( $R = K_{\min}/K_{\max}$ ), environment, cyclic loading frequency, and temperature.

The complex interactions between these factors are only poorly understood at the present time, and extensive experiments must be conducted to provide reliable information for lifetime analyses. The need for experimentation is one of the current drawbacks of using fracture mechanics, and can add greatly to the cost of performing a reliable lifetime analysis. A more complete understanding of the effect of influencing factors and their interactions would reduce the need for experimentation.

Many propulsion components are subjected to high frequency loadings and any initial cracks must be small in order to survive for the desired lifetime. Since some of these cracks are too small to be modeled with typical fracture mechanics methods, a means of treating the growth of short cracks is necessary. A more thorough understanding of the influence of environment and microstructure on fatigue crack growth thresholds, as well as the influence of load history, would be highly desirable.

In the more realistic case of variable amplitude cyclic loading, the crack growth per cycle is influenced by the past loading history, and the behavior becomes quite complex — even in the absence of environmental and threshold effects. Various models have been suggested for periodic overloads and other more general loading cases. These models typically consider the crack growth to be altered by threshold effects and either (1) the presence of residual stresses ahead of the crack or (2) crack closure and crack surface alteration produced by the overload. All the models have been shown to provide good correlations to selected test data. However, they are all

lacking in some regard. The largest gap of knowledge in lifetime prediction areas is in characterization of fatigue crack growth for the case of variable amplitude loading in the presence of an adverse environment.

Analytical tools for the analysis of subcritical growth of part-through cracks are currently not well developed, especially in the case of complex spatial stress gradients. Additionally, criteria for the transition of part-through cracks to through-wall cracks are currently of a highly empirical nature.

Although considerable additional understanding of fatigue crack growth remains to be attained, several automated computer programs provide an adequate level of predictive capability for many applications. However, consolidation of all available predictive procedures into one general-purpose program has yet to be accomplished.

#### Nonlinear Fracture Mechanics

The need for nonlinear fracture mechanics arises when plastic or viscoplastic deformation becomes appreciable. In oxygen/hydrogen propulsion components, plasticity occurs predominately at the crack location, such as at a surface crack emanating from a notch-like stress raiser that causes localized yielding. Plasticity effects can be very important for accurate life prediction, and few tools are available to address these problems. These methods include adaptation of Neuber's notch plasticity results<sup>2</sup> to prediction of nonlinear stress fields and attempts to define and use such parameters as the J-integral.

Although a comprehensive review of nonlinear fracture mechanics was not attempted as part of this study, three approaches to final failure criteria for nonlinear situations were considered: the failure assessment diagram, the design curve approach, and the J-integral approach. The first two are relatively easy to employ but generally are lacking in precision

and generality. The J-integral and related tearing modulus approach are the most strongly mechanics-based, and should be readily applicable to oxygen/hydrogen propulsion components. However, very little information on the J-resistance characteristics of relevant materials is available. Even though such data would have to be generated in order to employ this approach, relevant test methods are fairly well advanced based on progress made in other fields -- such as nuclear reactor pressure vessels and piping. In cases of low-cycle fatigue, nonlinear considerations of final failure can be important, and in cases where large cyclic stresses are imposed, nonlinear consideration of fatigue crack growth can be of use.

#### Other Topics

Numerous other topics of interest were also reviewed. One of growing interest is probabilistic fracture mechanics (PFM). Scatter in material properties, the stochastic nature of imposed loads, and uncertainties in initial crack sizes often lead to large uncertainties in lifetime calculations that are based on deterministic fracture mechanics predictions. Fracture mechanics calculations that incorporate probabilistic considerations provide a means of quantifying these uncertainties and assessing their influence on the reliability of the component. Probabilistic considerations will undoubtedly be of growing importance in fracture mechanics analyses.

Another topic of current interest and concern is the use of proof testing to assess the adequacy of component integrity. There are various approaches to selecting appropriate proof test loadings and cycles and various trade-offs to be considered between damaging good components during the proof test or allowing unsafe components to go into service. It was found that a divergence of opinion exists among various practitioners, based largely on dissimilar past experience in this area. Selection and optimization of proof test procedures is still fairly rudimentary, and this appears to be a topic for fruitful

future efforts -- especially as additional information on the nature of the randomness of various fracture mechanics inputs becomes available.

Because many life-limiting defects in oxygen/hydrogen propulsion components originate in welds, and because many cracked-weld problems combine several complexities of fracture mechanics life technology and material behavior, special aspects of the use of fracture mechanics to determine the influence of weld defects on structural integrity were examined.

### Directions for Development

As part of this study, NASA requested suggestions for enhancing existing technology for life prediction and for directing research into new and developing technologies. The fracture mechanics review revealed that many powerful tools and voluminous materials data now exist, and that the current technology is capable of providing adequate results under many circumstances. However, conflicting theories and inconsistent data have been reported, and there is an obvious need for both a better understanding of underlying phenomena and additional material data.

As noted before, the fracture mechanics analysis of crack growth in engine components often involves consideration of fatigue under extreme conditions of temperature and/or aggressive environment. For known loads, inaccuracies in prediction of component lifetime will therefore be dominated by inaccuracies in environmental and fatigue crack growth relations, stress intensity factor solutions, and methods used to model given loads and stresses. Therefore, the recommendations made below are heavily weighed towards filling the gaps in knowledge of the growth characteristics of cyclically loaded cracks. In addition, these recommendations are not restricted to fracture mechanics topics, but include closely allied areas that are necessary for comprehensive fracture control.

## Using and Improving Existing Technology

Current fracture mechanics technology is in many ways highly sophisticated and suited to the needs of the fracture mechanics practitioner. One problem is that the best available methods are not always utilized due to the inaccessibility of some tools and techniques and the degree of complexity involved in the use of others, such as automated computer codes that are difficult to use and available to only a limited number of users. Therefore, the first step in expanding the usefulness of fracture mechanics for lifetime prediction is to provide more easily used and accessed software.

Software Development. A logical starting point would be to develop a widely accessible, user-friendly software package for determining stress intensity factors for a wide range of crack configurations and loadings. This computerized "K-handbook" (see Tada<sup>3</sup>, Sih<sup>4</sup>, and Rooke and Cartwright<sup>5</sup>) should be interactive and functional on personal computers. Software should not require the user to be a programmer and should be designed to interface between personal, mini- and mainframe computers. Programs already exist (such as BIGIF<sup>6</sup>) which begin to meet these criteria, covering a wide range of loading and geometry combinations and easily expandable to accept new information and formats.

Provisions for easily interfacing the uncracked-structure stress analysis (especially finite element results) with the fracture mechanics code for the determination of stress intensity factors would be desirable. Suggestions for follow-on projects which could be developed separately and then incorporated into the "K-handbook" program include:

- Develop software that would use procedures such as the Neuber approach<sup>2</sup> to treat contained plasticity due to notches and other local stress raisers.

- Create a more widely accessible package for analyzing flaw growth. Currently available codes could be merged to form a code that would contain most of the required capabilities for practical applications.
- Develop software for predicting critical flaw sizes for various crack configurations in typical engine components and materials. Since accurate knowledge of critical crack sizes is not required for accurate lifetime prediction. A high degree of sophistication in this software is not necessary. Current codes and procedures capable of generating stress intensity factors for two-dimensional configurations not already analyzed should also be made more user-friendly and accessible.

A user-oriented code should also be developed to generate the J-integral, tearing modulus, and  $C^*$  (energy release rate due to creep) solutions required in some low cycle fatigue and/or high temperature applications. Nonlinear finite elements appear to be the best candidate for general applicability to two-dimensional problems. An alternative approach would be to generate new nonlinear solutions for geometries of relevance to engine components.

The development of widely available and user-friendly software for determination of stress intensity factors in two- and three-dimensional bodies would reduce the need for the following efforts. However, these efforts, which are specifically tailored to engine components, would assist in the transfer of technology to the day-to-day engine fracture mechanics practitioner. In brief they are:

- Identify typical engine component geometries (e.g., bolted, flange fillet radii, typical weld joint configurations) for which existing stress intensity factor or J-integral solutions are inadequate and generate such solutions for future use.

- The new stress intensity factor results should be exercised for both hypothetical and practical problems which encompass most geometries, stress, material and environmental combinations to be expected in the field. The analyses created could serve as modeling examples and guidelines.

Generating Test Data. While the existing fracture mechanics life prediction technology provides powerful tools for the prediction of crack growth, these tools depend heavily upon appropriate test results as input data. Suggestions for expanding the store of test data include:

- Identify key material/environment combinations of relevance to oxygen/hydrogen engine components for which adequate fatigue crack growth data is unavailable. Perform tests to characterize the subcritical crack growth of the material over a wide range of crack growth rates.
- Test to discriminate between various proposed models of crack growth under variable amplitude loading.
- Attain a clearer understanding of transition behavior of part-through cracks through limited testing.
- Generate J-resistance curves for ductile materials at temperatures at which critical crack lengths have an important influence on predicted lifetimes. The technology of such testing is fairly advanced, and these tests would therefore not be overly expensive. Tests to generate J-resistance curves for use in analysis of part-through cracks would also be useful.
- Research crack growth under mixed mode cyclic loading for typical engine materials.

## Filling the Gaps in Existing Technology

Improving Subcritical Crack Growth Models. A general model for estimation of fatigue crack growth under aggressive environments would be very useful -- even for the relatively simple case of constant cyclic load amplitude. The development of such a model is one of the most difficult undertakings suggested here, but is also the one with potentially the largest payoff. This model would allow predictions to be made of the influence of a particular environment on fatigue crack growth, including the effects of temperature, loading frequency, and R-ratio. This would circumvent the need to perform numerous tests each time a new loading condition or environment was encountered. Such a model has proven very elusive in the past because of the complexity of the phenomena involved as well as the interdisciplinary nature of the problem. Lacking a general model, several viable techniques for "interpolating" or "extrapolating" from test conditions to the desired conditions are available and should be pursued.

Research into improving methods of predicting crack growth under variable amplitude cyclic loading and understanding the influences of environment and previous load history on fatigue crack growth histories would be especially valuable as input to the "K-handbook" program suggested earlier. Further research into already established areas would also be desirable in order to establish creep crack growth characteristics, explore creep and fatigue interactions, and provide (through testing) crack growth rate-C\* correlations for relevant materials and temperatures.

The conditions under which net section stress ( $\sigma_n$ ), K, J, and/or C\* provide the suitable parameters for engine conditions needs to be clarified through solid mechanics-based studies of the relevant parameters for correlation of creep crack growth under typical oxygen/hydrogen engine conditions. Applicable tools for analyzing creep crack growth would also need

to be developed. The J or C\* solutions for relevant defects should be developed so that the laboratory correlations with crack growth characteristics can be used to predict the behavior of actual cracked components operated at high temperatures.

Integrating Crack Initiation Analysis with Fracture Mechanics. Many oxygen/hydrogen engine components are currently designed based on a fatigue analysis that assumes an initially flaw-free material. The analysis then proceeds with an S-N type of approach for predicting component lifetime. Since NASA currently has a research project underway to develop procedures for calculating lifetimes under random cyclic loading, and to verify the prediction by comparison with observed service conditions and corresponding failures, a follow-on research program is recommended for developing methodologies that combine the S-N approach with fracture mechanics. This combination provides a consistent tool for life estimation of initially unflawed components that includes both the initiation and propagation of cracks. Improved tools for the treatment of short cracks would be important in the treatment of the early behavior of initiated cracks. Procedures for treating the randomness of the initiation phase would be useful in probabilistic fracture mechanics (PFM) analyses.

Treating Residual and Assembly Stresses. Residual stresses, such as due to welding and assembly stresses, can be introduced into engine components during fabrication. These stresses can have an important influence on subcritical and catastrophic crack growth and should be better characterized. Through-thickness variations due to welding residual stresses have an important influence on the effect such stresses have on the behavior of cracks, and should be included in any research efforts in this area.

#### Implementing Probabilistic Fracture Mechanics.

Improvements in (deterministic) fracture mechanics resulting from research efforts recommended above should be closely coupled to research efforts for expanding the usefulness of PFM for engine components. As a first step, data bases should be developed for improved definition of the statistical distribution of the materials-related random variables. This would include studies of the distribution of toughness of typical engine materials as well as the distribution of cyclic crack growth properties for a given  $\Delta K$  and cycles to initiation for a given stress history. The applicability and utility of "effective-initial-crack-size" distributions presented in the literature should also be explored, and investigation into initial crack sizes is recommended -- including more data on initial crack depth and length, as well as the relationship between these two random variables. The often-made assumption that the crack depth and the aspect ratio are independent should be scrutinized.

It is suggested that any PFM research efforts be coordinated with on-going NASA programs related to NDE of engine components. Coordination of these projects would improve the likelihood that the NDE procedures would concentrate on the most relevant types and features of defects from a fracture mechanics standpoint while also providing the information on flaw detection probabilities necessary for the PFM evaluation. This is not the only research effort that would profit from such coordination, but it is one of the few for which a companion effort can at present be identified.

Optimizing Proof Test Procedures. A coordinated effort is recommended for the development of procedures to apply PFM to the optimization of proof test procedures. The magnitude of proof loading and the number of proof cycles could be optimized based on the cost of various types of failure and their probability of occurrence. Improved J-resistance curve information on engine materials subject to stable flaw growth

and improved data bases for random variables would provide important inputs to proof test optimization.

#### Expanding Existing Technology

Generalization of J-Integral. The J-integral is strictly applicable only to nonlinear elastic materials. This lack of generality makes its use suspect in applications involving either non-monotonic loading or crack growth. Atluri's T-integral<sup>7</sup> appears to be a promising beginning point for efforts to provide a more general parameter for the characterization of crack stress fields and/or energy release rates.

Cyclic Plasticity - Fatigue Crack Growth Interfaces. A research effort aimed at unifying the fracture mechanics approach to fatigue crack growth and the cyclic plastic deformation characteristics of materials would be worthwhile, in that it would unify these two largely independent areas to provide a better and more fundamental understanding of fatigue crack growth. Progress in this area could have an important impact on fatigue crack growth model development -- one of the directions already suggested for development.

Transient Creep Crack Growth. Current theories of creep crack growth assume that creep is occurring under steady-state conditions (i.e., secondary creep). This allows J-integral approaches to be employed, but ignores the transient portion of the creep behavior (primary creep), which could be important for the time-temperature combinations relevant to creep cracking of typical oxygen/hydrogen engine components. As additional information is gained on the creep crack behavior under relevant conditions, the suitability of ignoring transient creep should become apparent. The desirability of a research effort into this area could be assessed at that time.

## References

1. Besuner, P. M., D. O. Harris, and J. M. Thomas, "A Review of Fracture Mechanics Life Technology," FaAA-83-3-11, contract NAS8-34746, Marshall Space Flight Center, September 1983.
2. Neuber, J., "Theory of Stress Concentration for Shear-Strained Prismatical Bodies with Arbitrary Nonlinear Stress-Strain Laws," Journal of Applied Mechanics, Transactions of the ASME, pp. 544-550, December 1961.
3. Tada, H., P. C. Paris, and G. R. Irwin, "The Stress Analysis of Cracks Handbook," Del Research Corporation, Hellertown, Pennsylvania, 1973.
4. Sih, G. C. M., "Handbook of Stress Intensity Factors," Lehigh University, Bethlehem, Pennsylvania, 1973.
5. Rooke, D. P. and D. J. Cartwright, Compendium of Stress Intensity Factors, Her Majesty's Stationary Office, London, 1975.
6. Besuner, P.M. et al., BIGIF - Fracture Mechanics Code for Structures, Electric Power Research Institute RP700-5, EPRI Report NP-1830-CCM, 1981.
7. Atluri, S. N., "Path-Independent Integrals in Finite Elasticity and Inelasticity," Engineering Fracture Mechanics, Vol. 16, No. 3, pp. 341-364, 1982.

## FATIGUE LIFE EXTENSION

D. E. Matejczyk and J. Lin

Rockwell International/Rocketdyne Division  
Canoga Park, California

### Abstract

Potential fatigue rejuvenation processes have been carried out on fatigue-damaged material both with and without observable surface-connected fatigue cracks. The fatigue life of fatigue-damaged MAR-M246(Hf) (DS), a directionally solidified nickel-base superalloy used in turbine airfoils, was extended by reheat treatment. The fatigue life of fatigue-cracked Inconel 718, a wrought nickel-base superalloy used in a wide variety of advanced rocket engine components, was extended by electron-beam welding to close off the surface-connected crack, followed by hot isostatic pressing and reheat treatment.

### Introduction

This paper describes a continuing study of possible techniques for rejuvenating the fatigue life of materials through various combinations of surface treatment, hot isostatic pressing, and reheat treatment. Potential rejuvenation techniques were investigated for MAR-M246 (Hf) (DS), a directionally solidified nickel-base superalloy and for Inconel 718, a wrought nickel-base superalloy.

The rejuvenation techniques are directed at the removal of fatigue damage and restoration of the initial alloy microstructure. Rejuvenation techniques have received considerable attention with respect to aircraft gas turbine engine applications (Ref. 1, 2, and 3). In the refurbishment of engine components, hot isostatic pressing (HIP) and/or reheat treatment are commonly carried out for rejuvenation of creep and stress rupture properties (Ref. 4). Rejuvenation of fatigue damage has received less attention, with limited success (Ref. 5).

Because the multiple aspects of fatigue damage and fracture necessitate several approaches to rejuvenation, it was anticipated that damage prior to crack initiation might be repaired through reheat treatment, while damage that includes significant surface cracking would require a combination of surface treatment and hot isostatic pressing.

### Materials and Procedures

The alloys studied under this program include MAR-M246(Hf)(DS), a directionally solidified nickel-base superalloy, and Inconel 718, a wrought nickel-base superalloy. Alloy compositions are listed in Table 1 and heat treatments are listed in Table 2.

Table 1. Alloy Compositions

ALLOY	NOMINAL COMPOSITION, WEIGHT PERCENT												FORM
	Ni	Cr	Co	W	Mo	Ti	Al	Ta	B	Zr	Hf	C	
MAR-M246(Hf)(DS)	bal	9	10	10	2.5	1.5	5.5	1.5	0.015	0.05	1.7	0.15	DIRECTIONALLY SOLIDIFIED
INCONEL 718	bal	18.6	3.1	5.0	4.0	0.9	18.5	0.20	0.30	0.40		WROUGHT	

Table 2. Heat Treatment and Rejuvenation  
Process Parameters

	HEAT TREATMENT	HIP PARAMETERS
MAR-M246(Hf)(DS)	2230 F FOR 2 HOURS IN ARGON, COOL TO ROOM TEMPERATURE; 1600 F FOR 24 HOURS IN ARGON; COOL TO ROOM TEMPERATURE	2050 F 30 KSI 3 HOURS
INCONEL 718	1900 F FOR 30 MINUTES IN ARGON, COOL TO ROOM TEMPERATURE; 1400 F FOR 10 HOURS IN ARGON, FURNACE COOL TO 1200 F; TOTAL AGE TIME 20 HOURS	1800 F 30 KSI 3 HOURS

The experimental approach was to first obtain baseline fatigue data for each specific alloy heat and testing condition. Cylindrical fatigue test specimens (Fig. 1) were tested in air at a stress ratio ( $R = \text{minimum stress}/\text{maximum stress}$ ) of -1 at the temperatures and maximum stress levels listed in Table 3.

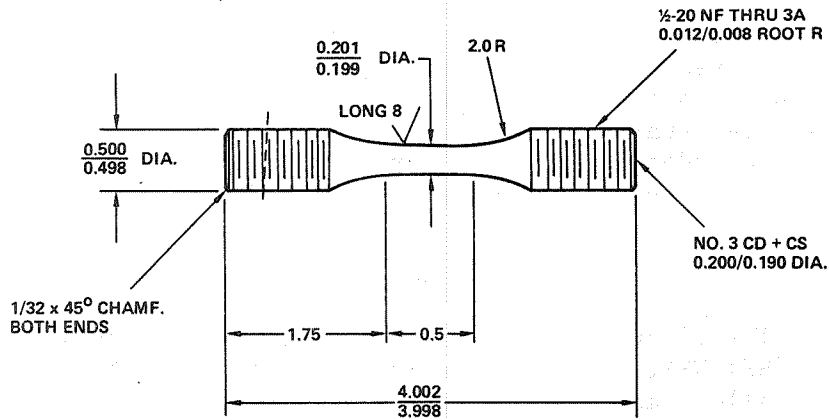


Fig. 1. Cylindrical Fatigue Test Specimen

Table 3. Baseline Fatigue Test Conditions

ALLOY	TEST TEMPERATURE		MAXIMUM STRESS	
	C	F	MPa	KSI
MAR-M246(DI)(DS)	843	1550	552	80
			441	64
			359	52
INCONEL 718	593	1100	662	96
			524	76
			441	64

These baseline tests of fatigue life to failure defined the fatigue-damage conditions for the fatigue rejuvenation testing. To test fatigue rejuvenation effects, specimens were initially damaged by cycling to 70 percent of the log mean value of the baseline fatigue life. Next, the planned rejuvenation processes were carried out, and finally, the fatigue-damaged rejuvenated specimens were tested to failure.

As a second method of preparing fatigue-damaged specimens for rejuvenation process testing, pre-cracked specimens were prepared by creating a fatigue crack in an oversized, prenotched cylindrical specimen. The original prenotch was thereafter removed

by machining the specimen to final size (Fig. 2). These specimens were used to test techniques for repair of existing fatigue cracks.

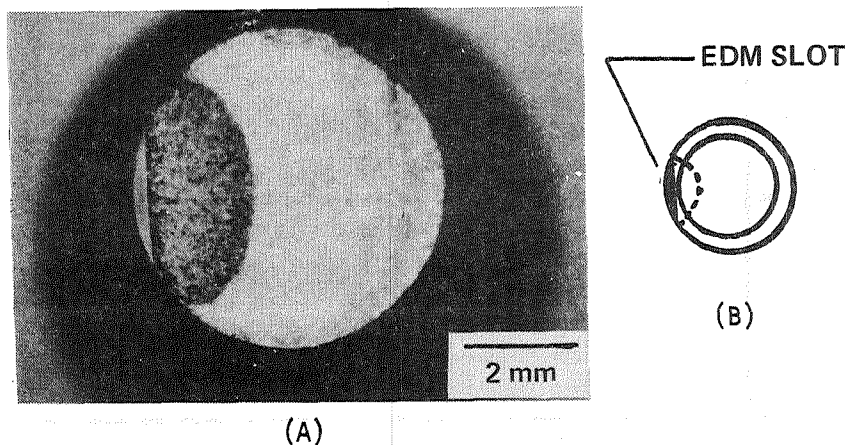


Fig. 2. (A) Heat-Tinted Area Indicates the Extent of the Fatigue Precrack Grown from the Notch. (B) As the Specimen is Machined to Final Dimensions, the Notch is Machined Away Leaving the Fatigue Precrack

At each specific stress level, statistical comparisons were made between the baseline data and the damaged, rejuvenation-processed material data using the statistical t-test (with all data transformed into log units) to assess the significance of differences between the two sets of data.

#### Results and Discussion

Figures 3 and 4 present the baseline fatigue lives for MAR-M246(Hf)(DS) and for Inconel 718.

MAR-M246(Hf)(DS) baseline fatigue fracture surfaces displayed several systematic features. At the higher stress levels, crack initiation was predominately at subsurface interdendritic porosity. Crack initiation and propagation were entirely Stage II, perpendicular to the principle stress. Figure 5 shows this initiation of interdendritic porosity and Stage II crack propagation.

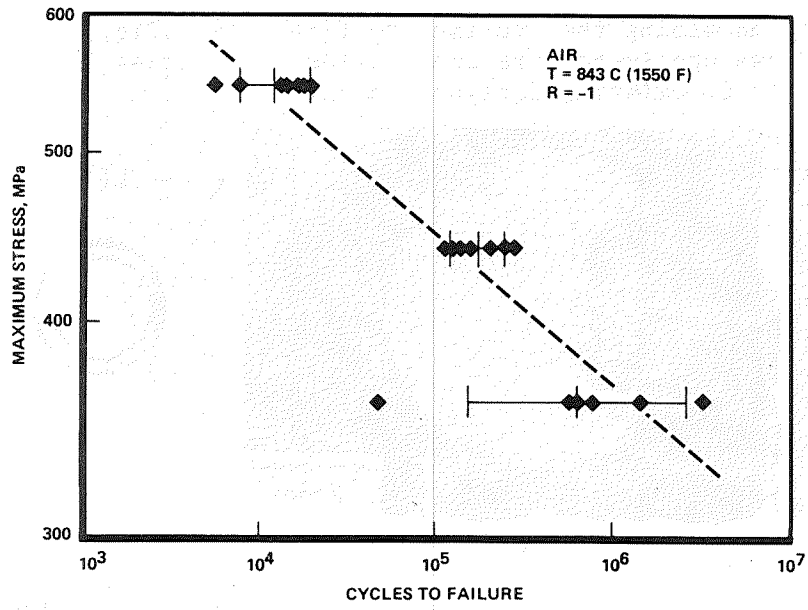


Fig. 3. MAR-M246(Hf)(DS) Baseline Fatigue Life

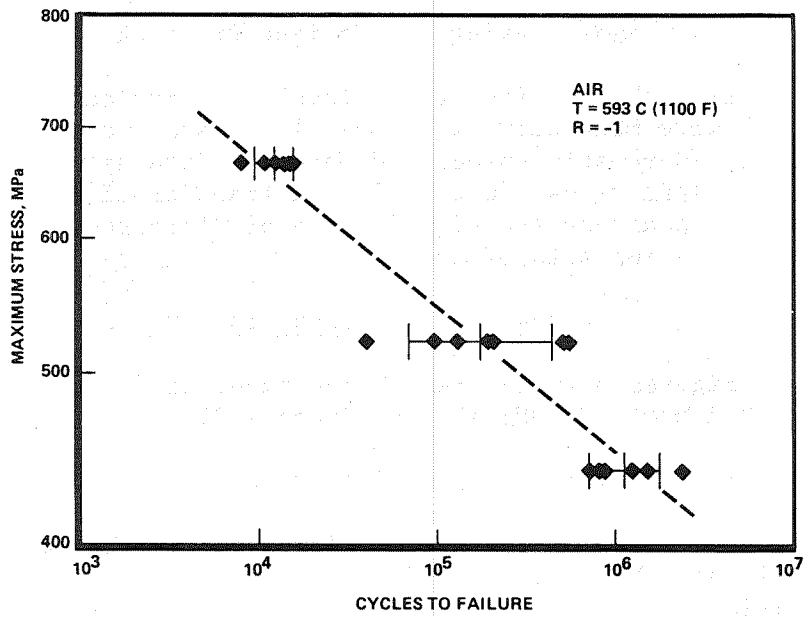
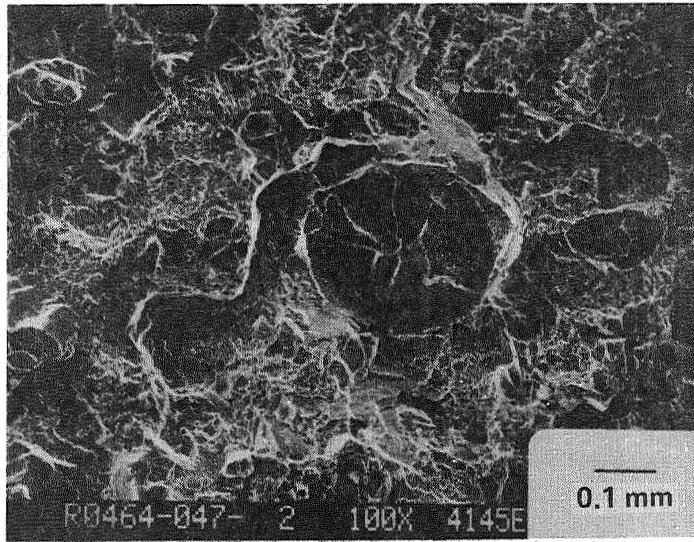
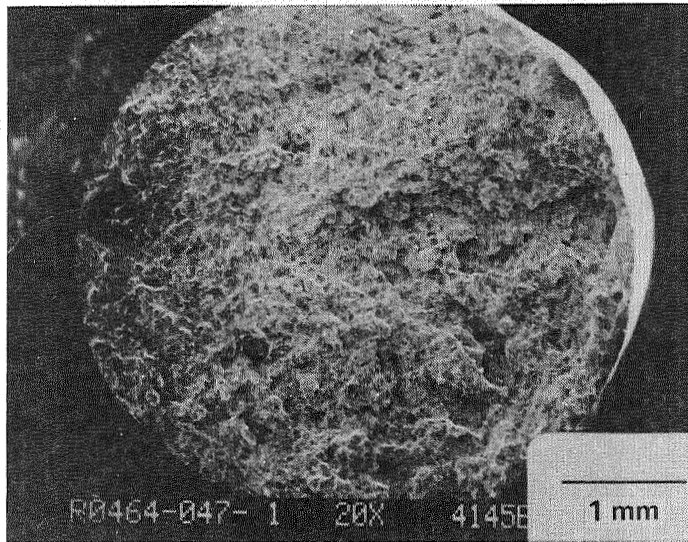


Fig. 4. Inconel 718 Baseline Fatigue Life



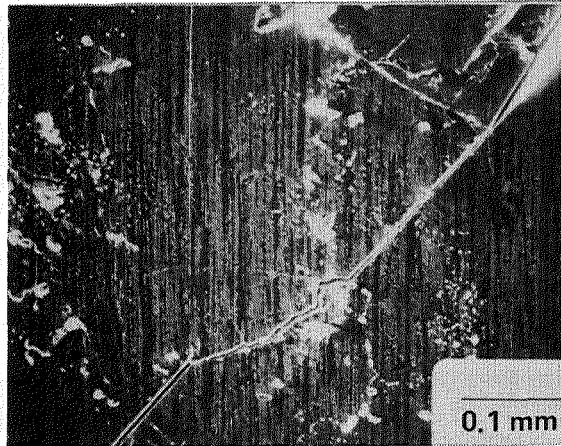
(A) CRACK INITIATION AT INTERDENDRITIC POROSITY



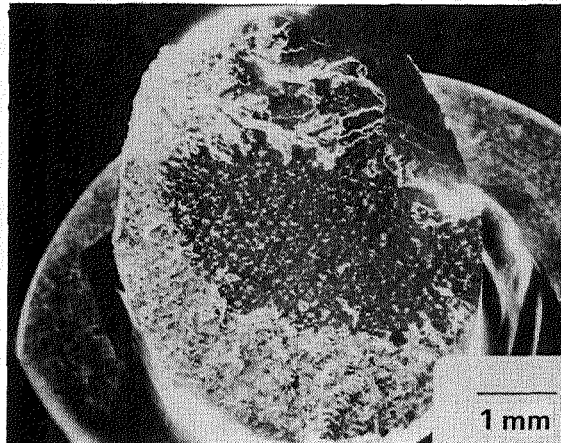
(B) STAGE II CRACK PROPAGATION

Fig. 5. Fatigue Fracture of MAR-M246(Hf)(DS) at a Maximum Stress of 552 MPa (80 ksi) at 843 C (1550 F) in Air at R = -1 (15,800 Cycles to Failure)

At the lower stress levels, initiation was predominately at the specimen surface. In several cases, carbides could be identified as probable initiation sites, and crack initiation and propagation were predominately Stage I, crystallographic. Figure 6 shows this crystallographic cracking at a surface carbide and the extensive crystallographic crack propagation.



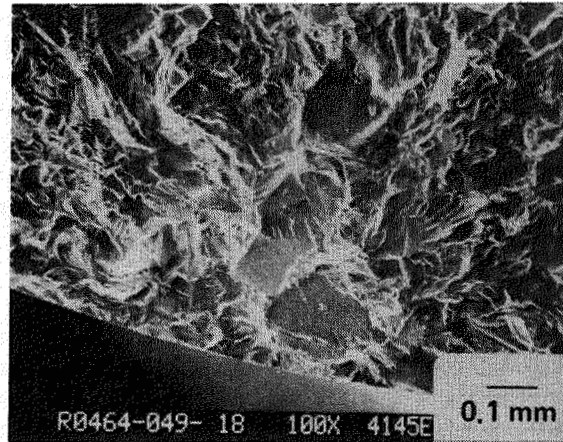
(A) SURFACE CARBIDE AT THE CRYSTALLOGRAPHIC CRACK



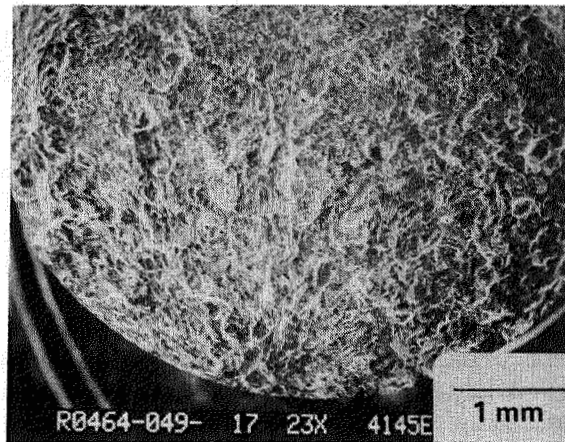
(B) STAGE I, CRYSTALLOGRAPHIC CRACK PROPAGATION

Fig. 6. Fatigue Fracture of MAR-M246(Hf) (DS) at a Maximum Stress of 359 MPa (52 ksi) (611,400 Cycles to Failure)

Inconel 718 baseline fatigue fracture surfaces, as shown in Fig. 7, generally displayed near-surface or surface crack initiation. The transgranular propagation mode was a mixture of Stage I and Stage II. No systematic variations as a function of stress level were noted in fatigue crack initiation or propagation mode.



(A) NEAR-SURFACE CRACK INITIATION



(B) MIXED STAGE I AND STAGE II TRANSGRANULAR  
CRACK PROPAGATION

Fig. 7. Fatigue Fracture Surface for Inconel 718  
at a Maximum Stress of 524 MPa (76 ksi)  
(515,000 Cycles to Failure)

## Rejuvenation of Fatigue-Damaged Material

The approach for evaluating the fatigue rejuvenation processes was to prepare fatigue-damaged specimens, apply to rejuvenation process, and test the remaining fatigue life. Specimens were fatigue to 70 percent of the mean log fatigue life at the same test conditions as in the baseline tests. Next, specimens were fluorescent penetrant inspected, and any with detectable surface-connected fatigue cracks were removed from the group of specimens. Typically, approximately 5 percent of the specimens either failed during this initial fatigue exposure or failed to pass the fluorescent penetrant inspection. Remaining specimens were processed through the candidate rejuvenation technique, then tested to failure, again at the same fatigue conditions as the baseline test.

Table 2 presents the rejuvenation process details for MAR-M246(Hf)(DS) and for Inconel 718. The reheat treatment schedules are identical to the standard initial heat treatments for the two alloys. In the case of MAR-M246(Hf)(DS), the HIP schedule was chosen based on microstructural studies that indicated significant carbide morphological changes during exposure of MAR-M246(Hf)(DS) to temperatures in the vicinity of 1149 C (2100 F) for 4 hours. The decision was made to HIP below that temperature.

In the case of Inconel 718, the HIP temperature was chosen based on studies of grain growth of wrought Inconel 718. This HIP temperature is near the maximum that may be utilized without producing significant grain growth.

Figure 8 presents results for fatigue-damaged reheat-treated MAR-M246(Hf)(DS) and for virgin heat treated MAR-M246(Hf)(DS). All comparisons are between the numbers of cycles to failure following rejuvenation (over and above any preceding damage cycles) and the baseline number of cycles to failure; therefore, if fatigue lives were completely rejuvenated, the two sets of data would be not significantly different.

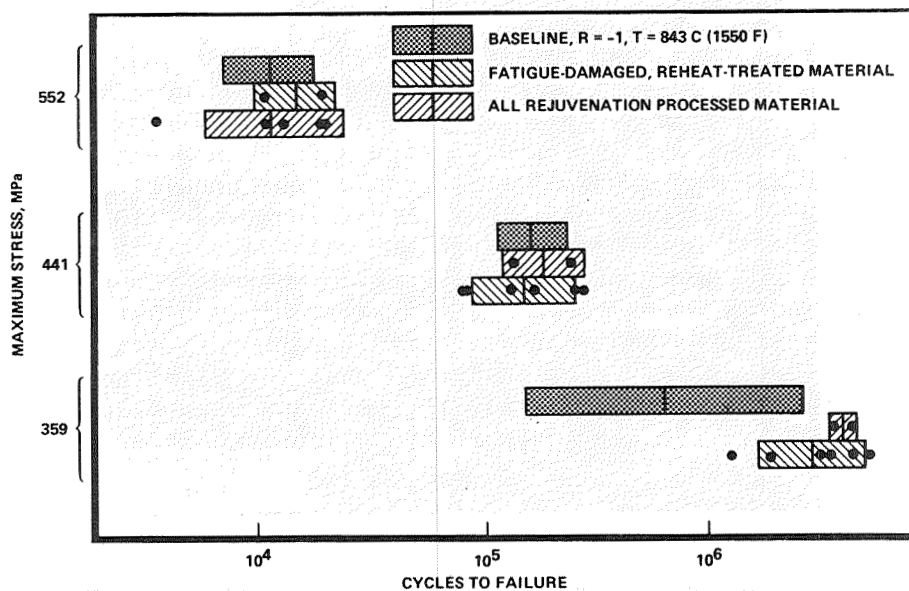
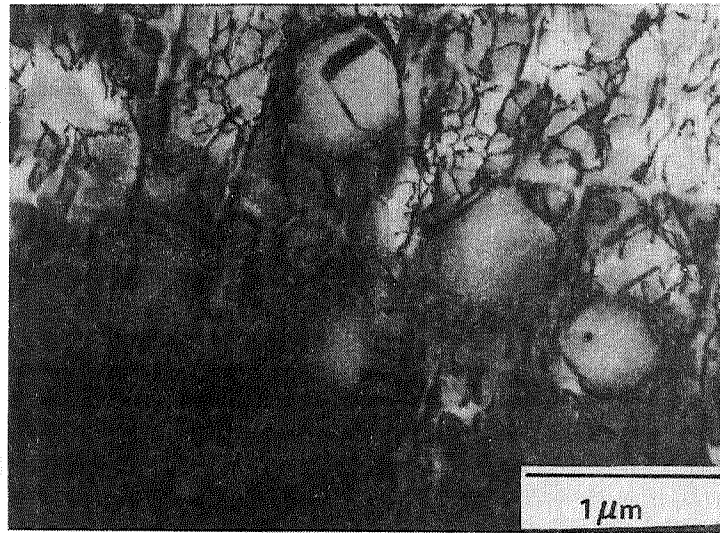


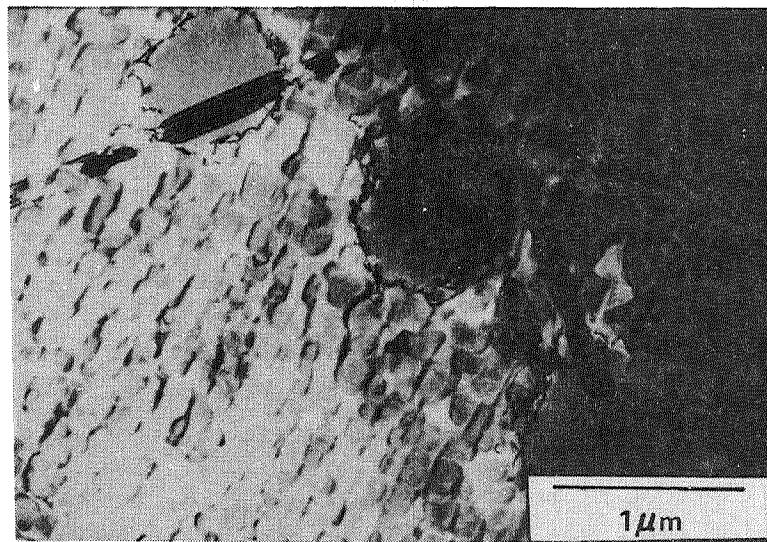
Fig. 8. Rejuvenation of Fatigue-Damaged MAR-M246(Hf) (DS)

At stress levels of 552 MPa (80 ksi) and 441 MPa (64 ksi), the lives of damaged rejuvenation-processed specimens are equivalent to the baseline lives, indicating complete rejuvenation. In the case of the 359 MPa (52 ksi) results, the lives following fatigue damage and rejuvenation are actually significantly higher than the baseline fatigue lives.

Reheat treatment, in this case, was shown to be very effective as a means of rejuvenating the fatigue life of fatigue-damaged MAR-M246(Hf) (DS). Transmission electron microscopy, shown in Fig. 9, revealed that the high dislocation density developed during fatigue exposure is annealed out during reheat treatment. The fatigue damage developed in the vicinity of carbides during fatigue exposure was also evident in the TEM observations (Fig. 10), and further TEM study indicated that some of this localized damage remained following reheat treatment.



(A)



(B)

Fig. 9. MAR-M246(Hf) (DS) TEM Micrographs Showing (A) High Dislocation Density Developed During Fatigue Damage and (B) Decreased Dislocation Density and Increase in Stacking Faults and Dislocations at Precipitate Interfaces After Reheat Treatment

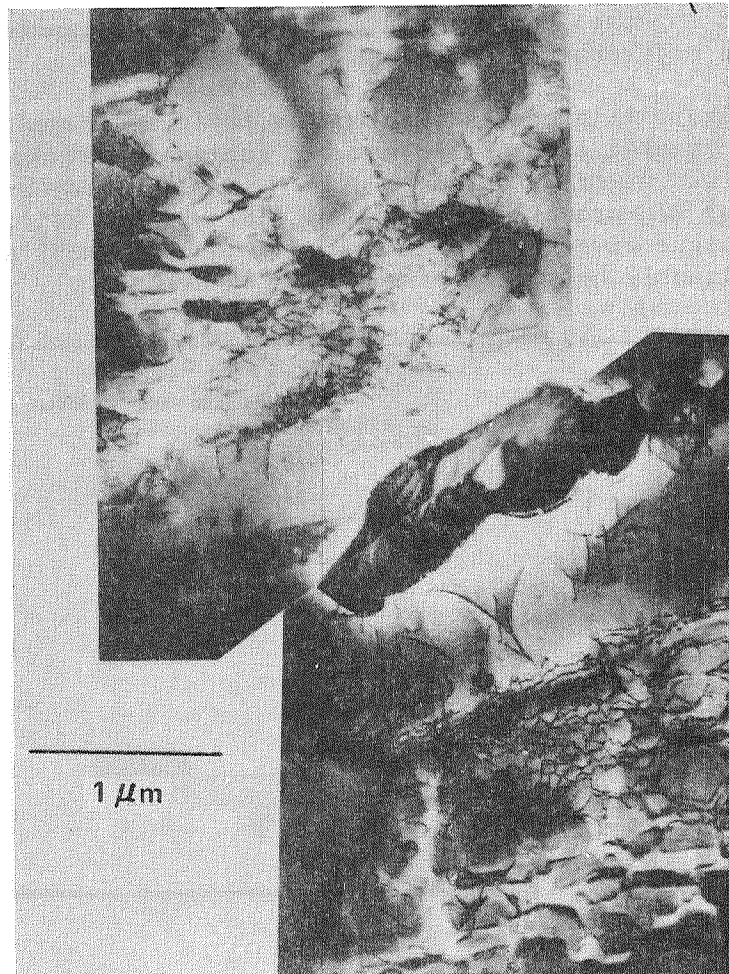


Fig. 10. TEM Micrograph of Fatigue Damage in MAR-M246(Hf) (DS) in the Vicinity of a Tungsten Carbide. Fatigue Exposure: 359 MPa (52 ksi), R = -1, 843 C (1550 F), 442,000 Cycles (70 Percent of Mean Life)

HIPing of fatigue-damaged MAR-M246(Hf) (DS) at 1112 C (2050 F)/3 hours/207 MPa (30 ksi) followed by reheat treating had no additional beneficial effect over reheat treatment alone. Both reheat treatment results and HIP plus reheat treatment results are

grouped together and plotted on Fig. 8 and designated as "all rejuvenation processed material."

Figure 11 presents results for fatigue-damaged, reheat-treated Inconel 718 and for fatigue-damaged HIPed, reheat-treated Inconel 718. In all cases except for HIP-processed material at 662 MPa (96 ksi), the fatigue lives following rejuvenation treatment are significantly below the baseline fatigue lives.

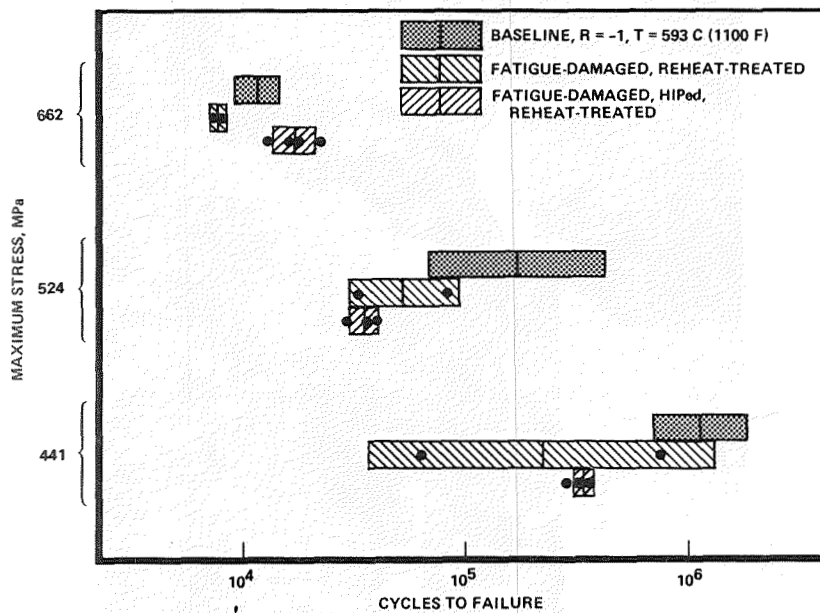


Fig. 11. Rejuvenation of Fatigue-Damaged Inconel 718

#### Rejuvenation of Precracked Material

A number of precracked specimens were prepared by propagating fatigue cracks in notched, oversized specimens, then machining to the final specimen diameters, leaving sharp surface cracks at the midpoint of the gage length in the cylindrical specimens.

Specimens were rejuvenated by electron-beam welding to seal the crack opening, HIPing at those conditions listed in Table 2 to heal the crack, and reheat treating to restore the precipitate microstructure (Fig. 12).



100  $\mu\text{m}$

Fig. 12. Inconel 718 that has been Pre-cracked, EB Welded, HIPed, and Reheat Treated. The EB Weld is at the Top of the Photograph. A Trace of the Healed Crack is Evident in the Center.

For Inconel 718, the pre-cracked, rejuvenated processed material lives, as shown in Fig. 13, approach, but do not equal, the baseline Inconel 718 fatigue lives, indicating partial recovery of fatigue damage.

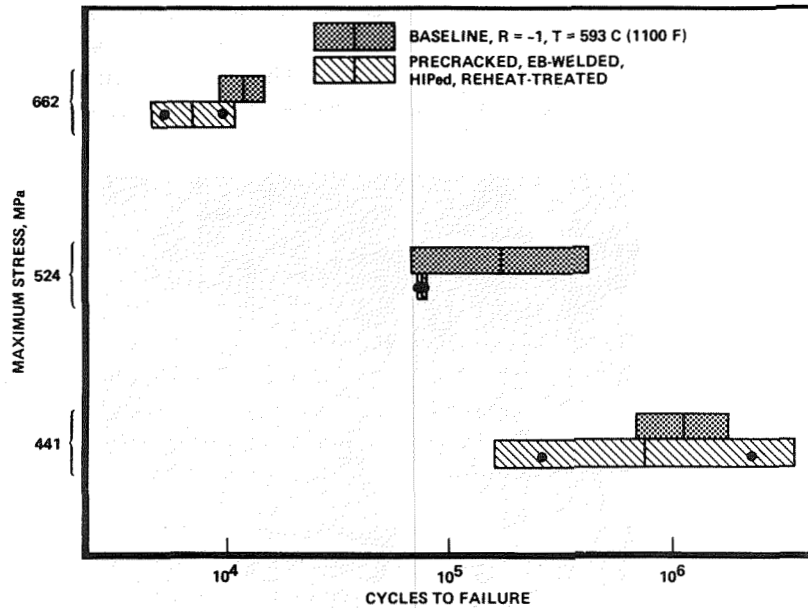


Fig. 13. Rejuvenation of Fatigue Precracked Inconel 718

#### Conclusions

1. Reheat treatment of fatigue-damaged MAR-M246(Hf) (DS) can remove previous fatigue damage and rejuvenate fatigue life.
2. HIPing of MAR-M246(Hf) (DS) at 1121 C (2050 F)/ 3 hours/207 MPa (30 ksi) prior to reheat treatment provides no additional beneficial effect.
3. Inconel 718 containing a single, large fatigue precrack may be partially rejuvenated by electron beam welding and HIPing to close off and heal the crack, followed by reheat treatment.
4. Attempts to rejuvenate fatigue-damaged Inconel 718 by reheat treatment or by HIPing and reheat treatment were unsuccessful.

These conclusions are based on progress to date under an on-going program. Continuing work is directed at obtaining further experimental data to

increase the level of confidence in the conclusions, and at obtaining more detailed understanding of the processes through further microstructural and fractographic examination.

#### Acknowledgements

This work was supported by NASA under contract NAS8-34618, under the direction of Mr. P. M. Munafa.

The authors also wish to thank Mr. J. C. Chesnutt, Mr. C. G. Rhodes, Mr. R. Kissinger, and Professor J. K. Tien for assistance in HIPing, for performing the transmission electron microscopy, and for helpful discussions, and the authors gratefully acknowledge the assistance of Mr. Bill Stross and Metcut Research Associates for carrying out the fatigue testing.

#### References

1. Dennison, J. P., I. C. Elliott, and B. Wilshire, Superalloys 1980, J. K. Tien et al. Eds., American Society for Metals, Metals Park, Ohio, 1980, p. 671.
2. Stewart, D. C., M. D. Ross, and G. T. Bennett (Pratt and Whitney Aircraft), AFML-TR-79-4032, 1979.
3. Stewart, D. C. and G. T. Bennett (Pratt and Whitney Aircraft), AFWAL-TR-80-4043, 1980.
4. Madhava, N. M., Private Communication, Chromalloy, Midwest City, Oklahoma, 1984.
5. Clauer, A. H., B. N. Leis, D. A. Seifert, and G. Hoover (Battelle Institute), AFML-TR-78-90, 1978.

## THRUST CHAMBER LIFE PREDICTION

Harold J. Kasper  
NASA Lewis Research Center  
Cleveland, Ohio

### Abstract

The reusable life of the Space Shuttle Main Engine (SSME) is influenced by the cyclic life of the regeneratively liquid cooled main combustion chamber (MCC). During an operational duty cycle the MCC liner is subjected to a large transient thermal gradient that imparts a high thermal cyclic strain to the liner hot gas wall. Life predictions of such chambers have usually been based on low cycle fatigue (LCF) evaluations. Hot-fire testing, however, has shown significant mid-channel wall deformation and thinning during accrued cyclic testing. This phenomenon is termed cyclic creep and appears to be significantly accelerated at elevated temperatures.

An analytical method that models the cyclic creep phenomenon and its application to thrust chamber life prediction is presented. The chamber finite element geometry is updated periodically to account for accrued wall thinning and distortion. Failure is based on the tensile instability failure criterion. Cyclic life results for several chamber life enhancing coolant channel designs are compared to the typically used LCF analysis that neglects cyclic creep. The results show that the usable cyclic creep life is approximately 30 to 50% of the commonly used LCF life.

### Introduction

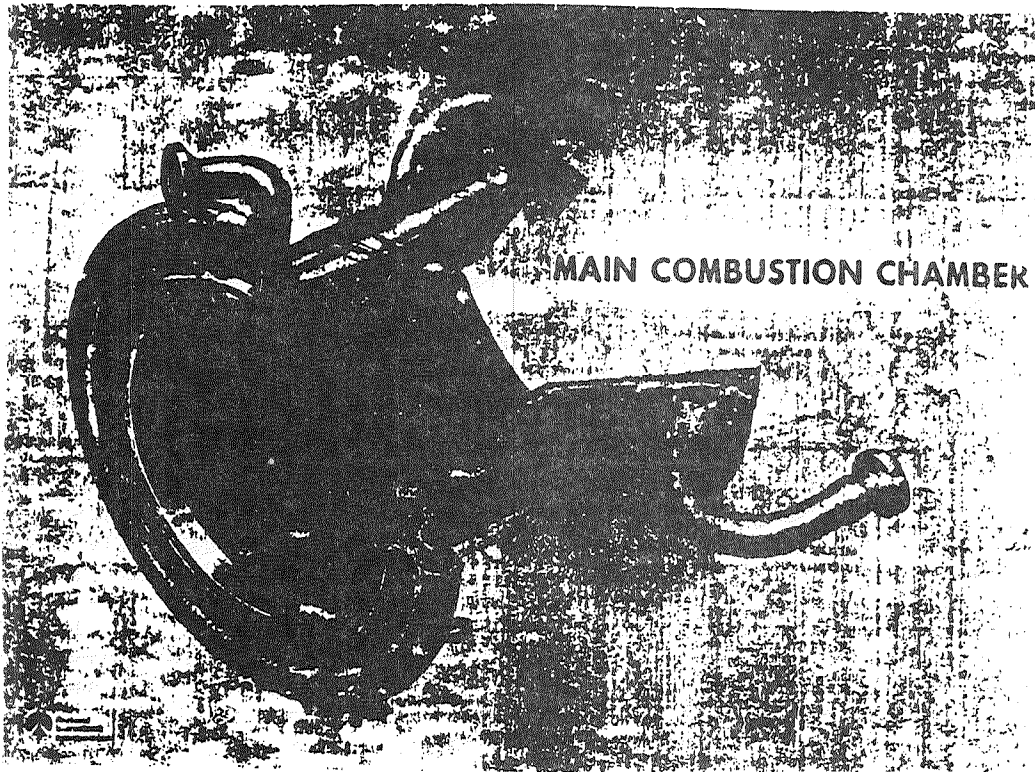
The reusable life of the Space Shuttle Main Engine (SSME) and future engines are greatly influenced by the cyclic life of several major components subjected to high temperature environments. The main combustion chamber (MCC) liner is exposed to an environment that produces a heat flux of approximately 100 BTU/in<sup>2</sup>-sec in the life limited throat region. To accommodate this high heat flux, the copper base MCC liner is regeneratively cooled through integral rectangular cooling channels. During operational duty cycles (missions) the MCC liner hot gas wall experiences large thermal plastic cyclic strains resulting from a large transient thermal gradient. These cyclic strains influence the fatigue life of the MCC liner hot gas wall.

Low cycle fatigue life is typically a function of the cyclic strain range, the material properties and the operating temperature. The theoretical reusable life is normally determined by the number of strain cycles that can be accrued before initiation of surface

cracks. Hot-fire testing of channel wall combustors at Rocketdyne and NASA Lewis Research Center (LeRC), however, indicates that fatigue is not necessarily the dominate failure mode. Significant mid-channel permanent deformation and wall thinning is witnessed during these hot-fire tests. It is concluded that the failure mode is one of strength once the wall has thinned to its critical thickness. The thinning phenomenon is termed cyclic creep and appears to be significantly accelerated at elevated temperatures. The sensitivity of the phenomenon to surface temperature is evidenced by the non-uniformity of channel wall deformation around the circumference of the combustors.

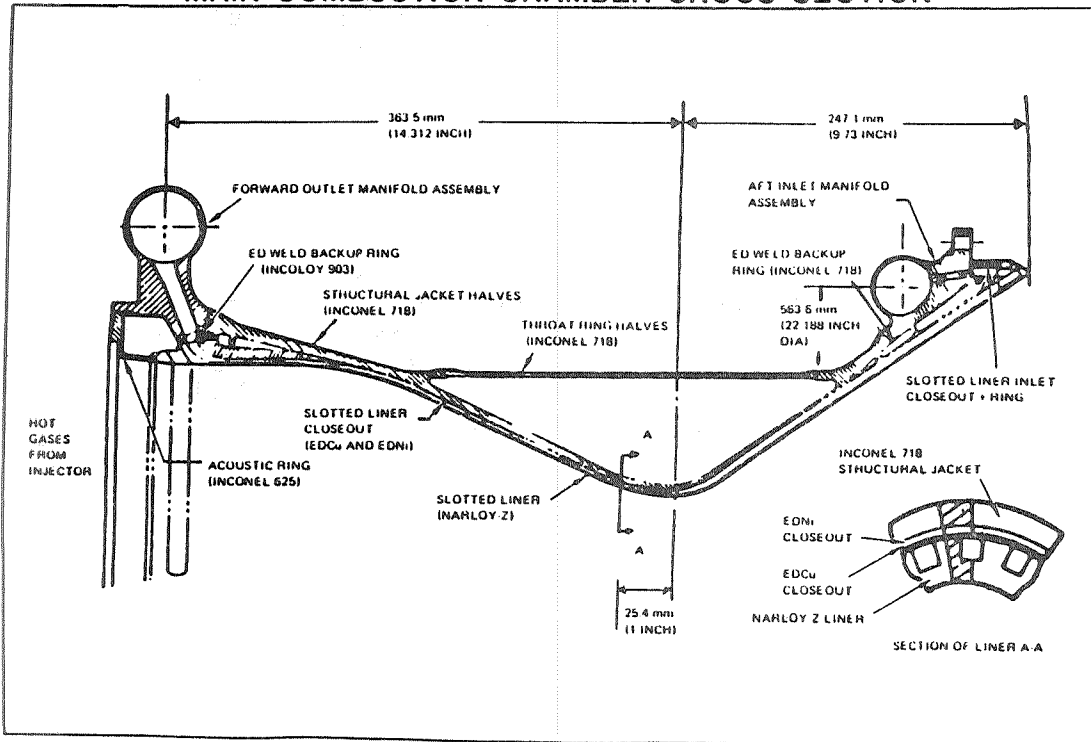
In 1973, work began at LeRC to systematically investigate the problem of thrust chamber life. The approach was to use cyclic testing under controlled conditions, and with a test procedure specifically designed to study thrust chamber life, finite element analyses were performed to compute strain range. Attempts were made to predict life assuming low cycle thermal fatigue failure mechanics and using life data from universal isothermal laboratory fatigue tests as a reference. This life prediction procedure was generally unsuccessful. Consequently, it was decided that an analytical method that models the observed cyclic creep phenomenon was needed to improve life prediction capability.

An analytical method was developed that periodically updates the chamber finite element geometry to account for accrued wall thinning and distortion. The methodology consists of analyzing the chamber considering more increments in the duty cycle and geometric deformation effects. The geometric deformation formulation allows the analysis to adjust to small geometry changes that occur during each duty cycle and are cumulative in nature. In order to minimize computer time, an extrapolation procedure is utilized. To perform the analysis, five duty cycles are sequentially analyzed and the change in geometric shape is extrapolated to the deformation conditions 15 cycles further on, e.g., 5 cycles + 15 cycles = 20 cycle condition. Using the new geometry, additional duty cycles are analyzed and another extrapolated shape projection made. This technique is continued until failure occurs. Failure is based on the tensile instability failure criterion. Cyclic creep life analysis results for several chamber life enhancing designs, when compared to the typically used low cycle fatigue (LCF) analysis results, show that the usable cyclic creep life is approximately 30 to 50% of the LCF life.

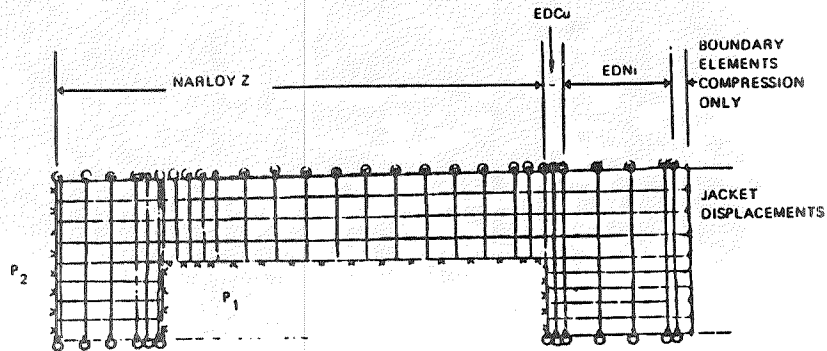


MAIN COMBUSTION CHAMBER

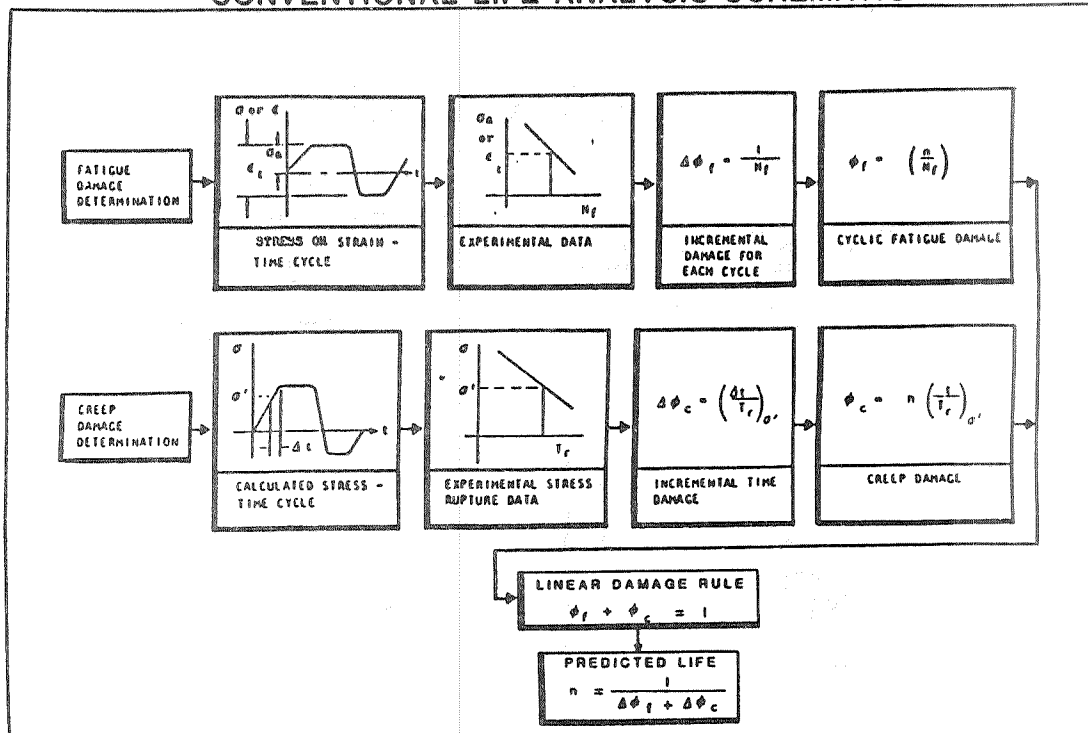
MAIN COMBUSTION CHAMBER CROSS SECTION

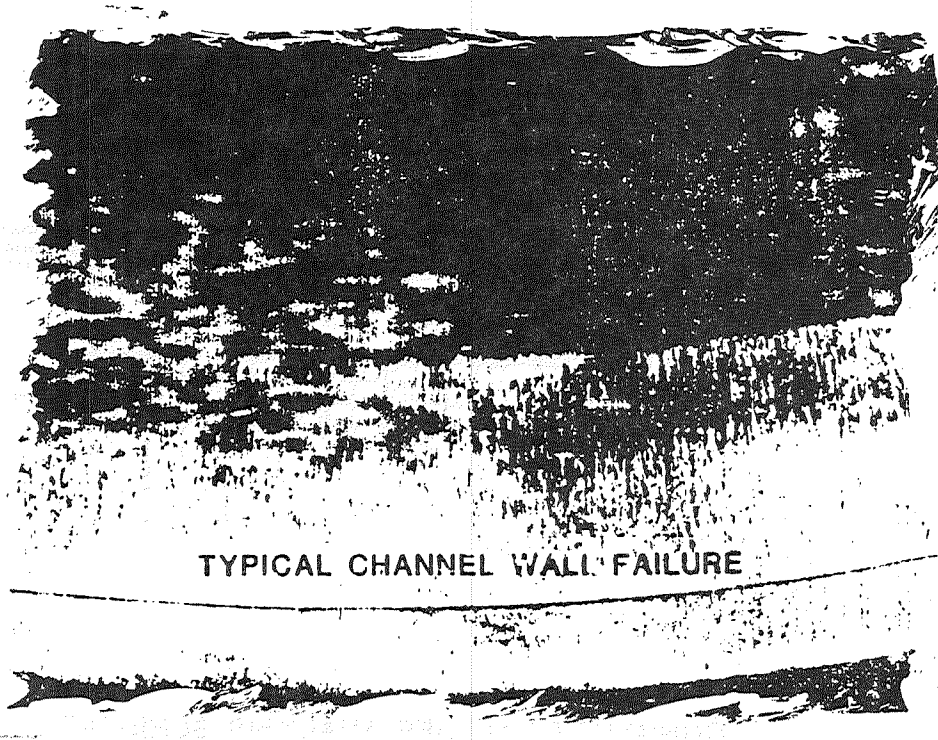


## STRUCTURAL ANALYSIS MODEL



## CONVENTIONAL LIFE ANALYSIS SCHEMATIC



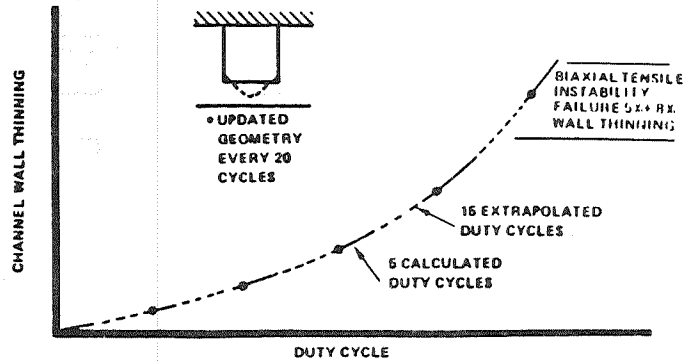
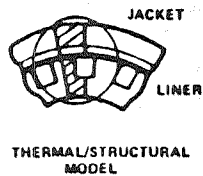
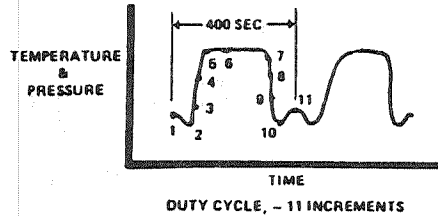


TYPICAL CHANNEL WALL FAILURE

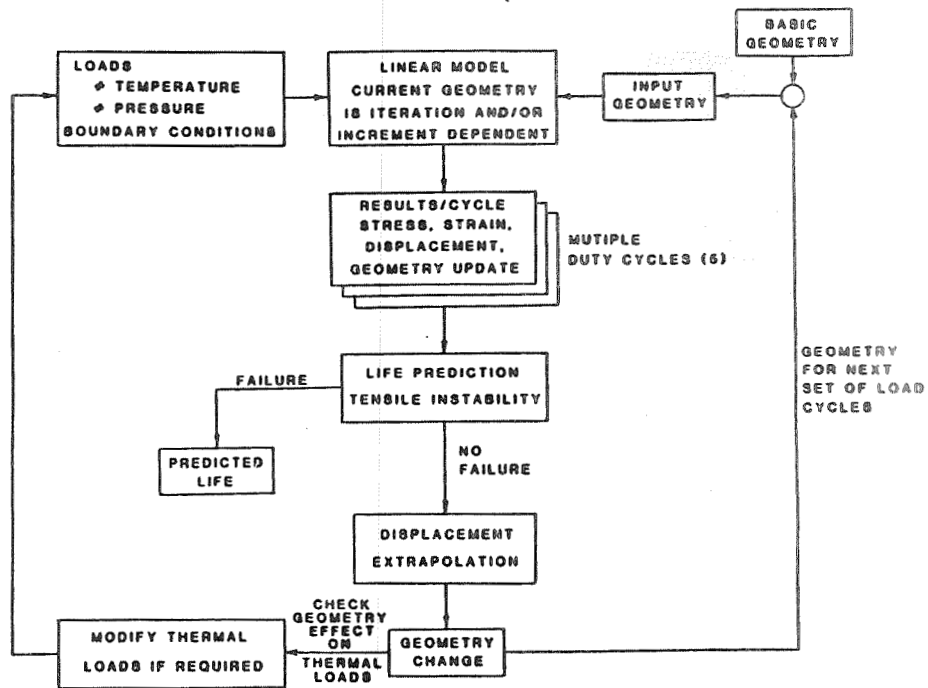
### CYCLIC CREEP LIFE ANALYSIS APPROACH

• CONSIDER

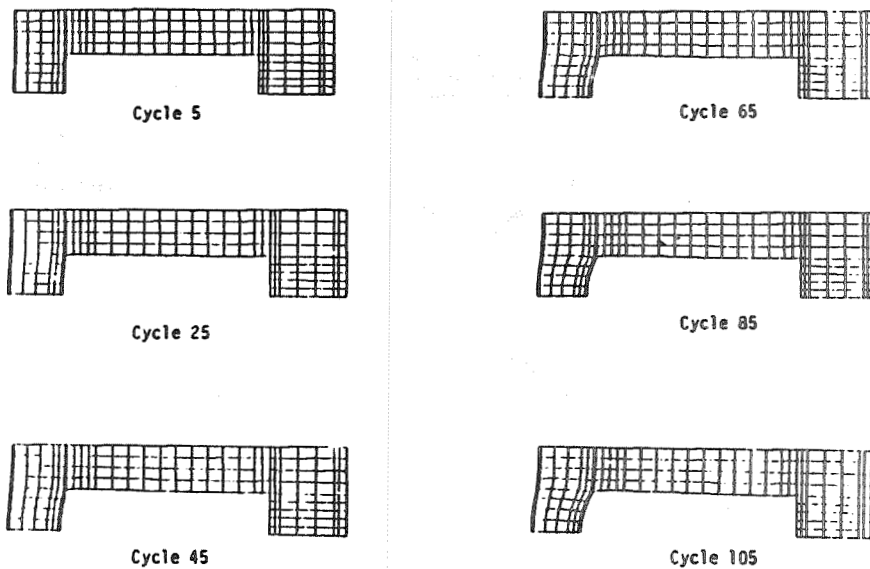
- TEMPERATURE AND PRESSURE HISTORY
- JACKET RADIAL DISPLACEMENTS AND AXIAL RESTRAINT
- INITIAL RADIAL LINER GAP 0.508 mm (0.020 IN.)
- STRUCTURAL MODEL
  - PLANE STRAIN CROSS SECTION
  - INELASTIC MATERIAL - KINEMATIC HARDENING
  - GEOMETRIC DISTORTIONS
  - CREEP/RELAXATION



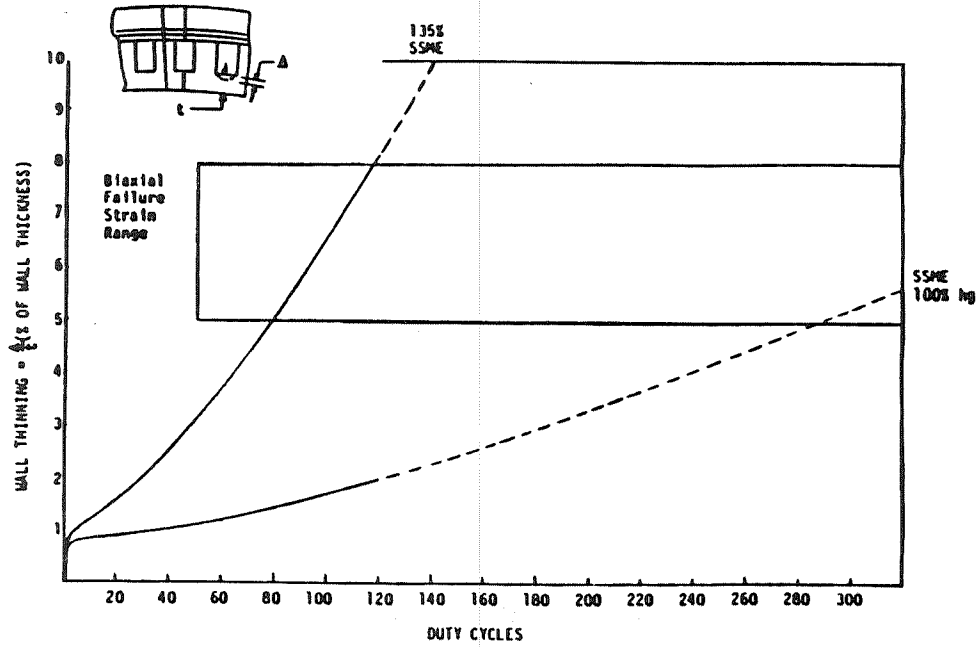
## CYCLIC CREEP LIFE ANALYSIS SCHEMATIC



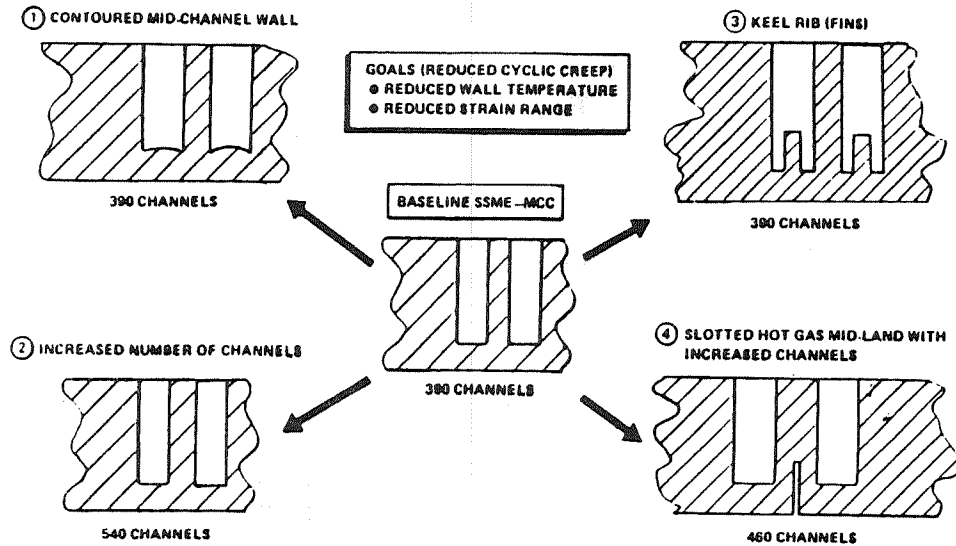
## TYPICAL GEOMETRIC SHAPE CHANGE WITH CYCLING



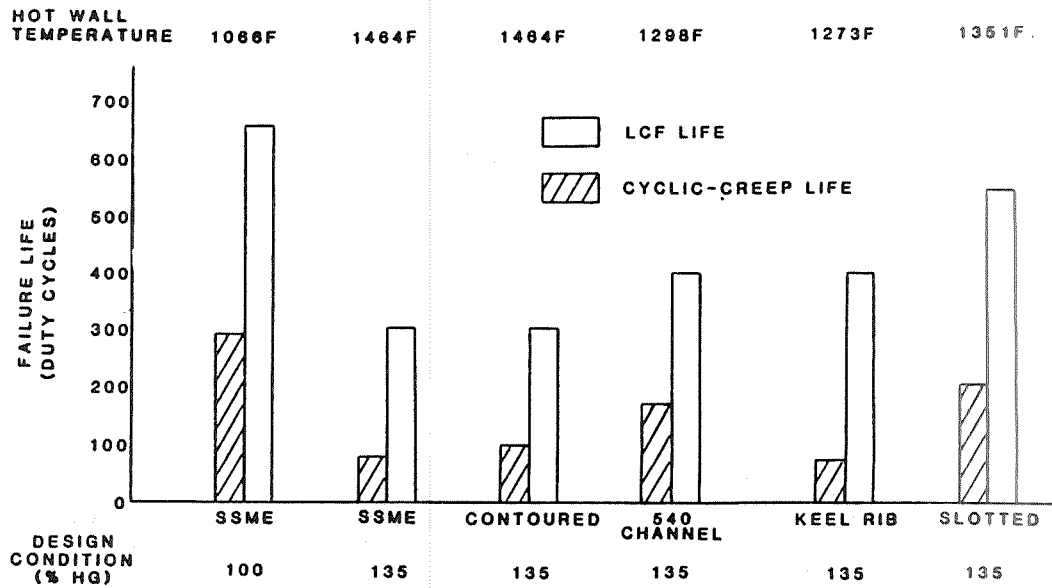
## MID-CHANNEL WALL PERMANENT DEFORMATION (THINNING)



## LIFE ENHANCED DESIGNS



## COMPARISON OF LIFE ENHANCED DESIGNS



### SUMMARY

- # Analytical model provides a refined analysis that models the observed failure mode
- # Predicted cyclic-creep life is typically 30 to 50% of the low-cycle-fatigue life
- # The most feasible approach to increasing SSME-MCC life is increasing the number of coolant channels

## MANUFACTURING AND PRODUCIBILITY TECHNOLOGY

### CO-CHAIRMEN:

JAMES D. HANKINS - NASA/MSFC  
ROBERT L. DRESHFIELD-NASA/LeRC

### Overview:

Manufacturing/Producibility is one of ten Working Groups within the Advanced High-Pressure O<sub>2</sub>/H<sub>2</sub> Technology Program. The objectives of the M/P Working Group are:

"To develop and evaluate process and manufacturing techniques for advanced propulsion hardware design and selected materials. To optimize the producibility of SSME components and assemblies by improved performance, increased life, greater reliability, and/or reduced cost."

The M/P Working Group activities are guided by a committee which has LeRC and MSFC membership representing a broad spectrum of organizations, disciplines, and technology users. The committee is co-chaired by LeRC and MSFC personnel, and includes the following members.

### Co-Chairmen:

J. D. Hankins	MSFC	Materials/Processes
R. L. Dreshfield	LeRC	Materials

Members:

O. K. Goetz	MSFC/EE51	Engine Development
R. P. Grimes	MSFC/EP23	Combustion Devices
T. D. McCay	MSFC/EP23	Turbomachinery
H. L. Goldstein	MSFC/EP23	Instrumentation
J. E. Gattis	MSFC/EF12	Controller
T. D. Byrd	MSFC/EP33	Valves & Actuators
R. R. Holmes	MSFC/EH43	Materials/Processes
L. D. Salter	MSFC/EP46	Stress
R. G. Zagrodzky	MSFC/EG03	Quality Assurance
M. A. Bryant	MSFC/SA55	SSME Project Office

Twelve work elements within the M/P Working Group have been identified. Six are active at MSFC or LeRC, as briefly described and noted in the following list. A seventh, Laser Welding, is proposed for a FY 85 start, and the initiation of the balance (5) will be FY 86, or later.

MANUFACTURING/PRODUCIBILITY

L1. VACUUM PLASMA COATING PROCESSES:

MSFC ACTIVE

To provide thermal shock resistant coatings and application process which will extend the service life of SSME components (blades, discs, heat shields, etc.) through vacuum plasma spray techniques, and subsequent application of these techniques to other space hardware.

L2. ADVANCED WELDING DEVELOPMENT:

MSFC ACTIVE

To assess the potentials of the plasma

arc and variable polarity plasma process on Inconel 718 and Incoloy 903. In particular, points to be investigated are: Number of weld passes, porosity, distortion, microfissuring, crater cracks, and equipment reliability.

L3. COMBUSTION CHAMBER WALL COATINGS:

LeRC ACTIVE

To develop technology for applying thermal barrier ceramic coatings to high-pressure rocket engines' metallic substrates, develop analytical models for predicting coating failure limits and thermal conductance, and determine appropriate mechanical and thermal properties of the coating system.

L5. HIGH-PERFORMANCE ALLOY ELECTROFORMING:

MSFC ACTIVE

To develop a system for electroforming materials with high-strength and high-temperature mechanical properties which can be used for fabricating advanced engine components. The use of such a system would have the potential for improving the life expectancy and reliability of engine components as well as weight reduction and simpler fabrication procedures.

L7. CERAMIC TURBINE ELEMENTS:

MSFC ACTIVE

To develop technology for manufacturing and utilizing high-strength turbine components that will improve the efficiency of operation of turbines by operating at higher temperatures than metallic elements.

L14. ADVANCED TURBINE BLADE COATINGS:

LeRC ACTIVE

Provide performance studies of various

thermal shock resistant/thermal barrier coatings relative to thickness, protective capability, strain tolerance, alternative disposition techniques and verification via hot gas rig testing.

L11. LASER WELDING:

MSFC            FY85

To develop and demonstrate laser welding and capability for fabrication via fusion joining SSME-type materials and joint configurations.

L9. NOZZLE TUBE FABRICATION FROM NEW MATERIAL:

MSFC            FUTURE

Candidate alloys will be characterized for application as nozzle tubes for an uprated SSME. One alloy will be selected for processing through a complete development phase and producibility study.

L13. SUPERPLASTIC FORMING/DIFFUSION BONDING TECH:

MSFC            FUTURE

Superplastic forming and diffusion bonding technology will be exploited for nickel base alloys. It is expected that implementation of this technology would substantially reduce costs and improve SSME component performance.

L15. CERAMIC MATERIALS EVALUATION:

LeRC            FUTURE

Evaluate silicon carbide/silicon nitride family of materials for application to high-temperature LOX/LH<sub>2</sub> engine components relative to failure modes and microstructures.

L16. INERTIA WELDING:

MSFC            FUTURE

To develop inertia welding technology and

parameters for increased reliability and producibility of LOX posts in current and future SSME combustion devices.

L17. ADVANCED PROCESS CONTROL TECHNOLOGY:

MSFC      FUTURE

To assess the application of weld-sensing techniques for advanced manufacturing processes, determine deficiencies that require improved or new technology, and update sensor technology for producing lower cost or higher quality O<sub>2</sub>/H<sub>2</sub> engines with closed loop, computer controlled processes.

Three of the above active M/P Elements (L1, L3, and L7) were selected as topics for papers in this technology conference.

"Rocket Thrust Chamber Thermal Barrier Coatings," by R. J. Quentmeyer, LeRC/NASA

"Ceramics for Advanced O<sub>2</sub>/H<sub>2</sub> Applications," by H. Carpenter, Rocketdyne Division, Rockwell International

"Vacuum Plasma Coatings for Turbine Blades," by R. Holmes, Materials and Processes Laboratory, MSFC/NASA

## ROCKET THRUST CHAMBER THERMAL BARRIER COATINGS

Richard J. Quentmeyer  
NASA Lewis Research Center  
Cleveland, Ohio

### Abstract

Subscale rocket thrust chamber tests were conducted to evaluate the effectiveness and durability of thin yttria stabilized zirconium oxide coatings applied to the thrust chamber hot-gas side wall. The fabrication consisted of arc plasma spraying the ceramic coating and bond coat onto a mandrell and then electrodepositing the copper thrust chamber wall around the coating. The remaining fabrication was completed in a conventional manner. Chambers were fabricated with coatings .008, .005 and .003 inches thick. The chambers were thermally cycled at a chamber pressure of 600 psia using oxygen-hydrogen as propellants and liquid hydrogen as the coolant. The thicker coatings tended to delaminate, early in the cyclic testing, down to a uniform sublayer which remained well adhered during the remaining cycles. Two chambers with .003 inch coatings were subjected to 1500 thermal cycles with no coating loss in the throat region, which represents a tenfold increase in life over identical chambers having no coatings. An analysis is presented which shows that the heat lost to the coolant due to the coating, in a rocket thrust chamber design having a coating only in the throat region, can be recovered by adding only one inch to the combustion chamber length.

### Introduction

High pressure, reusable rocket thrust chambers, such as the Space Shuttle Main Engine (SSME), encounter an irreversible plastic deformation and thinning of the cooling passage wall during each thermal cycle. After numerous thermal cycles, cracks form in the cooling passage wall which can lead to failure of the thrust chamber.

A thermal barrier coating (TBC), such as zirconia ( $ZrO_2$ ), applied to the thrust chamber inner wall could substantially increase the life of the chamber, or allow operation at an even higher chamber pressure. The coating reduces the very high thermal gradient between the hot-gas side wall and the cold back-side closeout. This reduces the cyclic induced plastic strain which causes the deformation of the cooling passage wall.

In recent years, TBCs have been proposed for use on gas turbine blades as well as on rocket thrust chambers. However, their use has not been widely accepted because the coatings are brittle and have a tendency to spall off during repeated thermal cycles. Since the heat flux in a gas turbine is relatively low compared to that in a high pressure rocket thrust chamber, a coating thickness greater than .010 inches is

required to be effective. The throat heat flux in the SSME approaches 100 BTU/in<sup>2</sup>sec. If a ZrO<sub>2</sub> TBC were to be used on the SSME and the hot-gas side wall temperature allowed to operate at 3500°R, the required coating thickness would be .0005-.001 inches, depending on the apparent thermoconductivity of the coating. Since experience has shown that thin coatings remain better bonded than thick coatings when subjected to thermal cycling, the use of a TBC on a high pressure rocket thrust chamber could be more successful than on a gas turbine, even though the thermal environment in the rocket thrust chamber is much more severe. However, to apply uniform ultra-thin coatings such as this requires some development.

Normally the use of a TBC would be incorporated in the initial design of a thrust chamber. A major drawback in using a TBC for life enhancement on an already-operational rocket thrust chamber such as the SSME is that the coating would reduce the heat which is picked up by the coolant and thus would upset the engine cycle balance. However, this effect could be reduced if only the throat section of the thrust chamber were coated.

The normal procedure of applying TBCs is to plasma spray a bond coat such as NiCr or NiCrAlY onto an already-fabricated thrust chamber and then plasma spray the ceramic layer over the top. Problems associated with this procedure include oxidation of the metallic substrate during the coating application, and a residual stress which remains in the coating when the coated chamber returns to room temperature. Both reduce the bond strength between the coating and the substrate.

Another method of applying the coating which reduces or eliminates the phenomenon described above is to build the thrust chamber inside out, i.e., start with the coating and fabricate the chamber around it. A method of fabricating coated thrust chambers inside out called the "electroform pick-up process," was developed at the Lewis Research Center. The process consists of plasma spraying the ceramic coating onto a mandrel, applying the bond coat, and then electrodepositing a liner around the coating using copper. The cooling channels are then machined into the copper liner after which the channels are closed out by electrodeposition. The mandrel is removed which leaves a smooth ceramic coating which possesses excellent bond strength.

At Lewis there has been an ongoing program to develop techniques of applying ultra-thin TBCs to rocket thrust chambers, both by applying the coating to already-fabricated chambers and by applying the coating using electroform pick-up process. However, the results discussed herein pertain only to thrust chambers having coatings applied by the electroform pick-up process.

In order to experimentally evaluate coatings for use on high pressure rocket thrust chambers, subscale rocket thrust chamber tests were conducted at Lewis using the Lewis plug nozzle thrust chamber test apparatus. Plug nozzle chambers having ZrO<sub>2</sub> coatings .008, .005 and .003 inches thick were fabricated by the electroform pickup process. The chambers were cyclically tested at 600 psia chamber pressure using oxygen-hydrogen as propellants and liquid hydrogen as the coolant. The test results are compared with identical chambers which had no coating.

Also presented are the results of an analysis performed on a high pressure advanced space engine (ASE) design, which shows the effect on the hot-gas side wall temperature, coolant pressure drop and coolant temperature rise if the throat region is coated with a TBC. The analysis also shows the affect of changing the combustion chamber length on the engine cycle balance.

## **PROGRAM OBJECTIVE**

**TO DEVELOP THERMAL BARRIER COATING TECHNOLOGY**

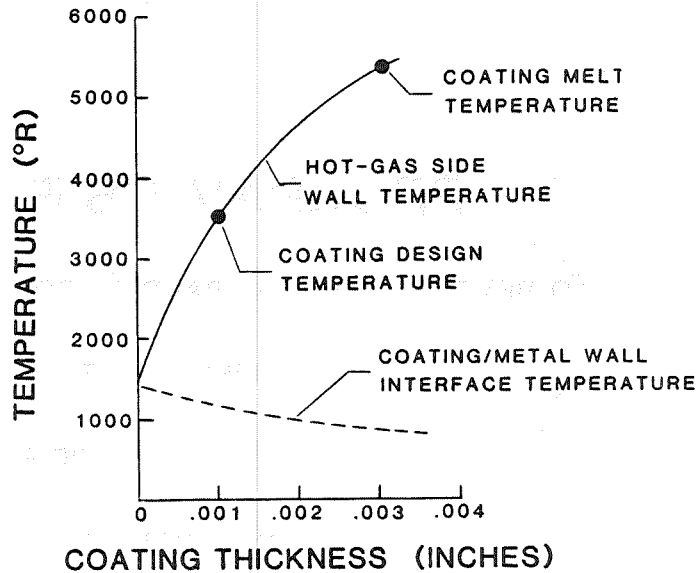
- CHAMBER LIFE EXTENSION
- HIGHER PRESSURE POTENTIAL
- FABRICATION FEASIBILITY
- EXPERIMENTAL VERIFICATION

## **TECHNOLOGY ISSUES**

- COATING DURABILITY
- LIFE EXTENSION, NOT SURVIVAL
- ULTRA THIN COATINGS

## THIN COATING REQUIREMENT

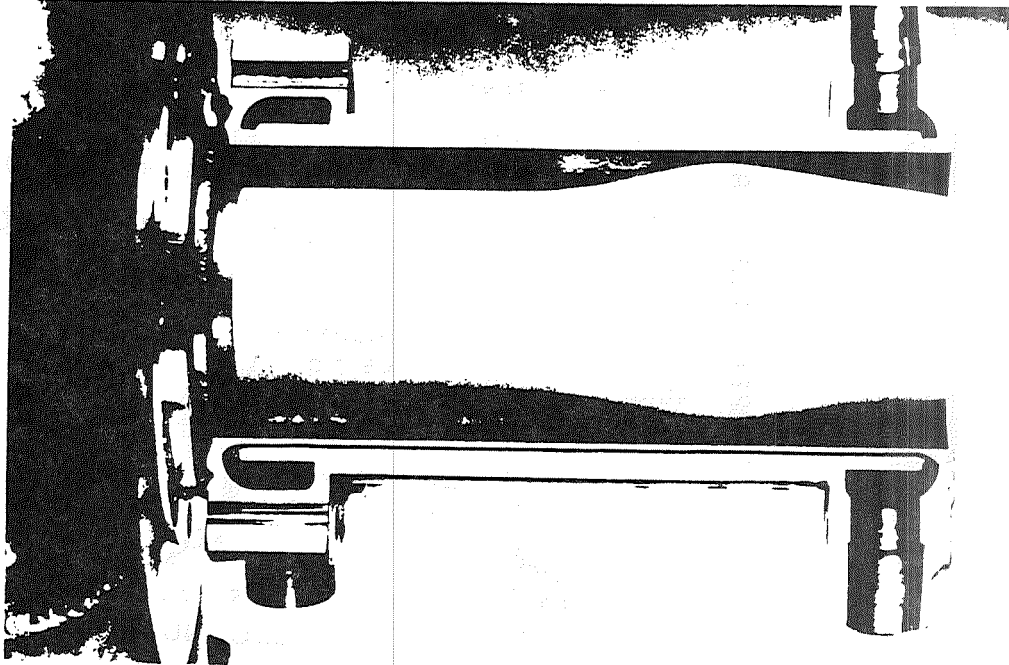
HIGH PRESSURE ROCKET THRUST CHAMBER



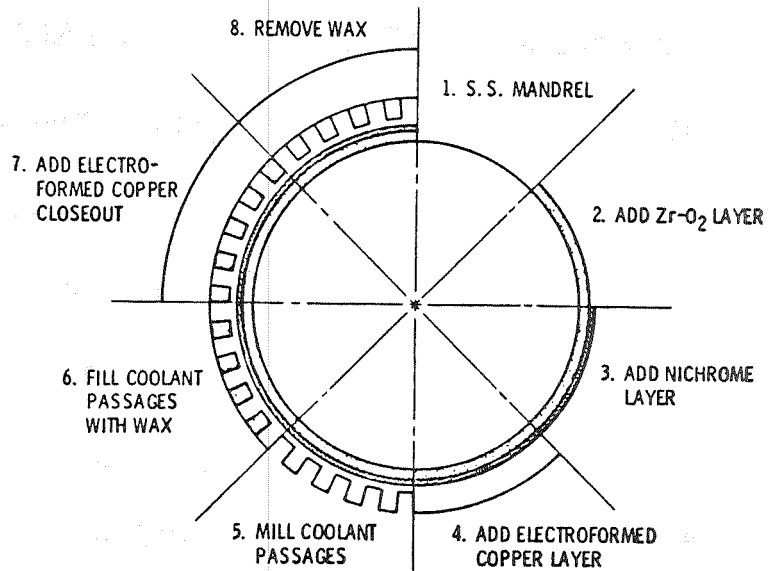
## APPROACH

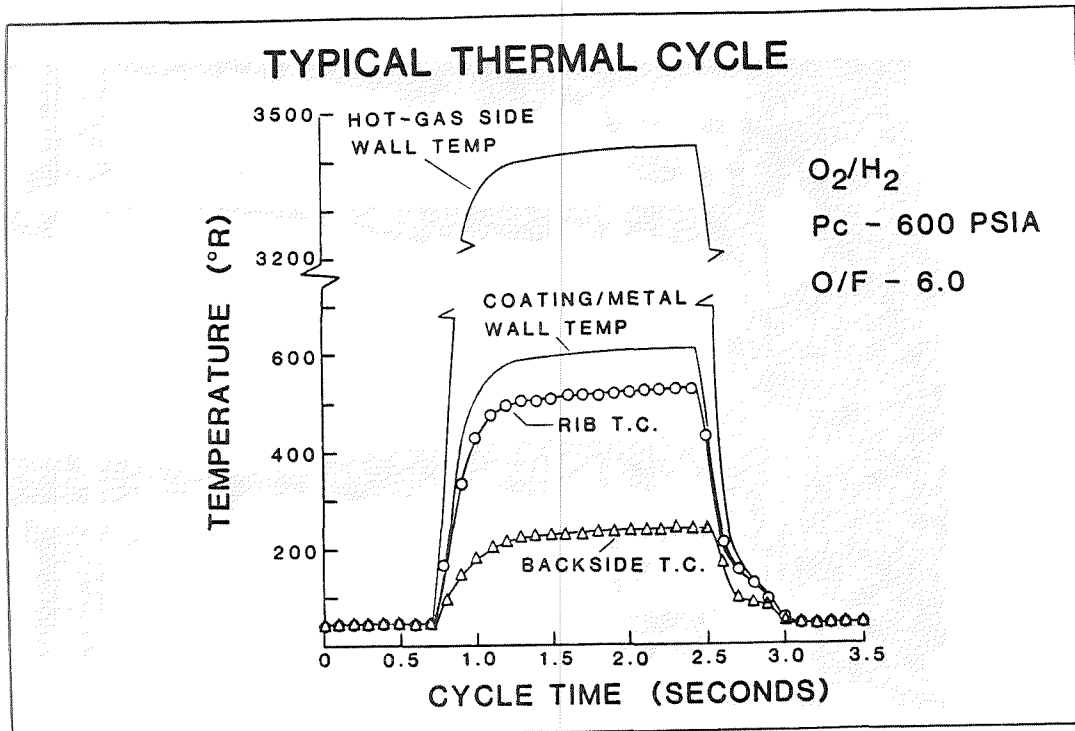
- APPLY COATINGS AS PART OF THE FABRICATION BY THE ELECTROFORM PICK-UP PROCESS
- APPLY COATINGS BY THE ARC PLASMA SPRAY PROCESS TO ALREADY FABRICATED THRUST CHAMBERS

# PLUG NOZZLE TEST APPARATUS



## CHAMBER FABRICATION SEQUENCE



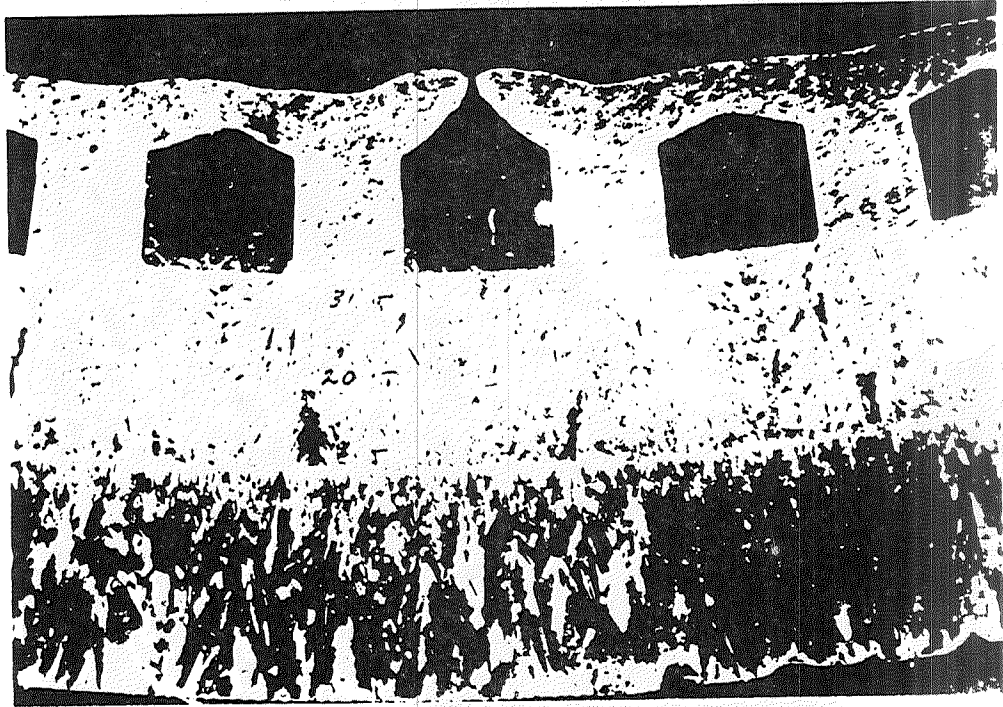


## EXPERIMENTAL RESULTS

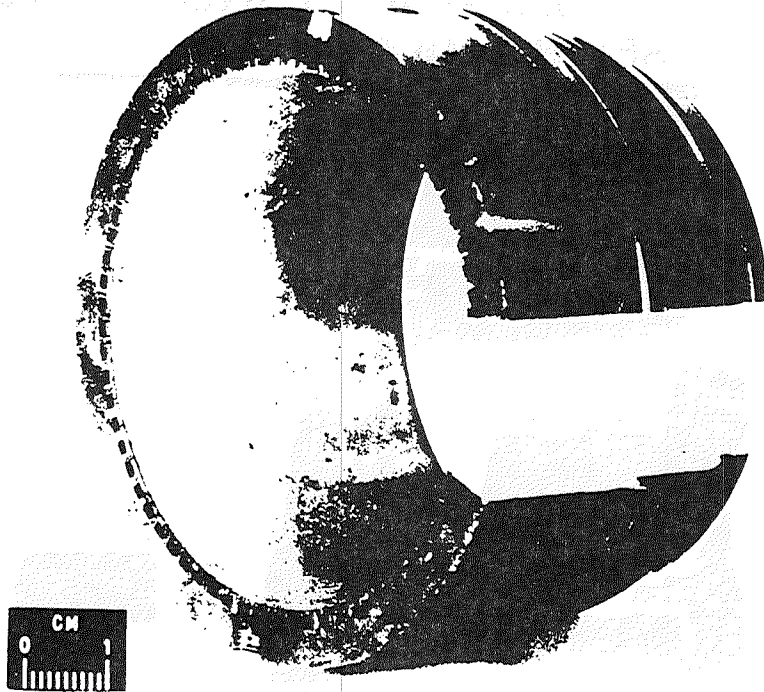
THICKNESS	CYCLES	RESULT
NO COATING	150 AVG	TYPICAL CHANNEL FAILURE
.008"	659	BLOCKED CHANNEL FAILURE
.005"	2413	NO FAILURE
.003"	1538	NO FAILURE
.003"	1448	NO FAILURE

- NO CHANNEL DEFORMATION FOR COATED CHAMBERS
- EXCELLANT METAL TO CERAMIC BOND IN ALL CASES

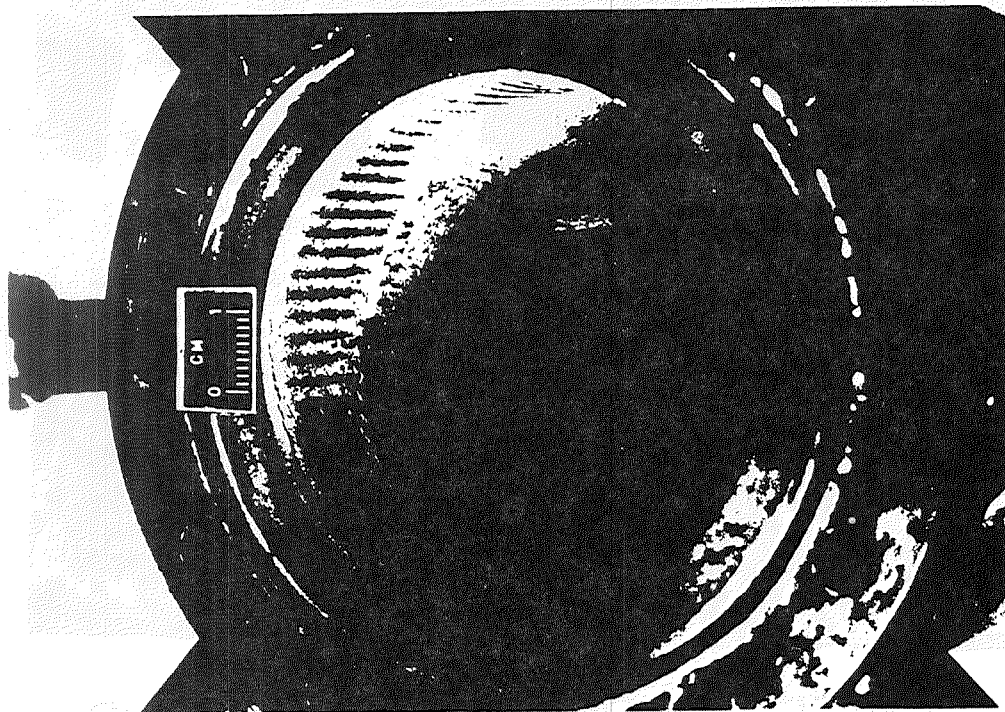
# COOLANT PASSAGE FAILURE



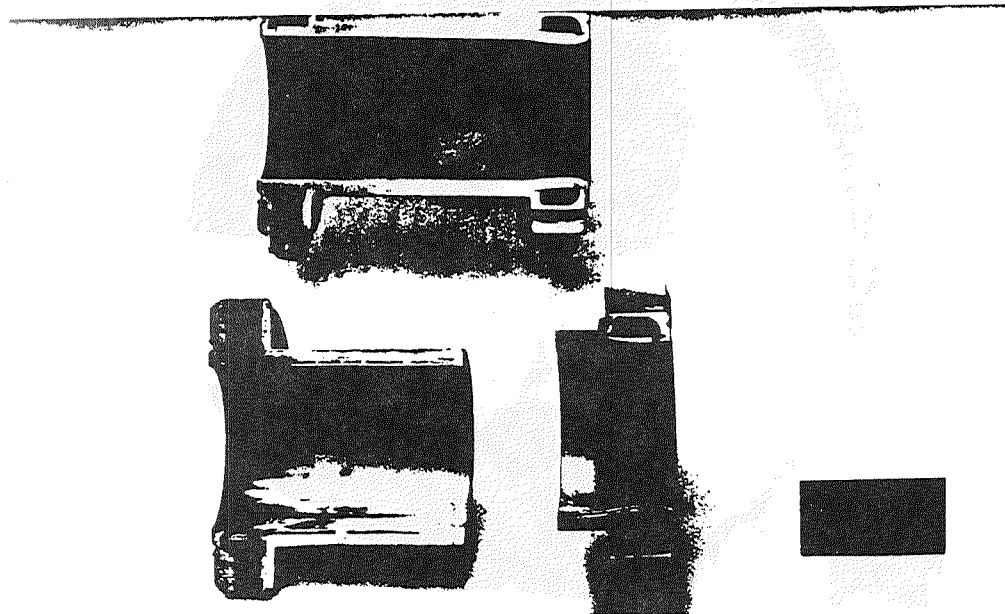
## COATED SURFACE CONDITIONS AFTER 659 CYCLES



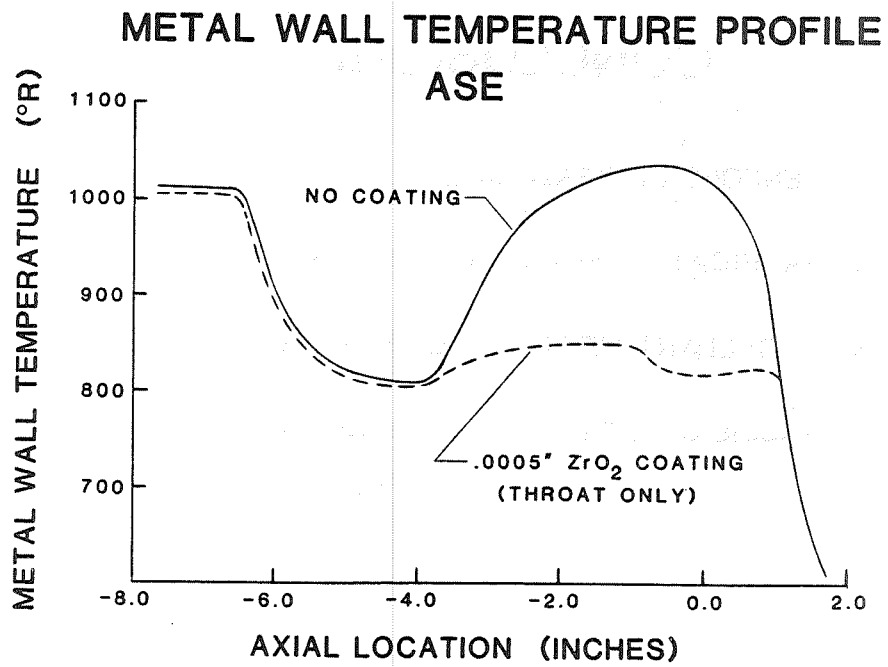
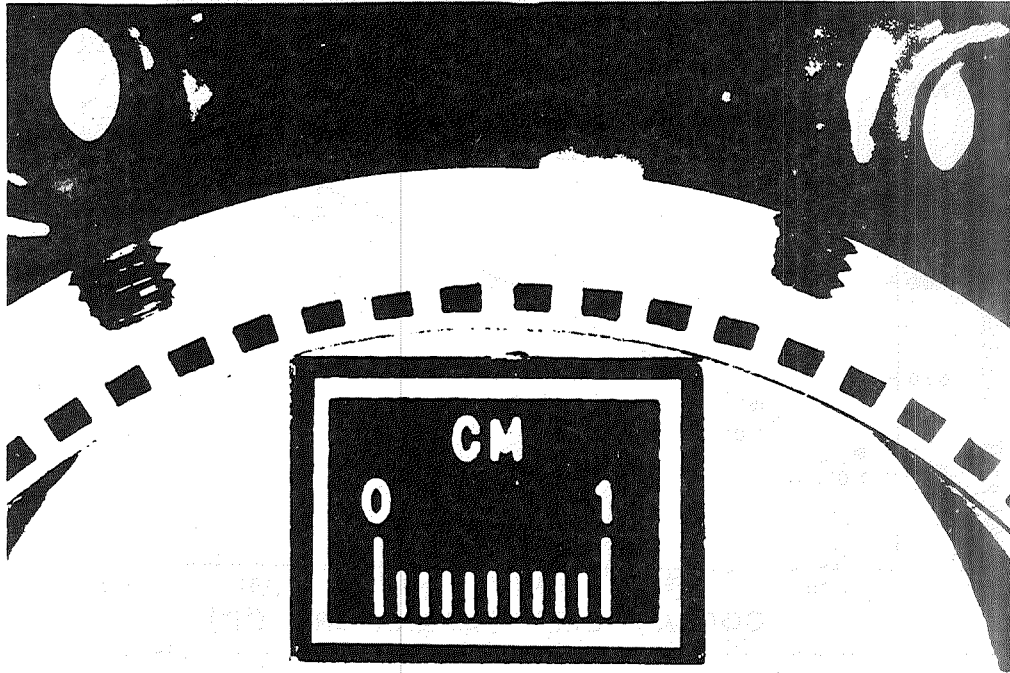
# COATED SURFACE CONDITIONS AFTER 2413 CYCLES

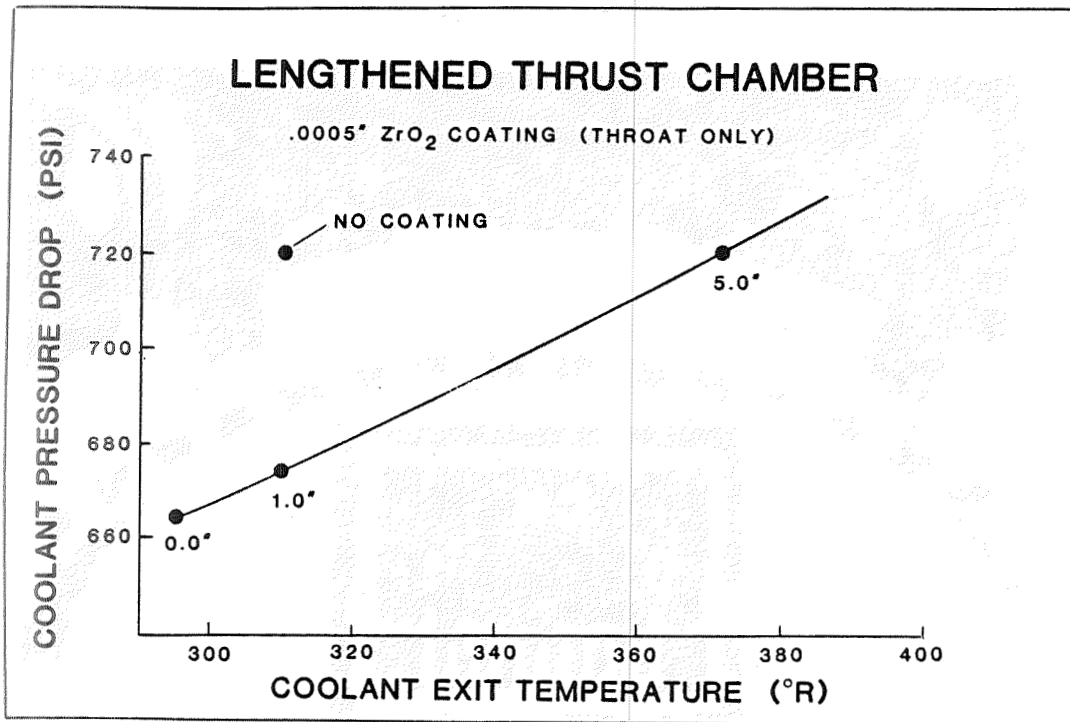


# COATED SURFACE CONDITIONS AFTER 1448 CYCLES



# COOLANT PASSAGE CONDITION AFTER 1448 CYCLES





## CONCLUSIONS

- TENFOLD INCREASE IN LIFE DEMONSTRATED
- FABRICATION FEASIBLE & REPEATABLE
- EXCELLANT METAL TO CERAMIC BOND
- ENGINE CYCLE BALANCE CAN BE MAINTAINED

## CERAMICS FOR ADVANCED O<sub>2</sub>/H<sub>2</sub> APPLICATION

H. W. Carpenter

Rockwell International/Rocketdyne Division  
Canoga Park, California

### Abstract

Ceramics are prime candidate materials for advanced rocket engines because they possess high-temperature capability, a tolerance for aggressive environments, and low density. This program was conducted to assess the applicability of structural ceramics to advanced versions of the Space Shuttle Main Engine. Operating conditions of ceramic turbine components were defined and each component in the hot-gas path was assessed in regard to materials selection, manufacturing process and feasibility, and relative structural reliability. The conclusion was that ceramic components would be viable in advanced SSME turbopumps.

### Introduction

Rocket engines for space missions beyond this decade must be capable of operating for longer periods of time, withstanding more duty cycles, and be more efficient than present engines. The most advanced liquid propellant rocket engine currently available is the Space Shuttle Main Engine (SSME). Materials for high-temperature components of the engine (e.g., turbine blades, stator vanes, and other elements in the hot-gas flowpath) are approaching the limits of their capabilities. Among the materials for use in advanced rocket engines, ceramics are prime candidates because of their high-temperature capability, low density, and tolerance for aggressive environments. This program was conducted to assess the capability of refractory structural ceramics to meet the severe requirements of advanced rocket engines

An objective of this program was to identify advanced SSME-type turbine components that would be promising candidates for application of advanced structural ceramics. The classes of ceramics of interest to this study program are silicon nitride, silicon carbide, and the new generation of ceramic composites such as transformation-toughened zirconia or alumina, and particulate- or whisker-reinforced ceramic matrices. The hardware of primary interest is in the hot section of an SSME-type turbine.

The program comprised two phases: the first phase defined the operating environment in which the ceramic turbine components will be exposed and the second phase identified those components that appeared to be promising candidates for manufacture from advanced structural ceramics.

## Results and Discussion

### Turbine Operating Environment

The effect of operating at turbine temperatures to 3000 R were explored with the aid of engine balance computer programs. Based on this information, the operational environment of the hot-gas path components under a turbine inlet temperature of 2400 R was defined in detail to provide pressures, flowrates, turbine speeds, nozzle velocities, temperatures, etc. Engine balance studies for staged-combustion cycle engines have demonstrated that modest increases in specific impulse ( $I_s$ ) and in thrust can result from increased turbine inlet temperature based on oxygen/hydrogen propellant systems. If different fuels than hydrogen are employed (e.g., methane), the situation becomes more favorable and increases in turbine temperature can provide more attractive improvements in specific impulse and thrust. Although engines based on other working cycles were not assessed during this study, future consideration should be given to the performance benefits possible due to increased turbine inlet temperature with

a gas-generator cycle rocket engine. The SSME staged-combustion engine utilizes a reaction turbine, while gas-generator engines have used impulse or velocity compounded turbines. The heat transfer within gas-generator engine turbine blading is considerably less severe than in a staged-combustion engine turbine due to decreased Reynolds numbers, and this should result in significant decreased thermal stresses. In addition, the lower turbine gas exhaust temperature would relieve the necessity of ceramic components downstream of the turbine (e.g., in the combustion chamber injector).

The use of ceramic materials in the turbine hot-gas path is motivated by the increased performance possible with increased turbine inlet temperatures. Performance benefits were considered for both oxygen/hydrogen and oxygen/methane propellants using a 500,000 pound thrust staged-combustion baseline engine design. Engine specific impulse gains for several different thrust chamber area ratios and for pump discharge pressures of 10,000 psia are shown in Fig. 1 and 2 (Ref. 1).

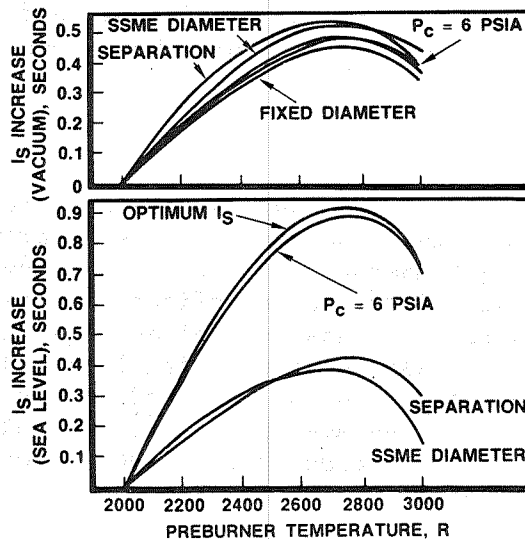


Fig. 1. Performance of a 500,000-Pound-Thrust Engine Using Oxygen/Hydrogen Propellants With Increasing Temperature

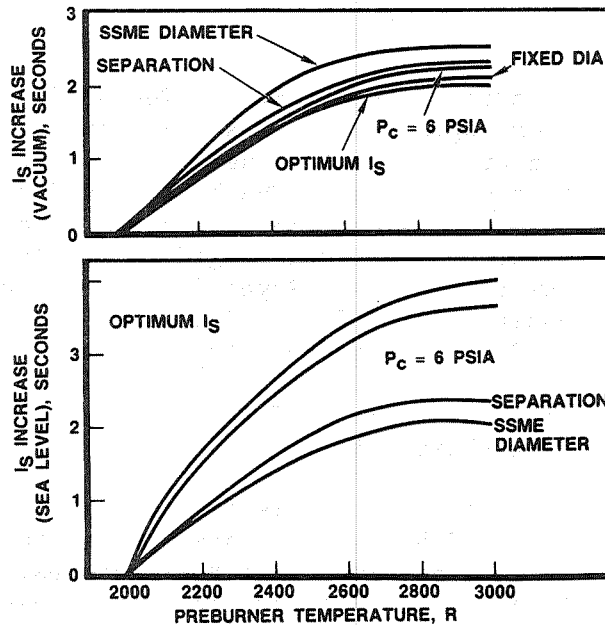


Fig. 2. Performance of a 500,000-Pound-Thrust Engine Using Oxygen/Methane Propellants With Increasing Temperature

Specific impulse increases are greatest for sea-level conditions compared to vacuum conditions, and are also significantly greater for oxygen/methane compared to oxygen/hydrogen.

#### Key Design Issues

Candidate ceramic components were selected for an advanced staged-combustion cycle engine to provide higher operating temperature or extended operating life, and the key design issues were defined. As part of this task, a structural analysis of an  $\text{Si}_3\text{N}_4$  turbine vane (Fig. 3) was assessed for reliability under the operational environment of an advanced rocket engine turbine. The projected average four-point MOR strength for the  $\text{Si}_3\text{N}_4$  body was assumed to be 90 ksi with a Weibull modulus of 15.

The maximum combined thermal and pressure stress in the hollow ceramic vane of Fig. 3 (37 ksi) occurs

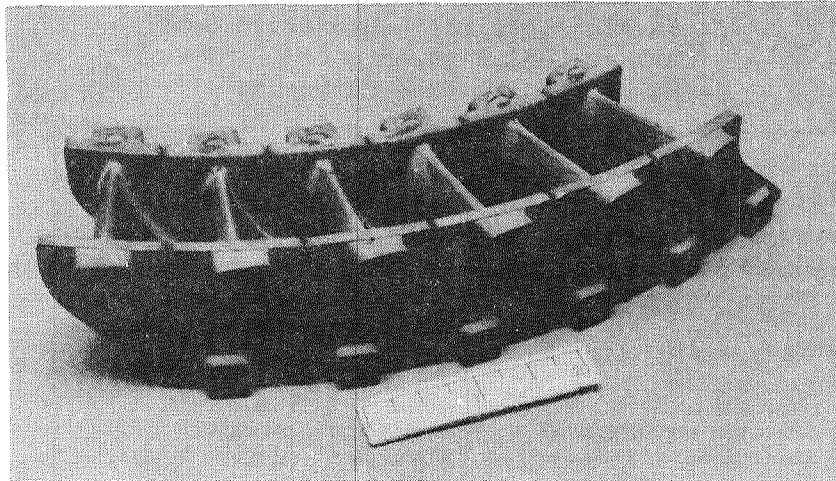


Fig. 3. Segmented Silicon Nitride Turbine Vanes

at the support rib inside the nozzle during the start-transient phase of engine hot firing. (The thermal ramp heating and cooling rates were based on those existing in the present SSME.) This translated to a reliability for any given nozzle of 0.999. Since this analysis was based on a fast fracture criterion, the reliability figure is valid for the 500 hot-firing cycles projected to be appropriate for an advanced engine. A reliability level of 0.999 indicates that the use of ceramic components in an advanced engine is feasible.

A fund of design analysis and test data are available as a result of the development of ceramic gas turbine engines for automotive applications. This information was used to compare the heat transfer conditions in a ceramic automotive gas turbine with those in an advanced rocket engine high-pressure fuel turbopump (HPFTP). This comparison is made in Table 1 (Ref. 2-7). Note that the conditions for a nozzle vane in the advanced high pressure fuel turbopump are considerably more severe than those for a nozzle vane in the automotive gas turbine environment. The film coefficient is up to 50 times higher, the pressure is 100 times higher, the thermal transients are 10 to 20

Table 1. Comparison of Thermal Environments  
for Ceramic Nozzles: Automotive Gas  
Turbine Engine vs Advanced SSME  
High-Pressure Fuel Turbopump

ITEM	AUTOMOTIVE AGT 101	ADVANCED SSME HPFTP (REF. 2)
FUEL	DIESEL (REF. 3)	HYDROGEN OR METHANE
OXIDIZER	AIR	LIQUID OXYGEN
FILM COEFFICIENT, BUU/HR-FT <sup>2</sup> -R		
SPIKE AT LEADING EDGE	1000 (REF. 4)	18,000
ALONG AIRFOIL SURFACE (AVG)	200 (REF. 4)	10,000
PRESSURE, PSI (MAX)	60 (REF. 4)	6000
FOR A NOZZLE VANE		
START TRANSIENT, FT/SEC (MAX)	640 (REF. 5)	6000
COOLDOWN RATE, FT/SEC (MAX)	900 (REF. 5)	18,000*
CUTOFF TRANSIENT, FT/SEC (MAX)	900 (REF. 5)	1700
TEMPERATURE, F (MAX)		
STARTUP SPIKE	2500 (REF. 3, 4, 5)	2400
STEADY STATE	2500 (REF. 4, 5, 6)	1940
COMPUTED TENSILE STRESS, KSI (MAX)	13.4** (REF. 4)	37*** (REF. 7)
NUMBER OF ENGINE STARTS (ESTIMATED)	10,000	55 TO 700
LIFE, HOURS (ESTIMATED)	3000	7.5 TO 100
*OCCURS DURING START TEMPERATURE SPIKE		
**OCCURS DURING DOWNSHOCK IN THE TRAILING EDGE NEAR THE OUTER SHROUD		
***OCCURS DURING UPSHOCK IN THE STRUT INSIDE THE HOLLOW VANE		

times more severe, and the nozzle vane in the advanced turbopump is projected to experience a temperature spike of 2400 F. These conditions produce a stress approximately 3 times that in the automotive nozzle. Thermal shock thus becomes a key material and design issue for ceramic rocket engine components.

### Ceramic Processing and Properties

Candidate Materials. Structural ceramic materials were evaluated for components in advanced SSME-type turbopumps. To qualify as a candidate ceramic material for SSME turbine components, the material should:

1. Exhibit adequate structural strength to the service temperature.

2. Possess a high Weibull modulus. A typical value for advanced structural ceramics is 8, but values above 20 are reported.
3. Be highly resistant to thermal shock. Thus, the material should have high strength, a low thermal expansion, and preferably a low elastic modulus. A high value of thermal conductivity also can be beneficial.
4. Be highly resistant to reaction with combustion products.
5. Maintain its toughness, stability, and strength over the design life of advanced turbines.
6. Be fabricable in complex shapes with close tolerances and at reasonable costs.
7. Have an acceptably high fracture toughness.

Efforts to develop strong, reliable structural ceramics for a variety of heat engines have been underway for the past decade, principally in the United States, Great Britain, Japan, Sweden, and West Germany. The emphasis so far has been directed at automotive applications and it is from these programs that many of the engineering properties data have been generated. Materials that can be considered as candidates for advanced rocket engine applications are:

1.  $\text{Si}_3\text{N}_4$  (SN)
2. SiC (SC)
3. Partially stabilized  $\text{ZrO}_2$  (PSZ)
4. Transformation-toughened ceramics
5. Particulate-toughened ceramics
6. Fiber-reinforced ceramics
7. Carbon-carbon composites with a protective coating

The materials that have exhibited the greatest promise for high-performance applications are  $\text{Si}_3\text{N}_4$

and SiC. These materials include sintered Si<sub>3</sub>N<sub>4</sub> (SSN), reaction-bonded Si<sub>3</sub>N<sub>4</sub> (RBSN), sintered reaction-bonded Si<sub>3</sub>N<sub>4</sub> (SRBSN), sintered SiC (SSC), and reaction-bonded SiC (RBSN). RBSC is also referred to as siliconized SiC (Si/SC). These materials are families of materials where the members have compositional modifications and are made by different fabrication routes. The microstructural features of these family members can be radically different and, as a consequence, so can the properties. Thus, it is essential to be aware of the basic fabrication processes.

Strength. The relative strengths of typical ceramic materials are shown in Fig. 4 (Ref. 8-12). The materials exhibiting the highest strengths are dense

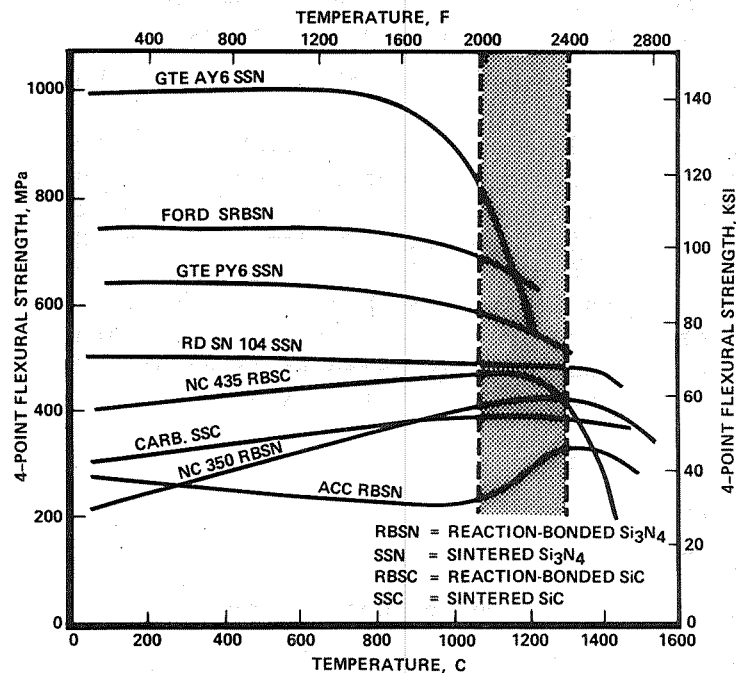


Fig. 4. Comparative Strengths of Representative Structural Ceramics

sintered silicon nitrides (SSN). Four-point bending strengths as high as 141 ksi have been reported (Ref. 8). The relative low strength of RBSN is a result of

its high porosity. Above 2400 F, however, RBSN has a strength level competitive with that of dense  $\text{Si}_3\text{N}_4$ . This is because RBSN does not contain a glassy phase in the grain boundaries. The relative strength ranges of the SiC materials are between those of dense SSN and RBSN.

It must be pointed out that the strength values reported in Fig. 4 are typical values, not design strength values. These typical strength values must be adjusted to produce design values based on size, test configuration, stress state in the hardware, and the required reliability.

Resist to Thermal Shock. Resistance to thermal shock is a critical consideration for ceramic turbo-pump components. Extensive testing has been performed on the subject materials (Ref. 13) by plotting (Fig. 5) the maximum quench temperature difference before

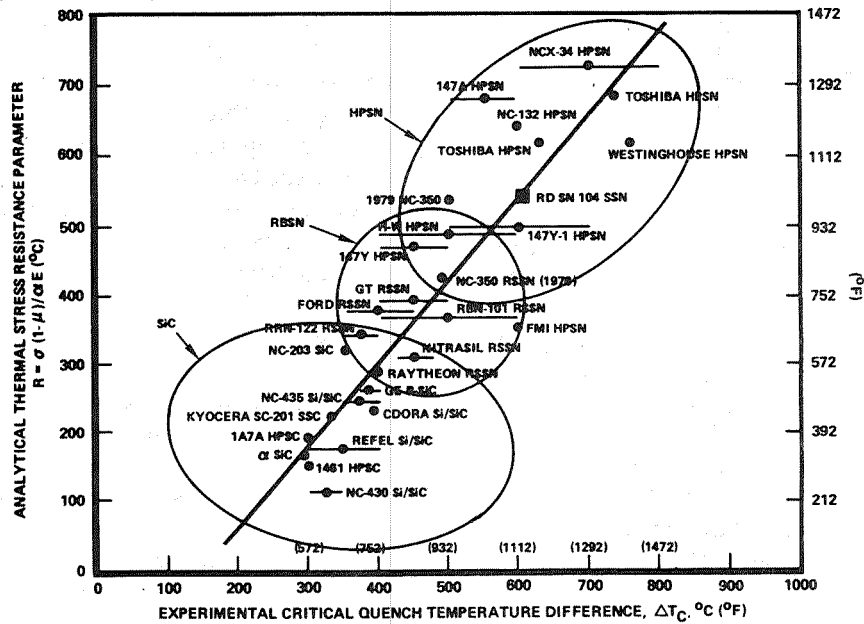


Fig. 5. Resistance to Thermal Shock of Candidate Materials

damage due to thermal shock occurred versus an analytical figure of merit, R, where:

$$R = \frac{\sigma(1 - \mu)}{\alpha E}$$

$\sigma$  = average flexural strength

$\mu$  = Poisson's ratio

$\alpha$  = thermal expansion coefficient

E = elastic modulus

The materials that best resist thermal shock are located in the upper right while those that least resist thermal shock are located in the lower left. Each of three families of materials are clustered together. Hot-pressed  $\text{Si}_3\text{N}_4$  (HPSN) exhibits the highest resistance to thermal shock, RBSN is next, while SiC materials exhibit the poorest resistance. Although SSN materials were not tested, they would be expected to fall in the circle drawn around the HPSN materials. SSN would exhibit similar results to those of HPSN because the microstructural features are similar and because it exhibits the same mechanical properties. The figure of merit for RD SN 104 SSN, shown by the square symbol in Fig. 5, falls in the center of the circle drawn around the HPSN data. HPSN offers limited use as turbine components because hardware is so expensive to make due to the extensive diamond grinding that is required.

Time-Dependent and Cyclic Properties. Long-term and cyclic properties, such as static fatigue, creep, and cyclic fatigue, are not yet well characterized on the newer SSN materials. Projections were made, however, based on data from similar materials. The effects of time-dependent and cyclic properties were small at the steady-state temperature, 1940 F, for 100 hours, and the stresses involving these properties are much lower than those that would cause fast fracture. Thus, the suitability of ceramics for turbopump application was demonstrated by satisfying fast-fracture criteria.

## Component and Materials Identification

Each potential component for ceramics in the hot-gas path (Fig. 6) of an advanced high pressure fuel turbopump was assessed in terms of fabrication feasibility and structural risk. Information generated in Tasks 1, 2, and 3, plus component designs from the existing high pressure fuel turbopump, was used as a

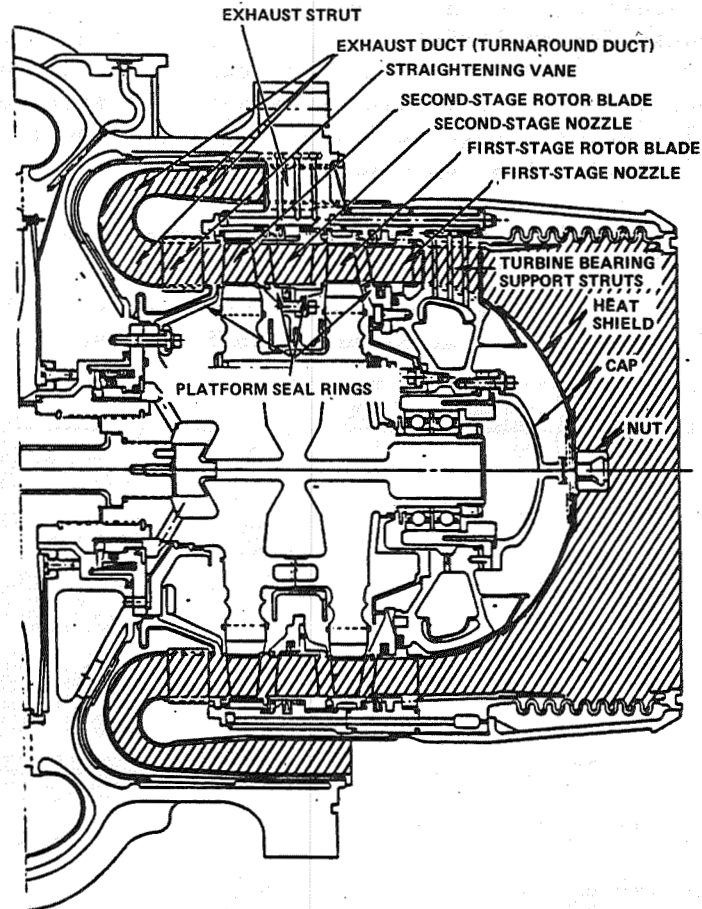


Fig. 6. Potential Components for Ceramics in the Hot-Gas Path of the Turbine Section in the SSME High Pressure Fuel Turbopump

basis for evaluation. Components showing good potential for benefit include stator nozzles, rotor blades, exhaust straightening vanes, and turbine inlet and exhaust struts.

Several of the turbine components can be made from high-performance ceramic materials at moderate to low risk. Experience has shown that ceramic components can replace metallic hardware only after careful and often major redesign. The most evident features of ceramic components for an SSME-type high pressure fuel turbo-pump are attention to attachment techniques, avoidance of excessive contact loading stresses, and fabricability. The major design challenge appears to be in devising methods of attachment.

Assessment of candidate hot-gas ceramic path components is summarized in Table 2.

Table 2. Assessment of Ceramic Components in the Hot-Gas Path of an Advanced SSME-Type HPFTP

COMPONENT	STRUCTURAL LOADS		CURRENT ATTACHMENT METHOD	FAB RISK	DEVELOPMENT PRIORITY	PRIMARY CONCERNS	COMMENTS
	MECH	THERM					
FIRST-STAGE NOZZLES	MOD	HIGH	LUGS	LOW	1	CONTACT STRESSES. TRANSIENT THERMAL STRESSES.	PRIMARY CANDIDATE FOR CERAMICS. STRUCTURAL ANALYSIS SHOWS THAT CERAMICS ARE VIABLE.
ROTOR BLADES	HIGH	HIGH	ROOT	LOW	2	CONTACT STRESSES. TRANSIENT THERMAL STRESSES. LACK OF FATIGUE DATA.	CENTRIFUGAL LOADS WILL BE LOWER THAN FOR METAL BLADES.
HEAT SHIELD	MOD	HIGH	NUT	MOD	4	CONTACT STRESSES. PRESSURE LOADING.	PROMISING CANDIDATE FOR CERAMICS BUT WOULD REQUIRE DETAILED STRUCTURAL ANALYSIS AND SOME REDESIGN.
CAP	HIGH	HIGH	FLANGE	MOD	..	HIGH LOADS. FLANGE ATTACHMENT	HIGH RISK FOR A CERAMIC COMPONENT WITH MODERATE REWARD. A METAL CAP WILL BE SATISFACTORY BECAUSE IT IS COOLED BY LH <sub>2</sub> AND IT IS NOT EXPOSED DIRECTLY TO HOT GASES.
TURBINE BLADE PLATFORM SEALS	MOD	HIGH	FLOATING SCREW	LOW-MOD	5	CONTACT STRESSES. RUBBING ON METAL PARTS.	FEASIBLE BUT REQUIRES REDESIGN OF CONFIGURATIONS AND ATTACHMENT CONSIDERATIONS.
EXHAUST STRAIGHTENING VANES	MOD	MOD-HIGH	WELDED	LOW	3	METHOD OF ATTACHMENT. ACCOMMODATING THERMAL EXPANSION	LOW RISK. PROVIDED A SUITABLE ATTACHMENT METHOD CAN BE DESIGNED.
EXHAUST DUCT	MOD	MOD-HIGH	WELDED	VERY HIGH	..	FABRICATION. ATTACHMENT.	THE PRESENT CONFIGURATION WOULD BE VERY DIFFICULT TO FABRICATE.
INLET AND EXHAUST STRUTS	HIGH	MOD-HIGH	INTEGRAL WITH SURROUNDING STRUCTURE	LOW	..	TENACITY OF CERAMIC COATINGS ON METAL STRUTS.	EXISTING COOLED METAL DESIGN COULD BE RETAINED BY PROTECTING THE STRUTS WITH A THIN CERAMIC THERMAL BARRIER.
INLET AND EXHAUST STRUT CANS	LOW	HIGH	WELDED	NOT FEASIBLE	..	THIN, COMPLEXLY SHAPED.	THESE CANS WOULD BE REPLACED WITH A CERAMIC THERMAL BARRIER.

### Conclusions and Recommendations

Structural analysis based on finite element models and reliability calculations showed that properly designed ceramic turbine elements would be viable under the extremely hostile environment of an advanced SSME-type engine. Critical factors are high-thermal stresses caused by the extreme thermal shocks occurring during startup and shutdown, and the contact stresses generated by attachment methods.

An immediate concern is to experimentally evaluate high-performance structural ceramic materials under the severe thermal transient conditions of the SSME. The viability of ceramics under these conditions needs to be verified and candidate materials need to be compared and ranked in order of resistance to extreme thermal shock.

Longer range recommendations for future effort include additional tasks that will complement the so-called "Automotive Ceramic Initiative" program as planned and funded by NASA and DOE (Ref. 14). These additional tasks, listed below, are specific to rocket engine applications:

1. Expand data base to supply design properties specifically for advanced rocket engines.
2. Implement brittle materials design methodology to account for manrated systems.
3. Develop ceramic hardware fabrication processes for producing net-shape advanced rocket engine components of superior quality.
4. Adapt nondestructive evaluation and proof testing methods to advanced rocket engine hardware.
5. Develop prototype testing devices for evaluating ceramic components under advanced SSME-type environmental conditions of high pressure and extreme thermal shock.

### References

1. High-Temperature Turbine Program, Air Force Contract F04611-81-C-0053.
2. Pidcoke, L. and J. Gerstley, Transient Thermal Analysis of a 500K H<sub>2</sub>/O<sub>2</sub> First-Stage Fuel Turbine Ceramic Nozzle Vane, Rocketdyne Report No. ATU-83-5179, 8 December 1983.
3. Trela, W., Personal Communication, Ford Motor Company, 21 March 1984.
4. Caverly, J. C. and D. L. Hartsock, Evaluation of Ceramics for Stator Applications - Gas Turbine Engines, Final Report, NASA CR-165270, November 1980.
5. Johnson, C. F. and D. L. Hartsock, "Thermal Response of Ceramic Turbine Stators," Ceramics for High-Performance Applications, J. J. Burke, A. E. Gorum, and R. N. Katz, Editors, Brook Hill, pp. 549-562, 1974.
6. Carpenter, H. W., Ceramic Turbine Elements, Monthly Report for February 1984, Contract NAS8-35327, 10 March 1984.
7. Rollins, C. T., High-Temperature Turbine Ceramic Nozzle Structural Analysis, Rocketdyne Internal Report, IL-4-21-003, 5 March 1984.
8. Pasto, A. F., J. T. Niel, and C. L. Quackerbush, "Microstructural Effects Influencing Strength of Sintered Silicon Nitride," presented at the International Conference on Ultrastructure Processing of Ceramics, Glasses, and Composites, Gainesville, Florida, 13-17 February 1983.
9. Quackerbush, D. L., ibid.

10. Mangels, J. A. and G. J. Tennehouse, "Densification of Reaction-Bonded  $\text{Si}_3\text{N}_4$ ," American Ceramic Society Bulletin 59 (12), p. 1216, 1980.
11. Larsen, D. C., Property Screening and Evaluation of Ceramic Turbine Materials, AFML-TR-4188, October 1979.
12. Schnittgrund, G. D., Interim Report on Silicon Nitride Development, Rocketdyne IL-169-271, 18 September 1980.
13. Larsen, D. C. and J. W. Adams, "Property Screening and Evaluation of Ceramic Turbine Materials," Semi-Annual Interim Technical Report No. 11, Contract No. F33615-79-6-5100, November 1981.
14. Ceramic Technology for Advanced Heat Engines, Preliminary Progress Plan, Oakridge National Laboratory, Materials and Ceramic Division, Contract NoW-7405, 26 July 1983.

## VACUUM PLASMA COATINGS FOR TURBINE BLADES

Richard R. Holmes  
Materials & Processes Laboratory  
NASA/MSFC  
Marshall Space Flight Center, Alabama 35812

### Abstract

Recent occurrences of air foil cracks in flight engine turbine blades have re-emphasized the need for improved coatings, and work is being expedited to develop durable thermal barrier coatings and coating application processes. Significant progress has been realized in the turbine blade coating program with an attendant potential for improved SSME performance, improved safety, increased producibility, and reduced engine maintenance costs. Turbine blades, vacuum plasma spray coated with NiCrAlY, CoCrAlY or NiCrAlY/Cr<sub>2</sub>O<sub>3</sub> under contract with Howmet Corp., were evaluated and rated superior to standard SSME coated blades. Ratings were based primarily on 25 thermal cycles in the MSFC Burner Rig Tester, cycling between 1700°F (gaseous H<sub>2</sub>) and -423°F (liquid H<sub>2</sub>). These tests showed no spalling on blades with improved vacuum plasma coatings, while standard blades spalled. Thermal barrier coatings of ZrO<sub>2</sub>, while superior to standard coatings, lacked the overall performance desired. Fatigue and tensile specimens, machined from MAR-M-246(Hf) test bars identical to the blades were vacuum plasma spray coated, diffusion bond treated, and tested to qualify the vacuum plasma spray process for flight hardware testing and application. While NiCrAlY/Cr<sub>2</sub>O<sub>3</sub> offers significant improvement over standard coatings in durability and thermal protection, studies continue with an objective to develop coatings offering even greater improvements.

### Introduction

On April 12, 1981 the first Space Shuttle, Columbia, lifted off Kennedy Space Center Complex 39 with an

initial force of 375,000 lbs. The turbine blades in the High Pressure Fuel Turbopump of the SSME (Space Shuttle Main Engine) that supplies hydrogen to the combustion chamber were rotating at 34,700 rpm. Each turbine blade, about the size of a quarter (Figure 1), was developing roughly 600 Horse Power. Gaseous hydrogen flowing thru the turbopump heated the blades to approximately 1500°F for 500 seconds of flight operation. The turbopump subsequently shutdown in a fuel rich environment, with the blades quenched in liquid hydrogen at -423°F. This extreme and rapid thermal shock from 1500°F to -423°F, with the turbine blades under tremendous dynamic stress is a major contributor to blade cracking. This same thermal shock causes ceramic coatings once plasma sprayed on the blades as protective thermal barrier coatings to spall or flake off. The protective ZrO<sub>2</sub> (zirconia) thermal barrier coatings are no longer used on replacement blades because of the spalling problem.

The current overhaul cycle for the SSME fuel pump turbine blades is 3000 seconds (6 flights) with an ultimate goal of 27,500 sec (55 flights). Turbine blade cracks have been occurring within the existing 3000 second changeout period demonstrating the need for more durable protective thermal barrier coatings. Cracks have formed along the leading edges of the air foil of first stage fuel pump turbine blades and in the shank portion of the trailing edge adjacent to the platform of second stage fuel pump turbine blades. Blades are presently coated only with NiCrAlY bond coating which provides minimum thermal protection.

The goal of the program discussed herein is to develop a durable thermal barrier coating that will reduce the tendency toward crack formation and extend the effective performance life of the turbine blades. More durable coatings will allow the changeout cycle for the turbopump to be extended to 10 flights (5000 sec.), 15 flights (7500 sec), etc. until the goal of 55 flights (27,500 sec) is reached.

Baseline coatings for the SSME turbine blades were applied initially by plasma spray coating both NiCrAlY (Ni-16Cr-5.6Al-0.6Y) bond coating, and yttria stabilized zirconia ( $ZrO_2 \cdot 12Y_2O_3$ ), thermal barrier ceramic coating, at atmospheric conditions. Even after the zirconia coating was deleted from the application procedure, the NiCrAlY coating, .007" thick, spalled during operation but to a lesser degree than before, as shown by the turbine wheel in Figure 2. A literature search<sup>2,3</sup> indicated that a significant improvement in coating durability could be realized by applying the plasma coating in a vacuum. Vacuum plasma coatings offered the following advantages over atmospheric plasma sprayed coatings (Figures 3 & 4):

- (1). Exclusion of oxides
- (2). Denser, less porous coating
- (3). Reverse transfer arc cleaning
- (4). Mach 3 velocities
- (5). More uniform application (15" spray distance vs 3")
- (6). Improved coating thickness uniformity

Based on the literature search<sup>4,5,6,7</sup> and telephone discussions with leaders<sup>8</sup> in the plasma spray field, metal alloy bond coatings were narrowed to NiCrAlY, CoCrAlY and NiCoCrAlY while the thermal barrier ceramic coatings were narrowed to zirconia stabilized with, 8% and 12% yttria and to chromia. All known companies with vacuum plasma spraying capabilities were contacted, with competitive bid contracts let to Howmet Corporation, Whitehall, Michigan and Plasma Technics, Inc, Hollywood, Florida. Turbine blades of MAR-M-246(Hf) alloy (Ni-9Cr-10Co-2.5Mo-10W-1.5Ta-5.5Al-1.5Ti-0.15C-.015B-.055Zr-1.5Hf), rejected because of minor anomalies for use in space flight, but satisfactory for plasma coating development were obtained from Rocketdyne. Only blades vacuum plasma sprayed at Howmet are discussed in this study.

#### Vacuum Plasma Spray Process

The vacuum plasma spray facility and process used at Howmet have been fully described by Shankar, Koeing and Dardi<sup>2</sup>. The pilot facility consists essentially of a 4-ft diameter vacuum chamber with a 120KW EPI-03 plasma head from Electro Plasma, Inc., Irvine, California. Minus 200/+325 or -400 mesh powder was supplied to the plasma head using Model 1250 Roto-feed powder hoppers from Plasmadyne, Inc., Santa Ana, California. An inert gas mixture of 80% argon, 20% helium was used as the plasma arc gas while pure argon was used as the powder carrier gas. Both plasma gun and workpiece motion were controlled by a computer. The chamber was maintained at 20-60 torr by regulating the vacuum for a given plasma spraying condition. The workpiece was preheated to 1500-1700<sup>o</sup>F with the plasma gun power regulated between 80 and 90KW. Prior to coating, the turbine blades were electrically cleaned by negatively biasing the workpiece relative to the gun anode. Powder particles injected into the plasma arc stream were melted (or softened) and simultaneously accelerated toward the workpiece where they adhered on impact. Coating thickness was .006+.0015" for "M" CrAlY used alone or .003+.0015" with MCrAlY as a bond coating plus .004+.0015" of MCrAlY/Cr<sub>2</sub>O<sub>3</sub> thermal barrier coating on top. All vacuum plasma applied MCrAlY and MCrAlY/Cr<sub>2</sub>O<sub>3</sub> coatings were diffusion bond treated 4 hours in vacuum at 1975<sup>o</sup>F to enhance the degree of bonding. The coated blades were surface finished to reduce drag. No further treatment was considered, such as hot isostatic pressing (HIP) or shot peening because of zero to minimal improvements from such work reported in the literature<sup>2</sup>.

#### Coating Studies

Table I shows the results of the initial studies. Four MAR-M-246(Hf) HPFTP (High Pressure Fuel Turbopump) turbine blades were vacuum plasma sprayed for each condition with three blades each tested in the MSFC Burner Rig cyclic thermal tester (Figure 5). Each cycle duration was 15 seconds, cycling between the temperatures of gaseous hydrogen/steam

(1700°F) and liquid hydrogen (-423°F) simulating operation of the SSME. Actual chamber and blade temperatures were recorded at 1700°F and -350°F (Figure 6). The blades were tested 25 cycles and were examined after 5, 10 and 25 cycles.

With the exception of NiCoCrAlY, all other vacuum plasma sprayed MCrAlY coatings performed extremely well, showing no spalling after 25 cycles while the control, atmospheric plasma sprayed turbine blades, baseline for the SSME, spalled severely (Figure 7). NiCrAlY (Ni-16Cr-5.6Al-0.6Y) (Figure 8) vacuum plasma sprayed using -200/+325 mesh powder which is identical to the powder, atmospherically plasma sprayed on baseline SSME turbine blades, was rated best. Although statistically all samples were in the same population, -400 mesh CoCrAlY and -400 mesh NiCrAlY were rated 2nd & 3rd in that order. Plasma powder -200/+325 mesh is considered the limit in fineness that can be sprayed atmospherically, while the finer -400 mesh is considered optimum in producing a superior coating for vacuum plasma spraying. NiCoCrAlY, utilized as a powder for vacuum plasma spray coating jet aircraft turbine blades, cracked and spalled severely during the Burner Rig cyclic thermal testing.

The 50/50 blend of Cr<sub>2</sub>O<sub>3</sub> (Figure 9) with NiCrAlY or CoCrAlY, was applied because a good uniform coating could be produced with the existing plasma spray nozzle. All 50/50 Cr<sub>2</sub>O<sub>3</sub>/MCrAlY coatings were rated comparable to the 100% MCrAlY coatings in durability. A uniform spray could not be obtained with 50/50 blends of ZrO<sub>2</sub> and NiCrAlY, nor with 100% amounts of Cr<sub>2</sub>O<sub>3</sub> or ZrO<sub>2</sub> at this time.

Blades were plasma coated with zirconia several months later using an automated atmospheric spray chamber specifically installed by Howmet to spray ceramic powders. Blades were first vacuum plasma sprayed with .003+.0015 NiCrAlY, then with .004+.0015 ZrO<sub>2</sub>. Burner Rig thermal cyclic testing of the ZrO<sub>2</sub> coated blades showed erosion rather than spalling for the top rated blades. The

best thermal barrier coatings were rated 65-70 on a 100 equals perfect basis, being downgraded primarily because of erosion (Table 2). The erosion was attributed to a lower than desired  $ZrO_2$  coating density. No statistical difference was found in the top three coatings (65, 66, 70 Rating) with results showing no difference between  $ZrO_2$  stabilized with either 8% or 12%  $Y_2O_3$ . The 7%  $Y_2O_3$  stabilized zirconia was a Howmet proprietary coating and basically different from the 8% and 12% yttria stabilized coatings. Cracks appearing in the uncoated shank portion of the turbine blades were attributed to the diffusion bonding treatment. Therefore additional blades were coated with NiCrAlY bond coating,  $ZrO_2 \cdot 12Y_2O_3$  thermal barrier coating, diffusion bond treated and then aged 24 hours at  $1600^\circ F$  (Figure 10). Aging is a normal treatment in the manufacture of turbine blades. Although the zirconia coating rating improved from 65 to 75, cracks still persisted in the shanks following 25 Burner Rig cyclic thermal tests.

#### Physical Testing

Test bars were previously obtained that were produced from the same heat as the turbine blades being used in this development work. In the normal process of manufacturing turbine blades, the MAR-M-246(Hf) blades are first cast, solution treated 2 hours in vacuum at  $2230^\circ F$ , aged 24 hours at  $1600^\circ F$ , machined, inspected, and later plasma spray coated with -200/+325 mesh NiCrAlY. The test bars were subjected to the same processing conditions as the turbine blades thru the aging cycle, and were machined into tensile strength test specimens (2 each condition) and fatigue test specimens (4 each condition) as shown in Table 3. The test specimens were vacuum plasma coated with NiCrAlY bond coating, plasma coated with  $ZrO_2 \cdot 12Y_2O_3$  thermal barrier coating and subsequently diffusion bond treated under identical conditions used for the turbine blades. Table 3 shows comparable tensile strengths for coated specimens non-treated and diffusion bond treated.

Fatigue specimens, diffusion bond treated 4 hours in vacuum at 1975°F and aged 24 hours at 1600°F, were in the same statistical population as the control, requiring 2.7 million cycles to break vs 2.9 million. The control was uncoated and untreated. Looking toward future blade coating studies, one set of fatigue specimens was solution treated 2 hours in vacuum at 2230°F, plasma sprayed first with NiCrAlY followed by  $ZrO_2 \cdot 12Y_2O_3$  and then diffusion bond treated 4 hrs at 1975°F and aged 24 hrs at 1600°F. These four fatigue specimens broke in a close tolerance range and averaged 5.2 million cycles to failure vs. 2.9 million for the control. This work offers the potential of not only producing improved coatings for turbine blades but also reducing the tendency toward cracking on the exposed shank and fir tree areas of the blades.

Studies are continuing in the Metallic Materials Division of the Materials and Processes Laboratory, to investigate the following for each plasma blade coating and treatment condition listed in Tables 1 & 2: (1) Microstructural changes, (2) Bond Interface, (3) Coating Integrity, (4) Mechanical Properties and (5) Crack Initiation.

During this development period, work has been in progress to procure and install an automated 120 KW LPPS (Low Pressure Plasma Spray) unit from Electro-Plasma Inc. This unit, bought thru competitive procurement, was placed in service at MSFC in July 1984.

Currently planned studies involve utilizing our new LPPS (Low Pressure Plasma Spray) unit at MSFC and the plasma expertise in Industry to continue our development effort to produce a durable thermal barrier coating for the SSME (Space Shuttle Main Engine) fuel turbopump turbine blades. These studies will continue our work with 50/50 blends of  $Cr_2O_3$  and NiCrAlY that have performed so satisfactorily in Burner Rig testing plus 50/50 blends of  $ZrO_2$  and NiCrAlY and 90/10 blends of

Cr<sub>2</sub>O<sub>3</sub> or ZrO<sub>2</sub> with NiCrAlY. Results of the metallurgical studies will be utilized in conjunction with refinements to blade heat treatments involving solutioning (2230°F), diffusion bonding (1975°F) and ageing (1600°F).

#### Conclusion

A 50/50 blend of Cr<sub>2</sub>O<sub>3</sub> and NiCrAlY plasma sprayed on SSME high pressure fuel turbopump turbine blades provided significant improvements in coating durability and thermal protection when tested in a simulated service environment. The success of these studies warrants their continuation and the expansion of testing to include qualification in flight configured turbines.

#### References

1. Hill, V.L. and Humphreys, V.E., "Thermal Fatigue And Oxidation Data For Directionally Solidified Mar-M-246 Turbine Blades", NASA CR-159798, Jan. 1980.
2. Shankar, S., Koenig, D.E. and Dardi, L.E., "Vacuum Plasma Sprayed Metallic Coatings", Journal of Metals, Vol. 33, No. 10, Oct. 1981, p. 13-20.
3. Gupta, D.K. and Pennisi, F.J., "Manufacturing Technology For Vacuum Plasma Spray Overlay Coatings" AFWAL/MLTM FR 16485, Seventh Interim Report, Apr. 1, 1982 thru June 30, 1982.
4. Stepka F.S., Liebert, C.H., and Stecura, S., "Summary Of NASA Research On Thermal-Barrier Coatings" Society of Automotive Engineers, International Automotive Engineering Congress and Exposition, Detroit, Mich. Feb. 28 - Mar. 4, 1977, Paper 27, p9.
5. Liebert C.H., Jacobs, R.E., Stecura, S. and Morse, C.R., "Durability Of Zirconia Thermal Barrier Ceramic Coatings On Air-Cooled Turbine Blades In Cyclic Jet Engine Operation" NASA TMX-3410, Sept.

1976.

6. Gladden, H.J. and Liebert, C.H., "Effects Of A Ceramic Coating On Metal Temperatures Of An Air-Cooled Turbine Vane", NASA TP-1598, Feb. 1980.

7. Stecura, Stephan, "Two-Layer Thermal Barrier Coating For Turbine Airfoils - Furnace And Burner Rig Test Results", NASA TMX-3425, Sept. 1976.

8. Gupta, D.K., Pratt & Whitney Aircraft Corp.; Frandsen, J.D., Rocketdyne; Dardi, L.E., Howmet Corp.; and Gilmore, H.L., NASA/MSFC private communications (1981).

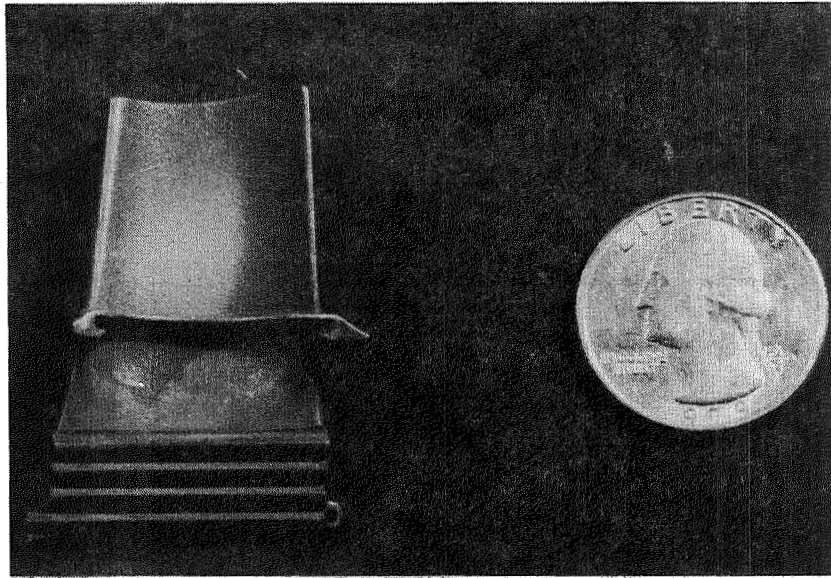


**FIGURE 1. SSME FIRST STAGE HIGH PRESSURE FUEL TURBOPUMP TURBINE BLADE THAT DEVELOPS ROUGHLY 600 HP AT LIFTOFF, COMPARED TO A 25¢ PIECE.**

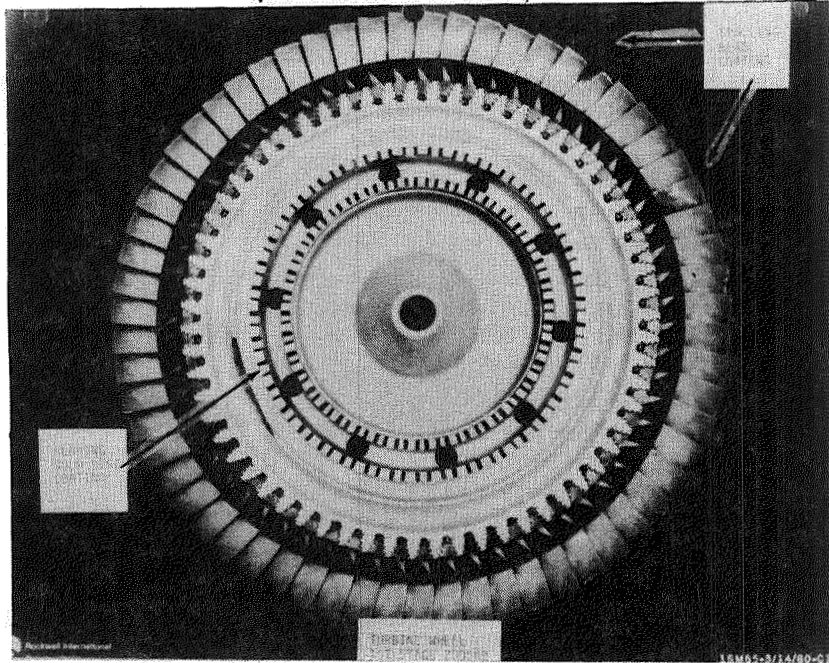


**FIGURE 2. SSME FIRST STAGE HIGH PRESSURE FUEL TURBOPUMP TURBINE WHEEL SHOWING SPALLED TURBINE BLADES.**

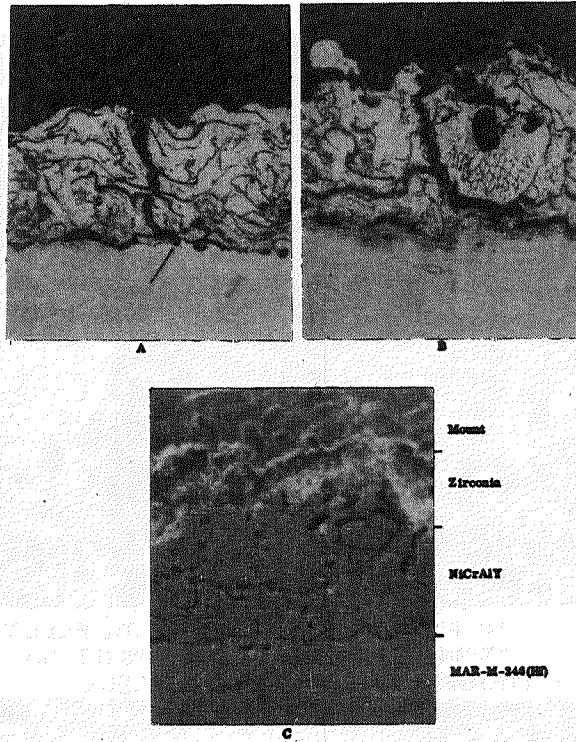


**FIGURE 3. NiCrAlY AIRFOIL LEADING EDGE CRACKING ON BLADE 9Z13 FROM HPFTP 9005 (A&B) AND THIN LAYER OF ZIRCONIA ON NiCrAlY (C). MAG. 400X**

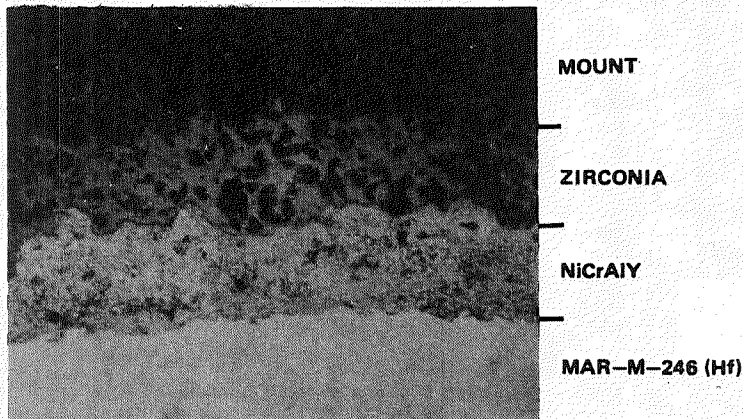


**FIGURE 4. NiCrAlY AIRFOIL LEADING EDGE APPLIED BY LOW PRESSURE PLASMA FLAME SPRAY SHOWING IMPROVEMENTS: (1) NO CRACKS IN NiCrAlY BOND COATING. (2) NO OXIDE LAYERS IN NiCrAlY BOND COATING. MAG. 200X**

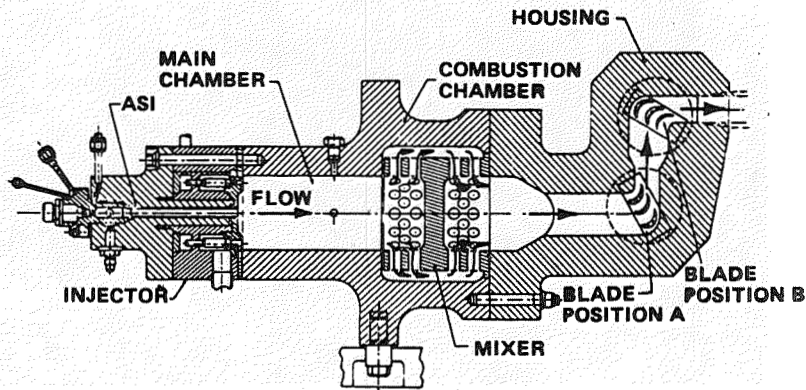


FIGURE 5. BURNER RIG THERMAL CYCLING TESTER

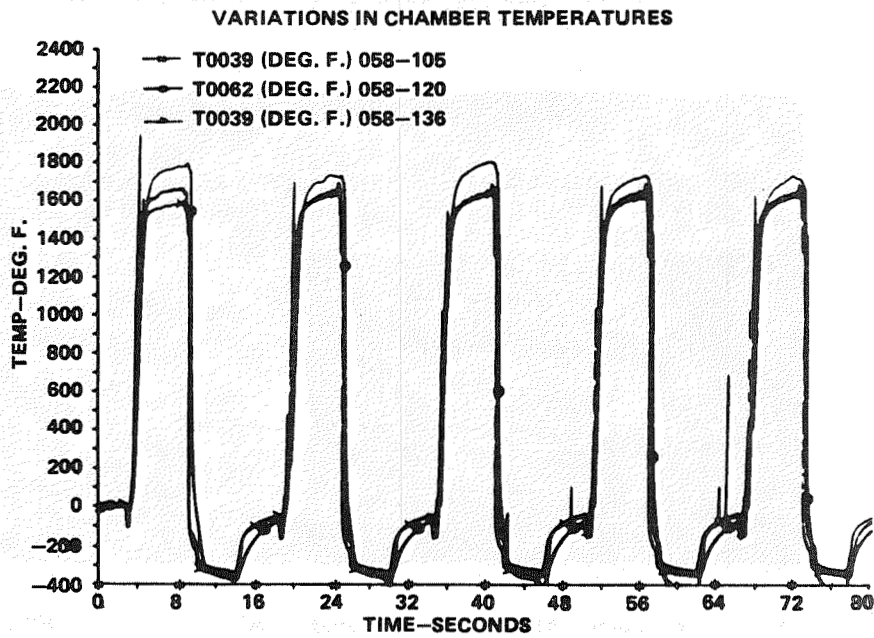
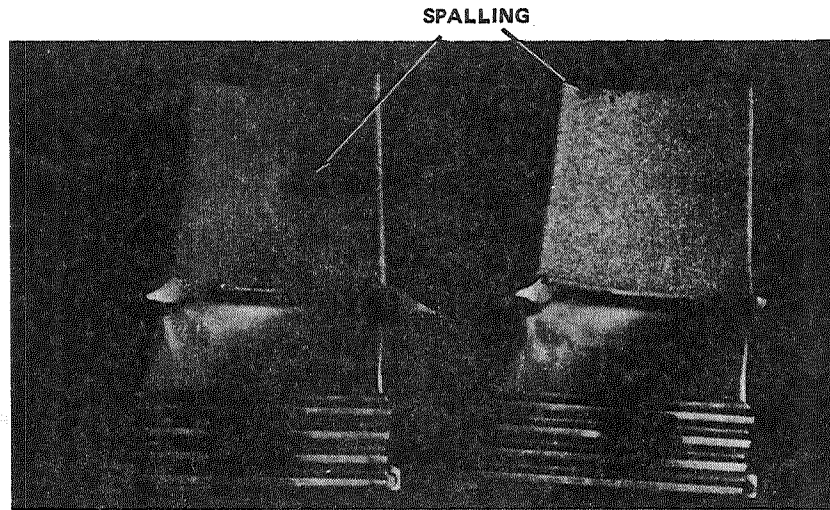
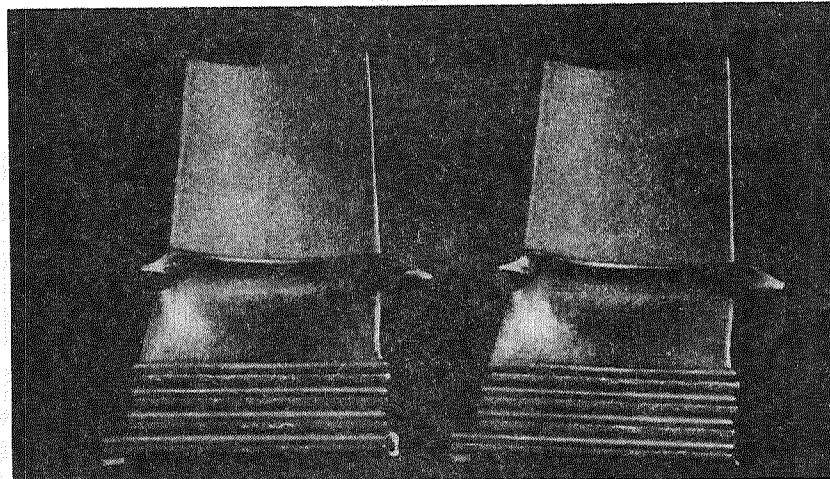


FIGURE 6. VARIATIONS IN BURNER RIG CHAMBER TEMPERATURE OVER FIVE 15 SECOND CYCLES BETWEEN 1700°F AND -350°F.



**FIGURE 7. BASELINE SSME TURBINE BLADES, ATMOSPHERICALLY PLASMA SPRAY COATED WITH .007" -200/+325 MESH NiCrAlY AND TESTED 25 CYCLES IN MSFC BURNER RIG BETWEEN 1700°F AND -350°F.**



**FIGURE 8. SSME TEST TURBINE BLADES VACUUM PLASMA SPRAY COATED WITH .006" -200/+325 MESH NiCrAlY AND TESTED 25 CYCLES IN MSFC BURNER RIG BETWEEN 1700°F AND -350°F.**

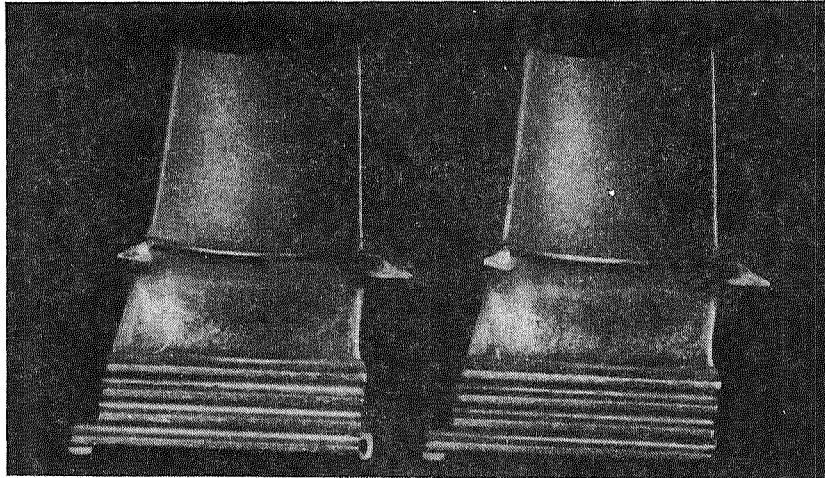


**FIGURE 9. SSME TEST TURBINE BLADES VACUUM PLASMA SPRAY COATED WITH .003" -400 MESH NiCrAlY, AND .004" 50/50 NiCrAlY/Cr<sub>2</sub>O<sub>3</sub> AND TESTED 25 CYCLES IN MSFC BURNER RIG BETWEEN 1700°F AND -350°F.**

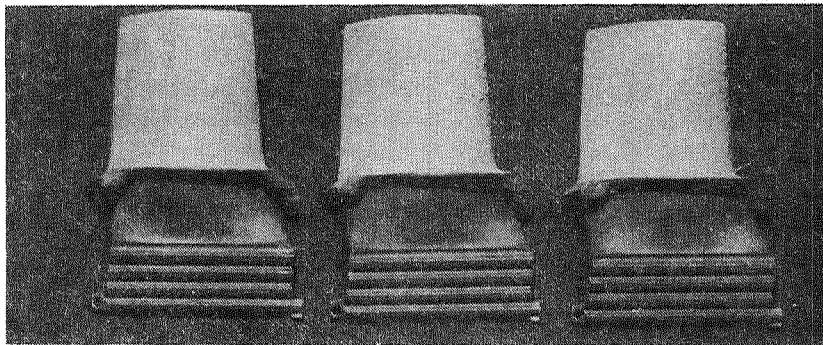


**FIGURE 10. SSME TEST TURBINE BLADES VACUUM PLASMA SPRAY COATED WITH .003" -200/+325 MESH NiCrAlY AND ATMOSPHERICALLY SPRAYED WITH .004" -200/+325 MESH ZrO<sub>2</sub> AND TESTED 25 CYCLES IN MSFC BURNER RIG BETWEEN 1700°F AND -350°F.**

TABLE 1  
 PLASMA COATED TURBINE BLADES  
 BURNER RIG CYCLIC THERMAL TESTING  
 25 CYCLES (1700°F TO -350°F)

<u>VACUUM SPRAY POWER MESH</u>	<u>BOND COATING*</u>	<u>THERMAL BARRIER COATING (4 MIL)</u>	<u>RATING** 100=PERFECT</u>	<u>COMMENTS</u>
-200/+325	NiCrAlY	-	95	NO SPALLING
-400	CoCrAlY	-	94	NO SPALLING
-400	NiCrAlY	-	93	NO SPALLING
-200/+325	NiCrAlY	Cr <sub>2</sub> O <sub>3</sub> .50 NiCrAlY	94	NO SPALLING
-400	CoCrAlY	Cr <sub>2</sub> O <sub>3</sub> .50 CoCrAlY	94	NO SPALLING
-400	NiCrAlY	Cr <sub>2</sub> O <sub>3</sub> .50 NiCrAlY	93	NO SPALLING
-200/+325	NiCoCrAlY	-	25	SPALLING
<u>ATMOSPHERIC SPRAY SSME BASELINE</u>				
-200/+325	NiCrAlY	-	35	SPALLING

\* BOND COATING ONLY : 6 MIL THICKNESS  
 BOND COATING BEFORE ADDING THERMAL BARRIER COATING: 3 MIL THICKNESS

\*\* 3 BLADES EACH SAMPLE

TABLE 2  
 PLASMA COATED TURBINE BLADES  
 BURNER RIG CYCLIC THERMAL TESTING  
 25 CYCLES (1700°F TO -350°F)

VACUUM SPRAY MESH	BOND COATING (3 MIL)	THERMAL BARRIER COATING (4 MIL)	DIFFUSION BOND 4 HRS VAC	RATING † 100=PERFECT
-200/+325	NiCrAlY	ZrO <sub>2</sub> . 12Y <sub>2</sub> O <sub>3</sub>	1975°F**	75
-200/+325	NiCrAlY	ZrO <sub>2</sub> . 8Y <sub>2</sub> O <sub>3</sub>	1975°F	66
-200/+325	NiCrAlY	ZrO <sub>2</sub> . 12Y <sub>2</sub> O <sub>3</sub>	1975°F	65
-200/+325	NiCrAlY	ZrO <sub>2</sub> . 7Y <sub>2</sub> O <sub>3</sub> *	1975°F	70
-400	NiCrAlY	ZrO <sub>2</sub> . 8Y <sub>2</sub> O <sub>3</sub>	1975°F	51
-400	NiCrAl*	ZrO <sub>2</sub> . 7Y <sub>2</sub> O <sub>3</sub> *	1975°F	31
-400	CoCrAl*	ZrO <sub>2</sub> . 7Y <sub>2</sub> O <sub>3</sub> *	1975°F	21

\* PROPRIETARY COATINGS

\*\* AGED 24 HRS @ 1600°F AFTER DIFFUSION BOND TREATMENT

† 3 BLADES EACH SAMPLE

TABLE 3  
PLASMA COATED TEST SPECIMENS  
TESTED AT 1500°F

VACUUM SPRAY MESH	BOND COATING	THERMAL BARRIER COATING	DIFFUSION BOND 4 HRS @ °F	AGEING 24 HRS	TENSILE <sup>†</sup> STREN. (LB/IN. <sup>2</sup> )
-200/+325	NiCrAlY	ZrO <sub>2</sub> .12Y <sub>2</sub> O <sub>3</sub>	—	—	147,000
-200/+325	NiCrAlY	ZrO <sub>2</sub> .12Y <sub>2</sub> O <sub>3</sub>	1975°F	1600°F	154,000
					FATIGUE LIFE <sup>†</sup> (CYCLES)
-200/+325	NiCrAlY	ZrO <sub>2</sub> .12Y <sub>2</sub> O <sub>3</sub>	1975°F	1600°F	2.7 x 10 <sup>6</sup>
-200/+325	NiCrAlY	ZrO <sub>2</sub> .12Y <sub>2</sub> O <sub>3</sub>	1975°F	1600°F	5.2 x 10 <sup>6*</sup>
-400	CoCrAl**	ZrO <sub>2</sub> .7Y <sub>2</sub> O <sub>3</sub> **	1975°F	1600°F	2.9 x 10 <sup>6</sup>
NO COATING	CONTROL	—	—	—	2.9 x 10 <sup>6</sup>

\* THESE TEST SPECIMENS DIFFER FROM THE OTHERS IN THAT AFTER MACHINING FROM TEST BARS, THEY WERE SOLUTION TREATED AT 2230°F FOR 2 HRS IN VACUUM BEFORE PLASMA SPRAYING WITH NiCrAlY FOLLOWED BY ZrO<sub>2</sub>.12Y<sub>2</sub>O<sub>3</sub>. ALL PLASMA COATED FATIGUE SPECIMENS WERE SUBSEQUENTLY DIFFUSION BOND TREATED 4 HRS AT 1975°F IN VACUUM AND AND AGED 24 HRS AT 1600°F IN AIR.

\*\* HOWMET PROPRIETARY COATINGS

† 2 TEST SPECIMENS EACH TENSILE TEST

† 4 TEST SPECIMENS EACH FATIGUE TEST

## MATERIAL TECHNOLOGY

Robert L. Dreshfield  
Metallic Materials Branch  
Lewis Research Center  
Cleveland, Ohio 44135

and

W. B. McPherson  
Materials & Process Laboratory  
Marshall Space Flight Center  
Huntsville, Alabama 35812

Advanced high pressure  $O_2/H_2$  propulsion systems as exemplified by the Space Shuttle Main Engine (SSME) create challenging operating environments for materials. For example, the high pressure fuel pump turbine materials are subjected to thermal transients without precedent in man-rated reusable turbo-machinery. Many components operate in either hydrogen or hydrogen-steam environments which may significantly degrade the performance of common alloys. These difficult operating conditions have caused a variety of durability concerns for this class of propulsion system.

The objective of the materials technology projects is to develop and evaluate candidate materials for application in advanced high pressure  $O_2/H_2$  propulsion systems. These new and improved materials are to improve the durability or performance of the SSME or derivative engine.

The program includes projects on the following topics:

- Hydrogen Resistant Alloys
- High Pressure  $O_2$  Ignition and Burning
- Improved Turbine Blades
- Improved Turbine Disk Material
- Impact Reactivity in High Pressure  $O_2$
- Fiber Reinforced Superalloys

Advanced Coating Techniques  
Advanced Turbopump Blade Materials Analysis  
Weld Cracking in Inconel 718  
Bearing Alloys for Cryogenic Applications

The papers that follow will include papers on: turbopump blade materials, effects of hydrogen on alloys, effects of oxygen on both metals and elastomers, understanding of microstructural relationship to weld cracking in Inconel 718 and requirements for advanced turbopump bearings. These papers are from industry, university, and government sources reflecting the integrated nature of our program which attempts to include work done in a variety of laboratories throughout the country.

DESIGN OVERVIEW OF FIBER-REINFORCED SUPERALLOY  
COMPOSITES FOR THE SPACE SHUTTLE MAIN ENGINE

J. R. Lewis

Rockwell International/Rocketdyne Division  
Canoga Park, California

Abstract

This preliminary design study evaluated the potential of fiber-reinforced superalloys (FRS) for hot-section components of Space Shuttle Main Engine turbo-pumps. Emphasis was placed on uncooled turbine blades, with a more limited evaluation of FRS turbine stator vanes. The study included FRS properties evaluation, current structural design capability, and preliminary design and structural analysis. In addition, key technology needs were identified, and a plan was generated to develop operational hardware for advanced versions of the SSME. Certain features of the program fell under the constraints of Federal Regulation 22 USC 2278, and will not be discussed in this paper.

Based on projections of design properties for FRS composites comprising 50 volume percent of W-4Re-0.38Hf-0.02C wire filaments in a ductile superalloy matrix, it was concluded that FRS turbine blades offer the potential of significant improved operating life and higher temperature capability over the MAR-M-246(Hf) (DS) blades currently used in the SSME.

A technology plan was devised to bring an FRS turbine blade to a state of operational readiness. It was recommended that the first priority in future work should be placed on acquiring an adequate design data base for tensile, fatigue, thermal shock, and environmental behavior of the FRS composite.

Introduction

Requirements for improved performance and longer life in advanced, liquid propellant rocket engines have

focused attention on the potential benefits of composite materials for high-temperature components of the turbines. Space Shuttle Main Engine (SSME) turbine blades (Fig. 1) are currently replaced after about 5000 seconds operation because of fatigue, and even more severe thermal and aerodynamic environments are projected for advanced versions of oxygen/hydrogen engines. It is for this reason that a study program was activated to explore the application of filament-reinforced

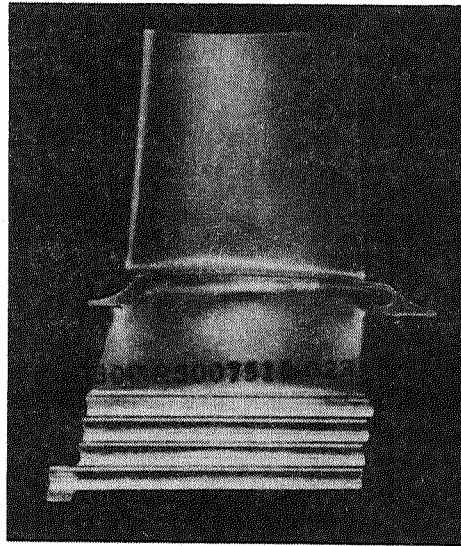


Fig. 1. Present SSME Blade Configuration for First-Stage High-Pressure Fuel Turbopump

superalloys (FRS) to hot-section elements of an advanced oxygen/hydrogen engine. The first-stage blades of the high-pressure fuel turbine were chosen as the reference system, and a preliminary design was undertaken based on high-strength tungsten alloy filaments in a ductile superalloy matrix. A final report for the program (Ref. 1) is available from NTIS, Springfield, VA.

#### Technical Issues

Historically, rocket engine materials have been drawn from an alloy pool developed for use in the airframe and air-breathing turbine industry. This has also been the case for composite materials, at least during the early developmental stages of composite rocket engine hardware. However, it is important to recognize that significant differences exist between the operating and design requirements for rocket engine turbines and those of their counterpart aircraft gas turbines. As can be seen from Table 1, rocket engine turbines may operate at considerably higher

Table 1. Comparison of Operation Characteristics  
Between Representative Rocket Engine  
and Aircraft Gas Turbines

ITEM	ROCKET ENGINE TURBINES	AIRCRAFT GAS TURBINES
FUEL	HYDROGEN OR METHANE	PETROLEUM DISTILLATE
OXIDIZER	OXYGEN	AIR
OPERATING RANGE, RPM	36,000 TO 110,000	15,000
BLADE TIP SPEED, FT/SEC	1,850	1,850
HORSEPOWER/BLADE	630	200 TO 400
TURBINE INLET TEMPERATURE, F	1,600 TO 2,200	2,600
HEAT TRANSFER COEFFICIENT, BTU/FT <sup>2</sup> -HR-F	54,000	500
THERMAL START/STOP TRANSIENTS, °F/SEC	32,000/7,000	100
ENGINE STARTS	55 TO 70	2,400
OPERATIONAL LIFE, HOURS	7.5 TO 100	8,000

temperature transients that produce higher temperature gradients and thus higher thermal fatigue strains. On the other hand, compared to aircraft gas turbines, rocket engine turbines design lifetimes are much shorter--in the vicinity of 10 hours versus thousands of hours. Thus, for rocket engine turbine materials, one is more interested in short-time tensile strengths; high-thermal strain, low-cycle fatigue; and high mean stress, high-cycle fatigue, but less interested in long-time creep strength and lower mean stress, high-cycle fatigue, which are of greater concern for aircraft gas turbines.

The high operating speeds of the SSME turbine ( 36,000 rpm) and the alternating bending loads imposed as turbine blades revolve past the stator nozzles lead to an expected fatigue life of the order of  $10^8$  cycles for the MAR-M246(Hf)(DS) blades presently used in the SSME turbine, so that the blade life is fatigue limited. It is a matter of policy to inspect all turbine blades at frequent intervals and to refit the turbine with new blades after about 5000 seconds (1.4 hours) of operation.

Rocket engine turbine materials are not exposed to sulfidation, and, because of the short times of operation, oxidation is less of a concern than in aircraft gas turbines. However, since the SSME turbine is in reality a hydrogen-rich steam turbine, there is a potential for hydrogen environmental embrittlement (HEE) when components are exposed to the high-pressure hydrogen fuel. This factor must also be considered in the selection of matrix alloys for the fiber-reinforced superalloy composites.

Currently, there are some quite sophisticated efforts under way to extend the functional capabilities of materials for aircraft gas turbines. Examples include the production of turbine blades from single crystals, from rapid solidification process (RSP) superalloy powders, directionally solidified eutectic (DSE) superalloys, oxide dispersion strengthened (ODS) superalloys, and fiber-reinforced superalloys (FRS). Fiber-reinforced superalloys have the potential for the highest strengths at high temperatures of any of these advanced superalloys, but they are in a relatively early stage of development and a number of details must be resolved (e.g., reaction and interdiffusion between reinforcing wire and matrix, reaction of reinforcing wire and matrix with environment, thermal fatigue behavior, and details of design and fabrication). Their higher density, particularly when tungsten is used as the reinforcing wire (and tungsten has been the most popular and highest strength reinforcing wire explored to date) is also a matter to be considered, particularly for turbine blade applications.

#### Fiber-Reinforced Superalloy Data Base

The FRS materials system selected as the baseline for this study was based on high-strength W-4Re-0.38Hf-0.02C wire filaments coupled with a high ductility superalloy matrix such as Waspaloy, Incoloy 903, FeCrAlY or type 316 stainless steel. Since experimental properties data for these specific composite systems are limited, it was necessary to project design properties through rule-of-mixtures or similar predictive methods.

It must be understood, therefore, that the properties cited in this paper are, for the most part, predicted properties and have yet to be substantiated by appropriate testing.

Recent investigations (Ref. 2-5) of fatigue behavior of composite materials indicate that when the strength of the fiber is significantly greater than that of the matrix, then both low-cycle fatigue (LCF) and high-cycle fatigue (HCF) are controlled by the fibers. Since the operational life of rocket engine turbine blades is expected to be fatigue limited, we selected the strongest known tungsten alloy (W-4Re-0.38Hf-0.02C) as the reference fiber material upon which the projected properties data were based.

The considerations for selecting the matrix material for the FRS blade included:

1. Compatibility with the environment, e.g., hydrogen or hydrogen/steam
2. Compatibility with tungsten wire (fiber degradation)
3. Bond strength between the reinforcement and matrix
4. Thermal fatigue resistance
5. High-cycle fatigue behavior

In the presence of hydrogen, particularly at high pressure and at moderate temperatures, the ductility and notch strength of susceptible alloys can be degraded and crack growth increased if the alloy is subjected to inelastic strain at the time of exposure. This effect has become known as Hydrogen Environment Embrittlement (HEE), and was one consideration in selection of matrix alloys for the fiber-reinforced superalloy systems.

Metallurgical compatibility between matrix and reinforcing filament requires a composite between two opposing requirements. On the one hand, a strongly bonded interface is desirable to accommodate transfer

and distribution of load within the composite structure; on the other hand, excessive diffusion of matrix alloying elements can degrade or embrittle the reinforcing fiber. Fiber degradation can be an important factor at operating temperatures above 980 C (1800 F) and for exposures greater than a few hundred hours; it is less of a factor, however, for operational exposures below 100 hours, as is the case for rocket engine applications.

Matrix alloys also play an important role in thermal fatigue, where the ductility of the matrix and its ability to accommodate plastic strain can govern thermal fatigue behavior of the composite (Ref. 6). The degree of mismatch between thermal coefficient of expansion of matrix and fiber is a key factor in thermal fatigue, since this will establish the internal strain at the matrix/fiber interface.

Based on the foregoing selection criteria, five materials were considered as candidate matrix materials. These were Incoloy 903, FeCrAlY alloy, 316L stainless steel, Astroloy, and Waspaloy. Projected design-minimum mechanical properties of these materials are listed in Table 2, and comparative thermal expansion curves are shown in Fig. 2. It is projected that the high-cycle fatigue and low-cycle fatigue behavior of the fiber-reinforced superalloy composite will be governed by the W-Re-Hf-C wire, and that the thermal fatigue behavior will be governed by the properties of the matrix. In this respect, it is desirable to have a ductile matrix material whose thermal expansion is near that of tungsten. The advantage of having ductile matrix materials is twofold: (1) to accommodate the microscopic isothermal strain generated from the differential thermal expansion coefficients between the fiber and the matrix and (2) to accommodate the macroscopic thermal strain generated by the transient thermal gradients during engine start and shutdown.

In Fig. 3 and 4, projections have been made of tensile and specific tensile strengths of candidate fiber-reinforced composite systems based upon incorporation of W-4Re-0.38Hf-0.02C fiber in various superalloy matrix alloys. In all cases, 50 volume

Table 2. Projected Design-Minimum Properties for Candidate FRS Matrix and Reinforcement Materials\*

MATERIAL	TEMPERATURE		F <sub>ty</sub>		F <sub>tu</sub>		ELONGATION, PERCENT	REMARKS
	°C	°F	MPa	ksi	MPa	ksi		
INCOLOY 903	-195	-320	930	135	1200	175	16	ADJUSTED FOR EXPOSURE TO HYDROGEN-STEAM ENVIRONMENT
	20	70	635	92	930	135	16	
	700	1300	480	70	620	90	8	
	845	1550	70	10	100	15	15	
	1090	2000	14	2	35	5	15	
316 STAINLESS STEEL	-195	-320	290	42	1070	155	40	NO SIGNIFICANT DEGRADATION IN HYDROGEN-STEAM ENVIRONMENT
	20	70	170	25	480	70	40	
	845	1550	35	5	110	16	38	
	1090	2000	14	2	30	4	60	
WASPALOY	-195	-320	1170	170	1550	225	10	ADJUSTED FOR HYDROGEN ENVIRONMENTAL EFFECTS
	20	70	1000	145	1240	180	12	
	370	700	930	135	1200	175	6	
	845	1550	275	40	510	75	23	
	1090	2000	35	5	70	10	30	
ASTROLOY	-195	-320	1030	150	1510	220	15	ADJUSTED FOR HYDROGEN ENVIRONMENTAL EFFECTS
	20	70	965	140	1310	190	15	
	370	700	930	135	1240	180	13	
	845	1550	550	80	760	110	30	
	1090	2000	35	5	70	10	30	
FeCrAlY (25 Cr)	-195	-320	--	--	--	--	--	EFFECTS OF HYDROGEN ENVIRONMENT UPON MECHANICAL BEHAVIOR ARE UNKNOWN
	20	70	240	35	410	60	10	
	845	1550	25	4	50	7	60	
	1090	2000	7	1	8	1.5	100	
W-Re-Hf-C (Wire)	-195	-320	--	--	--	--	--	PROPERTIES ESTIMATES BASED ON LIMITED DATA
	20	70	--	--	2750	400	4	
	845	1550	--	--	2060	300	4	
	1090	2000	--	--	1860	270	4	

\* SEE FIGURE 2 FOR THERMAL EXPANSION DATA

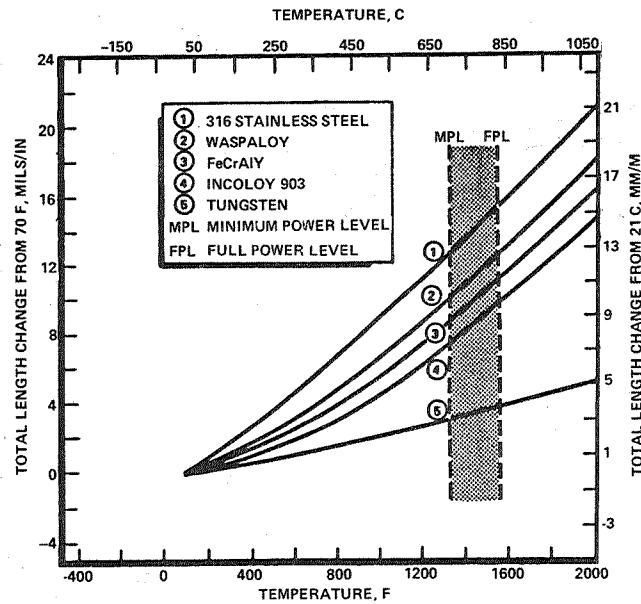


Fig. 2. Comparisons of the Thermal Expansion of Candidate FRS Materials

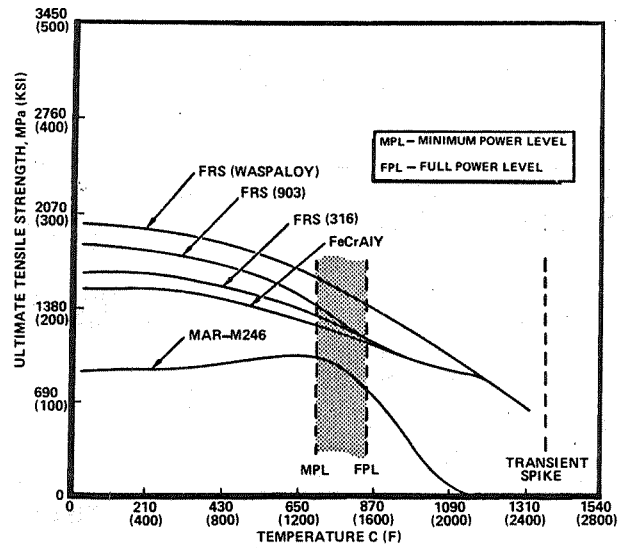


Fig. 3. Projected Tensile Strengths of Candidate FRS Composites

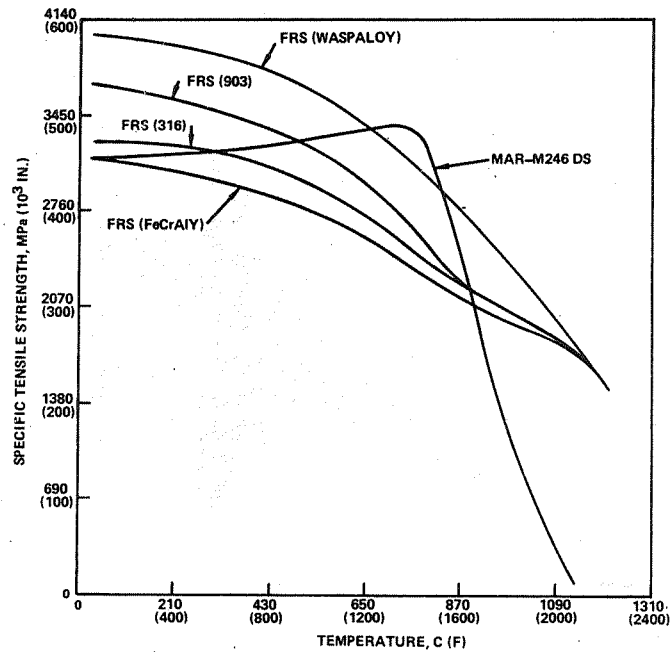


Fig. 4. Projected Specific Strengths of Candidate FRS Composites

percent of the tungsten alloy has been assumed. It will be noted that in all cases, an advantage in tensile strength is apparent over the MAR-M246(DS) blade material currently used in the SSME turbines. When specific strength is considered (Fig. 4), the advantage becomes less apparent below 870 C (1600 F). As a consequence of the higher density of the composite  $14 \text{ g/cm}^3$  ( $0.5 \text{ lb/in.}^3$ ), axial stresses in the denser blade will become higher as a result of centrifugal forces.

Using available fatigue data for FRS composites, a Goodman diagram has been projected (Fig. 5) showing the projected fatigue behavior of a W-Re-Hf-C/Waspaloy

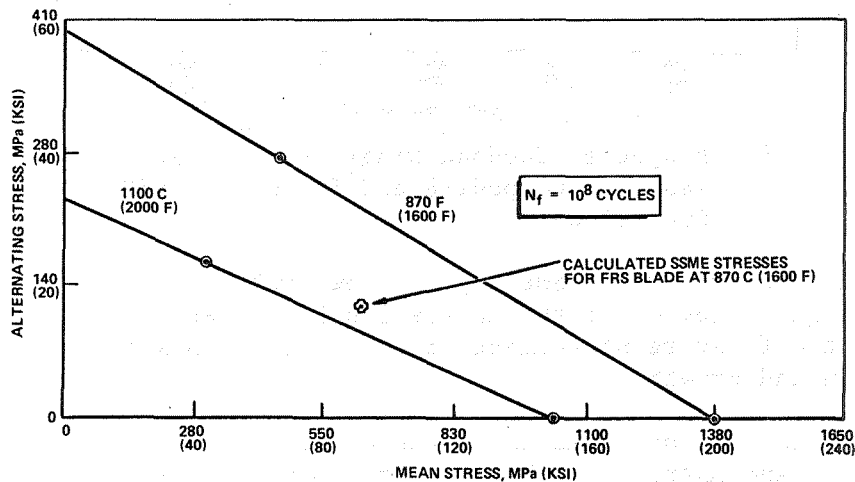


Fig. 5. Projected Goodman Diagram for W-Re-Hf-C/Waspaloy Composite

composite as a function of combined axial and flexural stresses. Curves are projected for 870 C (1600 F) and 1090 C (2000 F) for a fatigue life of  $10^8$  cycles. In addition, the calculated stresses at the root of the FRS airfoil devised for this application is also shown in Fig. 5. The projected high-cycle fatigue behavior of FRS turbine blades is compared to that of the current MAR-M246(Hf)(DS) alloy in Fig. 6. Fatigue behavior is expected to be influenced, under conditions

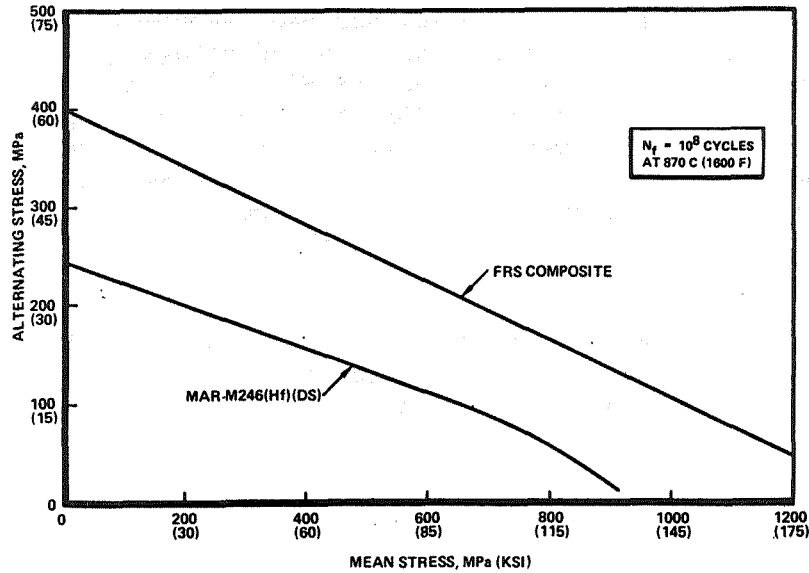


Fig. 6. Projected Goodman Diagrams for W-Re-Hf-C/Waspaloy Composite and for MAR-M246(Hf)(DS) Superalloy

encountered in the SSME, by the low-cycle (inelastic) fatigue behavior of the matrix and by the resistance of the fiber reinforcement to high-cycle crack initiation and growth.

Because of mismatch in thermal expansion between fiber and matrix, isothermal strain will occur. Figure 7 indicates the strain mismatch that will exist for four candidate matrix alloys, assuming equilibrium at 20 C (70 F). Incoloy 903 would result in the lowest thermal strain mismatch, with Waspaloy and FeCrAlY being about 30 percent higher. Waspaloy, on the other hand, is more ductile than Incoloy 903 and thus may be more capable of withstanding cyclic thermal strain. Although very little strain-controlled, low-cycle fatigue data have been generated for FRS composites, an attempt has been made to project a range of low-cycle fatigue behavior using the Manson-Coffin approach. The results are shown in Fig. 8. The upper and lower limits of the estimated range were derived

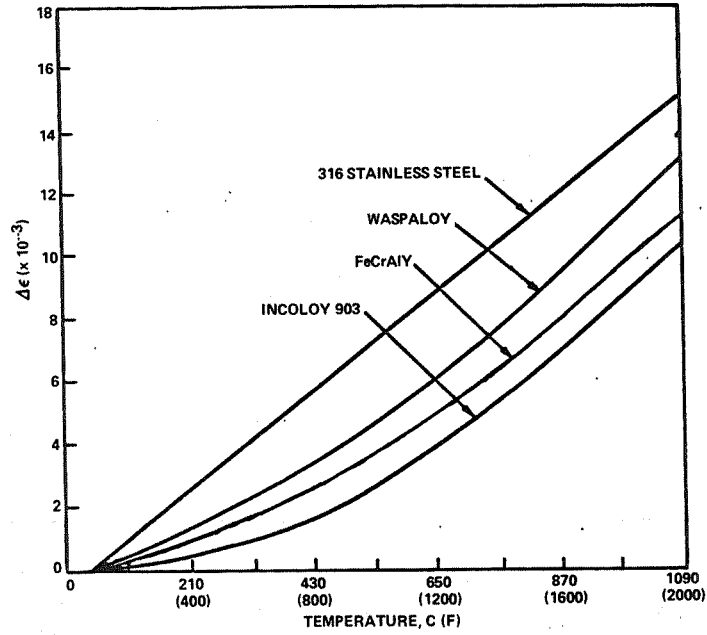


Fig. 7. Thermal Strain at Fiber/Matrix Interface for Candidate FRS Composites

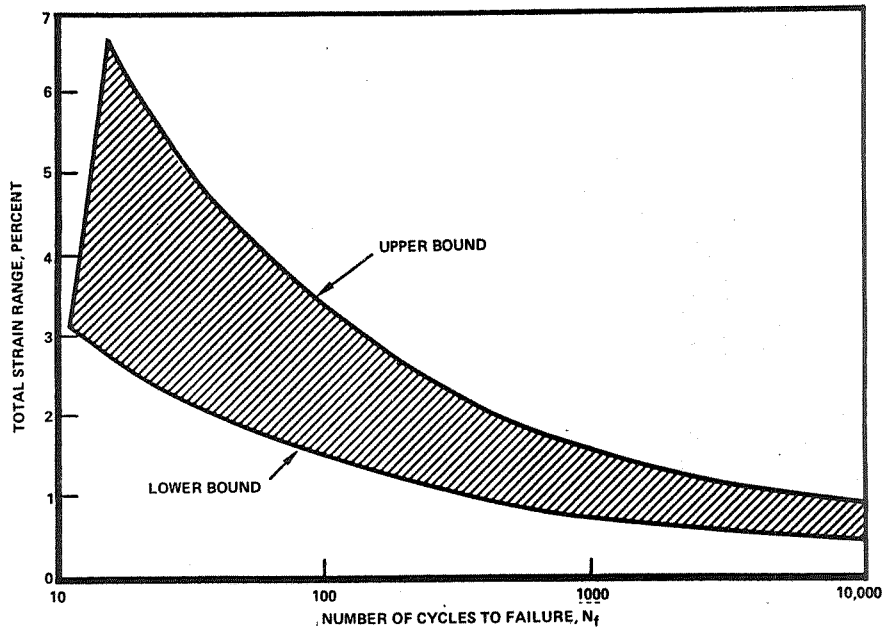


Fig. 8. Low-Cycle Fatigue FRS Composite (1600 F)

for a composite based on 50 volume percent W-Re-Hf-C in a Waspaloy matrix at 1600 F, using the mechanical properties noted in Table 3.

Table 3. Input Data Used in Manson Equation for Estimation of Low-Cycle Fatigue

	ELASTIC MODULUS, GPa( 10 <sup>9</sup> psi)	TENSILE STRENGTH, MPa(kksi)	DUCTILITY (PERCENT)
LOWER BOUND	255(37)(1)	1379(200)(3)	4(4)
UPPER BOUND	172(25)(2)	1379(200)(3)	23(5)

(1) STAGE I MODULUS (BEFORE MATRIX YIELD)  
 (2) STAGE II MODULUS (AFTER MATRIX YIELD)  
 (3) ULTIMATE STRENGTH OF FRS COMPOSITE  
 (4) DUCTILITY OF W-RE-HF-C WIRE  
 (5) DUCTILITY OF WASPALOY

The relatively high thermal conductivity of fiber-reinforced superalloy composites is a distinct advantage in reducing the transient thermal strains that accompany engine start and shutdown. As can be seen in Fig. 9, conductivities of the fiber-reinforced superalloy

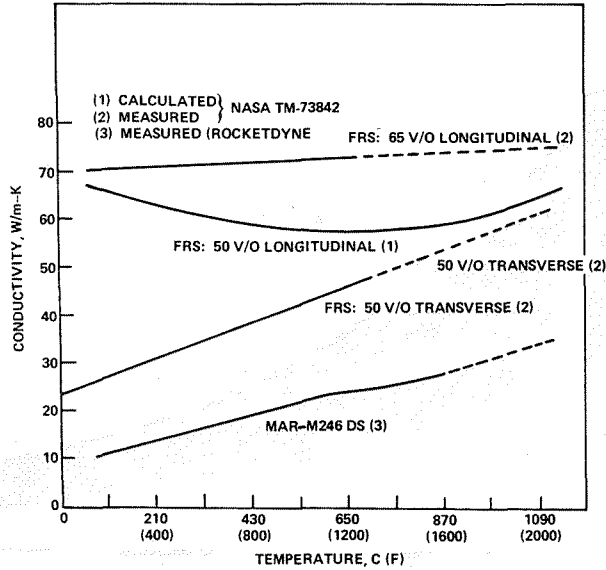


Fig. 9. Thermal Conductivity of FRS and MAR-M246(DS) Superalloys

composites are double that of MAR-M246 at 1600 F. Stress rupture projections are shown in Fig. 10.

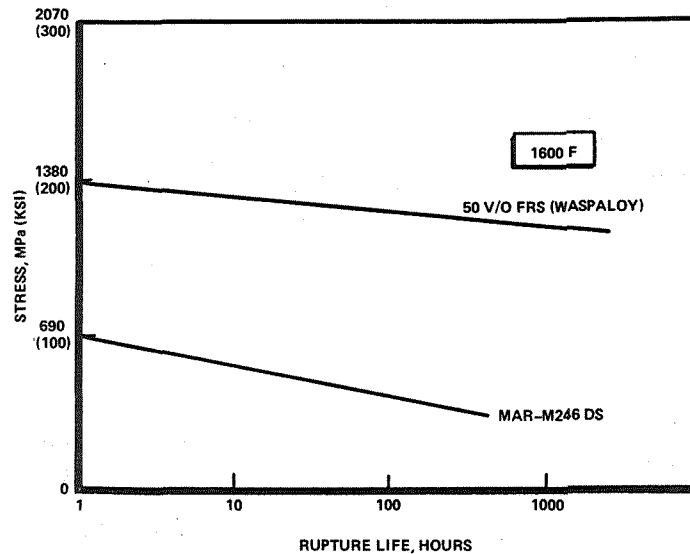


Fig. 10. Stress Rupture of MAR-M246 (DS) and FRS Composites

#### Blade Design

The objective of the fiber-reinforced superalloy blade design and analysis was to develop a preliminary design for an FRS version of an SSME turbine blade. The first-stage blade of the high-pressure fuel pump was chosen as the model, and a composite based on high strength W-4Re-0.38Hf-0.02C wire filaments in a ductile superalloy matrix was selected as the structural system for the blade airfoil. The operating premises upon which the SSME preliminary blade design was based were: (1) that the design properties should be projected from an existing fund of data (no new experimental properties data were generated under this contract) and (2) that the blade should be designed to fit within the current SSME operating parameters and dimensional envelope.

During the course of this program, several fiber-reinforced superalloy turbine blade/disk interface

design concepts evolved, including both detachable and integral blade/disk attachments. Although details of blade design and analysis are discussed in the final report for this program (Ref. 1), the constraints of Federal Regulation 22 USC 2278 foreclose any disclosure of these matters to other than citizens of the United States. For this reason, this paper has been limited to a discussion of projected properties. The final report, however, is available to qualified persons through the auspices of NTIS.

### Conclusions and Recommendations

The fiber-reinforced superalloy materials system selected as the baseline for this study comprises high-strength W-4Re-0.38Hf-0.02C wire filaments, coupled with a high-ductility alloy matrix such as Waspaloy, Incoloy 903, FeCrAlY or type 316 stainless steel. Experimental properties data for these specific composite systems are limited, and it thus has been necessary to project design properties using rule-or-mixture and engineering judgement. A thorough characterization of design properties, therefore, becomes a key technology issue for any follow-on program. The following are of the most immediate importance:

1. Production of developmental quantities of high-strength tungsten alloy wire (e.g., W-Re-Hf-C)
2. Fabrication of fiber-reinforced superalloy composite stock for testing and evaluation
3. Characterization of the following design properties for fiber-reinforced superalloy composites:
  - a. Tensile behavior from cryogenic to evaluated temperatures
  - b. Thermal fatigue and high-cycle fatigue properties
  - c. Hydrogen-environment embrittlement effects
  - d. Stability in hydrogen/water combustion environment

- e. Properties of brazed and/or diffusion-bonded joints
- f. Thermal shock behavior under SSME start and shutdown
- g. Stress-rupture behavior

The operating premises upon which the SSME preliminary design was based were: (1) that the design properties should be projected from an existing fund of data (no new properties data would be generated under this contract) and (2) that the components should be designed to fit within the current SSME operating parameters and dimensional envelope. Specific findings of the effort are summarized below:

1. The short, stubby blade of the SSME high-pressure fuel turbine is well suited for FRS composite application.
2. Design properties, based on projections of existing data, offer significant advantages in both operational life and high-temperature capability for FRS\* turbine components.
3. FRS turbine components lend themselves to a variety of advanced earth-to-orbit booster rocket engines.

The current SSME is a staged combustion cycle engine utilizing hydrogen as a fuel. Other engine systems can involve different fuels (e.g., methane) or other cycles (e.g., gas generator) to heat the working fluid which drives the turbopump. The advantage of FRS turbine blades lies in their capability to withstand exposure to the high temperatures involved in advanced engines, as well as to offer extended operating life.

---

\*50 volume percent W/Hf-Re-C fiber in a Waspaloy matrix.

4. A plan has been provided to develop the needed technology to create operational FRS turbopump components for advanced versions of the SSME.

A three-phase plan is visualized to bring an FRS blade to a state of operational readiness. The current study program, which constitutes Phase I, has identified the needed technologies and has recommended a turbine blade as the component for future effort. During Phase II, the needed technologies will be developed. The third and future phase of the projected program will be concerned with component fabrication, system integration, and demonstration through simulated service test-bed hot firings.

#### Acknowledgements

This paper is based on a program conducted under Contract NAS3-23521 for Lewis Research Center of the National Aeronautics and Space Administration. Donald W. Petrusek was Program Manager. Major credit for engineering support at Rocketdyne belongs to Jerry Lin (Materials) and Linsey Orr (Structures), and Irv Rosman (Design).

#### References

1. Lewis, J. R., Design Overview of Fiber-Reinforced Superalloy Composites for the Space Shuttle Main Engine, NASA CR-168185 (1983).
2. Petrusek, D. W., E. A. Winsa, L. J. Westfall, and R. A. Signorelli, Tungsten Fiber-Reinforced FeCrAl - A First Generation Composite Turbine Blade Material, NASA TM-79094 (1979).
3. Rosenkranz, G., et al., Journal of Mat. Sci. 17, p. 264 (1982).
4. Baskey, R. H., Fiber-Reinforced Metallic Composite Materials, AFML-TR-67-196, Wright-Patterson Air Force Base, Ohio (1967).

5. Fleck, J. N., Fabrication of Tungsten Wire/FeCrAl - Matrix Composite Specimens, TRW, Inc., Cleveland, Ohio, Report No. ER-8076 (1979).
6. Petrasek, D. W. and R. A. Signorelli, Tungsten Fiber-Reinforced Superalloys - A Status Review, NASA TM-82590 (1981).

Materials for Advanced Rocket Engine  
Turbopump Turbine Blades

W. T. Chandler  
Materials Engineering and Technology

Rockwell International/Rocketdyne Division  
Canoga Park, California

Abstract

A study program was conducted to identify those materials that will provide the greatest benefits as turbine blades for advanced liquid propellant rocket engine turbines and to prepare technology plans for the development of those materials for use in the 1990 through 1995 period. The candidate materials were selected from six classes of materials--single-crystal (SC) superalloys, oxide dispersion-strengthened (ODS) superalloys, rapid solidification processed (RSP) superalloys, directionally solidified eutectic (DSE) superalloys, fiber-reinforced superalloy (FRS) composites, and ceramics. Properties of materials from the six classes were compiled and evaluated and property improvements were projected approximately 5 years into the future for advanced versions of materials in each of the six classes. The projected properties were used in turbine blade structural analyses based on the design and operating conditions of the Space Shuttle Main Engine. It was concluded that the materials that warranted development were the SC superalloys for use at 870 C (1600 F), the FRS composite for use at 870 C (1600 F) and 1093 C (2000 F), and the ceramic for use at 1093 C (2000 F).

Introduction

Requirements for improved performance and longer life in advanced liquid propellant rocket engines have focused attention on the potential benefits of advanced, high-temperature structural materials for rocket engine turbopump turbine blades.

Compared to aircraft gas turbines, rocket engine turbines experience very severe thermal start/stop transients, high operating speeds, and hydrogen environments which result in the following unique requirements for rocket engine turbine blade materials: high thermal strain low-cycle fatigue strength; high mean stress high-cycle fatigue strength; resistance to hydrogen environment embrittlement; thermal shock resistance; and relatively short time stress-rupture/creep strength. Fatigue requirements are particularly severe as evidenced by the fact that the directionally solidified, hafnium modified MAR-M246 (MAR-M246(Hf) (DS)) turbine blades in both the High Pressure Fuel Turbopump (HPFTP) and High Pressure Oxidizer Turbopump (HPOTP) of the Space Shuttle Main Engine (SSME) are subjected to life-limiting fatigue cracking as outlined in Table 1. Thus, there is a need for improved turbine blade materials for increased life under current SSME turbine operating conditions and for increased temperature capability for improved rocket engine performance for future liquid propellant rocket engines.

Table 1. SSME Turbine Blade Life Limitations

<ul style="list-style-type: none"> <li>• DESIGN LIFE GOAL - 55 ENGINE FIRINGS, 27,500 SECONDS</li> <li>• 1st STAGE HPFTP BLADES             <ul style="list-style-type: none"> <li>• TRANSVERSE LEADING EDGE AIRFOIL CRACKS - LCF + HCF</li> <li>• CURRENT LIFE ~ 6-8 FIRINGS</li> </ul> </li> <li>• 2nd STAGE HPFTP             <ul style="list-style-type: none"> <li>• TRANSVERSE TRAILING EDGE SHANK CRACKS - HCF</li> <li>• CURRENT LIFE ~ 6 FIRINGS</li> </ul> </li> <li>• 1st STAGE HPOTP             <ul style="list-style-type: none"> <li>• TRANSVERSE TRAILING EDGE FIRTREE CRACKS - HCF</li> <li>• CURRENT LIFE ~ 6 FIRINGS</li> </ul> </li> </ul>
--

Currently, there are some quite sophisticated efforts underway to further extend the capabilities of turbine blade materials. These include not only the various classes of superalloys (single crystal (SC) superalloys, oxide dispersion strengthened (ODS)

superalloys, rapid solidification-processed (RSP) superalloys, fiber-reinforced superalloys (FRS), and directionally solidified eutectic (DSE) superalloys) but also structural ceramics. Thus, a program was conducted to identify those materials from among these six classes that would provide the greatest benefits as turbine blades for advanced liquid propellant rocket engine turbopump turbines in the 1990 through 1995 period, and to prepare development plans for advanced versions of those materials. The program included the gathering, evaluation, and projection of data for materials believed to show promise for the proposed application and performing structural analyses of blades using the selected materials.

The configuration and operating conditions of the SSME high pressure fuel turbopump first-stage turbine blade were used for the blade analyses. The turbine blade steady-state operating temperatures of interest range from 870 C (1600 F), the approximate steady-state operating temperature of turbine blades in the SSME, to above 1093 C (2000 F). Thus, the analyses and comparison of the potential of the candidate materials were conducted for those two temperature regimes. Based on the blade analyses, development plans were prepared and benefit analyses performed to permit the identification of those materials offering the best balance of benefits to the system, risk, and development costs.

## Results and Technical Discussion

### Evaluation and Projection of Data

The mechanical, physical, and environmental effects properties required to analyze and compare the potential of the various candidate materials for use in rocket engine turbine blades in the 1990 to 1995 period were acquired, evaluated, and projected.

As noted earlier, properties were required for structural analyses at both 870 C (1600 F) and 1093 C (2000 F).

A developmental time of approximately 5 years was assumed, at which time the specific optimum turbine blade material must be identified. Therefore, for each of the six classes of materials, mechanical properties were projected 5 years into the future, based on the properties of the best of the current materials and anticipated improvements. The projected mechanical properties were converted into design (minimum) values for use in blade structural analyses. For other properties, for example, thermal properties, current typical values were used in the analyses.

Single Crystal (SC) Superalloys. Data acquisition was initiated for over a dozen SC alloys. Based on an early comparison of properties, NASAIR-100, PWA 1480, and the CM SX alloys were selected as having the greatest near-term potential for rocket engine turbine blades, however NASAIR-100 was found to be very susceptible to hydrogen environment embrittlement (Ref. 1). Thus, the projected values for the mechanical properties for single-crystal superalloys are based on consideration of the properties of PWA 1480 and CM SX series alloys, with the majority of the projected values based on CM SX-2 data. Assumptions made in generating these projected properties were that single-crystal superalloys would be used in rocket engines at operating temperatures of approximately 870 C (1600 F), and that the projected properties appear to be attainable in 5 years through processing developments such as high gradient casting and hot isotatic pressing which reduce porosity that serve as fatigue crack initiation sites and crystal orientation control. In particular, high gradient casting has been shown in the laboratory to provide dramatic increases in high cycle fatigue properties (Ref. 2) and it was assumed in the projections that this process could be transformed into an industrial process in 5 years.

Oxide Dispersion Strengthened (ODS) Superalloys. After evaluation of various ODS alloys, it was concluded that Inconel MA 6000 which combines coherent  $\gamma'$  and incoherent  $Y_2O_3$  particles in a nickel-based

solid solution strengthened matrix, is the only commercial ODS superalloy that may be considered a candidate turbine blade material for use in the 870 C (1600 F) to 1093 C (2000 F) temperature range. International Nickel Company has also developed higher  $\delta'$  volume fraction ODS superalloys, and the most promising of these alloys, Alloy 51, has been well characterized (Ref. 3,4).

To project the potential physical and mechanical properties of ODS alloys 5 years into the future, the properties of Inconel MA 6000 and of Alloy 51, were examined and it was assumed that with appropriate development effort, the higher of the strength properties would be available at that time.

Rapid Solidification Processed (RSP) Superalloys. After evaluation of various RSP alloys, it was concluded that those showing the greatest promise for rocket engine turbine blades were the Pratt & Whitney Rapid Solidification Rate (RSR) processed Alloy 185 (a Ni-Al-Mo ternary alloy) and an Alloy X variant optimized for turbine blade applications that were developed under a DARPA/AFWAL contract (Ref. 5). Thus, projected properties were based on the properties of these alloys, assuming that processing of these alloys could be developed in 5 years.

Directionally Solidified Eutectic (DSE) Superalloys. Some 22 DSE alloys were surveyed and from these, four alloys, NiTaC-13, NiTaC-14B, CoTaC-744, and AG-170, were selected for evaluation. It was concluded that of these, NiTaC-14B has the greatest promise for rocket engine turbine blades because of greater high cycle fatigue strength and transverse ductility than the other alloys.

Thus, projections for the DSE alloy mechanical properties were based on the properties of NiTaC-14B (Ref. 7) assuming that this alloy could be developed for use in rocket engine turbine blades in 5 years with additional modest improvements in longitudinal strength (10 percent) and transverse ductility (15 percent).

Fiber-Reinforced Superalloy (FRS) Composite. A study program directed at applications of FRS to rocket engine turbines recently has been completed at Rocket-dyne Division of Rockwell International (Ref. 7). The findings of that program serve as the source of the projected properties for FRS composites. The selected composite on which projected properties were based was a W-4Re-0.38 Hf-0.02C fiber-reinforced Waspaloy assuming that this material can be developed for use in rocket engine turbine blades within 5 years.

Ceramics. A list of candidate materials for ceramic turbine blades was compiled at the onset of this program. Those materials on the list had to pass rigid requirements qualifying them as potential advanced turbine blade materials. The pertinent properties essential for designing an advanced ceramic turbine blade were then compiled. A first cut evaluation reduced the candidates to silicon nitride and silicon carbide processed by various methods. Upon further evaluation sintered silicon nitride (SSN) was selected as the ceramic with the greatest promise for rocket engine turbine blades mainly because of higher strength, Weibull modulus, and resistance to thermal shock.

Comparison of Projected Mechanical Properties. Figures 1 through 6 contain comparisons of the projected properties among the 6 classes of materials. Based on these data, the SC superalloy and the FRS composite appear to show the greatest promise for use at 870 C (1600 F) and the FRS composite and ceramic show the greatest promise for use at 1093 C (2000 F). Although very little strain-controlled, low-cycle fatigue data have been generated for FRS composites, low-cycle fatigue behavior was projected using the Manson-Coffin approach. The results are shown in Fig. 6, which was derived for a composite based on 50 volume percent W-Re-Hf-C fiber in a Waspaloy matrix at 870 C (1600 F) using the overall strength of the composite but other properties of the individual components to calculate the upper and lower limits shown. Comparison of Fig. 5 and 6 show that

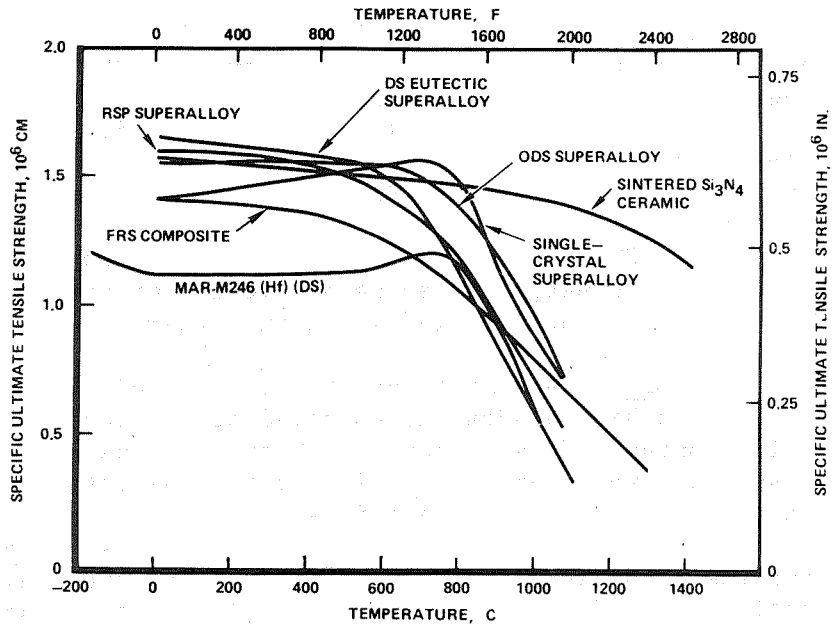


Fig. 1. Projected Design Specific Ultimate Tensile Strength

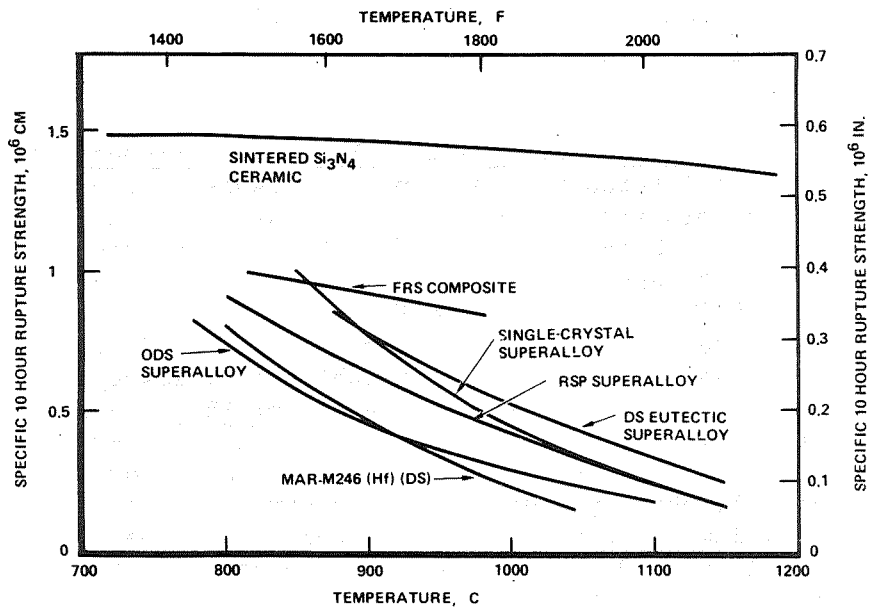


Fig. 2. Projected Design Specific 10-Hour Stress Rupture Strength

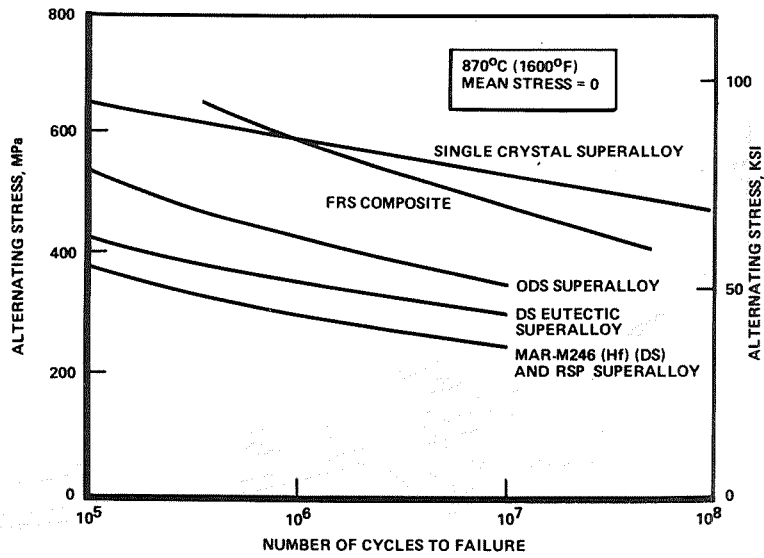


Fig. 3. Projected Design High-Cycle Fatigue Strength

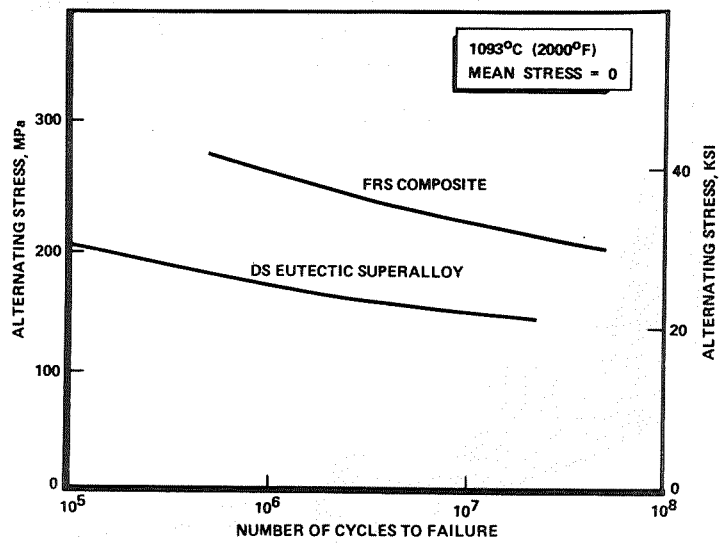


Fig. 4. Projected Design High-Cycle Fatigue Strength

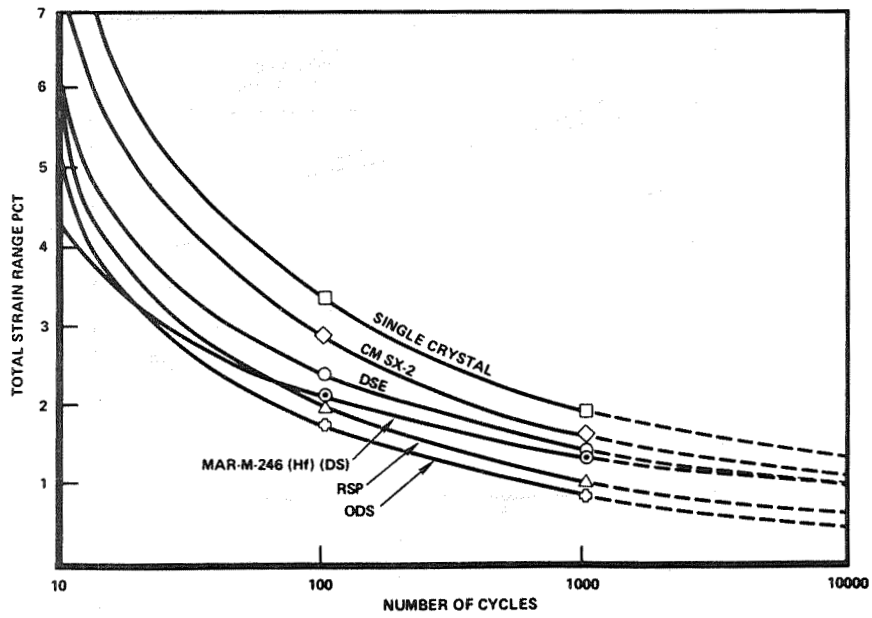


Fig. 5. Projected Design Low-Cycle Fatigue Properties (870 C, 1600 F)

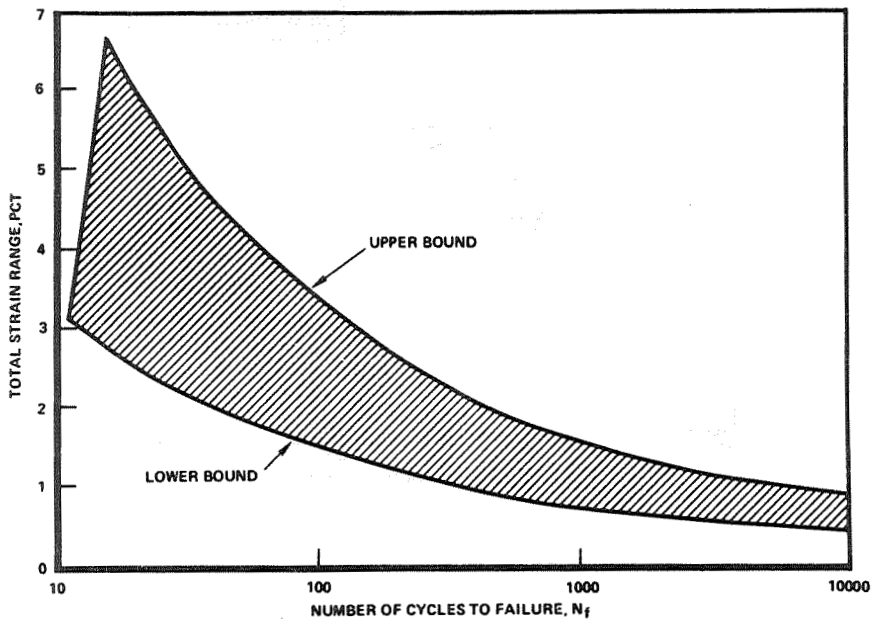


Fig. 6. Projected Design Low-Cycle Fatigue Properties for FRS Composite (870 C, 1600 F)

the projected extremes for the FRS composite embrace the entire behavior for all the other alloys considered during this program.

### Turbine Blade Structural Analysis

Turbine blade structural analyses were conducted using the projected properties for the advanced material in each of the six classes so that the impact on performance of using each of these materials could be compared with each other and with MAR-M246(Hf)(DS) and two current advanced materials, the CM SX-2 SC superalloy and the NiTaC-14B DSE superalloy. The analyses were conducted for a steady-state operating temperature of 870 C (1600 F) for eight materials: the projected material for each of the six classes and for MAR-M246(Hf)(DS) and CM SX-2 SC superalloy. Analyses also were conducted for a steady-state operating temperature of 1093 C (2000 F) for four materials: the projected DSE, FRS, and ceramic materials and the NiTaC-14B alloy. The turbine blade on which the structural analyses were based was the first-stage blade of the SSME high pressure fuel turbopump.

#### Stress Rupture Evaluation for 870 C (1600 F).

The stress rupture evaluation for 870 C (1600 F) was performed using the calculated mean stress due to centrifugal loading for the reference MAR-M246(Hf)(DS), calculating the mean stress for each of the other materials based on the ratio of its density to that of MAR-M246(Hf)(DS), and comparing these calculated stresses to the stress-rupture strengths from the previous section. The ranking order of the materials from the stress rupture evaluation for 870 C (1600 F) is shown in Table 2.

#### High-Cycle Fatigue Evaluation for 870 C (1600 F).

The high-cycle fatigue evaluation for 870 C (1600 F) was performed using mean stresses calculated as described for the stress rupture evaluation and basing the alternating stress on test data obtained by vibrating an extensively strain-gaged MAR-M246(Hf)(DS) blade at its fundamental frequency. The

Table 2. Stress Rupture Evaluation at  
870 C (1600 F)

MATERIAL	10 HOUR RUPTURE STRENGTH CALCULATED MEAN STRESS
MAR-M246 (Hf) (DS)	1.51
Si <sub>3</sub> N <sub>4</sub> CERAMIC	3.80
FRS COMPOSITE	2.68
SINGLE CRYSTAL SUPERALLOY	2.31
DS EUTECTIC SUPERALLOY	2.31
RSP SUPERALLOY	1.94
CM SX-2 SC SUPERALLOY	1.92
ODS SUPERALLOY	1.36

alternating stress was assumed to be due only to pressure pulses and thus was assumed to be the same for the different materials.

High-cycle fatigue capabilities were analyzed using a modified Goodman diagram that shows the failure limits for combinations of mean and alternating stresses. The failure limits are established by the materials endurance ( $10^7$  cycles) limit, ultimate tensile strength, and 10-hour stress-rupture strength. Figure 7 shows a modified Goodman diagram for MAR-M246(Hf)(DS) for four blade locations. The failure limit for a given ratio of mean and alternating stresses is represented by the length of a ray from the origin to the limit line (the limit length). The portion "used up" by the stresses at a given position on the blade is the length of the ray from the origin to that point (the point length). The high-cycle fatigue factor of safety is the limit length divided by the point length. The high-cycle fatigue minimum factors of safety for blades of all the materials for 870 C (1600) are listed in Table 3.

Low-Cycle Fatigue Evaluation for 870 C (1600 F).  
Different thermal strains will occur in blades of different materials when subjected to the same hot gas transients. The thermal strains are proportional to

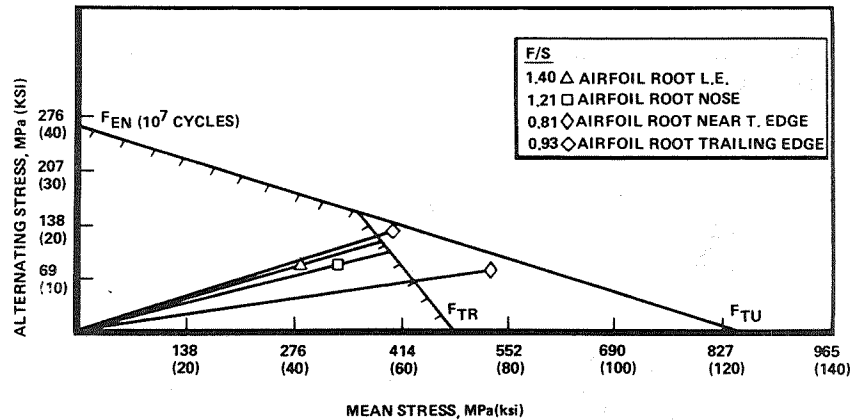


Fig. 7. MAR-M246 (Hf) (DS) Goodman Diagram at 870 C (1600 F)

Table 3. High-Cycle Fatigue Evaluation at 870 C (1600 F)

MATERIAL	HCF MINIMUM FACTOR OF SAFETY (FROM GOODMAN DIAGRAM)
MAR-M246 (Hf) (DS)	0.81
Si <sub>3</sub> N <sub>4</sub> CERAMIC	1.65
FRS COMPOSITE	1.24
SINGLE CRYSTAL SUPERALLOY	1.23
DS EUTECTIC SUPERALLOY	1.23
CM SX-2 SC SUPERALLOY	1.03
RSP SUPERALLOY	1.03
ODS SUPERALLOY	0.71

the coefficient of thermal expansion ( $\alpha$ ) and the difference between the bulk temperature and the temperature at a point. For a given geometry, the thermal transient temperature gradients were assumed proportional to the reciprocal of the thermal diffusivity of the material, which is a function of its thermal conductivity ( $K$ ), its density ( $\rho$ ), and its specific heat ( $C$ ).

Using MAR-M246(Hf)(DS) for a reference, the relative thermal strains for the other materials were calculated as follows:

$$\frac{\Delta\epsilon_x}{\Delta\epsilon_{\text{MAR-M246}}} = \frac{\alpha_x \left( \frac{K}{\rho C} \right)_{\text{MAR-M246}}}{\alpha_{\text{MAR-M246}} \left( \frac{K}{\rho C} \right)_x} \quad (1)$$

A strain range of 3 percent was assumed for MAR-M246(Hf)(DS) and the corresponding strain ranges for the other materials were calculated using Eq. (1). Using these strain ranges and the low-cycle fatigue curves of Fig. 5 and the lower-bound curve of Fig. 6 for the FRS composite, a cyclic life for a temperature transient that causes a 3-percent strain in MAR-M246(Hf)(DS) was calculated. The calculated comparative cycle lives are given in Table 4.

Table 4. Thermal Fatigue Evaluation  
870 C (1600 F)

MATERIAL	CYCLIC LIFE FOR A TEMPERATURE TRANSIENT WHICH CAUSES A 3% STRAIN IN MAR-M246 (Hf) (DS)
MAR-M246 (Hf) (DS)	24
FRS COMPOSITE	>1000
SINGLE CRYSTAL SUPERALLOY	240
CM SX-2 SC SUPERALLOY	130
DS EUTECTIC SUPERALLOY	120
RSP SUPERALLOY	120
ODS SUPERALLOY	65

Conclusions From Structural Analyses for 870 C (1600 F). Based on the results shown in Tables 2, 3, and 4, the single-crystal material appears very attractive for the 870 C (1600 F) turbine blade application. The ODS superalloy offers little or no improvement over MAR-M246(Hf)(DS) at this temperature. The RSP and DSE superalloys do provide improvements in capabilities over MAR-M246(Hf)(DS) but they

overall, do not measure up to the SC superalloy, and they are in earlier stages of development than the SC superalloys. The FRS composite also appears attractive for use at 870 C (1600 F) although there are open questions with regard to thermal fatigue capabilities. The FRS composite would require blade design modifications in the attachment area and the FRS composites are in an earlier stage of development than the SC superalloys. From stress-rupture and high-cycle fatigue considerations, the ceramic looks promising. However, its ability to withstand the thermal transients is of concern. The 870 C (1600 F) temperature is too low to require the unique high temperature capabilities of the ceramic and its development for this temperature application does not appear justified.

Structural Analyses for 1093 C (2000 F). A representative advanced high temperature staged combustion rocket engine design incorporating turbopumps for operation at approximately 1093 C (2000 F) was developed under a High Temperature Turbine Program (Ref. 8) conducted at Rocketdyne for AFRPL. Blade design and operating conditions for the structural analyses for the 1093 C (2000 F) temperature were taken from that program. The evaluation of the four candidate alloys for use in advanced rocket engine high temperature high pressure fuel turbopump turbine blades operating at 1093 C (2000 F) was directed at two modes of material failure--stress-rupture and high-cycle fatigue. The lack of comparative data or established analytical techniques precluded comparisons of thermal fatigue capabilities. This points up the need for appropriate thermal fatigue data for these materials. The procedures for comparing stress-rupture and high-cycle fatigue capabilities were as discussed for the 870 C (1600 F) temperature.

The comparisons of the candidate materials for stress-rupture and high-cycle fatigue for the 1093 C (2000 F) application are contained in Tables 5 and 6. It is obvious that the DSE materials do not have adequate properties for this application. Both the FRS composite and ceramic have excellent properties

Table 5. Stress-Rupture Evaluation  
at 1093 C (2000 F)

MATERIAL	10 HOUR RUPTURE STRENGTH CALCULATED MEAN STRESS
Si <sub>3</sub> N <sub>4</sub> CERAMIC	3.48
FRS COMPOSITE	2.15
DS EUTECTIC SUPERALLOY	1.03
NiTaC-14B DSE SUPERALLOY	0.93

Table 6. High-Cycle Fatigue Evaluation  
at 1093 C (2000 F)

MATERIAL	HCF MINIMUM FACTOR OF SAFETY (FROM GOODMAN DIAGRAM)
Si <sub>3</sub> N <sub>4</sub> CERAMIC	2.21
FRS COMPOSITE	1.34
DS EUTECTIC SUPERALLOY	0.82
NiTaC-14B DSE SUPERALLOY	0.73

and development of these materials for the 1093 C (2000 F) rocket engine turbine blade application appears justified.

Categorization of Materials. On the basis of the results of the turbine blade structural analyses, the candidate materials were categorized as follows:

1. Material warrants further development as a beneficial alternate material for the current SSME turbine blade design
  - a. Single-crystal (SC) superalloy--for use at 870 C (1600 F)
2. Material should be dropped from consideration
  - a. Oxide dispersion strengthened (ODS) superalloy, rapid solidification processed (RSP) superalloy, and directionally solidified eutectic (DSE) superalloy

3. Material warrants further development but design modifications would be required
  - a. Fiber-reinforced superalloy (FRS) composite--for use at 870 C (1600 F) and 1093 C (2000 F)
  - b. Ceramic--for use at 1093 C (2000 F)

#### Technical Development Plans

Based on the technology needs for each material, technical development plans, schedules, and costs were outlined for the material categorized as warranting development for use in advanced rocket engine turbo-pump turbine blades. The major technology needs identified for the materials warranting development are given in Table 7.

Table 7. Technology Needs

<ul style="list-style-type: none"><li>• <b>ADVANCED SC SUPERALLOY</b><ul style="list-style-type: none"><li>• DEVELOP HIGH GRADIENT CASTING PROCESS</li><li>• CONFIRM PROPERTY IMPROVEMENTS</li><li>• ESTABLISH AS VIABLE COMMERCIAL PRODUCTION PROCESS</li></ul></li><li>• <b>FRS COMPOSITE</b><ul style="list-style-type: none"><li>• DEVELOP DESIGN DATA BASE</li><li>• ESTABLISH PRODUCTION OF REQUIRED QUANTITIES OF HIGH-STRENGTH TUNGSTEN ALLOY WIRE</li><li>• DEVELOP BLADE DESIGN TECHNOLOGY</li><li>• ESTABLISH COMMERCIAL BLADE PRODUCTION PROCESS</li></ul></li><li>• <b>CERAMIC</b><ul style="list-style-type: none"><li>• IMPROVE RELIABILITY AND TOUGHNESS</li><li>• DEVELOP DESIGN DATA BASE</li><li>• DEVELOP NDE METHODS</li><li>• IMPROVE DESIGN METHODOLOGY</li></ul></li></ul>
--

It was estimated that if technical development programs are implemented, these materials could be qualified for use in rocket engine turbine blades by 1990 for the advanced single-crystal superalloy, by 1991 for the FRS composite, and by 2000 for the ceramic. It should be noted that the technical development program outlined for the ceramic depended heavily on, and was built upon, the DOE/NASA plan

for developing an advanced terrestrial heat engine (Ref. 9), the so-called Ceramic Initiative Program.

### Cost Benefit Analysis

A study was made to assess the cost benefits that can be realized by the use of advanced turbine blade materials for an advanced SSME-type engine. Cost benefit analyses were conducted for two areas: analysis of the cost savings that can accrue from extended blade life, operating at present temperature levels, i.e., 870 C (1600 F), and analysis of the increased income that will result from the increased payload that can be realized by operating the turbines at 1093 C (2000 F).

Increased Turbine Blade Life. The life of SSME high pressure fuel and oxidizer turbopump turbine blades at the present is approximately 3000 seconds. Development programs are underway that are expected to extend blade life to 5000 seconds by 1989 so this life was used as the basis for calculating cost benefits from increased life. The cost benefits result from decreasing the number of pump rebladings required. The cost of replacing the blades in an SSME turbopump including pump removal and reinstallation, reblading the turbopump, testing and propellants, and shipping is approximately \$1 million.

The average reblading cost per Orbiter mission or flight is shown as a function of blade life in Fig. 8. At the expected blade life of 5000 seconds, the average cost is \$600,000 per Orbiter flight. The steep slope of the curve in Fig. 8 for a blade life under approximately 10,000 seconds illustrates the significant gains to be made by relatively small increases in blade life.

Figure 8 also shows the total program cost incurred as a function of blade life. For the case of a five-Shuttle fleet with an Orbiter life of 100 missions each, the total cost for a blade life of 5000 seconds is \$300 million.

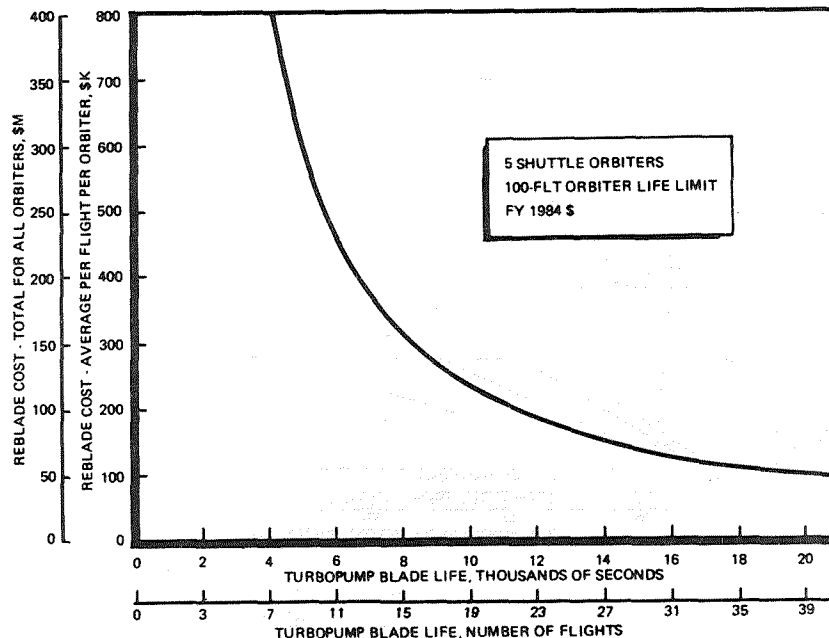


Fig. 8. Cost to Reblade Turbines as a Function of Blade Life

Figure 9 shows the maintenance cost savings realized by extending blade life from a reference value of 5000 seconds to various longer durations. Using the same case as above, i.e., at 500 missions, the gross cost savings in going from 5000 to 15,000 seconds blade life is \$240 million by reducing the total cost of reblading all engines of the Orbiter fleet from \$300 million to \$60 million.

Superimposed on the graph are cost levels that represent upper and lower estimates of the development effort. The material characterization and blade development costs in this example are set at \$10 million. This represents the lowest limit of development cost (i.e., just the technology acquisition) for turbine blade life extension using new blade materials. It assumes that turbopump and engine recertification would be charged entirely against other development or turbopump improvement program costs.

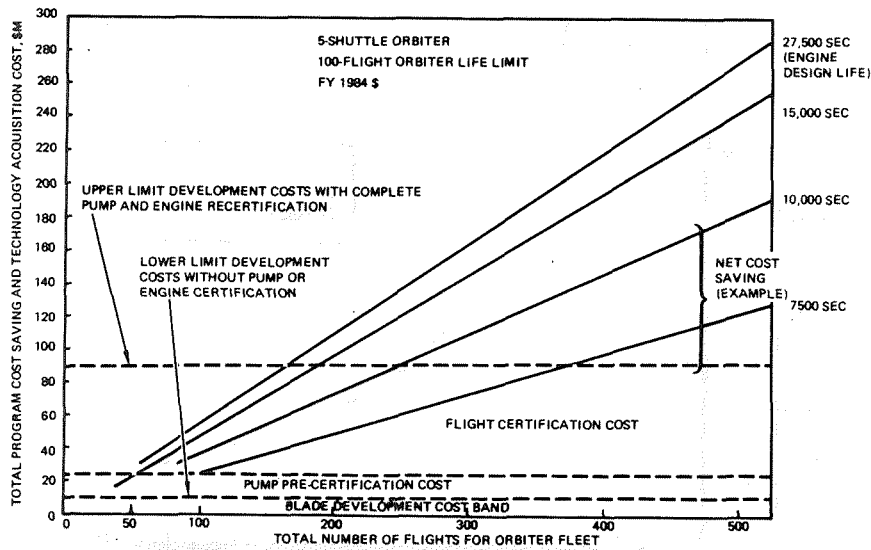


Fig. 9. Cost Saving Realized by Extending Blade Life From 5000 Seconds to Duration Shown

The upper limit of development costs for turbine blade life extension by new material substitution consists of the sum of blade development cost (\$10 million), turbopump precertification testing (about \$15 million), and engine flight certification (about \$65 million), i.e., a total of \$90 million. The development cost of \$90 million would be applicable only if turbine blade material substitution were the sole change in an advanced SSME-type engine requiring complete pump and engine recertification. However, it can be assumed that in a future advanced SSME-type engine, advanced turbine blade materials will be incorporated at the design stage, suggesting that the lower development cost level applies.

As shown in Fig. 9, extending blade life from 5000 to 15,000 seconds results in a gross cost saving of \$240 million for 500 flights (five Orbiters, 100 missions each). Subtracting the development cost band of \$10 million to \$90 million results in net cost savings of \$150 million to \$230 million. The

figure also shows that the development cost would be recovered after 25 to 190 Orbiter fleet flights, depending upon the development cost assumptions.

It is apparent that the estimated cost benefits resulting from extending life for the 870 C (1600 F) temperature are much larger than development costs for either the advanced single-crystal superalloy or the FRS composite.

Increased Turbine Operating Temperature. Raising the turbine operating temperature increases the Orbiter payload by increasing specific impulse. Specific impulse gains can be realized when the turbine operating temperature increase is accompanied by the incorporation into the engine design of advanced turbomachinery technologies (associated with higher turbopump speeds) and advanced thrust chamber cooling techniques.

For an advanced 500,000 lbf thrust, staged-combustion engine with oxygen/hydrogen propellants, with current engine technology, it is estimated that a specific impulse gain of 0.25 second is achievable if the preburner temperature is raised from 838 C (2000 R) to 1060 C (2400 R), Ref. 8. Larger gains can be realized if advanced technology in turbomachinery and thrust chamber cooling techniques are incorporated. For such engines, a 220 C (400 F) increase in preburner (or blade material) temperature is estimated to result in a specific impulse gain of approximately 0.75 second.

With a launch cost of \$1.2 million/thousand pounds of payload, based upon a Kennedy Space Center launch price for subsidized non-DOD, U.S. Government and commercial users, or \$1.9 million/thousand pounds for nonsubsidized launch costs, and a payload gain factor of 1100 pounds/sec of specific impulse, a cost benefit can be calculated. The total gross cost benefit equals the delta payload in thousand pounds, times the launch cost/thousand pounds of payload, times the total number of launches (500). The total number of launches has been established in

the groundrules as number of Orbiters (five) times number of flights per Orbiter life (100). The gross cost benefits are shown in Fig. 10 for the technology levels noted. The gross cost benefit attributable to a 200 C

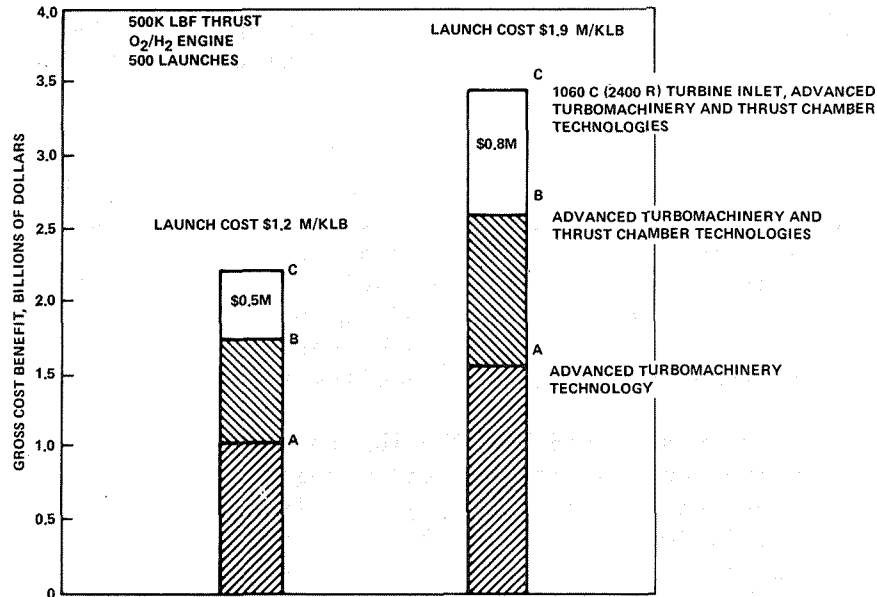


Fig. 10. Total Program Cost Benefit With Increased Turbine Inlet Temperature and Advanced TD Technologies

(400 R) increase in preburner temperature is from approximately \$500 million to \$800 million, depending upon the launch cost assumed.

From Fig. 10, it is apparent that large gross cost benefits can be achieved over the lifetime of a future Orbiter fleet if advances in turbomachinery and thrust chamber technologies are exploited fully in the next generation Orbiter engines. These gross cost benefits appear to justify the development of those technologies including the development of the FRS composite and ceramic turbine blades required to achieve the 1093 C (2000 F) turbine temperature.

### Conclusions

A program was conducted to identify those materials that would provide the greatest benefits as turbine blades for advanced liquid propellant rocket engine turbopump turbines in the 1990 through 1995 period, and to prepare development plans for advanced versions of those materials. The conclusions are as follows:

1. The materials warranting development for advanced rocket engine turbine blades are the SC superalloy for use at 870 C (1600 F), the steady-state turbine blade temperature in the Space Shuttle Main Engine, the FRS composite for use at 870 C (1600 F) and 1093 C (2000 F), and the ceramic for use at 1093 C (2000 F).
2. Technology plans were outlined indicating that the time at which the materials could be developed through rocket engine certification and acceptance tests are 1989 for the SC superalloy, 1991 for the FRS composite, and 2000 for the ceramic.
3. Estimated cost benefits so far outweigh any anticipated material development costs, even factoring in development risks, that it was concluded that the programs outlined for the development of the SC superalloy, the FRS composite, and the ceramic for use in advanced rocket engine turbine blades are justified for implementation.

### Acknowledgements

This paper is based on a program conducted by the Rocketdyne Division of Rockwell International under Contract NAS3-23536 for the Lewis Research Center of the National Aeronautics and Space Administration. R. L. Dreshfield was NASA Program Manager. F. M. Kirby was Rocketdyne Program Manager. Major technical contributions were provided by the following Rockwell International employees. Rocketdyne Division: Materials--D. F. Atkins, H. W. Carpenter, J. R. Lewis, D. E. Matejczyk, and F. T. Wimmer; Stress Analysis--L. M. Orr and C. T. Rollins; High-Temperature Turbine--

J. G. Tellier; Benefits Analysis--E. N. Eusanio and C. J. Meisl. Science Center: Materials--R. J. Richards-Frandsen. Valuable discussions with Professor John K. Tien, Columbia University, New York, are gratefully acknowledged.

#### References

1. Bashir, S., Unpublished data, Rockwell International, Rocketdyne Division, Canoga Park, CA.
2. Harris, K., G. L. Erickson, and R. E. Schwer, "Development of the Single Crystal Alloys CM SX-2 and CM SX-3 for Advanced Technology Turbine Engines," paper 83-GT-244, presented at the ASME International Gas Turbine Conference, March 1983.
3. Benn, R. C., "High  $\gamma'$  Content ODS Superalloy Characterization," TMS-AIME 112th Annual Meeting, Atlanta, GA, March 1983.
4. Benn, R. C., Oxide Dispersion Strengthened High-Volume Fraction  $\gamma'$  Nickel-Base Superalloy Characterization, NADS-79106-60, 1981.
5. Cox, A. R., et al., Application of Rapidly Solidified Alloys, DARPA Contract NO. F33615-76-C-5136, PWA Reports Nos. FR 8688 (May 1977), FR 9011 (August 1977), FR 9417 (November 1977), FR 9744 (February 1978), FR 10521 (May 1978), FR 10657 (September 1978), FR 11103A (December 1978), FR 11691 (February 1979), FR 13606 (August 1980), and later reports.
6. Dannemann, K., et al., "Microstructure and Fatigue Behavior of Nickel-Base Eutectic Composites," Strength of Metals and Alloys, (ICSMA 6), R. C. Gifkins, Ed., Pergamon Press, p. 141, 1982.
7. Lewis, J. R., Design Overview of Fiber-Reinforced Superalloy Composites for the Space Shuttle Main Engine, Final Report Rocketdyne Division Rockwell International, NASA CR-168185, May 1983.
8. Tellier, J. G., High-Temperature Turbine Study, Rockwell International/Rocketdyne Division, AFRPL Contract F04511-81-C-0053, in progress.

## DEVELOPMENT OF HYDROGEN RESISTANT ALLOYS

W. B. McPherson

National Aeronautics and Space Administration  
Marshall Space Flight Center, Alabama 35812

The most hostile operating environments in the  $O_2/H_2$  Space Shuttle Main Engine are gaseous hydrogen and hydrogen/water vapor. After years of evaluating commercially available alloys, only a few high strength alloys have been found that perform satisfactorily in these environments.

In a search for hydrogen tolerant alloys, this paper describes the evaluation of various compositions of the Fe-Ni-Co system with elemental additions of Cr, Cb, Ti and Al. After processing, notched tensile specimens were tested in 5000 psi hydrogen at room temperature as the prime screening test. The  $H_2$ /air ratio was used as the selection/rejection criteria.

## IGNITION OF METALS IN HIGH PRESSURE OXYGEN

James W. Bransford  
National Bureau of Standards  
Chemical Engineering Science Division  
Boulder, Colorado 80303

### Abstract

A description of an experimental facility used to determine the ignition and combustion characteristics of metallic materials is described. The results obtained for aluminum 6061, 302 stainless steel, and the nickel alloy--N06625--are given.

### Introduction

For a number of years, accidents involving the sudden ignition and combustion of metals in contact with liquid and gaseous oxygen have occurred. These accidents have occurred to many users of liquid and gaseous oxygen. Some of the accidents have resulted in injury and/or death to personnel close to the accident.

During the development of the Space Shuttle main engine, several major failures occurred due to the sudden ignition and combustion of metallic materials in contact with liquid and gaseous oxygen. As these failures were analyzed it became apparent that data on the ignition and combustion characteristics of many materials was either limited or not available.

To alleviate this problem, a program was initiated at the National Bureau of Standards, by the George C. Marshall Space Flight Center to determine the ignition and combustion characteristics of specific alloys in high pressure oxygen systems. In addition to the data generation part of the program, the determination of fundamental ignition mechanisms are to be determined.

## Experimental

Specimens of aluminum 6061, 302 stainless steel, and nickel alloy N06625, 5 mm in diameter by 5 mm in height, were ignited in commercially pure oxygen. Oxygen pressure varied from atmospheric to 5.171 MPa (750 psia) the maximum pressure at which reliable ignition could be obtained. Specimen ignition was carried out by heating the top surface with an 80 W cw CO<sub>2</sub> laser operating predominantly in the TEM<sub>00</sub> mode. The sample size utilized was the largest that would meet heating rate and maximum temperature requirements.

The ignition studies were carried out in a high pressure combustion chamber, Figure 1, which was

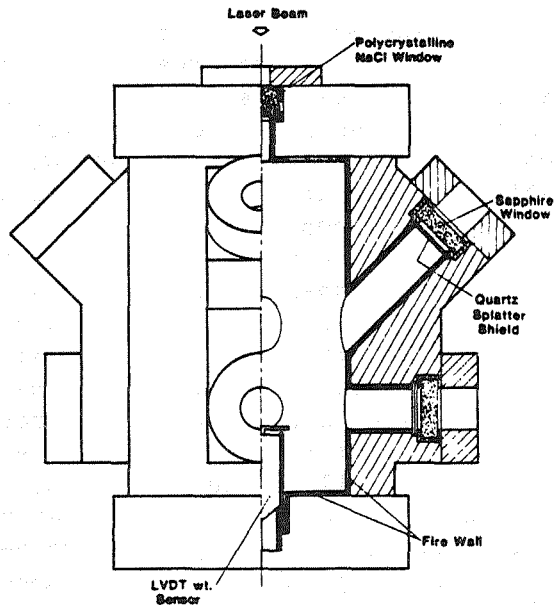


Figure 1. High pressure combustion chamber.

designed to allow the manual mounting and adjustment of the specimen and to minimize pressure changes during the experiment. The free volume of the chamber is approximately 2.5 liters. The chamber has eight

general purpose ports; four were equally spaced at 45° to the chamber axis, and four equally spaced at 90° to the chamber axis. All port axes intersect at a common point on the chamber axis. Each port has a clear aperture of 6.5 cm<sup>2</sup>.

Five measurements were made as follows:

- 1) mass,
- 2) brightness,
- 3) interior temperature,
- 4) mean top surface temperature, and
- 5) selected top surface spot temperature.

Mass data were obtained from a linear variable differential transformer (LVDT) sensor which has a 100 g capacity. The mass sensor/data acquisition unit was set up to give a mass resolution of 0.25 mg. Brightness data, not quantitative measurements, were obtained from a silicon photodiode. These data were used to compare present results to past work; they will probably be eliminated in future studies, since the mean top surface temperature was a much better indicator of surface events. The interior temperature was measured by inserting a W 6% Re vs. W 26% Re or Pt vs. Pt 10% Rh thermocouple into a 0.64 mm diameter hole drilled to within 0.25 to 0.40 mm of the top surface. The thermocouple wire was insulated with an aluminum-oxide-doped fiber-reinforced silicate cement. Two-color ratio pyrometers were used to measure the mean overall top surface temperature and the selected top surface spot, 0.5 mm diameter, temperature. The two-color ratio pyrometers were not adversely affected by problems such as smoke or dirty windows. In addition to the above measurements, high-speed cinematography was used to obtain ignition and combustion behavior. A framing rate of 250 fps was used.

The test specimens were machined from commercially available material. Specimens of nonaluminum based alloys were flame oxidized (blued) to reduce

reflectivity and improve absorptivity to the laser beam.

To assemble the experiment, the insulated thermocouple was inserted through the bottom of the graphite block into the containment well and weakly cemented in place. The containment well was then lined with packed aluminum oxide powder to a thickness of 2 mm on the bottom and 1 mm along the side. The specimen was inserted firmly over the thermocouple and seated firmly on the aluminum oxide powder, breaking the weak thermocouple/graphite block cement bond. This allowed the thermocouple to float and follow changes in position of the top surface of the specimen. This assembly was placed on a contoured section of foam firebrick and then seated on the platen of the LVDT, Figure 2. A cylindrical glass

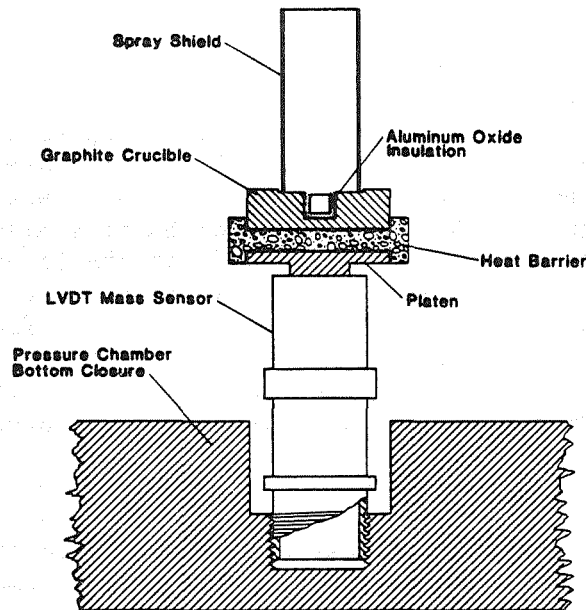


Figure 2. Experimental set-up.

shield was placed over the containment well in order to reduce the amount of molten/burning material

ejected from the combustion zone and also to reduce the effects of convection on the LVDT mass sensor.

All sensor signals were digitized by 12 or 15 bit analog-to-digital converters. Data acquisition times were either 10 or 20 ms per point for a total experiment run time of 20 or 40 s.

### Discussion and Results

The ignition and combustion results for three metal alloys are reported. These alloys are representative of large classes of alloys from which the alloys were taken.

#### Definitions

##### Ignition Point

Ignition was considered to have occurred when an accelerating or abrupt mean surface temperature increase develops from the general heating rate trend. The data point preceding this development was taken as the ignition point. For vapor burning alloys this point was usually well defined. For the liquid burning alloys, considerable care was taken to differentiate temperature steps due to oxide scale from the temperature step due to the oxidation of the alloy. The ignition point for these materials usually must be confirmed from mass and interior temperature data.

##### Ignition Temperature

Ignition temperatures are derived from the various sensor signals at the ignition point. Smoothing or extrapolating procedures may be used.

##### Aluminum 6061

Aluminum and aluminum-based alloys burn in the vapor phase. Aluminum oxide is a protective oxide and prevents the transfer of significant amounts of oxygen to the molten metal surface. For pure

aluminum to ignite and burn, the covering aluminum oxide layer must be raised above the melting point or the vapor pressure of the molten metal must be sufficient to break the layer.

Two possible effects can be generated by alloying elements on the aluminum/aluminum oxide system. First, the protective oxide layer may be modified to become nonprotective, thereby lowering the ignition temperature. Second, there exists the possibility of energetic reactions between aluminum and alloying element oxides, effectively lowering the ignition temperature.

To test the possible effects of alloying elements, ignition tests using aluminum 6061 were carried out. This alloy has a nominal composition of 0.2% Cr, 0.27% Cu, 1.0% Mg, and 0.6% Si. Some or all of these alloying elements are present in various percentages in many other aluminum-based alloys. No iron is present; therefore the known iron oxide/aluminum reaction will not confuse the results. Initially, tests were planned for oxygen pressures from atmospheric to 13.790 MPa (2000 psia). However, low surface absorptivity to the laser beam and higher convective cooling rates in the pressurized oxygen limited ignition to a maximum pressure of 2.413 MPa (350 psia).

The preignition oxidative behavior of the alloy was highly variable. Oxidation rates from undetectable to 15 mg  $[O_2]$ /s were observed. If detectable preignition oxidation occurred during a test, the event began at temperatures greater than 1800 K but did not necessarily continue throughout the experiment.

The ignition sequence was of two types--abrupt and accelerating. The abrupt ignition sequence took place within one data acquisition time period, 10 or 20 ms, and was concurrent with combustion. The accelerating ignition sequence usually lasted for 40 to 60 ms, but has lasted for as long as 140 ms; it

usually ended abruptly. This would imply that more than one mechanism is responsible for ignition and combustion or that one mechanism begins the process and a second is available to accelerate the event.

The specimen underwent a slow but constant change in geometry during heating. The original flat top surface became dome-like before ignition. In addition to the top surface change, the specimen sagged, becoming up to 1 mm shorter; the sagging slightly shifted the relative position of the top surface. Because of changes in the specimen geometry, the original 0.5 mm diameter central measurement point for the spot temperature measurement was randomly shifted from the original position. Using spot temperature data at low pressures plus data from special calibration tests, it was found that the maximum surface temperature was less than 2275 K. The calibration tests, which were conducted in air to prevent specimen combustion and failure of the tungsten-based thermocouple, also demonstrated that the mean surface temperature was an excellent indicator of the maximum interior temperature to within +20 K.

Using the previous definition of ignition point, the mean surface temperature at ignition was determined. Oxygen pressure varied from 0.069 MPa (10 psia) to 2.413 MPa (350 psia). These data are presented in Figure 3. Three of the data points, marked by a triangle, represent ignition that occurred on specimen cooling after failure to reach ignition temperature on heating. Insufficient laser power was the cause of the failures to reach ignition temperature. These data are considered unique and will be discussed separately. Five data points are marked by diamonds. These data are considered to deviate from the main body of data because the pyrometer field of view was set excessively high on the specimen. As the specimen sagged and the upper surface geometry changed, the only area within the field of view of the instrument would be the upper part of the dome, the highest temperature area of the surface.

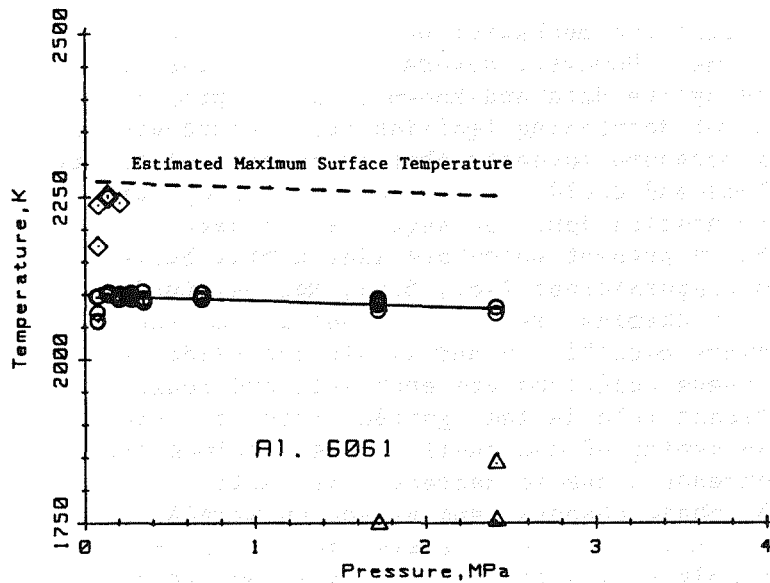


Figure 3. Mean surface temperature at ignition.

These data confirm the maximum spot temperature data, which peaked at 2266 K. Utilizing data from the low pressure experiment and the calibration test, an estimate of the temperature differential across the top oxide surface can be established. The most probable experiment-to-experiment value of the temperature differential would lie in the range 150 K to 200 K.

The highest mean surface temperature at ignition occurred at 0.138 MPa (20 psia). A linear least squares curve fit of the data from 0.138 MPa to 2.413 MPa gave an ignition temperature dependency on oxygen pressure of  $-9.11626 \text{ K/MPa}$  ( $-0.06285 \text{ K/psi}$ ). It is reasonable to assume that the peak surface temperature and peak interior temperature also followed this trend; this is shown in Figure 3. Observation of the specimen indicates that the ignition zone

occurred in the central 50% of the top surface. This was the area of highest temperature.

The ignition mechanism has not been determined at this time. However, several possibilities are suggested by the data and known physical properties. The trend of decreasing ignition temperature with increasing pressure suggests that an oxygen solubility is involved and could also explain the abrupt and fast accelerating ignition sequence. Several oxides are probably present which are liquid well below the ignition temperatures; i.e.,  $\text{SiO}_2$ ,  $\text{MgSiO}_3$ ,  $\text{Cu}_2\text{O}$ . A number of chemical reactions involving molten aluminum are possible on and within the oxide shell. Many of these reactions are energetic and could play a significant role in the ignition process. The steady weakening of the shell as the specimen temperature increases, due to decreased mechanical strength, phase changes, and expansion stress, is an additional complication. Several individual mechanisms probably play a role in the ignition process.

The ignition of several specimens on cooling, that had failed to reach ignition temperature on heating, was considered to be significant. The ignition was abrupt and considered to have occurred when the specimen surface either cracked or imploded from the negative differential volume change due to the larger expansivity of the liquid alloy. The energy produced by the oxidizing surface was thought to be trapped within the cracked or imploded area. Additional energy may have been added to the system by the chemical reaction of molten aluminum with various alloying element oxides. The total energy thus released was sufficient to raise the temperature of the surrounding oxide material past the ignition point, resulting in combustion. This would imply that molten aluminum alloys can be ignited at temperatures significantly below the normal ignition temperature.

### 302 Stainless Steel

The 300 series stainless steels have been extensively used in oxygen systems due to the many desirable properties shown by various alloys within this series. It has been considered desirable to determine the ignition and combustion characteristics of a number of alloys in this series because of their usefulness.

A large number of ignition tests have been made on seven alloys of the 300 series. The ignition and combustion characteristics have been similar for all seven alloys. The data for one alloy, 302, are presented here.

The 302 alloy has a nominal composition of 17-19% Cr, 8-10% Ni, 2% Mn, 1% Si, 0.15% C, 0.045% P, 0.030% S; the balance is Fe. The alloy has a melting range from 1672 to 1694 K. In the case of the stainless steels, the higher absorptivity of the oxidized specimen surface and the lower ignition temperatures allowed tests to be performed to oxygen pressures of 5.171 MPa (750 psia).

The preignition oxidative behavior of this alloy was uneventful. A black oxide surface would develop and gradually increase in thickness. Between 1500 and 1600 K, a detectable oxidation rate of up to 0.4 mg [O<sub>2</sub>]/s developed. The surface oxide layer took on a granular appearance and became thermally insulating.

The ignition sequence began with the development of a small hot-spot within the central 50% of the top surface. The hot-spot increased irregularly in size until the specimen began to melt and self-sustained combustion developed. If the external heat source was removed during the ignition sequence, self-sustained combustion did not develop. A typical preignition-ignition sequence for a test at 1.724 MPa (250 psia) is shown in Figure 4.

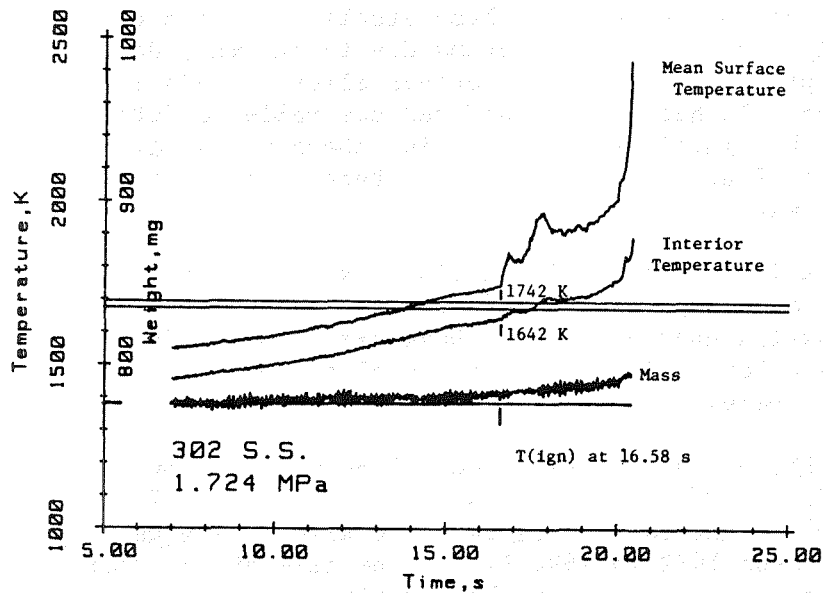


Figure 4. Typical waveforms about the ignition point for 302 stainless steel.

Interior temperatures at ignition are presented in Figure 5. The solid lines represent the lower and upper melting range of the alloy and the dashed line represents the melting point of ferrous oxide or iron deficient ferrous oxide. Analysis of the waveforms of the interior temperature as well as the interior temperature values at ignition strongly indicates that ignition cannot begin until the ferrous oxide at the alloy-oxide interface begins to melt. Thus the ignition temperature of 302 stainless steel has a lower bound of 1650 K. The interior temperature waveform analysis also strongly indicates that at oxygen pressures of 0.689 MPa (100 psia) and greater, ignition will take place before the alloy-oxide interface temperature reaches the upper melting range bound, 1694 K.

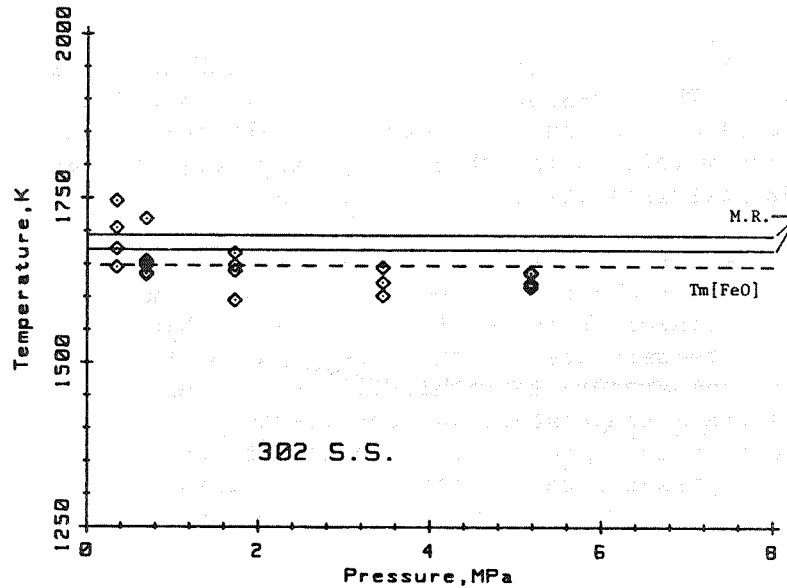


Figure 5. Interior temperature at ignition.

#### Nickel Alloy N06625

Several nickel alloys are to be studied. However, the alloy N06625 is the only one for which data have been generated for oxygen pressures greater than 0.345 MPa (50 psia). Those data are presented here.

The N06625 alloy had a ladle analysis of 22.10% Cr, 8.77 Mo, 3.90% Cb+Ta, 2.44% Fe, 0.26% Ti, 0.17% Al, 0.04% C, 0.02% Si, 0.03 Mn, 0.005% P, 0.002% S and balance Ni. The alloy has a melting range of 1561 to 1622 K.

The preignition oxidative behavior of this alloy was uneventful. A thin black oxide layer would form until the alloy surface began to melt. At this point, if the heating rate was too slow, a thick solid oxide layer would form and could prevent

ignition. If the heating rate was adequate, ignition would occur shortly after the upper surface began to melt.

The ignition sequence began with the development of a small hot-spot within the central 50% of the top surface. The hot-spot would rapidly expand and unsupported combustion would develop. The temperature and mass waveforms for this alloy were very similar to 302 stainless steel.

Interior temperatures were available for ignition taking place below 1700 K. For those ignitions for which interior temperatures are available, the interior temperature was the same value as the mean surface temperature to within  $\pm 15$  K. Therefore the mean surface temperature was considered to be a good estimate of the interior temperature at ignition. Figure 6 presents the ignition temperatures. The

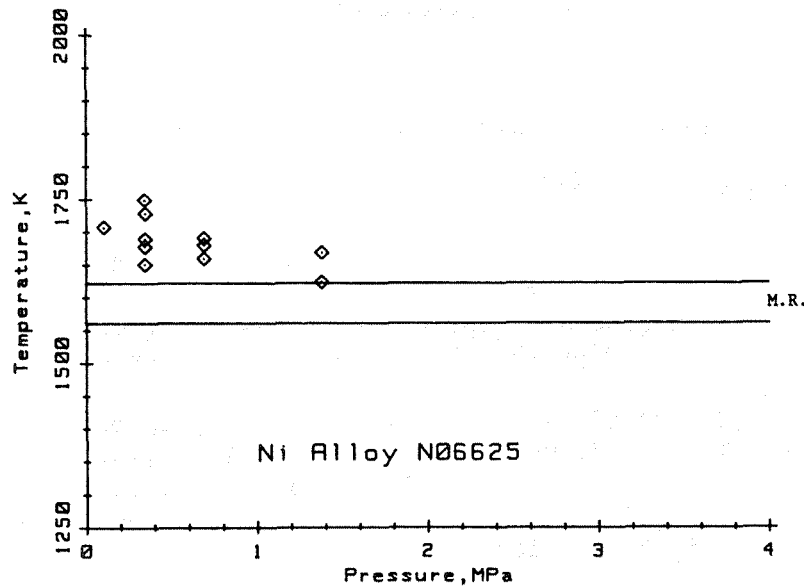


Figure 6. Mean surface temperature at ignition.

limited data do not warrant any conclusions on the dependence of ignition temperatures with oxygen pressure.

### Conclusions

The conclusions given below are based upon a bulk specimen, i.e., low surface to volume ratio, undergoing nonuniform heating. The upper surface of the specimen, where ignition occurs, was freely radiating. Experiments carried out on high surface to volume materials, i.e., powders or small particles, or under uniform heating conditions may give different ignition data and thus change or modify the conclusions.

#### Aluminum 6061

1. For a heated undisturbed surface:
  - a. the ignition temperature was less than the melting point of aluminum oxide.
  - b. the ignition temperature decreased with increasing oxygen pressure.
  - c. the preignition and ignition sequence data indicated that several mechanisms were in the ignition sequence.
2. For a previously heated undisturbed oxidized surface, ignition could occur during cooling.
3. Conclusion 2 would imply that either a heated or a previously heated cooling disturbed surface could ignite at temperatures significantly below the undisturbed ignition temperature.

#### 302 Stainless Steel

1. For a heated undisturbed surface, ignition occurred at temperatures equal to the melting point of ferrous oxide, 1650 K, or higher; but below the liquidus temperature.

2. For oxygen pressures up to 5.171 MPa (750 psia), unsupported combustion was not concurrent with ignition.
3. For a heated undisturbed surface, the ignition temperature range was independent of oxygen pressure beyond 0.345 MPa (50 psia) and up to 5.171 MPa (750 Psia), the present data limit.

#### Nickel Alloy N06625

1. For a heated undisturbed surface, ignition occurred within or beyond the alloy liquidus temperature.
2. For a heated undisturbed surface, unsupported combustion was not concurrent with ignition.

#### Acknowledgments

The author would like to express his gratitude to Mr. James D. Breuel, Mr. James A. Hurley, and Mr. Ke Nguyen for their assistance in performing this work, and to the George C. Marshall Space Flight Center for supporting this program.

DEVELOPMENT AND EVALUATION OF ADVANCED LOX/GOX  
COMPATIBLE FLUORO-ELASTOMERS

J. W. Martin  
TRW Electronics & Defense  
Redondo Beach, California 90278

Abstract not available.

HIGH-PRESSURE HYDROGEN TESTING  
OF SINGLE CRYSTAL SUPERALLOYS FOR ADVANCED  
ROCKET ENGINE TURBOPUMP TURBINE BLADES

Richard A. Parr, Wendy S. Alter,  
Dr. Mary H. Johnston  
Materials and Processes Laboratory  
National Aeronautics and Space Administration

and

Joseph P. Strizak  
Oak Ridge National Laboratory  
Operated by Martin Marietta Energy Systems, Inc.

A screening program determined the effects of high-pressure hydrogen on selected candidate materials for advanced single crystal turbine blade applications. The alloys chosen for the investigation were CM SX-2, CM SX-4C, and PWA 1480. Testing was carried out in hydrogen and helium at 34 MPa and room temperature, with both notched and unnotched single crystal specimens. Results show a significant variation in susceptibility to Hydrogen Environment Embrittlement (HEE) among the four alloys and a marked difference in fracture topography between hydrogen and helium environment specimens.

## INTRODUCTION

The selection of the present SSME turbine blade alloy, MAR-M246(Hf)DS, was based to a great extent on its performance in material development programs for aircraft gas turbines. However, the operating environment of a rocket engine turbine requires material properties which differ in certain respects from those required for an aircraft gas turbine. Candidate materials for the next-generation SSME turbine blades are being evaluated by criteria more specific to their unique application.

One significant difference between rocket engine turbines and aircraft gas turbines is the use of hydrogen fuel rather than petroleum distillates. This creates an aggressive rocket engine operating environment in which high strength materials may exhibit hydrogen environment embrittlement (HEE). Until recently, however, little attention was given to the effect of a hydrogen environment on the mechanical properties of turbine blade materials. As part of the effort to select candidate materials best suited for the rocket engine, Marshall Space Flight Center initiated a contract with Oak Ridge National Laboratory to establish facilities for high pressure hydrogen testing.

## OBJECTIVE

This program was designed strictly for screening purposes. Its goal is to rank the performance of candidate single crystal turbine blade materials under hydrogen conditions. Although researchers are attempting to understand the mechanism and the factors that influence hydrogen embrittlement of various alloys, as yet there is insufficient information to predict HEE susceptibility. Consequently, a hydrogen screening program such as this is indispensable.

## EXPERIMENTAL PROCEDURE

The four materials chosen for the study, PWA 1480, CM SX-2, CM SX-4C and Rene N-4, are all single crystal superalloys which have demonstrated good mechanical performance in air. All were received in a heat-treated condition. The CM SX-2 and CM SX-4C material had received the standard heat treatment rather than the recently developed ONERA heat treatment.<sup>1</sup> The PWA 1480 material had been heat treated according to Pratt and Whitney's modified regime, and the Rene N-4 received its normal heat treatment.

The test apparatus (Fig. 1) is located in an underground pit, with only the servo-hydraulic control instrumentation (a standard MTS system) and the hydrogen supply on the ground floor above. The system may be isolated, evacuated and purged with helium to flush out air and moisture. Then hydrogen or inert test gas is introduced and raised to 34 MPa within the autoclave by means of a booster pump. The specimen is mounted in the specimen grips; these, in turn, are mounted to the cap of the autoclave. A spherical bushing is used to maintain specimen alignment.

Both smooth and notched specimens of each alloy were tested (Fig. 2). The notched configuration was designed with a stress intensity factor of 8.0. All specimens were stress relieved at 850°C for 8 hours.

Three specimens of each alloy were tested in each of the categories in the test matrix (Table 1). Cross-head speed in all cases was  $2.12 \mu\text{ms}^{-1}$ , and the helium and hydrogen tests were conducted at 34 MPa and room temperature. The results which follow are the mean value of the three tests. In most cases, the coefficient of variation is less than 5%, indicating good consistency.

## RESULTS

Smooth tensile testing shows only a small difference between the helium properties and those obtained in air for both ultimate and yield strength (Table 2). The difference between the UTS values and yield strength is an indicator of the alloy's ductile behavior in helium. Hydrogen yield strength is not significantly different from that in helium; but the impact of the hydrogen environment is seen in the ultimate tensile strength, which is virtually identical to yield strength in hydrogen. This represents a severe loss of ductility. As soon as the specimens begin to yield, they fail. In the smooth tests, all alloys performed comparably, showing no obvious ranking of performance among the four alloys.

Reduction in area measurements on the smooth specimens reveal the extent of the ductility loss in HEE: approximately 50% in most cases. But it is in the notched strength that the difference among the alloys is clearly seen (Table 3). When the results are expressed as a ratio, the degradation of performance in hydrogen is most apparent for standard heat treated CM SX-2, and the alloys are easily ranked, with PWA 1480 showing the least loss of ductility.

An inspection of the fracture surfaces supports this ranking (Fig. 3). The high-pressure helium notched fracture surfaces show very little difference among the alloys. They are all predominantly ductile, reflecting the similar notched strengths. However, the hydrogen surfaces clearly differ. CM SX-2 shows an almost entirely brittle fracture, representing nearly instantaneous failure. As the notched ratio increases, the fracture surfaces show increasing areas of ductility.

A closer look at the fracture surfaces by the scanning electron microscope shows some ductility at both the edge and the center of the CM SX-2 specimen in helium (Fig. 4). In hydrogen, the surface is cleavage fracture. Note the orthogonal cracking in the last-to-fail region, correlating to a crystallographic fracture plane. In helium, the fracture surface of CM SX-4C is similar to that of CM SX-2 (Fig. 5). All the samples tested in helium show similar characteristics. In the hydrogen specimen both cleavage and ductility can be seen, corresponding to this alloy's better notch ratio. The properties of Rene N-4 are better still; cleavage is apparent at the edge, with a larger ductile area in the center (Fig. 6). Cleavage is less pronounced in PWA 1480, even at the edge (Fig. 7). Thus, there is a direct correspondence between the notched ratio and fractography of a specimen, and material performance in HEE can be clearly ranked.

#### CONCLUSIONS

This screening program is not conclusive in that it is not yet possible to specify one recommended alloy for use in SSME turbine blades. Work by other researchers has indicated that the ONERA heat treatment may significantly improve hydrogen properties;<sup>2</sup> therefore it would be premature to rule out the alloys in this study which showed poor performance. However, several conclusions can be drawn at this point. First, susceptibility to HEE differs dramatically among superalloys. Furthermore, mechanical testing in atmospheres other than hydrogen yields no useful information on predicting material performance under actual engine operating conditions. Therefore, hydrogen testing is essential in an SSME turbine blade superalloy screening program.

#### REFERENCES

1. T. Khan and P. Caron: "Effect of Heat Treatments on the Creep Behavior of a Ni-Base Single Crystal Superalloy," Fourth RISO Int. Symp. on "Metallurgy and Mat. Science", Roskilde (Denmark), Sept. 5-9, 1983.
2. W. T. Chandler: "Materials for Advanced Rocket Engine Turbopump Turbine Blades", Contract NAS 3-23536 Third Quarterly Technical Progress Narrative, July 28, 1983.

Fig. 1

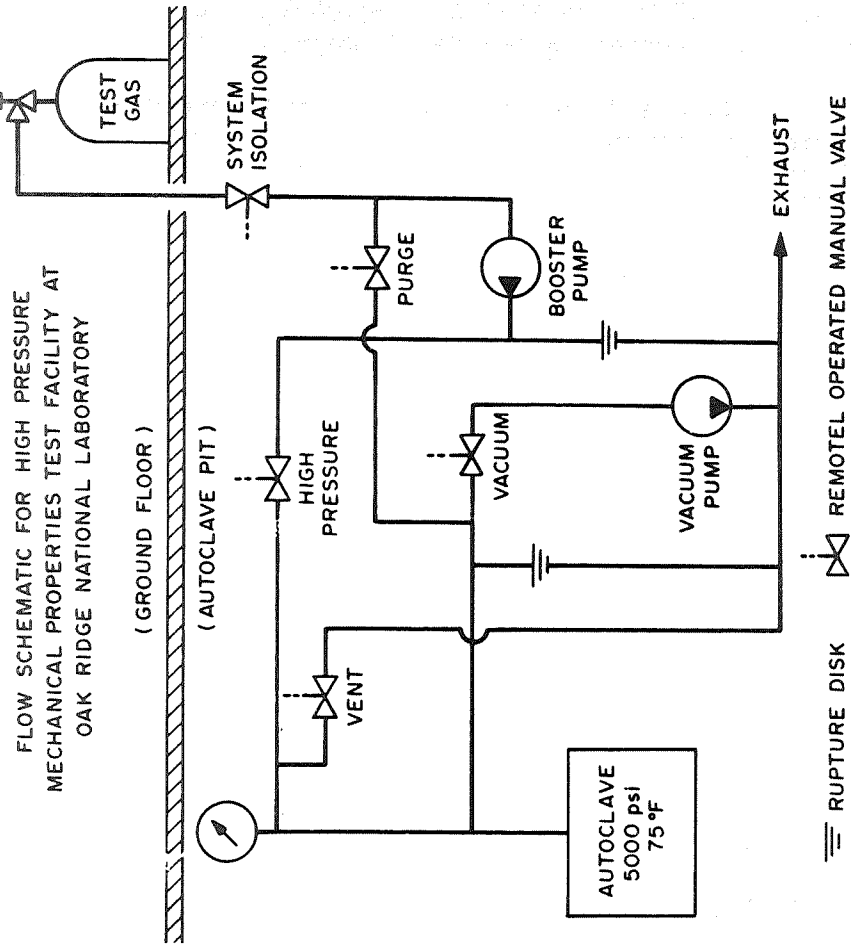


Fig. 2

TENSILE SPECIMENS

NOTES

1. ALL DIAMETERS CONCENTRIC WITHIN .005 FIR
2. ALL DIMENSIONS IN INCHES
- ③ SLIGHT TAPER TO CENTER PERMITTED
- ④ DO NOT UNDERCUT RADIUS

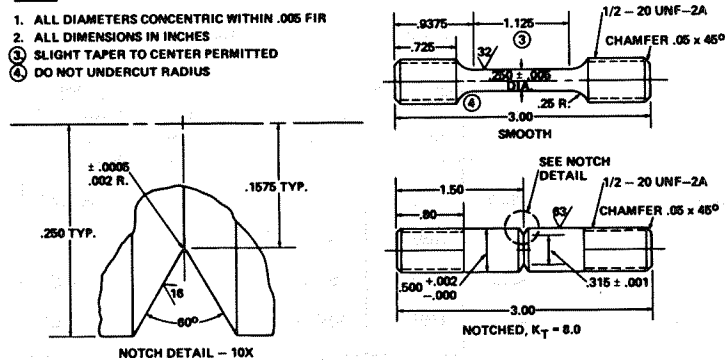


Table 1

TEST MATRIX

SPECIMEN <sup>a</sup>	ENVIRONMENT <sup>b</sup>	TEMPERATURE
NOTCHED	He	R. T.
NOTCHED	H <sub>2</sub>	R. T.
SMOOTH	He	R. T.
SMOOTH	H <sub>2</sub>	R. T.
SMOOTH	AIR	816°C

a CROSSHEAD SPEED -  $2.12 \mu\text{ms}^{-1}$ ; NOTCH -  $K_T = 8$ ; STRESS RELIEVED AT 850°C FOR 8 HOURS - VACUUM

b HELIUM AND HYDROGEN TESTS - 34 MPa; O<sub>2</sub> (H<sub>2</sub>) << 10 ppm

Table 2  
SMOOTH TENSILE TEST

ALLOY <sup>a</sup>	UTS <sup>b</sup> (MPa)			Y. S. (MPa)		
	AIR 816°C	He 20°C	H <sub>2</sub> <sup>c</sup> 20°C	AIR 816°C	He 20°C	H <sub>2</sub> <sup>c</sup> 20°C
CM SX-2	980.9	1046.1	928.2	882.9	969.7	928.2
CM SX-4C	1004.2	1087.4	987.4	870.5	996.5	967.4
RENE N-4	969.0	1157.8	970.6	854.6	976.8	970.6
PWA 1480	995.4	1151.7	1047.2	916.5	1041.8	1047.2

<sup>a</sup> ALL SPECIMENS STRESS RELIEVED AT 850°C FOR 8 HOURS/VACUUM

<sup>b</sup> CROSS HEAD SPEED OF 2.12  $\mu$  ms<sup>-1</sup>

<sup>c</sup> OXYGEN CONTENT << 10 ppm

Table 3  
NOTCHED TENSILE TEST

ALLOY <sup>a</sup>	R. A. <sup>b</sup> (%)		NOTCHED STRENGTH <sup>c</sup> (MPa)		NOTCHED RATIO H <sub>2</sub> /He
	He	H <sub>2</sub>	He	H <sub>2</sub>	
CM SX-2	14.3	6.4	1498.5	215.9	0.14
CM SX-4C	10.6	8.6	1536.6	546.8	0.36
RENE N-4	10.6	5.1	1472.8	677.6	0.46
PWA 1480	12.4	6.5	1518.0	739.6	0.49

<sup>a</sup> ALL SPECIMENS STRESS RELIEVED AT 850°C FOR 8 HOURS/VACUUM

<sup>b</sup> FINAL CROSS SECTIONAL AREA ASSUMED ELLIPTICAL

<sup>c</sup> NOTCH K<sub>T</sub> = 8

Fig. 3  
**NOTCHED TENSILE FRACTURE SURFACES**  
 2.5 X

CM SX-2      CM SX-4C      RENE N-4      PWA 1480

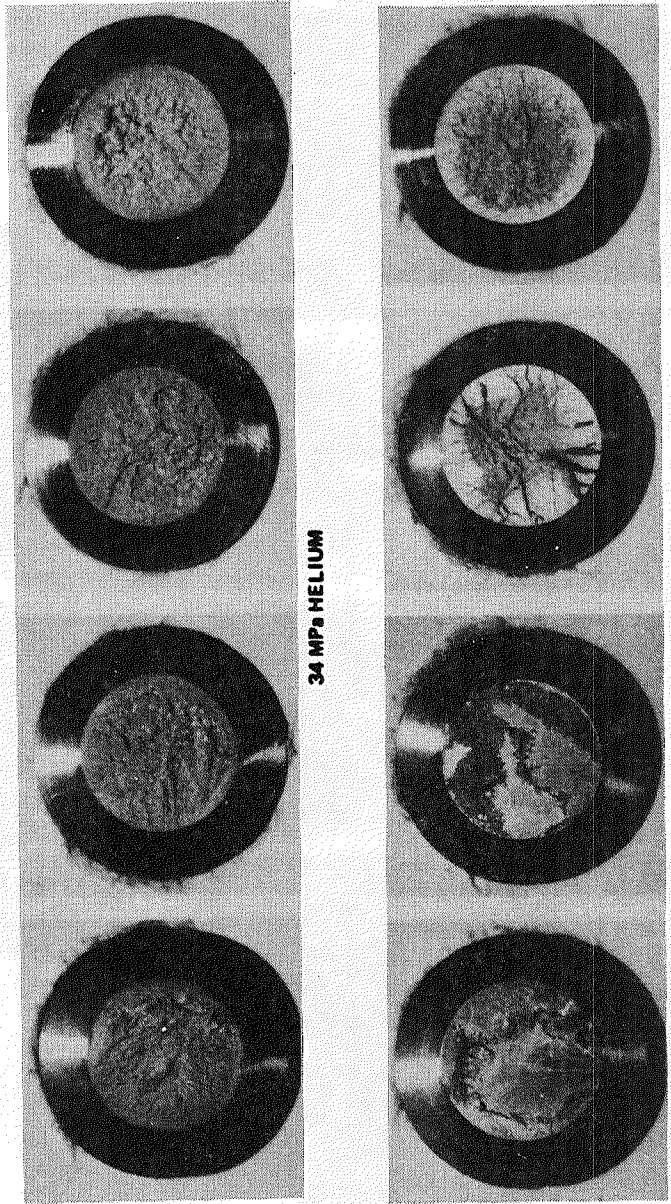


Fig. 4

CM SX-2

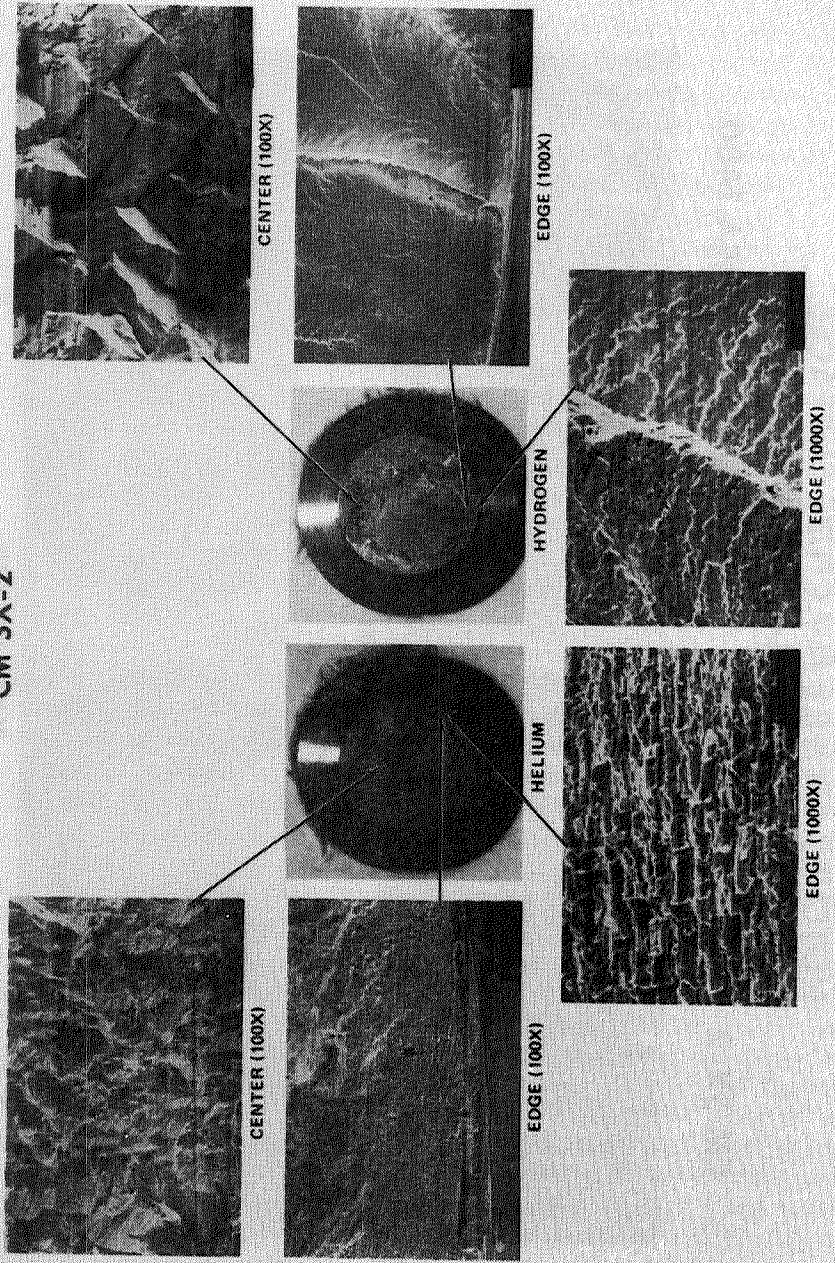


Fig. 5

CM SX-4C

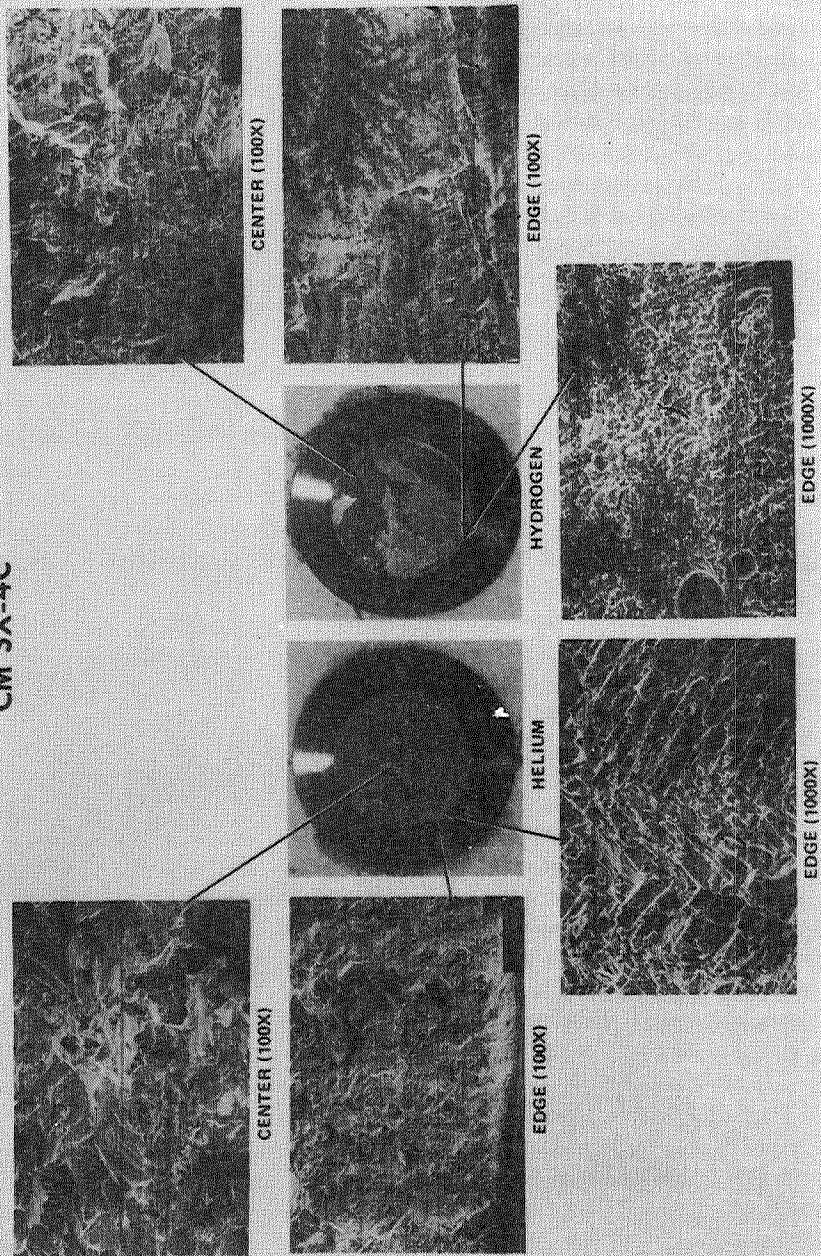


Fig. 6

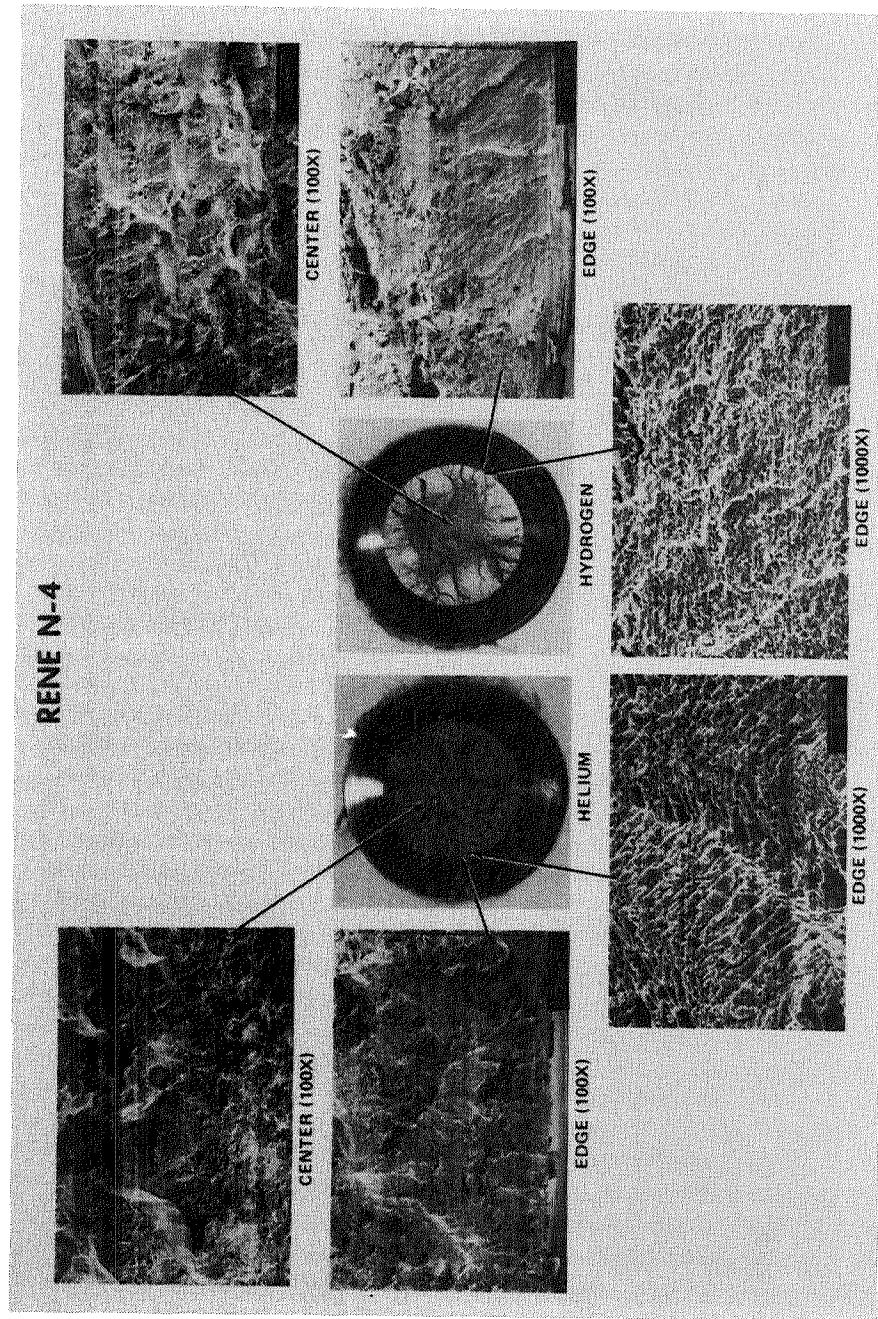
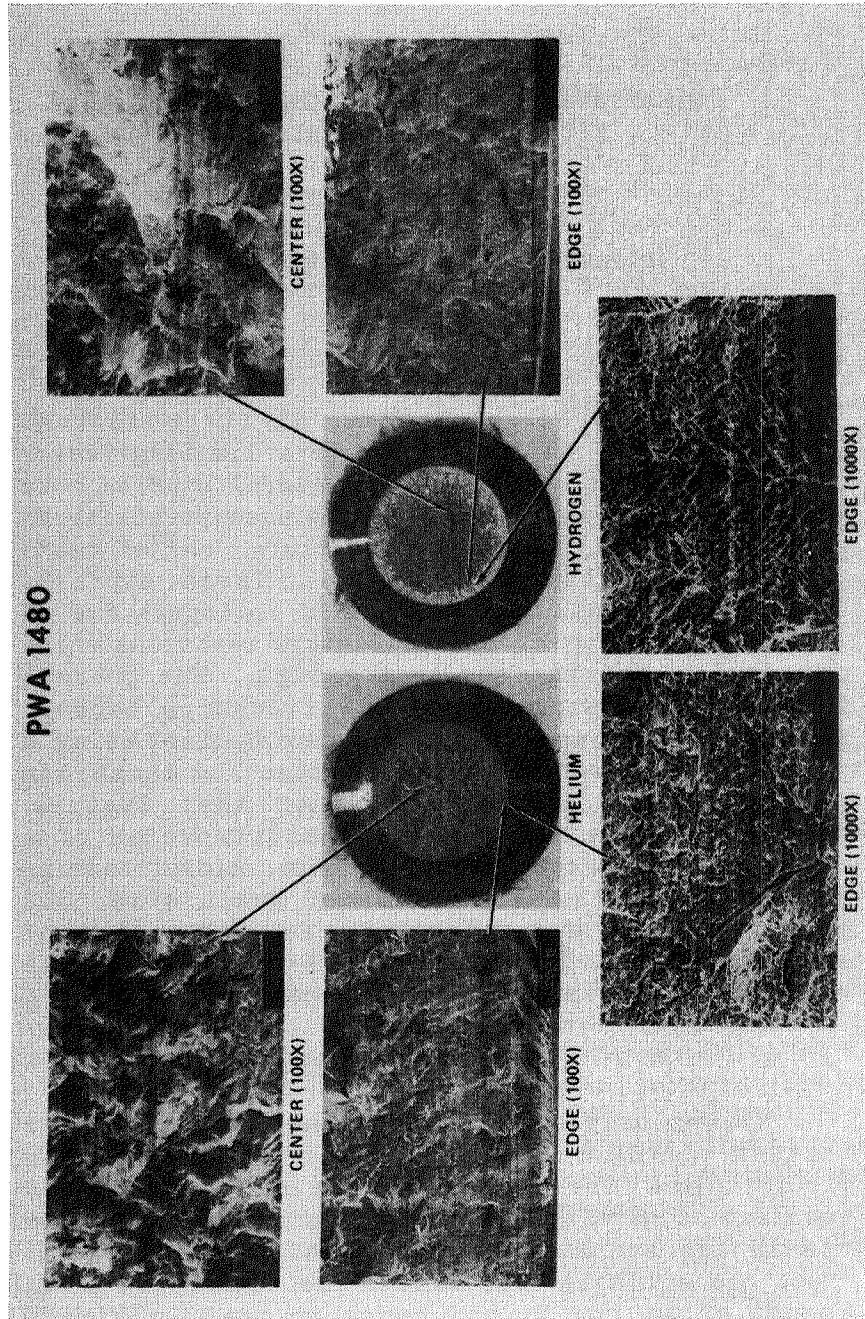


Fig. 7



RELATIONSHIPS BETWEEN MICROSTRUCTURE AND  
MICROFISSURING IN ALLOY 718

R. G. Thompson  
Materials Engineering  
University of Alabama in Birmingham  
Birmingham, AL 35294

Abstract

Microfissures which occur in the weld heat affected zone of alloy 718 can be a limiting factor in the material's weldability. Several studies have attempted to relate microfissuring susceptibility to processing conditions, microstructure, and/or heat-to-heat chemistry differences. These studies, however, are usually difficult to interpret due to the multiplicity of microstructure reactions which occurred in the various test groups. The present investigation studies the relationships between microstructure and microfissuring by isolating a particular microstructural feature and measuring microfissuring as a function of that feature. Results to date include the identification of a microstructure-microfissure sequence, microfissuring susceptibility as a function of grain size, and microfissuring susceptibility as a function of solution annealing time ( $\text{Ni}_3\text{Nb}$ - $\delta$  phase). This research effort is still in progress.

Introduction

Nickel base superalloys generally get their maximum strength from  $\gamma'$  [ $\text{Ni}_3(\text{Al},\text{Ti})$ ] age hardening precipitates. The precipitation is very rapid and can lead to strain age cracking during welding. The strain age cracking problem limits weldability. Thus, the weldable superalloys are limited in their amount of Al and Ti and hence in their ultimate strength.

One method of increasing the ultimate strength of a superalloy while avoiding strain age cracking

is the addition of Nb (alias Cb). This produces  $\gamma'$  [Ni<sub>3</sub>Nb] age hardening and, when used in conjunction with a limited amount of  $\gamma'$ , results in an increase in strength without strain age cracking problems. The  $\gamma''$  does not lead to strain age cracking because its transformation kinetics are too slow to allow its formation during ordinary welding practice. This combination of  $\gamma'$  and  $\gamma''$  strengthening was incorporated into the 718 type alloys.

Although the 718 alloy avoided the strain age cracking problem, it inherited a heat-affected zone (HAZ) microfissuring problem due to the Nb additions. Various studies were carried out to determine the cause of the microfissuring. These studies suggested that heat-to-heat chemistry differences had a strong influence on microfissuring susceptibility.<sup>2,3</sup> They also showed that processing prior to welding<sup>2</sup> and heat treatment prior to welding<sup>2,4,5</sup> both strongly influenced microfissuring susceptibility during welding. It was also strongly felt that grain size controlled microfissuring although experimental evidence was not conclusive.<sup>5</sup>

The present research builds on both prior experimental studies and practical experience to establish relationships between microstructure and microfissuring. These relationships are directly applicable to the wrought condition and, by judicious extrapolation, can be applied to cast and forged conditions as well. The research is divided into three sections which represent the three distinct experimental approaches used to study different microstructural features. Each section is capable of standing alone as a separate investigation. These three sections will be brought together in the Summary and Conclusions.

### Microstructure-Microfissuring Sequence

#### Introduction/Procedure

Little was known of the sequence of events that

led to the formation of microfissures in alloy 718 when this investigation was initiated. It was believed that carbide<sup>4</sup> or Laves<sup>2,5,6</sup> phase liquation was involved in producing a zero ductility condition in the HAZ along grain boundaries. The hot ductility test using a Gleeble machine was widely used to determine this zero ductility condition for correlation with weld microfissuring.<sup>2,4</sup>

The present study used a standard hot ductility test to generate typical hot ductility curves. A modified hot ductility test was also used in which samples were quenched to freeze the microstructure. A correlation was then made between the microstructure and hot ductility response as a function of the welding thermal cycle. A full description of this study has been published<sup>7</sup> and the reader is referred to that expanded text for more details.

#### Results/Discussion

A typical hot ductility curve with corresponding microstructures is shown in Figure 1. These microstructure-ductility curves were produced for high temperature annealed, solution annealed, and age hardened conditions. Although these preweld heat treatments showed a wide range of microfissuring susceptibilities, they all showed the same microfissuring sequence. Figure 2 shows evolution of NbC into liquid and finally Laves phase. Figure 3 depicts our scheme of the microfissure formation in the presence of this intergranular liquid.

Several important conclusions can be drawn from the results of this study. First, results from microstructure-ductility curves typical of Figure 1 showed that no on-cooling ductility was lost until NbC melting started. Thus one prerequisite for microfissuring is the formation of intergranular liquid through NbC liquation. A second interesting point is that Laves phase precipitates from this

liquid. This would explain why many investigators associated microfissuring with Laves phase.

The Ni-Nb binary phase diagram supports these observations. It is found that a eutectic point exists at the temperature which NbC liquation occurs. The composition of this eutectic is about 50 w/o Nb. The Laves phase does not have this much Nb and thus could only cause liquation through a concentration of some low melting element such as sulfur. NbC on the other hand would act like a sink of pure Nb and could easily cause the eutectic composition.

The third point to be made is that preweld heat treatments altered microfissuring susceptibility. They do not, however, change the basic microfissuring mechanism of NbC liquation. Heat treating apparently affects the manner in which the intergranular liquid spreads across the grain boundaries. Figure 4 shows an intergranular fracture surface from alloy 718. By controlling the intergranular wetting of this liquid, perhaps the microfissuring of the alloy could be controlled.

#### Microfissuring-Grain Size Relationship

##### Introduction/Procedure

Grain size is so widely recognized as a contributing factor in microfissuring that it is often used to screen incoming 718 metal for weldability. Yet there is only one reference<sup>5</sup> in the 718 literature which relates microfissuring to grain size and it is inconclusive. The purpose of the present study was to determine the relationship between grain size and microfissuring.

It was determined that a wide range of grain sizes could best be produced by using a high temperature grain growth anneal. The starting material was a single heat of 718 which was mill

processed into a uniform sheet with an average grain size of  $\sim 10 \mu$  (ASTM #10). This grain size was progressively enlarged by holding to progressively longer times at  $\sim 2160\text{F}$ . Specimens were quenched from  $2160\text{F}$  to prevent precipitation of unwanted secondary phases. It was felt that this treatment would minimize analytical variables such as heat-to-heat chemistry differences, impurity segregation, and secondary phases. It should be noted that the carbides were left undissolved since the thermal treatment was below the carbide liquation temperature.

The microfissuring susceptibility as a function of grain size was determined using a spot vareststraint test.<sup>8</sup> In this test, microfissures were forced to occur around the periphery of a GTAW spot weld by straining the hot HAZ of the weld. The magnitude of microfissuring was correlated with grain size as shown in Figure 5.

#### Results/Discussion

As seen in Figure 5, microfissuring showed an almost linear dependence on grain size at all strain levels. The relative effect of grain size was to increase microfissuring 0.4% per micron ( $1 \times 10^{-6}\text{m}$ ) increase in grain size. This represents substantial increases in microfissuring as the ASTM grain size number increases (Table 1).

TABLE 1

#### Microfissuring Dependence on Grain Size

ASTM Grain Size	Percentage Increase in Microfissuring above Baseline
9	baseline
7	5%
5	12%
3	38%
1	82%
00	175%

It is interesting to note that the relationship between microfissuring and grain size is independent of the strain level. It is also noteworthy that there is not a critical grain size below which microfissuring did not occur. Thus, if grain size is to be used as a weldability criterion, then it should be realized that such a criterion at best defines some microfissuring level of significance. It could not specify a microfissure, no-microfissure condition for a wide variety of welds.

### Microfissure-Heat Treating Relationship

#### Introduction/Procedure

Heat treatments of interest in the 718 microfissuring problem are the solution anneal (1900-1700F) and age hardening (1400-1200F) treatments. Isothermal transformation diagrams are available in the literature which could be used to predict the precipitation reactions which might accompany these standard heat treatments. However, it was found that such diagrams are highly dependent on Nb segregation. Thus, published transformation diagrams are not generally applicable.

Given the above misgivings about predicted 718 transformations, certain generalities can be helpful when considering solution anneal and age hardening heat treatments. First, solution annealing usually is associated with reduced microfissuring while age hardening is usually associated with increased microfissuring. Solution annealing is also generally associated with  $Ni_3Nb$  ( $\delta$ ) precipitation while age hardening is associated with  $\gamma'$ ,  $\gamma''$  precipitation. The present work sought to identify some relationship between microfissuring and the precipitation of  $Ni_3Nb(\delta)$  and  $\gamma'$ ,  $\gamma''$ .

Specimen preparation followed directly from the grain growth procedures already described. The grain growth procedure was carefully designed to eliminate secondary phases. It was thus uniquely

suited for the introduction of a specific second phase for analysis. A solution anneal of 1700F for 1 to 8 hours was used to produce a volume fraction range of  $Ni_3Nb(\delta)$  precipitated into a 718 matrix of specific grain size. Samples thus prepared were tested in the spot vareststraint machine as previously described.

It should be possible to correlate microfissuring with the volume fraction of  $Ni_3Nb(\delta)$ . These volume fractions have not yet been measured so that microfissuring is plotted against solution annealing time as in Figure 6. Microfissuring versus either volume fraction of  $\gamma'$ ,  $\gamma''$  or hardness will also be presented in the final report but at this time the data is not yet ready.

#### Results/Discussion

Figure 6 shows that the solution anneal heat treatment was effective in reducing microfissuring only in the metal with large grain size. It is also evident that most of the beneficial effect is achieved in the first hour of heat treating. The last point of significance is that the reduction in microfissuring susceptibility was realized before  $Ni_3Nb(\delta)$  precipitation was detected in the alloy.

The fact that microfissuring was reduced prior to  $Ni_3Nb(\delta)$  precipitation is interesting. It might have been suspected that  $Ni_3Nb(\delta)$  precipitation was the reason that solution annealing seemed to reduce microfissuring. That doesn't appear to be the case and other theories as to the mechanism of reduced microfissuring should be considered. One such theory is that of impurity or alloy segregation during the solution anneal heat treatment.

#### Summary

Microfissuring in wrought alloy 718 is due to the liquation of NbC and the subsequent intergranular liquid which is produced. If

sufficient strain is produced in the HAZ while the intergranular liquid is present, then microfissuring will result.

It is evident from Figure 5 that the magnitude of microfissuring in the HAZ is a function of both the strain level and the susceptibility of the microstructure to microfissure.

The susceptibility of the microstructure to microfissure can be easily understood if we assume that this susceptibility is defined by the distribution of the intergranular liquid as a function of temperature. Smith<sup>9</sup> has defined the distribution of intergranular liquid in terms of the liquid's wetting angle. The boundaries seen in Figure 4 represent the case where liquid has not quite wet the grain boundary faces. This would be equivalent to a wetting angle slightly greater than zero. The HAZ would be most susceptible to microfissuring when the wetting angle reaches zero. One must also consider the temperature response of the wetting angle. The metal will be microfissure sensitive over the temperature range which the wetting angle remains zero during cooling from the weld. A large microfissure-sensitive temperature range translates into a long period of time over which cooling strains can concentrate in the HAZ and cause microfissuring.

### Conclusions

1. NbC liquation is a prerequisite for microfissuring.
2. TiC has a higher stability temperature than does NbC and is not involved in the NbC liquation.
3. Laves phase is often associated with microfissuring because it precipitates from the Nb-rich intergranular liquid onto the microfissure fracture surfaces.

4. Increasing grain size increases microfissure susceptibility at the rate of 0.4% per micron ( $1 \times 10^{-6}$ m) increase in grain size.
5. The grain size effect is independent of the applied strain.
6. Solution annealing significantly reduces microfissuring only in metal with a large grain size.
7. The major reduction of microfissuring during solution anneals occurs during the first 30 to 60 minutes at 1700F.
8. The observed reduction in microfissuring during solution annealing does not appear to be related to the  $\text{Ni}_3\text{Nb}(\delta)$  precipitation which often accompanies that heat treatment.
9. It was found that age hardening increased microfissuring, but it has not yet been determined if the increased microfissuring correlates with matrix hardness.

#### References

1. Eiselstein, H. S. 1965. Metallurgy of a columbium-hardened and nickel-chromium-iron alloy. ADVANCES IN TECHNOLOGY OF STAINLESS STEEL AND RELATED ALLOYS, ASTM STP 369:62-79.
2. Thompson, E. G. 1969. Hot cracking studies of alloy 718 weld heat-affected zone. Welding Journal 48 (2):70-s to 79-s.
3. Morrison, T. J., Shira, C. S., and Weisenberg, L.A. 1969. Effect of Minor Elements on Alloy 718 Weld Microfissuring. Effects of Minor Elements on the Weldability of High-Nickel Alloys. Welding Research Council, N.Y.,N.Y.:47.

4. Duvall, D. S., and Owczarski, W. A. 1967. Further heat-affected zone studies in heat resistant nickel alloys. Welding Journal 46(9):423-s to 432-s.
5. Valdez, P. J. and Steinman, J. B. 1969. Effect of Composition and Thermal Treatments on the Weldability of Nickel-Base 718 Alloy. Effects of Minor Elements on the Weldability of High-Nickel Alloys. Welding Research Council. N.Y., N.Y.:93.
6. Vincent, E. R. 1980. The microstructure of welds in Inconel 718. Department of Physics, University of Bristol, United Kingdom.
7. Thompson, R. G. and Genculu, S. 1983. Microstructural Evolution in the HAZ of Inconel 718 and Correlation with the Hot Ductility Test. Welding Journal 62(12):337-s to 345-s.
8. Savage, W. F., Nippes, E. F. and Goodwin, G. W. 1977. Effects of Minor Elements on Hot Cracking Tendencies of Inconel 600. Welding Journal 56:245-s.
9. Smith, C. S., 1948. Grains, phases and interfaces: an interpretation of microstructure. Trans. A.I.M.M.E. 175:175.

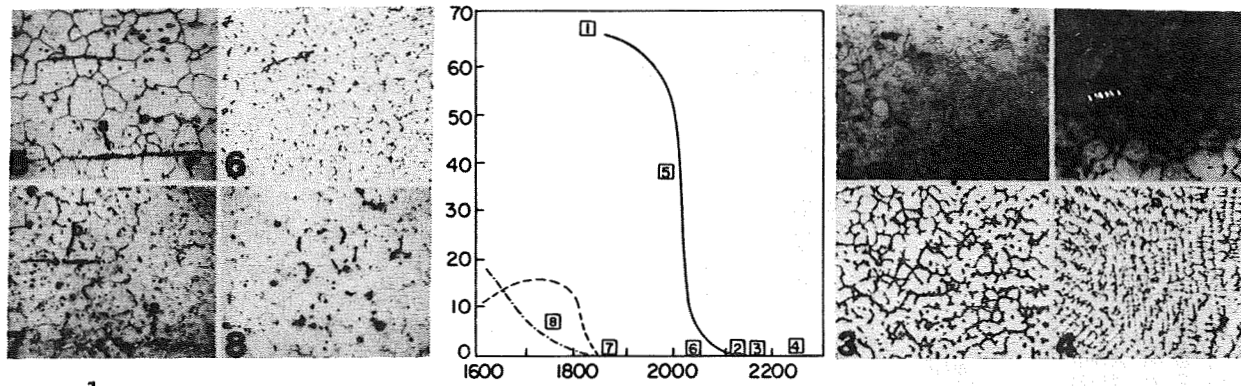
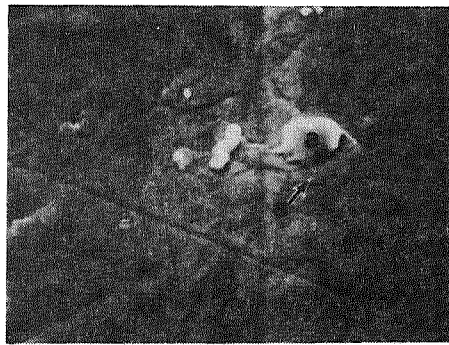


**FIGURE 1.**  
**MICROSTRUCTURAL EVOLUTION IN AS RECEIVED 718 DURING HOT DUCTILITY TEST.**



a - NbC particle

d - Laves phase precipitation from liquid e

e - Liquid from liquated NbC particle

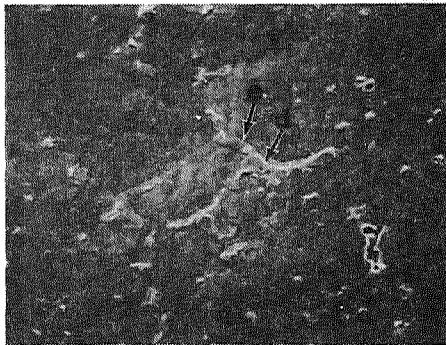
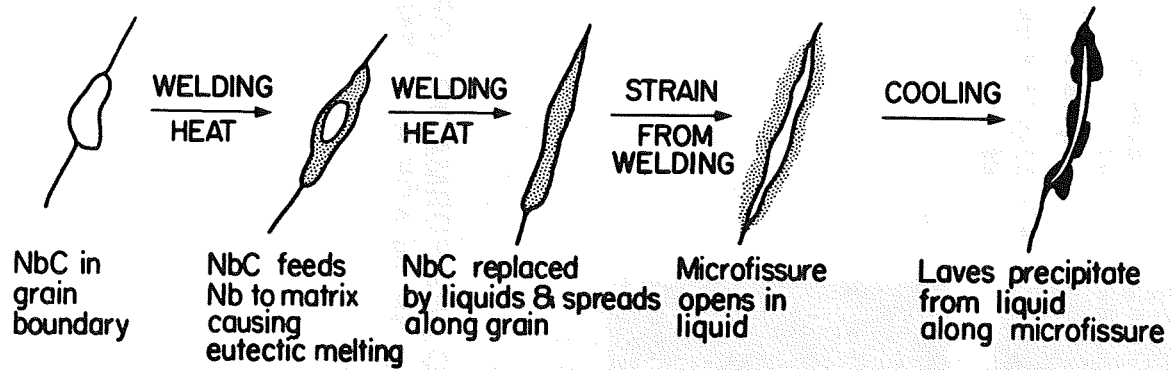


Figure 2

**DISSOLUTION OF NbC AND FORMATION OF INTERCRANULAR PHASE IN AGE HARDENED 718.**



### Microstructure - Microfissure Sequence

FIGURE 3

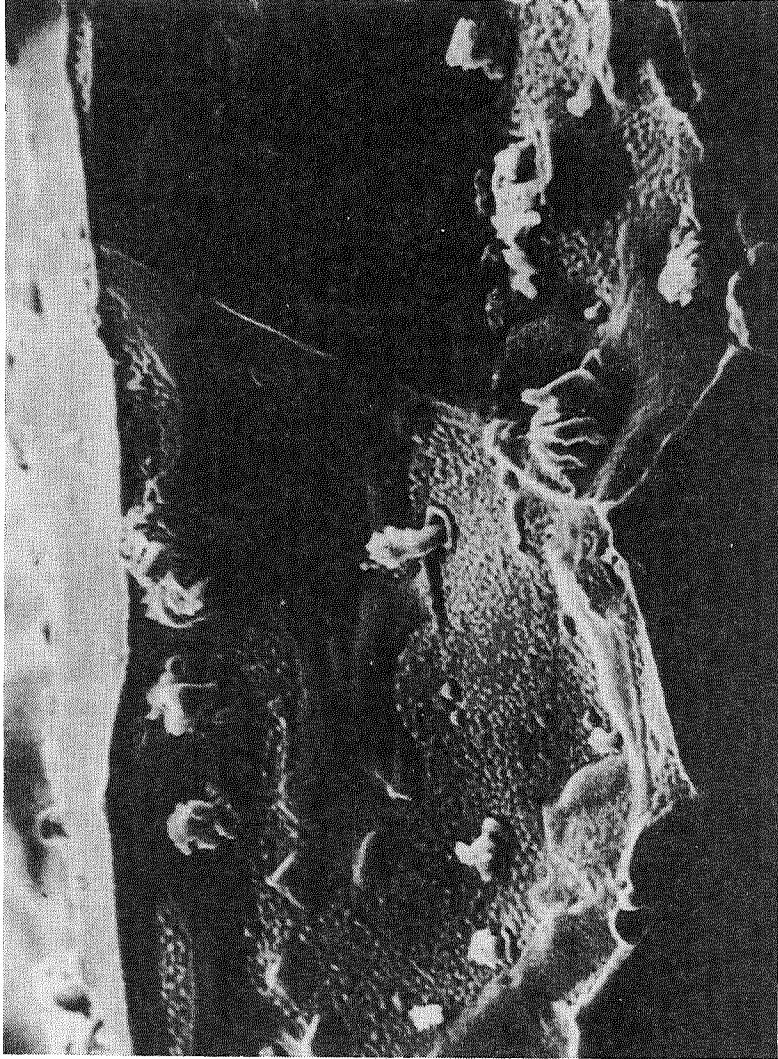


**FIGURE 4**  
FRACTURE SURFACE - 2200°F, 500X

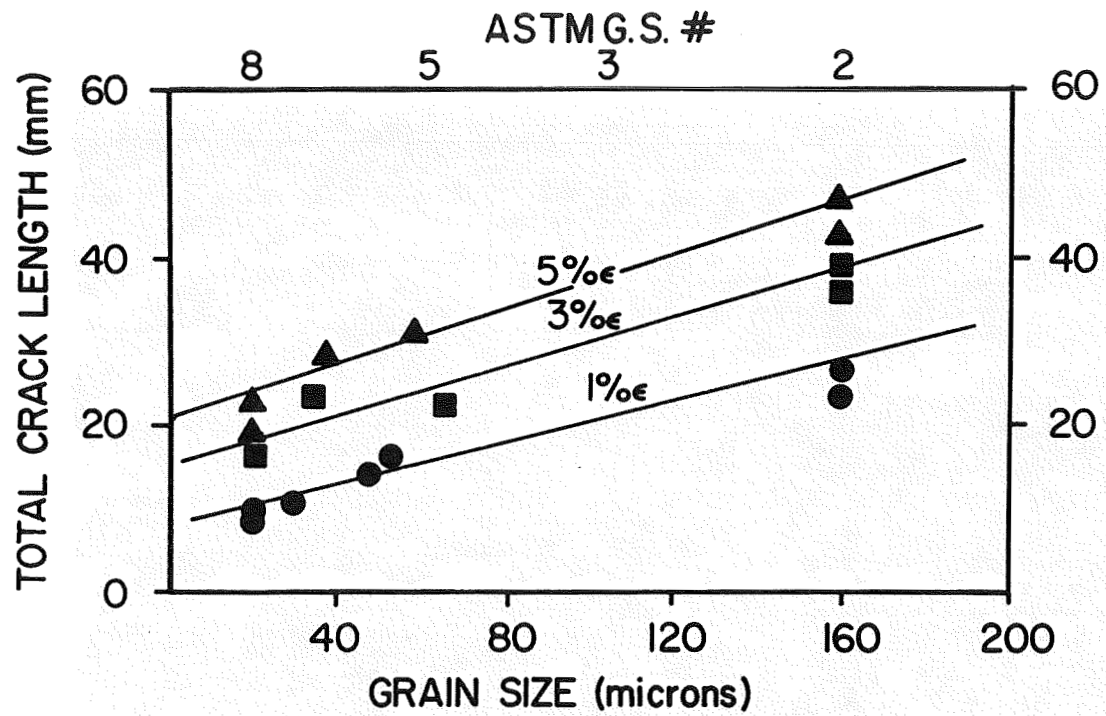
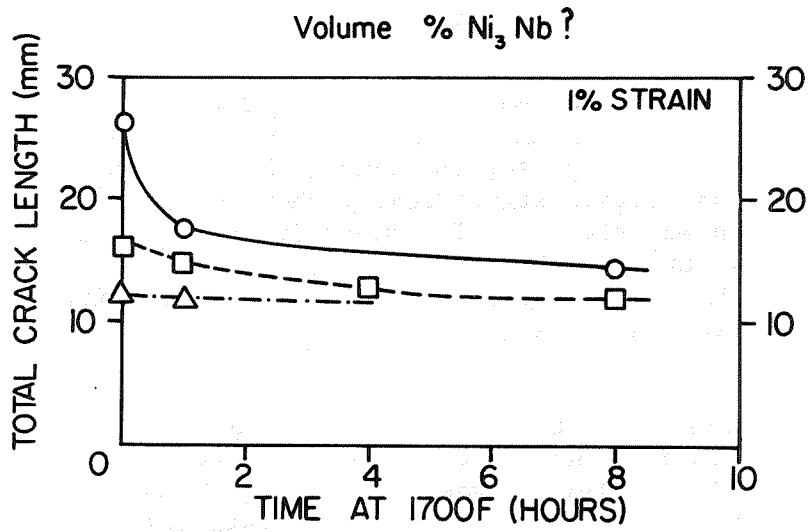


FIGURE 5 Effect of Grain Size on Total HAZ Crack Length in the Spot Varestraint Test

- Initial G.S. 160 $\mu$  (#1.8)
- Initial G.S. 55 $\mu$  (#5)
- △ Initial G.S. 45 $\mu$  (#6)



Effect of Annealing Time at 1700F on  
Microfissuring Susceptibility  
**FIGURE 6**

## DEVELOPMENT OF NEW MATERIALS FOR TURBOPUMP BEARINGS

Robert E. Maurer and Robert A. Pallini  
SKF Industries, Inc.  
King of Prussia, PA

### Abstract

The life requirement for the angular contact ball bearings in the Space Shuttle Main Engine (SSME) high pressure oxygen turbopump (HPOTP) is 7.5 hours. In actual operation, significantly shorter service life has been experienced. The objective of this current program is to identify bearing materials and/or materials processing techniques offering significant potential for extending HPOTP bearing performance life.

Interactive thermomechanical analysis of the HPOTP bearing-shaft system was performed with the SHABERTH computer program. Bearing fatigue life, ball-race contact stress, heat generation rate, bulk ring temperatures and circumferential stress in the inner rings were quantified as functions of radial load, thrust load and ball-race contact friction. Criteria established from the output of this analysis are being used for material candidate selection.

### Introduction

The space shuttle main engine cryogenic turbopumps, and in particular the high pressure oxygen turbopump, (HPOTP), have been experiencing premature bearing degradation. Bhat and Dolan<sup>1</sup> have reported heavy spalling and prominent wear of the rings and rolling elements of the HPOTP bearings after only

2406 seconds of total running time with only 1090 of those seconds at full power level. Other failure analyses<sup>2,3</sup> have revealed heavy wear, smearing, microcracking and pitting indicative of surface distress associated with inadequate lubrication. The bearings in these analyses experienced total operating times of less than 6000 seconds. In addition to the above mentioned failure observations, surface oxide films indicative of high operating temperatures have been observed on rolling element and race surfaces of the bearings after 100 to 4000 seconds total operating time. These latter observations are consistent with the failure scenario proposed by Bhat and Dolan<sup>1</sup>, which attributes the abbreviated HPOTP bearing life to a thermal runaway mechanism.

In an investigative study<sup>4</sup> performed on these bearings, analytical work showed that with full film lubrication the predicted bearing life is on the order of 100 hours (360,000 seconds). The life requirement is 7.5 hours or 27,000 seconds. The current HPOTP bearing lubrication scheme consists of MoS<sub>2</sub> films on the balls and raceways, and a woven glass reinforced Teflon (Armolon) cage intended to provide a transfer film to the balls during bearing operation. The very short life of the MoS<sub>2</sub> films and the lack of Teflon film formation in the liquid oxygen (LOX) environment results in inadequate lubrication. The attendant wear and thermally induced bearing loading have resulted in the much shorter lives experienced to date.

The failure analysis work highlighted above indicates that significant life improvements may be realized by providing low friction, wear resistant rolling contact surfaces. Computer stress analysis indicates that the means by which low friction and wear resistance are obtained must be consistent with metallurgical requirements associated with successful bearing performance in a very severe rolling contact stress environment.

This paper reports the results to date of a study aimed at identifying new bearing materials offering significant potential for extending bearing performance life in advanced cryogenic turbopumps. State-of-the-art bearing analysis techniques were employed to parametrically quantify bearing material property requirements in high pressure cryogenic turbopumps, with emphasis placed on the HPOTP. The results of this analysis were used to establish well defined criteria for the selection of new materials and associated processing techniques. Materials and processing techniques can now be reviewed and rated in compliance with the selection criteria.

#### HPOTP Rotor/Bearing System

Figure 1 is a cross-section of the high pressure liquid oxygen turbopump (HPOTP) showing the locations of the two pairs of preloaded angular contact ball bearings that support the pump rotor. The bearings are mounted in a back-to-back arrangement with a pair on each side of the main pump impeller. The rotor is designed to act as a floating piston (balance piston) to balance out as much as possible any residual thrust loads on the bearings from the fluid pressures acting on the rotor. Preload springs between the bearings in each pair and apply thrust preloads of 3.8 to 4.5 kN (850 to 1000 lbf) to prevent skidding, depending on bearing size.

The rings and balls in the angular contact ball bearings in these turbopumps are made of CEVM 440C martensitic stainless steel. The cages are made of Armalon, a woven glass reinforced Teflon composite, which is intended to provide lubrication for the ball and race contacts by Teflon transfer films to the balls from the cage pockets. Bearing cooling is achieved by a substantial flow of the LOX through the bearings. The extreme temperatures of the environment preclude use of any conventional type of bearing lubrication.

The bearings are designed with 52% to 53% ball groove conformities and nominal unmounted contact angles of 20° to 28°. The ring mounting fits are designed to be a sliding fit on the outer rings and a tight fit on the inner rings, which is to become essentially line-to-line during operation, taking into account differential thermal growths and centrifugal effects on both the inner ring and shaft.

#### Analytical Studies

The bearing system analyses were conducted with the SHABERTH<sup>3</sup> (SHaft-BEaring-THERmal) computer program. This approach provided an efficient means of calculating the stress, kinematic, and thermal information required to describe the bearing internal operating environment. Bearing stresses, fatigue lives, heat generation rates, temperatures, rolling and sliding velocities were calculated. The analysis incorporates the effects of thermal contractions, shaft stiffness, bearing preload, coolant temperature and flow rate, solid lubricant traction coefficients, and material elastic and heat transfer properties.

Two key features of SHABERTH with respect to the cryogenic turbopump bearing analyses are the inclusion of a general thermal analysis model and a dry lubrication option. The high bearing heat generation rates due to the use of solid lubrication make consideration of thermal and mechanical interactions very important in analyzing the bearings. The dry lubrication option makes use of a coulomb friction model to calculate bearing heat generation rates.

All of the possible heat transfer mechanisms including conduction, free and forced convection, and fluid flow are considered in the SHABERTH thermal model. The thermal analysis is coupled with the bearing mechanical analysis enabling consideration of thermomechanical interplay. Steady state or time transient temperatures may be calculated.

An interactive thermomechanical analysis of the aforementioned HPOTP shaft/bearing system was performed with the objective of parametrically quantifying HPOTP bearing operating environments from a materials viewpoint. Table 1 is a listing of the loading conditions modelled in the analytical studies.

Bearing fatigue life calculated in SHABERTH is based on classical subsurface initiated failure. Empirically derived multipliers are often applied to this calculated value to reflect observed effects of bearing material quality and lubrication conditions in an adjusted rating life, or expected life. In the current analytical studies no multipliers were used, so the values indicated are the unadjusted, calculated lives that may be achieved if surface integrity is protected against wear and lubrication related surface distress. The surface characteristic that was parameterized was coefficient of sliding friction. This permitted characterization of the effect of coefficient of friction on bearing heat generation and the associated thermally induced loading, and the resulting effect of thermal loading on bearing fatigue life.

Figure 2 is a plot of bearing fatigue life versus friction coefficient for Bearings #2 and #3, for two of the radial load conditions that were analyzed. Under the worst case radial load conditions (i.e. 22.2 kN (5000 lbf) total radial shaft load) the life of Bearing #3 decreases from a calculated 9 hours at coefficient of friction ( $\mu$ ) = 0.08 to a life of less than 1 hour at  $\mu$  = 0.5. Under the minimum radial load condition plotted (i.e. 8.5 kN (1915 lbf) total radial shaft load), the calculated life for Bearing #3 shows a very dramatic decline from approximately 44 hours at  $\mu$  = .08, to 3 hours at  $\mu$  = 0.5. (A coefficient of friction for unlubricated 440C-440C sliding of 0.65 is reported by Spalvins<sup>6</sup>).

The life degradation is severely aggravated by the application of thrust load (possibly caused by

the failure of outer race axial movement) resulting in the trends in bearing life reduction plotted in Figure 3.

Figures 2 and 3 indicate that even if surface initiating mechanisms can be ruled out as causes for failure, the HPOTP bearings will have difficulty achieving the required fatigue lives unless friction coefficient can be minimized and the occurrence of applied thrust load can be eliminated.

Figures 4 and 5 present bearing element-to-raceway stress levels versus friction coefficient and applied thrust load, respectively. Again, a dramatic sensitivity to friction coefficient is indicated. With the application of thrust load the contact stress levels can exceed 3447 MPa (500 ksi).

These high stress levels and low fatigue lives are a result of thermally induced loading. The radial expansion of the bearing created by the heat generated within the bearing is causing a radial preloading effect. Even though the bearings are operating in a cryogenic environment and coolant flow is present through the bearings, the ball/race contacts are still a source of considerable heat generation. Figures 6 and 7 illustrate the heat generation rates for the HPOTP bearings.

The figures (6 and 7) show total bearing heat generations, however, it should be noted that 55% to 65% of this generated heat is at the inner race contacts. This is due to the fact that the computer modeling has assumed outer race control, which means that all the ball spinning takes place at the inner race contact. Since there is no gross sliding present (axial spring preload are sufficient to prevent sliding) the spin at the inner race is the major contributor to the heat generation. Spin-to-roll ratios for the inner race contacts ranged from 0.1 to as high as 0.6 under light loads. A spin/roll ratio of 0.3 was typical for nominal operating conditions.

Other bearing performance parameters examined included, operating contact angles, subsurface stresses, and circumferential ring stresses. The trends in the results for these parameters were consistent with those already examined.

In summary, the analytical studies highlighted the following key points about the HPOTP bearing operating environment:

- 1) Due to the short duration of the MoS<sub>2</sub> films on the balls and raceways, and the inability of the Teflon transfer to be effective in the LOX environment, the HPOTP bearings most likely operate with friction coefficient values approaching that of dry metal-to-metal contact (i.e.  $\mu > .35$ ).
- 2) At these high friction levels and under maximum operating conditions the bearing heat generation rates reach levels on the order of 20 to 50 kilowatts (19 to 47.4 Btu/sec).
- 3) The high rate of heat generation creates a situation of inner ring thermal expansion which creates high [up to 3447 MPa (500 ksi)] bearing contact stress levels and greatly reduced bearing rolling contact fatigue lives.
- 4) Any applied thrust load dramatically aggravates the above scenario and provides increased potential for a thermal runaway type failure.
- 5) The analysis indicates that much improved bearing life may be realized at low (<0.15) friction coefficient levels coupled with minimized bearing wear and thrust loading.

#### Bearing Material Consideration

Bearing material candidate eligibility is to be assessed on the basis of compatibility of their pro-

property offerings with the property requirements identified in the analytical studies.

The required material properties include:

- ° rolling contact fatigue life consistent with the 7.5 hour design goal
- ° dimensional stability at cryogenic temperatures
- ° fracture toughness sufficient to preclude catastrophic component fracture in service
- ° corrosion resistance at least equal to that of 440C steel
- ° ball-race contact friction coefficient less than 0.15
- ° wear resistance consistent with maintaining the required contact friction through the life goal of 7.5 hours.

Bulk material requirements for hardness, rolling contact fatigue life, dimensional stability and fracture toughness are adequately provided by conventional, high quality, through hardening bearing steels such as 440C, 52100 and M50. Of these materials, 440C is the only one offering corrosion protection, but with a sacrifice in rolling contact fatigue performance compared to 52100 or M50. The required friction and wear resistance properties are not provided by these materials.

Coefficients of friction obtained from unlubricated 4-ball wear tests are reported by Kannel, et al<sup>7</sup>, for 52100, 440C, BG-42 and Star J. The values are in the range of 0.4 to 0.6 for all of the materials. It is doubtful that appreciably different values would be demonstrated with any other bearing steel composition. As previously discussed, the solid film lubrication methods used in the current

HPOTP system appear inadequate to prevent metal-to-metal contact between the balls and raceway surfaces. With the constraints of the HPOTP operating environment, and restrictions on the types of lubricating substances that can be introduced into the LOX system, no outstanding replacement candidates for Armoloy have been identified. Consequently, friction and wear control of the required magnitude necessitates measures offering significantly more reliability and efficiency than that provided by the current lubrication scheme.

There are several surface treatment techniques, compatible with hardened steel substrates, that provide substantial reductions in friction, and improved wear and corrosion resistance. Some have been tested in rolling contact fatigue and have demonstrated excellent performance. These include reactively sputtered (RS) TiN, a reactively sputtered material referred to as "Hard Molybdenum" and electrodeposited chromium via the Armoloy process<sup>8,9</sup>. Although the rolling contact tests were oil lubricated, specimens of M50 steel coated with RS TiN survived 167.5 hours ( $86.4 \times 10^6$  cycles) at a contact stress of 5419 MPa (786 ksi) without failure, demonstrating remarkable coating adherence<sup>8</sup>.

Coefficient of friction values in the range of 0.05 to 0.1 are reported by Jamal, et al<sup>10</sup>, for unlubricated test couples when both surfaces are coated with TiC or TiN. Ramalingam<sup>11</sup> reports coefficient of friction values in the range of 0.13 to 0.16 for TiN coated AISI 1018 steel (annealed) running against 52100 steel (RC62). Wear rate reductions of approximately two orders of magnitude were obtained with TiN coated 1018 steel as compared with uncoated 1018 steel. A value of 0.16 is reported by the Armoloy Corporation for uncoated steel against Armoloy coated steel.

Increased adhesive and abrasive wear resistance of both carbide and high speed steel cutting tools

coated with TiN and TiC is credited by Bunshah<sup>12</sup> for life improvement factors of 2 to 8 over uncoated tools.

Exceptional corrosion and wear resistance, reported coefficient of friction values in the vicinity of 0.15 demonstrated adherence under extremely high rolling contact stress, and compatibility with conventional, high performance bearing steel add up to provide solid endorsement of hard coatings as candidates for evaluation in HPOTP bearing services.

An enduring surface coating exhibiting low friction in unlubricated conditions (compared to an unlubricated steel-steel contact) not only offers potential for significant reductions in bearing heat generation and the associated thermal loading, but also provides for lower surface tractions, thereby diminishing life reduction effects described by Smith and Liu<sup>13</sup>. Additionally, substrate material selection can be based on rolling contact fatigue performance, uncompromised by bulk material requirements for corrosion and wear resistance.

Information is being compiled concerning application techniques, properties and performance characteristics of hard coatings as well as that pertaining to alternate surface treatments. Specific substrate-surface treatment combinations will be identified and recommended for further evaluation as HPOTP bearing material candidates.

#### Summary and Conclusions

- 1) The current HPOTP bearing lubrication methods are inadequate, resulting in ball-race friction approaching that of unlubricated metal-to-metal contact (i.e.  $\mu = .35$  to  $.60$ ).
- 2) Under these high friction conditions and maximum load, bearing heat generation rates reach levels

on the order of 20 to 50 kilowatts (19 to 47.4 Btu/sec).

- 3) The high rate of heat generation results in thermally induced bearing loading and greatly reduced bearing fatigue life.
- 4) Applied thrust load significantly increases bearing heat generation rates.
- 5) Bearing life approaching the design goal of 7.5 hours may be realized with a coefficient of friction for ball-race contact of 0.15 or less, coupled with minimized bearing wear and thrust loading.
- 6) Hard coatings (e.g. reactively sputtered TiN) used in conjunction with a high performance bearing steel (e.g. M50) offer significant potential to provide the combination of properties indicated by the analytical studies as requisite for HPOTP bearing design life attainment.

#### Acknowledgement

This work is being performed under NASA/MSFC Contract No. NAS8-35341 with SKF Industries, Inc., King of Prussia, PA. The authors acknowledge the assistance provided by Mr. Gordon Marsh, NASA/MSFC Program Manager, Dr. Biliyar N. Bhat, Metallurgy Research Branch, Metallic Materials Division and Mr. Fred J. Dolan, Chief, Lubrication and Surface Physics Branch, Engineering Physics Division, Materials and Processes Laboratory, MSFC.

#### References

1. Bhat, B. N. and Dolan, F. J., "Past Performance Analysis of HPOTP Bearings," NASA TM-82470, March 1982.

2. Broschard, J. L., "Turbopump Bearing Analysis," SKF Report No. AT83X001, March 1983.
3. Dufrane, K. F. and Kannel, J. W., "Evaluation of Space Shuttle Main Engine Bearings from High Pressure Oxygen Turbopump 9008," Final Report, Contract No. NAS8-33576, Task No. 102, July 11, 1980.
4. Sibley, L. B., "Analysis of Turbopump Bearings from Space Shuttle Test Engine No. 5," SKF Report No. AL79T004, January 1979.
5. Crecelius, W. J., "User's Manual for Steady State and Transient Thermal Analysis of a Shaft Bearing System (SHABERTH)," Contract Report ARBRL-CR-00386, submitted to U.S. Army Ballistic Research Laboratories, November 1978.
6. Spalvins, Talivaldis, "Coatings for Wear and Lubrication," Thin Solid Films, Vol. 53, 1978, pp. 285-300.
7. Kannel, J. W., Merriman, T. L., Stockwell, R. D. and Dufrane, K. F., "Evaluation of Outer Race Tilt and Lubrication on Ball Wear and SSME Bearing Life Reductions," Final Report, NASA/MSFC Contract NAS8-34908, July 1983.
8. Dill, J. F., Gardos, M. N., Hinterman, H. E., and Boving, H. J., "Rolling Contact Fatigue Evaluation of Hardcoated Bearing Steels." To be presented at the International Solid Lubrication Conference, Denver, August 1984.
9. Maurer, R. E., Hahn, D. E. and Ninos, N. J., "Functional Testing of Armoloy, Noblizing and Electroless Nickel Coatings in Rolling Contact," SKF Report No. AL76M001, August 1976.
10. Jamal, T., Nimmagadda, R., and Bunshah, R. F., "Friction and Adhesive Wear of Titanium Carbide

and Titanium Nitride Overlay Coatings," Thin Solid Films, Vol. 73, 1980, p. 245.

11. Ramalingam, S., "Magnetron Sputtering as a Technique for Applying Tribological Coatings," Tribology in the 80's, NASA Conference Publication 2300, Vol. 2, 1983, pp. 753-772.
12. Bunshah, R. F., "Hard Coatings for Wear Resistance by Physical Vapor Deposition Processes," SAMPE Quarterly, Vol. 12, No. 1, October 1980.
13. Smith, T. O. and Liu, C. K., "Stress Due to Tangential and Normal Loads on an Elastic Solid with Application to Some Contact Stress Problems," ASME Journal of Applied Mechanics, June 1953, pp. 157-166.

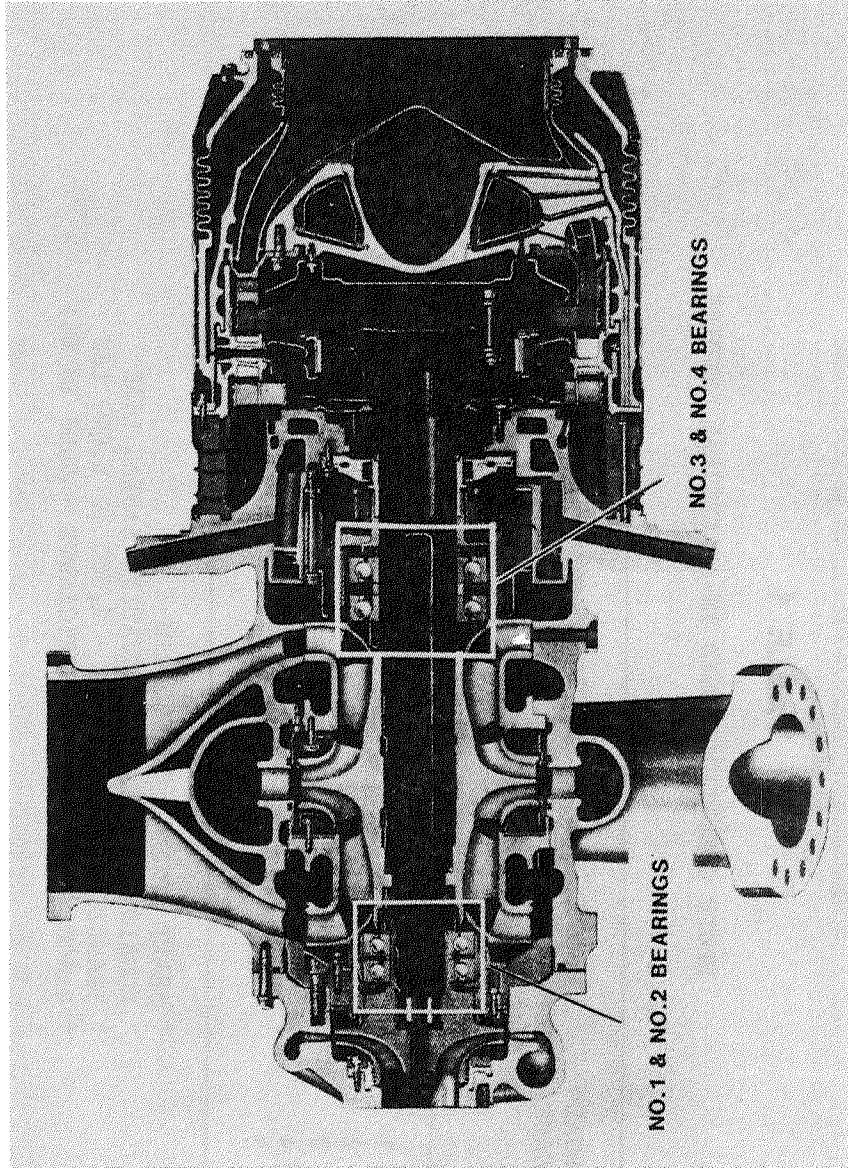


FIGURE 1. SSME HPOTP

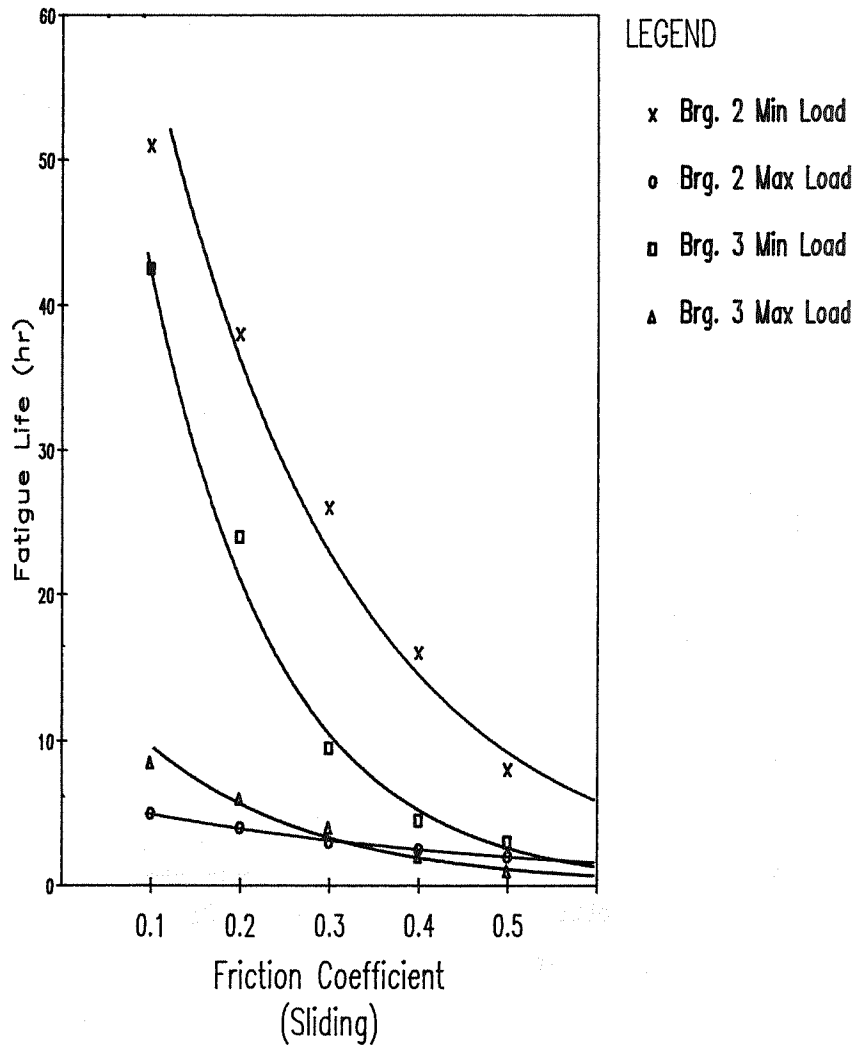
**TABLE 1**

HPOTP CONDITIONS USED IN ANALYTICAL STUDIES

LOAD CASE	RADIAL NON-ROTATING LOAD COMPONENT (LBS)	RADIAL ROTATING LOAD COMPONENT (LBS)	ORIENTATION OF ROTATING & NON-ROTATING LOAD COMPONENT (DEG)	RESULTANT RADIAL LOAD (LBS)
1	2500	2500	0	5000
2	2500	2500	45	4620
3	2500	2500	90	3535
4	2500	2500	135	1915
5	2500	2500	180	0

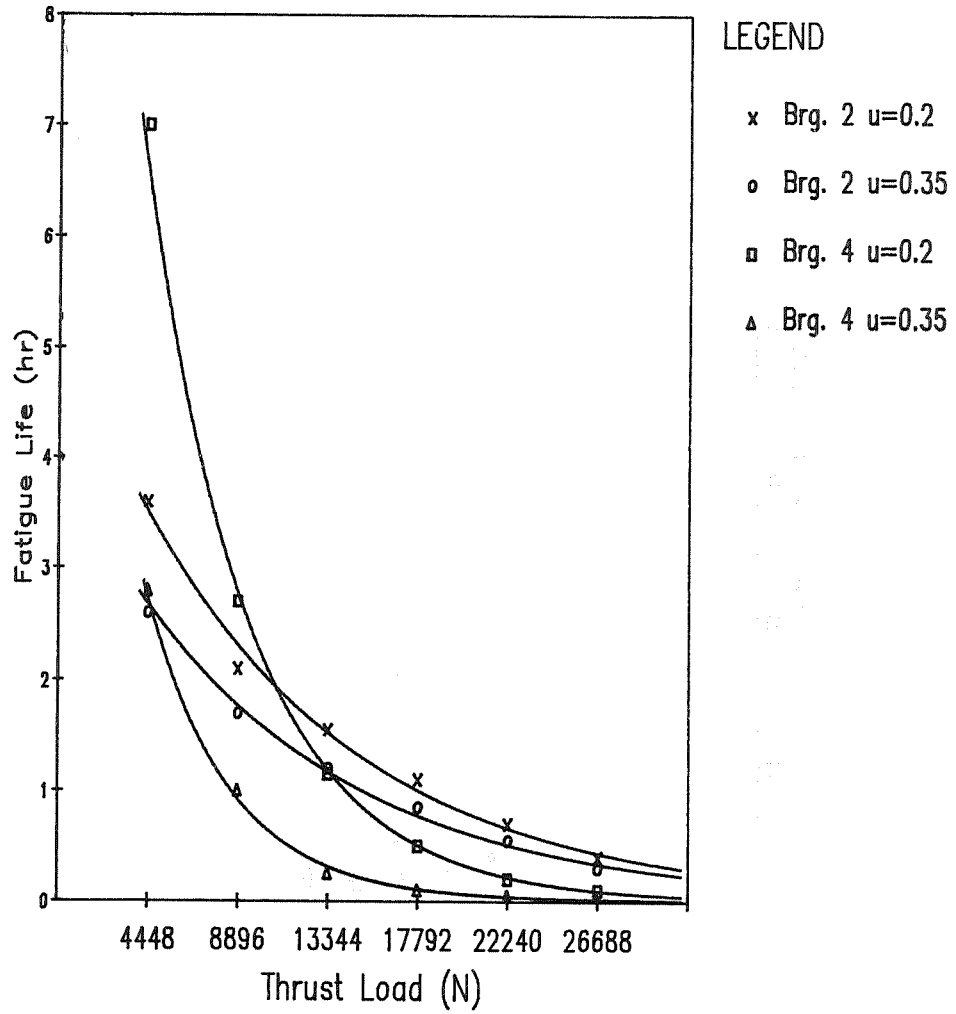
- ° SHAFT SPEED - 30,000 RPM
- ° COMBINED STATIC AND ROTATING RADIAL LOAD
- ° TRANSIENT AXIAL LOADS - 2,000 TO 8,000 LBS
- ° RANGE OF FRICTION COEFFICIENTS - 0.08 TO 0.5

FIGURE 2  
SSME HPOTP  
Fatigue Life vs Friction Coefficient



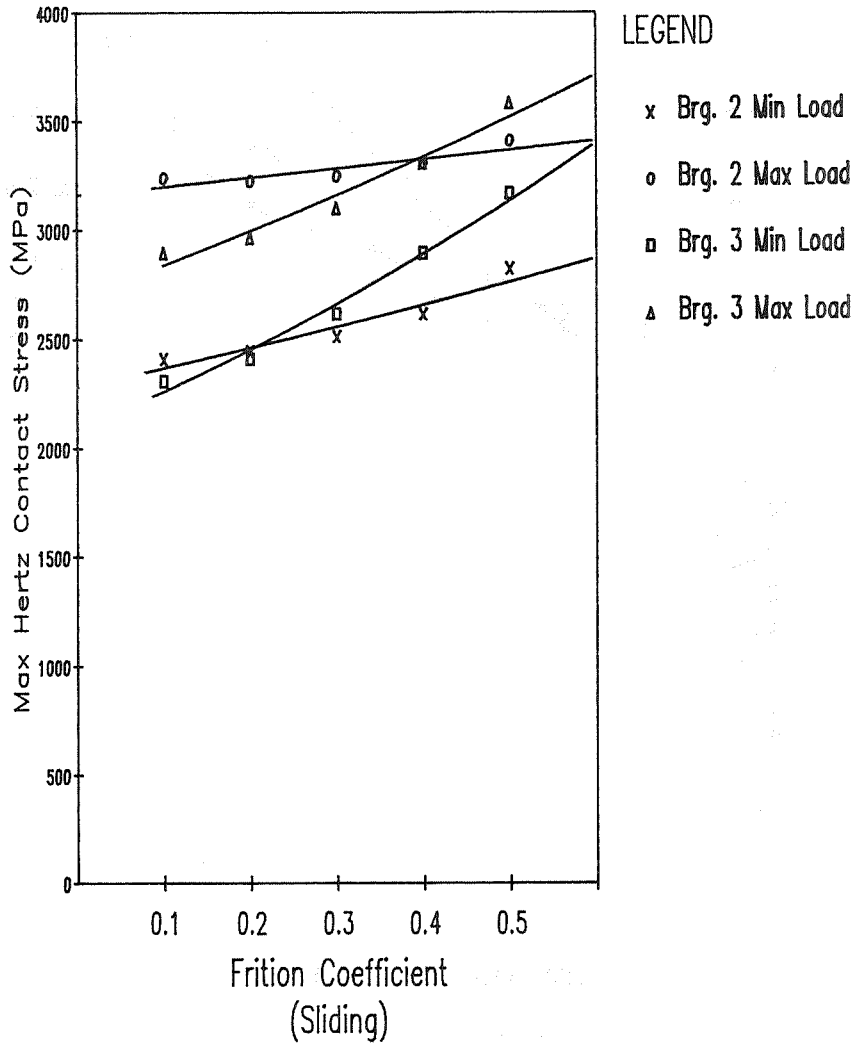
Min=8518 N Max=22240 N

FIGURE 3  
 SSME HPOTP  
 Fatigue Life vs Thrust Load



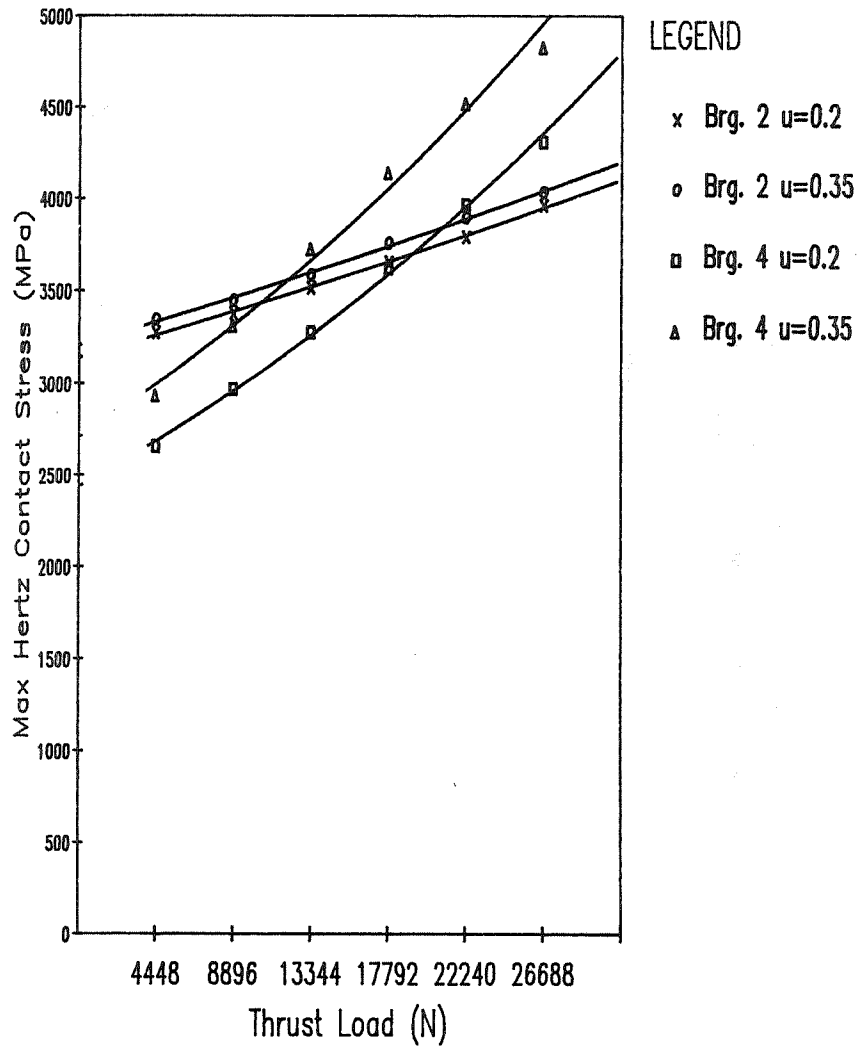
Max Shaft Load=22240 N

FIGURE 4  
 SSME HPOTP  
 Contact Stress vs Friction Coefficient



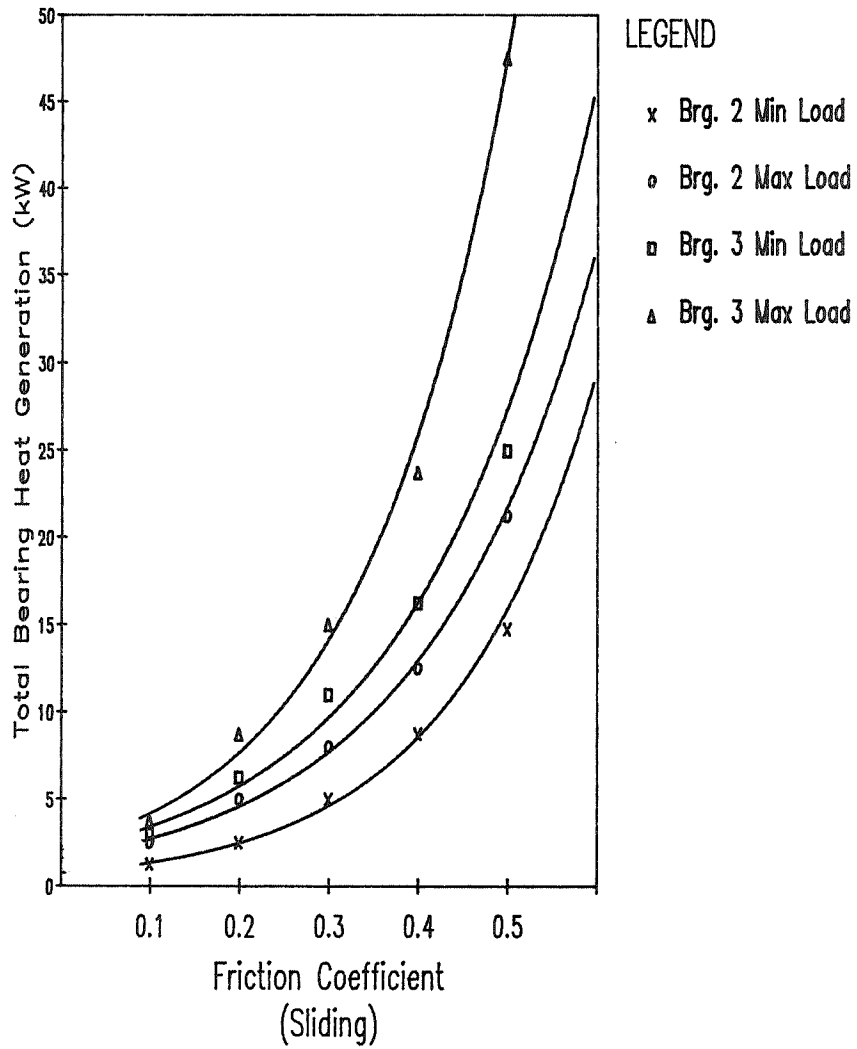
Min=8518 N Max=22240 N

FIGURE 5  
 SSME HPOTP  
 Contact Stress vs Thrust Load



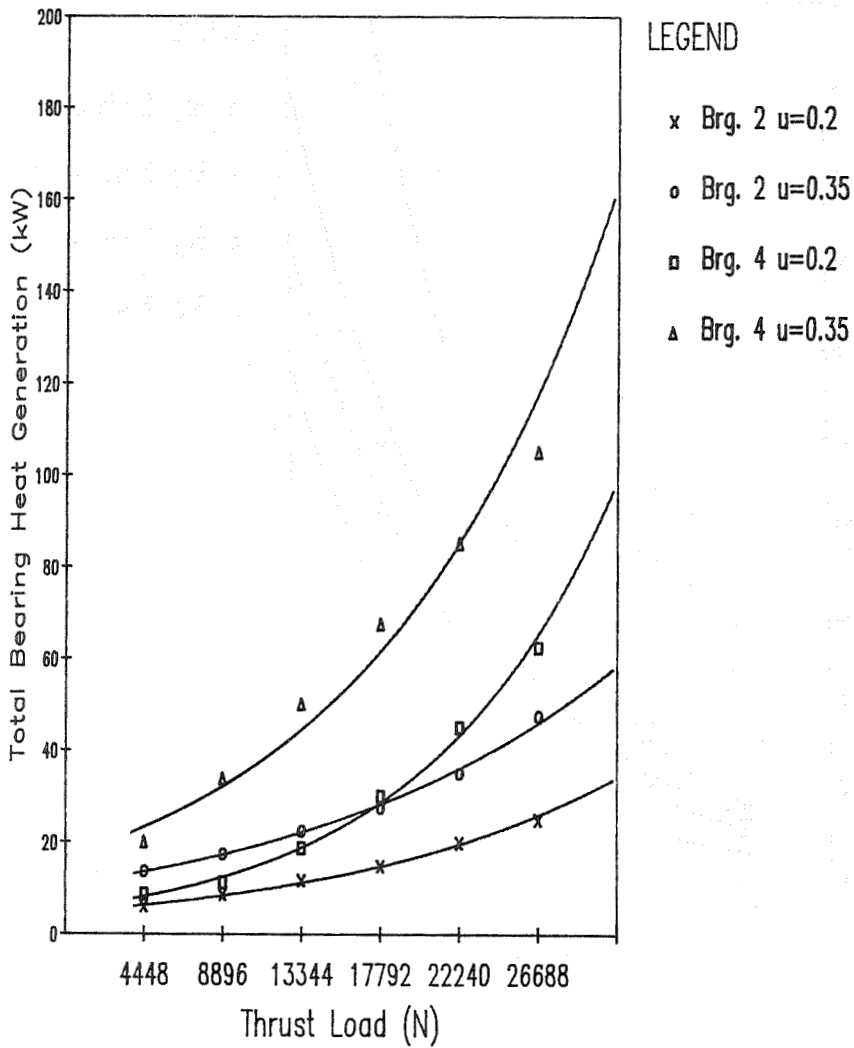
Max Shaft Load=22240 N

FIGURE 6  
 SSME HPOTP  
 Heat Generation vs Friction Coefficient



Min=8518 N Max=22240 N

FIGURE 7  
 SSME HPOTP  
 Heat Generation vs Thrust Load



Max Shaft Load=22240 N

## BEARINGS WORKING GROUP

### Introduction

The service life of the Space Shuttle Main Engine (SSME) turbomachinery bearings has been a predominant factor in engine durability and maintenance problems. Recent data has indicated that bearing life is about one order of magnitude lower than our goal of seven and one-half hours particularly those in the High Pressure Oxidizer Turbopump (HPOTP). There are several reasons for this limited life situation as follows: The turbopumps are high speed, very high power-to-weight ratio, high efficiency units. The turbopump mainshaft rotors operate above the first critical speed; therefore, rotor loads imposed on the bearings are relatively high. Engine systems' pressures impose high transient axial loads on the HPOTP bearings during start and shutdown, particularly at shutdown. Finally the bearings operate submerged in the cryogenic fluid being pumped so conventional fluid lubricants cannot be utilized and the dry film lubricants being applied have limited life. In addition to working toward reducing the loads being imposed on turbopump bearings, it was decided that improvements in bearing design, modeling, materials, substrate surface modification, coatings, and lubrication methods would be researched, since the 440C steel being used was not particularly good in either rolling contact fatigue or wear resistance, the other materials and techniques being applied were not recent state-of-the-art and significant improvement was believed possible.

In order to structure a program which would have a high probability of success and one which would fully address the SSME problems being encountered, a Bearings Working Group was established which included technological expertise from both the Lewis Research and the Marshall Space Flight Centers in areas of turbopump

and engine development, mechanical design, stress, rotor dynamics, instrumentation, metallurgy, lubrication, bearings, hydrostatic bearings, bearing modeling, seals, and test engineering. The objective adopted is shown below.

### Objective

To advance the state-of-the-art in bearing technology, primarily cryogenic turbomachinery bearing technology, by exploring the life and performance effects of design changes, design concept changes, materials changes, manufacturing technique changes and lubrication system changes, and to compare each new variation against the current bearing design in full scale cryogenic tests.

### Program Elements

Cryogenic Turbopump Bearing Data Analysis and Computer Modeling Updating - The compilation and analysis of cryogenic bearing test data and its use in generating a computer math model.

Cryogenic Turbopump Roller Bearing Research and Technology - A feasibility study, which if successful, would advance to the design and manufacture of cryogenic turbopump roller bearings for test and use.

Hydrostatic Bearing for LH<sub>2</sub> and Lox Turbopumps - A feasibility study, which if successful, would lead to the design, fabrication and test of a hydrostatic or hybrid cryogenic bearing.

Investigate and Characterize Magnetic Bearings in a Cryogenic Environment - A feasibility study, which if successful, would be followed by the design and manufacture of demonstration unit hardware which would be tested at MSFC with contractor assistance.

Application of Powder Metallurgy Techniques to Produce Improved Bearing Elements - A feasibility study, which if successful, would lead first to the manufacture of balls for evaluation and full scale tests,

then second to the manufacture of entire bearings for evaluation and test.

Cryogenic Turbopump Ball Bearing Research and Technology - An in-house MSFC cryogenic bearing test program wherein measurements of bearing stiffness, damping and coolant requirements will be made, test of new bearing materials, surface treatments and coatings, and different lubrication schemes will be made, plus where data will be accumulated which will permit the adjustment of a cryogenic bearing math model.

Ion Plated Bearing Materials Study and Evaluation - A feasibility study, which if successful, would lead to the manufacture of ion plated bearings for full scale tests.

Although all of the Program Elements in the bearings area are active and good progress is being made in each, four were chosen for the presentation of papers because of their relative accomplishments. The paper given concerning detailed internal cryogenic bearing thermal modeling reported that current jet engine models are not appropriate and that a model has been generated which can accommodate bearing heat transfer across the phase change of a cryogenic coolant. It can also accommodate different LN<sub>2</sub> or LO<sub>2</sub> coolant inlet conditions, flowrates and axial loads. More work remains to be accomplished in modeling LH<sub>2</sub> coolant, radial load cases, and coupling the thermal and mechanical models needed for this application. The paper concerning development of a hydrostatic bearing reported successful design optimization, bearing manufacture, and completion of the first test series in LH<sub>2</sub> (liquid hydrogen). More test work remains with LH<sub>2</sub> and configurations for test and use in LO<sub>2</sub>. The paper presented concerning the application of powder metallurgy bearing elements showed data which indicated improved rolling contact fatigue resistance with three of the alloys being tested. One of them appears to be a significant improvement over 440C. Again, this was a status report and considerable work remains to be accomplished.

The paper concerning chromium ion plated 440C reported improved rolling contact fatigue life with thin coatings. This effort has been expanded to include ion implantation methods and much work remains to be done in this area.

ADVANCED ROCKET ENGINE CRYOGENIC  
TURBOPUMP BEARING THERMAL MODEL

Joe C. Cody, Linda New, Bruce Tiller  
Aerospace Systems & Products Division  
Spectra Research Systems, Huntsville Division

Abstract

A lumped node thermal model has been developed representing the Space Shuttle Main Engine (SSME) liquid oxygen (LOX) turbopump turbine end bearings operating in a cryogenically cooled bearing tester. Bearing elements, shaft, carrier, housing, cryogen flow characteristics, friction heat, and fluid viscous energy are included in the model. Heat transfer characteristics for the regimes of forced convection boiling are modeled for liquid oxygen (LOX) and liquid nitrogen ( $LN_2$ ). Large temperature differences between the cryogenic fluid and bearing contact surfaces require detailed nodal representation in these areas. Internal loads and friction heat are affected by temperature dependent operating clearances requiring iterations between bearing thermal and mechanical models. Results compare favorably with limited data from the Marshall Space Flight Center (MSFC) Bearing Materials Tester (BMT). Analyses indicate a thermal-mechanical coupling resulting in reduced operating clearances, increased loading and heating which can contribute to premature bearing failure. Contact surfaces operate at temperatures above local saturation resulting in vapor rather than liquid in the contacts, precluding possible liquid film lubrication. Elevated temperatures can reduce lubrication, increase friction, and reduce surface hardness supporting a surface failure mode rather than subsurface fatigue. Future efforts include modeling the SSME liquid hydrogen turbopump bearings, model refinements, and further correlation of modeling techniques with BMT data.

## Introduction

This thermal modeling development supports an overall MSFC Bearing Materials evaluation program designed to formulate and experimentally verify failure modes and life prediction models for high speed rolling bearings operating in cryogenics. This research supports development and improvement of hardware such as the Space Shuttle Main Engine liquid oxygen (LOX) and liquid hydrogen (LH<sub>2</sub>) turbopumps which are highly efficient lightweight machines operating at high power levels and shaft speeds. The pump main shafts are supported by angular contact ball bearings operating in the cryogen being pumped.

State of the art bearing codes are not adequate for thermal simulation of high speed rolling bearings operating in cryogenics. Although sufficient for analysis of conventionally lubricated bearings, treatment of the various regimes of boiling, large temperature gradients, and significant variations in material properties is beyond the scope of these codes. The current thermal modeling effort is directed toward improved treatment of these important characteristics of cryogenic bearing systems, and to provide a better understanding of the thermal influences on cryogenic bearing operating characteristics and life. Objectives are to develop and refine the bearing model, correlate results with BMT data, and provide a verified design tool for predicting the thermal characteristics of high speed rolling bearings operating in cryogenics.

## Approach

### Model Description

A state of the art thermal code "SINDA" was selected for modeling the cryogenic bearing system. This code has the capability for temperature and time varying boundary conditions, and temperature varying material properties. It also provides for modeling of fluid networks which is necessary to simulate the cryogenic fluid flow. The internal arrangement of

the BMT is shown in Figure 1. Since the right and left bearing pairs are essentially similar, only one bearing pair requires modeling. The cryogen, acting as a coolant, enters a manifold at each end of the tester, flows through each bearing and exits via a common flow path. Although the tester can be loaded in both the axial and radial directions, the current computer simulation treats only the axially loaded case. Since this produces axially symmetric loading a radial slice of the system is all that requires modeling. Figure 2, a schematic of the bearing set, illustrates a representative radial section of the model. The bearing is a 57 mm bore angular contact ball bearing with thirteen balls.

Due to the large temperature differences in the bearing contact surfaces and cryogenic fluid, large thermal gradients are present in the balls and races near the highly loaded contacts. This, in addition to the extreme sensitivity of the fluid heat transfer coefficient to surface temperature, required many very small nodes in the contact areas of the model. The nodal representation of the inner race, ball, and outer race for the 57 mm LOX pump turbine end bearing is shown in Figure 3. There are 642 nodes in the model. Surface nodes are connected by appropriate thermal resistors to the cryogenic fluid. These resistors are varied as the surface temperature of the node changes to represent the appropriate fluid heat transfer regime. The ball contacts the inner and outer races in a small elliptical area that varies in size and location with speed and load. The detailed nodal representation allows flexibility to account for these variations without renoding the model.

#### Fluid Heat Transfer Coefficients

Wide variations in component surface temperatures carries the fluid heat transfer mechanisms through the range of forced convection in liquid, high velocity forced convection boiling, and forced convection in vapor. Since test data are absent for high velocity, high pressure forced convection

boiling of cryogenics, a superposition method<sup>2</sup> was used to evaluate the appropriate flow regimes depending on the surface superheat.

Figure 4 provides a graphical illustration of the method for evaluating the heat transfer regimes as a function of surface superheat for  $LN_2$ . As shown, when the forced convection heat flux<sup>2</sup> equals the nucleate boiling flux incipient boiling is assumed to occur. As the surface superheat exceeds about  $3.3^\circ R$  the surface is assumed to be vapor blanketed and forced convection vapor is the mode of heat transfer. Since this indicates about an order of magnitude reduction in heat transfer, the significance of the superheat value at which transition occurs becomes apparent. Heat fluxes for the different regimes were calculated from the following equations—the Dittus-Boelter equation for forced convection on all components except the balls, Katsnellson's equation for forced convection on the balls, the Borishanskiy-Minchenko correlation for nucleate boiling, and the Kutateladze correlation for the peak heat flux.<sup>2</sup> This technique was tentatively verified with tester data as illustrated in Figure 5, where a comparison of predicted and measured bearing outer race temperatures is shown. The predicted values are provided as a function of surface superheat and indicate that a superheat range of 2 to 6 degrees provides reasonable agreement with the measured BMT test data. A similar analysis was conducted for  $LOX$ <sup>2</sup>.

#### Heat Generated by Friction in the Bearing Contact Area

Heat is generated in the raceway contacts due to ball spin and roll. Additional frictional heat, not yet included in the model, is generated by the ball contacting the cage, and the cage contacting the inner surface of the outer raceway. The cage effects are in the process of being incorporated into the model.

The raceway frictional heat generated is obtained from the SHABERTH<sup>3</sup> bearing code. This code also provides bearing operating characteristics such as contact angles, operating clearances, contact stresses, deflections, ball and cage speeds and bearing reactions. Shown in Figure 6 is an example of the frictional heat generated in the inner race contacts for the conditions noted. The two minimum points indicate the areas of ball roll and the maximum value is caused by the high relative velocities due to ball spin. Similar information may be generated for the outer race. These values are used as input to the bearing thermal model.

#### Heat Generated by Mechanically Working the Fluid

Considerable heat is generated in the shaft bearing system due to mechanical work on the coolant fluid. Heat generated<sup>4</sup> from fluid stirring and friction was estimated<sup>4</sup> for each component. A BMT heat balance provided a measure of the total heat into the system. Estimated values were adjusted to match the BMT heat balance. The estimated values were from 45% to 80% too low with the larger deviation at the lower shaft speeds. Results are shown in Figure 7. Included are values of contact frictional heat for the loading conditions shown. This data illustrates the large percentage of heat input to the system from fluid work.

#### Thermal Model Results

Results of the bearing thermal model show high local temperatures and steep temperature gradients in the ball/race contact areas. Examples are shown in Figures 8, 9 and 10. Figure 8 illustrates representative surface temperatures and gradients in the ball. There is a wide variation in surface temperature, and much of the surface is above the local saturation temperature ( $-241^{\circ}\text{F}$ ) of the  $\text{LN}_2$  coolant. Inner race temperatures are shown in Figure 9. These surface temperatures are also above the local fluid saturation temperature as are most of the outer race track nodes shown in Figure 10. These temperatures

show that for the conditions analyzed the bearing contacts are operating in vapor rather than liquid. In addition, the maximum temperature shown in the ball track (461°F) is approaching temperatures that can affect surface hardness of the 440C steel.

#### Thermal-Mechanical Interactions

The inner races of high speed rolling bearings reach a higher operating temperature than the outer races because of the increased ball spin at the inner race. This causes inner race growth relative to the outer race and has the effect of increasing loads and reducing internal operating clearances and contact angles. If bearing clearances and/or cooling capacity is marginal, this effect can amplify causing increased loading and heating and possible premature bearing failure. Examples of this trend are shown in Figures 11 and 12. Figure 11 shows the reduction in internal clearance as the coolant flow is decreased, and Figure 12 shows the corresponding increase in component temperature.

#### Comparison of Model and Test Results

Shown in Figure 13 are comparisons of the measured and calculated outer race temperature and the coolant outlet temperature. These results show fair agreement between the measured temperatures and model predictions even though a slight difference in coolant flow rate exists because the thermal model predictions were conducted well before the actual test run and at that time the flow rates were not precisely known. BMT test data is limited at this time. As additional test data becomes available further verification and/or model refinements will be made.

#### Conclusions

Development of a bearing thermal model capable of accounting for two-phase cryogenic flow characteristics has revealed unexpected high temperatures in the loaded contacts. These contact areas operate

at temperatures well above the local saturation temperature and are operating in a vapor rather than liquid environment. The lubrication benefits that might be expected from a liquid film separating the contacts does not occur. For some loading and coolant flow conditions, the model shows that there is a thermal-mechanical coupling that can cause loss of operating clearances, increased loading, and increased heat generation that can contribute to premature bearing failure. Elevated temperatures can reduce lubrication, increase friction, and reduce surface hardness. These conditions support a surface failure mode rather than the subsurface fatigue experienced by conventional oil lubricated rolling bearings.

Bearing modeling techniques are providing valuable tools for the assessment of new materials for high speed bearings operating in cryogenics. However, due to the complexity of the system and lack of experimental data in many areas, especially high flow two-phase cryogenic heat transfer characteristics, additional data from the MSFC BMT is vital for verification of cryogenic bearing systems modeling methods.

#### References

1. SINDA Engineering Program Manual (Contract No. NAS9-10435) June 1971.
2. Bearing Tester Data Compilation, Analysis, and Reporting and Bearing Math Modeling (Contract No. NAS8-34686), May 1984, Final Report.
3. SHABERTH Computer Program Operation Manual, Technical Report AFAPL-TR-76-90, October 1976.
4. NASA Report No. 793, "Experiments on Drag of Revolving Disks, Cylinders, and Streamline Rods at High Speeds", by T. Theodorsen and A. Regier.

FIGURE 1 SHAFT, BEARINGS & CARRIER APPLIED LOADS

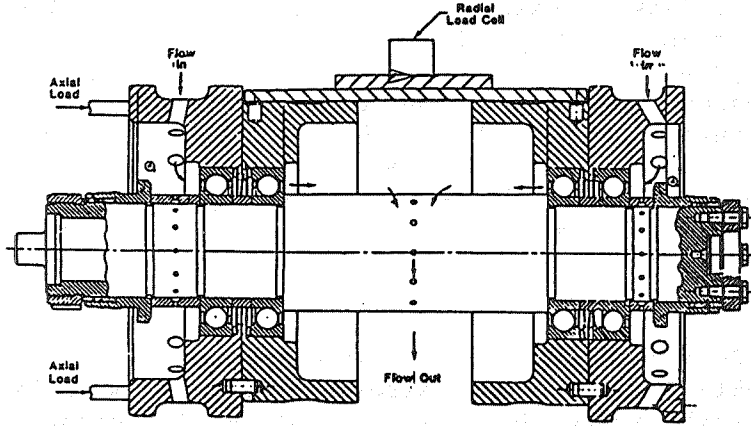
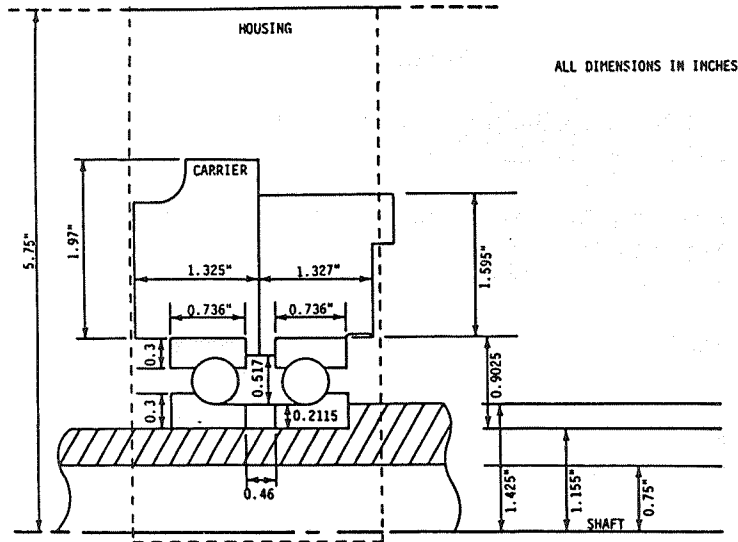


FIGURE 2 SCHEMATIC OF BEARING SET



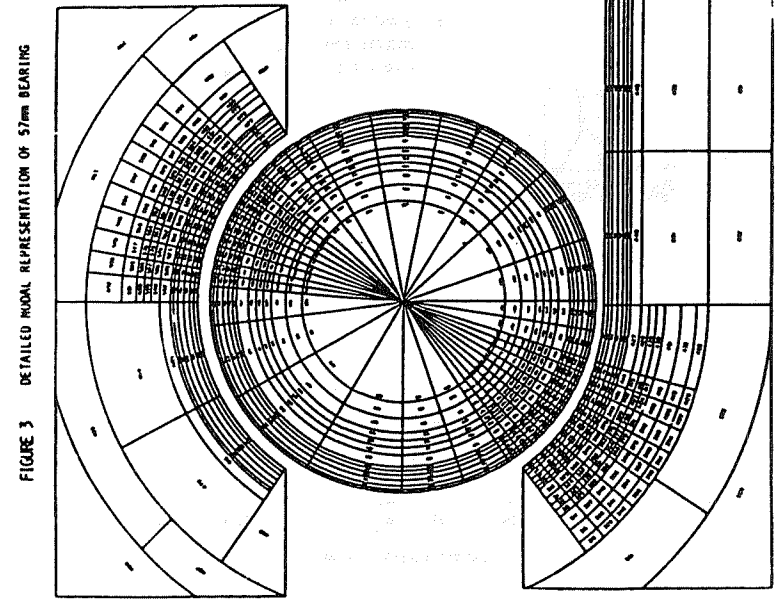
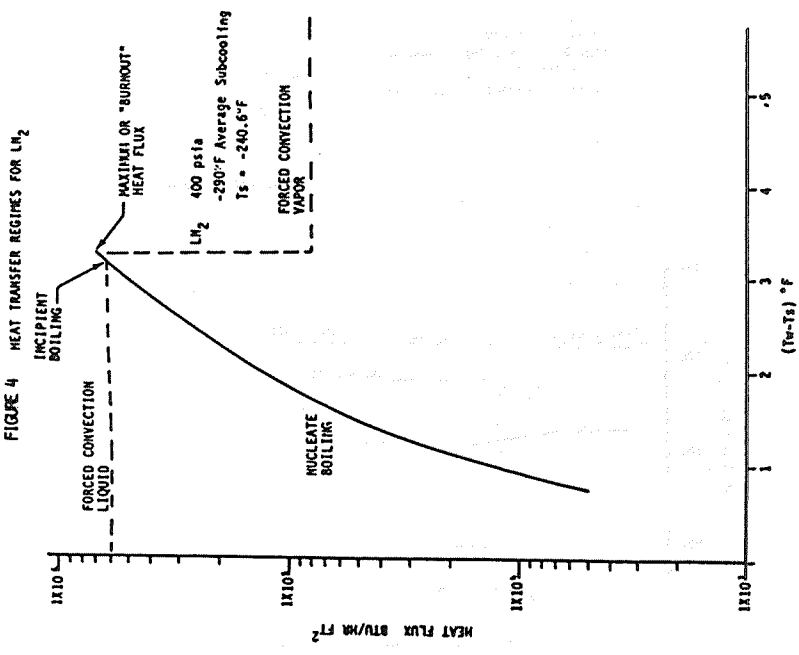


FIGURE 5 Outer Race Node Temperature As A Function of  
Ball Superheat at Max Flux Conditions  
(LOX Turbopump Turbine End Bearing - 57 mm)

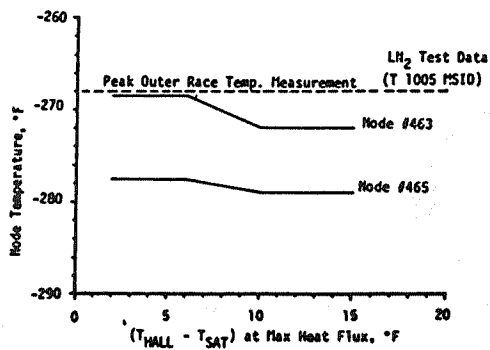
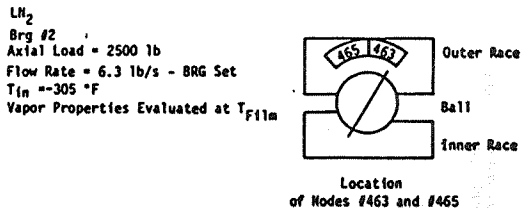


FIGURE 6 INNER RACE HEAT GENERATED AT CONTACT ELLIPSE

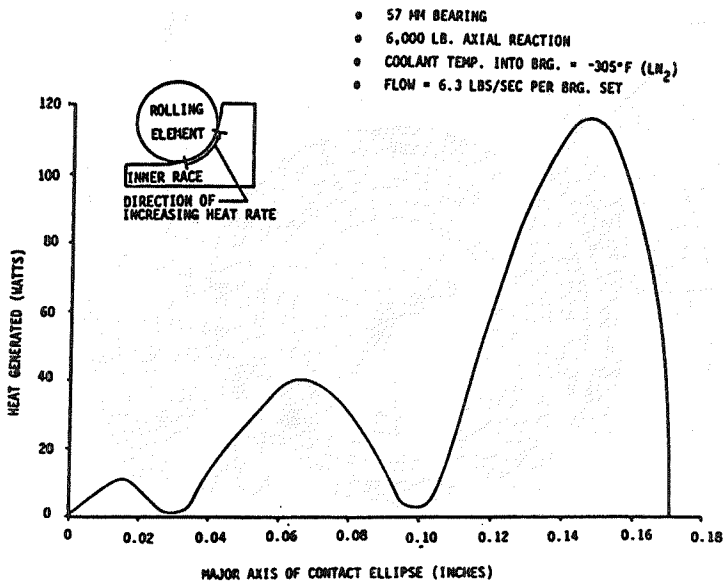


FIGURE 7  
HEAT GENERATED (kW) AT LOAD END OF THE BMT AS A FUNCTION OF  
SHAFT SPEED AND AXIAL LOAD (LN<sub>2</sub> COOLANT)

COMPONENT LOADS(LBS)	SHAFT SPEED (RPM)							
	15,000		20,000		25,000		30,000	
	2500	4000	2500	4000	2500	4000	2500	4000
SLINGER	3.11	3.11	7.1	7.1	11.2	11.2	17.84	17.84
SPACER	1.18	1.18	2.7	2.7	4.45	4.45	6.87	6.87
SHAFT	4.0	4.0	9.15	9.15	15.	15.	23	23
BGR #1								
VISCOUS	5.77	5.77	14.	14.	23.	23.	40.2	40.2
FRICTION	.40	.40	.72	.72	1.12	1.12	1.9	1.9
BGR #2								
VISCOUS	1.17	1.17	2.66	2.66	4.38	4.38	7	7
FRICTION	2.42	4.48	3.64	6.44	5.29	8.86	7.3	11.5
TOTAL	18.	20.	40.	42.8	64.4	68.2	104.1	108.3

FIGURE 8 TEMPERATURE -VS- DEPTH BELOW SURFACE OF ROLLING ELEMENT

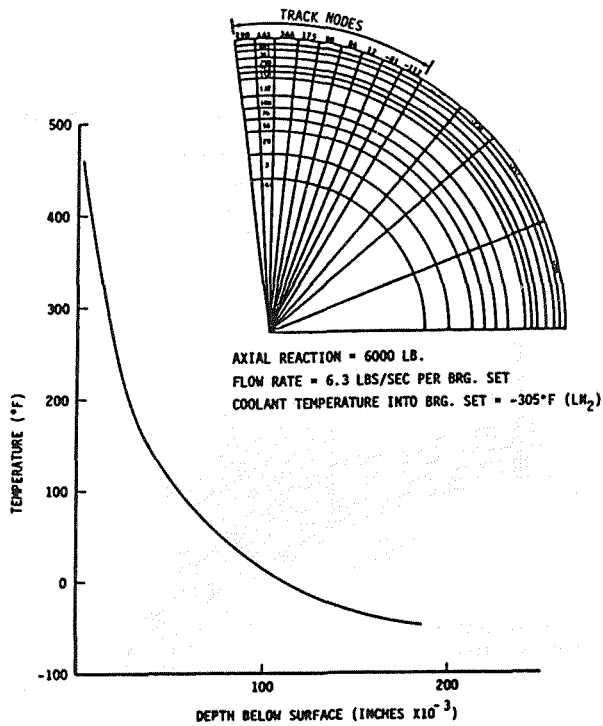


FIGURE 9 INNER RACE TEMPERATURE DISTRIBUTION FOR LOX PUMP TURBINE END BEARING

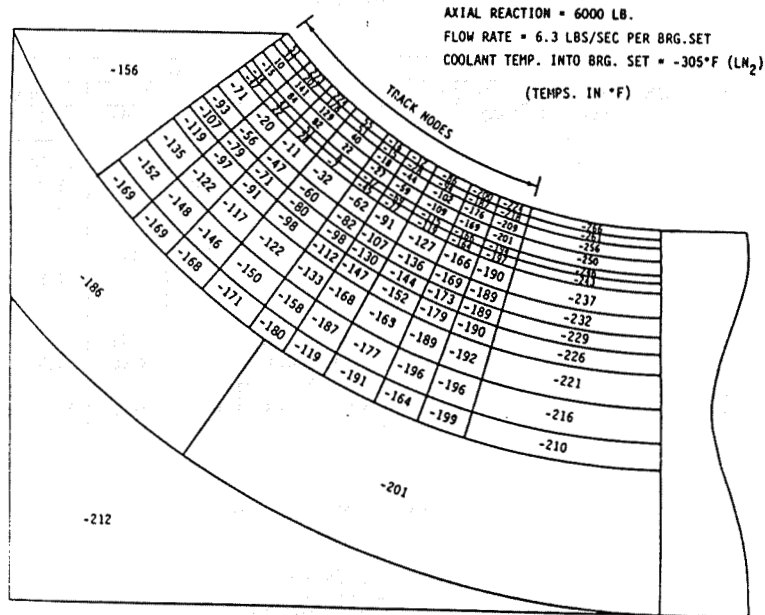


FIGURE 10 OUTER RACE TEMPERATURE DISTRIBUTION FOR LOX PUMP TURBINE END BEARING

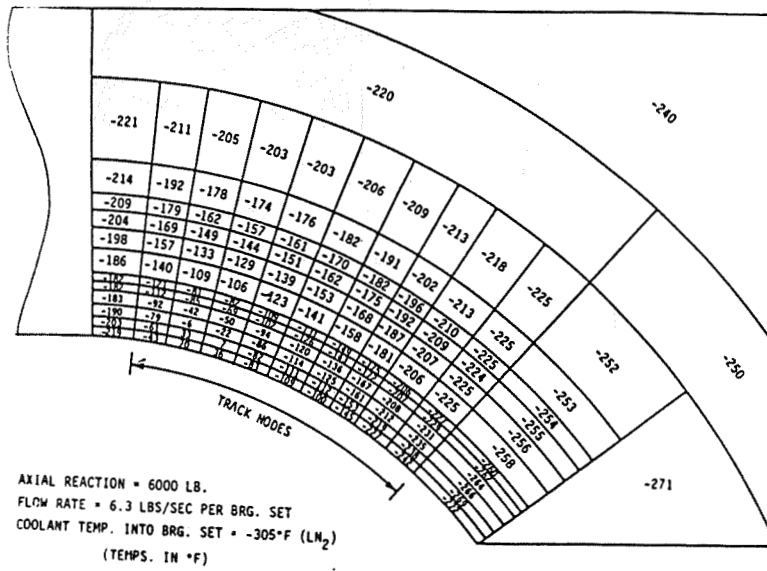


FIGURE 11 OPERATING CLEARANCE VS COOLANT FLOW

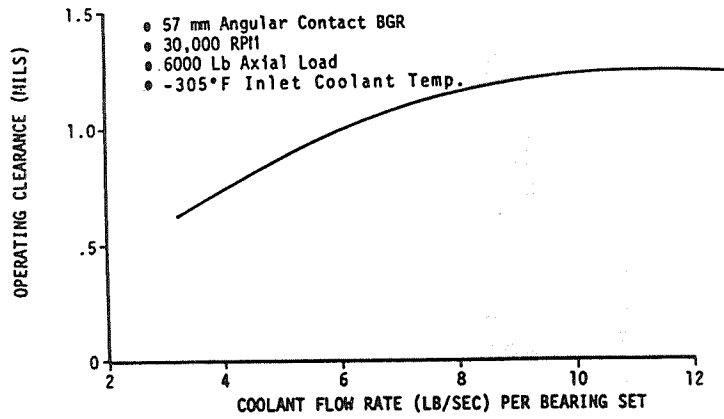


FIGURE 12  
AVERAGE BEARING COMPONENT TEMPERATURE VS COOLANT FLOW

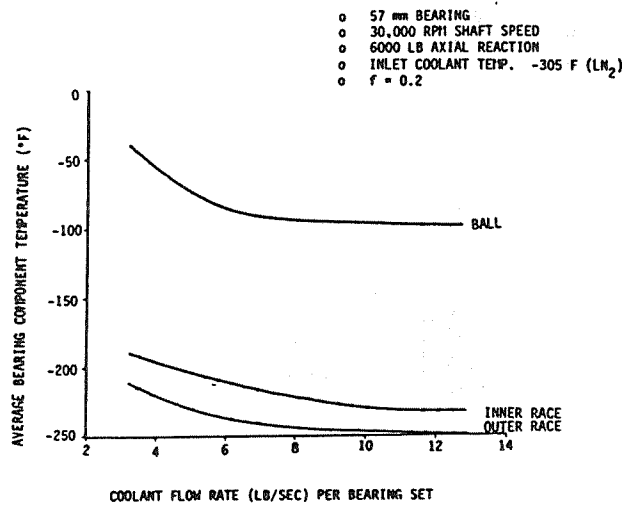


FIGURE 13  
COMPARISON OF MODEL PREDICTIONS AND TEST RESULTS

OPERATING PARAMETERS	BEARING THERMAL MODEL RESULTS RUN DATE 9-29-83	BEARING MATERIALS TESTER DATA	
		TEST DATE 4-26-84 TEST # 201N0409	TEST DATE 5-15-84 TEST # 201N0501
SHAFT SPEED (RPM)	25,000	25,000	25,000
LN <sub>2</sub> COOLANT FLOW RATE (LB/SEC PER BRG. PAIR)	6.0	6.4	6.3
INLET COOLANT TEMPERATURE (°F)	-300	-300.5	-296
COOLANT TEMPERATURE OUT OF LOADED BEARING (°F)	-283.8	-281.5	-275
OUTER RACE BEARING TEMPERATURE (°F)	-278.2	-279	-276

FIGURE 14  
 COMPARISON OF MODEL PREDICTIONS AND TEST RESULTS

OPERATING PARAMETERS	BEARING THERMAL MODEL RESULTS RUN DATE: 11-10-83	BEARING MATERIALS TESTER DATA LN <sub>2</sub> ROTATION 82-62-17-40-12-121
SHAFT SPEED (RPM)	30,000	30,000
LN <sub>2</sub> COOLANT FLOW RATE (LB/SEC PER BRG. PAIR)	6.3	6.3
INLET COOLANT TEMPERATURE (°F)	-305	-303
COOLANT TEMPERATURE OUT OF LOADED BEARING (°F)	-275.1	-274
OUTER RACE BEARING TEMPERATURE (°F)	-268.5	-269

## HYBRID BEARINGS FOR LH<sub>2</sub> AND LO<sub>2</sub> TURBOPUMPS

M. F. Butner and F. C. Lee

Rockwell International/Rocketdyne Division  
Canoga Park, California

### Abstract

Hybrid combinations of hydrostatic and ball bearings can improve bearing performance for liquid hydrogen and liquid oxygen turbopumps. Analytic studies were conducted to optimize hybrid bearing designs for the SSME-type turbopump conditions. A method to empirically determine damping coefficients was devised. Four hybrid bearing configurations were designed, and three were fabricated. Six hybrid and hydrostatic-only bearing configurations will be tested for steady-state and transient performance, and quantification of damping coefficients. The initial tests have been conducted with the liquid hydrogen bearing.

### Turbopump Bearing Improvement is Needed

In the Space Shuttle Main Engine (SSME) turbopumps, the use of propellant-cooled ball bearings achieves reduced turbopump size and weight by eliminating the need for separate lubricants, and the attendant seals and heaters. The SSME High Pressure Oxidizer Turbopump (HOPTP) represents this practice (Fig. 1). Ball bearings are capable of functioning in the severe environments typical of turbopumps, where high speeds and loads are combined with large temperature excursions, negligible lubrication and particulate contamination. Ball bearings with 440-C balls and races and Teflon-fiber-glass cages were entirely satisfactory for liquid hydrogen and liquid oxygen service in single-flight engines like the J-2 used in the Apollo Program.

With the advent of reusable vehicles, the SSME and other advanced engine requirements have placed progressively greater demands on turbopump bearings in terms of life, load capacity, speed capability, and rotor support

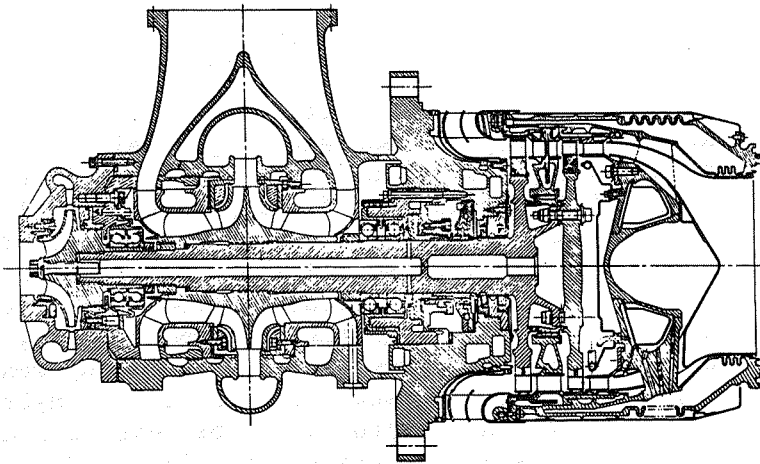


Fig. 1. SSME HPOTP Cross Section

characteristics, taxing the capabilities of ball bearings. For example, the SSME service life requirement of 7.5 hours exceeds the 1 to 3 hours bearing life currently attained under operating conditions like those listed in Table 1. Speed capabilities exceeding  $2 \times 10^6$  DN, with service lives of 10 hours are required for advanced applications in the near future with further increases anticipated. Ball bearings are currently limited to approximately  $2 \times 10^6$  DN by centrifugal loading and wear. Rotordynamic response could often be improved if increases in shaft diameter, bearing stiffness, and/or damping were available.

Table 1. SSME HPOTP Bearing Operating Conditions

	HPOTP		HPFTP
	PREBURNER	TURBINE END	
COOLANT	LO <sub>2</sub>	LO <sub>2</sub>	LH <sub>2</sub>
COOLANT TEMPERATURE, R	210	210	90
SPEED, RPM	30,000	30,000	36,000
BEARING DN, 10 <sup>6</sup>	1.4	1.7	1.6
LOAD (PER BEARING)			
AXIAL, TRANSIENT	SMALL	4,000	NEGLIGIBLE
AXIAL, STEADY STATE	850	1,000	700
RADIAL, FIXED	500	500	SMALL
RADIAL, SYNCHRONOUS	600	600	400 - 900

## Hybrid Bearings Can Fill Need

Hydrostatic bearings are attractive alternates to ball bearings, as they can operate at journal speeds up to approximately  $5 \times 10^6$  DN, show increased load capacity (providing sufficient fluid pressure and flow are available), and in addition can provide improved shaft support through greater stiffness and damping. However, since they require pressurization from an external source to develop significant load capacity, hydrostatic bearings need some means of avoiding wear and heat generation during start and shutdown. Hybrid combinations of ball and hydrostatic bearings such as shown in Fig. 2 possess dry start capability and can exploit the advantages of the film bearing. These bearings are adaptable to rocket turbomachinery, since typical liquid rocket flow systems can supply the high pressure fluid required for hydrostatic bearings without significant performance penalty. One or more of the possible hybrid bearing forms possess the characteristics necessary for achievement of life and performance goals for individual bearing positions in the SSME and future engine turbopumps. Hybrid bearings have been tested, demonstrated to be feasible, and are actively considered for incorporation into new designs (Ref. 1-3).

### Program to Develop Hybrid Bearing Technology

NASA/Lewis Research Center (LeRC) initiated the SSME Long Life Bearing Program under Contract NAS3-23263 with the goal of extending bearing capabilities by providing practical design information for radial hybrid bearings suitable for SSME and other advanced propulsion systems. The program comprises design studies, bearing fabrication, testing, and correlation of analytic and empirical results.

### Design Studies

#### Hybrid Bearing Designs

Hydrostatic and ball bearing elements can be combined to share speed or load; working fluid may be

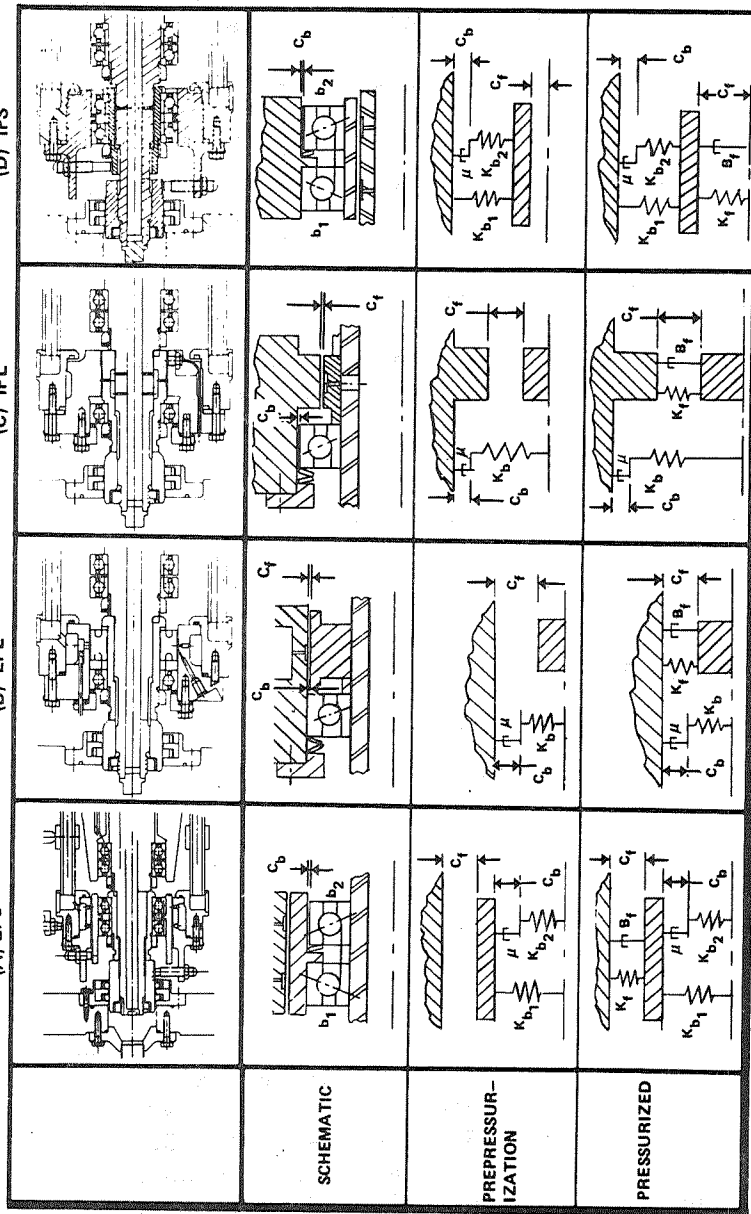


Fig. 2. Hybrid Bearing Types

supplied externally or from the shaft center. Figure 2 presents the four types of hybrid bearing most applicable to rocket engine turbopumps. The following abbreviations will be used to identify the several configurations in the balance of this paper:

1. EPS--Externally Pressurized, Parallel Speed
2. EPL--Externally Pressurized, Parallel Load
3. IPL--Internally Pressurized, Parallel Load
4. IPS--Internally Pressurized, Parallel Speed

In Fig. 2, the top row is a cross section of the design as installed in the test rig. The second row contains the bearing pictorial schematic. Functional schematics are shown prior to pressurization (Row 3) and fully pressurized (Row 4). Symbols for Fig. 2 are defined as:

- b - designates ball bearing (also used as subscript)
- f - designates film bearing (also used as subscript)
- c - radial clearance
- $\mu$  - Coulomb friction
- B - viscous damping
- K - stiffness

#### Bearing Analyses

Hybrid bearing performance was predicted by combining the characteristics of the hydrostatic and ball bearing members for conditions representing start, steady-state, and shutdown conditions based on SSME speeds and loads. Hydrostatic bearing analyses were performed using the computer program HBEAR written by Artilles, Wallwit, and Shapiro (Ref. 4). Stiffness, friction torque, and flow were determined as functions of speed and clearance for selected bearing geometry. The hydrostatic bearing analytical model assumes incompressible fluid and isothermal flow, in which the

turbulent effect on the fluid's viscosity and the inertia effect at the recess boundary are included. The last two effects are important for liquid-hydrogen and liquid-oxygen-fed bearings because of the low fluid kinematic viscosity values.

The ball bearing element's characteristics of fatigue life, stiffness, and friction torque were calculated as functions of axial and radial load for the applicable ranges of inner and outer race speeds using a computer program written by A. B. Jones (Ref. 5).

### Parametric Design Studies

To organize the large number of variables and interactions, nondimensional relations were combined into the design charts for liquid hydrogen and liquid oxygen hybrid bearings (Ref. 6). Studies were also made of the effects of manufacturing tolerance ranges and the use of surrogate fluids for test. It was found impractical to incorporate all hydrostatic bearing variables in universally applicable charts. However, a reasonable number of curves can be utilized to characterize bearings with the same recess configuration and similar Reynold's number. The use of nondimensional charts can effect a reduction in the computer time required to optimize the design for a particular application.

Examples of nondimensional parameters are the pressure ratio ( $\bar{P}_R$ ), nondimensional stiffness ( $\bar{K}$ ), and damping ( $\bar{B}$ ). The relation of  $\bar{K}$ ,  $\bar{B}$  to  $\bar{P}_R$  (Fig. 3) allows assessment of multiple dimensional variables with one chart. Other nondimensional parameters such as an L/D (journal length divided by diameter) and C/R (radial clearance divided by journal radius) can be used to assess bearing performance in response to a great many variables.

### Detail Designs

All four hybrid configurations shown in Fig. 2 were analyzed and detail designs produced. Table 2

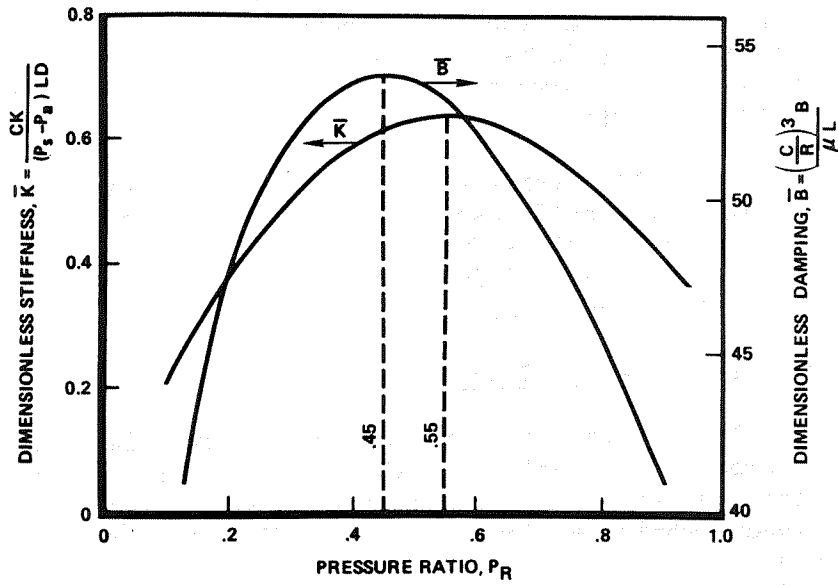


Fig. 3. Liquid Hydrogen Hydrostatic Bearing

Table 2. Hydrostatic Bearing Design Features

	HYDROSTATIC BEARING			
	EPS	EPL	IPL	IPS
DIAMETER, IN.	3.5	3.0	2.15	1.31
LENGTH, IN.	1.5	1.0	1.0	1.7
RADIAL CLEARANCE, IN.	0.00175	0.0015	0.0015	0.0009
ORIFICE DIAMETER, IN.	0.048	0.050	0.053	0.017
NO. OF RECESSES	12	6	6	12
RECESS AREA RATIO	0.08	0.1	0.1	0.08
NO. OF ROWS	2	1	1	2
RECESS WIDTH, IN.	0.183	0.449	0.322	0.274
RECESS LENGTH, IN.	0.300	0.350	0.350	0.340
SILL LENGTH, IN.	0.300	0.325	0.325	0.340

lists the major dimensional characteristics. In view of the existence of practical experience with EPS bearings and in the interest of gaining experience with new concepts, the EPL, IPL, and IPS configurations (Fig. 2B, C, and D) were fabricated as test bearings. The predicted major performance characteristics are listed in Table 3.

Table 3. Hydrostatic Bearings Performance

	HYDROSTATIC BEARING					
	EPS		EPL		IPL	IPS
	TURB.	INLET	TURB.	INLET		
<b>OPERATING CONDITION:</b>						
FLUID	LH <sub>2</sub>	LH <sub>2</sub>	LH <sub>2</sub>	LH <sub>2</sub>	LO <sub>2</sub>	LO <sub>2</sub>
SPEED, RPM	36,600	36,600	36,600	36,600	29,800	29,800
SUPPLY PRESSURE, PSIA	5,600	2,350	5,600	2,350	2,003	2,003
SUMP PRESSURE, PSIA	3,700	350	3,700	350	407	407
FLUID TEMPERATURE, R	90	90	90	90	196	196
<b>FLUID PROPERTIES:</b>						
VISCOSITY, LB-SEC/IN. <sup>2</sup> x 10 <sup>9</sup>	1.86	1.12	1.86	1.12	20.0	20.0
DENSITY, LB-SEC <sup>2</sup> /IN. <sup>4</sup> x 10 <sup>4</sup>	0.069	0.0473	0.069	0.0473	1.0	1.0
<b>PERFORMANCE:</b>						
FLOWRATE, LB/SEC	0.99	0.86	0.54	0.464	1.6	0.40
DIR. STIFF., LBF/IN. x 10 <sup>-6</sup>	3.49	3.55	1.59	1.69	1.09	2.27
CROSS-CPL. STIFF., LBF/IN. x 10 <sup>-5</sup>	2.87	2.30	1.00	0.81	2.4	10.2
DIR. DAMPING, LBF-SEC/IN.	150.3	121.0	52.4	42.5	152.4	655.3
PRESSURE RATIO	0.46	0.44	0.47	0.45	0.68	0.51
POWER LOSS, HP	2.71	1.92	1.02	0.71	2.21	0.66

In selecting the hydrostatic test bearing designs, priority was assigned to maximizing stiffness and damping with a satisfactory degree of stability. Optimization for some applications might require greater emphasis on achieving low friction torque or flowrate, resulting in alternate design details of clearance, recess configuration, and orifice diameter.

Initial sizing of the hydrostatic bearing may be dictated by turbopump design or selected from operating conditions by applying

$$\frac{W}{(P_s - P_a) L/D} \approx 0.25 \quad (1)$$

The radial clearance for the first design iteration can be assumed so that (Ref. 7):

$$C/R = 0.001 \quad (2)$$

The next step, selection of a recess configuration, is affected by several considerations. The recess volume should be limited to preserve stability, but the recess should be deep enough to achieve uniform pressure over the recess area. The number, length, and width of

the recesses should be chosen so that the recess to total bearing area ratio is less than 0.15 (an adaptation of MTI experience). The number of recesses should be four or more to achieve uniform directional load capacity, while the use of more than six is not generally necessary (Ref. 8). For EPS bearings, where the free-rotating member has considerable angular compliance, two rows of recesses are probably beneficial, which leads to more but smaller recesses.

After selecting the recess configuration, the compensating orifices are sized to achieve equal orifice and film flow resistances, producing near-maximum stiffness and damping as illustrated in Fig. 3. The computer program is then used to calculate the stiffness, damping, flow, and friction torque for comparison to design constraints.

If necessary, bearing geometric variations are repeated until the desired result is achieved. In general, increased stiffness, damping, and friction torque with decreased flow result from decreases in clearance or increases in length.

#### EPS Bearing

For maximum ball bearing life extension, the outer race cartridge speed should approach shaft speed as illustrated by Fig. 4. This condition requires that film friction be less than that of the ball bearings.

Such conditions are predicted for liquid hydrogen hybrid bearings, and have been confirmed experimentally (Ref. 1 and 2). However, use of liquid oxygen in a similar bearing will produce a relatively low speed ratio due to the higher fluid viscosity and density.

In the EPS bearing, the journal must be larger than the shaft to contain the ball bearing. Therefore, if the maximum speed is limited by the tensile strength of the cartridge to  $5 \times 10^6$  DN, the actual

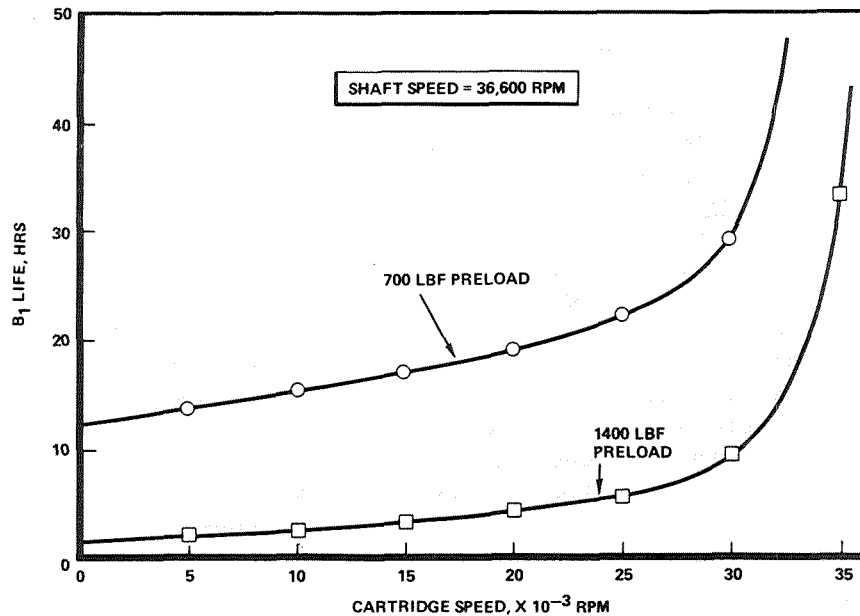


Fig. 4. 45-mm Ball Bearing Life  
(EPS Hybrid Bearing)

shaft-based DN limit will be in the range of  $3 \times 10^6$  DN, representing a significant extension to the unaided ball bearing speed limit of approximately  $2 \times 10^6$ .

In optimizing the EPS design, the relatively large centrifugal growth of journal diameter made it advantageous to reduce steady-state radial clearance to below the theoretical optimum so that a reduction could be made in clearance at start and low speed. The resulting greater stiffness throughout the speed range offset the disadvantage of higher friction. Because rotordynamic response may be sensitive to bearing stiffness and deadband, clearance tradeoffs should be part of the detail design of any EPS bearing. Conclusions drawn from the design studies for the EPS bearing are:

1. The EPS bearing can offer significant bearing life extension for high speed liquid

hydrogen applications. It should be considered for incorporation in the high pressure fuel turbopump.

2. The EPS bearing is not suitable for liquid oxygen use at high speeds.

### EPL Bearing

The EPL bearing offers significant increases over ball bearing load capacity and stiffness. By supporting a part of the radial load, ball bearing life is extended as shown in Fig. 5. This characteristic is desirable because life limitations for propellant-cooled bearings are chiefly caused by radial loading rather than axial preloads. A second significant advantage of the EPL bearing is that the hydrostatic film couples the journal directly to the housing thus making available all the stiffness and damping of the fluid film.

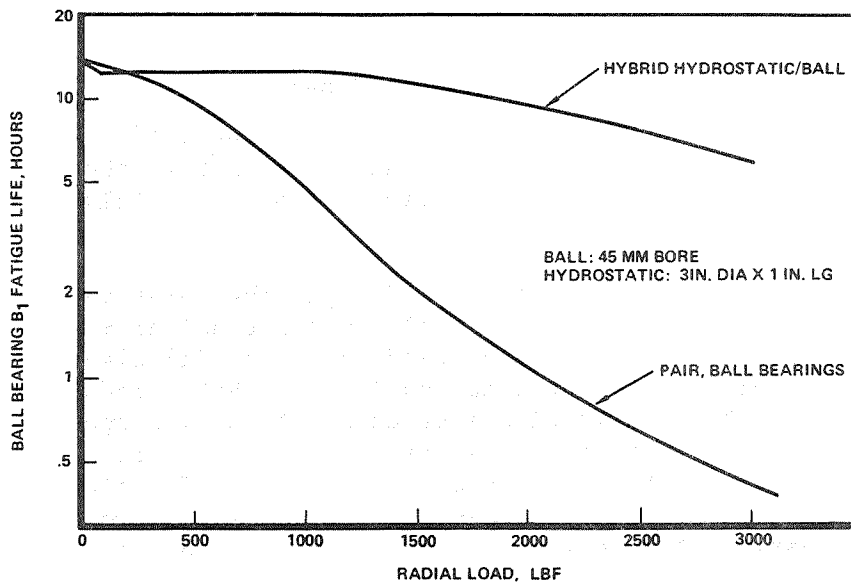


Fig. 5. Load Sharing Effect on 45-mm Ball Bearing Life (3- by 1-Inch Parallel Load Hybrid Bearing)

Rubbing during startup and shutdown can be reduced or avoided completely, a significant advantage for liquid oxygen bearings. Not only is the film clearance typically greater than the ball bearing OD clearance, but also the centrifugal growth of the journal can be advantageously used to increase the startup clearance. Conclusions concerning the EPL bearing were:

1. The EPL bearings' potential advantages warrant fabrication and test.
2. Although applicable to both liquid hydrogen and oxygen, the potential for avoidance or rubbing is of greatest advantage for liquid oxygen.
3. Due to direct coupling, the EPL bearing offers major benefits in terms of increased stiffness, damping, and load capacity.
4. Since ball bearing speed is not reduced, the speed and life increasing potential cannot approach that of the EPS bearing.

#### IPL Bearing

The IPL bearing offers the same increases in load capacity, stiffness, life, and avoidance of rubbing contact as noted for the EPL configuration. A potential disadvantage of unknown magnitude is the increased fluid tangential velocity that may result in increased cross-coupling effects. Conclusions relative to the IPL studies were similar to those for the EPL configuration. A test bearing was fabricated and tests are planned using liquid nitrogen and liquid oxygen.

#### IPS Bearing

Extension of life and speed can be obtained with liquid oxygen as well as liquid hydrogen when the IPS configuration (Fig. 2D) is employed. The reduced diameter of the hydrostatic bearing journal results in lower film friction, better speed ratio, and improved ball bearing life. For the IPS test bearing design, the film will theoretically assume 22,000 rpm

of the 30,000 rpm shaft speed, raising the ball bearing  $B_1$  life from 19 to 42 hours (Fig. 6).

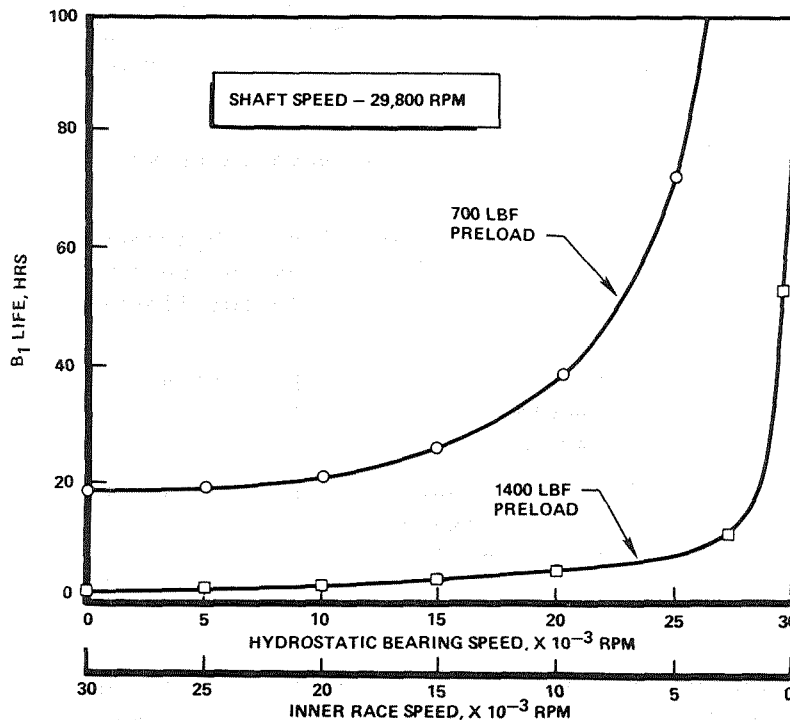


Fig. 6. 45-mm Ball Bearing Life vs Cartridge Speed (IPS Hybrid Bearing)

Additional advantages of the IPS bearing, when compared to the EPS configuration, include:

1. A speed limit of approximately  $5 \times 10^6$  DN is realizable, since only the shaft rotates at maximum speed.
2. Less kinetic energy dissipation will occur at touchdown during the shutdown transient because the cartridge is smaller.
3. Less centrifugal growth will occur, therefore less clearance change and sensitivity to speed will result.

4. The potential for internal feed exists in the high pressure oxidizer turbopump and the turbine end of the high pressure fuel turbopump.

As a consequence of internal feed, the working fluid's tangential velocity in the film will be higher, possibly increasing cross-coupling effects. Conclusions based on the IPS design studies are:

1. IPS bearing's potential advantages justify fabrication and test.
2. The IPS bearing is particularly advantageous in extending speed limits of ball bearings.
3. The IPS bearing is a viable candidate for the high pressure oxidizer turbopump and the high pressure fuel turbopump turbine bearing positions.

#### Damping Studies

To define the benefits of the damping available from hybrid bearings, studies were conducted to provide insight in three areas:

1. How much damping is desirable from a rotor-dynamic response aspect?
2. How much damping can be obtained from liquid hydrogen- and oxygen-fed hydrostatic bearings?
3. How can damping coefficient be confirmed empirically?

Using a rotordynamic model representation of SSME-type high pressure turbopumps, it was shown that the optimum magnitude of damping (that which attains the minimum response) increases with bearing stiffness. For the model used, Fig. 7 illustrates that added damping can increase response amplitudes below resonances, but may increase them at greater speeds. Optimum damping for the second resonant speed is greater than that for the first resonance. The conclusion

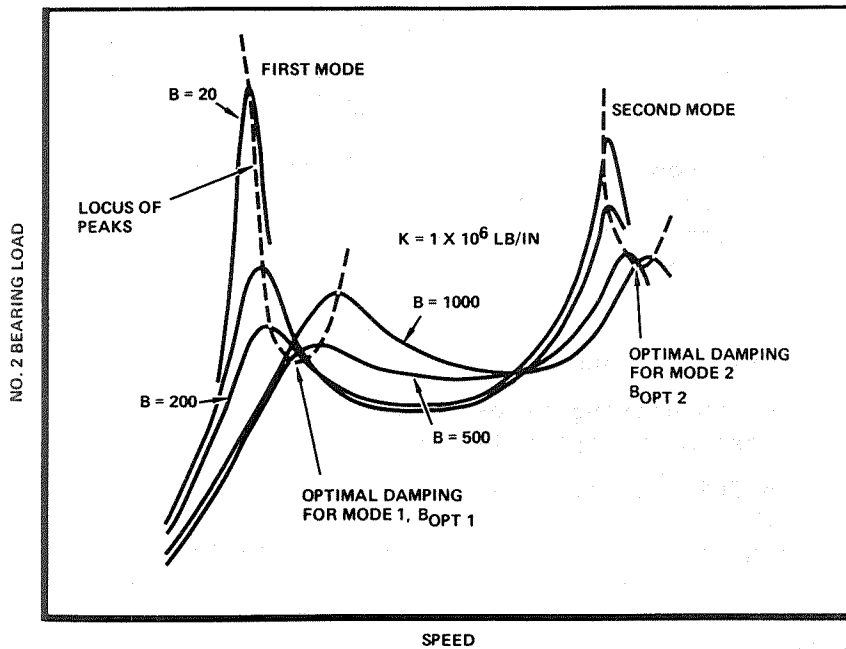


Fig. 7. Optimized Damping

drawn from the study is that optimization of damping requires a parametric study of bearing location, stiffness, and damping at the conceptual stage of rotor design.

#### Bearing Damping Potential

The magnitude of damping obtainable from liquid hydrogen and oxygen hydrostatic bearings was defined analytically in a parametric study of the effects of variations in bearing length, L/D, clearance, overall and film pressure ratios, recess geometry, orifice diameter, speed, eccentricity, and fluid properties. As shown in Table 4, the damping from a liquid hydrogen bearing responded most significantly to bearing size and clearance.

The magnitude of damping available from a similar sized liquid oxygen bearing was approximately four times that for liquid hydrogen, but the response to

Table 4. LH<sub>2</sub> Hydrostatic Bearing Damping Sensitivity

PARAMETER	SYMBOL	RANGE	DAMPING, Bxx, LBF-SEC/IN.		
			0	500	1000
L/D RATIO (D = 3.5")	L/D	.2 TO 1.0	[Bar chart showing sensitivity across the range]		
RADIAL CLEARANCE	C	.004" TO .003"	[Bar chart showing sensitivity across the range]		
SPEED (OVERALL EFFECT)	N	0 TO 40000 RPM	[Bar chart showing sensitivity across the range]		
L/D RATIO (LD = 5.25 IN <sup>2</sup> )	L/D	.2 TO 1.0	[Bar chart showing sensitivity across the range]		
PRESSURE DROP	(P <sub>s</sub> -P <sub>a</sub> )	1000 TO 5000 PSI	[Bar chart showing sensitivity across the range]		
SUPPLY/AMBIENT PRESSURE RATIO	P <sub>s</sub> /P <sub>a</sub>	1.5 TO 5.0	[Bar chart showing sensitivity across the range]		
PRESSURE RATIO	$\bar{P}_R$	.1 TO .7	[Bar chart showing sensitivity across the range]		
FLUID DENSITY	$\rho$	4 TO 9 (X 10 <sup>-6</sup> LB-S <sup>2</sup> /IN <sup>4</sup> )	[Bar chart showing sensitivity across the range]		
FLUID VISCOSITY	$\mu$	.5 TO 3.5 (X 10 <sup>-9</sup> LB-S/IN <sup>2</sup> )	[Bar chart showing sensitivity across the range]		
NUMBER OF RECESS	n	6 TO 20	[Bar chart showing sensitivity across the range]		
ECCENTRICITY RATIO	$\epsilon$	0 TO .9	[Bar chart showing sensitivity across the range]		
RECESS AREA RATIO	A <sub>r</sub>	.06 TO .15	[Bar chart showing sensitivity across the range]		
ORIFICE DIAMETER	d <sub>o</sub>	.032" TO .046"	[Bar chart showing sensitivity across the range]		
SPEED (SOLE EFFECT)	N	0 TO 40000 RPM	[Bar chart showing sensitivity across the range]		

geometric and operational variations followed a similar pattern (Table 5).

Table 5. LO<sub>2</sub> Hydrostatic Bearing Damping Sensitivity

PARAMETER	SYMBOL	RANGE	DAMPING, Bxx, LBF-SEC/IN.			
			0	1000	2000	3000
L/D RATIO (D = 3.5")	L/D	.2 TO 1.0	[Bar chart showing sensitivity across the range]			
RADIAL CLEARANCE	C	.0004" TO .003"	[Bar chart showing sensitivity across the range]			
L/D RATIO (LD = 5.25 IN <sup>2</sup> )	L/D	.2 TO 1.0	[Bar chart showing sensitivity across the range]			
SPEED (OVERALL EFFECT)	N	0 TO 30,000 RPM	[Bar chart showing sensitivity across the range]			
PRESSURE RATIO	$\bar{P}_R$	.1 TO .8	[Bar chart showing sensitivity across the range]			
PRESSURE DROP	(P <sub>s</sub> -P <sub>a</sub> )	200 TO 2,000 PSI	[Bar chart showing sensitivity across the range]			
PRESSURE RATIO	P <sub>s</sub> /P <sub>a</sub>	1.5 TO 6.0	[Bar chart showing sensitivity across the range]			
ECCENTRICITY RATIO	$\epsilon$	.0 TO .9	[Bar chart showing sensitivity across the range]			
FLUID DENSITY	$\rho$	.8 TO 1.2 (X 10 <sup>4</sup> LB-S <sup>2</sup> /IN <sup>2</sup> )	[Bar chart showing sensitivity across the range]			
SPEED (SOLE EFFECT)	N	0 TO 30,000 RPM	[Bar chart showing sensitivity across the range]			
FLUID VISCOSITY	$\mu$	.8 TO 3.0 (X 10 <sup>-8</sup> LB-S/IN <sup>2</sup> )	[Bar chart showing sensitivity across the range]			
NUMBER OF RECESSES	n	6 TO 20	[Bar chart showing sensitivity across the range]			
RECESS AREA RATIO	A <sub>r</sub>	.06 TO .15	[Bar chart showing sensitivity across the range]			
ORIFICE DIAMETER	d <sub>o</sub>	.025" TO .067"	[Bar chart showing sensitivity across the range]			

Damping Measurement

Empirical determinations of damping coefficients are planned to confirm analytic predictions. The

experimental method employs a journal eccentricity to produce a synchronous motion across the fluid film, which will be measured by proximity devices. Motions of the stator will be determined by proximity devices and accelerometers. Forces transmitted between the stator and the tester housing will be measured by strain gages in preloaded stiffening spokes. The dynamic force and motion data are to be recorded on magnetic tape for subsequent Fourier analysis to extract damping and stiffness coefficients.

#### Hardware Fabrication

The hydrostatic elements of the test bearings were constructed of Alloy 718 as were the mating parts of the tester to minimize relative thermal growths. Recesses in the EPL and IPL bearings were formed by EDM (Electric Discharge Machining). Recesses in the IPS journal are being produced by grinding.

Opposing materials in the EPL bearing for liquid hydrogen service are thin-dense chrome (bearing) vs bare Alloy 718 (journal). This combination was chosen to provide a wear-resistant surface to mate with the ball bearing outer diameter.

Both the IPL AND IPS bearings have thick silver-plated inner surface opposing chrome-plated journals following current practice in liquid oxygen turbopumps for potential rub locations.

#### Testing

The device shown in Fig. 8 was designed and built especially to test hydrostatic and hybrid bearings. Working fluid can be supplied through the test bearing housing for external feed, or, by the addition of a third shaft seal, through the shaft for internal feed. The rotor is turbine driven so that turbopump shaft speed and acceleration can be simulated. Fixed radial loads can be applied to the test bearing with a load cylinder acting on the bearing support flexure. Strain gages on the support beams are used to monitor

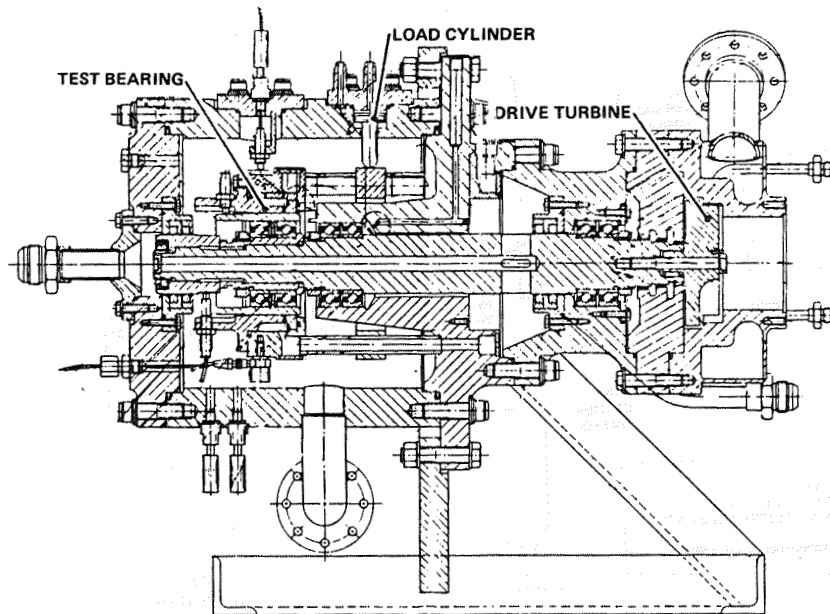


Fig. 8. Hybrid Bearing Tester

applied loads. Eddy current proximity devices are used to measure motions of the bearing and shaft, and also to measure speeds of the shaft and cartridge. For damping tests, a high bearing support stiffness is required to ensure measurable motion across the fluid film. In these tests, four strain-gaged spokes are radially pre-loaded against the test bearing housing to provide this additional stiffness. Strain gages and proximity probes were laboratory calibrated at ambient and liquid nitrogen temperatures.

The liquid hydrogen test facility, shown schematically in Fig. 9 provides liquid hydrogen for the test bearing supply from a 200-gallon tank. Gaseous hydrogen from a high-pressure source is used to pressurize the bearing supply, turbine drive, and load cylinder. Servocontrolled valves regulate test bearing supply and sump pressure, shaft speed, radial load, and when required, fluid inlet temperature. Timing of variations of each of these parameters can be controlled to six set points for a given test. Strip charts are used to monitor control function. Pressure, temperature

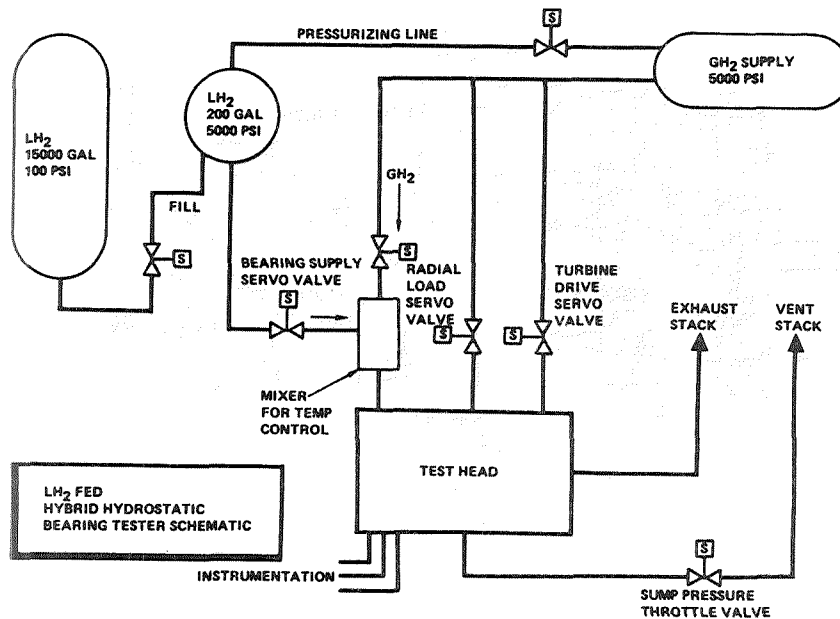


Fig. 9. Liquid Hydrogen Test Schematic

and speed data are recorded for later transcription to CRT plots. Digital data are tabulated for selected "time slices." Dynamic data from proximity devices and strain gages are recorded on FM tape for subsequent processing at the analog facility.

Redline cutoffs are used to terminate the test in the event of undesired test conditions of speed, pressures, temperatures, or accelerations.

Six bearing configurations were selected (Table 6) for testing with cryogenic working fluids (liquid hydrogen, nitrogen, or oxygen) under conditions of steady state and simulated turbopump transient start/shutdown. As previously described, eccentric journals will be used to extract dynamic coefficients of stiffness and damping.

### Test Results

In Test 012 (Table 7), flowrate was observed to decline as speed increased (Fig. 10) due largely to the

Table 6. Six Test Bearing Configurations To Be Evaluated

BUILD	DESCRIPTION	TESTS
1	EPL BEARING	STATIC AND PREPRESSURIZED ROTATING FLOW AND STIFFNESS TRANSIENT START AND SHUTDOWN
	LIQUID HYDROGEN FED ONE 45-MM BALL BEARING	
2	HYDROSTATIC ELEMENT OF BUILD 1 ECCENTRIC JOURNAL	DAMPING MEASUREMENT
3	INCREASED L/D HYDROSTATIC ELEMENT ECCENTRIC JOURNAL	DAMPING MEASUREMENT
4	IPL BEARING	STATIC AND PREPRESSURIZED ROTATING FLOW AND STIFFNESS TRANSIENT START AND SHUTDOWN
	LIQUID NITROGEN AND OXYGEN FED ONE 45-MM BALL BEARING	
5	HYDROSTATIC ELEMENT OF BUILD 4 ECCENTRIC JOURNALS	DAMPING MEASUREMENT
6	IPS BEARING	STATIC AND PREPRESSURIZED ROTATING FLOW AND STIFFNESS TRANSIENT START AND SHUTDOWN
	LIQUID NITROGEN AND OXYGEN FED PAIR OF 45-MM BALL BEARINGS	

Table 7. Test Result Summary

TEST NO.	TEST TYPE	SPEED, RPM	PRESSURES				TEMPERATURES		RADIAL LOAD, LB	STIFF 10 <sup>6</sup> LB/IN	FLUID INLET DENSITY	FLOW LB/SEC
			SUPPLY	SUMP	RECESS 1	RECESS 2	SUPPLY	SUMP				
012	LH <sub>2</sub> SPIN NO LOAD	8028	2357	352	1515	1511	104	87	0		3.56	0.37
		19564	2360	352	1585	1600	106	90	0		3.51	0.35
		32796	2358	353	1778	1799	112	97	0		3.38	0.31
019	LH <sub>2</sub> SPIN FIXED RADIAL LOAD	36676	2359	349	1869	1891	118	102	0		3.22	0.29
		38560	2328	346	1820	1894	91	82	0		3.58	0.32
		36065	2325	350	1816	1783	93	83	166	3.37	3.82	0.31
		36195	2324	349	1763	1831	93	83	0		3.82	0.32
		35624	2325	350	1869	1723	95	84	340	3.16	3.77	0.32
		36451	2326	350	1773	1845	95	84	0		3.78	0.32
022	LH <sub>2</sub> TRANSIENT	35824	2323	351	1891	1716	95	84	386	3.45	3.77	0.32
		0	100	~ 10	~ 40	~ 40	56	52	0		-	-
		39229	2106	284	1763	1726	84	81	300*		4.00	0.26
		36961	2252	349	1853	1788	90	82	800*		3.91	0.33
		27634	1704	270	1246	1168	94	76	470*		3.45	0.32
		37257	2264	352	1876	1798	94	84	800*		3.81	0.32
		15668	1611	258	1041	1039	96	78	~ 0		3.31	0.32

\*INTENDED LOAD, ACTUAL LOAD MAY BE LESS

clearance reduction as the journal grows centrifugally. Changes not attributable to journal growth are most probably due to increased hydrodynamic (Couette) flow in the film and increased flow resistance of the adjacent ball bearing as speed increases. When the ball bearing was removed for the damping tests, the resulting decrease in recess pressure and increase in flow was attributed to reduced restriction of flow to one

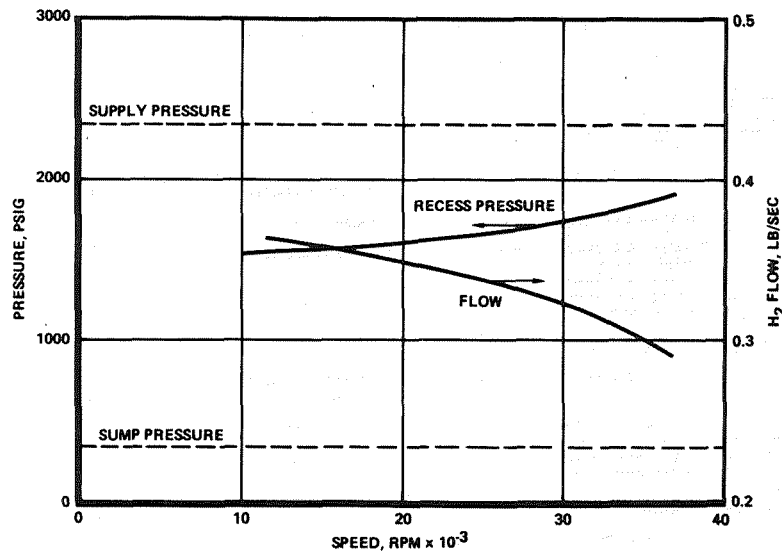


Fig. 10. Speed Effects - Test 012 EPL Bearing

side of the hydrostatic bearing. Based only on experimental results, correlation of the measured flow and recess pressures with analytic predictions suggests adjustments to the orifice discharge coefficient ( $C_D$ ) from the assumed 0.98 to 0.94. The lowered effective discharge coefficient may be the result of greater than normal losses due to fluid turbulence and sudden velocity changes at the orifice exit in the small recess volume. A corresponding adjustment is indicated for the land clearance entrance loss coefficient ( $K_e$ ) from the assumed 0.5 to 0.39. A possible reason for a lower-than-expected entrance loss is that the circumferential recess boundaries are tapered rather than being fully sharp due to the manufacturing process. Recess pressures showed an increase with speed (Fig. 10), corresponding to the flow decrease and also probably due chiefly to centrifugal journal growth. The decline in recess pressure that followed removal of the ball bearing was probably in response to lowered downstream flow resistance, even though that change applies to only one side of the bearing.

The calculated stiffness values from Test 019 are in the range of  $3 \times 10^6$  lb/in. for the composite total for the ball and hydrostatic bearing. Deducting the ball bearing calculated stiffness results in an apparent stiffness of  $2.7 \times 10^6$  lb/in. for the hydrostatic bearing, exceeding the predicted value by 70 percent. This result is comparable with those obtained by Hannum and Nielson (Ref. 3). Stiffness magnitude will be further assessed by comparison with the results of the damping tests and with repeated steady-state tests of the hydrostatic bearing alone.

Two transient tests based on the high pressure fuel turbopump start/shutdown profile were completed as programmed. Figure 11 illustrates the simultaneous ramps of speed, supply and sump pressures, and radial load as they would occur during launch, throttling, and shutdown in an SSME flight at the Challenger power levels. The simulated total run duration is compressed to avoid liquid hydrogen depletion prior to shutdown.

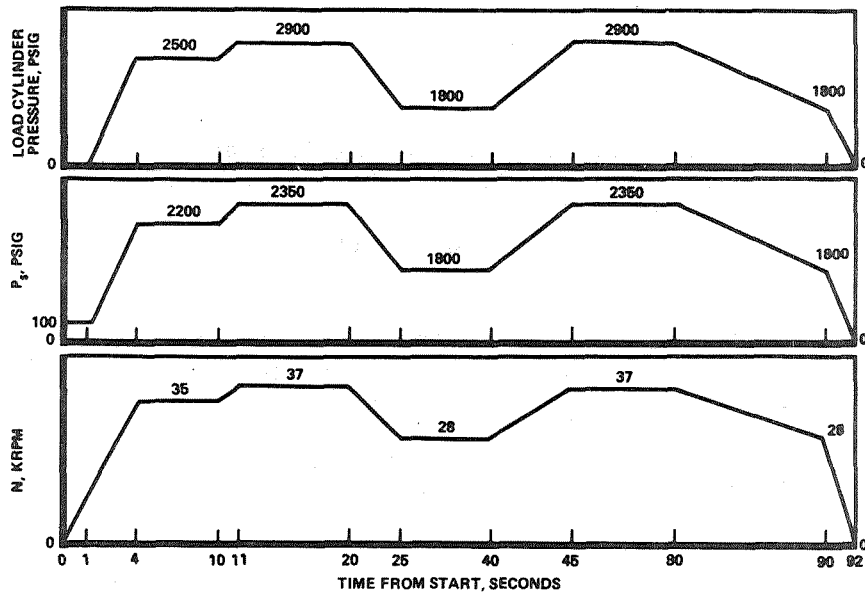


Fig. 11. HPFTP Start/Shutdown Transient (Challenger Profile)

Two damping tests were conducted incorporating an eccentric journal and stiffened bearing support. Three ramps were included at speeds from 10,000 to 14,000 rpm, 22,000 to 26,000 rpm, and 32,000 to 36,000 rpm. Data examination and analysis is currently underway.

### Looking Ahead

Analytic treatment and test results have shown that hybrid bearings have potential to improve turbopump bearing and rotordynamic performance, and that they are viable and practical machine elements. The current SSME Long Life Program will provide empirical and operational data concerning externally fed liquid hydrogen and oxygen hybrid bearings.

Two additional areas of study are recommended to support the incorporation of load sharing elements into current and future turbopump designs:

1. EPL (Externally Fed Parallel Load) hybrid bearings for liquid oxygen service
2. Load sharing seals for liquid oxygen - This concept is currently showing outstanding potential for extension of bearing life and improvement of rotor stability. An effort to quantify or confirm analytic seal coefficients for liquid oxygen operation would be extremely valuable.

These elements can be designed and fabricated for incorporation into the currently used test device for functional evaluation and correlation of analytic and test results.

### Nomenclature

- $A_o$  = orifice area, in.<sup>2</sup>  
 $A_r$  = recess area ratio =  $\bar{x} \bar{y}$   
 $B_{xx}$  = direct damping, lbf-sec/in.  
 $\bar{B}_{xx}$  = nondimensional damping  $(c/R)^3 B_{xx} / \mu L$

- $c$  = clearance, inches  
 $C_D$  = coefficient of discharge  
 $D$  = journal diameter, inches  
 $d_o$  = orifice diameter, inches  
 $g$  = gravitational constant = 386.4 in./sec<sup>2</sup>  
 $G_p$  = turbulent correction factor for viscosity  
 $K$  = stiffness, lbf/in.  
 $\bar{K}$  = nondimensional stiffness =  $cK/(P_s - P_a)$   
 $K_{xx}$  = direct stiffness, lbf/in.  
 $K_{xy}$  = cross-coupling stiffness, lbf/in.  
 $K_e$  = inertia coefficient  
 $L$  = bearing length, inches  
 $m$  = number of rows  
 $n$  = number of recesses  
 $N$  = rotational speed, rpm  
 $P_a$  = ambient pressure, psia  
 $P_r$  = recess pressure, psia  
 $P_s$  = supply pressure, psia  
 $\bar{P}_R$  = pressure ratio  
 $R$  = journal radius, inches (=  $D/2$ )  
 $\bar{R}_f$  = nondimensional film resistance =  $\left[ \frac{\rho g G_p c^3 \bar{P}_R}{\mu \left(\frac{L}{D}\right) \left(1 - \frac{\bar{Y}}{m}\right)} \right]^2 (P_s - P_a) R_f$   
 $R_o$  = orifice resistance, sec<sup>2</sup>/lb-in.<sup>2</sup>  
 $\bar{R}_o$  = nondimensional orifice resistance =  $\left[ \frac{\rho g G_p c^3 \bar{P}_R}{\mu \left(\frac{L}{D}\right) \left(1 - \frac{\bar{Y}}{m}\right)} \right]^2 (P_s - P_a) R_o$

W = bearing load, lbf

$\epsilon$  = eccentricity ratio

$$\Lambda_r = \text{orifice restrictor parameter} = \frac{\rho(P_s - P_a) c^6 R}{\mu(A_o C_D)^2}$$

### References

1. Wolf, J. E., Mark 25 Pump Hybrid Hydrostatic Bearing Test at Nuclear Rocket Development Station, Rockwell International/Rocketdyne Division, Canoga Park, CA, Report R-9117, Contract SNSN-65, 20 November 1972.
2. Hannum, N. P. and C. E. Nielson, "The Performance and Application of High Speed Long Life LH<sub>2</sub> Bearings for Reusable Rocket Engine Turbomachinery," NASA TM-83417, AIAA 83-1389, June 1983.
3. Reddecliff, J. J. and J. M. Vohr, "Hydrostatic Bearings for Cryogenic Rocket Engine Turbopumps," J. of Lubrication Technology, July 1969.
4. Artiles, A., J. Wallowitz, and W. Shapiro, "Analysis of Hybrid, Fluid Film Journal Bearings With Turbulence and Inertia Effects. Advances in Computer-Aided Bearing Design," Proceedings of ASME-ASLE Lubrication Conference, American Society of Lubrication Engineers, New York, October 1982.
5. Jones, A. B., Rolling-Element Bearing Analysis Program, 1978.
6. Lee, F. C., Parametric Study of Hybrid Bearings, Rockwell International IL TPME 3172-6642, 23 November 1982.
7. Vohr, J. H., Journal Bearing Section, RPI-MTI Gas Bearing Design Course, 1967.
8. Aston, R. L. and J. P. O'Donoghue, "The Effect of the Number of Recesses on the Performance of Externally Pressurized Multi-Recess Journal Bearings," Tribology, May 1971.

POWDER METALLURGY BEARINGS FOR ADVANCED  
ROCKET ENGINES

J. N. Fleck, B. J. Killman and H. Munson  
TRW Aircraft Components Group  
Cleveland, Ohio 44117

Traditional ingot metallurgy has been pushed to the limit for many demanding applications including antifriction bearings. New systems require corrosion resistance, better fatigue resistance, and higher toughness. With conventional processing, increasing the alloying level to achieve corrosion resistance results in a decrease in other properties such as toughness.

Advanced powder metallurgy affords a viable solution to this problem. During powder manufacture, the individual particle solidifies very rapidly; as a consequence, the primary carbides are very small and uniformly distributed. When properly consolidated, this uniform structure is preserved while generating a fully dense product. Element tests including rolling contact fatigue, hot hardness, wear, fracture toughness, and corrosion resistance are underway on eleven candidate P/M bearing alloys and results are compared with those for wrought 440C steel, the current SSME bearing material.

Several materials which offer the promise of a significant improvement in performance have been identified.

ROLLING CONTACT FATIGUE LIFE OF  
CHROMIUM ION PLATED 440C BEARING STEEL

Biliyar N. Bhat  
Materials and Processes Laboratory  
NASA/MSFC  
Marshall Space Flight Center, Alabama 35823  
U.S.A.

Jack H. Davis  
Department of Physics  
The University of Alabama in Huntsville  
Huntsville, Alabama 35899  
U.S.A.

ABSTRACT

Rolling contact fatigue (RCF) test specimens of heat treated 440C bearing steel were chromium ion plated in thicknesses from  $0.1 \mu\text{m}$  to  $8.0 \mu\text{m}$  and tested in RCF tester using 700 ksi maximum Hertzian stress. Heavy coatings, greater than about  $5 \mu\text{m}$  in thickness, peeled off or spalled readily, whereas thin coatings, less than  $3 \mu\text{m}$  thick, were tenacious and did not come off. Furthermore, significant improvement in RCF life was obtained with thin chromium ion plated test specimens. The average increase in  $B_{10}$  life was 75% compared with unplated 440C. These preliminary results indicate that ion plating is a promising way to improve bearing life.

ROLLING CONTACT FATIGUE LIFE OF CHROMIUM  
ION PLATED 440C BEARING STEEL

Introduction

The high efficiency operation of the Space Shuttle Main Engine (SSME) appears to limit the service life of 440C steel bearings in the engine, especially those of the high pressure oxidizer turbopump (HPOTP). Bearing life enhancement is expected to contribute significantly to increased life and reliability of space transportation systems. To achieve this goal, efforts have been made to thoroughly understand the complexities of turbopump bearing service life.<sup>1</sup> Improved bearing materials with greater resistance to fatigue and wear are being developed through powder metallurgy techniques.<sup>2</sup> Furthermore, surface modification techniques such as ion plating and ion implantation appeared to offer potential for improving the fatigue life of bearing materials.<sup>3</sup> Ion plating, in particular, seemed to have several positive qualities, the most important of which are outstanding film adhesion and deposition on all sides of the substrate (including some coverage into cavities), whereas normal vacuum deposition and ion implantation give the usual line-of-sight coverage. Other qualities are fine grain structure, low coefficient of friction and improved mechanical properties. The latter two qualities of ion plated coatings make it attractive for application in turbopump bearings. Therefore, a study of ion plating 440C with chromium was conducted. This paper presents some preliminary results obtained in that study.

### Ion Plating Procedure

Chromium was selected for ion plating 440C steel because of its common use in electroplating steel for corrosion resistance. Furthermore, 440C steel contains about 16-18 wt. % chromium, thus providing a continuity in chemistry which is an important consideration in obtaining a good bond. The test specimen used in this study and the heat treatment are shown in Figure 1. The apparatus used for ion plating is shown schematically in Figure 2. Chromium is melted by an electron beam and vaporized. Some chromium atoms are ionized in the plasma glow discharge formed by the ionized argon gas, accelerated by the applied electric potential and deposited on the 440C rolling contact fatigue (RCF) test specimen. The specimen rod axis was mounted coaxially with the jar axis to produce a symmetric uniform coating. The specimen was initially sputter-cleaned in situ to remove the oxide layer before the electron beam was turned on to vaporize chromium. Plating thickness was varied so that the effect of plating thickness on RCF life could be determined. The plating thickness was calculated based on weight gain during plating. Argon pressure during plating was typically 15-30  $\mu\text{m}$ . Substrate temperatures using an infrared pyrometer varied between 200°C-300°C. Table 1 gives a summary of the test specimens ion plated with chromium in this program. Estimated plating thickness varied from 0.1  $\mu\text{m}$  to 8.0  $\mu\text{m}$ . Coating appearance was variable, from nearly invisible and bright to bluish, grey and dark.

### Metallurgical Analysis

All RCF test specimens were examined under a stereo viewer. Where the coatings were very thin (< 1  $\mu\text{m}$ ) it was difficult to tell that the specimens were coated. Dark coatings were generally porous and were readily scratched by knife. Good, thin coatings were not scratched by knife. One such specimen (No. 5) was sectioned, electroless nickel plated, mounted in epoxy, polished, etched and

examined under optical microscope. A thin ion plated chromium layer was observed (Figure 3). The plating was uniform and followed the surface contours. There was a good bond between the chrome plating and the surface, especially with the carbides.

#### Rolling Contact Fatigue (RCF) Testing

RCF testing was done using the Polymet model RCF-1 machine which used two, 7.5 in. diameter loading discs (Figure 4). The specimen was loaded to a maximum Hertzian stress of 700,000 psi. The testing speed was 10,000 rpm. The number of revolutions were counted automatically by a revolution counter. The testing machine was shut down automatically by a failure sensor which picked up vibrations that increased sharply when the specimen failed by spalling. The number of revolutions to failure was noted. About eight tests were run with each specimen, four on each end. The data were plotted on a Weibull probability chart, which plotted cumulative percent failure versus number of cycles to failure (Figure 5). The  $B_{10}$  life was read off the chart. The results are summarized in Table 1. Some specimens had coatings that were too thick and readily spalled off. These samples were not tested any further. Specimen No. 1 (in Table 1) was not ion plated, but was simply sputter cleaned by argon. Auger analysis of this sample showed a chromium rich (40 wt. % Cr) surface layer, approximately 15 nm thick. Such a surface layer obviously provides a good transition layer for ion plating chromium. RCF testing produced typical wear tracks and spalls in the specimen. Figure 6 gives three examples. The spalls of both ion plated and standard specimens were examined in the scanning electron microscope (Figure 7). Failure mode appears to be the same in both cases.

## Discussion

On examination of RCF test results (Table 1) chromium ion plating obviously helped to improve the RCF life of 440C steel test specimens. The ratio  $B_{10}$  (specimen)/ $B_{10}$  (standard) is listed in the last column of Table 1. This ratio varied from 1.07 to 2.86. The average was 1.75, indicating a 75% improvement in RCF life. The failure mode in RCF testing was by spalling (Figure 7). In this mechanism subsurface crack initiation occurs under high Hertzian stresses and the crack propagates to the surface resulting in spalling. The reason for the improvement in RCF life may be due to the fact that a thin chromium layer is likely to produce a more even distribution of contact stresses which results in a somewhat reduced maximum shear stress, thus extending the fatigue life. It is not clear how well the coating would perform under actual service conditions of the turbopump where some sliding motion is present and where lubrication is marginal. To answer this question it would be necessary to run cryogenic tests with ion plated bearings. The preliminary results obtained in this study are encouraging. However, there is a considerable scatter in the  $B_{10}$  lives of ion plated specimens, taken as a whole. The reason for this scatter is not very clear. One possibility is that the ion plating process is not fully optimized yet. For instance, further optimization in electron beam current (which determines the rate of chromium evaporation) may be necessary. However, it does appear that the highest  $B_{10}$  lives are associated with thin coatings (0.1  $\mu\text{m}$  and 0.2  $\mu\text{m}$ , Table 1). This avenue should be pursued further to gain confidence in the improved RCF life of ion plated 440C bearing steel.

### Summary and Conclusions

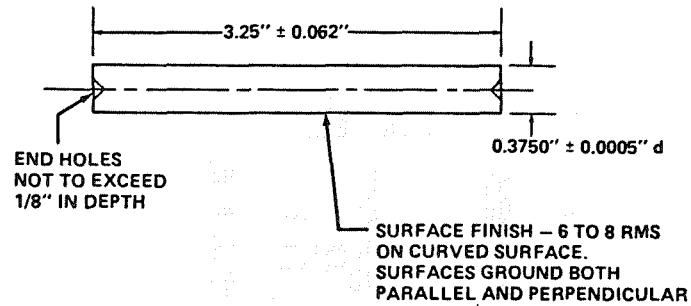
RCF tests were conducted with chromium ion plated 440C bearing steel specimens. The results showed significant improvements in B<sub>10</sub> life. The average improvement was 75% for all samples. Thin coatings, 0.1 to 0.2  $\mu\text{m}$  thin, gave the best results, with B<sub>10</sub> life improvements greater than 150%. Further process optimization and tests in cryogenic environments are necessary to qualify these coatings for use in the SSME turbopump bearings.

### Acknowledgements

The technical support of F. J. Dolan, R. R. Rowe, and other personnel of Materials and Processes Laboratory, NASA-MSFC, and the advice and assistance of A. P. Biddle of Space Science Laboratory, NASA-MSFC, in setting up and operating the ion plating unit are gratefully acknowledged.

## References

1. B. N. Bhat, "Fracture Analysis of HPOTP Bearing Balls," NASA-TM-82428, May 1981; B.N. Bhat and F. J. Dolan, "Past Performance Analysis of HPOTP Bearings", NASA-TM-92470, March 1982; B.N. Bhat and F.J. Dolan, "Analysis of Cryogenic Turbopump Bearing Service Life," unpublished report, May 1983.
2. "Application of Powder Metallurgy Techniques to Produce Improved Bearing Elements for Liquid Rocket Engines," by TRW, Inc., Materials and Manufacturing Technology Center, Cleveland, Ohio. (NASA Contract NAS8-34763) Work in progress.
3. "Ion Plating" by R.F. Hochman and D.U. Mattox; "Ion Implantation" by R.F. Hochman, Metals Handbook, Volume 5, American Society for Metals (1982).
4. Jack H. Davis, "Aluminum and Chromium Ion Plating Studies for Enhancement of Surface Properties," NASA CR-162051 and NASA CR-161851, University of Alabama in Huntsville, AL, August 11, 1981 and August 18, 1982.

**A. RCF TEST SPECIMEN****B. HEAT TREATMENT OF RCF TEST SPECIMEN**

AFTER ROUGH MACHINING, HEAT TREATMENT IS CARRIED OUT AS FOLLOWS:

- A. AUSTENITIZE AT  $1930^{\circ} \pm 30^{\circ}\text{F}$  FOR ONE HOUR AT TEMPERATURE.
- B. HARDEN (OIL QUENCH  $120^{\circ} - 150^{\circ}\text{F}$  OIL TEMP.).
- C. TEMPER ONE HOUR MIN. AT  $325^{\circ} + 25^{\circ}\text{F}$   
 $- 0^{\circ}\text{F}$
- D. COOL IN AIR TO  $70^{\circ} \pm 10^{\circ}\text{F}$  (ROOM TEMP.)
- E. COLD SOAK IN LIQUID NITROGEN FOR 30 MINUTES.
- F. TEMPER ONE HOUR MINIMUM AT  $325^{\circ} + 25^{\circ}\text{F}$   
 $- 0^{\circ}\text{F}$

FINAL HARDNESS - TYPICALLY Rc 59-61

FIGURE 1. RCF TEST SPECIMEN CONFIGURATION AND HEAT TREATMENT

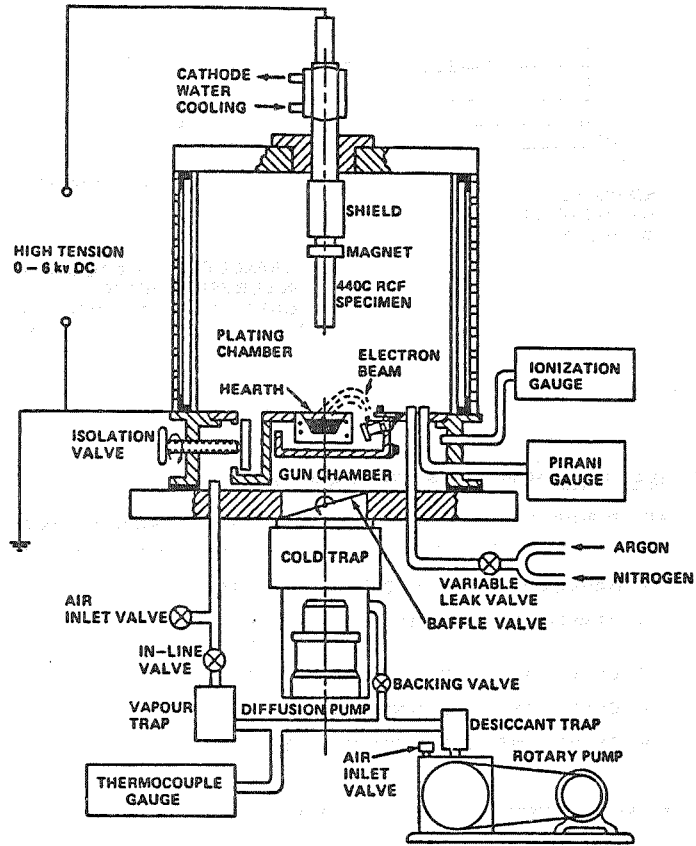


FIGURE 2. ION PLATING APPARATUS WITH AN ELECTRON BEAM GUN (SCHEMATIC)

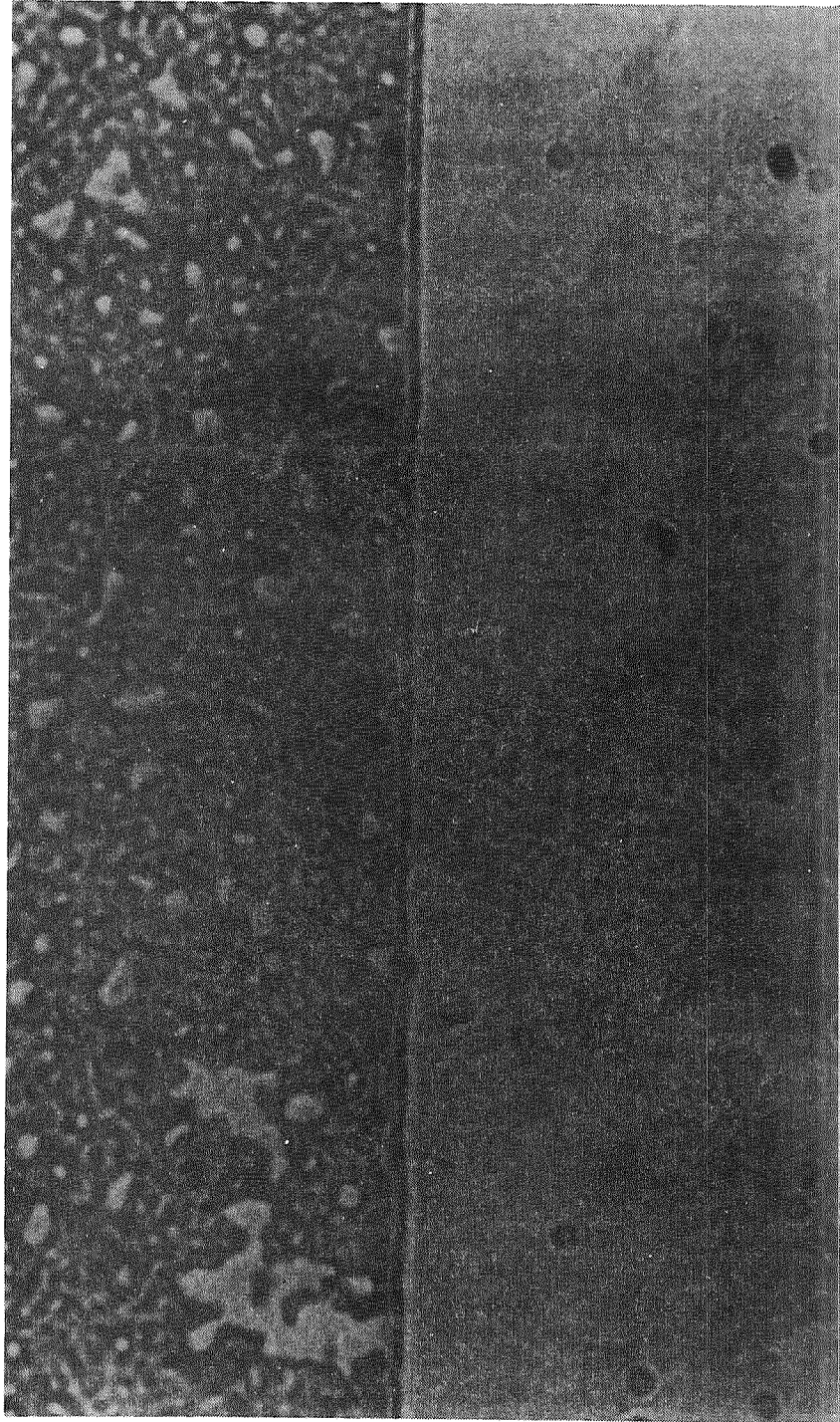


FIGURE 3. - PHOTOMICROGRAPH OF ION PLATED 440C RCF TEST SPECIMEN (NO. 6).

FIGURE 3 - PHOTOGRAPHIC COPY OF THE ROLLING CONTACT FATIGUE TESTER (RCF-1) OF

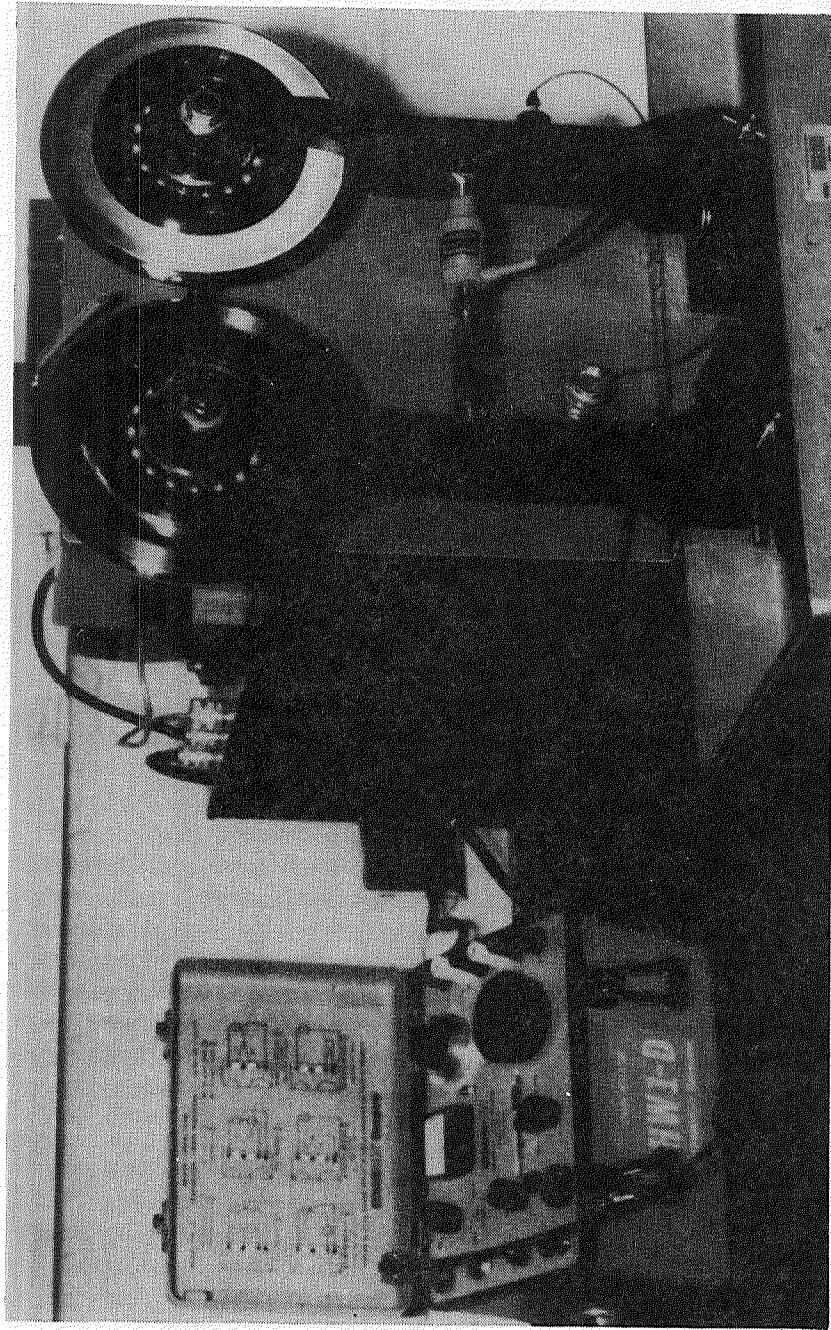


FIGURE 4. - ROLLING CONTACT FATIGUE TESTER (POLYMET MODEL RCF-1).

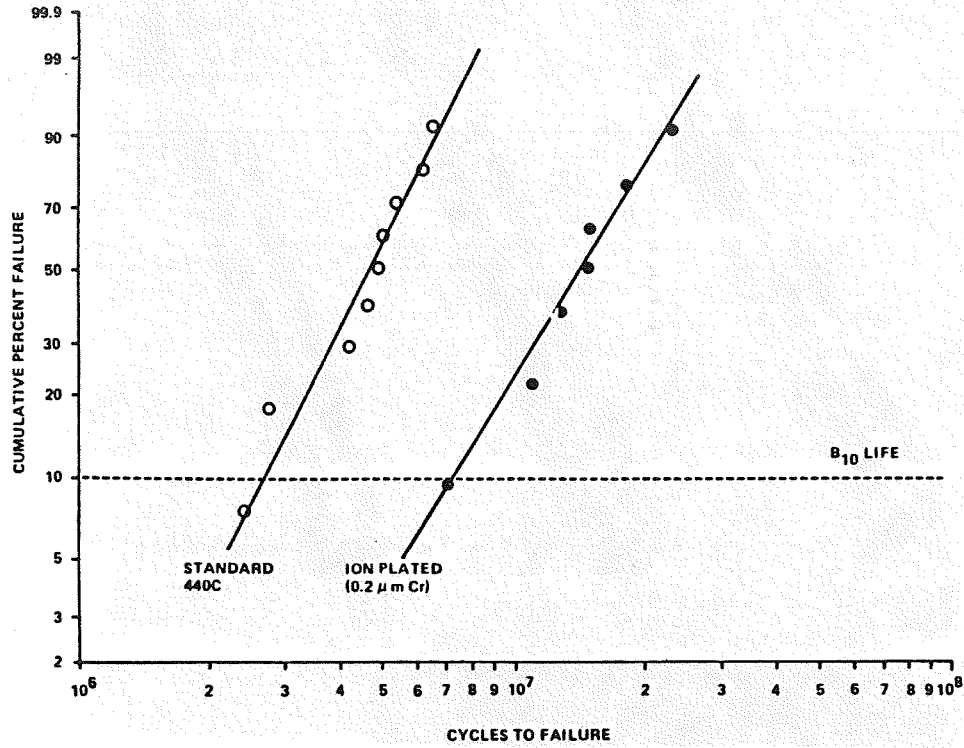


FIGURE 5. WEIBULL PLOT OF RCF TEST RESULTS FOR STANDARD AND CHROMIUM ION PLATED 440C

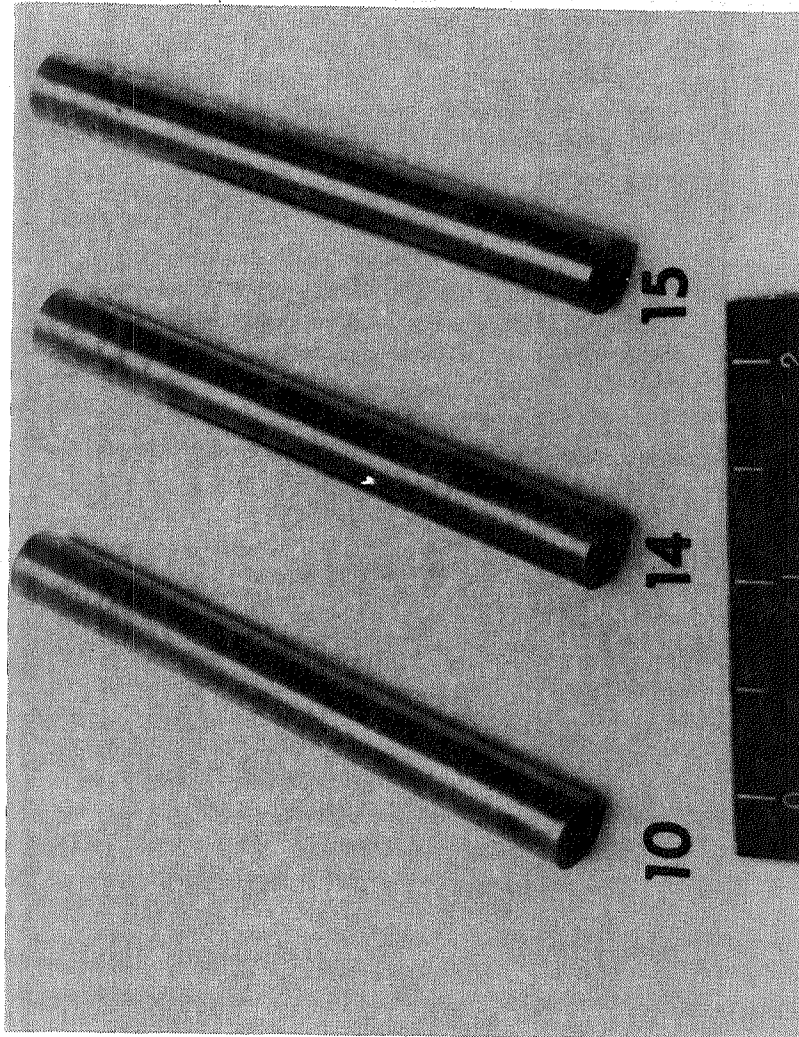


FIGURE 6. - RCF TEST SPECIMENS - AFTER TESTING. NOTE WEAR TRACKS AND SPALLS.  
(NUMBERS REFER TO SPECIMEN NUMBERS IN TABLE 1.)

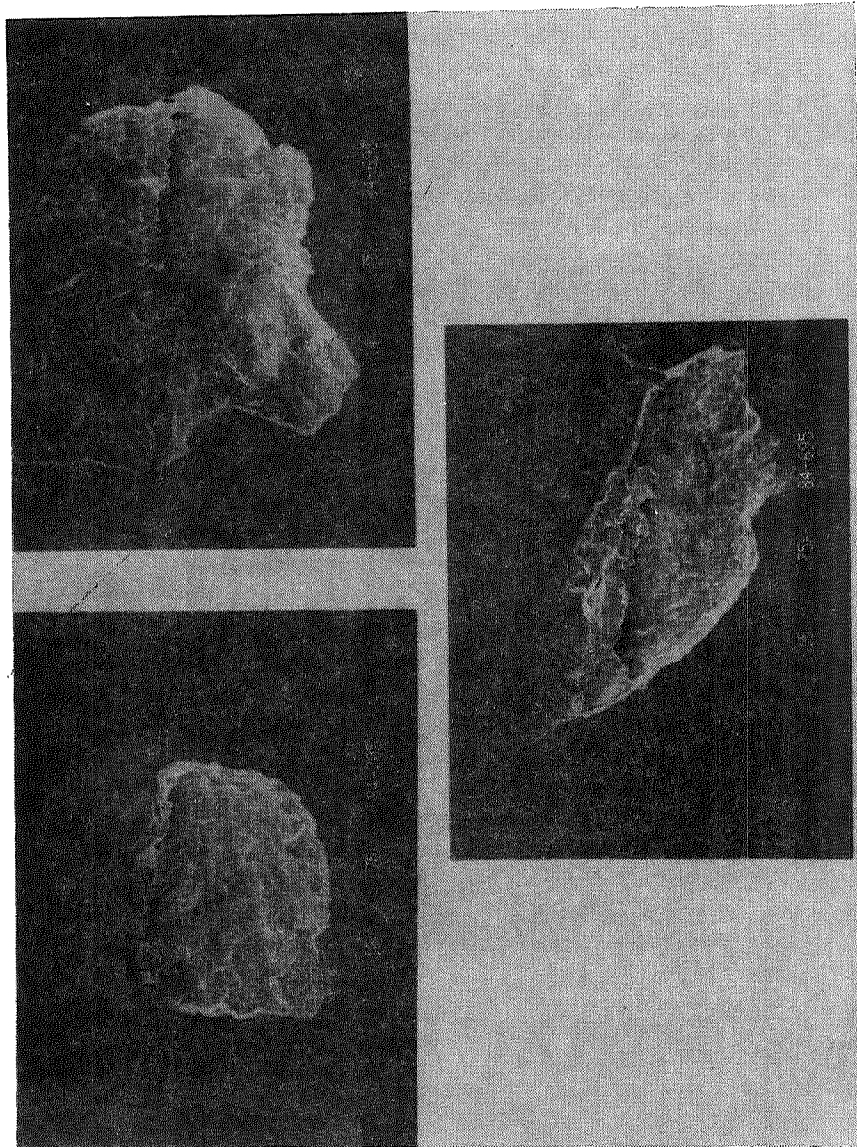


FIGURE 7. - TYPICAL SPALLS IN ION PLATED (NOS. 10, 14) AND UNPLATED (NO. 15) RCF TEST SPECIMENS.

TABLE 1: SUMMARY OF TEST SPECIMENS

Sample Number	Average Coating Thickness ( $\mu\text{m}$ )	Color of Coating	Comments	RCF Test Results	
				B <sub>10</sub> Life (Cycles)	B <sub>10</sub> (Specimen) B <sub>10</sub> (Standard 440C)
1	0.0	Light gold	Sputter-cleaned, but not ion plated		
2	4.5	Grey to dark	Thick coating, peeled off during RCF test		
3	8.0	Dark	Coating easily scratched by knife; not tested		
4	6.0	Bright	Coating peeled off during RCF test		
5	5.0	Bright	Easily scratched, not tested		
6	0.2	Bright	Good coating; RCF tested	7.2X10 <sup>6</sup>	2.57
7	6.6	Dark	Readily scratched, coating peeled off during RCF test		
8	6.0	Grey	Readily scratched, not tested		
9	1.0	Blackish	RCF tested	3.6X10 <sup>6</sup>	1.29
10	3.0	Bluish	RCF tested	5.0X10 <sup>6</sup>	1.79
11	0.1	Bright	RCF tested	8.0X10 <sup>6</sup>	2.86
12	2.0	Bluish	RCF tested	3.0X10 <sup>6</sup>	1.07
13	0.9	Bright	RCF tested	4.2X10 <sup>6</sup>	1.5
14	0.4	Bright	RCF tested	3.4X10 <sup>6</sup>	1.21
15	0.0	Bright	Standard 440C specimen	2.8X10 <sup>6</sup>	----
				AVG.	1.75

TECHNICAL OVERVIEW  
STRUCTURAL DYNAMICS

Larry Kiefling  
Systems Dynamics Laboratory  
NASA/MSFC  
Marshall Space Flight Center, Alabama 35812 U. S. A.

Structural dynamics technology development in support of SSME was initiated in November 1980. The objective identified were to develop improved understanding of the operating dynamic characteristics of high-performance liquid rocket systems in order to:

- o increase lifetime and performance
- o decrease weight
- o identify incipient failures
- o meet deflection requirements
- o decrease costs
- o predict effect of imposed changes
- o determine changes to meet specified requirements

A series of tasks was identified and work was started on the most urgent tasks. In 1983, the program was made into a joint program with NASA-Lewis Research Center. A complete description can be found in the RTOP.

The papers presented at this conference give results from some of the earlier tasks as they near completion. A considerable amount of effort is represented and significant progress is reported.

SIGNAL ANALYSIS TECHNIQUES  
FOR INCIPIENT FAILURE DETECTION  
IN TURBOMACHINERY

Thomas Coffin  
Wyle Laboratories, Huntsville, Ala.

Abstract

This paper reviews the status of an investigation to develop, implement, and evaluate signal analysis techniques for the detection and classification of incipient mechanical failures in turbomachinery. Signal analysis techniques available to describe dynamic measurement characteristics are reviewed. Time domain and spectral methods are described, and statistical classification in terms of moments is discussed. Several of these waveform analysis techniques have been implemented on a computer and applied to dynamic signals. A laboratory evaluation of the methods with respect to signal detection capability is described. Plans for further technique evaluation and data base development to characterize turbopump incipient failure modes from Space Shuttle main engine (SSME) hot firing measurements are outlined.

Introduction

Although little can be done to anticipate mechanical failures which exhibit very short periods of growth, most failures are preceded by growing tolerances, imbalance, bearing element wear, and the like, which may manifest themselves through subtle modifications in the waveform observed by dynamic measurements. Incipient failure detection is based on observing and recognizing measurable phenomena that occur as a result of nominal system operation and those associated with component degradation. The techniques are analytical, but their application is necessarily empirical, based on correlation between derived signature characteristics and observed mechanical condition.

Turbomachinery malfunction may result from a number of distinct failure modes such as turbine blade wear or bearing element fatigue. Each of these mechanisms may be expected to influence the waveform or spectral content measured by a transducer in a somewhat different fashion. Thus, it is clear that a single best signal analysis technique or indicator is not to be expected for system condition monitoring. A series of tests, each designed to detect a given failure mode, is therefore desirable.

The Space Shuttle main engines have and are presently undergoing extensive hot firing tests at which time vibration measurements on the high pressure fuel and oxidizer turbopumps are acquired. Thus, a wealth of vibration data is available from these components under widely varying operational conditions. Under contract with NASA/MSFC, Wyle is investigating techniques of analyzing these data to indicate SSME component condition.

#### Techniques and Applications

Review of the literature on machinery condition diagnostic methodologies indicate approaches employing thermal, chemical, metallographic, and vibration analysis techniques.<sup>1,2</sup> This discussion is limited to the assessment of motion detected by a transducer fixed to the machine during operation. (Appropriate sensor selection and location is not a trivial consideration with respect to component fault detection.) Historically, the most common diagnostic approach has been to detect and track the root-mean-square vibration level (displacement, velocity, or acceleration) as an indication of machinery condition. Performing the same analysis in separate frequency bands provides some improvement in fault identification since gross failure modes, such as imbalance, may show up at well-defined frequencies with respect to the synchronous speed. Signature analysis techniques thus fall naturally into two categories, time domain methods and characterization in the frequency domain. Several of these techniques presently under evaluation are next described.

### Time Domain Methods

Time Domain Averaging. This method is a well-known technique for extracting periodic signals from noisy or complex waveforms.<sup>3,4</sup> The procedure can be explained by assuming a given signal  $x(t)$  is the sum of a periodic component  $p(t)$ , and additive noise,  $n(t)$ :

$$x(t) = p(t) + n(t).$$

By summing one time slice of  $x(t)$  with another but delayed one period later than the previous, the periodic component will add coherently, and the noise component, if uncorrelated, will not. After  $N$  additions of the signal with itself, the time domain average signature,  $D(t)$ , may be expressed as

$$D(t) = \frac{1}{N} \sum_{n=0}^{N-1} x(t+nt).$$

This process is equivalent to a comb filter in the frequency domain as illustrated in figure 1.<sup>4</sup> As the number of replications increases, so does the sharpness of the main lobes and attenuation of nonharmonic frequencies. The TDA method has been effectively applied to large rotating machinery evaluations, and implementation on a small computer is quite direct. It is noted that the process is coherent, requiring that the period of the signal to be extracted be known or assumed.

Random Decrement Analysis. The response of a structural dynamic system is a function of both the applied loading and system properties. Changes in system characteristics such as modal frequencies or damping may be indicative of component degradation. The so-called random decrement signature has been applied extensively to the extraction of structural system characteristics in the presence of complex loading.<sup>5,6</sup> The procedure is similar to the TDA

method described above in that the measured signal is repetitively shifted and added to itself:

$$\delta(\tau) = (1/N) \sum_{n=1}^N x(t_n + \tau).$$

However, in the present case, the time delay between successive segments,  $t_n$ , is no longer a fixed period but is determined by the amplitude and/or slope of the signal attaining specified values. The most popular choice in defining a trigger level for acquiring successive samples is to simply specify an amplitude threshold,  $x_s$  (such as the rms value of the signal), at which time each segment is initiated, giving

$$t_n = t \text{ when } x(t) = x_s.$$

Figure 2 illustrates the evolution of a random decrement signature from a complex response measurement. An advantage of the randomdec method is that system characteristics need not be known a priori. As structural flaws or cracks develop in a component, the altered structural characteristics will modify the randomdec signature, providing an indication of possible incipient failure.

Characterization by Moments. If our measurement,  $x(t)$ , be assumed a representative sample function drawn from a stationary process, statistical moments can be estimated in terms of time averages:

$$m_n = (1/T) \int_0^T [x(t) - m_1]^n dt$$

$$m_1 = (1/T) \int_0^T x(t) dt.$$

The first two moments are the familiar mean and variance, respectively. Note that if the signal is symmetric about the mean, all odd order moments are zero.

Of special interest is the normalized fourth moment, or kurtosis coefficient:

$$K = m_4/m_2^2.$$

Similar to the peak/rms ratio, the kurtosis provides an indication of the spread of the distribution, i.e. the proportion of extreme values with respect to the rms level. For example,

K = 1, square wave  
K = 1.5, sine wave  
K = 3, random signal with Gaussian amplitude distribution

Bearing faults or seal rubs often cause intermittent contact over a fraction of a revolution of the machine. The onset of such behavior therefore imparts an impulsive nature to a measurable signal, which may be detected as an increase in the kurtosis coefficient. Since the kurtosis coefficient is normalized by the signal variance, this parameter should be relatively insensitive to machinery loading conditions.

Adaptive Noise Cancellation. Measurements obtained on the SSME turbopump housing during engine operation are corrupted with a high level of undesired noise from a multitude of sources. The concept of adaptive noise cancellation is a means by which signals corrupted by additive noise or interference can be estimated. An adaptive filter is a recursive numerical algorithm which, for stationary stochastic inputs, closely approximates the performance of a fixed Wiener estimation filter. The method uses a "primary" input containing both the desired signal and noise along with a "reference" signal correlated in some unknown way with the primary input noise. The reference input is weighted based on its past values and subtracted from the primary input to yield an estimate of the desired signal. The general concept of adaptive noise cancellation is discussed in detail in reference 7, and use of the process as applied to machine monitoring is presented in reference 8. Reference 8 also describes the application of

statistical moment and cepstrum analysis techniques to turbine bearing fault detection subsequent to adaptive filtering. Application of the adaptive filtering technique to SSME turbopump measurements is illustrated in the next section.

Envelope Detection. Bearing element and transmission gear mesh frequencies have been observed as an amplitude modulation superimposed on a measured complex vibration time history. Envelope detection has therefore been applied to the identification of related defects. The general approach is to detect the envelope of the measured signal followed by spectrum analysis to extract predominant frequency contributions in the envelope time history. These frequencies have been associated with flaws, which may not be detectable in the spectrum of the original wideband signal. In 1958, Dugundji introduced the concept of a pre-envelope function defined as

$$z(t) = x(t) + i \hat{x}(t)$$

where  $x(t)$  is the original time signal, and  $\hat{x}(t)$  is Hilbert transform of  $x(t)$ .

The pre-envelope is a (mathematically) complex time signal, the modulus of which is the signal envelope.

$$|z(t)| = \left\{ x^2(t) + \hat{x}^2(t) \right\}^{\frac{1}{2}}.$$

The availability of microprocessors and the fast Fourier transform (FFT) algorithm has made it possible to implement envelope detection software on Fourier-based analyzers due to the duality between Fourier/Hilbert transforms. Thus, the pre-envelope function may be extracted by Fourier transforming the original vibration signal, discarding all negative frequencies, doubling the positive frequency values, and taking the inverse transform of this one-sided spectrum. The modulus of the resulting complex valued time history yields the desired signal envelope. An obvious computational advantage of the above approach is that the envelope function can be directly

extracted using a standard FFT analyzer and calculator. Subsequent spectrum analysis of the envelope time history is then a simple additional step in the computation. It might be noted that the resulting envelope signal may also be analyzed by the above time averaging techniques to investigate signal characteristic/fault correlations.

### Frequency Decomposition

Turbomachinery components exhibit distinct characteristic frequencies associated with machine operation such as shaft speed, impeller blade passage, bearing element rotation, etc. Spectral representation of measurements, either by band-pass filtering or frequency transformation, is therefore the most popular approach in practice for machine condition trending and fault identification.

Power Spectral Density (PSD). If a measurement time history is viewed as a representative sample function from a stationary random process, the mean-square density spectrum (or PSD) describes the frequency distribution of the process mean-square. The PSD may be estimated in several ways but is now most commonly extracted by applying the discrete Fourier transform on a digital spectrum analyzer and defined by

$$S_x(f) = (1/T) \langle x^*(f) x(f) \rangle$$

where  $S_x(f)$  is the PSD at frequency  $f$ ,  $x(f)$  is the discrete<sup>x</sup> Fourier transform of a segment of the time history of length  $T$ , and the asterisk denotes the conjugate complex; the brackets indicate an ensemble average. Due in part to the availability and efficiency of digital analyzers, the PSD and cross PSD have become the standard format for complex signal description and system parameter identification. Another reason for its popularity is the straightforward interpretation of linear excitation/response relations and system characteristics in the frequency domain.

Bispectrum Analysis. As the PSD is the spectrum of the process second moment, the bispectrum represents the (two-dimensional) spectrum of the third joint moment and can be estimated by

$$B(f_1, f_2) = 1/T \langle x(f_1)x(f_2)x^*(f_3) \rangle, f_1 + f_2 = f_3.$$

The PSD and bispectrum may be seen to be the first two of a hierarchy of higher order statistical descriptions as the mean and variance are to higher order moments. Higher order spectra have been applied for some time to define joint correlations in statistical data<sup>9</sup> and more recently to dynamic system parameter identification.<sup>10,11</sup> As a diagnostic tool, the normalized bispectrum may be applied to detect the onset of nonlinear system behavior and possible associated component degradation. The bispectrum analysis technique can be implemented on contemporary FFT analyzers since only one-dimensional transforms are required. Symmetry of the function permits evaluation over only a portion of the two-dimensional frequency plane.

Cepstrum Analysis. The power cepstrum<sup>12</sup> was first defined as the power spectrum of the logarithm<sup>13</sup> of the ordinary PSD and may be written as

$$C_x(\tau) = \left| \mathcal{F} \left\{ \log S_x(f) \right\} \right|^2$$

where  $\mathcal{F}$  denotes the Fourier transform and the variable  $\tau$  in the cepstrum is called the quefrequency. Alternative expressions for the power cepstrum include the absolute value of the above, without squaring, and the indicated transform, which is real, as opposed to its squared modulus. In any event, the power cepstrum serves to indicate periodicities in the PSD. Thus, an increase in the harmonic content or uniform sidebands in the signal will be indicated by peaks in the power cepstrum. The quefrequency at which a given peak occurs defines the period (or frequency difference) between a series of harmonic components. It may be noted that the power cepstrum is, in truth, a time domain characterization of the measured signal since the quefrequency has units of time. The cepstrum technique has been applied successfully to remove echoes (periodic

reflections) in acoustic and sonar applications as well as to enhance the harmonic content in bearing element vibration spectra.

### Implementation and Simulation

Five of the above techniques have been implemented on a computer and applied to the extraction of known signals from noise and to SSME turbopump vibration measurements. Software development and results are documented in references 1 and 2. We here illustrate several results indicative of technique performance.

The TDA method was implemented on a Hewlett Packard 5451-C computer system and applied to the extraction of a sinusoid with additive noise. The results of this exercise are illustrated in figure 3. The spectrum of the sinusoid is shown in figure 3(a). The spectrum of the same sine plus noise is shown in figure 3(b). Improvement in the discrimination of the spectral component is illustrated in figure 3(c), representing 50 TDAs and figure 3(d), after 150 TDAs. As noted previously, the TDA method requires a priori knowledge of periodicities sought. However, based on ordered sampling corresponding to tachometer or synchronous speed measurements, improved resolution of significant spectral components by this method has been obtained.

Performance of the randomdec method on a sine wave plus noise process is illustrated in figure 4. The input signal is shown in the top illustration. The associated randomdec signature is shown in the center. Increased periodicity in this signature is evident though the signature is still quite complex. As a matter of interest, a second randomdec was extracted using the first as input and is shown in the lower time history. The imbedded sine wave is here seen to be well identified. As noted in the above discussion, the randomdec algorithm has the advantage of not requiring prior knowledge of periodicities in the signal. The establishment of optimum threshold

conditions for signature extraction requires further investigation.

The adaptive filter concept was implemented using an available hard-wired digital filter (DAC 1025I). A schematic of the data analysis setup is shown in figure 5. Typical pre- and post-filtered PSDs from a high pressure oxidizer turbopump measurement are shown in figure 6. The first spectrum represents the ordinary PSD of the signal obtained with a 12.5-Hz resolution. The second illustrates the same spectral decomposition obtained after processing of the signal with the adaptive filter. A marked improvement in resolution of turbopump periodic components is clear. Identification of synchronous and blade passage harmonics has been enhanced significantly. Work remains in the engineering interpretation of spectral values obtained from adaptive filtered measurements.

As a final illustration, figure 7 shows some results from a bearing life investigation where the statistical moment technique was applied.<sup>14</sup> This figure illustrates the time history of rms acceleration and kurtosis coefficient measured on the bearing housing of a roller bearing during endurance test on a Timken test machine. Note the distinct increase in kurtosis coefficient at approximately 457 hours, which is not reflected in the acceleration time history. Inspection at this time revealed a small fatigue crack on the inner race though the test continued for 657 hours, at which time extensive bearing damage was observed.

The above results are quite promising. Implementation of moment spectra, envelope spectra, and bispectral methods is presently in progress. Generation of a data base of adaptive filtered spectra for SSME hot firing measurements is also being performed. Recent additional SSME measurements obtained internal to the turbopump casing will be most useful to detection technique evaluation. Upon completion of this evaluation, the most promising techniques will be

optimized computationally and integrated into the MSFC diagnostic data evaluation system.

#### Acknowledgments

Software development and computer simulation in the course of this study was performed by Messrs. T. Gardner and G. Anderson, II. This work is being performed under contract with NASA/MSFC. Mr. J. Jones, MSFC/ED24, has provided continuing technical advice and encouragement throughout the investigation.

#### References

1. Gardner, Tony G. Incipient SSME Bearing Failure Detection--Data Enhancement Techniques. Wyle Laboratories Rept. TM 81-6, May 1981, 79 pp.
2. Anderson, Granville R. Data Enhancement Techniques for Incipient Failure Detection. Wyle Laboratories Rept. TM 83-1, Feb. 1983.
3. Braun, S. The extraction of periodic waveform by time domain averaging. Acoustica, v. 32, No. 2, 1975, pp.69-77.
4. \_\_\_\_\_. Signature analysis methods and applications for rotating machines. ASME paper 77WA/AUT5, American Society of Mechanical Engineers, 1977.
5. Cole, H. A., Jr. On-line failure detection and damping measurement of aerospace structures by random decrement signatures. NASA CR 2205, Mar. 1973.
6. Ibrahim, S. R. Random decrement technique for modal identification of structures. J. Spacecraft, v. 14, No. 11, 1977, pp. 696-700.
7. Widrow, B., et al. Adaptive noise cancelling: Principles and applications. IEEE Proc., v. 63, No. 12, Dec. 1975.

8. Chaturvedi, C. K., and D. W. Thomas. Adaptive noise cancelling and condition monitoring. J. Sound Vib., v. 76, No. 3, 1981, pp. 391-405.
9. Brillinger, D. R. An Introduction to Polyspectra. Annals of Mathematical Statistics, 36, 1964, pp. 1351-1374.
10. Kim, Y. C., and E. J. Powers. Digital bispectral analysis and its applications to nonlinear wave interactions. IEEE Trans. Plasma Sci., PS-7, 1979, pp. 120-131.
11. Bendat, J. S., and A. G. Piersol. Spectral analysis of nonlinear systems involving square-law operations. J. Sound Vib., 18(2), 1982, pp. 199-213.
12. Bogert, B. P., M. J. R. Healy and J. W. Tukey. The quefrency analysis of time series for echoes: Cepstrum, pseudo-autocovariance, cross-cepstrum and Sape cracking. Proc. Symp. Time Series Anal. (M. Rosenblatt, ed.), 1963, pp. 209-243.
13. Randall, R. B. Application of B&K Equipment to Frequency Analysis, Bruel and Kjaer, Naerum, Denmark, 1977.
14. Dyer, D., and R. M. Stewart. Detection of rolling element bearing damage by statistical vibration analysis. J. Mech. Design, v. 100, Apr. 1978, pp. 229-233.

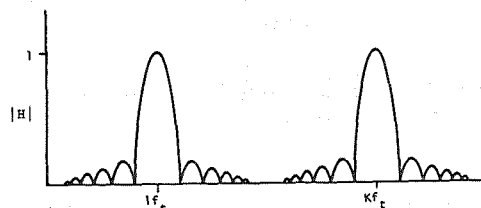


Figure 1. Time domain average comb filter

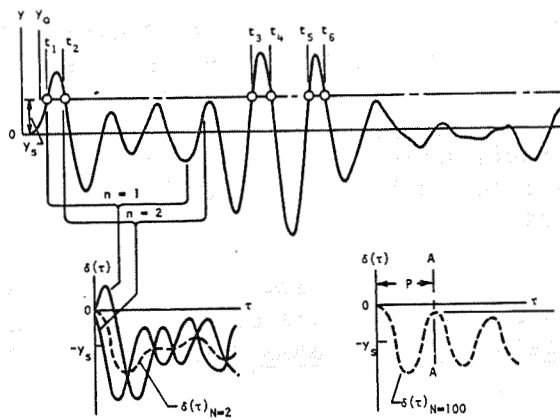


Figure 2. Evolution of a random decrement signature<sup>5</sup>

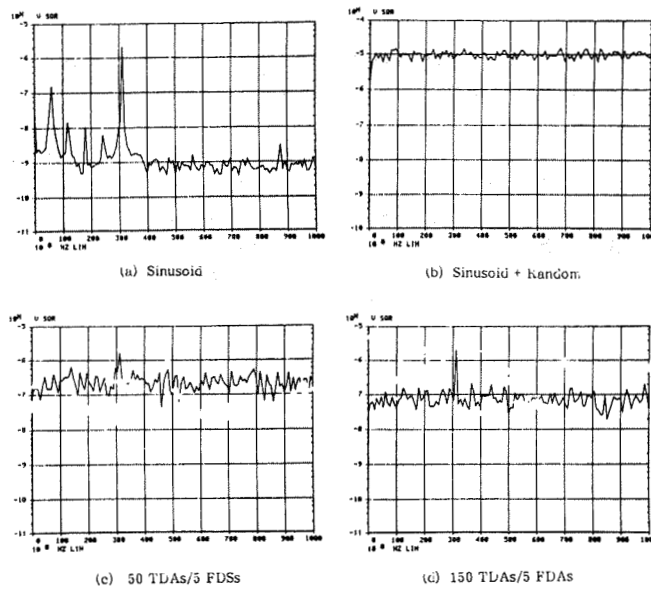


Figure 3. Spectrum of time domain averaged signal of sinusoid with additive random noise

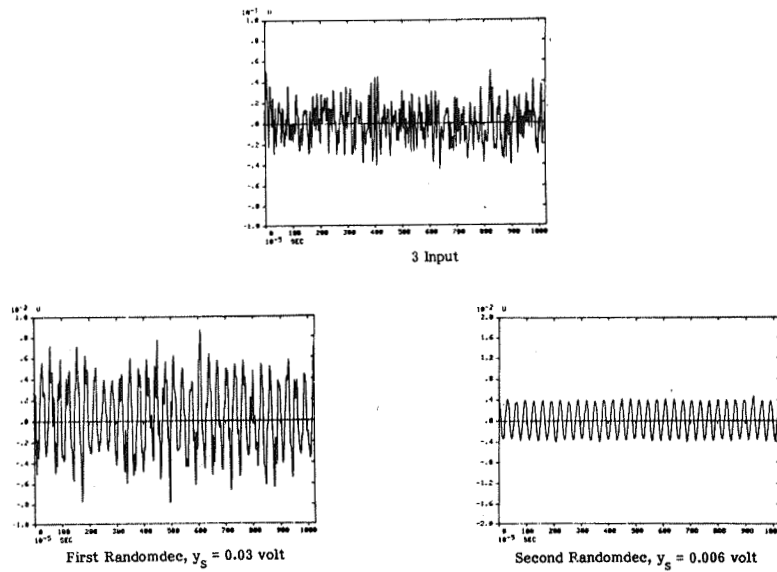


Figure 4. Random decrement signature of sinusoid plus noise

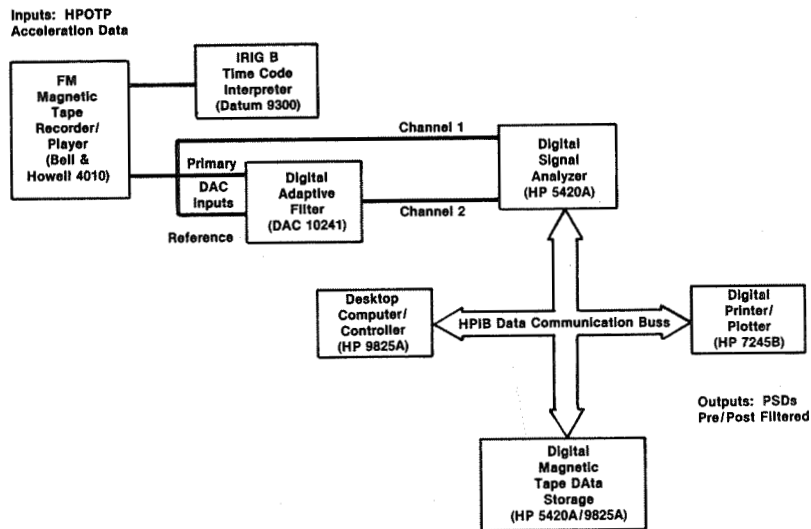
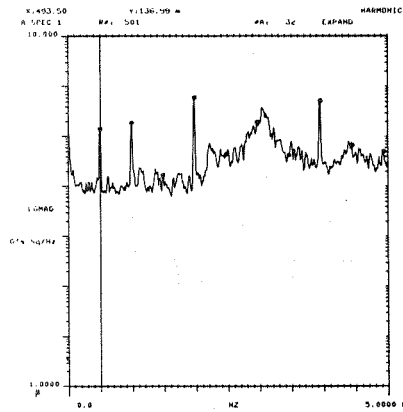


Figure 5. Data reduction flowchart for implementing adaptive noise cancellation

SSME TEST 001-301 HPOT RAD 140 ACCEL. 100% PHL  
 TYPE OF ANALYSIS: PSD DATA TAPE: 06 CH. NO. 19  
 DATA SLICE TIME INTERVAL: 13:11:05-13:11:35  
 BANDWIDTH: 12.5 Hz  
 COMPOSITE: 1.707e 01 0's rms



SSME TEST 001-301 HPOT RAD 140 ACCEL. 100% PHL  
 TYPE OF ANALYSIS: TFE-PSD DATA TAPE: 06 CH. NO. 19  
 DATA SLICE TIME INTERVAL: 13:11:05-13:11:35  
 BANDWIDTH: 12.5 Hz  
 COMPOSITE: 3.520e 00 0's rms

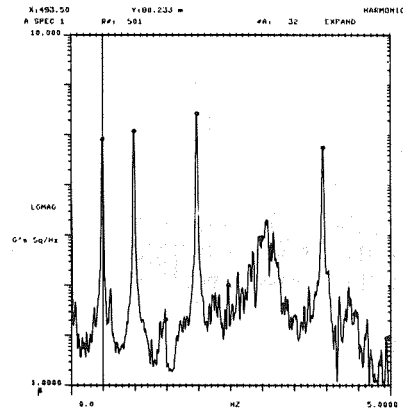


Figure 6. Spectrum of SSME turbopump measurement before and after adaptive filtering

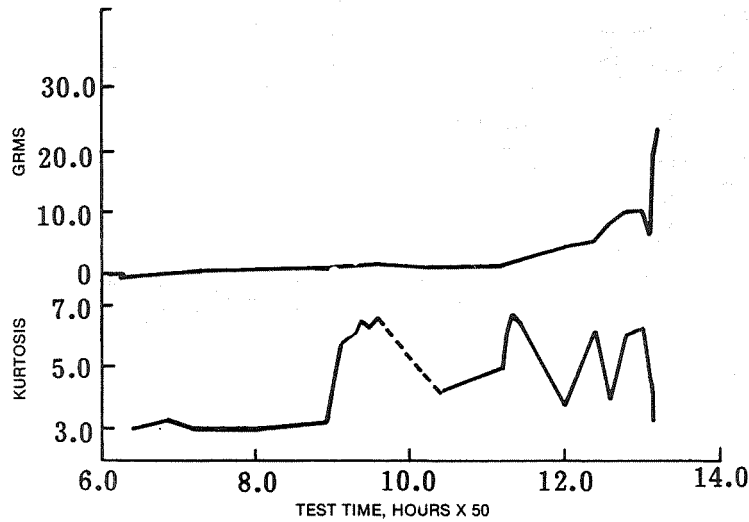


Figure 7. Variation of acceleration and kurtosis coefficient with test time<sup>14</sup>

FLOW DYNAMIC ENVIRONMENT  
DATA BASE DEVELOPMENT FOR THE SSME

C. V. Sundaram  
Wyle Laboratories, Huntsville

Abstract

This paper describes the studies being carried out on the fluid flow-induced vibration of the Space Shuttle main engine (SSME) components. This study is being carried out with a view to correlating the frequency characteristics of the pressure fluctuations in a rocket engine to its operating conditions and geometry. An overview of the data base development for SSME test firing results and the interactive computer software used to access, retrieve, and plot or print the results selectively for given thrust levels, engine numbers, etc., is presented. The various statistical methods available in the computer code for data analysis are discussed. Plots of test data, nondimensionalized using parameters such as fluid flow velocities, densities, and pressures, are presented. Comparative studies of these results with results available in the literature are made. Correlations between the resonant peaks observed at higher frequencies in power spectral density plots with pump geometry and operating conditions are discussed. Finally, an overview of the status of the investigation is presented and future directions are discussed.

Introduction

The development efforts expended on the main engine of the Space Shuttle has resulted in the evolution of highly complex machinery which is capable of generating high thrust levels. Even from the earliest days of spacecraft engine development, achieving the highest possible specific thrust, based on engine weight or overall size, has been identified as one of the prime goals. The earlier spacecraft, however, were equipped with power sources which were designed for just one mission. The advent of the concept of reusable space vehicles added a new dimension to the

engine design, that they not only satisfy the requirements on thrust but also that they be capable of carrying out multimissions into outer space with, ideally, the least amount of maintenance and component replacements between missions. This has imposed a greater emphasis on preventing failures and prolonging the fatigue life expectancy of the SSME during operation. Furthermore, specific knowledge relating to the frequency characteristics of the pressure fluctuations in rocket engine systems is not well understood. It is important to understand the functional relationships between pressure fluctuations in these systems in terms of the geometrical and performance characteristics because of their effect on hardware lifetime.

The SSME has been subjected to extensive hot firing and flow tests. During these tests, system failures and malfunctions have occurred from time to time. These failures range from wear on component bearings and flow-induced failures to explosions due to intense pressure fluctuations and accompanying dynamic stresses in the pumps, valves, and/or propellant lines. The large volume of data on pressure fluctuations, strain, and acceleration obtained from these tests provide a good basis for studies on the flow-induced vibrations taking place in the SSME.

The sheer volume of test data available makes it absolutely essential that a computerized data base management system be employed to perform any meaningful analysis. Wyle Laboratories is engaged in the development of such a data base management software. This paper provides an overview of the work being performed on the software development and discusses the method of approach suggested for analyzing the data.

#### SSME Data Base Management

The SSME data base management and analysis system developed at Wyle Laboratories has been designed for use on an Interdata 8/32 computer system and other computer systems utilizing similar file name structures.

## Data Filing System

The data base management system is designed to accommodate two types of data: time histories and power spectral density or other frequency domain data. The time history (rms pressure or thrust) data files consist of a pair of values in each record, the first value being the number of seconds into the test and the second being the magnitude. The file may consist of any number of data points (records), but most of the routines presently have an upper limit of 500 points.

Each PSD file consists of a single real number in each record. These are the spectral magnitudes. Since the PSD test data is recorded using constant bandwidth filters, the frequencies corresponding to each PSD value is automatically calculated by the program when the frequency range is entered. A considerable saving in computer disc storage space has been realized by this method because of the large amount of PSD data involved.

Data entry into files can be performed through a digitizing tablet. When the volume of data is large, however, use of a digitizing tablet can be very time consuming. Hence the data in this case is directly read from a digital tape using the dedicated magnetic tape drive units. File names are automatically assigned by the software based on test numbers, engine numbers, channel descriptors, etc., to uniquely identify each data set. Figure 1 provides an insight into the operational sequences and capabilities of the SSME data base management and analysis software.

Figure 2 shows a plot of power versus time, and figure 3 shows the rms pressure variations with time for the low pressure fuel pump. These plots were generated using the data retrieval system described above. Figure 4 shows a PSD plot generated from the digitized data for the high pressure oxidizer pump. The input to the computer to generate these plots are the file names for the time history plots and the test

number, time slice, and maximum frequency for the PSD plots.

Statistical parameters, such as mean, standard deviation, rms values, third and fourth central moments, and minimum and maximum values and range, can be calculated and plotted with ease for any number of data sets selected based on engine, HPFP, and HPOP numbers; thrust level; and channel descriptors. The abscissa and the ordinate can have any combination of linear and logarithmic scales, and any statistical parameter can be plotted against any other or a frequency scale. The uniqueness of the set of PSDs selected for statistical analysis can be controlled by specifying or leaving out, in any combination, the engine, HPOP, and HPFP numbers.

A detailed description of all the capabilities of the data base management and analysis software is presented in reference 1.

### General Character of Turbomachinery Noise

#### Background

The jet noise theory gained importance with increasing use of jet engines in aircraft. It is well known that the acoustic power generated by a jet exhaust is strongly dependent on the exit velocity (Lighthill's 8th power law<sup>2</sup>). However, during approach configuration of the aircraft, when the jet noise level is generally low, the engine compressor noise was observed to be a major noise source. The study of compressor noise, especially the multistage axial flow types, has acquired great importance during the last 25 years.

#### Noise Sources in Axial Flow Compressors

In general, the noise spectra of different types of compressors exhibit similar gross characteristics. In this paper, we limit our attention to axial flow compressors because it is believed that their noise characteristics should be more relevant to the noise

generation mechanism of the axial flow pumps on the SSME.

The general form of an acoustic spectrum of an axial flow compressor would indicate broadband noise extending over a wide range of frequencies. Superimposed on this are a number of discrete peaks which represent the blade passage frequencies and their harmonics.

The broadband noise component has been attributed to various mechanisms. At least three that merit consideration are

1. The random force fluctuations due to a moving flow on the surface. These fluctuations can be interpreted to act as acoustic sources located within the turbulent boundary layer.
2. The shedding of vortices from the trailing edges of a body immersed in a moving fluid. This vortex shedding imparts to the body fluctuating lift forces that are periodic at low Reynolds number flows and become random as the Reynolds number increases. (It is believed that the periodic component of the shedding does not disappear completely.) This random excitation force of vortex shedding is also considered to be instrumental in the broadband characteristic of the acoustic spectrum.
3. A turbulent flow at the inlet to the compressor sets up fluctuating forces due to flow incidence on the surface. The perturbation velocity component in a turbulent flow is random in nature, and hence the acoustic energy due to the fluctuating forces can be expected to have a broadband nature.

Another significant broadband component in the case of the SSME would be the structurally transmitted secondary vibrations due to the close proximity of the components, all having highly turbulent flow taking place within them. A challenging task in the analysis of SSME component vibration is the development of a prediction scheme that will provide quantitative

estimates of the acoustic energy due to flow-induced and structurally transmitted vibrations in a frequency spectrum at various locations on the SSME.

The pure tones, which are a result of the spinning modes of the pressure field, exhibit decaying trends downstream of the rotor when the impeller tip Mach number is below critical, as in the case of a subsonic rotor. For a rotor-stator combination, however, a number of spinning modes are generated, many of which spin at Mach numbers above the critical tip Mach numbers, and these modes exhibit strong propagation characteristics.

#### SSME Flow-Induced Vibration Characteristics

In this section, preliminary studies conducted on pressure spectra obtained from SSME firing tests are discussed. Fluid flow variables, which may be of lesser importance in conventional axial flow compressors, but which may be of greater significance in the SSME flow environment, are highlighted.

The initial efforts in the data analysis have been directed toward obtaining nondimensional PSD as a function of Strouhal number. The power spectral densities, which have dimensions of mean square pressure per hertz, were normalized as follows:

$$S_p = Q_p(f) / \rho_f^2 V^3 D \quad (1)$$

where  $S_p$  is nondimensional PSD,  $Q_p(f)$  is the measured PSD,  $\rho_f$  is the local fluid density,  $V$  is the mean velocity, and  $D$  is a characteristic length. Strouhal number is defined as

$$S_t = fD/V \quad (2)$$

where  $f$  is the frequency.

Figures 5 and 6 show nondimensionalized PSD plotted as a function of Strouhal number for the high pressure oxidizer pump discharge pressure. Similar analyses have been carried out to estimate the

pressure fluctuations due to turbulent flow of water at the wall of a duct. Figure 7, reproduced from reference 5, shows the pressure fluctuation dependence on Strouhal number. Figures 5, 6, and 7 indicate similar trends in the variation of nondimensionalized PSD for increasing Strouhal number. The scaling applied to the SSME data is based on the assumption that the pressure fluctuations are flow induced. This assumption is somewhat oversimplified as it does not address the various other noise-generating mechanisms present during turbomachinery operation.

Dimensional analysis studies of blower noise<sup>6</sup> provide a functional relationship,

$$E = F(D, N, Q, f, \rho, \mu, C) \quad (3)$$

where E is the acoustic power/hertz; D, the blower diameter; N, the rpm; Q, the flow rate; f, the frequency;  $\rho$ , the fluid density;  $\mu$ , the viscosity; and C, the acoustic speed. A similar analysis on the SSME turbopump would require accounting for the acoustic propagation characteristic of the structure.

Another important factor that should be considered is the fluid properties. The fluid flow conditions in the SSME undergo extreme variations in temperature and pressure. The mechanism of propagation of disturbances in fluids at extremely low temperatures and very high pressures requires further studies for proper mathematical modeling. Since the fluid flow conditions experience wide variations in the SSME, it is reasonable to expect variations in local propagation velocities and hence local Mach numbers.

The studies on the flow dynamic environment of the SSME being carried out at Wyle Laboratories are directed toward applying the existing theories on noise generation mechanism in turbomachinery after modifications to reflect the flow environment present in the SSME. An approach that would involve developing an empirical formulation rather than a very rigorous and purely analytical solutions seems to indicate

promise. The basic idea involves modeling the noise generation mechanism due to turbulent flow and the pressure pulses generated by the spinning modes of the pressure field due to rotor-stator interactions separately and combining the two components to obtain the total frequency spectrum. That an empirical approach, though somewhat complicated, is not totally impossible has been amply demonstrated through similar studies performed by Van Niekerk and others.

#### Acknowledgements

The author wishes to acknowledge the help provided by Mr. T. Coffin in directing the research efforts, Dr. G. T. Meares, the chief architect of the data base software development. This project was sponsored by the NASA, Marshall Space Flight Center under contract No. NAS8-34343.

#### References

1. Meares, G., T. Coffin, and J. Reinhardt. Flow Dynamic Environments in High Performance Rocket Engines." Wyle Laboratories Research Staff Technical Memorandum TM 84-01, Jan. 1984.
2. Lighthill, M. J. On Sound Generated Aerodynamically, II, Turbulence as a Source of Sound. Proc. Roy. Soc., A222, 1954, pp. 1-32.
3. Sharland, I. J. Sources of Noise in Axial Flow Fans. J. Sound Vib., V. 1, No. 3, July 1964.
4. Tyler, J. M., and T. G. Sofrin. Axial Flow Compressor Noise Studies. Soc. Auto. Engr., Aeronautical meeting, preprint 345D, 1961.
5. Clinch, J. M. Prediction and Measurement of the Vibrations Induced in Thin-Walled Pipes by the Passage of Internal Turbulent Water Flow. J. Sound Vib., V. 12, No. 4, 1970, pp. 429-451.

6. Maling, G. C. Jr. Dimensional Analysis of Blower Noise. J. Acoust. Soc. Am., V. 35, No. 10, Oct. 1963, pp. 1556-1564.

7. Van Niekerk, C. G. Noise Generation in Axial Flow Fans. J. Sound Vib., V. 3, No. 1, Jan. 1966.

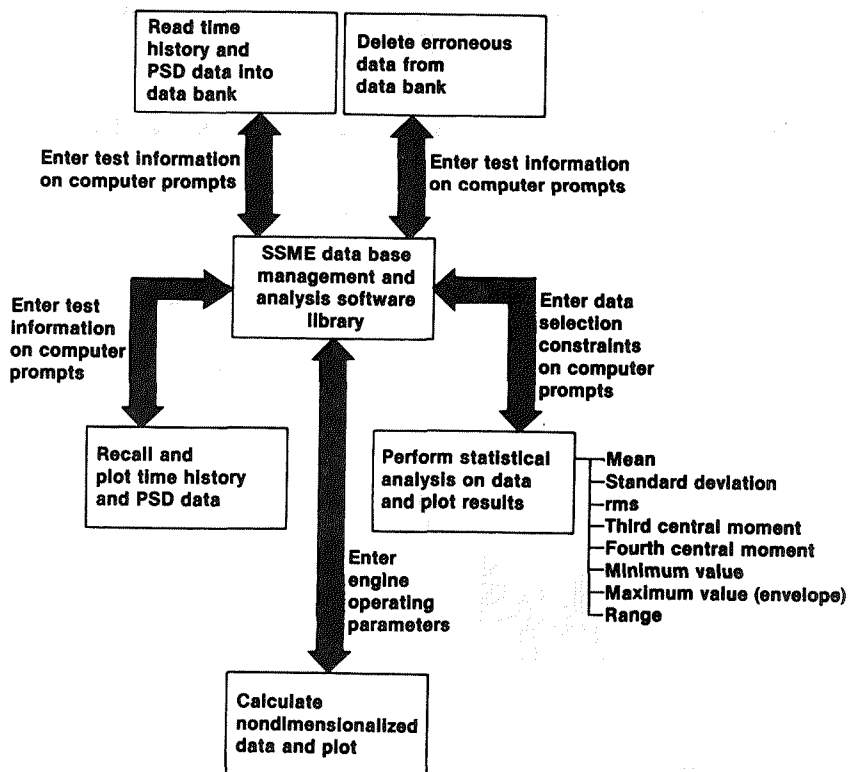


Figure 1. SSME data base management and analysis software operational sequence and capabilities

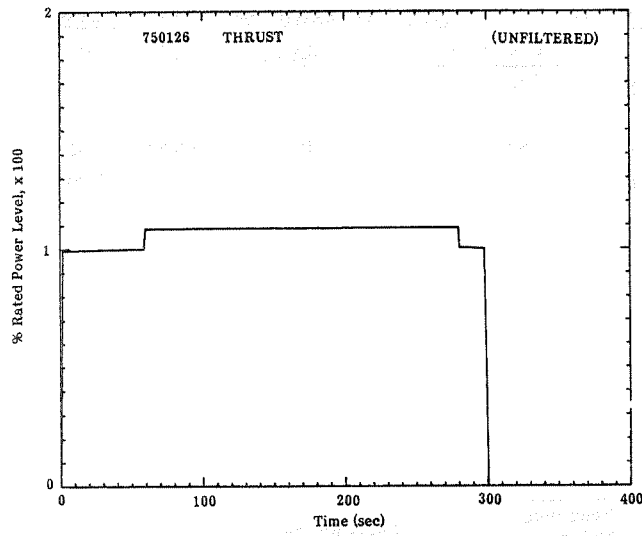


Figure 2. SSME power level variations as a function of time

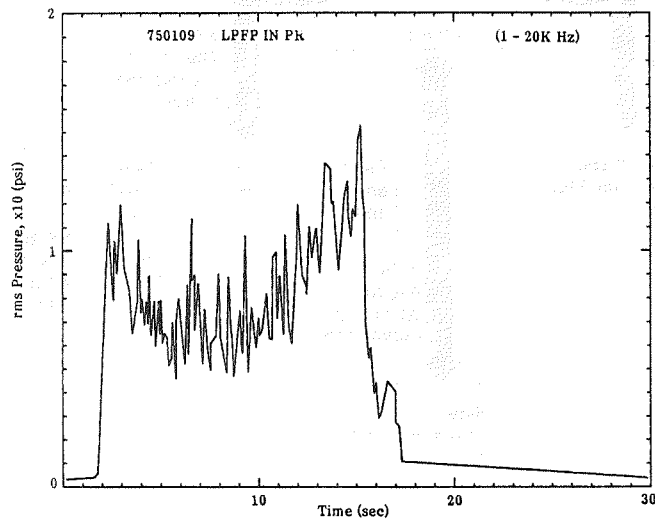


Figure 3. rms pressure time history at the inlet of the low pressure fuel pump

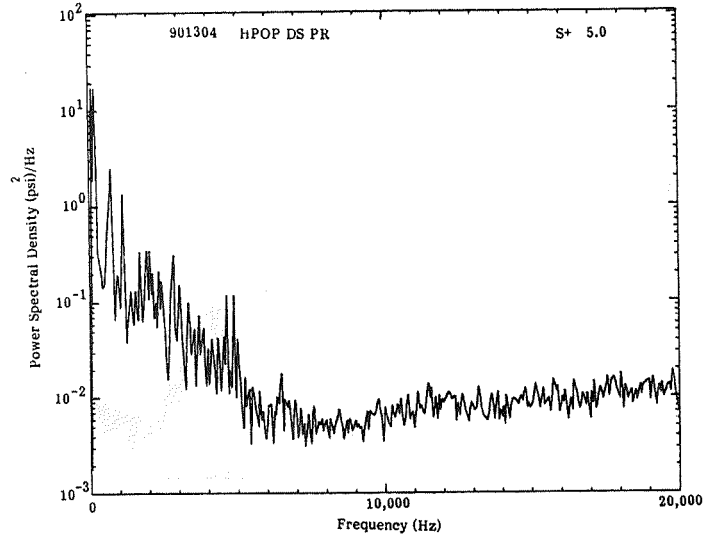


Figure 4. Power spectral density of the high pressure oxidizer pump discharge pressure 5 seconds after SSME startup

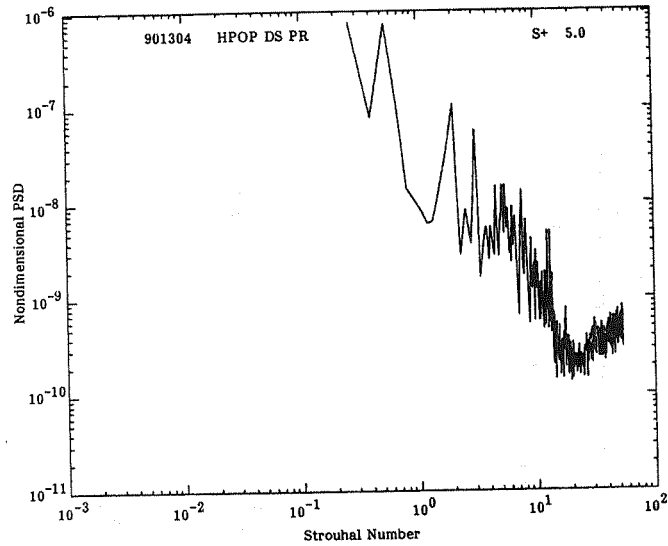


Figure 5. Nondimensionalized frequency spectrum for high pressure oxidizer pump discharge pressure, 5 seconds after SSME startup

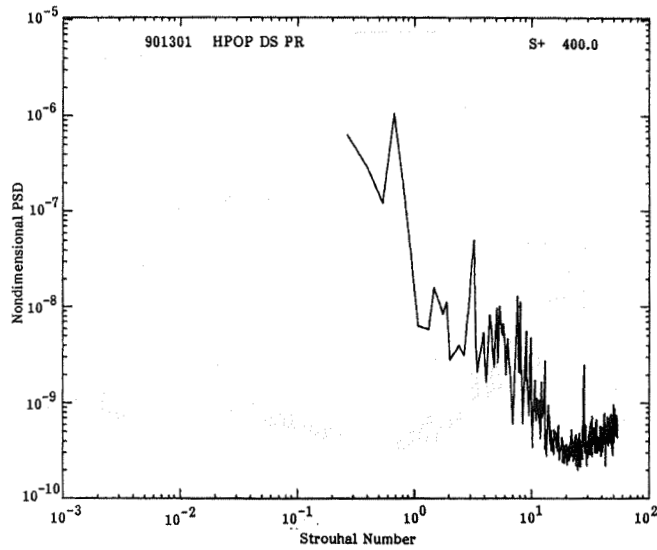


Figure 6. Nondimensionalized frequency spectrum for high pressure oxidizer pump discharge pressure 400 seconds after SSME startup

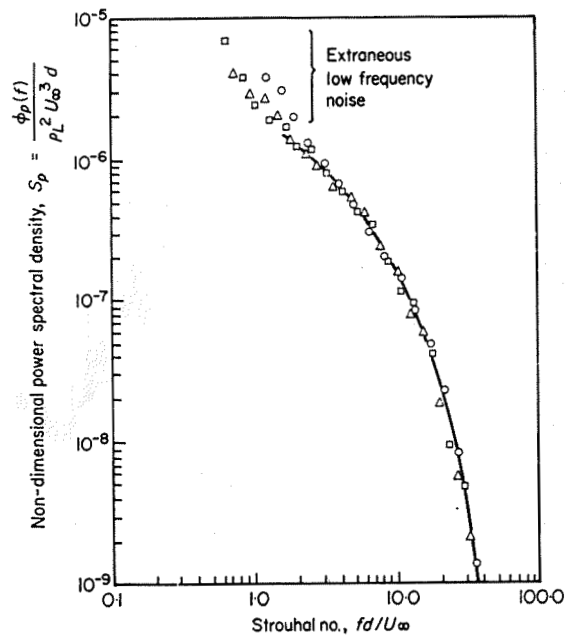


Figure 7. Frequency spectrum of turbulent wall pressure field. (O), 267 in/sec; ( $\Delta$ ) 450 in/sec; ( $\square$ ) 520 in/sec

## TURBINE BLADE FRICTION DAMPING STUDY

Robert J. Dominic  
University of Dayton Research Institute  
Dayton, Ohio 45469

### Abstract

An analytical and test evaluation were conducted to determine the performance of turbine blade platform friction dampers used to control the lower order flexural modes of a blade. The configuration used in the study was the first stage turbine of the high pressure fuel turbopump (HPFTP) of the space shuttle main engine (SSME). The analytical study used the lumped parameter method developed by Jones and Muszynska<sup>1</sup> as implemented on a VAX 11/780 computer. It showed that the primary parameters affecting the friction damper performance are: the damper-blade coefficient of friction; the normal force applied to the friction interface; the amplitude of the periodic forcing function; the relative phase angle of the forcing functions for adjacent blades bridged by a damper (effectively, the engine order of the forcing function); and the amount of hysteretic damping that acts to limit the vibration amplitude of the blade in its resonance modes. In addition, the analytical study showed that overdamping of the blade, resulting in fixity at the platform and a consequent lightly-damped flexural resonance mode of the blade airfoil section alone, is likely to occur in a high-speed turbine such as the HPFTP because of the high normal force applied to the friction interface by the centrifugal force acting on the damper. A test study was performed in a high speed spin pit to evaluate the low order flexural resonance vibration modes of HPFTP blades without dampers, with production dampers, and with two types of lightweight experimental dampers. The test program results agreed with the results of the analytical study in that blades fitted with production friction dampers experienced the airfoil-alone flexural resonance mode, while those without dampers or with lighter weight dampers did not. Likewise, no blades

fitted with dampers experienced the whole blade flexural resonance mode during high speed tests, while those without dampers did.

#### Background

Three catastrophic failures of HPFTP first stage turbine blades occurred during test stand runs early in the SSME development program. These failures were attributed to lockup of the platforms of adjacent blades, in one case due to welding of the underplatform friction dampers to the platforms because of overtemperature conditions during the run, in another case due to extrusion of a nickelplate antifriction coating on the dampers into the interplatform gap, and in a third case due to an out of tolerance build that reduced or eliminated the interplatform gap for some blades in the stage. The mechanism of the failures was determined to be high cycle fatigue caused by excessive vibration of the blades. Failures occurred near the base of the airfoil section of the blades, just above the platform. Figure 1 shows two of the subject blades and the friction dampers that are placed in slots below the platforms and act on the bottom surface of the platforms to reduce the flexural vibrations of the blades through the absorption of energy by friction heating.

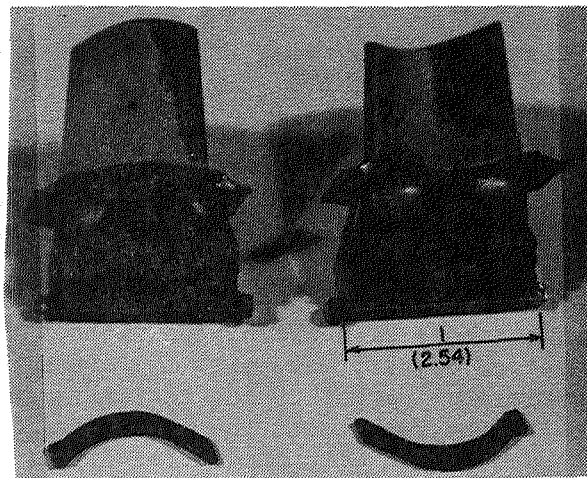


FIG. 1 HPFTP 1st STAGE BLADES AND DAMPERS

During pump operation the dampers also act to limit the leakage of cooling hydrogen, which is routed over the blade roots, into the turbine drive fluid stream. The dampers are forced against the under surface of the platforms by a combination of centrifugal force and the differential pressure between the cooling hydrogen and the turbine drive fluid.

The 63 blade turbine wheel is fed by 41 first stage nozzles. Thirteen shaft front bearing support struts are aligned with 13 of the nozzles in a necessarily unsymmetrical arrangement with 11 struts aligned three nozzles apart and two struts aligned four nozzles apart. Pressure pulses caused by the wakes off the nozzles, and particularly the higher amplitude pulses for the nozzles aligned with struts, excite vibrations in the blades that cause the high cycle fatigue problems. The repetition frequencies for these pulses are  $10\frac{1}{4}$  per rev for struts spaced four nozzles apart,  $13\frac{2}{3}$  per rev for struts spaced three nozzles apart, and 41 per rev for the symmetrically spaced nozzles. Sum and difference frequencies of these excitation components and their harmonics occur also to provide wide band excitation of the blades. The  $13\frac{2}{3}$  per rev (14E) excitation of the blades is shown later to be a critical excitation frequency in the operating regime of the blades.

The nature of the blade fatigue failures caused them to be attributed to flexural resonance modes of the blades. Modal studies of the blades showed that the first two bending modes of the blade occurred at approximately 4,500 and 18,000 Hz. Later, during a whirligig spin test program<sup>2</sup> conducted by Rocketdyne, a resonance condition near 8,500 Hz was found. This resonance condition was first described as the first torsional mode of the blade (which actually occurs at approximately 11,000 Hz), but it was later identified by the University of Dayton Research Institute (UDRI) as the first flexural mode of the airfoil section of the blade when the platforms are constrained from motion. The 14E excitation pulses occur at this airfoil-alone flexural resonance frequency of the

blades during the long (relatively) time periods of engine operation at RPL.

As a result of the early studies the strut contour was changed to reduce the energy in the excitation pulses and the platform friction damper weight was reduced to provide more optimum damping. However, fatigue cracking continued to occur near the airfoil root with the platform at much lower than the specified and predicted life for the blades. Subsequently, UDRI contracted with NASA to evaluate the operation of the blade-damper system analytically, using the lumped parameter analysis, and to evaluate the operation of a test system in a high speed spin pit.

#### Analytical Study Using the Lumped Parameter (Lumped Mass) Analysis

The lumped mass analysis used evaluates a blade only in its lower order flexural modes and only for the steady state solution. The blade is represented by two concentrated masses ( $m_1, m_2$ ) supported in series by two flexural springs ( $k_1, k_2$ ) with a hysteretic loss factor ( $\eta_1, \eta_2$ ) associated with each spring. The hysteretic loss factors represent the combination of root damping, aerodynamic damping, and material damping in the operating blade. The concentrated masses and flexural springs represent the modal parameters of the blade in the flexural plane. The modal parameters for the SSME HPFTP first stage blade can be determined from the resonance equations of the blade in three flexural resonance conditions, as shown in Figure 2. The resonance frequencies  $f_1, f_2, f_3$  have been measured in test programs as follows:  $f_1$  has been measured by Rocketdyne Division of Rockwell International (RDRI) in siren tests and by UDRI in impact tests;  $f_2$  has been measured by (RDRI) in siren tests;  $f_3$  was shown in the (RDRI) whirligig test data<sup>2</sup> on blades with welded platforms and on blades with friction dampers when the dampers greatly limited platform motion. These values are average values for several blades.

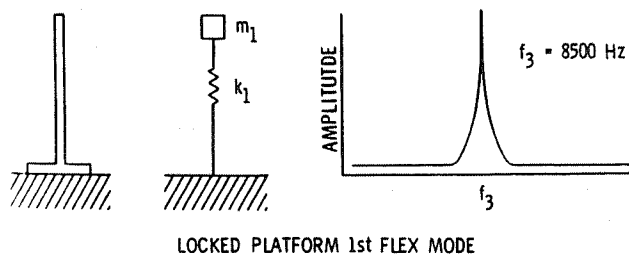
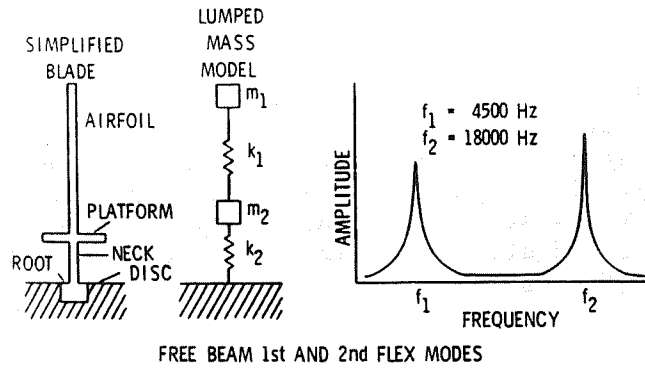


FIG. 2 HPFTP 1st STAGE BLADE FLEX MODES

Three resonance equations can be derived, two for the free blade and one for the platform locked blade, as below.

$$\frac{k_1 k_2}{m_1 m_2} = (4\pi^2 f_1 f_2)^2 \tag{1}$$

$$\frac{k_1 + k_2}{m_2} + \frac{k_1}{m_1} = 4\pi^2 (f_1^2 + f_2^2) \tag{2}$$

$$\frac{k_1}{m_1} = (2\pi f_3)^2 \tag{3}$$

These three equations can be simplified algebraically to state three of the unknown parameters in terms of the fourth. Then if one is assigned a value the other three parameters are defined. Any consistent set of units can be used. We assigned  $m_1 = 0.02$  pound, then

$m_2 = 0.0079757$  pound,  $k_1 = 5.705 \times 10^7$  pounds/inch, and  $k_2 = 2.859 \times 10^7$  pounds/inch.

If a series of these blades are installed in a rigid disk with platform friction dampers between the blades and with airfoil excitation forces imposed, the discrete bladed disk model shown in Figure 3 is evolved. This system is a modal analog of the HPFTP first stage bladed disk in the frequency range of 0 to perhaps 20,000 Hz.

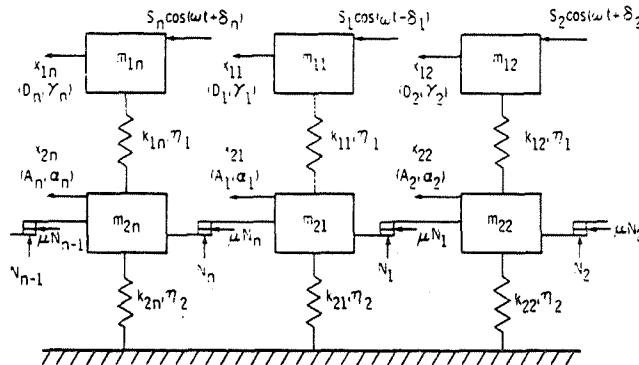


FIG. 3 LUMPED MASS MODEL OF BLADED DISK SYSTEM

The equations of motion for the  $v$ th blade in Figure 3 are:

$$m_{1v} \ddot{x}_{1v} + k_{1v} (x_{1v} - x_{2v}) + \frac{k_{1v} \eta_1}{\omega} (\dot{x}_{1v} - \dot{x}_{2v}) = S_v \cos(\omega t + \delta_v) \quad (4)$$

$$m_{2v} \ddot{x}_{2v} - k_{1v} x_{1v} + \frac{k_{1v} \eta_1}{\omega} (\dot{x}_{2v} - \dot{x}_{1v}) + \frac{k_{2v} \eta_2}{\omega} \dot{x}_{2v} + \mu N_v \text{sign}$$

$$(\dot{x}_{2v} - \dot{x}_{2,v+1}) + \mu N_{v-1} \text{sign}(\dot{x}_{2v} - \dot{x}_{2,v-1}) + (k_{1v} + k_{2v}) x_{2v} = 0 \quad (5)$$

for  $v = 1, 2, \dots, n$ , where  $n$  is the number of blades in the system. These are a set of nonlinear equations of the second order, the only nonlinear terms representing a Coulomb model of the friction forces on the platform. The previously undefined terms in these equations are the harmonic excitation force,  $S_v \cos(\omega t + \delta_v)$ , the

coefficient of friction,  $\mu$ , the normal force on the friction surface,  $N_v$ , and the deflections of the modal masses,  $X_1$  and  $X_2$ . The phase angle,  $\delta_v$ , represents the time lag of a traveling wave excitation around the disk system. This is representative of the spinning blade system passing through pressure disturbances caused by the nozzle vane and shaft front support strut wakes.

This system of equations is solved using the method of harmonic balance. A nonlinear matrix iteration is used to obtain a numerical solution.<sup>1</sup> The solution, obtained by computer, consists of the deflection amplitudes  $D_v$ ,  $A_v$ , and the phase angles  $\gamma_v$ ,  $\alpha_v$ , for the outboard (airfoil) and inboard (platform and neck) modal masses of each blade as a function of the system parameters  $m_{1v}$ ,  $m_{2v}$ ,  $k_{1v}$ ,  $k_{2v}$ ,  $N_v$ ,  $S_v$ ,  $\delta_v$ ,  $\mu$ ,  $\eta_1$ ,  $\eta_2$ , and  $\omega$ . Since most of the system parameters are input to the computer as arrays many types of mistuned systems can be evaluated. Only solutions for a tuned system have been evaluated to date, specifically, a tuned system with the HPFTP average blade.

The usual analysis is a series of computer runs with  $\eta_1$ ,  $\eta_2$ ,  $\mu$ , and  $S$  constant and  $N$  varying from 0 to a selected upper limit in steps for successive runs. In each run solutions are obtained from a lower starting frequency to an upper ending frequency at fixed increments of the frequency range. The range from 3,000 to 12,000 Hz has been evaluated in 100 Hz or 250 Hz increments in most runs because failures at the 8,500 Hz mode when platform lockup occurs are of major interest. A few runs from 3,000 to 20,000 Hz have been processed and show that the friction damping is as effective at the second flexural mode of the free blade (18,000 Hz) as it is at the first flexural mode (4,500 Hz).

Another controlling parameter of the friction damper performance is the blade to adjacent blade phasing. One would expect that when adjacent blades are in phase no damping by the interplatform friction dampers would occur. Conversely, maximum damping

would be expected when blades are out of phase. The interblade phase angle is controlled by  $\delta_v$ , the phase shift of the harmonic forcing function  $S \cos(\omega t + \delta_v)$ , and is input to each run as an array. The value of  $\delta_v$ , the phase angle of the  $v$ th blade for a phase tuned system is defined as:

$$\delta_v = \frac{2\pi E(v-1)}{n} \quad (6)$$

where  $E$  is the engine order of the vibration mode and  $n$  is the total number of blades in the disk. The blade to blade phase shift is designated  $\theta$ , defined as:

$$\theta = \frac{2\pi E}{n} = \delta_v - \delta_{(v-1)} \quad (7)$$

A sample of program output data for the outboard modal mass deflection is presented in Figure 4 as a plot of amplitude  $D$  versus frequency and a similar set of data for the inboard modal mass deflection (amplitude  $A$ ) is presented in Figure 5 for the same computer runs. These data sets arise from runs of the lumped mass program with the  $N$  variable successively assigned the values shown in the tables on the figures. The other system parameters for these runs were:

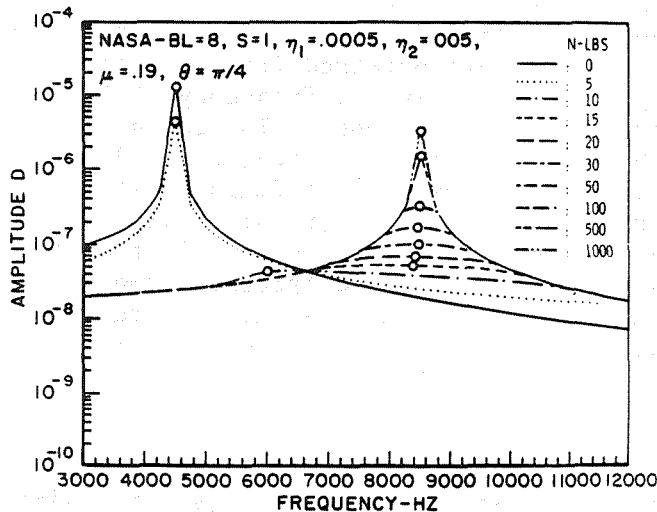


FIG. 4 AMPLITUDE OF HPFTP BLADE MODAL MASS  $m_1$  VERSUS FREQUENCY OF EXCITATION

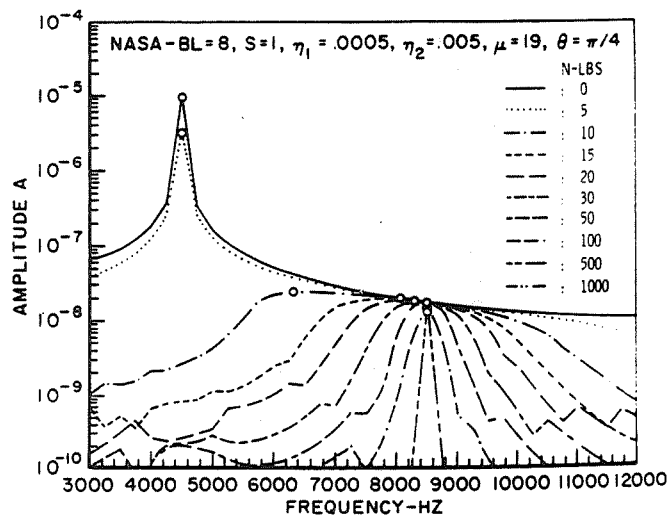


FIG. 5 AMPLITUDE OF HPFTP BLADE MODAL MASS  $m_2$  VERSUS FREQUENCY OF EXCITATION

$$\theta = \pi/4 \text{ (8 bladed disk)}$$

$$S = 1.0 \text{ lb. } \cos(\omega t + \frac{2\pi(\nu-1)}{8})$$

$$\mu = 0.19$$

$$\eta_1 = 0.0005$$

$$\eta_2 = 0.005$$

and  $m_1, m_2, k_1, k_2$  = HPFTP average blade modal values for the tuned first stage disk system. The  $\eta_2$  value of 0.005 is an average value obtained during modal tests of blades hard-clamped in a broach block. Figures 4 and 5 show that the blade transitions very quickly from the 4,500 Hz mode to the 8,500 Hz mode at low values of  $N$  or  $\mu N/S$  and that the minimum response of the blade occurs in this transition region near the midfrequency of the region.

Figure 6 shows the plots of the peak amplitude of the airfoil modal mass deflection relative to the platform-neck modal mass deflection (D-A) versus the ratio

$\mu N/S$ , the ratio of the friction force opposing platform motion to the blade forcing function amplitude.

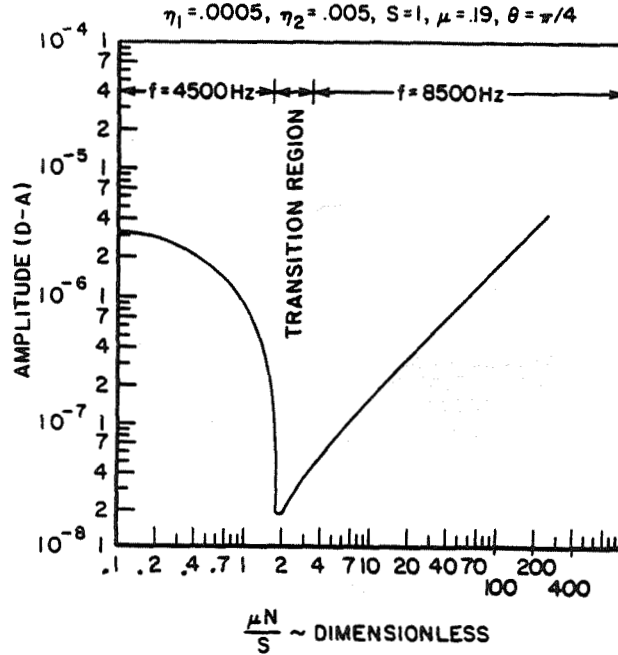


FIG. 6 AMPLITUDE OF  $m_1$  RELATIVE TO  $m_2$  VS  $\frac{\mu N}{S}$

The data points selected for the Figure 6 plot are circled on Figures 4 and 5. Figures 4 and 5 show that the blade vibration amplitude is reduced optimally by friction damping at relatively low values of  $N$ . This fact is depicted very graphically in Figure 6. The transition region also is shown in Figure 6.

Figure 7 shows the effect of changes in the hysteretic loss factors  $\eta_1$  and  $\eta_2$  while all other parameters remain unchanged. Figure 7 shows that hysteretic damping is effective at the 4,500 Hz modal frequency. After the friction damping forces the frequency into the transition region, however, the effect of the hysteretic damping becomes negligible.

Figure 8 shows the effect of variation of  $\theta$ , the blade to blade phase angle. It is seen that a larger phase shift between blades up to an equivalent engine

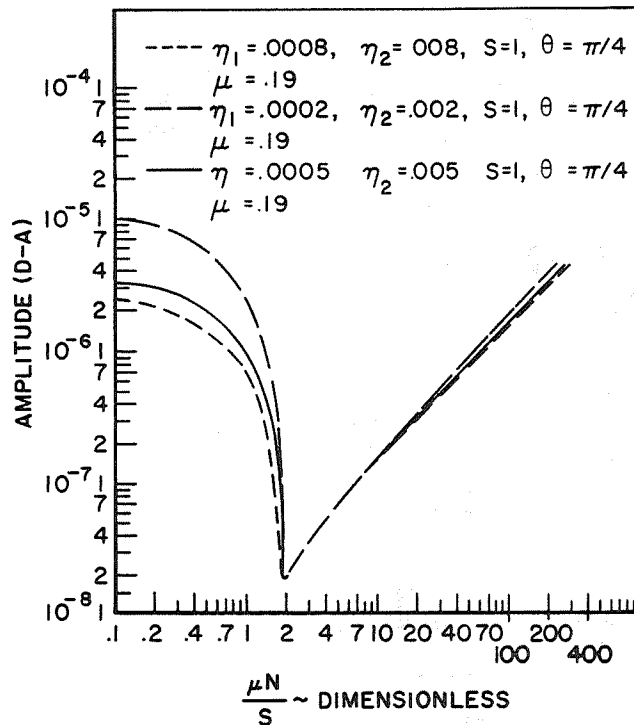


FIG. 7 AMPLITUDE OF  $m_1$  RELATIVE TO  $m_2$  VS  $\frac{\mu N}{S}$ ,  
VARIATION OF  $\eta_1 \eta_2$

order (E) of vibration  $n/2$ , produces a higher level of Coulomb friction damping, as expected. However, this is not usually a controllable parameter in an operational turbine, as may be true of most of the other parameters. The figure does show the characteristics of the curves for various engine orders of excitation, and provides useful design or evaluation information. It should be noted that the amplitude reduction possible is the same for all values of  $\theta$  but at different values of  $\mu N/S$ .

Figure 9 shows the effect of variation of  $S$ , the forcing function amplitude. It should be noted that the three curves shown have identical shapes, but that for an order of magnitude increase in  $S$  the airfoil response amplitude (D-A) as a function of  $\mu N/S$  increases by an order of magnitude. This shows the

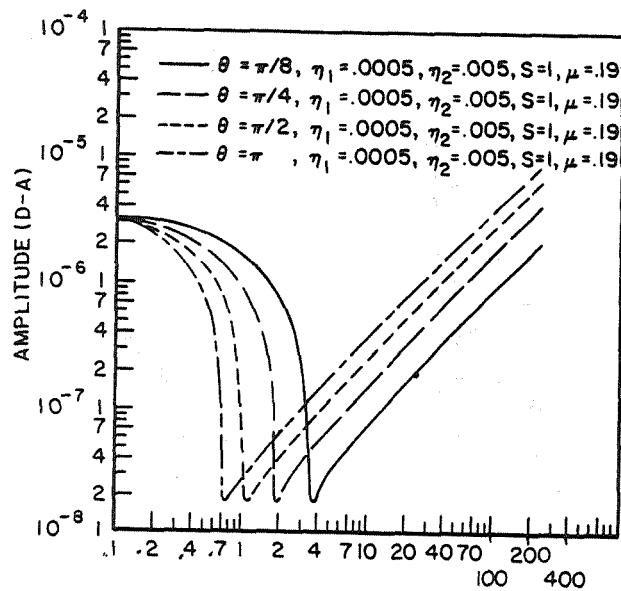


FIG. 8 AMPLITUDE OF  $m_1$  RELATIVE TO  $m_2$  VS  $\frac{\mu N}{S}$ ,  
VARIATION OF  $\theta$

system to be linear with  $S$  and indicates that a unit curve ( $S=1$ ) can be used to define a system. Then, the response amplitude can be scaled by the amplitude of  $S$  for any operating system having otherwise identical operating parameters.

All the previous data sets represent systems having a  $\mu$  (the damper to platform coefficient of friction) of 0.19, an arbitrary value. A set of data was generated for a system having  $\mu$  of 0.38, double the previous value. When a data point for  $\mu N/S$  of  $\frac{0.38 \times 5}{1}$  was plotted, the amplitude fell identically on that for  $\frac{0.19 \times 10}{1}$ , and similarly for all values of  $0.19 \times N$  equivalent to  $0.38 \times N$ . Obviously  $\mu$  and  $N$  are not independent variables, which is a basic tenet of Coulomb friction. It is necessary to know the values of  $\mu$  and  $N$  and their characteristics throughout the operating temperature-pressure-speed regime of a turbine. They may be amenable to some modification if design problems are encountered, or if operational fatigue problems are

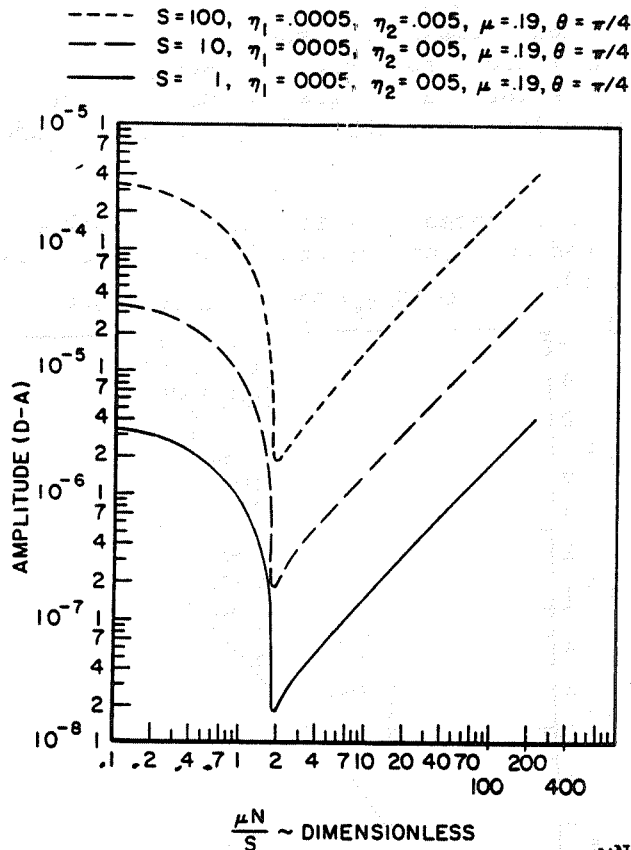


FIG. 9 AMPLITUDE OF  $m_1$  RELATIVE TO  $m_2$  VS  $\frac{\mu N}{S}$ ,  
 VARIATION OF S

encountered later that necessitate modification of the system.

A limit of this dynamic analysis is that the Coulomb friction ends at some value of  $\mu N/S$  and a regime of stick-slip friction begins. The stick-slip regime is followed by the end of slip, the lockup regime where friction ends and the surfaces are locked firmly together. The consequence of platform lockup has been shown to be quite severe for the system under study, being almost immediate failure of the turbine blade. After the loss of friction damping the airfoil vibration amplitude at excited resonance modes is limited only by the blade material hysteretic loss

factor (perhaps 0.0001) combined with whatever aerodynamic viscous damping is imparted to the blade by the driving fluid. For this analysis the outboard blade section loss factor was estimated to be an order of magnitude less than that of the inboard blade section.

The consequences of stick-slip and lockup have been sketched on a copy of the Figure 6 graph as shown in Figure 10.

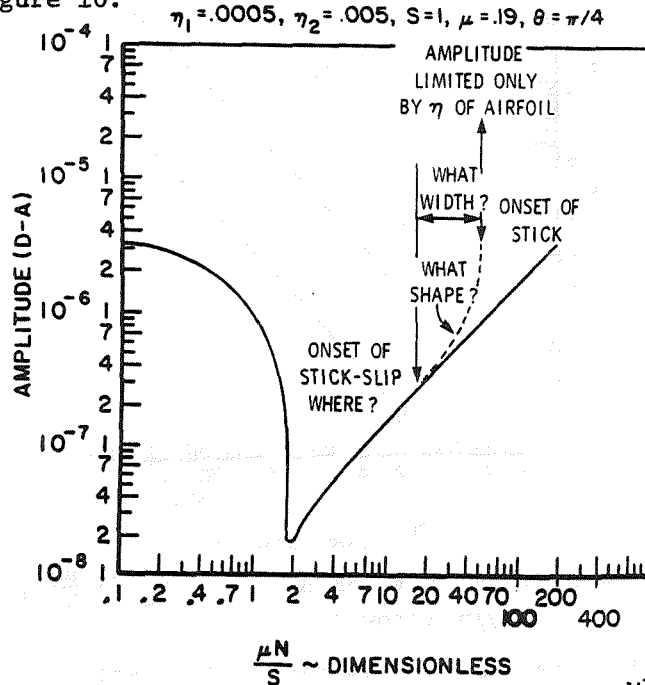


FIG. 10 AMPLITUDE OF  $m_1$  RELATIVE TO  $m_2$  VS  $\frac{\mu N}{S}$ ,

#### EFFECTS OF STICK-SLIP AND STICK

The location of stick-slip onset, the breadth of the stick-slip range and the effective damping in that range may be critical to system survival. This information is likely to be indeterminate without a careful and costly test program. Such a program may yield only marginally satisfactory results. What is needed is instrumentation data readings during system operation. Acquisition of such data is still beyond the state of the art for some high performance systems

such as the HPFTP.

The following conclusions are drawn from this study.

1. The lumped mass analysis shows the qualitative effects of the platform friction dampers on the flexural resonance response modes of the subject blade in the frequency range of 0 to 20,000 Hz.
2. Good quantitative analysis is dependent on reliable knowledge of the parameters upon which the analysis is based, i.e.,  $m_1$ ,  $m_2$ ,  $k_1$ ,  $k_2$ ,  $\eta_1$ ,  $\eta_2$ ,  $\mu$ ,  $N$ ,  $S$  and  $\theta$  or  $\delta$ , these latter being functions of the engine order of the excitation and the number of blades in the disc.
3. The analysis shows that effective friction damping is achieved in the lower range of the parameter  $\mu N/S$  up to the value where  $\mu N/S$  causes the onset of stick-slip friction. The airfoil amplitude response during stick-slip is undefined and if stick is encountered the airfoil amplitude will be controlled only by the damping of the airfoil section of the blade.
4. The response amplitude of the airfoil is reduced more than two orders of magnitude (more than 99 percent) at the minimum response in the frequency transition region ( $\mu N/S$  range approximately 1 to 10, dependent on  $\theta$ ).
5. The hysteretic damping of the blade does not appreciably affect its response in the effective friction damping range.
6. The curves shown in Figures 7 through 9 define the effects of variations of  $\eta$ ,  $\theta$ , and  $S$  in the  $\mu N/S$  region where stick-slip and stick are not encountered.
7. Figure 9 shows that response curves for  $S=1$  can be used for design or redesign of this blade-damper system since the response amplitude scales linearly as a function of  $S$ .

8. The values of  $\mu N/S$  that cause onset of stick-slip and stick are critical to the damper system design. If these regions can be avoided the Coulomb friction damping is very effective.

#### Test Evaluation in the Spin Pit

A vibration test evaluation of a simulated HPFTP first stage bladed disk was conducted in a high speed spin pit. For purposes of test, a used set of blades and dampers was acquired from NASA and a titanium disk and two types of experimental dampers were fabricated. Blade vibration responses were measured with strain gages as the blades were excited magnetically during high speed spins in vacuum.

Twelve blades were instrumented with 1/16 inch square strain gages on the suction side of the airfoil. The gages were centered 1/4 inch above the platform and 1/8 inch from the trailing edge, a high stress region of the blade. Leadwires were routed down the aft face of the blade through a slot cut in the platform to terminals on the aft face of the firtree area. A photograph of a strain gage installation is shown in Figure 11.

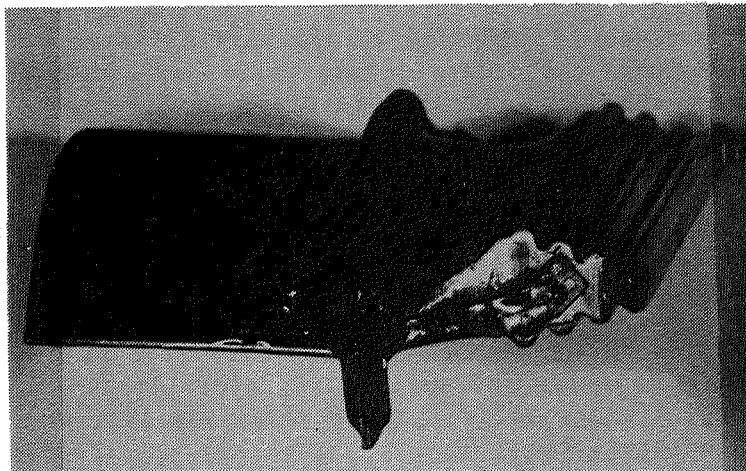


FIG. 11 HPFTP STRAIN GAGED BLADE

The blades were installed in a test disk .

fabricated from a forged and heat-treated 6Al4V titanium blank. The firtree slots in the disk were cut by computer controlled wire EDM, which achieved production tolerance on the slot configuration and the blade to disk firtree fit. The test disk was fabricated with 64 slots in order that a symmetrical test specimen could be assembled.

In addition to the disk, two types of lightweight experimental platform friction dampers were fabricated. These dampers were formed of nichrome wire on bending jigs designed for the purpose. Figure 12 shows the production 0.56 gram dampers and the experimental 0.20 gram and 0.10 gram dampers.

After 0.5 gram magnetic cobalt weld beads were added to the blade tips, the blades were tested in a broach block to identify the first flexural and first torsional mode resonance frequencies. They were subsequently x-rayed to verify the adequacy of the welds and the absence of serious cracks. They then were weighed and were installed in the test disk in the scheme shown in Figure 13. As shown, eight groups of

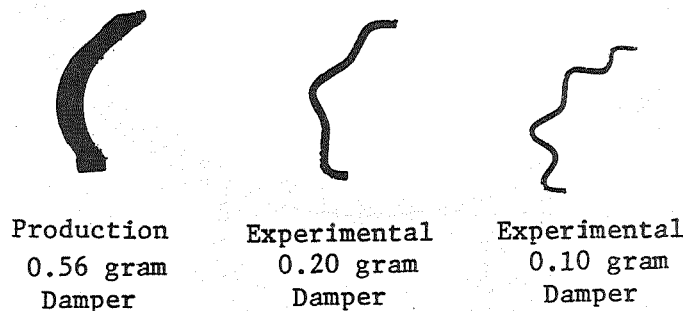


FIG. 12 TEST DAMPERS

eight blades were installed in test octants consisting of oppositely balanced octants of each of the three test damper types and two opposite groups of blades without dampers. Two strain gaged blades and one spare gaged blade were included for each configuration type. In addition, two gages were installed to measure radial strain on the test disk. The blade strain gages were connected to leadwire pairs on the disk with

<u>Octant</u>	<u>Damper Type</u>
1,5	None
2,6	0.56 gram production
3,7	0.10 gram wire
4,8	0.20 gram wire

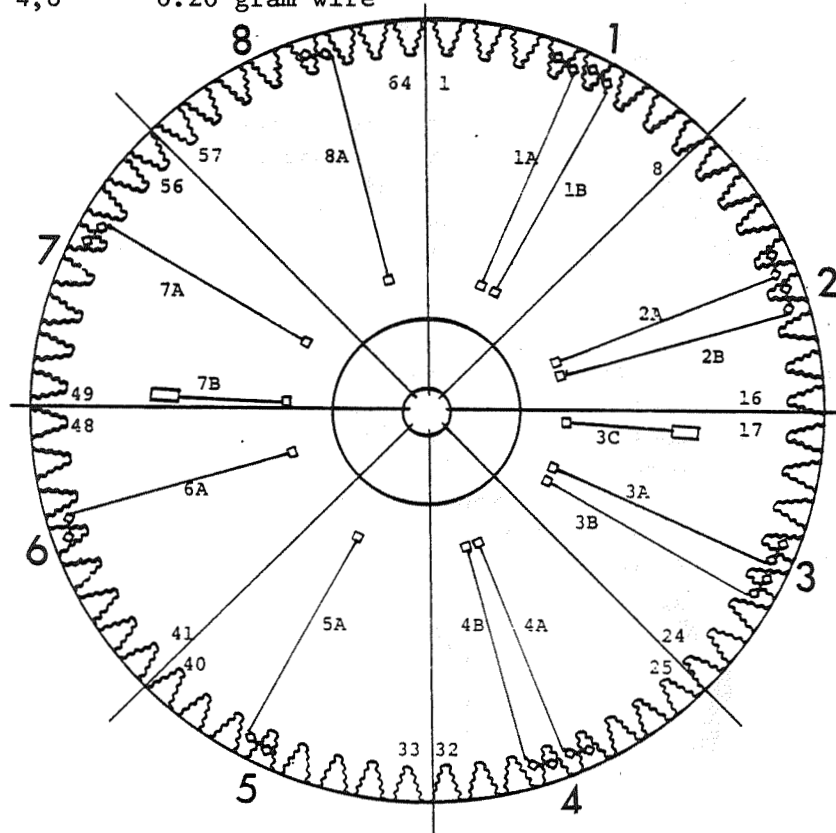


FIG. 13 TEST DISK LAYOUT

jumpers over the firtree gap.

The bladed disk was installed to an arbor shaft assembly and the strain gage leadwires were routed from terminals on the disk up through the arbor shaft. The disk-arbor assembly was precision dynamically balanced and then was installed in the spin pit test assembly shown in Figure 14. The strain gage leads were routed from the arbor shaft through the quill shaft to the high speed slip ring on top of the spin assembly. They then were routed to strain signal

amplifiers and on to an FM reorder and to test monitoring oscilloscopes and a frequency analyzer.

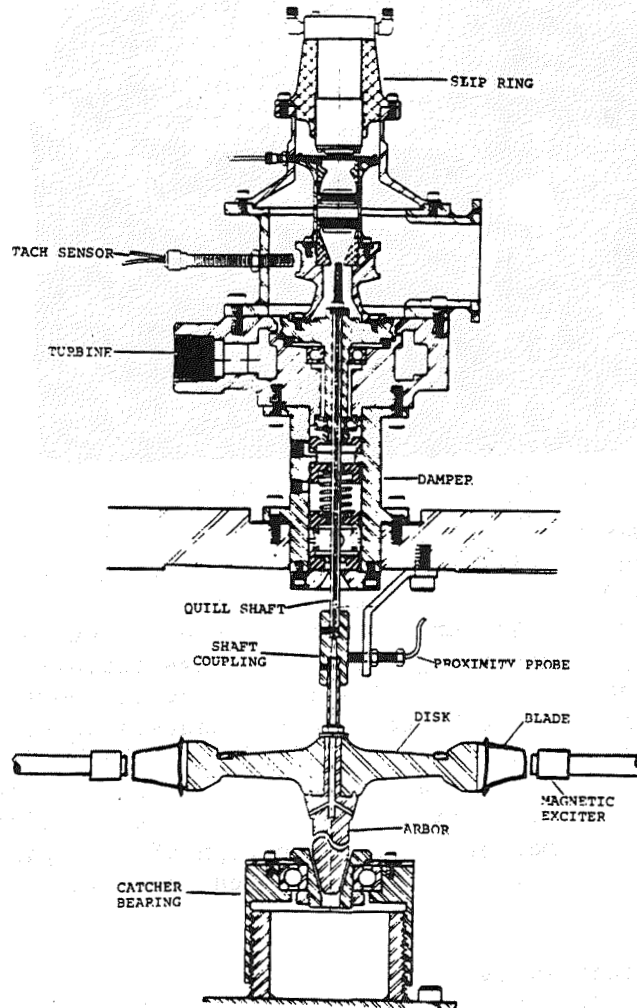


FIG. 14 SPIN TEST ASSEMBLY

As shown in Figure 14, the blades were excited by radially mounted samarium cobalt permanent magnets that were spaced symmetrically around the disk with an at-rest gap of 0.12 inch between the magnets and the cobalt weld beads on the blade tips. The magnet support

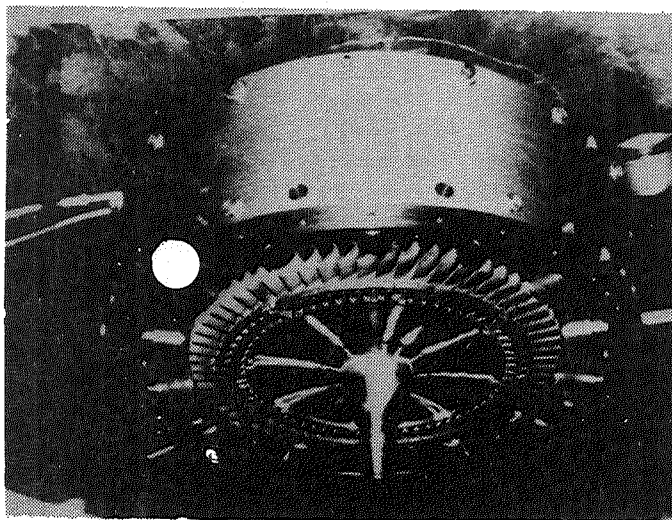


FIG. 15 SPIN TEST SET-UP

fixture was provided with 28 magnet mounts and tests were conducted with both 28 and 14 magnets installed, providing 28E or 14E excitation of the bladed disk for two series of test runs. Whether 28 or 14 magnets were installed, adjacent magnets were always installed with opposite polarity, i.e. if a magnet had its north magnet pole facing the blade tips the magnets on either side had their south magnet pole facing the blade tips. The blades were excited primarily by magnetic drag pulses as the blade tips passed through the fields of the permanent magnets. A photograph of the spin pit test setup with 14 magnets installed is shown in Figure 15.

The test assembly was always spun in a vacuum that ranged from 2.5 to 3.0 torr for various test spins. In early testing, high whirl modes of the test assembly were encountered but these were reduced to tolerable levels by redesigning the arbor to quill shaft coupling. The first spin test was conducted with 28 excitation magnets installed. It was expected that this 28E excitation would induce the first flexural resonance mode of the blades (4,800 Hz was the mean frequency for 64 blades hard clamped in the broach block) at about 10,000 rpm and that the 8,500 Hz airfoil-alone first flexural mode might occur near 18,000 rpm, at least on

the blades with the heaviest (production 0.56 gram) dampers since frequency increases linearly with rpm and normal force of the dampers increases with the square of the rpm.

The first test spin covered the range from 0 to 23,000 rpm. The only significant test data from this spin are shown in Figures 16, 17, 18 and 19.

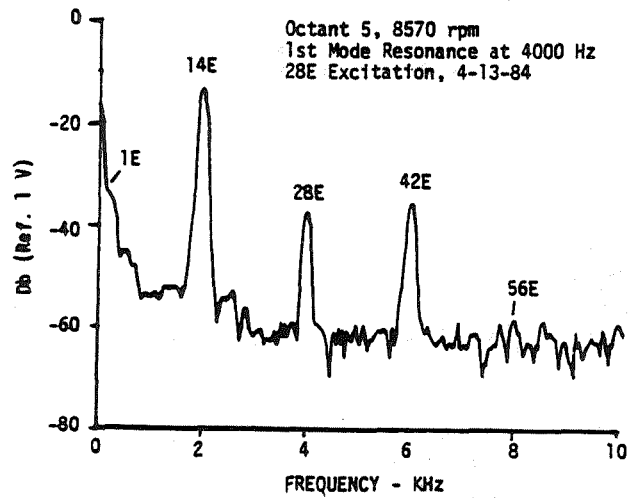
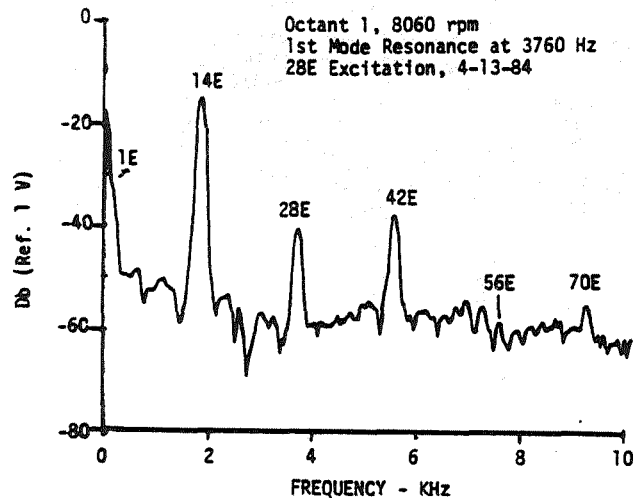


FIG. 16 VIBRATION SPECTRA - UNDAMPED BLADES

First flexural resonance vibration of all the monitored test blades is shown clearly at the 28E excitation frequency. The peaks at 14E and 42E are due to magnetically induced EMF in the strain circuits and the 1E peak is due to one-per-rev unbalance-induced strain. The signal noise floor is caused by sum and difference frequencies of the one-per-rev signal and its harmonics with the other major signal components.

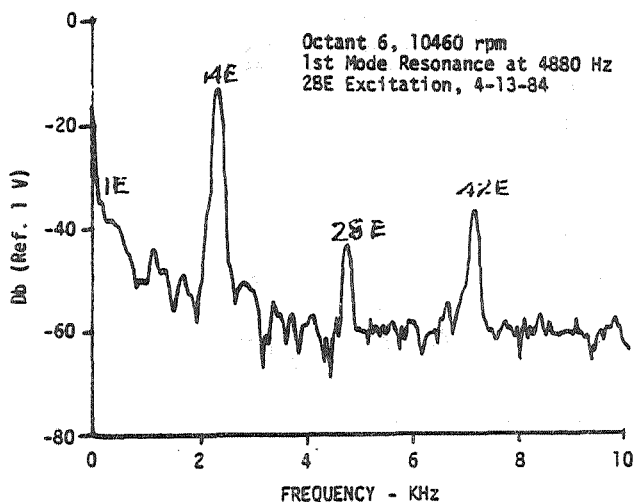
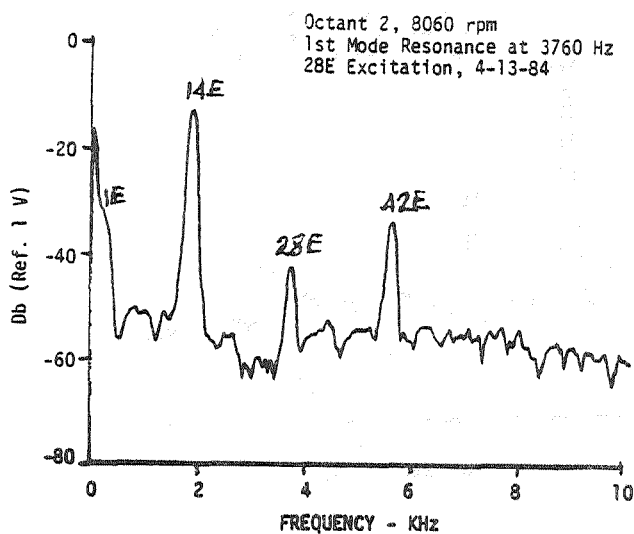


FIG. 17 VIBRATION SPECTRA-PRODUCTION 0.56 GRAM DAMPERS

By contrast, Figure 20 shows strain gage signals for 28E and 14E excitation spins when no blade resonance vibration is occurring.

The significant factors shown by the low speed spin data of Figures 16 through 19 are that the blade first flexural mode resonance occurred at lower than expected

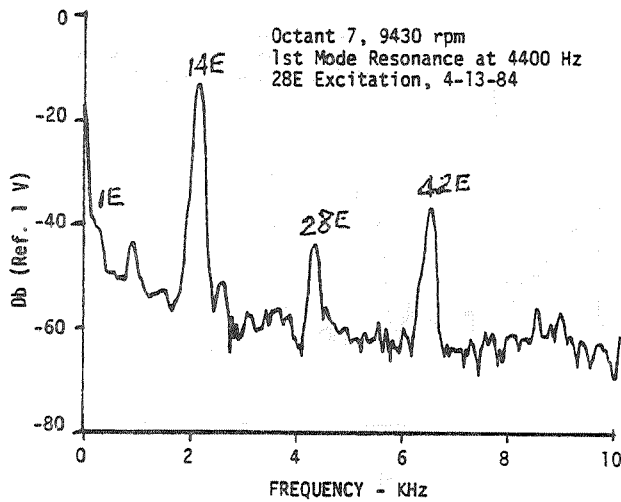
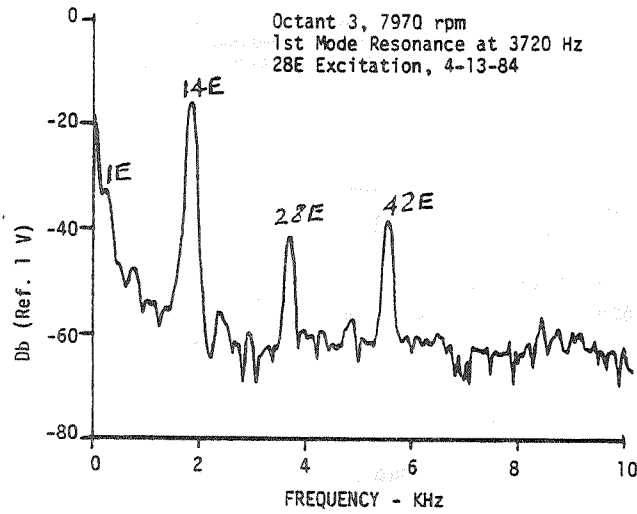


FIG. 18 VIBRATION SPECTRA - EXPERIMENTAL  
0.10 GRAM DAMPERS

frequencies for all four test configurations and that no airfoil-alone resonances occurred for any of the instrumented blades. The first torsional mode resonance was found for two blades near 10,700 Hz and 23,000 rpm, but at a relatively low amplitude. The surprisingly low first flexural mode frequencies found during this spin test are attributed to a relatively

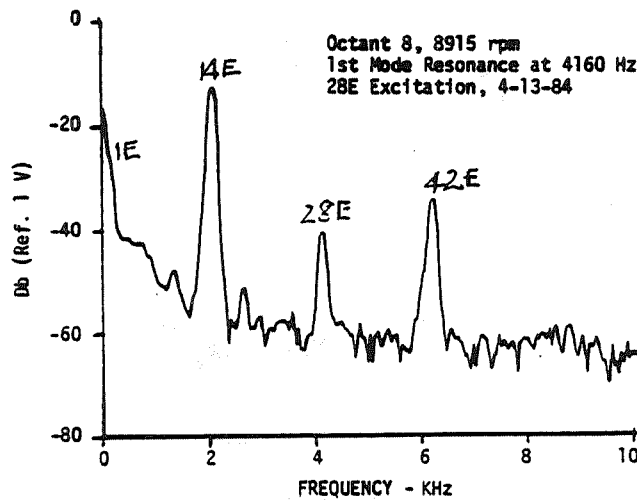
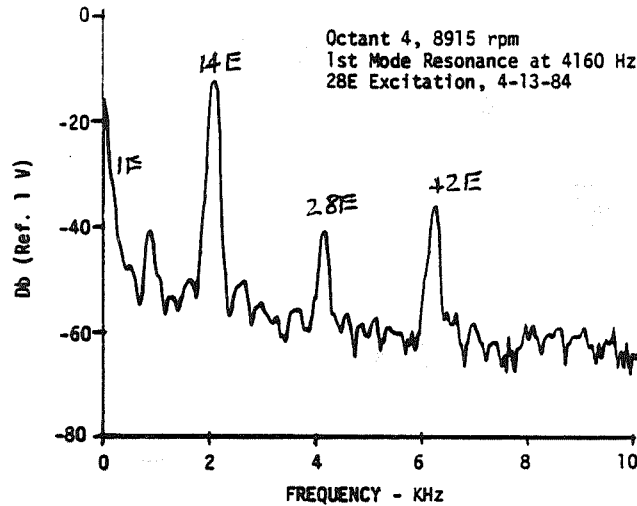


FIG. 19 VIBRATION SPECTRA - EXPERIMENTAL  
0.20 GRAM DAMPERS

soft mount condition of the blades at the firtree root for this low speed spin condition.

After the magnets were reconfigured for 14E excitation, a high speed spin test to 38,000 rpm was performed. The only significant blade resonance vibrations found during this test are shown in Figures 21 and 22. Figure 21 shows the first flexural mode

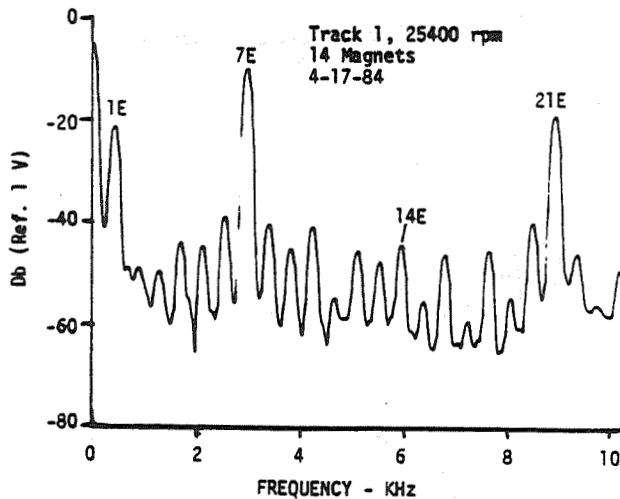
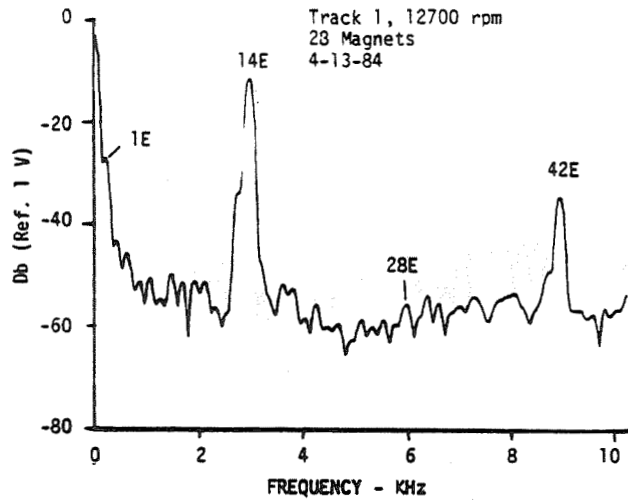


FIG. 20 OCTANT 1 FREQUENCY SPECTRA - NO RESONANCE

vibration of the whole blade for the blades with no friction dampers and Figure 22 shows the airfoil-alone flexural resonance mode for blades with production 0.56 gram dampers. Neither mode was found for the blades with lightweight experimental dampers indicating vibrations of these blades occurred at very low amplitude in the transitional region between the two resonance

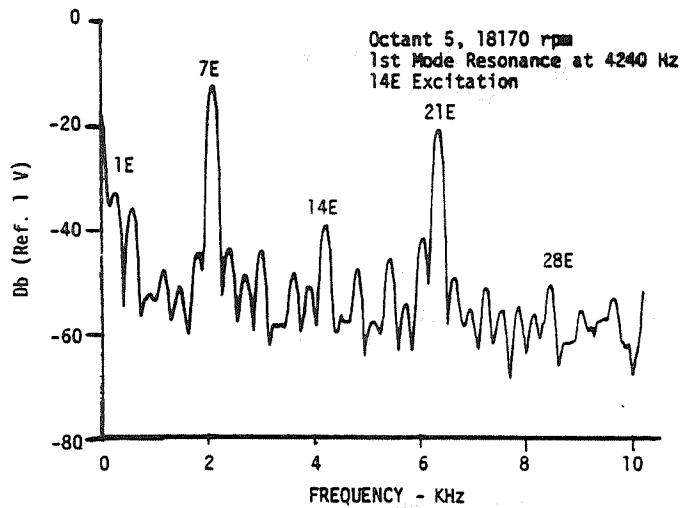
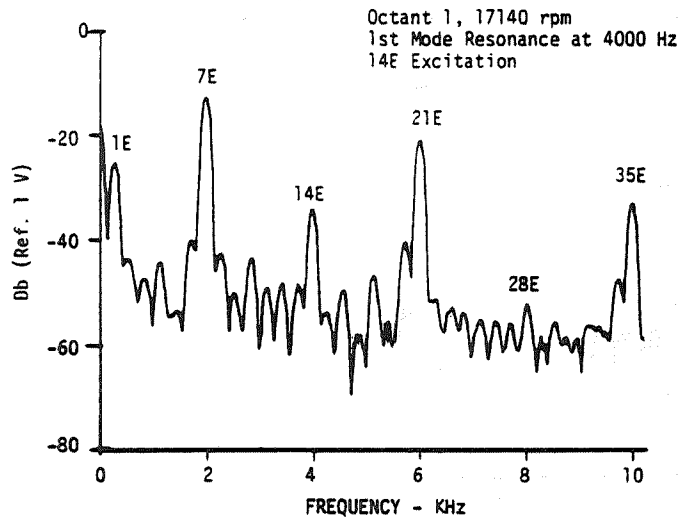


FIG. 21 VIBRATION SPECTRA - 14E EXCITATION OF UNDAMPED BLADES

modes. In other words, these friction dampers worked very well at the excitation force levels produced by the permanent magnets. Conversely, the production 0.56 gram dampers caused an airfoil-alone resonance vibration strain signal in test octant 6 that was more than 6 dB higher, or double the strain amplitude, than any of the resonance vibrations that occurred in the

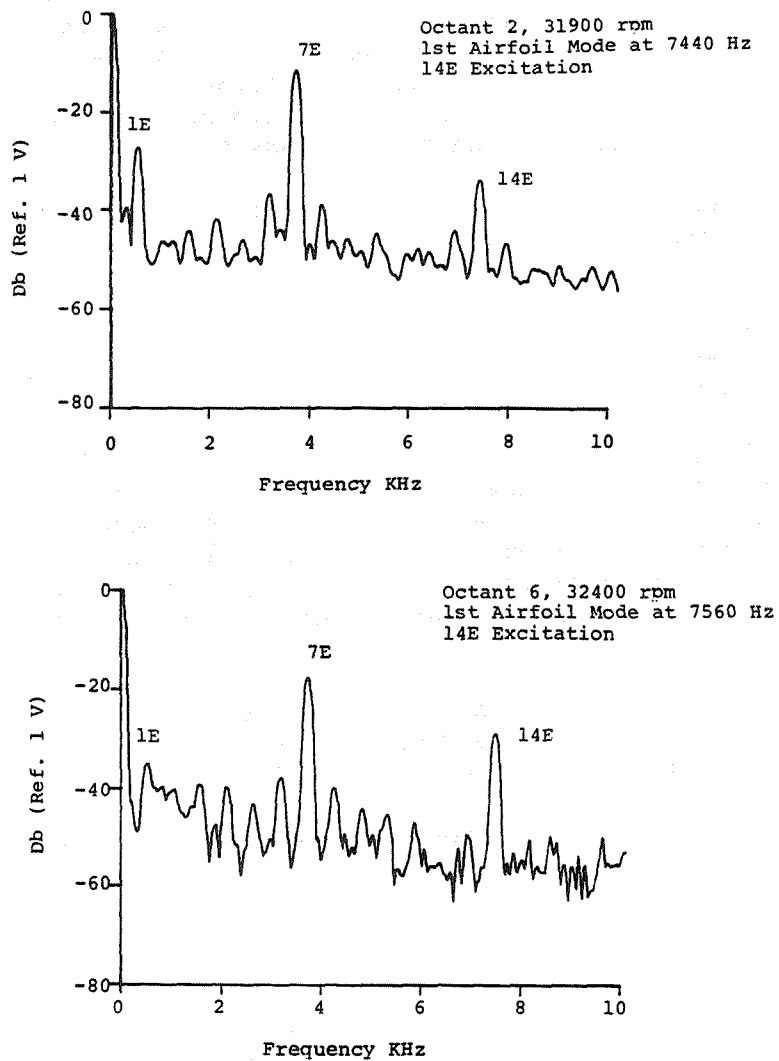


FIG. 22 VIBRATION SPECTRA - AIRFOIL FLEX MODE -  
PRODUCTION 0.56 GRAM DAMPERS

undamped blades or in any of the blades in the whole blade first flexural resonance mode.

The resonance vibrations shown for undamped blades in Figure 21 again occurred at a lower than expected frequency but at a higher frequency than in the low speed spin test. This shows a relatively soft, but hardening, root fixity at the firtree. The airfoil-alone flexural resonance modes shown in Figure 22 also occurred at a lower than expected frequency. This is attributed to the addition of the 0.5 gram magnetic cobalt weld beads added to the blade tips.

The following conclusions are drawn from the test program.

1. Low speed spin conditions are not adequate to seat the blades and dampers firmly enough to produce data related to conditions during operational speeds of the HPFTP.
2. The production 0.56 gram dampers did constrain the platforms at operational spin speed and caused excessive airfoil-alone first flexural mode resonance vibration, though probably at a lower than operational excitation amplitude, at the 14E excitation frequency that is known to occur in the HPFTP.
3. Lightweight experimental dampers eliminated both lower order flexural modes of the blade for the excitation level that occurred in the test.
4. The test data confirmed the results of the analytical study.

#### Acknowledgement

This work was performed for Marshall Space Flight Center (MSFC) of NASA under contract NAS8-34682. Mr. Larry Kiefling, the project technical monitor, of the Structural Dynamics Division of MSFC, was very helpful in providing data and guidance for the work.

### References

1. Muszynska, A., D.I.G. Jones, T. Lagnese, and L. Whitford, "On Nonlinear Response of Multiple Blade Systems," Paper presented at 51st Shock and Vibration Symposium, San Diego, CA, October 1980, and published in Shock and Vibration Bulletin 51, Part 3, May 1981.
2. Sutton, R.F., "Nasa, High Speed Rotating Diagnostic Laboratory Testing, SSME High-pressure Fuel Turbopump Blade/Damper Evaluation," Rocketdyne Division of Rockwell International Report RSS-8626, November 2978.
3. Dominic, R.J., "Parametric Study of Turbine Blade Platform Friction Damping Using the Lumped Parameter Analysis," ASME Paper 84-GT-109, 1984.
4. Dickerson, E.O., "Turbine Blade Structural Dynamic Analysis," AIAA Paper 80-0782, 1980.
5. Scott, L.P., J.E. Pond, C.C. Myers, G.A. Teal, G.F. Lewis, and J.K. Robinson, "Assessment of HPFTP Turbine Blade Environment and Fatigue Life Study on the SSME, Volumes I and II," Lockheed Missiles and Space Company, Inc., Huntsville Research and Engineering Center Report LMSC-HREC TR D784198, May 1981.
6. Dominic, R.J., Philip A. Graf, and B. Basava Raju, "Analytical and Experimental Investigation of Turbine Blade Damping - Final Report," University of Dayton Research Institute Report UDR-TR-82-39, August 1982. (AD-A120470, AFOSR-82-0911TR, or NTIS HC A04/MF A01).
7. Soni, J.L., and T.W. Held, "Users Manual for a Computer Program for Dynamic Response of Bladed Systems," University of Dayton Research Institute Report UDR-TR-84-38, May 1984.

## NONLINEAR STRUCTURAL ANALYSIS FOR FIBER-REINFORCED SUPERALLOY TURBINE BLADES

D. A. Hopkins and C. C. Chamis  
Structures and Mechanical Technologies Division  
NASA Lewis Research Center  
Cleveland, Ohio 44135

### Abstract

A computational capability for predicting the nonlinear thermomechanical structural response of fiber-reinforced superalloy (FRS) turbine blades is described. This capability is embedded in a special-purpose computer code recently developed at the NASA Lewis Research Center. Special features of this computational capability include accounting for; fiber/matrix reaction, nonlinear and anisotropic material behavior, complex stress distribution due to local and global heterogeneity, and residual stresses due to initial fabrication and/or inelastic behavior during subsequent missions.

Numerical results are presented from analyses of a hypothetical FRS turbine blade subjected to a fabrication process and subsequent mission cycle. The results demonstrate the capabilities of this computational tool to; predict local stress/strain response and capture trends of local nonlinear and anisotropic material behavior, relate the effects of this local behavior to the global response of a multilayered fiber-composite turbine blade, and trace material history from fabrication through successive missions.

### Introduction

Fiber-reinforced superalloys (FRS) are becoming more attractive for hot-section applications in aircraft gas turbine and liquid-propellant rocket engines. Recently, specific investigations<sup>1-3</sup> have focused on the benefit of using FRS for components (rotor blades) of aircraft engine high-pressure

turbines and Space Shuttle Main Engine high-pressure fuel turbopumps. In short, these investigations demonstrated, qualitatively at least, the potential of FRS to provide a substantial improvement in component durability and maximum temperature capability beyond that presently achieved with monolithic materials.

Despite the apparent advantages of FRS, the prospects for having a production engine with FRS turbine components in the near future are remote. This is largely due to the fact that no adequate (accurate and economical) means currently exist for making a quantitative assessment of the mechanical performance and structural integrity of composite materials in such complex structural applications as turbine blades. The availability of adequate structural analysis/design tools is imperative if the use of FRS, or any advanced composite material, for engine hot-section components, or any complex structural application, is to become a reality.

In response to the deficiency mentioned above, research is being conducted at the NASA Lewis Research Center to develop computational nonlinear structural mechanics methodologies for high-temperature composite engine structures. One recent result of these efforts has been the development of a computational capability specifically tailored for the nonlinear structural/stress analysis of FRS turbine blades.<sup>4</sup> The intent here is to provide a brief and general overview of this analytical tool together with some typical results obtained from a recent exercise using this capability.

#### Computational Capability

Clearly, the utility of any structural analysis tool depends on the accuracy with which it describes or predicts the actual physical event being modeled. In this light, the primary goal in developing the computational capability mentioned above was to account for the physics governing this application

in the analytical formulation of the problem. In doing so, it was assumed that the behavior of a FRS turbine blade could be predominantly attributed to certain physical characteristics and/or phenomena associated with this application, including;

- local (intralaminar) heterogeneity of a fiber-reinforced composite ply
- global (interlaminar) heterogeneity of a multilayered angleplied composite structure
- fiber/matrix metallurgical reaction due to extended exposure in elevated temperature environments
- nonlinear (stress-temperature-time dependent) and anisotropic constituent material behavior due to complex and cyclic thermomechanical loading conditions
- complex and nonuniform microstress distribution in the composite constituents due to intralaminar heterogeneity and anisotropic nonlinearities
- residual stresses due to initial composite fabrication process and/or inelastic behavior during subsequent mission cycles

Accountability of these factors, then, was judged to be most critical to the development of an appropriate and adequate structural analysis tool.

To develop the computational capability alluded to above, the existing COBSTRAN computer code was used as a foundation. COBSTRAN (COmposite Blade STRuctural ANalysis) is a special-purpose code developed several years ago at the NASA Lewis Research Center to perform linear-elastic structural analysis of composite blade-like structures. This recently developed nonlinear version of COBSTRAN is an integrated structural analysis tool incorporating; a

fiber degradation model, a nonlinear material model/cumulative damage model, composite micromechanics theory, laminate theory, and global finite element structural analysis.

The analytical procedure of nonlinear COBSTRAN is based on an incremental/iterative solution strategy. This strategy entails the successive solution of a linear formulation for distinct increments of the total load/time domain of the problem. During the process, results from the solution of each load/time increment are used to update the problem formulation for solution of the next increment. In this manner, the solution strategy embedded in nonlinear COBSTRAN resembles the forward-Euler type scheme.<sup>5</sup>

As implemented in nonlinear COBSTRAN, the solution strategy described above involves two levels of iteration. The primary iteration occurs for the load/time stepping process. For each distinct increment then, the secondary iteration occurs to achieve convergence at an equilibrium solution. Presently, a criterion based on the error in nodal displacement components for successive iterations is used to establish equilibrium-solution convergence.

The functional essence of the computational capability embodied by nonlinear COBSTRAN is depicted graphically in Figure 1. The schematic summarizes the major elements comprising this integrated structural analysis tool while the circular arrangement portrays the iterative nature of the solution strategy. Moreover, a distinct computational "hierarchy" is evident from the schematic. In other words, there is a clear progression from a description of material properties at the "micro" level to a prediction of structural response at the "macro" level, and back. In short, the analytical process illustrated in Figure 1 can be described as an "upward integration" of the structural analysis model and a "downward decomposition" of the structural response variables.

As implied in Figure 1, the problem of material nonlinearity is treated at the lowermost level in the computational hierarchy i.e., in the constituent materials comprising each ply. To describe the nonlinear material behavior, a simple thermoviscoplastic constitutive model was formulated on the premise that the nonlinearity could be expressed in terms of a stress-temperature-time dependency of the constituent material properties. As such, the model relates the incremental stress in the constituent to the incremental strain in a manner similar to the Hooke's Law relationships. However, in this case the material properties are taken to be dependent functions of stress, stress-rate, temperature, and time. The material model also incorporates a simple cumulative damage/life fraction model based on the concept of residual strength.

The fiber/matrix reaction phenomenon is accounted for in conjunction with the treatment of material nonlinearity. An empirical expression is used to quantify the reduction in cross-sectional area of the intact fibers. The resulting growth of an interphase of material between the intact fiber and matrix is accommodated by providing for the separate characterization of this material as an additional constituent of the ply.

Composite micromechanics theory and laminate theory comprise the two intermediate levels in the computational hierarchy depicted in Figure 1. In effect, the two theories constitute an idealization of the inherently heterogeneous composite structure as an equivalent "pseudo-homogeneous" one. In the upward integration process these theories provide the means to predict equivalent properties of a pseudo-homogeneous finite element based on the properties of the constituent materials and the geometrical characteristics of the composite (ply and laminate). In the downward decomposition process the theories provide the means to relate the global response of the composite structure back to the local response of the individual constituents of each ply.

Global structural analysis by the finite element method (FEM) represents the uppermost level of the computational hierarchy illustrated in Figure 1. A superficial summary of the governing equations of linear structural analysis, from a FEM perspective, is given in Figure 2. Part of the analytical process of nonlinear COBSTRAN involves solution of these equations for each successive increment of the total load/time domain of the problem, as depicted in the accompanying schematic. At present, the nonlinear COBSTRAN code interfaces with the MSC/NASTRAN<sup>6</sup> code for global FEM structural analysis requirements.

### Turbine Blade Analyses

In an effort to demonstrate the utility and capabilities of the integrated structural analysis tool described above, some typical results are given below from a recent exercise involving analyses of a hypothetical FRS turbine blade airfoil. The analyses were conducted to investigate the effects on the airfoil of a fabrication process and the subsequent response of the airfoil to a mission cycle.

An illustration of the airfoil geometry used in the analyses is given in Figure 3. Overall, the approximate dimensions of the airfoil are; 2.15 in. along the span, 1.20 in. across the chord, and 0.040 in. through-the-thickness of the wall. The airfoil has a slight axial twist and a tapered cross-section from root to tip. The discretized finite element model of the airfoil shown in Figure 3 contains 220 quadrilateral isoparametric membrane-bending elements and 240 nodal points (1200 degrees-of-freedom less those constrained by imposed boundary conditions).

A summary of the specific FRS composite system used for the analyses is also given in Figure 3. The system entails a 4-ply laminate with a configuration of  $[\pm 45^\circ]_S$ . The individual plies are 0.010 in. thick and consist of Fe-25Cr-4Al-1Y matrix reinforced with 0.008 in. diameter continuous W-1.5ThO<sub>2</sub> fibers yielding a fiber volume fraction of 0.50.

The objective of the first analysis of the FRS airfoil was to investigate the residual stress state induced by thermal loading experienced during a fabrication process. The process simulated for the analysis was adapted from an actual hot isostatic pressing (HIP) process used in the fabrication of laboratory test specimens. The complete HIP process consists of; a 20-minute heat-up transient (room temperature to 1950° F), a 30-minute constant temperature/pressure transient (1950° F/15,000 psi), and a 16-hour cool-down transient (1950° F to room temperature).

The analysis of the fabrication process simulated only the cool-down portion of the HIP process inasmuch as the transition from the constant temperature/pressure transient to the cool-down transient was judged to be a reasonable point in the process to assume the onset of composite behavior. Moreover, it was assumed that the individual plies were being consolidated simultaneously with the fabrication of the airfoil in order to neglect the existence of any initial residual microstress in the ply constituents prior to component fabrication.

The cool-down transient, illustrated in Figure 4, was simulated using 30 load/time increments. The temperature was assumed to be uniform over the entire airfoil (spanwise, chordwise, and through-the-thickness). Boundary conditions for the analysis were specified so as to provide immobility of the airfoil model with minimal constraint. A maximum error tolerance of one percent was prescribed for the equilibrium-solution convergence criterion. The analysis required a total of 61 iterations and consumed approximately 20 minutes of CPU time on a Cray 1S computer system.

Results from the analysis of the fabrication cool-down process indicated a practically uniform state of ply residual stress throughout the airfoil, as anticipated in view of the uniform temperature distribution and "quasi-isotropic" ply configuration.

Magnitudes of longitudinal normal ply stress,  $\sigma_{L11}$  (see ply coordinate system, Figure 5), varied from -11.5 ksi to -13.4 ksi with the majority of values falling in the range  $-12.5 \pm 0.3$  ksi. Magnitudes of transverse normal ply stress,  $\sigma_{L22}$ , were similar to  $\sigma_{L11}$  but of opposite sense, i.e. tensile rather than compressive. Also evident were ply in-plane shear stresses,  $\sigma_{L12}$ , ranging in magnitude from 0.0 to  $\pm 0.4$  ksi. These small shear stresses and the deviation in normal stresses are attributed primarily to small-scale local bending and/or twisting of the airfoil due to the asymmetric airfoil geometry.

The build-up of residual stress in a ply and the resulting microstress state in the ply constituents throughout the duration of the cool-down process is illustrated in Figure 5. These results are of the longitudinal normal stress/microstress ( $\sigma_{11}$ ) in the outermost ( $+45^\circ$ ) ply and its constituents at a location on the airfoil corresponding to the root leading edge point (see arrow, Figure 4). What is noteworthy about the results illustrated in Figure 5 is that, despite a relatively low magnitude of ply stress, the constituent constituent microstress magnitudes are quite large. This reflects the substantial contribution of thermally induced microstress due to the mismatch in thermal expansion characteristics of the two materials.

Similar to Figure 5, results are presented in Figure 6 of transverse normal stress/microstress ( $\sigma_{22}$ ) for the same ply at the same airfoil location. Different from  $\sigma_{11}$  however, the interaction of constituents in the transverse direction causes the distribution of  $\sigma_{22}$  (and  $\sigma_{12}$ ) in the matrix and interphase to be nonuniform through-the-thickness of the ply. This intraply nonuniformity is characterized by three distinct regions (A-B-C) as shown in the schematic. A review of the results for matrix microstress, for example, indicates the significance of this intraply nonuniformity. A transition occurs from a tensile microstress in regions A and B to a compressive microstress in region C.

One ramification of the intraply nonuniformity of  $\sigma_{22}$  (and  $\sigma_{12}$ ) for the matrix and interphase concerns the potential for the microstress in a select region to exceed the yield point of the material. This localized inelastic behavior would result in an induced anisotropy of the material that serves to exacerbate the already complex physical characteristics of this problem. With this in mind, it is easier to envision how local flaws might initiate, propagate, and eventually cause complete failure in a turbine blade, for example. The point to be taken from this is the importance of being able to account for behavior on the "micro" scale, and therein lies the utility of the integrated computational capability embodied by nonlinear COBSTRAN.

The second analysis of the FRS turbine blade airfoil was conducted to investigate the response to the thermal, pressure, and centrifugal loads experienced during a mission cycle. Complete details of the loading conditions are excluded here for the sake of brevity and because they are unimportant within the scope of this discussion. It will suffice to say that the temperature and pressure distributions over the airfoil surfaces (pressure and suction) had a bicubic variation (spanwise and chordwise) throughout the mission cycle.

The mission cycle was simulated with 43 load/time increments. The imposed boundary conditions most closely represented those of a cantilevered structure. The same maximum error tolerance of one percent was prescribed for the convergence criterion. The analysis required a total of 112 iterations and consumed approximately 50 minutes of CPU time.

Results from the mission cycle analysis indicated an overall change in the ply residual stress state from prior (initial fabrication residual stresses) to after the mission. In general, the magnitudes of  $\sigma_{L11}$  were decreased for all plies while the magnitudes of  $\sigma_{L22}$  were increased for all plies. In all cases  $\sigma_{L11}$  remained compressive and  $\sigma_{L22}$  remained tensile.

The extent of this change in ply residual stress magnitude varied depending on the location on the airfoil. For example, the change was most noticeable at the root section and least noticeable at the tip, as might be expected since the effects of the pressure and centrifugal loads vanish at the tip. Likewise, the change was more significant at mid-chord, and especially on the suction surface, than at the leading or trailing edges. As an illustration, the maximum ply residual stress at the end of the mission cycle was approximately +19.0 ksi and occurred in the  $\sigma_{22}$  component for the outermost ply on the suction surface at the root mid-chord location.

Results similar to those shown earlier for the analysis of the fabrication cool-down process are presented now for the mission cycle analysis, using the same ply at the same airfoil location (outermost ply, root leading edge). Figures 7 through 9 illustrate the temperature, pressure, and centrifugal load variations, respectively, throughout the mission for this location. Figure 10 illustrates the variation of longitudinal tensile strength ( $S_{11T}$ ) in the constituents and for the ply. These results reflect a dependence of strength on primarily temperature. Figure 11 illustrates the variation of stress/microstress magnitude throughout the mission.

The first point to note from the results shown in Figures 7 through 11 is the large variation in the constituent microstress state despite a relatively constant ply stress. Again, this reflects the contribution of thermally induced microstress due to the mismatch in thermal expansion characteristics of the two materials. Secondly, and perhaps most intriguing, is that the microstress state is minimum at maximum load conditions and when available strength in the constituents is minimum. This suggests a potential design flexibility which is unique to composite material systems.

A final result from the analysis of the mission cycle is illustrated in Figure 12 showing the

variation throughout the mission of natural vibration frequencies for the airfoil. The results reflect the change in frequency corresponding to the change in stiffness of the airfoil, due initially to the variation in temperature and then to the inelastic deformation in the airfoil.

#### Conclusions

The numerical results presented above serve as examples of the type of information provided by the nonlinear COBSTRAN code. The results demonstrate the unique capabilities of this computational tool to relate local nonlinear constituent material behavior to the global response of an FRS composite turbine blade. Moreover, the results manifest the utility of the "upward integration/downward decomposition" approach, in general, for nonlinear structural analysis of any composite structure.

#### References

1. P. Melnyk and J. N. Fleck, "Tungsten Wire Reinforced Superalloys for 1093 C (2000° F) Turbine Blade Applications", NASA CR-159720, 1979.
2. D. W. Petrasek and R. A. Signorelli, "Tungsten Fiber Reinforced Superalloys - A Status Review", NASA TM-82590, 1981.
3. J. R. Lewis, "Design Overview of Fiber Reinforced Superalloy Composites for the Space Shuttle Main Engine", NASA CR-168185, 1983.
4. D. A. Hopkins, "Nonlinear Analysis for High-Temperature Multilayered Fiber Composite Structures", NASA TM-83754, 1984.
5. O. C. Zienkiewicz, The Finite Element Method, 3rd ed., McGraw-Hill Book Company (UK) Limited, London, 1977.

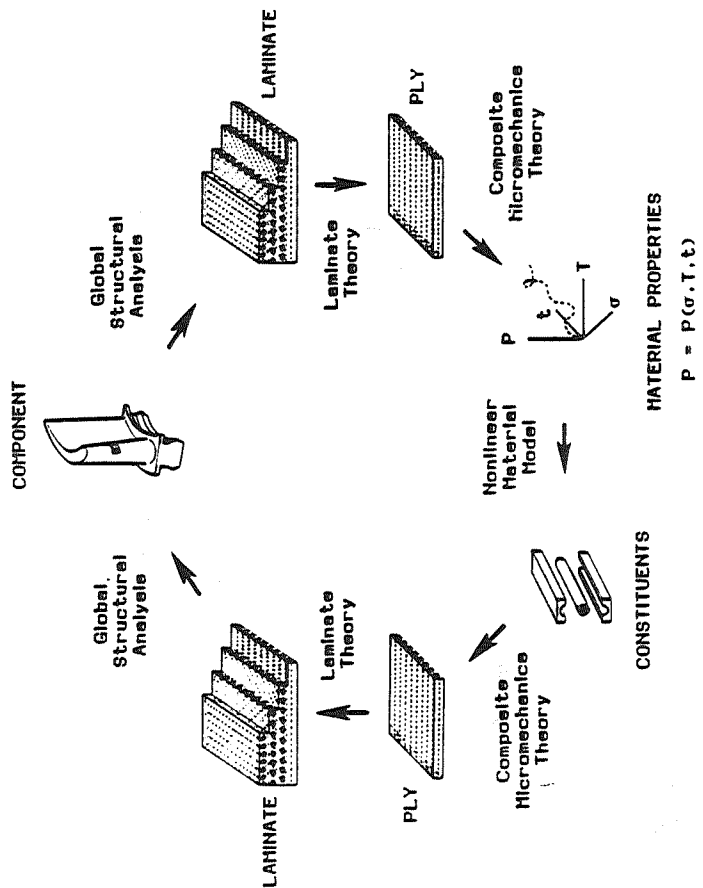


Figure 1 - Integrated Approach to Nonlinear Structural Analysis of FRS Turbine Blades

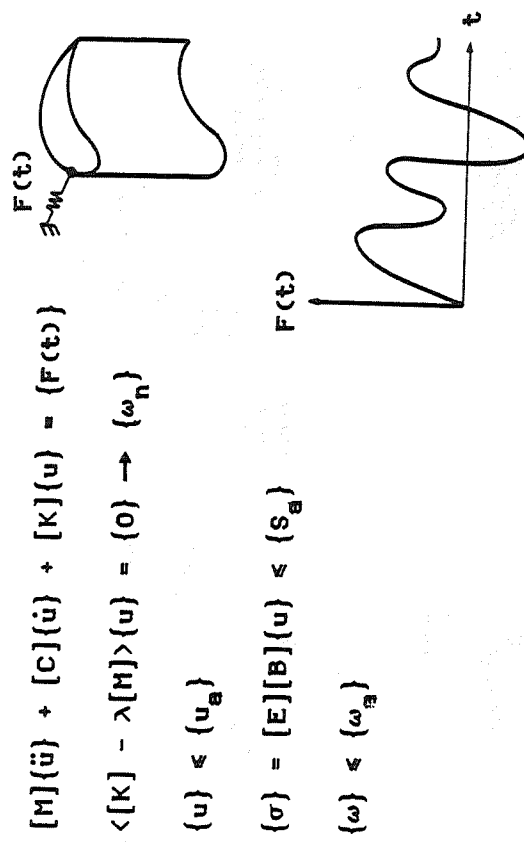


Figure 2 - Summary of Governing Equations for Global Linear Structural Analysis

$WThO_2/FeCrAlY$

$v_f = 0.50$

$t_1 = 0.010''$

$\theta = [\pm 45]_e$

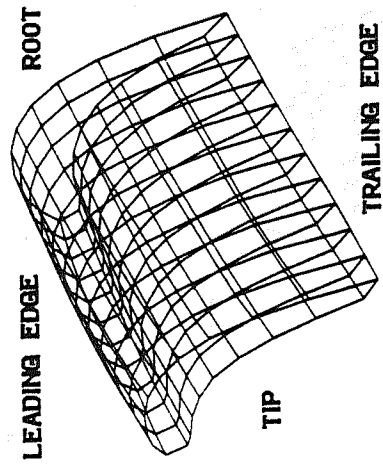
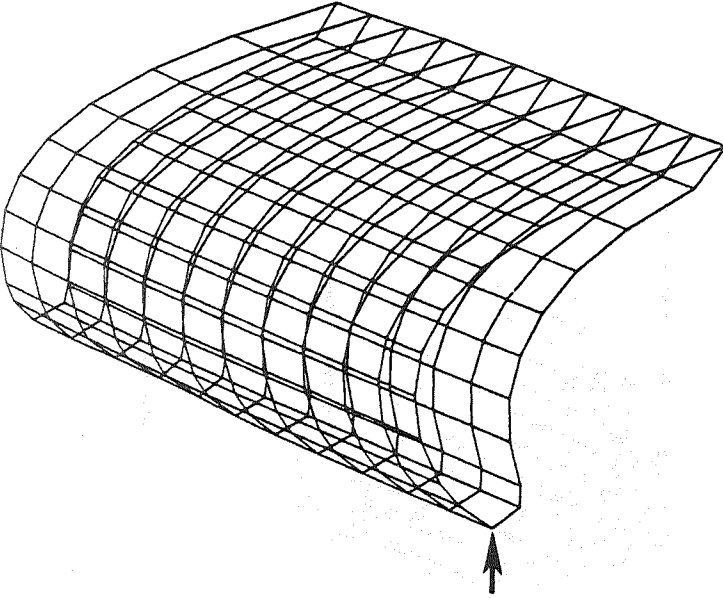


Figure 3 – FRS Turbine Blade Model and Material System



NODE NO. 11  
PLY NO. 1

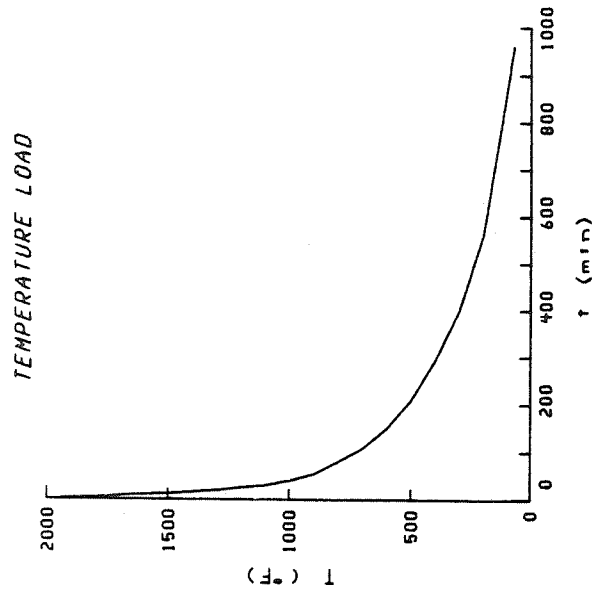


Figure 4 - Fabrication Cool-Down Process and Airfoil Root Leading Edge Location

NODE NO. 11  
 PLY NO. 1  
 F FIBER  
 M MATRIX  
 D INTERPHASE  
 L PLY

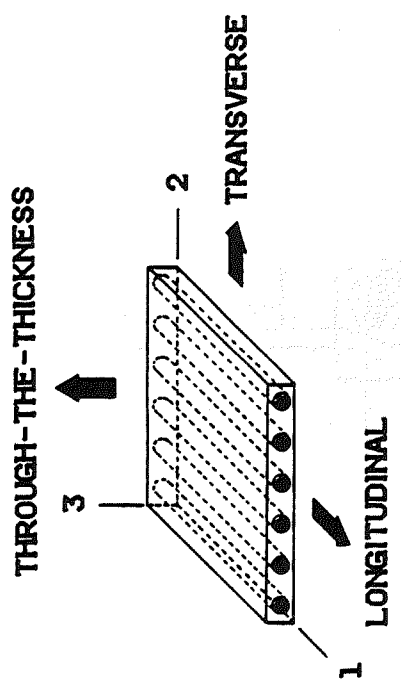
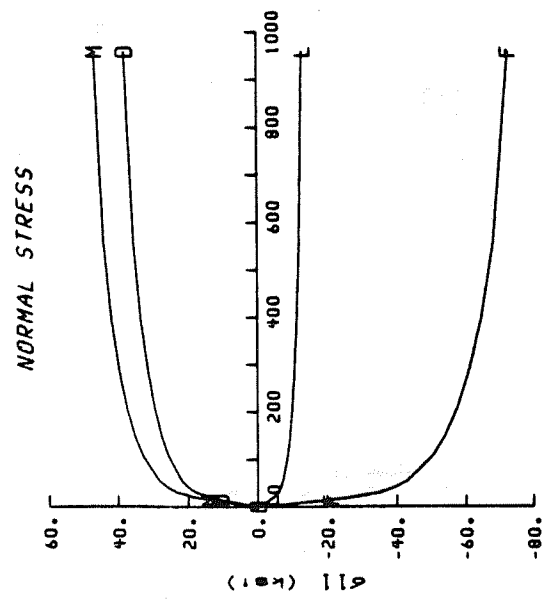


Figure 5 - Fabrication Residual Stress/Microstress ( $\sigma_{11}$ )  
 Build-up and Ply Coordinate System

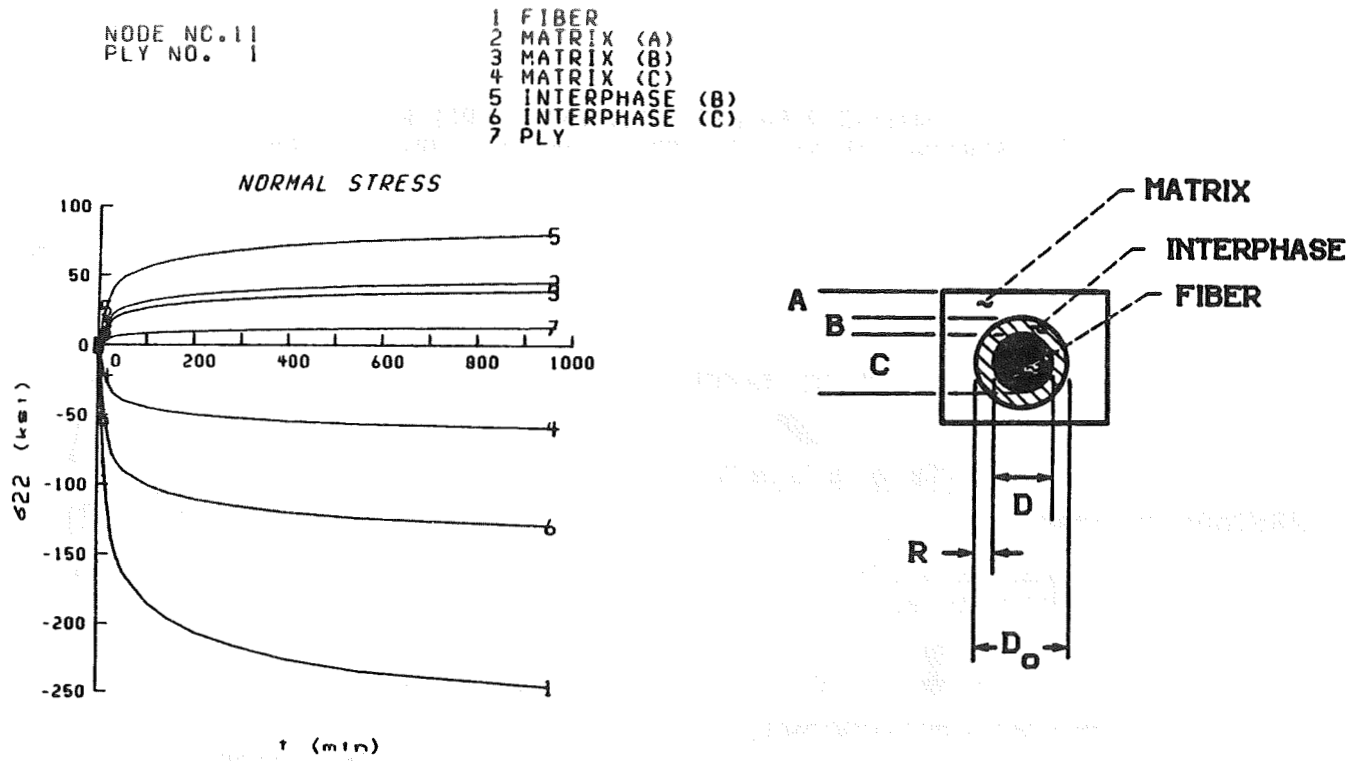


Figure 6 - Fabrication Residual Stress/Microstress ( $\sigma_{22}$ ) Build-up and Regions (A-B-C) of Nonuniformity

NODE NO. 11  
PLY NO. 1

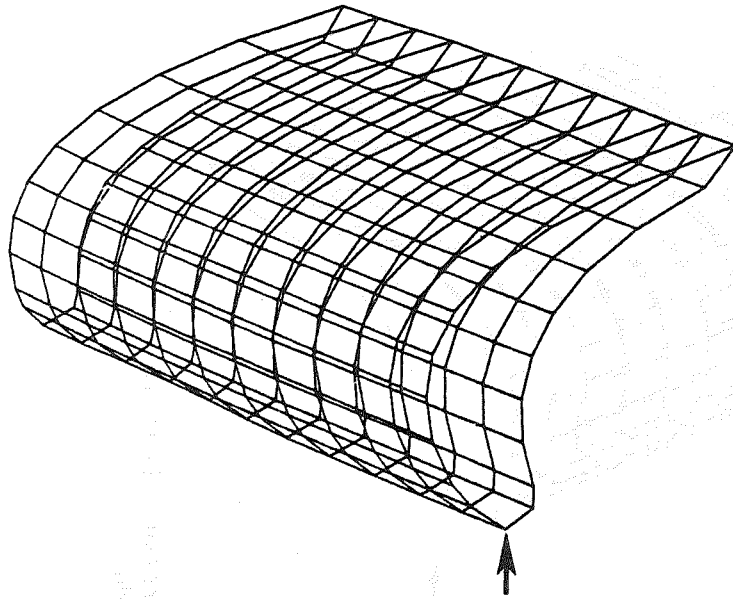
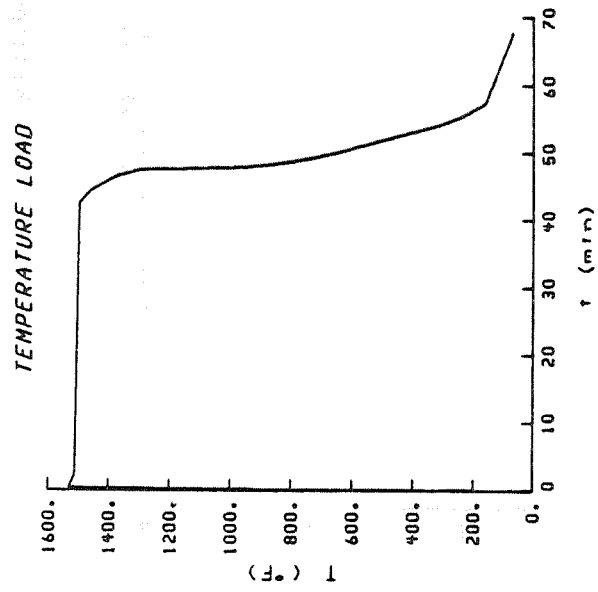


Figure 7 - Mission Cycle Temperature Load at Root Leading Edge

NODE NO. 11  
PLY NO. 1

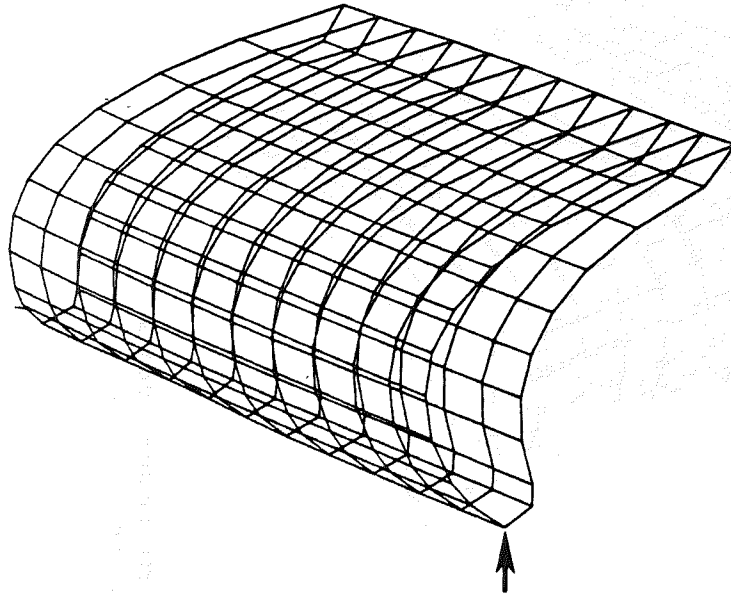
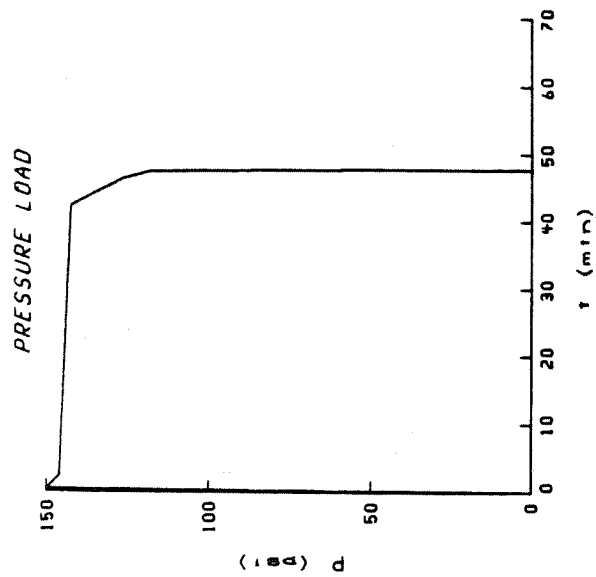


Figure 8 - Mission Cycle Pressure Load at Root Leading Edge

NODE NO. 11  
PLY NO. 1

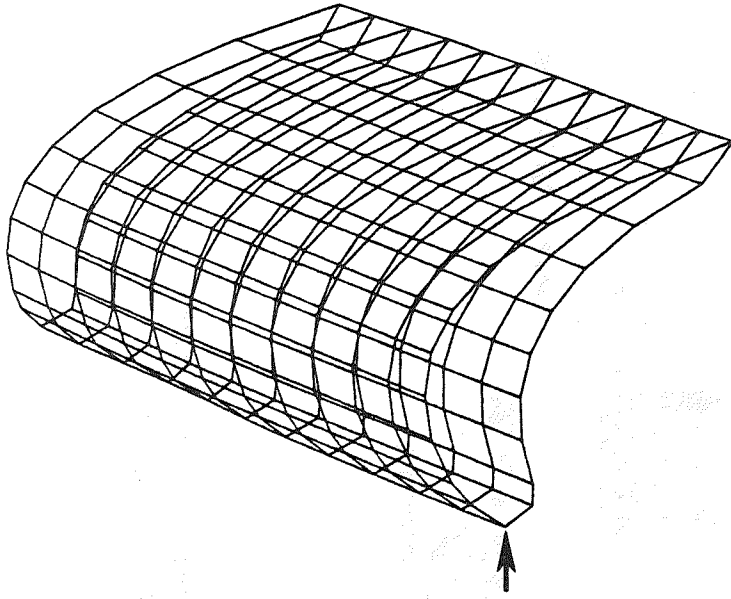
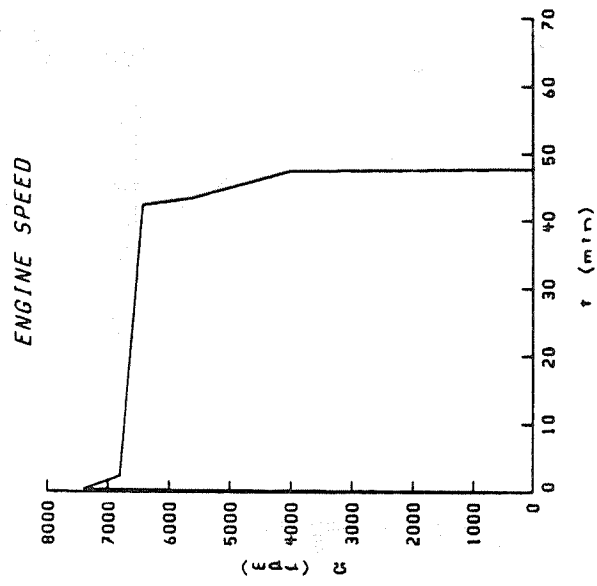


Figure 9 - Mission Cycle Engine Speed

NODE NO. 11  
PLY NO. 1

F FIBER  
M MATRIX  
D INTERPHASE  
L PLY

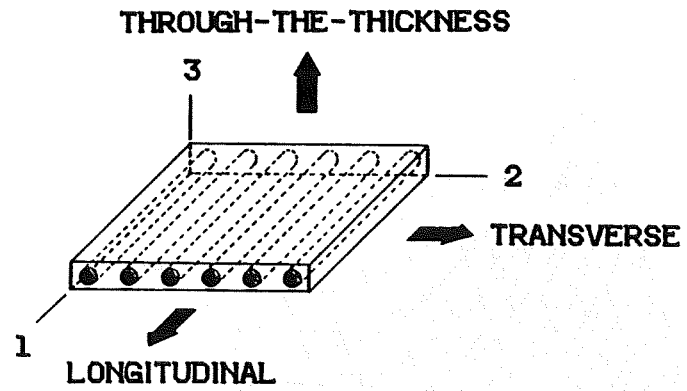
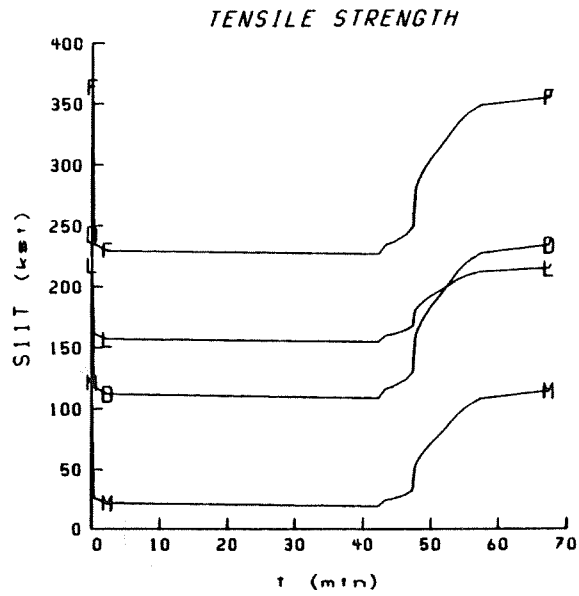


Figure 10 - Variation of Longitudinal Tensile Strength ( $S_{11T}$ )

F FIBER  
M MATRIX  
D INTERPHASE  
L PLY

NODE NO. 11  
PLY NO. 1

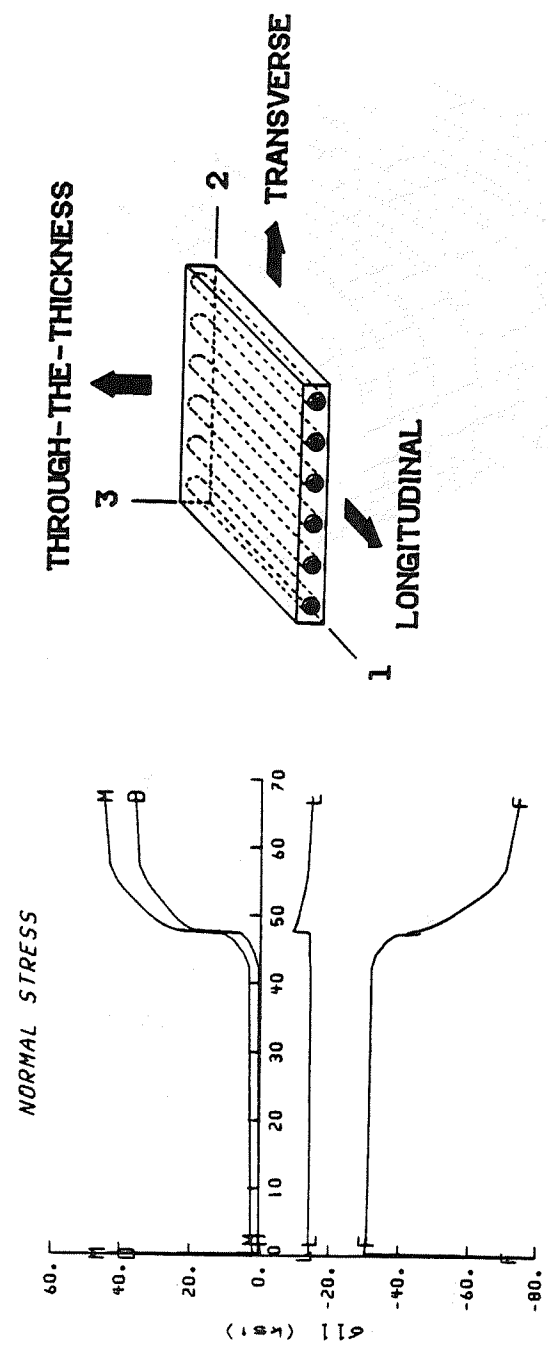


Figure 11 - Variation of Longitudinal Normal Stress/Microstress ( $\sigma_{11}$ )

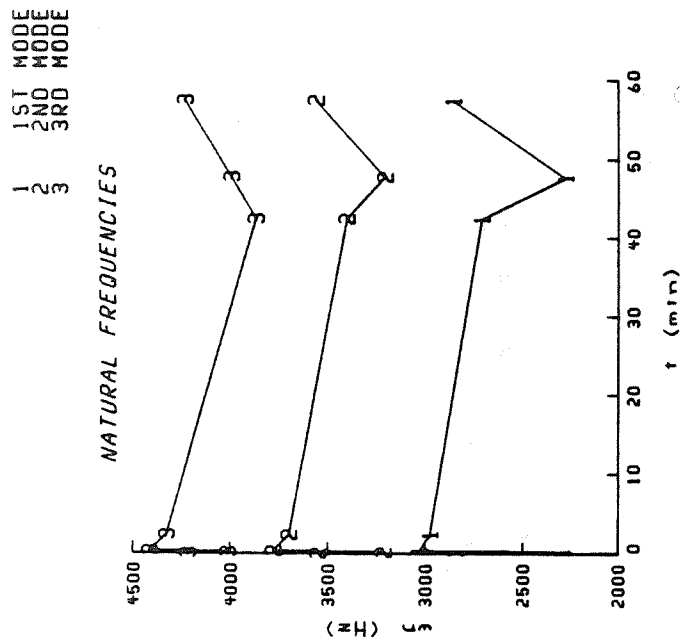
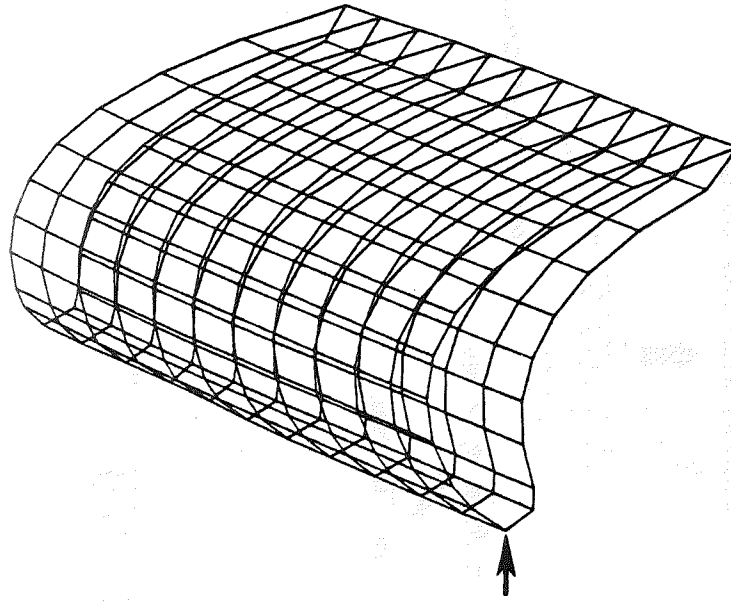


Figure 12 - Variation of Airfoil Natural Frequencies

## SESSION VI. ROTORDYNAMICS

LUKE A. SCHUTZENHOFER  
SYSTEMS DYNAMICS LABORATORY  
NASA, MARSHALL SPACE FLIGHT CENTER  
HUNTSVILLE, ALABAMA 35812 USA

### INTRODUCTION

In rotational systems that operate at high speeds, i.e., in excess of their critical speeds, and where the tolerances between rotating members are close, careful consideration must be given to rotordynamic design. In the design and development phase of the SSME, some of the rotordynamic design considerations were bearing loads, whirl instability, excessive deflections that result in rubbing, unbalance, deadband, sideforce, transmission of dynamic loads, rotor stack buildup/shift (internal rotor friction), etc. The purpose of rotordynamic design is to minimize all detrimental effects; this usually results in optimizing all of the aforementioned effects with respect to each other and with respect to system performance and life.

The rotordynamic analyses that are required to support the SSME design while sophisticated with respect to the present state-of-the-art still require additional advances because of the far reaching SSME operational conditions. The goal of the rotordynamic working group is to plan generic, but SSME related, research activities that ultimately lead to optimum rotordynamic design. Specifically, the plan is to improve the description and analysis methods pertaining to rotordynamic loads and response, to define more accurately and completely the significant rotordynamic forces, and to define design requirements

that influence rotordynamic loads, deflections and stability. Consistent with this plan, tasks have been defined to: (1) develop new analysis and simulation techniques, (2) define forces which result from the rotor and surroundings, (3) determine the effect of rubbing, (4) improve balancing, (5) develop damping methods, i.e., eddy-current and damping seals, (6) develop methods to quantify internal friction, and (7) develop supporting test apparatus.

The papers that have been presented during this session illustrate some of the accomplishments achieved under the aforementioned plan. The activities related to deadband by J. R. Glaese and A. P. Buckley have extended previous work to illustrate the nonlinear effects on loads and stability in addition to developing a limit cycle algorithm. The model applied by J. R. Glaese and A. P. Buckley was a generic model while in the paper presented by Dara W. Childs, a nonlinear multiple degree-of-freedom model was utilized. D. W. Childs' results showed that (1) a reduction in whirl frequency could result from bearing clearances, (2) the computed whirl frequency matches test data, (3) damping seals are effective toward suppressing subsynchronous whirl, and (4) under certain conditions synchronous bearing loads were more important than subsynchronous bearing loads.

Results of activities related to improved balancing were presented by M. J. Hine, C. E. Landis, and R. F. Beatty. The significant results achieved in this activity include the (1) definition of HPOTP and HPFTP balance sensitivity, (2) effectiveness of low speed multiplane balancing, (3) demonstration of potential improvements due to rotor stiffness, (4) definition of nonlinear deadband effects, (5) interrelationship between balance planes, balance runs and

speed, and (6) modeling of time dependent unbalance changes for analysis of self-enhanced unbalance. E. S. Zorzi and J. Walton also presented results related to unbalance. Their results showed (1) multiplane/multispeed balancing can decrease machine vibrations, (2) low speed single plane trim balancing does not allow control for high speed vibration suppression, (3) a low speed balancing approach may be acceptable provided sufficient balance planes are available, and (4) effects of bearing tilt were shown to minimally effect rotor unbalance response.

Results related to damping seals were presented by G. L. von Pragenau. These seals are a new technology and the results are encouraging in that these seals are retrofittable in machines beset with whirl instability. At the present time, damping seals are being tested in the SSME program. An apparatus to test damping seals is discussed in the paper presented by K. L. Cappel. This apparatus has been designed and fabrication is in progress. It will operate at speeds up to 37,000 rpm with various flow rates up to 300 gpm and pressures up to 2,300 psi. R. E. Cunningham, also addressed seals; however, his approach consisted of developing an eddy-current damper test rig. Results from the eddy-current damper program are as follows: (1) damping potential was demonstrated on a vibrating beam in liquid  $N_2$ , (2) computer codes were developed to characterize eddy-current dampers at cryogenic temperatures, (3) a 12,000 rpm rotating apparatus for testing several eddy-current dampers in liquid  $N_2$  was developed and tested, and (4) an eddy-current test rig that will operate to 36,000 rpm in liquid  $H_2$  was designed.

In summary, some of the papers presented in this session focused attention upon

understanding loads, response and whirl instability utilizing rotordynamic computational methods. Other papers emphasized activities related to unbalance with their end goal being to reduce the unbalance loads and consequential vibrations at high speed operations. A new method to suppress whirl instability with retrofittable damping seals was presented along with the development of a test apparatus to test damping seals at conditions similar to SSME operating condition. Finally, the test results related to eddy-current dampers were presented.

## EFFECTS OF BEARING DEADBANDS ON BEARING LOADS AND ROTOR STABILITY

John R. Glaese and Angelia P. Bukley  
Control Dynamics Company  
Huntsville, Alabama 35805

### Introduction

The problem of determining bearing loads and stability properties of rotating machines such as the turbopumps used in high performance rocket engines like the Space Shuttle Main Engine (SSME) is complex. Very high speeds are attained with significant fluid flows. As a consequence, bearing loads are potentially high with subsynchronous whirling likely. Typically, models used to analyze such systems are very complicated and nearly impossible to use for gaining insight into the basic phenomena involved. Linear models containing large numbers of degrees of freedom have been developed and applied to the analysis with mixed success. A significant nonlinearity is ignored by these models. The bearings typically have clearances of the order of .0005"-.0025". Since these machines are balanced to very high precision, the eccentricity of the rotor, i.e. the distance between the rotor center of mass and its geometric axis is of the same order or smaller in magnitude. Thus, bearing clearances or deadbands as they are more typically called, significantly affect the dynamics of these systems and must be taken into account. Taking this nonlinearity into account makes the analysis of the dynamics much more difficult. It is very desirable to have a simplified model of a turbopump which retains the significant driving forces known to be present but readily lends itself to analysis. Such a model is available and is usually referred to as the Jeffcott model. We have modified this model by adding deadband effects along with fluid seal forces as currently understood. Further, we have rewritten the equations of motion for the model in

polar coordinates. This formulation is more naturally suited to the symmetry of the problem because the whirl orbits tend to be circular.

In addition to seal forces and deadbands, we have added a constant side force to the model to account for the likely misalignments between bearings and seals and also to account for hydrodynamic forces resulting from pumping fluids which may not be perfectly balanced due to slight imperfections in the internal geometry of the pump. The side force and deadband effects, working together, significantly affect the stability properties of the system in an interesting way. Stability may be enhanced under proper combinations but is only local stability in that it is possible to drive the system into instability by impulsive disturbances or large rotor imbalances.

The Jeffcott rotor is closer to reality than it may appear to the casual observer. Periodic synchronous or nonsynchronous orbiting motions of the rotor, referred to as whirls, are normally the motions of the system exhibited. Such an orbital motion can be described by a planar model. Thus, values for the effective mass, stiffness, deadband and seal coefficients can be found which will approximate the behavior of the more complex models. While exact frequencies of critical speeds and stability boundaries cannot be inferred from Jeffcott models, very good qualitative behavior can be investigated with these models and refined by higher fidelity hybrid simulations. For this reason, we consider the augmented Jeffcott model as the model of choice for developing an understanding of rotor whirl phenomena.

### Force Models & System Equations of Motion

The assumed geometry for the derivation of the equations of motion of the simple rotor model is depicted in Figure 1. The vector  $\underline{r}$  is the displacement of the rotor center from its equilibrium position (rotor at rest). The angle  $\phi$  is the angle made by  $\underline{r}$  with the horizontal axis and is referred to as

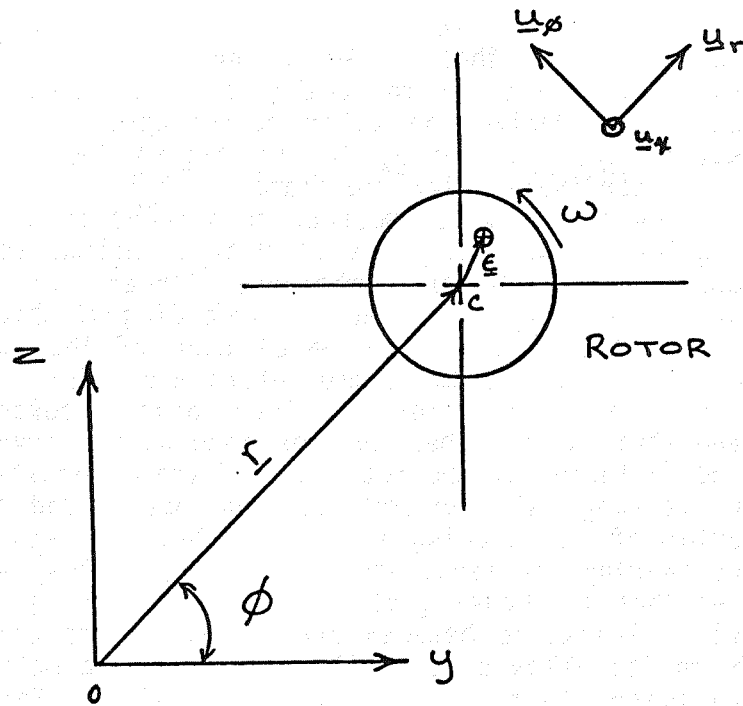


Figure 1. Assumed rotor geometry.

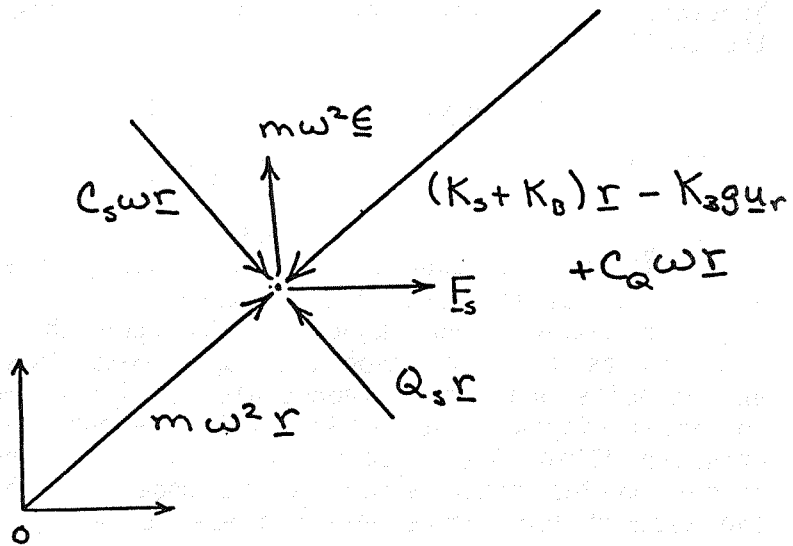


Figure 2. Vector force diagram.

the whirl angle. The rotor eccentricity is represented by the vector  $\underline{\varepsilon}$ , the magnitude of which is constant. The shaft speed is denoted by  $\omega$  and is assumed constant for the analysis. The equations of motion are derived in polar coordinates. The unit vectors  $\underline{u}_r$ ,  $\underline{u}_\phi$ , and  $\underline{u}_x$  in the figure indicate the polar coordinate reference frame.

The forces which must be considered in the formulation of the equations of motion include bearing forces, seal forces, imbalance forces, and side forces. Figure 2 is a vector force diagram which indicates the direction in which each of the various forces acts. The turbopump rotors are maintained in position by bearing forces. These bearing forces are generated by a rather complex interaction involving bending forces of the rotor shaft, the deformation of the bearing balls or rollers, the motion and deformation of the bearing races, the bearing retainers, the bearing carriers, etc. For our purposes, we assume that the bearing acts as a linear spring. However, clearances between bearing races and carriers or shafts allow some small region of free motion of the rotor shaft relative to its housing. For simplicity, we idealize the bearing balls or rollers as a uniform annular ring separating the rotor shaft and housing. The bearing force curve is idealized for the analysis as

$$\underline{F}_B = \begin{cases} K_B (\underline{r} - g \underline{u}_r) & |\underline{r}| > g \\ 0 & |\underline{r}| \leq g \end{cases} \quad (1)$$

where  $K_B$  is the bearing stiffness and  $g$  is the dead-band. If the magnitude of  $\underline{r}$  is less than  $g$ , then the bearing forces are assumed to be zero.

The fluid being pumped reacts upon the rotor with forces that are dependent upon rotor position and velocity and can be represented by linear models for small displacements.<sup>1</sup> The seals prevent the high pressure fluid from leaking away and also generate forces on the rotor which can be modeled linearly. The assumed form representing these forces is given by

$$\underline{F}_{\text{seal}} = -C_S \dot{\underline{r}} - K_S \underline{r} + Q_S \underline{u}_X \times \underline{r} + C_Q \underline{u}_X \times \dot{\underline{r}} \quad (2)$$

where  $K_S$  is the seal stiffness,  $C_S$  is the seal damping coefficient,  $Q_S$  is the cross coupling stiffness, and  $C_Q$  is the cross coupling damping. These forces have the potential to drive whirl instability.

The force due to the mass eccentricity is a rotating force whose magnitude varies as the square of the rotor speed and is directed toward the rotor center of mass. This force is potentially destructive and must be minimized by stringent balancing of the turbopump rotors. The form of this force is

$$\underline{F}_e = -m \omega^2 \underline{\epsilon} \quad (3)$$

with  $m$  representing the mass of the rotor. The values of the parameters in the equations above are chosen such that the system model is representative of the SSME high-pressure oxygen turbopump. These values are:  $K_B = 10^6$  lbs/in;  $K_S = 2.0 \times 10^5$  lbs/in;  $C_S = 200$  lbs-sec/in;  $C_Q = 40$  lbs-sec/in;  $Q_S = C_S \omega / 2$  lbs/in; and  $m = 0.20422$  lbs-sec<sup>2</sup>/in. Five deadband values are considered and are 0.5, 1.0, 1.5, 2.0, and 2.5 mils. Two values of rotor eccentricity are also used, they are 0.1 and 0.2 mils. Side force values range from 600 to 1200 pounds in the investigation.

The force equation for the system may be written as

$$m(\ddot{\underline{r}} + \underline{\ddot{\epsilon}}) = \sum_i \underline{F}_i \quad (4)$$

with the summation representing the forces due to the seals, bearings, and the side force. The vector equation for the system is, therefore

$$m\ddot{\underline{r}} = -K_B (\underline{r} - g\underline{u}_r) - K_S \underline{r} - C_S \dot{\underline{r}} + Q_S \underline{u}_X \times \underline{r} + C_Q \underline{u}_X \times \dot{\underline{r}} + \underline{F}_S + m \omega^2 \underline{\epsilon} \quad (5)$$

Performing the vector cross products and derivatives indicated in equation 5 above, the following second

order differential equations which describe the system are obtained.

$$\ddot{r} = \frac{-K_B}{m} (r-g) - \frac{K_S}{m} r - \frac{C_S}{m} \dot{r} - \frac{C_Q}{m} r\dot{\phi} + \frac{F_S}{m} \cos\phi + r\dot{\phi}^2 + \omega^2 \epsilon \cos(\omega t - \phi) \quad (6)$$

$$\ddot{\phi} = \frac{Q_S}{m} - \frac{C_S}{m} \dot{\phi} + \frac{C_Q}{m} \frac{\dot{r}}{r} - \frac{F_S}{m} \sin\phi - \frac{2r\dot{\phi}}{r} + \frac{\omega^2 \epsilon}{r} \sin(\omega t - \phi) \quad (7)$$

#### Limit Cycle Analysis

Analysis of the system is more readily carried out when the equations of motion are cast in state variable form.

Let

$$p_1 = r \quad p_2 = \dot{r} \quad p_3 = \phi \quad p_4 = \dot{\phi} \quad (8)$$

Then

$$\dot{p}_1 = p_2 \quad (9)$$

$$\dot{p}_2 = \frac{-(K_B + K_S)}{m} p_1 + K_B g - \frac{C_S}{m} p_2 - \frac{C_Q}{m} p_1 p_4 + \frac{F_S}{m} \cos p_3 + \omega^2 \epsilon \cos(\omega t - p_3) + p_1 + p_4^2 \quad (10)$$

$$\dot{p}_3 = p_4 \quad (11)$$

$$\dot{p}_4 = \frac{Q_s}{m} - \frac{C_s}{m} p_4 + \frac{C_Q p_2}{m p_1} - \frac{F_s}{m p_1} \sin p_3$$

$$+ \frac{\omega^2 \epsilon}{p_1} \sin (\omega t - p_3) - \frac{2 p_2 p_4}{p_1}$$
(12)

In this form, the system is amenable to solution by numerical methods. Three different types of orbits are observed when the system of equation is solved for different values of deadband, side force, and rotor eccentricity. These are referred to as A-type, B-type, and C-type motion.<sup>2</sup> Illustrations of the three are shown in Figures 3 through 5. A-type motion is periodic and does not encircle the origin. B-type motion is nonperiodic and somewhat random in nature. C-type is periodic and does surround the origin. The A-type and C-type motions are limit cycles.

To characterize the limit cycle motions present in the rotor system, an algorithm has been developed which will converge to a set of initial conditions for the four system states which, when input into a simulation of this system, will cause the system to immediately exhibit the limit cycle behavior. The algorithm is based on the fact that the function for which the limit cycle initial conditions are sought is periodic. That is, the orbit comes back around to the same point once each cycle. The idea is to determine that such a point exists and the values of the system states which satisfy this condition.

Given the state equations which describe the system, a solution to the states may be obtained through integration. The mathematical statement of the problem is:

$$\dot{\underline{p}} = \underline{f}(\underline{p}, t)$$
(13)

the solution to which is

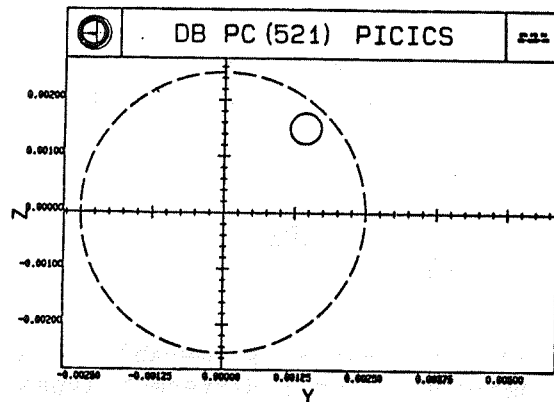


Figure 3. A-type rotor motion.

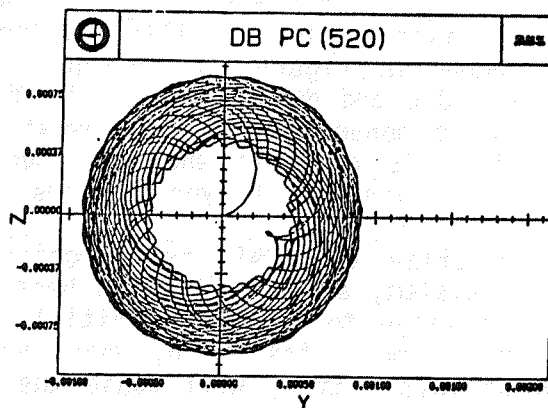


Figure 4. B-type rotor motion.

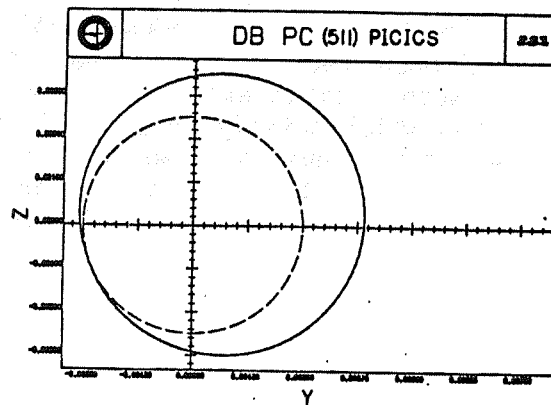


Figure 5. C-type rotor motion.

$$\underline{p}(t) = \underline{p}_0 + \int_0^t \underline{f}(\underline{p}, \tau) d\tau \quad (14)$$

where  $\underline{p}_0$  is some initial state. It is desired to determine the  $\underline{p}_0$  such that

$$\underline{p}(t) = \underline{p}_0 \quad \text{for } t = T \quad (15)$$

$$\text{where } T = \frac{2\pi}{\omega}, \quad (16)$$

the period of the function. In other words, we wish to determine  $\underline{p}_0$  so that the integral in Equation 14 is zero. The problem may be restated as

$$\underline{g}(\underline{p}) = \underline{p}(T) - \underline{p}_0 \quad (17)$$

If  $\underline{g}(\underline{p})$  can be driven to zero, then  $\underline{p}(T) = \underline{p}_0$ .

The function  $\underline{g}(\underline{p})$  may be approximated to 1st order by

$$\underline{g}(\underline{p}) = \underline{g}(\underline{p}_0) + \left. \frac{\partial \underline{g}}{\partial \underline{p}} \right|_{\underline{p}_0} \cdot \Delta \underline{p} \quad (18)$$

where  $\Delta \underline{p}$  is some incremental change in the state vector  $\underline{p}$ . This is the quantity to be determined. It will be added to the original state vector. Because we wish  $\underline{g}(\underline{p})$  to be zero, Equation 17 is rewritten as

$$\underline{0} = \underline{g}(\underline{p}_0) + \underline{J} \cdot (\underline{p} - \underline{p}_0) \quad (19)$$

where

$$\Delta \underline{p} = \underline{p} - \underline{p}_0 \quad (20)$$

and  $\underline{J}$  is the Jacobian of  $\underline{g}(\underline{p})$ . The solution for  $\Delta \underline{p}$  is

$$\Delta \underline{p} = \underline{J}^{-1} (-\underline{g}(\underline{p}_0)) . \quad (21)$$

A new set of initial states is formed as

$$\underline{p}_{0\text{new}} = \underline{p}_{0\text{old}} + \Delta \underline{p} . \quad (22)$$

For orbits which are C-type, another modification to the algorithm is required. Because the whirl angle,  $\phi$ , is not periodic but increasing with time, this method left unmodified will not converge to a solution. To force  $\phi$  to appear to be periodic, the value  $2\pi$  is subtracted from the  $\phi$  component of the state vector value at time  $t = T$ . This procedure will, in fact, allow the algorithm to converge to a solution to the C-type orbit initial conditions.

The plot of the limit cycle shown in Figure 3 is obtained using the initial conditions obtained with the algorithm described above. Figure 6 is a plot of that same limit cycle including the transients that occur when a simulation of the system is executed with the initial conditions set at zero. Likewise, the plot in Figure 5 is obtained using limit cycle initial conditions obtained with the algorithm. Figure 7 is a plot of the same orbit obtained from zero initial conditions.

### Stability Analysis

The approach taken in the determination of system stability is to examine the equations of motion, omitting the imbalance force terms. This procedure greatly simplifies the analysis. Our studies indicate that side forces and deadbands are influential on local stability. Under the influence of a side force, the rotor shifts to a position of equilibrium when no imbalance is present. The addition of an imbalance, in general, causes the rotor to whirl about the equilibrium point. The position of the equilibrium point is dependent upon the magnitude of the side force, the deadband, and the stiffness coefficients. The position of the equilibrium, with respect to the deadband, determines the type of orbit

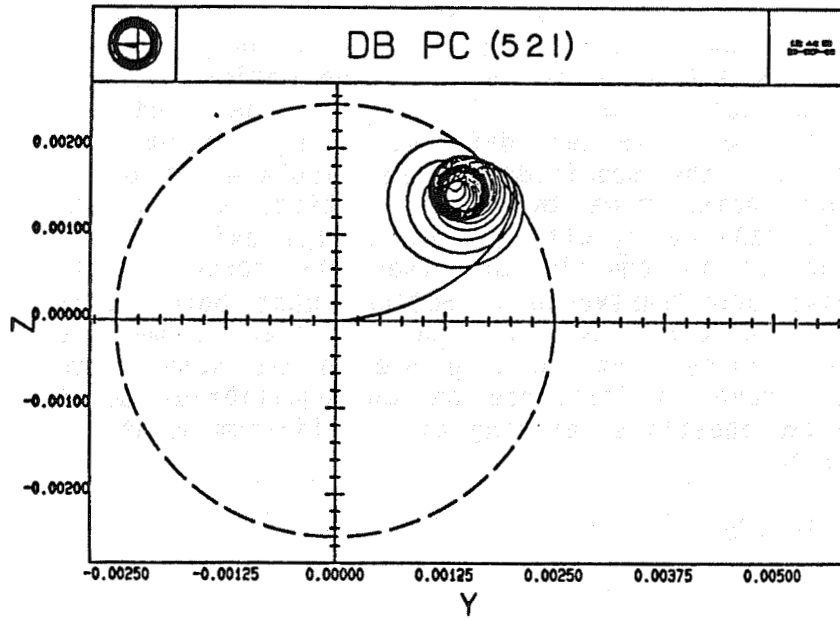


Figure 6. A-type motion with transients.

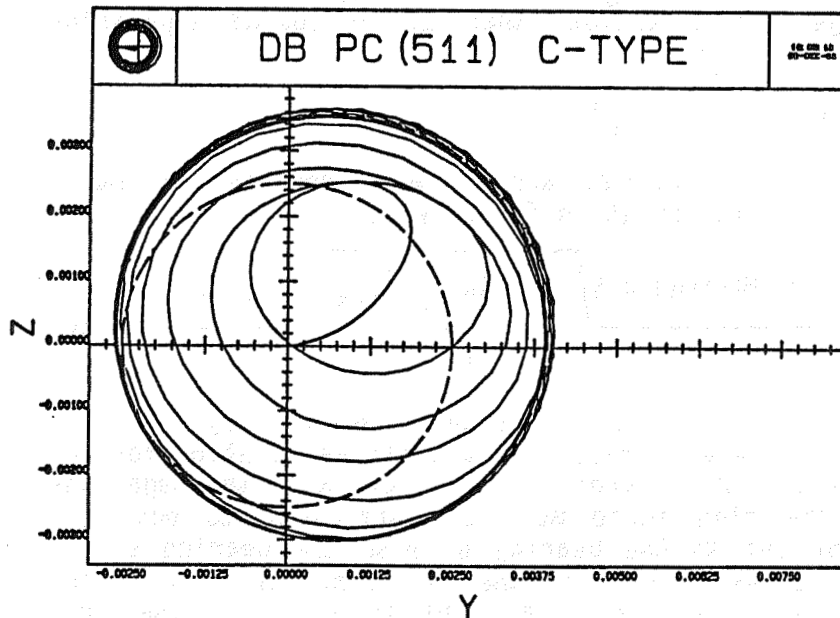


Figure 7. C-type motion with transients.

in which the rotor will whirl. Generally, if the equilibrium point is outside the deadband, the rotor exhibits A-type motion with C-type motion resulting if the equilibrium point is inside the deadband.

The two parameters defining the equilibrium point are  $r_0$ , the magnitude of the displacement of the rotor center from the rest position, and  $\phi_0$ , the angle made by  $r_0$  with the horizontal axis. If the rotor is in equilibrium, then the forces in the radial and transverse directions must both sum to zero. Because they have been balanced by the side force, force terms arising due to the spin of the shaft have no influence on the equilibrium point. The two equations defining the equilibrium point are, therefore,

$$K_B (r_0 - g) + K_S r_0 = F_S \cos \phi_0 \quad (23)$$

$$Q_S r_0 = F_S \sin \phi_0 \quad (24)$$

where  $F_S$  is used to denote side force magnitude. If we define  $F_r$  to be the side force in the radial direction and  $F_\phi$  to be the side force in the tangential direction, then the following expression is true.

$$F_S^2 = F_r^2 + F_\phi^2 \quad (25)$$

Using equations 23 and 24 with equation 25 makes possible the solution for  $r_0$  which is

$$r_0 = \frac{(K_B + K_S)K_B g \pm \sqrt{F_S^2 [(K_B + K_S)^2 + Q_S^2] - Q_S^2 K_B^2 g^2}}{(K_B + K_S)^2 + Q_S^2} \quad (26)$$

Note that when there is no deadband, any value of side force will result in a positive solution for  $r_0$ . However, in the presence of a deadband, the magnitude of the side force must be sufficient to push the rotor out to the bearing or else the bearing stiffness plays no role in the determination of  $r_0$ . The minimum side force required to overcome the seal

stiffness is denoted  $F_{SMIN}$  and is defined by the expression

$$F_{SMIN} = \sqrt{(K_S^2 + Q_S^2)g^2} \cdot \quad (27)$$

For any value of side force less than  $F_{SMIN}$ , the value of  $r_0$  is the positive solution to Equation 26 with  $K_B$  set to zero. For cases in which the side force is greater than  $F_{SMIN}$  and two positive solutions result, then  $r_0$  is equal to the larger of the two values because it will lie outside the deadband due to the side force being sufficient to move the rotor to such a position. The angle  $\phi_0$  is easily obtained once the solution for  $r_0$  is determined.

With the equilibrium points well in hand, we may now proceed. Recall the vector equation which describes the system. It is repeated here, with the imbalance term omitted.

$$\begin{aligned} m\ddot{\underline{r}} = & -K_B(r - g) \underline{u} (r - g) \underline{e}_r - K_S r \underline{e}_r + Q_S \underline{e}_x \times r \underline{e}_r \\ & - C_S \dot{\underline{r}} + C_Q \underline{e}_x \times \dot{\underline{r}} \end{aligned} \quad (28)$$

We make the following definitions for  $\underline{r}$  and  $\underline{e}_r$ ,

$$\underline{r} = \underline{r}_0 + \underline{\delta} \quad (29)$$

$$r = r_0 + \delta y \quad (30)$$

$$\underline{e}_r = \underline{e}_{r_0} + \delta \underline{e}_r \quad (31)$$

where  $\underline{r}_0$  is the equilibrium position vector,  $\underline{e}_{r_0}$  is the unit vector in the direction of  $\underline{r}_0$ , and  $\underline{\delta}$  and  $\delta \underline{e}_r$  are the perturbations associated with  $\underline{r}$  and  $\underline{e}_r$ , respectively. The radial component of  $\underline{r}$  with its perturbation is Equation 30. Another way to express  $\underline{e}_r$  is

$$\begin{aligned} \underline{e}_r = \frac{\underline{r}_0 + \underline{\delta}}{|\underline{r}_0 + \underline{\delta}|} = \frac{\underline{r}_0}{|\underline{r}_0|} + \frac{\underline{\delta}}{|\underline{r}_0|} - \frac{\underline{r}_0 \underline{r}_0}{|\underline{r}_0|^2} \cdot \underline{\delta} \\ + \dots \end{aligned} \quad (32)$$

which is equivalent to:

$$\underline{e}_r = \underline{e}_{r_0} + \frac{\delta z}{r_0} \underline{e}_\phi \quad (33)$$

We now examine the nonlinear deadband term in Equation 27. In the small and to a first order approximation,

$$\begin{aligned} & -K_B (r - g) u (r - g) \underline{e}_r \\ = & -K_B r_0 \underline{e}_{r_0} + K_B g \underline{e}_{r_0} - K_B \delta y \underline{e}_{r_0} - K_B \frac{(r_0 - g)}{r_0} \delta z \underline{e}_\phi \end{aligned} \quad (34)$$

with  $\delta y$  and  $\delta z$  being the small perturbations about the equilibrium. It follows, therefore, that in terms of the perturbation variables, the system may be expressed in the following form:

$$m \begin{bmatrix} \ddot{\delta y} \\ \ddot{\delta z} \end{bmatrix} = - \begin{bmatrix} K_s + K_B & Q \\ -Q & K_s + K_B (1 - g_0) \end{bmatrix} \begin{bmatrix} \delta y \\ \delta z \end{bmatrix} - \begin{bmatrix} C_s & C_Q \\ -C_Q & C_s \end{bmatrix} \begin{bmatrix} \dot{\delta y} \\ \dot{\delta z} \end{bmatrix} \quad (35)$$

$$\text{Where } g_0 = \frac{g}{r_0} .$$

The effects of side forces are now inherent in the formulation. Stability may be assessed through examination of equation 35. State assignments for the perturbation variables are given below.

$$x_1 = \delta y \quad x_2 = \dot{\delta y} \quad x_3 = \delta z \quad x_4 = \dot{\delta z} \quad (36)$$

Rewriting 34 in state variable format yields the following differential equations.

$$\dot{x}_1 = x_2 \quad (37)$$

$$\dot{x}_2 = -\frac{K}{m} x_1 - \frac{C_s}{m} x_2 - \frac{Q_s}{m} x_3 - \frac{C_Q}{m} x_4 \quad (38)$$

$$\dot{x}_3 = x_4 \quad (39)$$

$$\begin{aligned} \dot{x}_4 = & \frac{Q_s}{m} x_1 + \frac{C_Q}{m} x_2 - \frac{K_s + K_B (1 - g_0)}{m} x_3 \\ & - \frac{C_s}{m} x_4 \end{aligned} \quad (40)$$

The sum  $K_B + K_s$  has been replaced by  $K$  for simplicity's sake. The system matrix is formed as before from which the characteristic equation is derived by solving the determinant of  $[sI - A]$ .

$$\begin{aligned} P(s) = & \left[ s^2 + \frac{C_s}{m} s + K + \Delta^2 - \frac{Q_s^2}{m^2} \right] \\ & \left[ s^2 + \frac{C_s}{m} s + K - \Delta^2 - \frac{Q_s^2}{m^2} \right] \end{aligned} \quad (41)$$

The stability boundaries established are plotted in Figure 8. Several interesting facts are observed when this figure is examined. The stability boundary for a deadband of zero is a constant 4848 radians/second, the dashed curve in the figure. This is the same stability boundary which may be established for the simplest form of the system.<sup>3</sup> This frequency is considered to be the global stability boundary. That

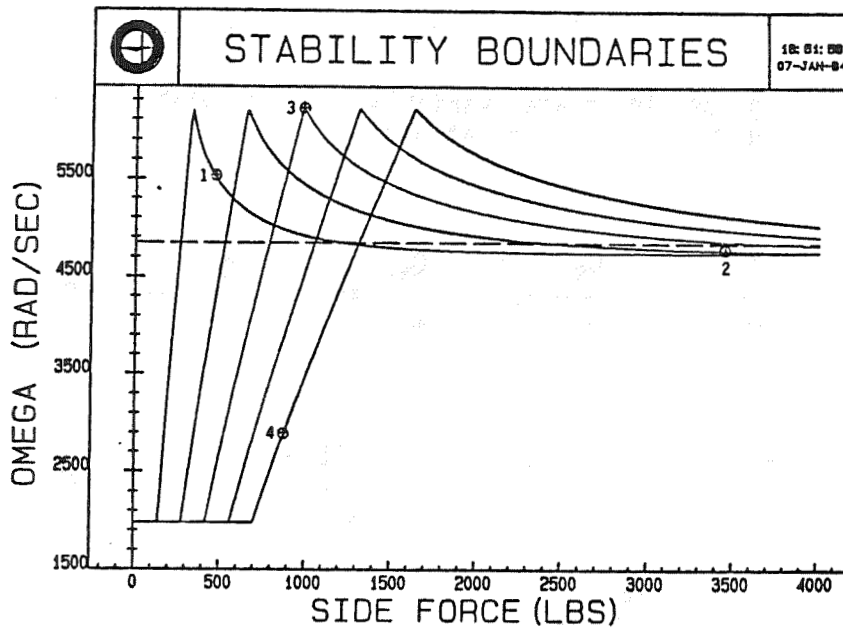


Figure 8. Stability boundaries.

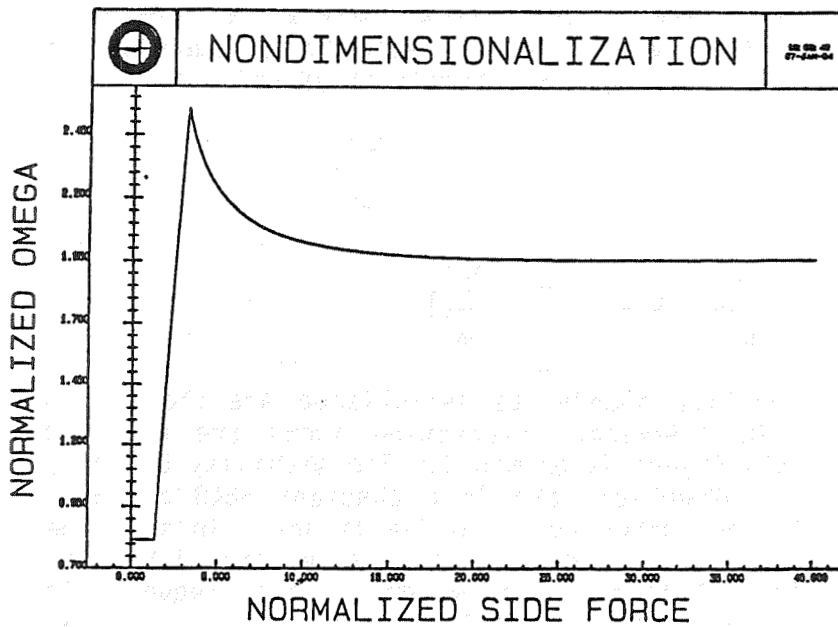


Figure 9. Nondimensionalized stability boundary.

is, the system is globally unstable when run at frequencies higher than this value. Local stability, or stability in the small, may be enhanced by other factors.

Notice that all five of the non-zero deadband stability curves are very similar in their general character. The maxima appear at approximately the same spin frequency as do their minima. We have shown that these curves do, indeed, collapse into a single curve when the system is nondimensionalized. To accomplish this, the units of displacement, force, and time are modified in such a way that the system parameters become unitless. Displacements are expressed in units of  $g$ , the deadband. Forces may be expressed as the product of the seal stiffness and deadband. Time is expressed in terms of the system natural frequency is  $\sqrt{m/(K_S + K_B)}$ . Figure 9 is a plot of the stability boundary for the normalized system. With this curve and the given conversion factors, one may determine the stability boundary for any deadband value.

### Bearing Loads Considerations

One of the major points of the study is to determine the effects of the system parameters on bearing loads. If these loads become too large, the effects are detrimental. Initially, we will look into this matter using a system with no side forces present, but with a rotor imbalance. We will then take into consideration the added effects of a side force present in the system.

Plotted in Figure 10 are the bearing loads which result when the rotor eccentricity is 0.1 mils. The deadband range is from 0.0 to 0.2 mils. The general behavior is that the smaller deadband produces the largest bearing load. This makes sense because the seal forces must be overcome before there is any interaction between the rotor and the bearings. The more distance between the rotor and the bearing there is, the more effect the seal forces have. It has been shown that if the rotor eccentricity is doubled, the bearing loads also double if all other parameters are left unchanged.<sup>3</sup>

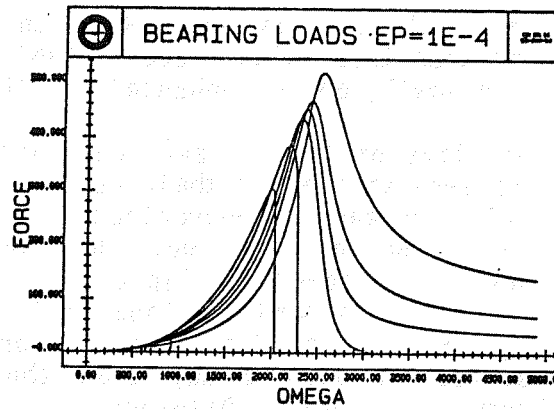


Figure 10. Bearing force curves.

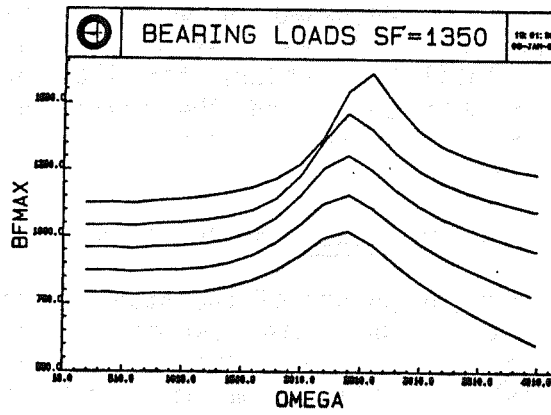


Figure 11. Bearing force curves.

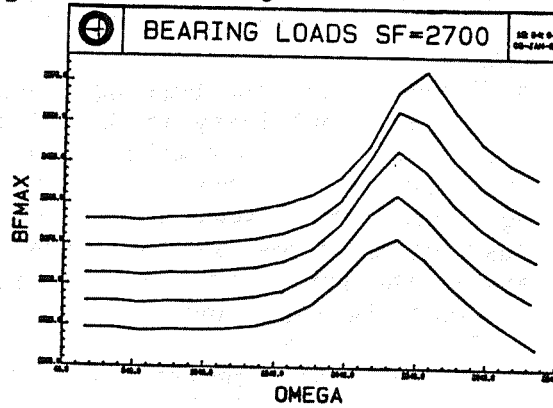


Figure 12. Bearing force curves.

Bearing load analysis is performed for two non-zero side force values. A value of side force is chosen so that it is always greater than  $F_{SMIN}$  for any of the five deadbands considered up to a frequency of 5000 radians per second. Figure 11 is a plot of the bearing loads for the deadbands of 0.5 to 2.5 mils for the side force of 1350 pounds. The maximum bearing loads occur at the system natural frequency of approximately 2424 radians/second, the smallest deadband producing the largest load. The load curves are plotted only up to a shaft spin frequency of 4000 radians because the system becomes unstable for frequencies higher than that. The presence of the rotor eccentricity of 0.2 mils is responsible for the unstable behavior.

A similar family of curves is produced when the side force is increased to twice that of the "minimum" side force, or, 2700 pounds. The plots of these bearing loads are given in Figure 12. The same general behavior is exhibited as before. Instability occurs somewhat sooner, at 3400 radians/second. The loads are much greater, as well.

The curves presented were generated using the simulation to determine the maximum rotor displacement, after steady-state is achieved. Having this value, it is a simple matter to compute the bearing load. Equation 43 is used.

$$BF_{MAX} = K_B(r_{MAX} - g) \quad (43)$$

### Conclusions

In the previous sections we have discussed the modeling and analysis of the problem. It is now time to review and summarize our results.

1. Observed 3 motion types called A, B, C;
  - A - Periodic but does not enclose origin, may include higher harmonics;
  - B - Nonperiodic;
  - C - Periodic enclosing origin, synchronous or nonsynchronous;

2. Limit Cycle Algorithm developed and employed, both A & C types observed.

3. Deadband does not affect stability-in-the-large.

4. Stability-in-the-small are affected (enhanced) by deadband and sideforce.

5. Bearing loads are largest for C-type motion.

6. Side force acting in concert with deadband effects may either increase or decrease bearing loads.

7. Bearing loads in a stable pump are determined primarily by rotor imbalance and side forces.

These results are quite significant in our understanding of the effects of bearing deadbands. Harmonics of synchronous and nonsynchronous oscillations have been observed. This is clearly a nonlinear effect. Stable limit cycle whirls have been observed occurring at synchronous and nonsynchronous rotor speeds in our results.

The limit cycle algorithm that we have developed can be generalized to more complex turbopump models with more degrees of freedom. It will be useful for loads analysis with nonlinear forces for rotor dynamics and other applications. It is capable of converging to periodic motions (solutions) which generally result in the highest load-producing conditions.

Since stability-in-the-large is ultimately determined by behavior at extremely large amplitudes of motion, deadband effects become negligible. Thus, linear models remain adequate for analysis of global stability properties. Stability-in-the-small is significantly altered by the nonlinear effects of deadbands. We have shown that sideforces can significantly enhance stability provided imbalance offsets and/or impulsive disturbances do not cause significant displacement from the equilibrium position of the rotor.

Bearing loads have been shown to be significantly modified by deadband effects. Critical speeds are altered. Loads may increase or decrease. The shape of the critical response curve is altered with higher loading at lower frequencies due to the deadband.

These results have been obtained using a relatively simple 2 degree-of-freedom model. This may lead one to believe the results are not applicable to real machines. This is not the case, however, and indeed one can argue and demonstrate with more sophisticated models that these effects are real. Since rotor responses are most often periodic, such motions can be described adequately by an effective mass responding to effective stiffnesses and deadbands, i.e., a 2-dimensional model. Thus, our results are at least qualitatively valid for the description of turbo-pump motions.

### References

1. Gunter, Edgar J. Jr., Dynamic Stability of Rotor-Bearing Systems, NASA SP-113; 1966.
2. Several G. C. Marshall Space Flight Center, ED14, Internal Memoranda and presentations covering period 1978-1980.
3. Final Report on Contract No. NAS8-35050, "Effects of Bearing Deadbands on Bearing Loads and Rotor Stability", Prepared for G. C. Marshall Space Flight Center by Control Dynamics Company, Huntsville, Alabama, January, 1984.

PRELIMINARY RESULTS ON PASSIVE EDDY CURRENT DAMPER  
TECHNOLOGY FOR SSME TURBOMACHINERY

Robert E. Cunningham  
NASA Lewis Research Center  
Cleveland, Ohio 44135

ABSTRACT

Some preliminary results have been obtained for the dynamic response of a rotor operating over a speed range of 800 to 10,000 rpm. Amplitude frequency plots show the lateral vibratory response of an unbalanced rotor with and without external damping. The mode of damping is by means of eddy currents generated with 4 "c" shaped permanent magnets installed at the lower bearing of a vertically oriented rotor. The lower ball bearing and its damper assembly are totally immersed in liquid nitrogen at a temperature of  $-197^{\circ}\text{C}$  ( $-320^{\circ}\text{F}$ ). These preliminary results for a referenced or base line passive eddy current damper assembly show that the amplitude of synchronous vibration is reduced at the resonant frequency. Measured damping coefficients were calculated to  $\mathcal{P} = .086$ ; this compares with a theoretically calculated value of  $\mathcal{P} = .079$ .

INTRODUCTION

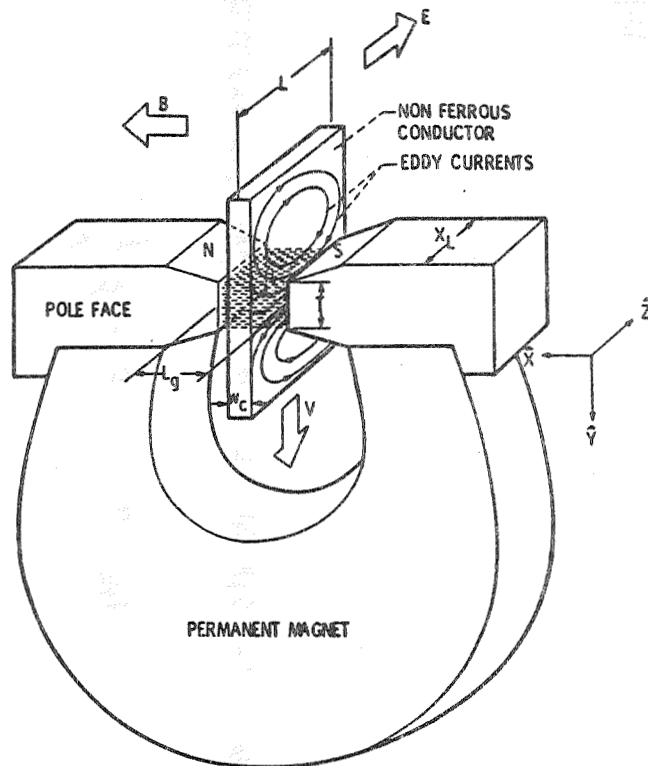
- o Improved performance and durability of SSME turbopumps will depend, to a large degree, on an effective and predictable mechanism for dissipating vibrational energy in the rotors.
- o Properly designed dampers located at or near bearing supports can be effective in controlling vibrations produced by rotor unbalance, commonly known as synchronous whirl.
- o Dampers can also be effective in controlling non-synchronous whirl, the type often produced by shaft internal hysteresis, hydrodynamic seals, interference fits, tie bolts, etc.
- o Dampers can reduce the dependence on ultra precision balancing or the need for frequent rebalancing.
- o Dampers along with properly designed flexible bearing supports can reduce magnitude of transmitted forces thru the ball bearings to the casing, and thus extend ball bearing life.
- o A unique method of damping is by means of eddy current generation in a conductor caused to vibrate in a magnetic flux field.
- o The low temperatures encountered in the turbopumps actually increase the available energy dissipation and thereby make this mechanism an attractive candidate for SSME turbomachinery.

- o An objective of this work is to verify by experimentation the derived relationship that define the eddy current damping coefficient.
- o A rotating rest apparatus was designed and fabricated in order to properly evaluate candidate damper designs over a speed range of 800 to 10,000 rpm while operating in liquid nitrogen at  $-195^{\circ}\text{C}$ .
- o Measured rotor response to unbalance forces with and without applied damping are compared to theoretical results from a computer code.

### SUMMARY AND CONCLUSIONS

- o Demonstrated the successful attenuation of synchronous vibration at the first system resonance using passive eddy current damping in liquid nitrogen.
- o Obtained reasonable agreement between theoretical and measured response of an unbalanced rotor for both the undamped and damped cases. A measured damping coefficient of  $\mathcal{D} = .086$  was obtained while the predicted damping coefficient was calculated to be  $\mathcal{D} = .079$ .

SCHMATIC OF EDDY CURRENT DAMPER SHOWING  
EDDY CURRENT PATHS IN CONDUCTOR



- STATING FARADAY'S AND LENZ'S LAWS IN EQUATION FORM

IT CAN BE SHOWN THAT:

$$(eq. 1) \quad F_M = \frac{B^2 \ell^2}{R} \quad V \quad (\text{NEWTONS})$$

WHERE: B, FLUX DENSITY,  $\frac{\text{WEBERS}}{\text{M}^2}$

$\ell$ , CONDUCTOR LENGTH, M

R, RESISTANCE, ohms

V, VELOCITY, M/sec

- OBTAINING  $F_M$  IN TERMS OF MATERIAL CONDUCTIVITY WHERE:

$$(eq. 2) \quad R = \rho \frac{\ell}{A}$$

WHERE  $\rho$ , ohms-meters

AND

$$(eq. 3) \quad F_M = \left( \frac{B^2 \ell A}{\rho} \right) V$$

(NEWTONS)

V-2184

- THE CONSTANT OF PROPORTIONALITY IS KNOWN AS THE DAMPING COEFFICIENT,  $C_D$  THEREFORE:

$$(eq. 4) \quad F_d = C_D \quad V \quad (\text{NEWTONS})$$

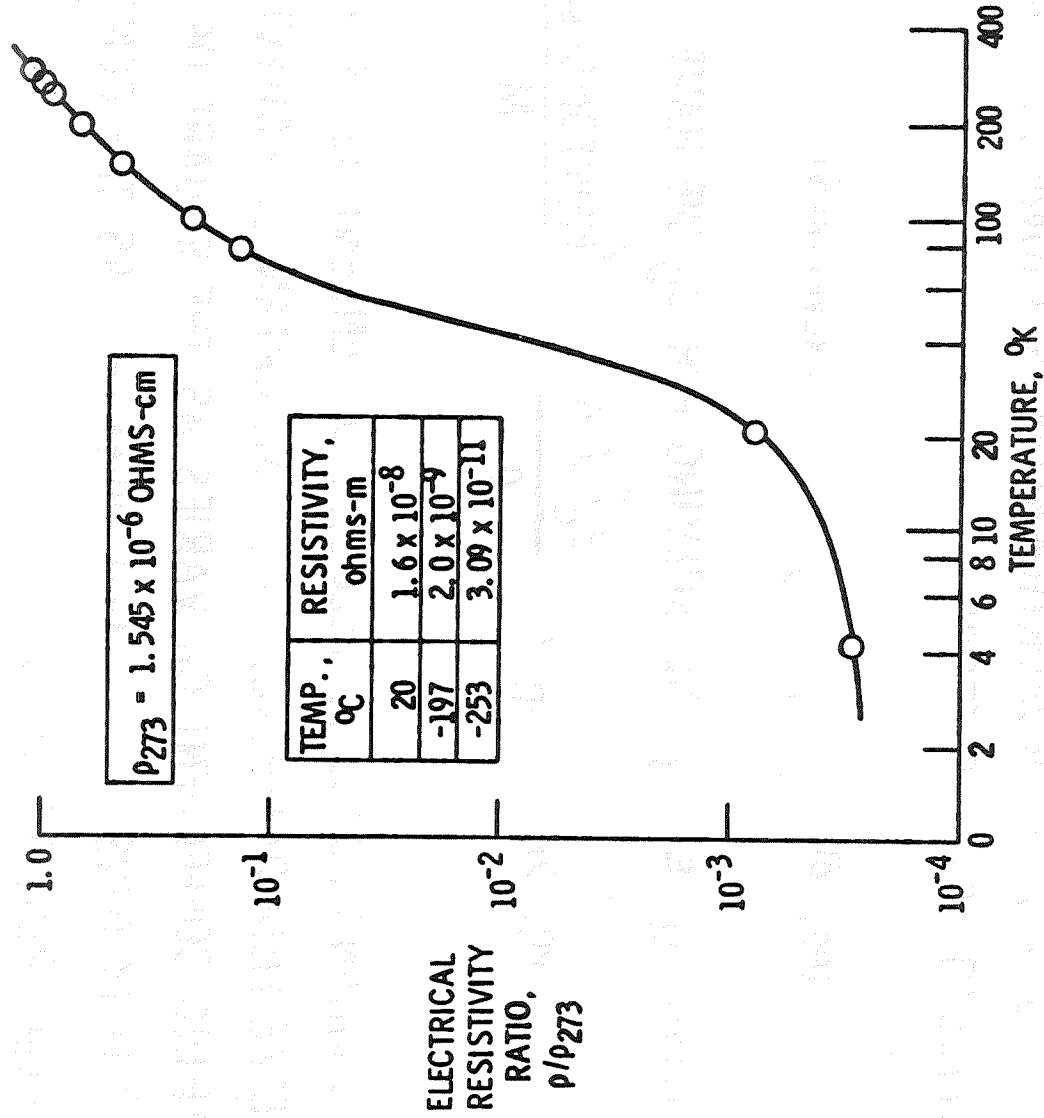
- EQUATING  $F_M \dot{\epsilon}$  &  $F_d$  AND SOLVING FOR  $C_D$  WE HAVE

$$(eq. 5) \quad C_D = \frac{B_g^2 \ell A}{\rho} \left( \frac{\text{NEWTONS-sec}}{M} \right)$$

- THE DAMPING FORCE IS VELOCITY DEPENDENT AS IS VISCOUS OIL SQUEEZE FILM DAMPING. MOST IMPORTANTLY HOWEVER THE DAMPING COEFFICIENT  $C_D$  VARIES AS THE SQUARE OF THE MAGNETIC FLUX DENSITY,  $B_g$  AND INVERSELY AS THE CONDUCTOR MATERIAL RESISTIVITY  $\rho$

# ELECTRICAL RESISTIVITY OF COPPER AS A FUNCTION OF TEMPERATURE

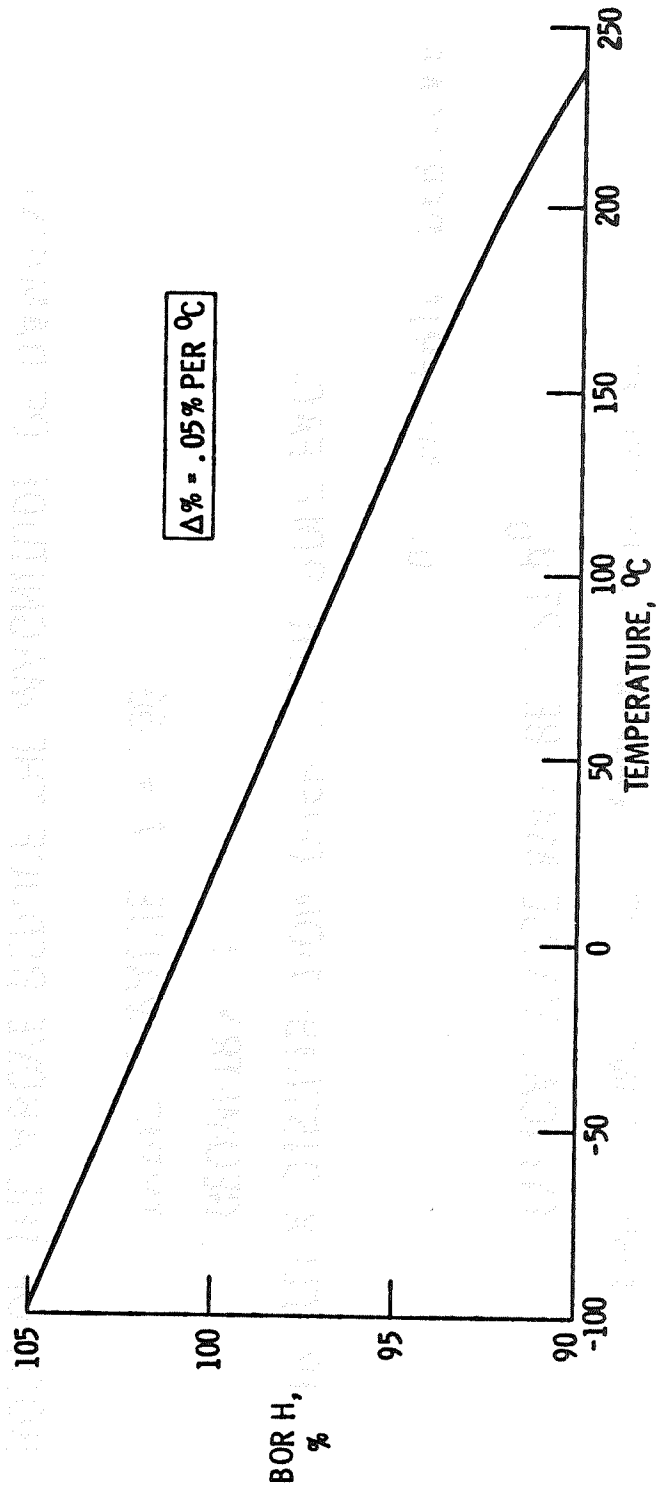
REF: NBS CRYOGENIC DATA MEMORANDUM NO. M-11



CS-84-0496

# REVERSIBLE TEMPERATURE CHANGES IN REMNANCE FLUX AND COERCIVITY

REF: ARNOLD ENG'R



● THE EQUATION FOR DAMPING COEFFICIENT  $C_D$  MUST BE MODIFIED TO ACCOUNT FOR:

(A) FINITE CONDUCTOR GEOMETRY, INDUCTIVITY,  $L_i$   
TYPICAL VALUE MAY BE,  $.27 \mu_0$

$\mu_0$ , MATERIAL PERMEABILITY

(B) FLUX DISTRIBUTION OVER FINITE POLE FACE  
GEOMETRY,  $f$

TYPICAL VALUE,  $f = .66$

● BOTH OF THE ABOVE REDUCE THE MAGNITUDE OF DAMPING COEFFICIENT THEORETICALLY AVAILABLE

$$C_D' = \frac{(f B_g)^2 \ell A L_i}{\rho \mu_0} \left( \frac{N\text{-sec}}{M} \right)$$

THE FLUX DENSITY ACROSS AN AIR GAP, REF. FIG. 1, IS DETERMINED BY THE MAGNET MATERIAL AND ITS HYSTERESIS CURVE AND THE MAGNET GEOMETRY. THE FOLLOWING RELATIONSHIP IS GIVEN IN MAGNET DESIGN MANUALS.

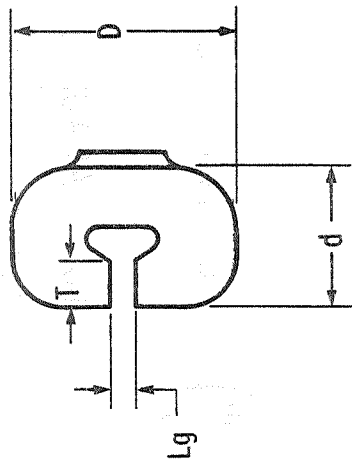
$$B_g = \left( \frac{A_m}{A_g} \right) \frac{B_R}{\sigma}$$

WHERE:  $A_m$ , CROSS SECTIONAL AREA  
 NORMAL TO MAGNETIC AXIS  
 $A_g$ , CROSS SECTIONAL AREA OF  
 POLE FACES  
 $B_R$ , REMNANCE FLUX  
 $\sigma$  FLUX LEAKAGE

$\left( \frac{A_m}{A_g} \right)$ , FOCUSING EFFECT

$\sigma$ , FLUX LEAKAGE IS A FUNCTION OF GEOMETRY. TYPICAL VALUES FOR "C" SHAPED MAGNET 2.5 TO 4

PERMANENT MAGNET DESIGNS FOR EXPERIMENTAL  
EVALUATION IN LIQUID N<sub>2</sub> AND LIQUID H<sub>2</sub>

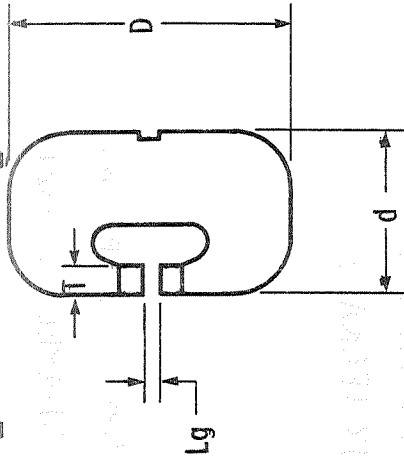


DESIGN A

"c" MAGNET MATERIAL, ALNICO V

DIMENSIONS

- D = 2.4 in
- d = 1.5 in
- T = .5 in
- Lg = .25 in
- W = 1.2 in



DESIGN B\*

"c" MAGNET MATERIAL, ALNICO V  
POLE FACES, SAMARIUM COBALT

DIMENSIONS

- D = 3.0 in
- d = 1.75 in
- T = .313 in
- Lg = .156 in
- W = 1.2 in

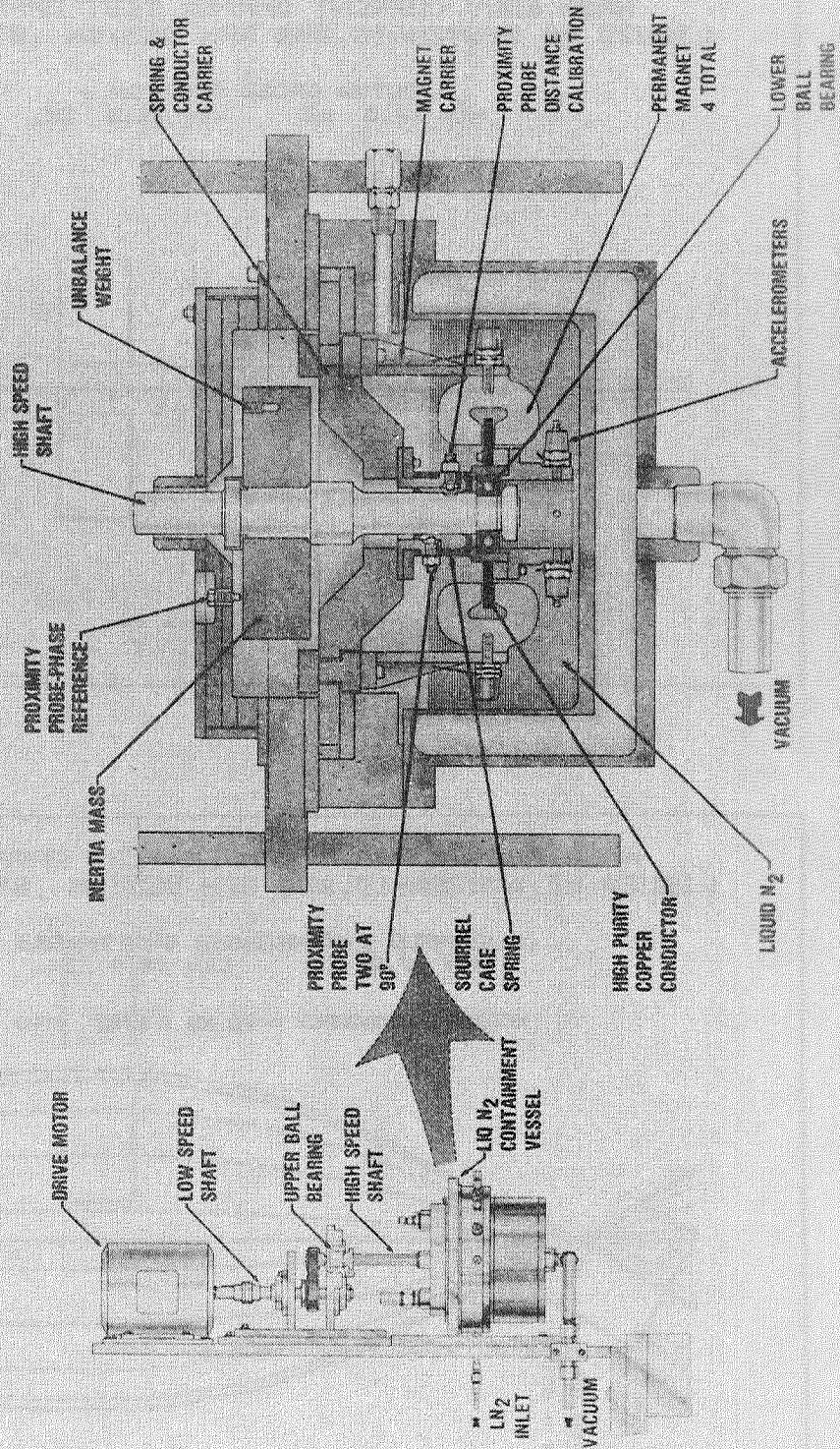
THEORETICAL DAMPING COEFFICIENTS

- ROOM TEMP. (20° C)  
C<sub>D</sub> = .122 lb-sec/in
- LIQUID N<sub>2</sub> (-197° C)  
C<sub>D</sub> = 1.02 lb-sec/in
- LIQUID H<sub>2</sub> (-253° C)  
C<sub>D</sub> = 66.2 lb-sec/in
- ROOM TEMP (20° C)  
C<sub>D</sub> = 1.31 lb-sec/in
- LIQUID N<sub>2</sub> (-197° C)  
C<sub>D</sub> = 10.95 lb-sec/in
- LIQUID H<sub>2</sub> (-253° C)  
C<sub>D</sub> = 707 lb-sec/in

\* OPTIMIZED GEOMETRY, COMPUTER PROGRAM

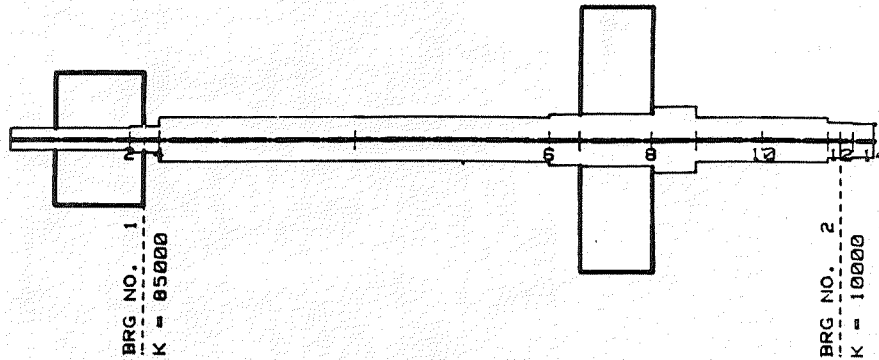
# EDDY CURRENT DAMPER

## TEST APPARATUS - LN2



NASA EDDY CURRENT DAMPER TEST APPARATUS  
 LIQUID N2 SYSTEM-15,000 RPM DESIGN ,STIFF SHAFT

- ROTOR CROSS SECTION -  
 Mt= 17.5 LB Lt= 19.5 IN.

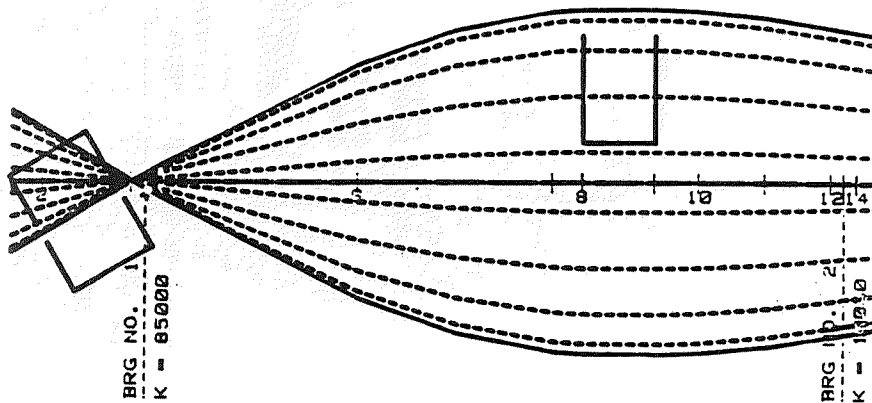


NO. OF STATIONS = 14  
 NO. OF BEARINGS (&SEALS) = 2

NASA EDDY CURRENT DAMPER TEST APPARATUS  
 LIQUID N2 SYSTEM-15,000 RPM DESIGN ,STIFF SHAFT

UNDAMPED SYNCHRONOUS SHAFTMODES  
 Mt= 17.5 LB Lt= 19.5 IN.

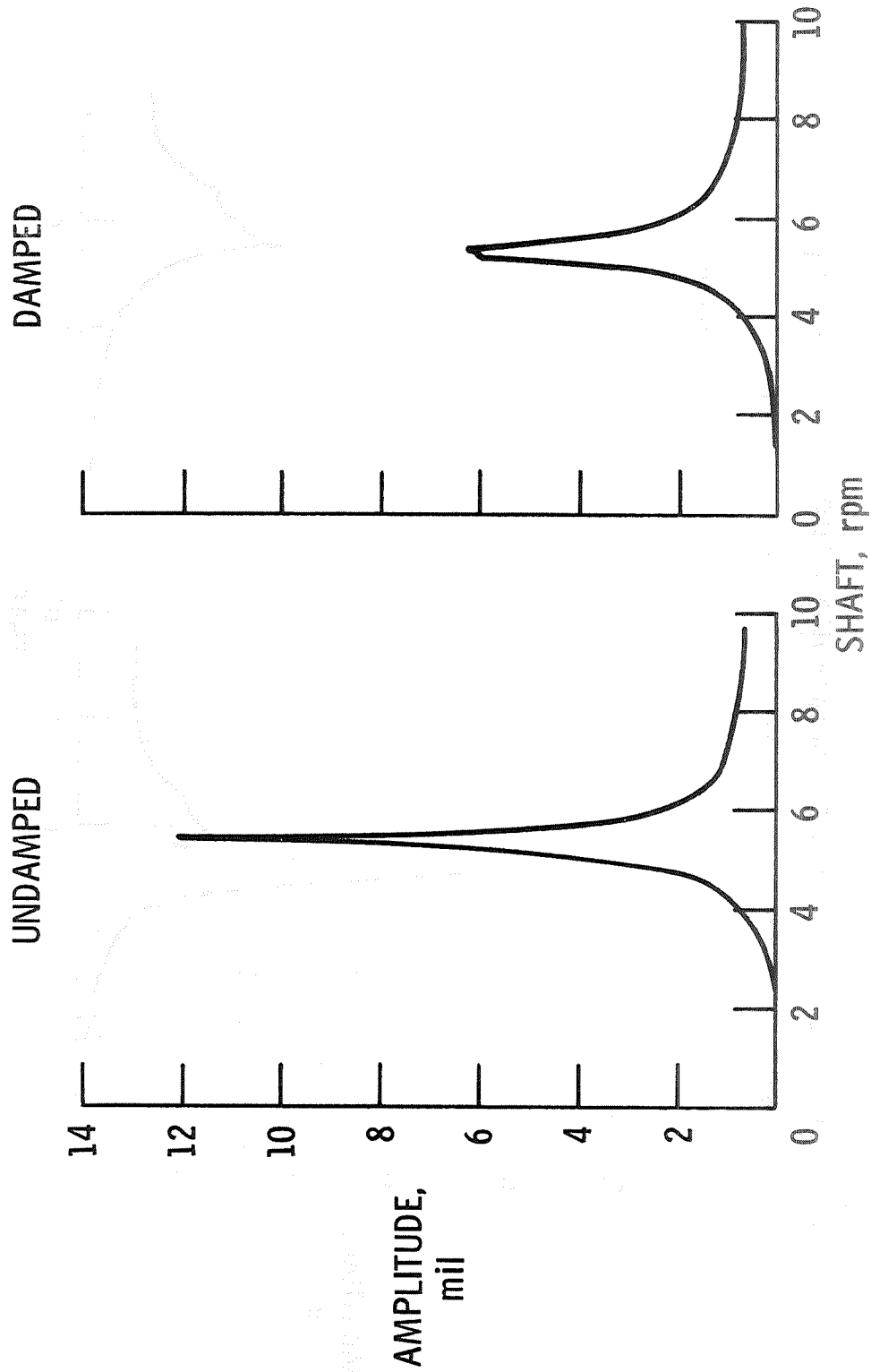
MODE 1 FREQUENCY = 98 HZ ( 6120 RPM)



NO. OF STATIONS = 15  
 NO. OF BEARINGS (&SEALS) = 2

# THEORETICAL RESPONSE OF UNDAMPED VERSUS DAMPED ROTOR

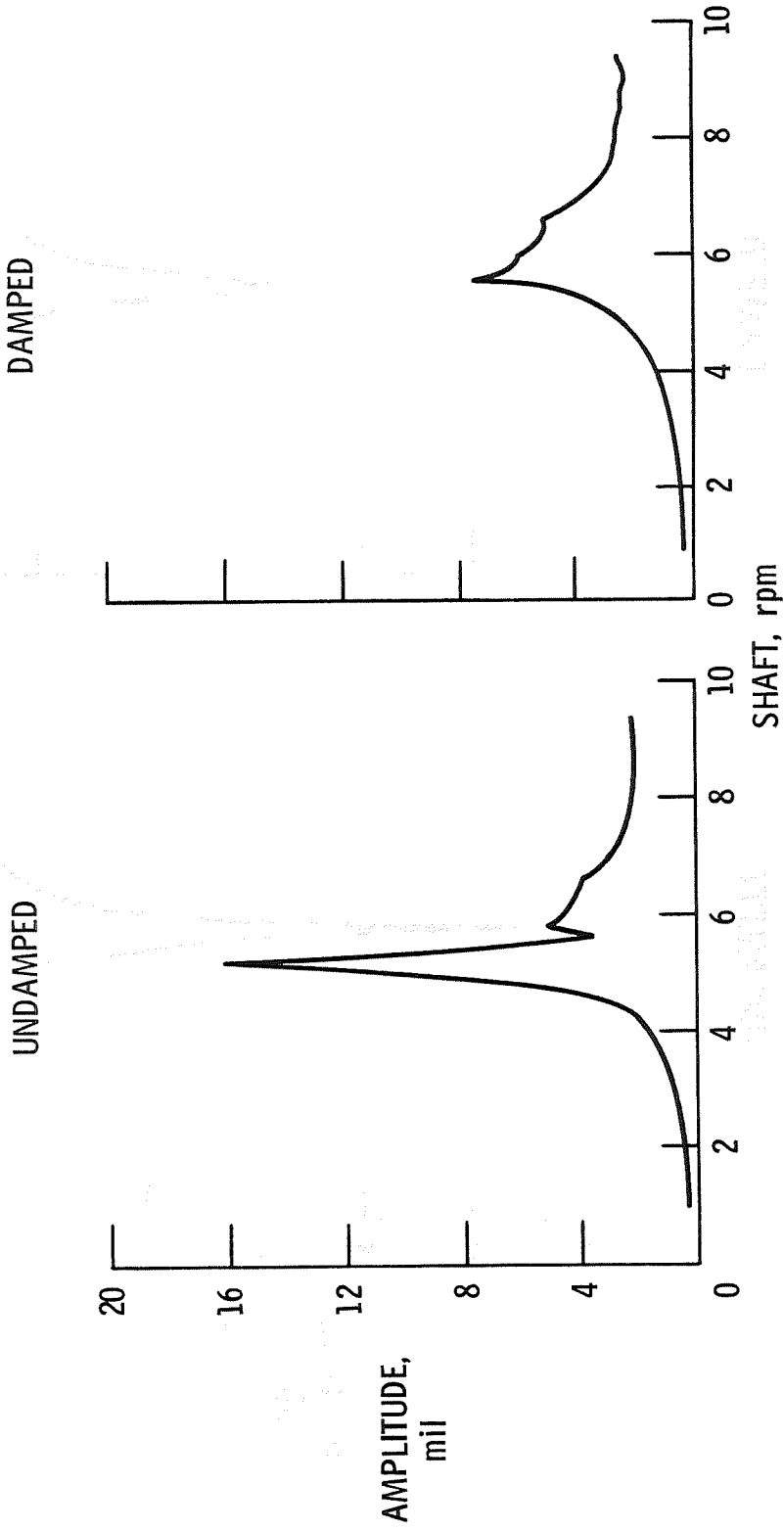
UNBALANCE, 0.149 oz-in. ; THEORETICAL DAMPING COEFFICIENT  $\zeta$ , 0.084



V-2144

# MEASURED RESPONSE OF UNDAMPED VERSUS DAMPED ROTOR

UNBALANCE, 0.149 oz-in. ; MEASURED DAMPING COEFFICIENT  $\zeta$ , 0.079



SUMMARY OF THEORETICAL VS MEASURED RESPONSE FOR LN<sub>2</sub> TEST ROTOR

ROTOR UNBALANCE, .149 OUNCE - INCHES

SPRING CONSTANT,  $K_s = 11,100$  lb/in

THEORETICAL RESPONSE

MEASURED RESPONSE

379

	<u>UNDAMPED</u>	<u>DAMPED</u>	<u>UNDAMPED</u>	<u>DAMPED</u>
RESONANT FREQ. (CPM)	5400	5400	5200	5600
MAX. AMPLITUDE AT RESONANCE (MILS)	11.9	6.2	16.1	7.3
DAMPING COEFFICIENT	≈ .002	.084		.079

V-2185

SUMMARY OF THEORETICAL VS MEASURED RESPONSE FOR LN<sub>2</sub> TEST ROTOR

ROTOR UNBALANCE, .149 OUNCE - INCHES

SPRING CONSTANT, K<sub>s</sub> = 11,100 lb/in

	<u>THEORETICAL RESPONSE</u>		<u>MEASURED RESPONSE</u>	
	<u>UNDAMPED</u>	<u>DAMPED</u>	<u>UNDAMPED</u>	<u>DAMPED</u>
RESONANT FREQ. (CPM)	5400	5400	5200	5600
MAX. AMPLITUDE AT RESONANCE - (MILS)	11.9	6.2	16.1	7.3
DAMPING COEFFICIENT	≈ .002	.084		.079

DEVELOPMENT AND APPLICATION OF A UNIFIED BALANCING  
APPROACH  
WITH MULTIPLE CONSTRAINTS

Edward S. Zorzi, C. Chester Lee, John C. Giordano  
Mechanical Technology Incorporated  
968 Albany-Shaker Road  
Latham, New York 12110

The development of a unified balancing approach with multiple constraints offers the engineer a powerful and flexible tool, broad in scope and not restricted to special rotor configurations. This method imposes no restrictions on the use of modal trail weight sets and/or modal influence coefficients, which have been proven effective for balancing high-speed rotors in previous "unified" approaches. This approach overcomes the limitations of earlier unifying efforts by permitting the application of orbit and/or weight constraints at any balancing speed not just at critical speeds. Modal trail weight sets for subsequent balancing can be predicted which will not disturb previously balanced speeds. An orbit constraint applied at an off-critical speed will only affect that individual orbit, but if applied at a critical speed, will affect all orbits and constrain the entire mode shape. In addition, correction weights may be constrained at any balance speed if, for example, a balance plane becomes unavailable (i.e. maximum weight removal limit reached) or if redundant planes exist. This method provides an analytic extension of the general influence coefficient methods and offers a least squares formulation that incorporates the constraints within the optimization procedure.

A special test facility is described which has been used to evaluate this approach to balancing. As

demonstrated, the analytic approach has been fully tested and found to be easily implemented. Test results compare favorably with the analytic methodology offered. No special problems have been encountered either in software implementation or obtaining excellent correlation from test rig experimental results.

## INTRODUCTION

Two widely used and distinct linear approaches to balancing have been developed within the past 20 years. One is the modal approach, which has been widely accepted by industry and has been very effective in balancing a wide variety of high-speed rotating equipment [1].\* The other approach consists of a group of balancing procedures, generally classified as influence coefficient methods, which has also attracted many supporters [2,3]. Recent publications have focused on the attractiveness of a combined or so-called "unified" approach, Darlow et al., [4,5]. The unified technique defines the use of modal trial weights which do not disturb previously balanced critical speeds (modes) and that are used to determine influence coefficients. The modal trial and correction weights are prescribed from experimentally determined influence coefficients, thus coupling the advantages of a modal technique with the influence coefficient approach.

These "unifying" efforts have encountered limitations in determining correction weights. The earlier approaches are, in effect, modal methods since they are predicated on the control of all orbits at a speed with a single modal weight set. Generally, such a procedure is not sufficient for balancing at off-critical speeds, such as balancing gas turbines at operating speed. To address this limitation, a final trim balance, using standard influence coefficient balancing, has been recommended [4]. It is apparent that these unifying approaches use a form of modal balancing to traverse critical speeds and the standard influence coefficient approach for trim balancing. This procedure is limited when general coupled modes are present or when synchronous orbit control is required at both the critical speed and at off-critical speeds. A truly unified approach would offer a single, integrated solution form for both steps and allow the engineer to evaluate the

---

\*Numbers in brackets refer to references.

trade-offs between balancing at the critical speeds and at off-critical speeds [6]. If modal constraints are to be imposed, the general flexibility of the influence coefficient balancing method should be extended to include such constraints.

This work describes the development of a general analytic approach to constrained balancing that is consistent with past influence coefficient methods (weighted least squares, point speed, etc.). The approach uses Lagrange multipliers [7] to impose orbit and/or weight constraints; these constraints are combined with the least squares minimization process to provide a set of coupled equations that result in a single solution form for determining correction weights. Proper selection of constraints results in the capability to: 1) balance higher speeds without disturbing previously balanced modes, thru the use of modal trial weight sets, 2) balance off-critical speeds, and 3) balance decoupled modes by use of a single balance plane. Furthermore, if no constraints are imposed, this solution form reduces to the general weighted least squares influence coefficient method.

This paper includes test data generated from a balancing rig operated at Mechanical Technology Incorporated. The test facility was used to examine the use of the general constrained balancing procedure and application of modal trial weight ratios. The data are compared to results obtained by using the general weighted least squares influence coefficient method. As the rig was designed to traverse up to two critical speeds, the algorithm for modal balancing, as well as off-mode correction, may be fully examined.

#### ANALYTIC DEVELOPMENT

Consistent with past influence coefficient approaches to balancing, a linear relationship is assumed. Defining the orbit response vector as  $\eta$ , the influence coefficient matrix as  $[A]$ , and  $T$  as the weight vector, this basic relationship is given by:

$$\eta = \eta_0 + [A] T \quad (1)$$

where  $\eta_0$  represents the synchronous response orbits prior to balancing. The response vector, influence coefficient matrix, and weight vector are represented as complex quantities.

Orbit constraints are specified by the orbit constraint vector  $D_0$ , and the orbit constraint matrix  $[G_0]$ , as:

$$[G_0]\eta = D_0 \quad (2)$$

Similarly, balance weight constraints are specified by the weight constraint vector  $D_w$ , and the weight constraint matrix  $[G_w]$  as:

$$[G_w] T = D_w \quad (3)$$

By defining a weighted summation of the residual orbits which includes the Lagrange balance weight and orbit constraints, the following relationship holds:

$$S = \eta^T [W] \eta + ([G_0]\eta - D_0)^T \lambda_0 + ([G_w]T - D_w)^T \lambda_w^{**} \quad (4)$$

Where  $[W]$  is the least squares weighting matrix, and the vectors  $\lambda_0$  and  $\lambda_w$  are the Lagrange multipliers for orbit constraints and weight constraints respectively. The solution to the constrained balancing problem requires minimization of Equation (4) with respect to  $\lambda_0$ ,  $\lambda_w$  and  $T$ . Thus, by substituting Equation (1) into Equation (4), and taking the appropriate partial derivatives, the following Equations result:

$$[\bar{A}]^T [W] \eta + ([G_0][A])^T \lambda_0 + [G_w]^T \lambda_w = 0 \quad (5)$$

---

\*\*Superscript T is used to indicate matrix transpose and bar is used to indicate complex conjugate.

$$[G_o]\eta - D_o = 0 \quad (6)$$

$$[G_w]T - D_w = 0 \quad (7)$$

Further substitution of Equation (1) into Equations (5) and (6) provide the following relationships:

$$([\bar{A}]^T[W][A])T + (G_o[A])^T \lambda_o + [G_w]^T \lambda_w = -[\bar{A}]^T[W]\eta_o \quad (8)$$

$$[G_o][A]T = D_o - [G_o]\eta_o \quad (9)$$

Equations (7), (8) and (9) are a set of simultaneous linear equations in  $\lambda_o$ ,  $\lambda_w$ , and T. The solution of these equations for T satisfies the orbit constraints specified in Equation (2), the weight constraints specified in Equation (3) and minimizes the weighted response error term specified in Equation (4). Therefore, correction weights can be determined which satisfy the imposed constraints and minimize the residual response in the least squares sense. This solution form offers the flexibility of specifying orbit and/or weight constraints. Furthermore, if orbit constraints are imposed which require that the correction weight not disturb previously balanced speeds, the predicted correction weights are modal sets.

Modal trial weight ratios can be calculated using a formulation similar to that shown in equations [1] - [6]. That is, a modal weight constraint is applied and orbits are minimized. In this case the constraint matrix in equation [3] is replaced by a modal constraint matrix  $[G_M]$ . The resulting unweighted equations analogous to [7] and [8] are:

$$([\bar{A}]^T[A])T + [G_M]^T \lambda_M = 0 \quad (10)$$

$$[G_M]T = D_M \quad (11)$$

With this solution methodology, the user has great latitude in specifying the constraints as seen in the flow chart shown in Figure 1.

#### DESCRIPTION OF TEST FACILITY

An experimental rig was used to verify the previously discussed analysis. This rig is shown schematically in Figure 2. It consists of a shaft with overall length 660.0 mm (26 in.) supported on grease packed ball bearings. There are four disks on the shaft - two between the bearings and one outboard of each bearing. The disks between the bearings are made of aluminum and consist of a hub and rim with overall outside diameter 101.6 mm (4.00 in.). The overhung disks are made of steel and are 76.2 mm (3.00 in.) thick and have an outside diameter of 101.6 mm (4.00 in.). Each disk has 36 equally spaced circumferential holes for insertion of trial or correction weights. The rig is driven through a shaft mounted pulley and drive belt. The belt is driven with a universal motor and variable AC power supply. The maximum speed with this drive system is 10,000 rpm.

An undamped critical speed analysis of the rig indicated that there are two criticals below the maximum rig speed of 10000 rpm and are predicted to occur at 4648 and 6156 rpm. These two modes are flexible and the predicted mode shapes are shown in Figure 3. The rig is instrumented with eddy current displacement probes at the disks in both horizontal and vertical directions. A fiber optic probe and signal conditioning circuit was used to acquire timing signal. Data from these probes was displayed on oscilloscopes. The synchronous vibration components (amplitude and phase with respect to the timing mark) were acquired digitally using a PDP 11/03 based data acquisition system.

#### Least Square Balancing

The unbalanced rotor was run to a speed where orbits began to grow rapidly to determine a baseline

unbalanced condition. The resulting response is shown in Figure 4 for probe #1. Due to excessive vibration, it was not possible to exceed 4400 rpm. From this baseline condition, 4400 rpm was chosen as the balancing speed. Using the general least square influence coefficient method, the rotor was balanced as shown in Figure 4.

### Constraint Balancing

Following the least squares balancing, a series of constrained balancing tests, as outlined in Table 1, were conducted.

Case No.	Number of Constraints	Condition
1	1	Weight Constraint at Plane #2 with 1.0 gm at 330° to simulate maximum weight removal limitation
2	2	Weight at Plane #2 with 0.9 gm at 15° Orbit at probe #1 with 0.0 mm
3	1	Modal Trial Weight Set Prediction. Plane #1 and #3 will be selected to have modal trial weight set installed.

Table 1 Constrained Balance Condition

As indicated in the following paragraphs, the constraints imposed were successfully matched by the test results.

Case 1: In Case #1, a single weight constraint was imposed. The correction weight for plane 2 was

constrained to be 1.0 gm at  $330^\circ$ . The results for this balance run are shown for probe #1. (Figure 5). The response is slightly better than the least square balance response.

Case 2: Both weight and orbit constraints are imposed in this case. That is, the correction weight is specified at 0.9 gm at  $15^\circ$  in plane #2, while the orbit at probe #1 at 4400 rpm was constrained to be zero. The results for this run are shown in Figure 6. The response for probe 1 indeed approaches zero as specified.

Case 3: After balancing the rotor at 4400 rpm, trial weights were predicted for balancing at a higher speed which would not disturb the balanced state at 4400 rpm. Constraints were again used to specify that the modal trial weight set was to be installed in planes #1 and #3 only. The weight ratios were predicted as:

- Plane #1 1.89 at  $358^\circ$
- Plane #2 0.00
- Plane #3 2.63 at  $180^\circ$

The response was plotted as shown in Figure 7 after the following modal weights were installed.

- Plane #1 0.70 gm. at  $360^\circ$
- Plane #3 0.98 gm. at  $180^\circ$

The result indicated that the balanced speed(4400 rpm) was not disturbed.

### CONCLUSIONS

The analytic formulation of the constrained balance procedure as developed provides a balancing methodology that offers the flexibility of a unified approach yet removes restrictions imposed by earlier unified approaches. In particular, it offers the capability to impose constraints at critical and off-critical speeds. Since this method uses a single, consistent solution form, it allows for the evaluation of trade-offs between these balance conditions. Furthermore, it is totally compatible with influence

coefficient methods and, in fact, reduces to the general weighted least squares solution when constraints are eliminated.

No limitations for determining the influence coefficients are imposed. Accordingly, using "modal" trial weight sets and/or redefining influence coefficients to be consistent with modal sets is possible. Therefore, one may use the full capabilities of modal weight sets for determining influence coefficients and directly integrate these results with the constrained balancing algorithm.

The test data has verified that this method offers a viable approach to balancing high-speed rotors; it also offers a great deal of flexibility to engineers when confronted with difficulties common to balancing rotating machinery. For example, orbits can be specified at any speed, to allow for smooth machine operation at the design operating speeds, control of bearing loads, etc. Balance weights can also be specified to compensate for balance planes which cannot accommodate more correction weight addition or removal. Furthermore, combinations of these types of constraints can be imposed simultaneously.

Application of modal trial weight sets will not affect the lower speeds that have already been balanced. This practice is especially useful when rotors are very sensitive to imbalance. In fact, the application of modal trial weight set can reduce the number of trial weight runs since the set will not disturb those balanced lower modes.

### ACKNOWLEDGEMENTS

The authors gratefully acknowledge the assistance of Mr. James Walton of Mechanical Technology Incorporated for his valuable suggestions and contribution and Mr. David Smith in providing the PDP11/03 computer based data acquisition system for use in this study.

## REFERENCES

1. Bishop, R.E.D., and Gladwell, G.M.L., "The Vibration and Balancing of an Unbalanced Flexible Rotor", Journal of Mechanical Engineering Science, Vol. 1, No. 1, 1959, pp. 66-77.
2. Goodman, T.P., "A Least-Squares Method for Computing Balance Corrections", Journal of Engineering for Industry, Trans. ASME, Series B, Vol. 86, No. 3, August 1964.
3. Zorzi, E.S., and Flemming, D., "Balancing of a Power-Transmission Shaft with Axial Torque", ASME 80-GT-143, March 1980.
4. Darlow, M.S., "A Unified Approach to the Mass Balancing of Rotating Flexible Shafts", PhD. Dissertation, University of Florida, 1980.
5. Parkinson, A.G., Darlow, M.S., Smalley, A.J., and Badgley, R.H., "An Introduction to a Unified Approach to Flexible Rotor Balancing", ASME paper presented at the ASME Gas Turbine Conference, March 1979.
6. Zorzi, E.S., Giordano, J.C., and Lee, C.C., "A Unified Approach to Balancing with Multiple Constraints", IFTOMM Conference on Rotordynamic Problems in Power Plants, Sept. 28 - Oct. 2, 1982, Rome, Italy.
7. Weinstock, R., Calculus of Variations, McGraw-Hill, 1952.
8. Tessarzik, J.M., Badgley, R.H., and Anderson, W.J., "Flexible Rotor Balancing by the Exact Point-Speed Influence Coefficient Method", Journal of Engineering for Industry, Vol. 94, No. 1, pp. 148-158, February 1972.

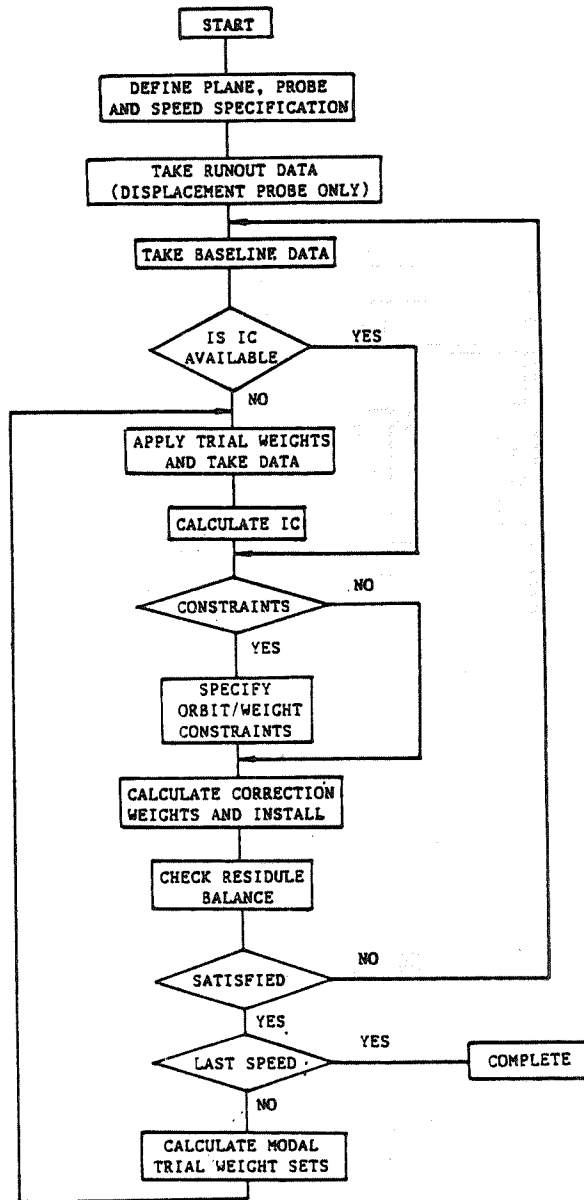


Fig. 1 Balancing Procedure Flow Chart

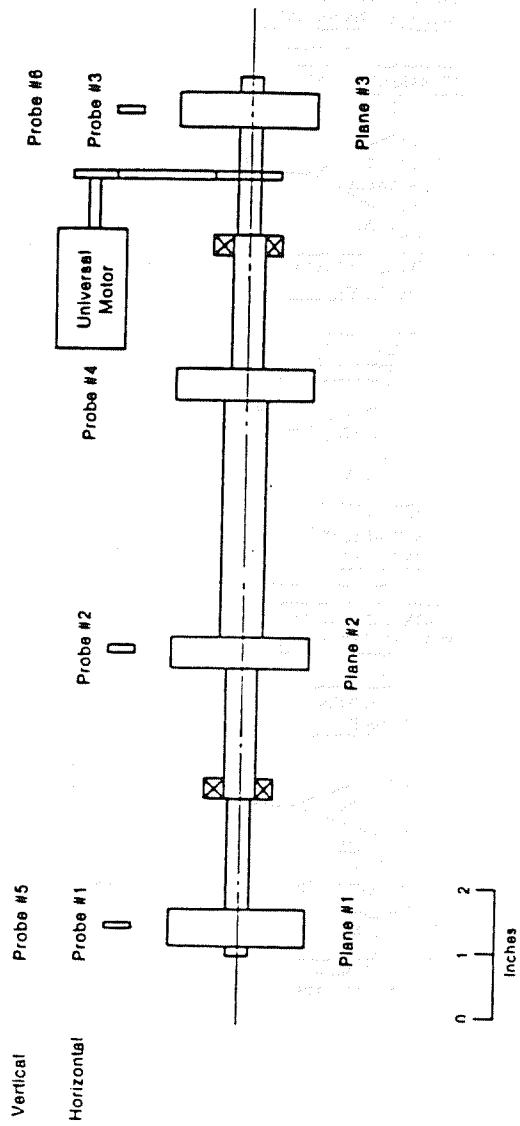
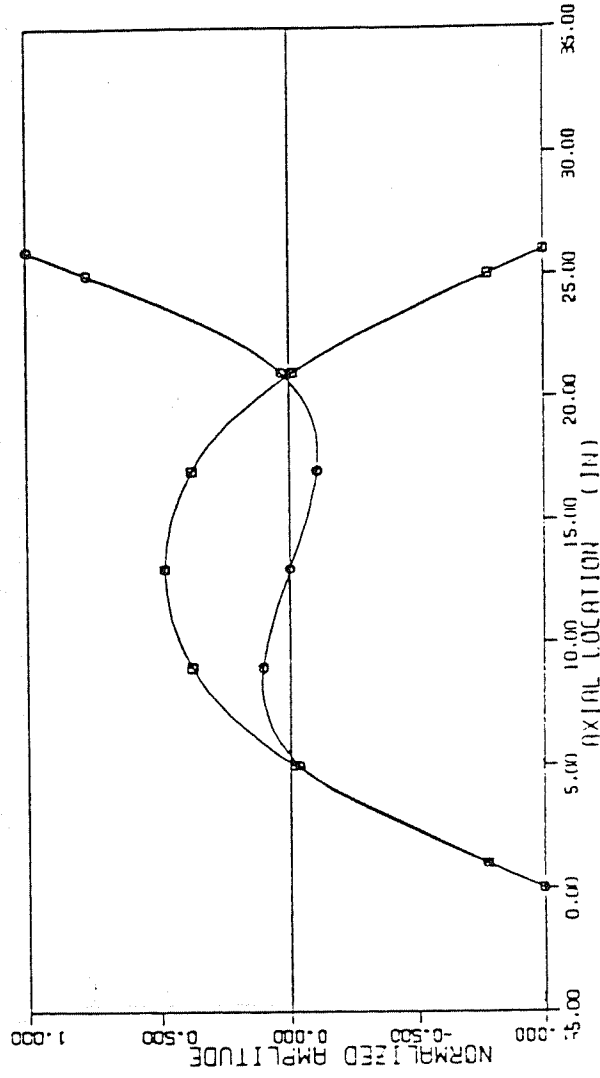


Fig. 2 Schematic of Balancing Rig

R41011

MTI BALANCING DEMO RIG

MODE	RPM	□	○
1	4648.00	□	○
2	6156.00	○	□



81818

Fig. 3 Mode Shape Plot

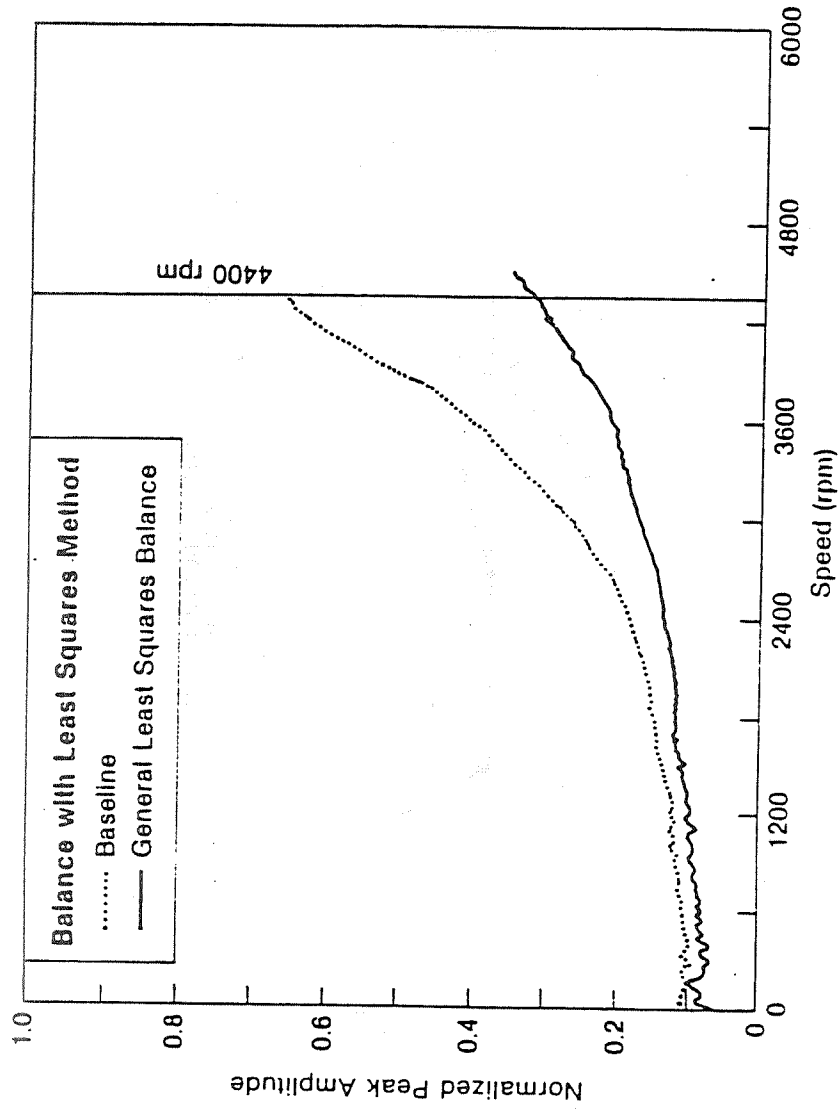


FIG. 4 Response vs. Speed (Balance with General Least Squares Method)

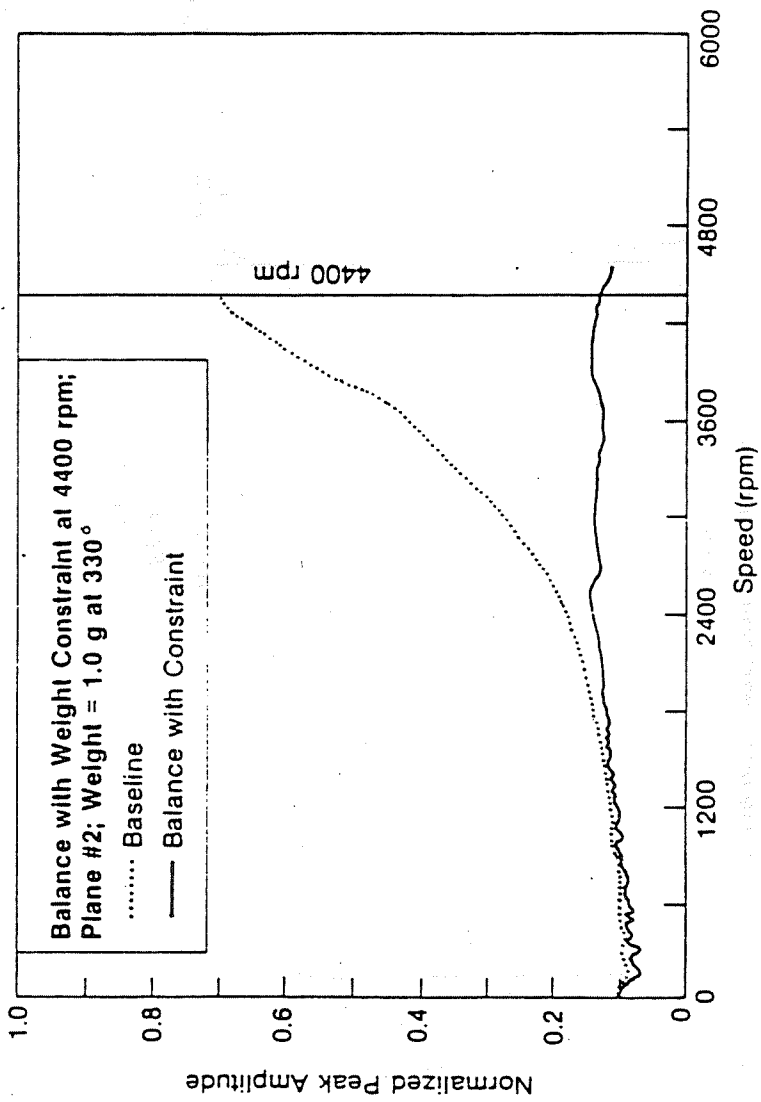


Fig. 5 Response vs. Speed (Balance with Weight Constraint)

641014

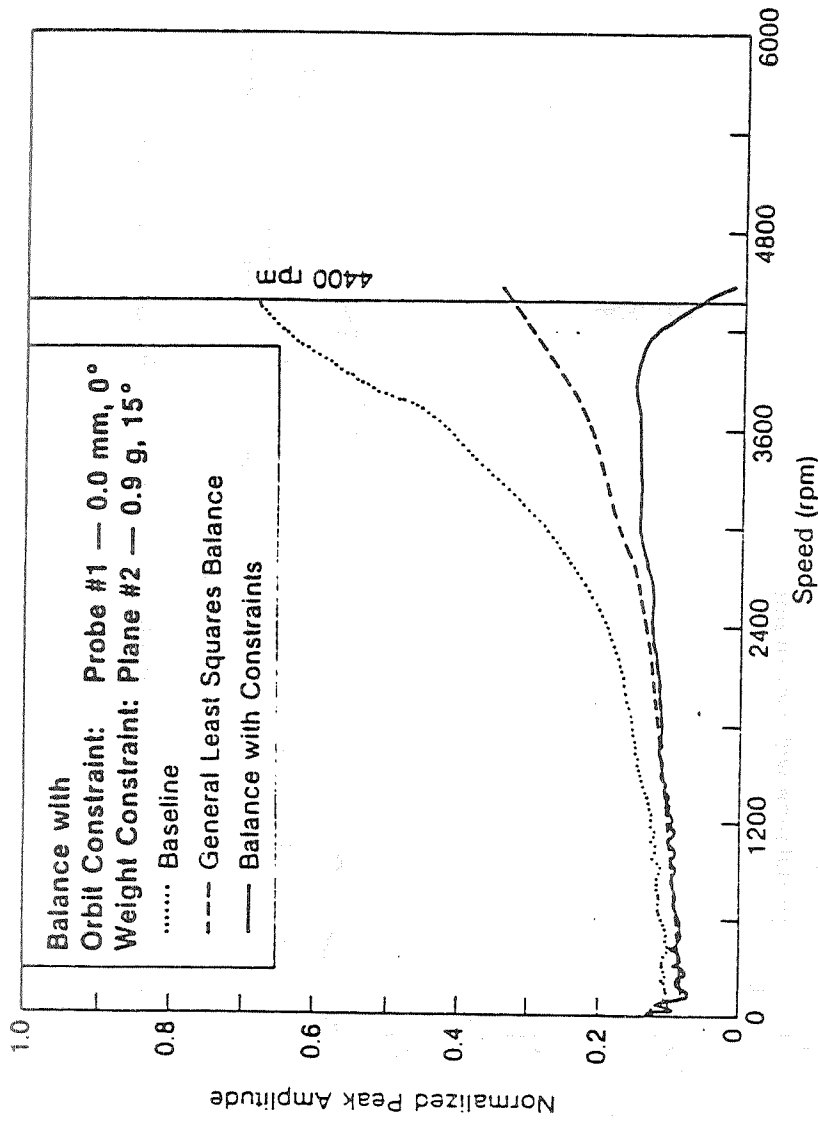


Fig. 6 Response vs. Speed (Balance with Orbit and Weight Constraints)

81115

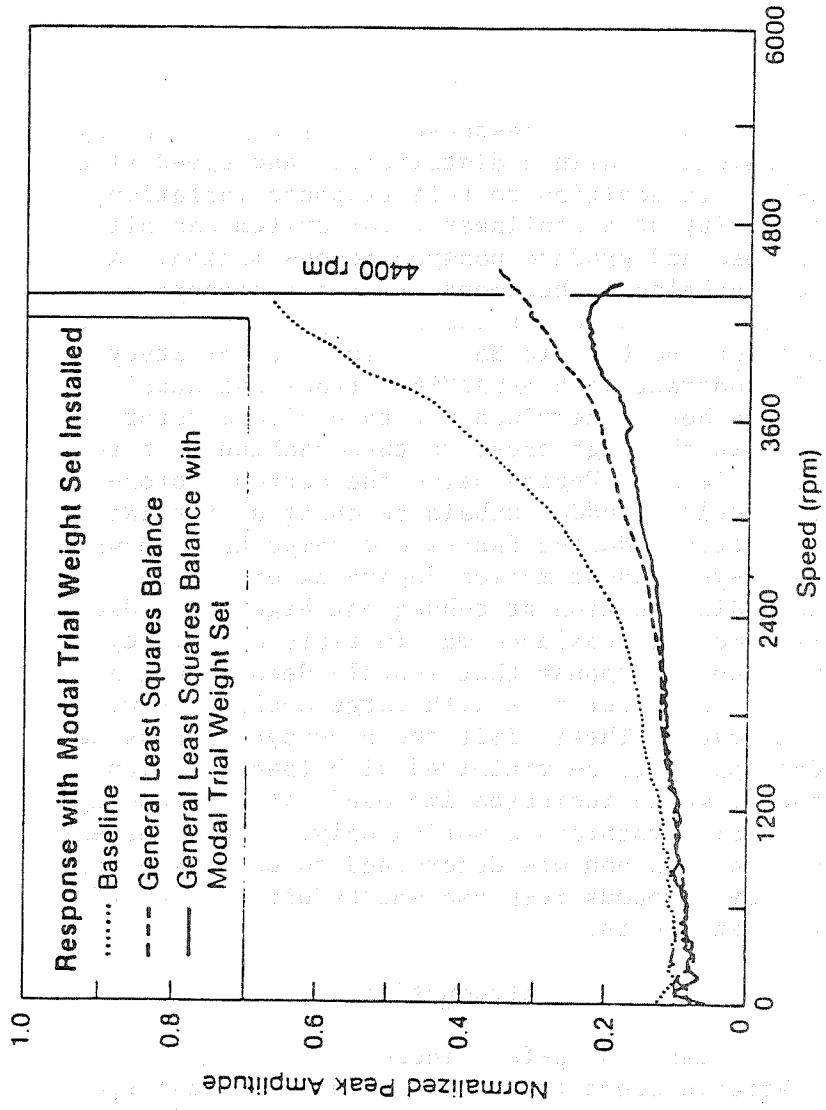


Fig. 7 Response vs. Speed (with Modal Trial Weight Set Installed)

841816

## ROTOR RESPONSE FOR TRANSIENT UNBALANCE CHANGES IN A NONLINEAR SIMULATION

M. J. Hine, C. E. Landis,  
and R. F. Beatty

### Abstract

Synchronous rotor response varies significantly with transient unbalance distribution and speed simultaneously. In addition to this response variation, the complexity of a nonlinear rotor system can alter the response and produce nonsynchronous motion. A transient unbalance phenomena created a concern about a perturbation source for unstable operation. As an outgrowth of the Dynamic Balance Improvement Study Phase II contract with NASA/MSFC, transient unbalance shifts have been determined not to excite a rotor instability in the high pressure turbomachinery of the Space Shuttle Main Engine using the current rotor-dynamic models. Sudden unbalance changes of relatively small magnitudes during fast-speed ramps have shown stable nonsynchronous motion depending on the resultant unbalance distribution at subsequent high speed dwells. Transient moment unbalance may initiate a limit cycle subsynchronous response that shortly decays, but a persistent subsynchronous with large amplitudes was never achieved. These limit cycle subsynchronous amplitudes appear to be minimized with lower unbalance magnitudes, which indicates improved rotor balancing would sustain synchronous motion only. The transient unbalance phenomenon was determined to be an explanation for synchronous response shifts often observed during engine tests.

### Introduction

Throttleable pump-fed liquid rocket engines require variable speed turbopumps capable of fast-speed ramp rates. A high rate of change in the applied torque may cause rotor components to reposition and alter the rotor mass unbalance. This concern, along with other possible unbalance changing mechanisms,

was expressed as a self-enhanced unbalance concern by NASA. It was suggested that transient unbalance changes could initiate an asynchronous rotor instability close to the spin frequency. The focus of concern was with the high performance turbopumps of the Space Shuttle Main Engine (SSME). The SSME powerhead with the main combustion elements and attached turbopumps is shown in Fig. 1. The throttleable SSME has high

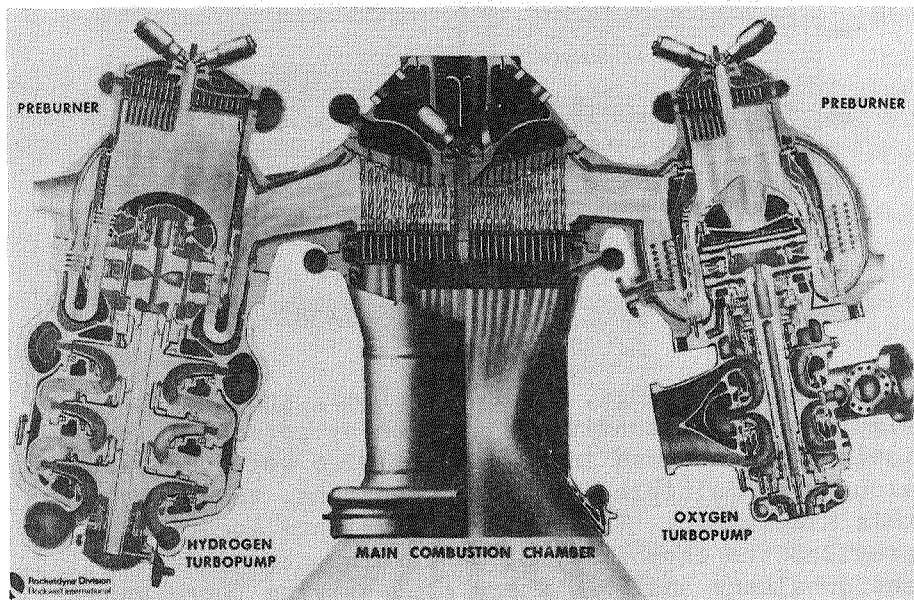


Fig. 1. SSME Powerhead Component Arrangement

pressure liquid oxygen and liquid hydrogen turbopumps, which have had stability problems in the past, and this transient unbalance mechanism was investigated as a technology item. The primary concern for this phenomenon was an initiation mechanism for a roughly 90 percent of speed subsynchronous whirl on the high pressure oxygen turbopump. Test data would normally indicate this subsynchronous response at the maximum shaft speed, or directly after a speed ramp, as shown in the example frequency versus time data plot of Fig. 2.

To perform this complex transient analysis, non-linear models were required and included such effects

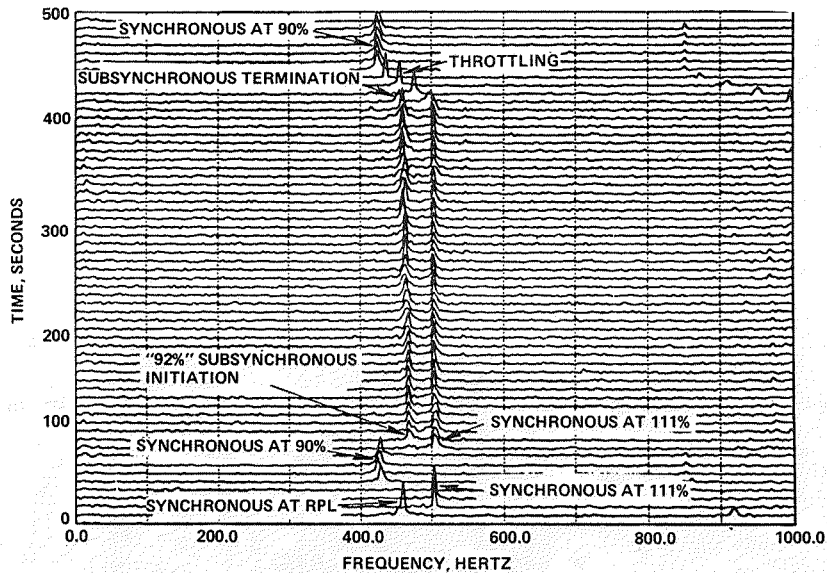


Fig. 2. HPOTP 2212 Test 901-382-2214  
Accelerometer Data

as deadband bearings, fixed sideload, and rubbing to simulate actual conditions as much as possible. Variable unbalance and speed capabilities were necessary, along with multiple unbalance locations, to accomplish this simulation. The multiple unbalance locations provided the capability of performing transient moment unbalance analyses where time-varying force unbalance magnitudes on adjacent turbine disks form a variable couple. These conditions require unique simulation programming and would generally create a large computer cost. However, hybrid computer usage made it possible to perform the analysis for a minimal cost and significant time savings.

#### Survey Turbopumps

The existing nonlinear simulation models of the high pressure oxygen turbopump (HPOTP) and high pressure fuel (liquid hydrogen) turbopump (HPFTP) were used to perform the analysis. The following is a brief description of these turbopumps.

The high pressure oxidizer turbopump is shown in Fig. 3 and a summary of its performance characteristics are provided in Table 1. Basically, the high pressure

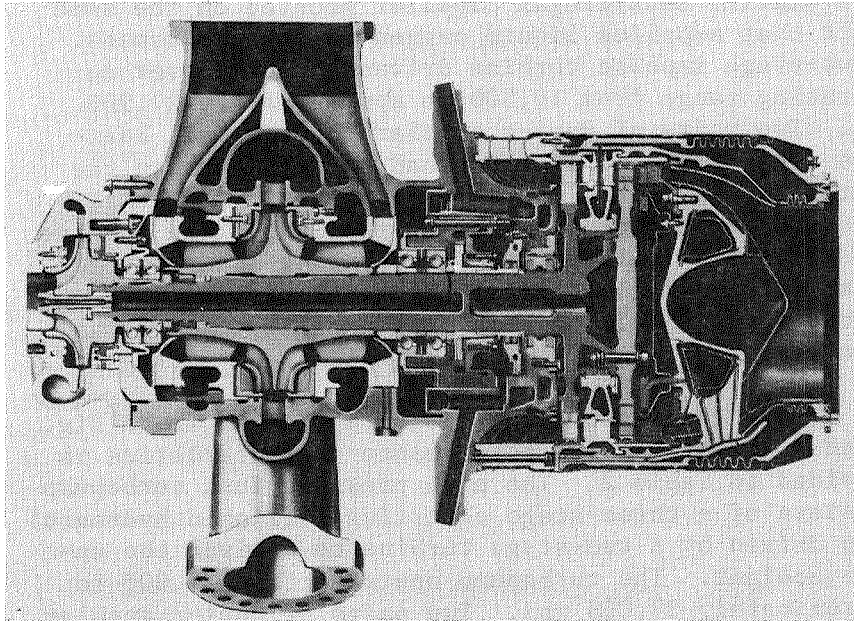


Fig. 3. SSME High Pressure Oxidizer Turbopump

Table 1. SSME HPOTP Performance Data

KEY PERFORMANCE PARAMETERS BASELINE DATA JAN. 1984				
	RPL		FPL	
	MAIN	BOOST	MAIN	BOOST
PUMP INLET FLOWRATE, LB/SEC	1070.6	111.6	1157.8	129.4
PUMP INLET PRESS, PSIA	379.3	3985.9	392.4	4403.6
PUMP DISCHARGE PRESSURE, PSIA	4108.7	7106.7	4556.0	7861.2
PUMP EFFICIENCY	0.684	0.809	0.650	0.800
TURBINE FLOWRATE, LB/SEC	61.8		69.0	
TURBINE INLET PRESSURE, PSIA	5015.3		5660.8	
TURBINE INLET TEMP, R	1407.2		1596.3	
TURBINE PRESS RATIO	1.506		1.550	
TURBINE EFFICIENCY	0.749		0.755	
TURBINE SPEED, RPM	27102		29675	
TURBINE HORSEPOWER	22902		29174	

oxidizer turbopump consists of a double-entry centrifugal impeller supplying liquid oxygen to the main chamber. A portion of this discharge flow is diverted to a smaller centrifugal impeller mounted on the same shaft that supplies liquid oxygen to the preburners. A two-stage impulse turbine drives the pump over an operating range from 19,500 to approximately 27,900 rpm. Two pairs of duplex angular contact ball bearings support the rotor. Preload springs between the bearing outer races in each pair maintain the axial load independent of rotor axial position. The turbine hot gases are isolated from the pump by a series of floating ring seals. Axial thrust on the rotor is reacted by a double balance piston built into the main impeller.

The high pressure fuel turbopump is shown in Fig. 4 and a summary of its performance characteristics is provided in Table 2. The high pressure fuel turbopump consists of a three-stage centrifugal (liquid hydrogen) pump driven by a two-stage turbine to deliver the engine coolant. The turbopump operates from 27,000 to approximately 37,000 rpm. Two pairs of duplex angular

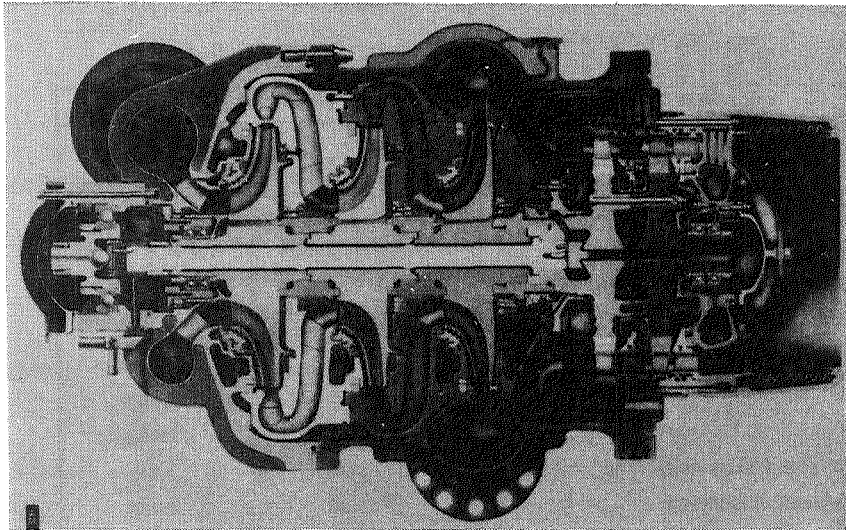


Fig. 4. SSME High Pressure Fuel Turbopump

Table 2. SSME HPFTP Performance Data

KEY PERFORMANCE PARAMETERS	RPL	FPL
PUMP INLET FLOWRATE, LB/SEC	148.4	161.7
PUMP INLET PRESSURE, PSIA	204.1	214.0
PUMP DISCHARGE PRESSURE, PSIA	6254.8	7036.8
PUMP EFFICIENCY	0.758	0.757
TURBINE FLOWRATE, LB/SEC	147.5	164.0
TURBINE INLET TEMPERATURE, R	1898.4	1989.2
TURBINE PRESSURE RATIO	1.522	1.558
TURBINE EFFICIENCY	0.770	0.780
TURBINE SPEED, RPM	34,931	37,076
TURBINE HORSEPOWER	63,288	77,142

contact ball bearings support the rotor radially and a thrust bearing is provided for start and shutdown axial positioning. A balance piston built into the third-stage impeller reacts the axial thrust during steady-state operation. Straight smooth annular seals between the impeller stages ensure the rotor stability.

#### Mathematical Models Description

The finite element models of the rotors and housings for the high pressure oxidizer and fuel turbopumps have been verified by years of empirical correlation and are generally accepted as producing the correct trends. The rotors are constructed of beam finite elements and the load line diagrams are shown in Fig. 5 and 6 for the high pressure oxidizer and fuel turbopumps, respectively. The high pressure oxidizer turbopump housing model, shown in Fig. 7, is constructed of plate elements and equivalent support beams that tie the housing to the engine chamber ground. The high pressure fuel turbopump housing model, shown in Fig. 8, is of beam and empirically sized spring construction, which is also tied to the engine chamber ground. The coupled system was analyzed using modal synthesis techniques that combine substructures of the rotor and housing-to-engine

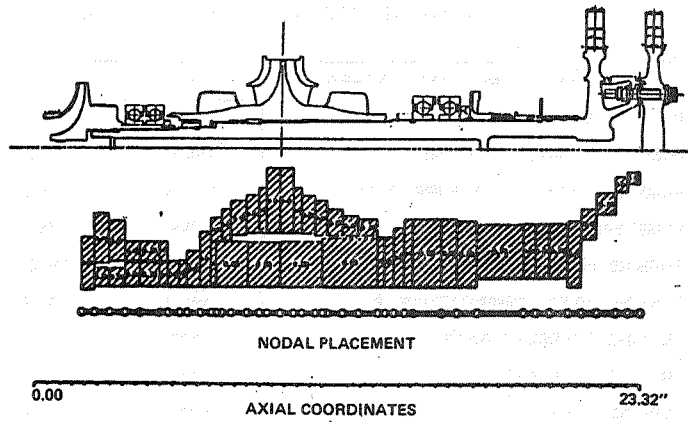


Fig. 5. SSME HPOTP Rotating Assembly  
Finite Element Model

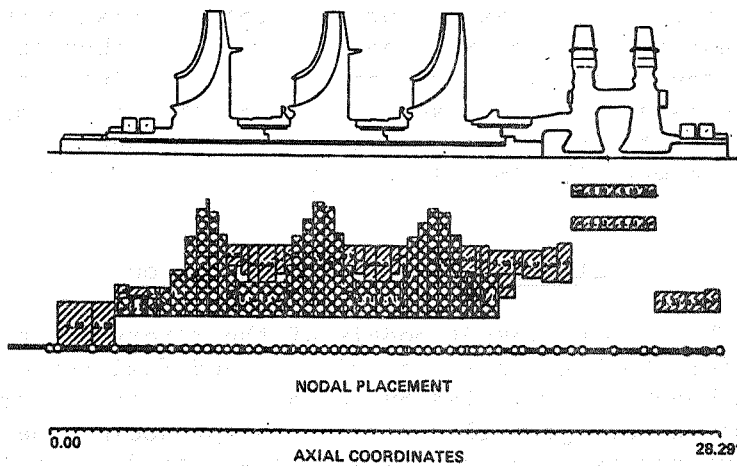


Fig. 6. SSME HPFTP Rotating Assembly  
Finite Element Model

support structure coupled through nonlinear bearings, hydrostatic seals, impeller-diffuser interaction, turbine aerodynamic cross-coupling, bearing damping, and fixed radial loads. Output capabilities include the ability to predict bearing loads, rotor displacements, and housing accelerations as a function of time and speed, and determine the response spectra.

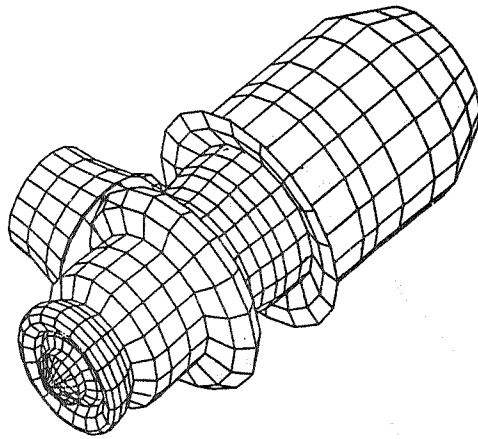


Fig. 7. SSME HPOTP Housing Finite Element Model

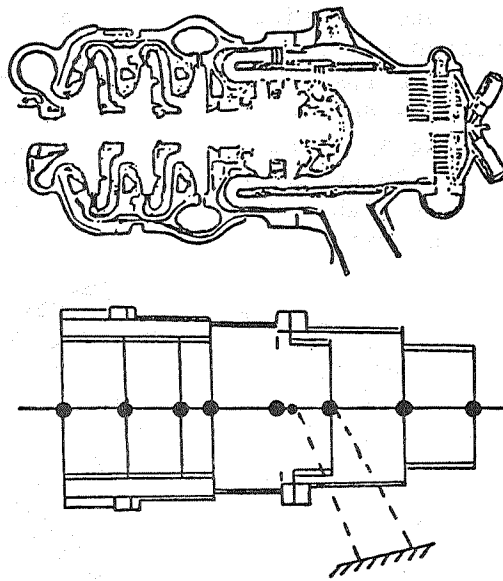


Fig. 8. SSME HPFTP Housing Model

The high pressure oxidizer turbopump operates between its first and second rotor critical speeds at approximately 12,000 and 32,500 rpm, respectively. The lowest rotor critical speed is the turbine overhang mode and is shown in Fig. 9. The higher rotor critical speed is the main impeller mode and is shown

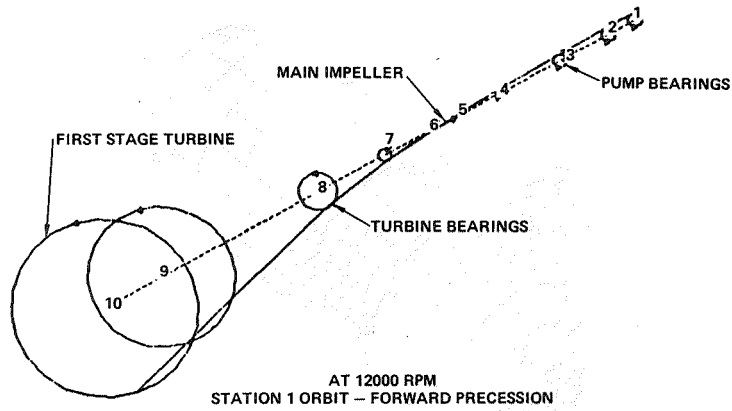


Fig. 9. SSME HPOTP Lowest Rotor Critical Turbine Overhang Mode

in Fig. 10. The high pressure fuel turbopump operates above its first rotor critical speed at about 17,000 rpm, but the second critical is in the speed range at approximately 32,000 rpm. The lower rotor mode has its maximum relative deflection approximately halfway between the bearing span and is shown in Fig. 11. The high pressure fuel turbopump 32,000 rpm rotor mode shown in Fig. 12 is highly damped by the straight smooth impeller interstage seals.

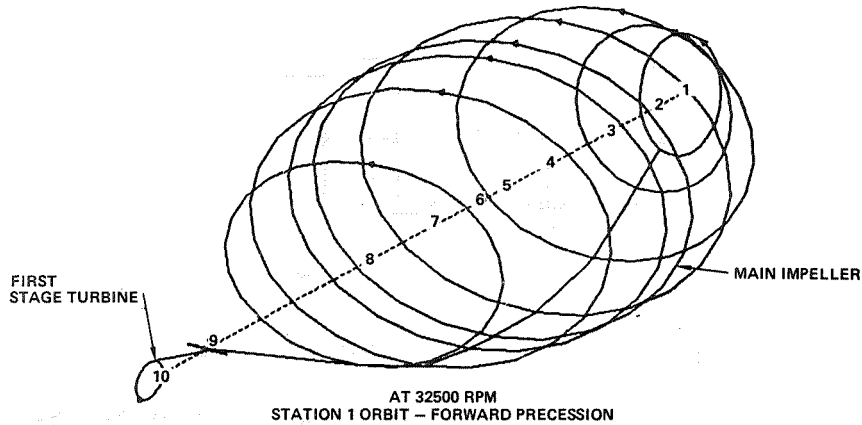


Fig. 10. SSME HPOTP Higher Rotor Critical Main Impeller Mode

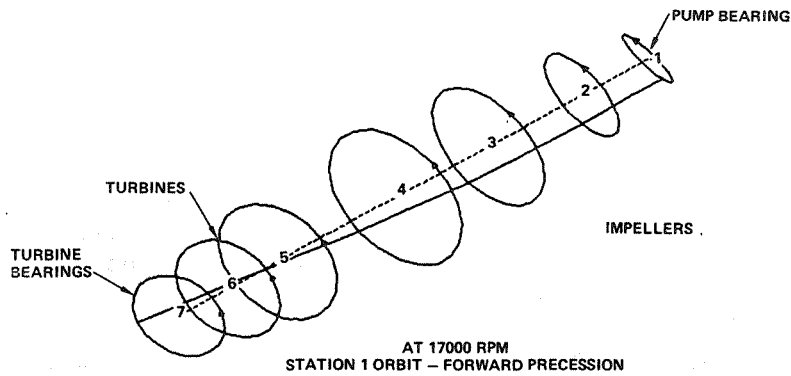


Fig. 11. SSME HPFTP Lowest Rotor Critical Skip Rope Mode

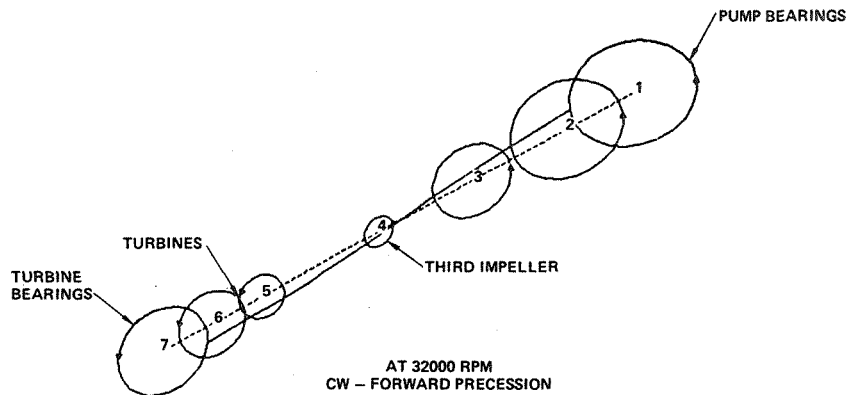


Fig. 12. SSME HPFTP Higher Rotor Mode Node at Third Impeller

#### Hybrid Model

These nonlinear rotordynamics models mechanized on an AD10 hybrid computer were used to study the transient unbalance changes. The hybrid computer allows the complete interactive operation of the model during these parametric studies.

Location, magnitude, and rate of change of the unbalances can be changed on-line and the resulting bearing loads and housing acceleration can be monitored on time-history brush charts. If, for example,

an undesirable unbalance was used, the analysis could be terminated immediately and new unbalance values entered for a repeat case. The time-history data from the hybrid model is digitally stored for post-processing to obtain spectral information.

A slight model modification had to be made to model time and speed varying unbalances since these variables were not normal parametric options of the model. To the best of our knowledge, Rocketdyne has the only time and speed variable unbalance analysis capability anywhere. To acquire this capability, an existing program option to simulate step unbalances at a discrete time was modified. This is mechanized as:

$$U = U_I \text{ if time } < t_u$$

$$U = U_I + U_s \text{ if time } \geq t_u$$

where

$U$  = effective unbalance

$U_I$  = constant unbalance

$U_s$  = increase in unbalance at time  $t_u$

$t_u$  = time the step unbalance occurs

Graphically, this would look like Fig. 13.

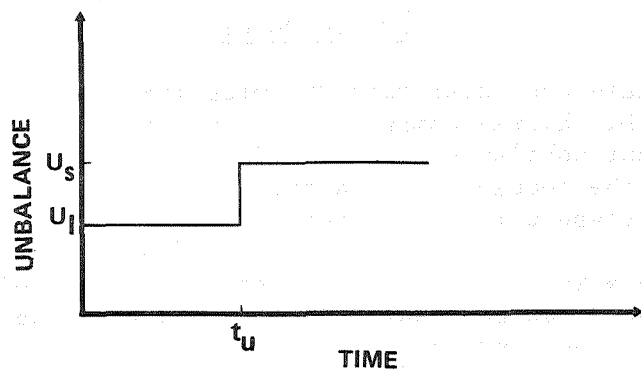


Fig. 13. Step Unbalance With Time

To simulate time and speed varying mechanisms, this was modified to:

$$\begin{aligned}
 U &= U_I \text{ if time } < t_u \\
 U &= U_I + \dot{U}_s (\text{time} - t_u) \text{ if } t_u \leq \text{time} \leq t_s \\
 U &= U_I + \dot{U}_s (t_s - t_u) \text{ if time } > t_s
 \end{aligned}$$

where

$$\begin{aligned}
 \dot{U}_s &= \text{rate of unbalance change, gm-in./sec} \\
 t_s &= \text{time the unbalance stops changing}
 \end{aligned}$$

Graphically, this appears as Fig. 14.

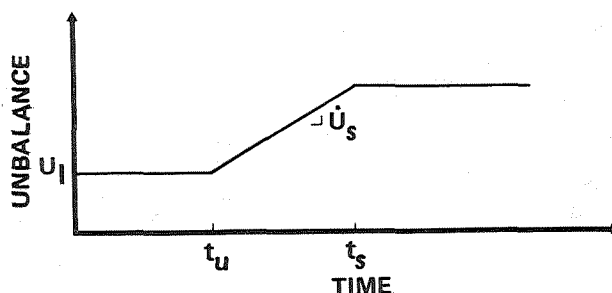


Fig. 14. Ramp Unbalance With Time

This mechanization permits complete flexibility in specifying the transient unbalance and also maintains the capability for simulating step unbalances.

#### Response Results

The initial state of balance in these simulations was established at all the major disks along both rotors based on build tolerances. Nominal state of balance conditions for the high pressure oxidizer and fuel turbopumps are shown in Fig. 15 and 16. It was determined for all self-enhanced unbalance mechanisms proposed that a significant unbalance change was not possible with the SSME turbopumps because splines, pilots, and normality tolerances were sufficient for maintaining rotor positioning. However, to study the

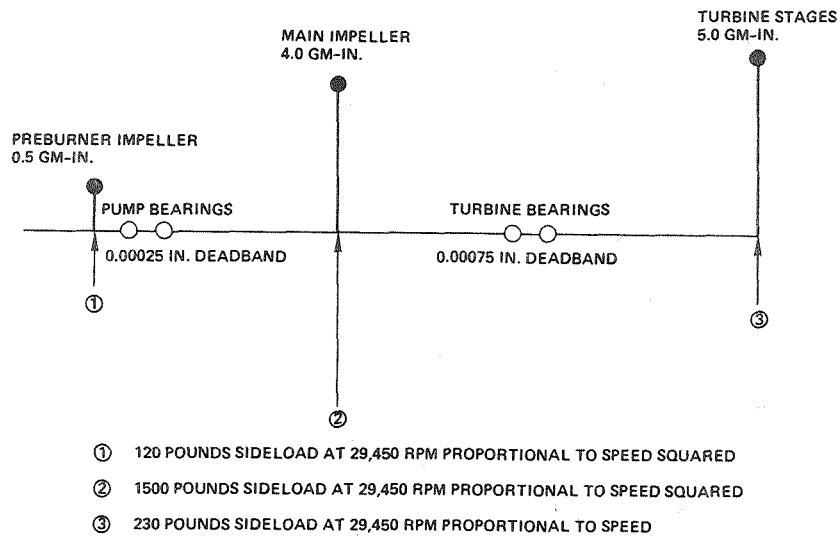


Fig. 15. HPOTP Model Initial Conditions

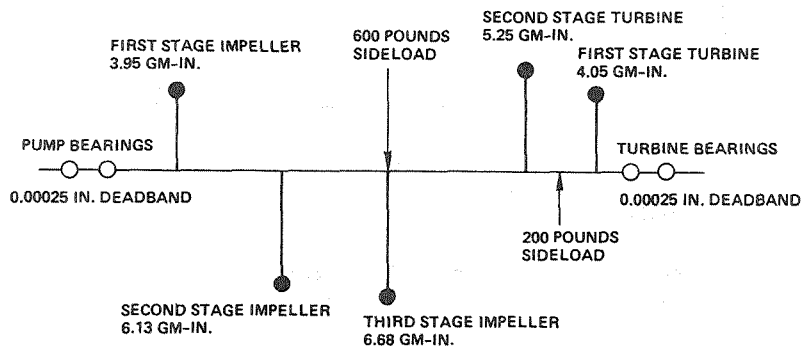


Fig. 16. HPFTP Model Initial Conditions

effect of changing unbalance for information only, it was arbitrarily decided to vary the unbalance magnitude by a factor of two over the speed ramp. Numerous simulations were performed with typically stable and well behaved synchronous only results. Some of the more interesting results will now be discussed.

#### HPFTP Time-Varying Unbalance

The unbalance at the first stage impeller was varied above and below the maximum anticipated

unbalance during an increasing speed ramp as in Fig. 17. The resultant acceleration response at the pump flange is shown in Fig. 18. All response parameters showed stable behavior following the ramp. Since the rotor unbalance distribution is altered, the rotor displacement constantly varies along the rotor length.

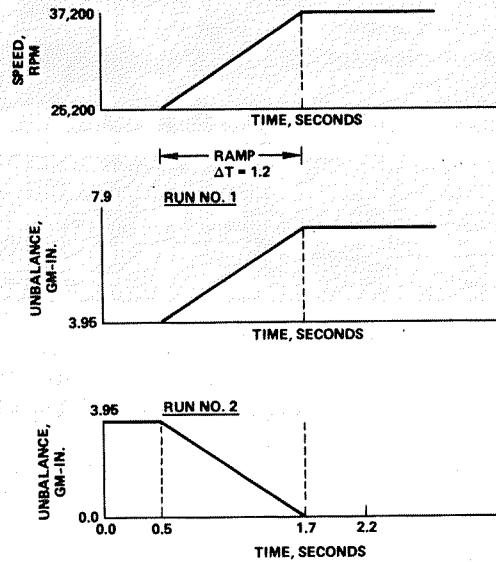


Fig. 17. HPFTP Computer (AD-10) Model Input for Time-Dependent Unbalance Increase and Decrease Applied at the First Impeller

#### HPFTP Time-Varying Moment

A transient moment was simulated by varying opposing unbalances at the first- and second-stage turbine disks above and below the maximum anticipated values during a speed ramp as in Fig. 19 and 20. The resultant acceleration response of the pump flange is shown in Fig. 21.

The pump appears to be basically unaffected by the moment changes themselves after the speed ramp. Following the speed ramp, for both increasing and decreasing turbine moment unbalance cases, a limit cycle subsynchronous response is present as shown in examples (Fig. 22 and 23) for a turbine bearing load and

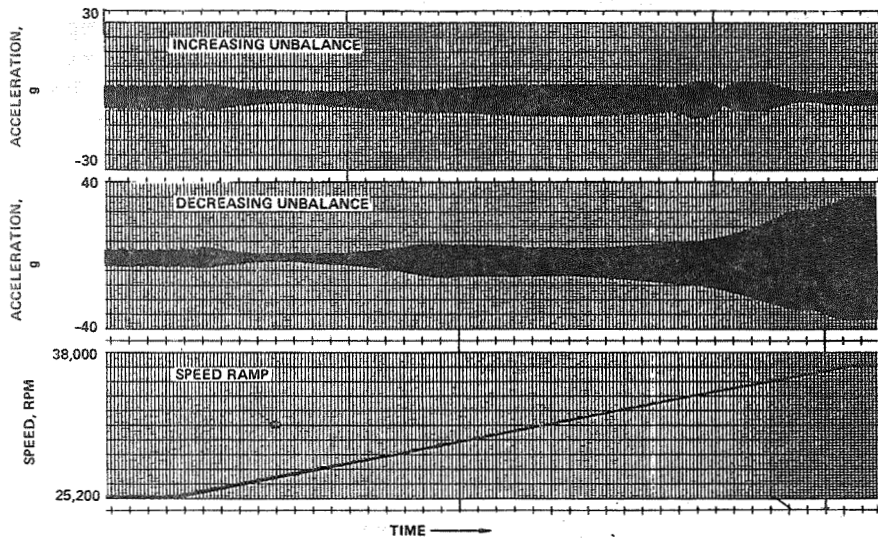


Fig. 18. HPFTP Housing Acceleration Response to Unbalance Changes at First Impeller

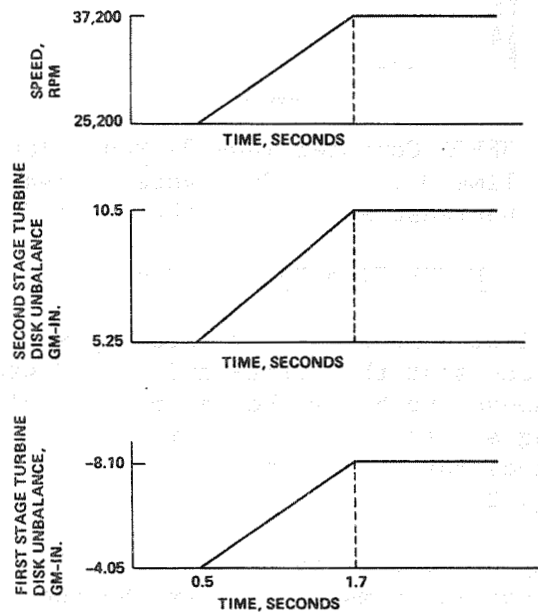


Fig. 19. HPFTP Computer (AD-10) Model Input for Time-Dependent Moment Unbalance Increase

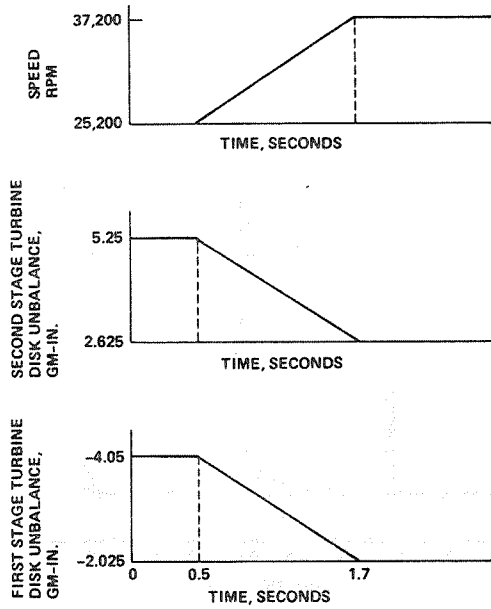


Fig. 20. HPFTP Computer (AD-10) Model Input for Time-Dependent Moment Unbalance Decrease

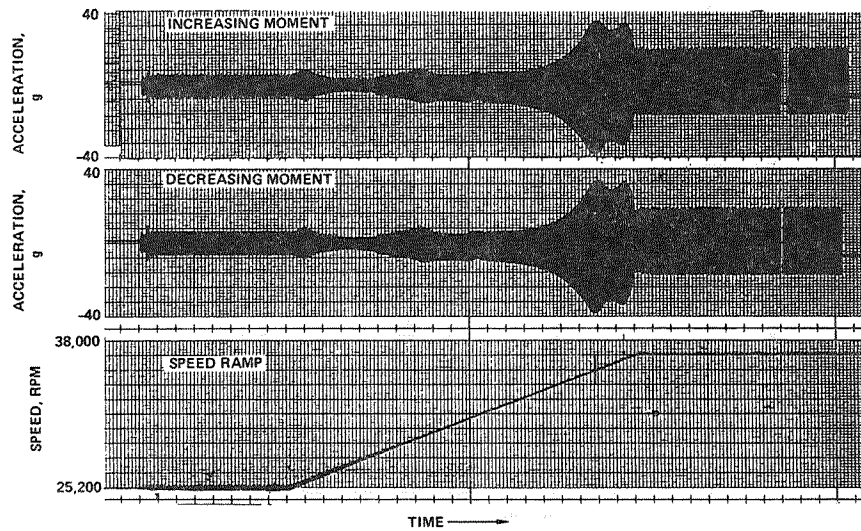


Fig. 21. HPFTP Housing Acceleration Response to Varying Moment Unbalance at Turbine

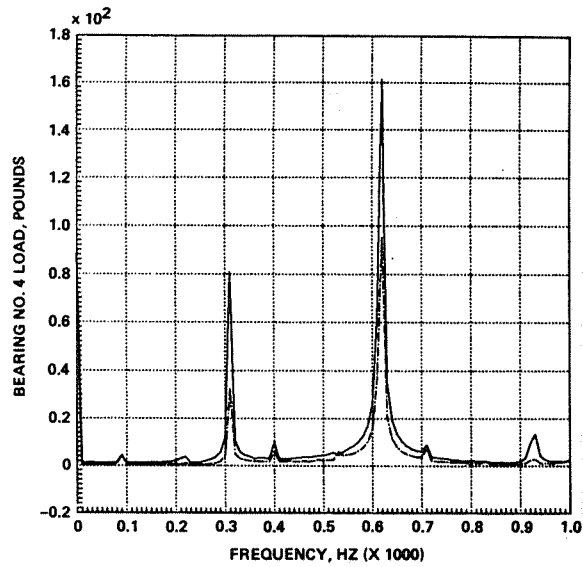


Fig. 22. HPFTP Spectra at 37,200 rpm with Increasing Moment Unbalance

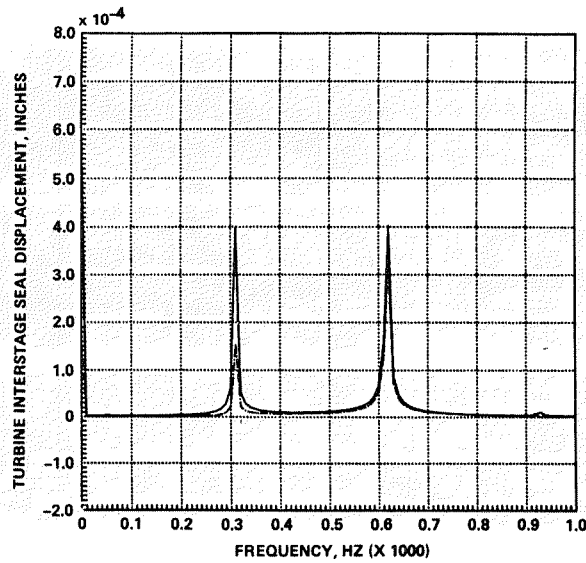


Fig. 23. HPFTP Spectra at 37,200 rpm with Increasing Moment Unbalance

turbine interstage seal displacement with an increasing moment unbalance. This lowest rotor mode subsynchronous response is attributed to the changes during the ramp since during normal operation at high speeds, the subsynchronous response is not present in the simulations. This level of subsynchronous response in the 300 Hz range is typically not experienced with a straight smooth impeller interstage seal configuration high pressure fuel turbopump during engine hot-fire testing. For normal steady-state unbalance distributions and high-speed dwell conditions, the typical response spectra is shown in Fig. 24, which the data represented in Fig. 22 and 23 eventually decays to reflect. Sensitivity to the initial conditions is typical in nonlinear simulation work.

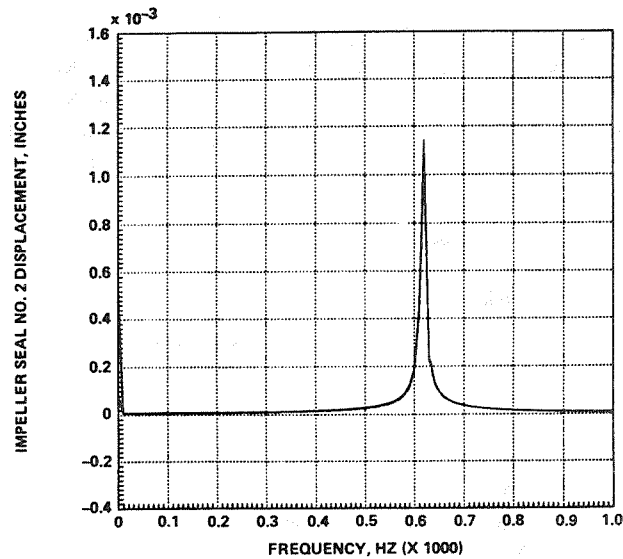


Fig. 24. Typical HPFTP Response Spectra at 37,200 rpm

#### HPOTP Time-Varying Unbalance

The effect on the rotor response of a time-varying unbalance during a speed ramp was studied with the unbalance occurring separately on the turbine and main impeller. Both increasing and decreasing unbalances were studied during a speed increasing ramp as

shown in Fig. 25 and 26. The acceleration of the housing flange is shown in Fig. 27 for the unbalance changes occurring at the main impeller. As expected, the increasing unbalance case produced larger residual response magnitudes than the decreasing case. The pump housing acceleration response to unbalance changes at the turbine is shown in Fig. 28.

The steady-state pump response was determined by the final unbalance magnitude and speed for the main impeller unbalance case. Variations in the response were observed during the speed ramp for the two analysis conditions where resonant activity was observed near the rotor critical speed and housing resonances.

The pump was dwelled at high speed for both unbalance conditions with subsynchronous activity at one-half synchronous speed, or the lowest rotor mode in the spectral displacement data at the turbine stages which was not present in the bearing loads or housing accelerations.

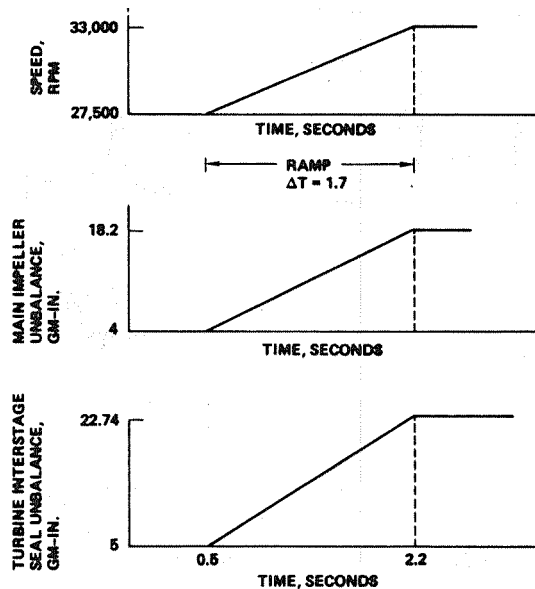


Fig. 25. HPOTP Computer (AD-10) Model Input for Time-Dependent Unbalance Increase

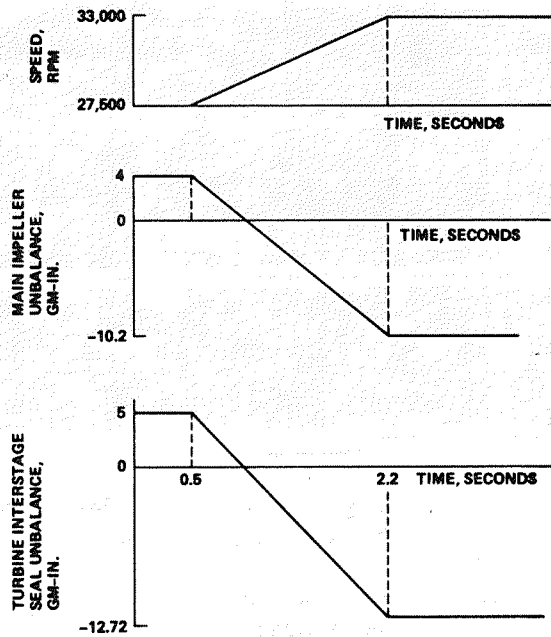


Fig. 26. HPOTP Computer (AD-10) Model Output for Time-Dependent Unbalance Decrease

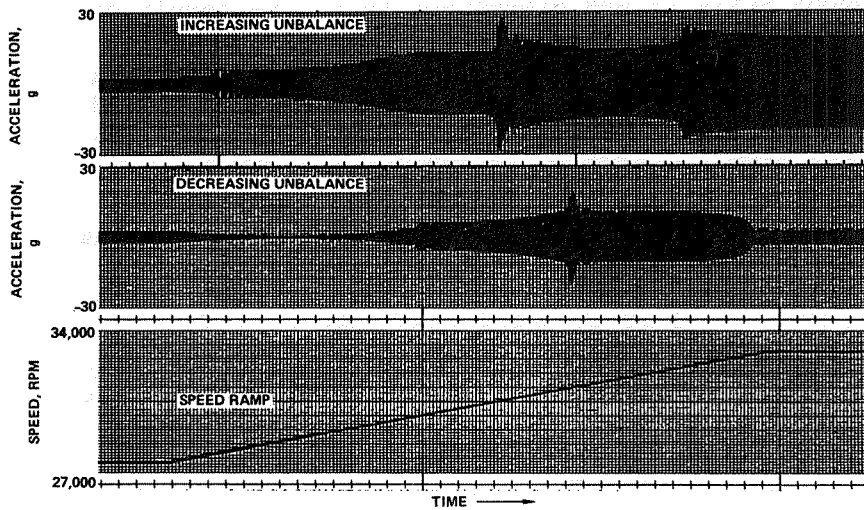


Fig. 27. HPOTP Housing Acceleration Response to Varying Unbalance at Main Impeller

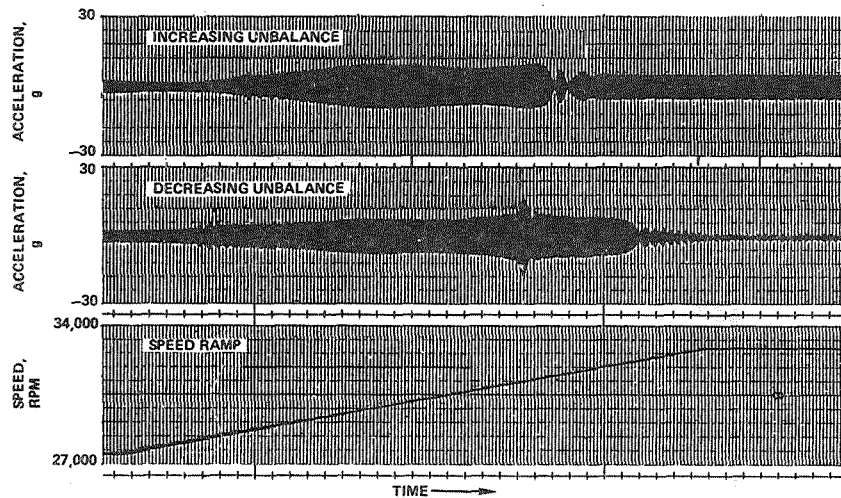


Fig. 28. HPOTP Housing Acceleration Response to Varying Unbalance at Turbine

Turbine response is shown in Fig. 29 and 30 for the increased and decreased main impeller unbalances, respectively. Of note here is that the subsynchronous amplitudes after an unbalance increase were higher than those after an unbalance decrease. This subsynchronous activity was proven not to be the result of the unbalance changes and speed ramp by operating at a constant speed of 33,000 rpm with the unbalance existing at the end of the speed ramp. Figures 31 and 32, respectively, show similar subsynchronous activity for high constant speed and similar unbalance conditions at the end of the ramps. It should be noted that 33,000 rpm is far in excess of the maximum running speed of 28,200 rpm at 104 percent of rated power. A modified turbine interstage seal for the up-rated high pressure oxidizer turbopump (109 percent thrust) has been shown to eliminate the turbine disks subsynchronous response, even at this excessive speed as shown in Fig. 33. As previously mentioned, the subsynchronous response was never observed in the housing acceleration data, which is monitored on every engine hot-fire test and is a reflection of the bearing loads.

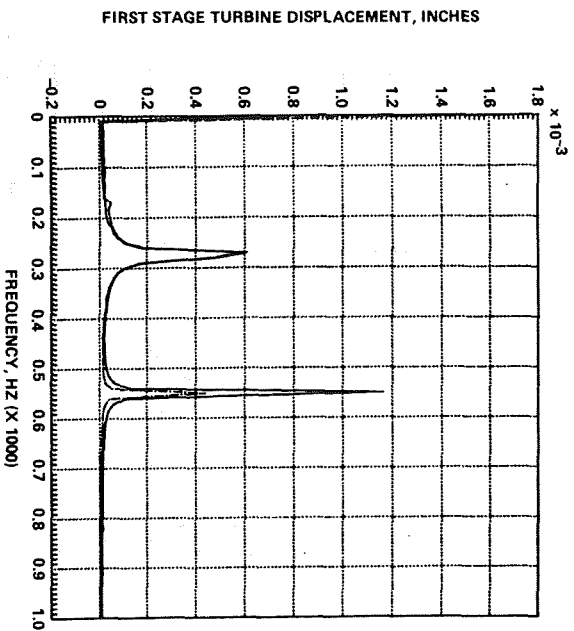


Fig. 29. HPOTP Increased Impeller Unbalance Response After Speed Ramp

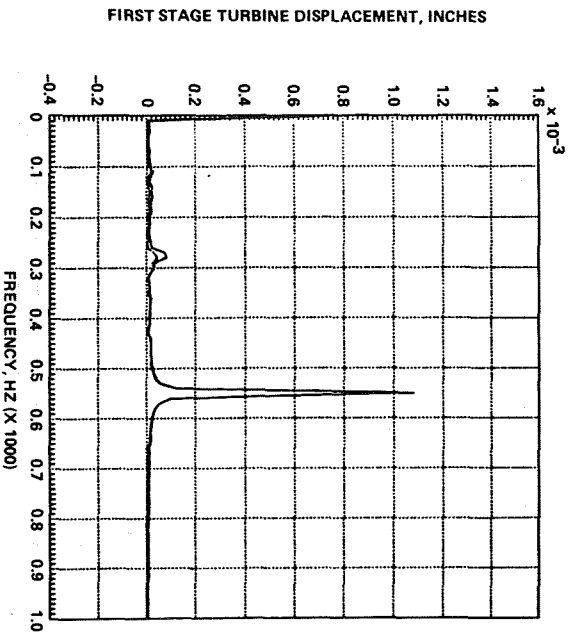


Fig. 30. HPOTP Decreased Impeller Unbalance Response After Speed Ramp

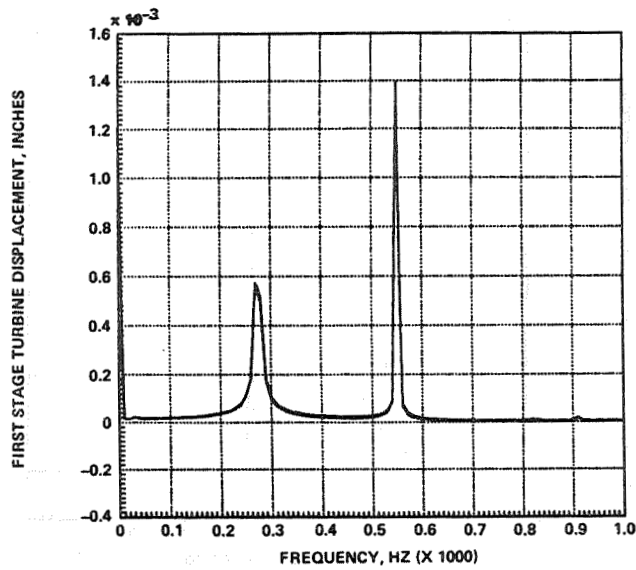


Fig. 31. HPOTP Response Spectra at 33,000 rpm Turbine Unbalance Increase

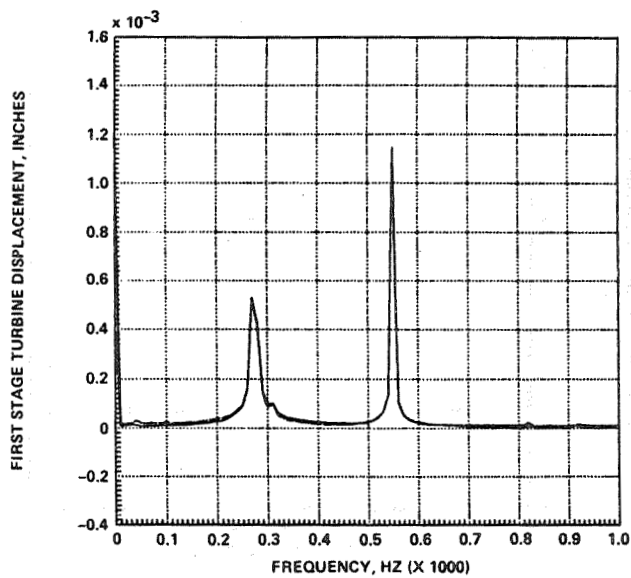


Fig. 32. HPOTP Response Spectra at 33,000 rpm Turbine Unbalance Decrease

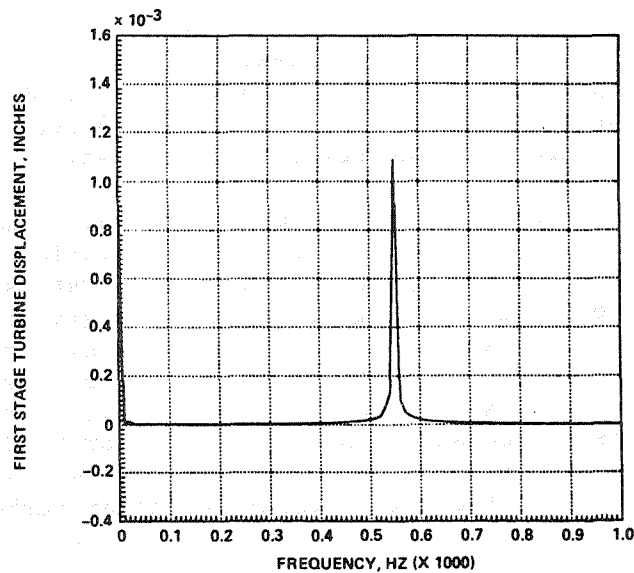


Fig. 33. Typical HPOTP Response Spectra at 33,000 rpm With Modified Turbine Interstage Seal

#### Conclusions

Numerous transient unbalance cases were performed on speed ramps and a divergent rotor instability, or nonsynchronous motion close to the operating speed, was never achieved. Unbalance changes in excess of reasonable analytically predicted magnitudes caused significant synchronous response variation due to the resulting unbalance distribution exciting different system modes. The limit cycle subsynchronous rotor motion detected for both turbopumps was always at the lowest rotor mode frequency, never at a higher rotor mode frequency. The lower rotor mode stability for either turbopump has not been a problem since well before the first Shuttle launch. The high pressure fuel turbopump subsynchronous rotor mode response was shown at a speed slightly above the maximum operating speed and has not been experienced during hot-fire testing since the conversion to straight smooth impeller interstage seals. The high pressure oxidizer

turbopump lowest rotor mode subsynchronous response is not present at speeds up to a maximum operating speed of 30,000 rpm and the low levels shown at 33,000 rpm can be suppressed with a turbine interstage seal modification currently in the development stages.

Lower transient unbalance magnitude shifts may explain some of the synchronous response variation occasionally seen during engine test or the "haystack" phenomenon observed in flight, which was a gradual increase in high pressure oxidizer turbopump synchronous response followed by a short decrease to the original levels. However, as a result of this study, a transient unbalance mechanism cannot explain, or be described as, the trigger for 90 percent of speed subsynchronous whirl on the high pressure oxidizer turbopump.

## DAMPING SEAL VERIFICATION SETUP

Klaus L. Cappel  
Wyle Scientific Services and Systems Group  
Huntsville, Alabama

### Introduction

The heart of the Space Shuttle Main Engine (SSME) is a set of turbopumps that propel cryogenic fluids at very high pressures and flow rates, at rotor speeds up to 37,000 rpm. The interaction and phase relations between the rotor's elastic and inertial forces with fluid restoring and damping forces is apt to give rise to subsynchronous whirl, a type of self-excited vibration at frequencies near the lowest critical frequency of the rotor. This potentially destructive dynamic phenomenon imposes limits on the performance of the engine.

Bushing seals that cause the flow in the fluid film to become turbulent, by means of a multiplicity of pockets, have been shown theoretically, Reference 1, not only to inhibit subsynchronous whirl, but to reduce leakage as well. However, experimental data that relate these two desirable characteristics to such parameters as pocket depth, Reynolds number (based on clearance and axial flow rate), and rotating speed are limited.

To obtain the required data, NASA's Marshall Space Flight Center (MSFC) commissioned Wyle Laboratories to design, build and operate a test rig in which the damping efficacy and leakage reduction of typical candidate seals are to be evaluated. Experimental conditions will either reproduce operating conditions, such as rotating speed and seal geometry, or will be relatable to them, such as Reynolds Number and dynamic characteristics.

## Experimental Design

### Rotor Dynamics

Normally, a flexible rotor turns in rigid seals and bearings. Here, the test setup order is reversed: a softly suspended bushing moves about a stiff rotor. The damping seal responds similarly in either case, by inducing, with the fluid film stiffness, damping, mass, and whirl cross coupling effects. The mass of the damping seal bushing is suspended against the rotor by the fluid film stiffness. The gap flow is established by axial pressure difference and by the Couette flow from the shaft rotation. Dynamically, the real and test systems are analogous.

### Seal Test Configuration

Two principal objectives determined the design of the Damping Seal Test Rig: minimization of risk, and reduction of variables in the machinery. To attain the first of these, water was substituted for cryogenic fluids, as the substance most nearly comparable with respect to specific gravity and viscosity.

Simplification was achieved by replacing the flexible rotor and rigidly mounted seal by a rigid shaft (i.e. one with a critical speed above the highest operating speed) and a seal virtually unrestrained in a plane normal to the shaft axis, but, obviously, prevented from rotation due to circumferential viscous shear forces. The effect of shaft bending stiffness is eliminated, and the only forces acting on the seal are those due to its mass, and the fluid film. In contrast to the actual turbopump, the shaft is externally driven.

### Experimental Variables

Seal: The seal to be tested is shown in Fig. 1. It has a length of 1.8 in. and fits a shaft with a diameter of 3.6 in. The inside surface is machined in a pattern consisting of right-angle triangles

separated by lands .020 in. wide. Four seals are to be retested, three with pocket depths of .020, .040 and .100 in., respectively, and a smooth seal for comparison.

Flow Rates: Axial flow rates through the seal will be varied from full through 1/2, 1/4, 1/8 and 1/16, for a total of five conditions.

Reynolds Number: All twenty configurations of pocket depth and flow rates are to be tested at two maximum flow rate settings, based on Reynolds Numbers of 100,000 and 200,000. The absolute viscosity of water can be varied only through rather narrow limits, by a factor of approximately 2, if one eliminates the need for costly cooling facilities and keeps the highest inlet temperature low enough to prevent flashing of the pressurized water emerging from the seal.

Of the two remaining variables in the Reynolds Number, the axial flow velocity through the seal is specified to lie between 75% and 125% of the shaft surface velocity at 36,000 rpm, or 5089 to 8432 in./sec. All but the lowest of these values were found to be impractical because of the high pressures required to overcome fluid friction in the seal, entrance and discharge losses. Concern was felt over potential problems due to deformation of the shaft seals at pressures much above 2000 psi, as well as the high leakage flow rates through these seals at high pressures, which would increase the already high flow requirements beyond practical limits.

Reduction in the damping seal gap width, as a means of lowering flow, was precluded by the high temperatures required to achieve the specified Reynolds Numbers. These considerations narrowed the feasible gap widths to .015 to .025 in. Because of the cost of the seals, and of the assembly and disassembly, a single gap width of .020 was selected. The resulting maximum calculated entrance pressure is 2150 psi, and the flow rate, 299 gpm, excluding leakage through the

shaft seals that must contain this pressure, in addition to the exit pressure. Inlet temperatures for the two Reynolds Numbers at maximum flow are 108 and 183 degrees F. All calculated values are based on the smooth seal. The seal analysis is derived from Reference 2.

#### Test Method

With water flowing through the seal, and the shaft rotating, the seal carrier is forced off center and released. Its subsequent motions are measured, in two orthogonal directions, by two proximity probes with respect to the shaft, and in inertial space by two accelerometers. The force required to decenter the shaft is also measured to give the static spring rate and cross coupling coefficient. Damping coefficients are derived from the amplitudes and phase relations of the seal motion in the plane normal to the shaft axis.

#### Test Setup

The damping seal test setup comprises three major subsystems: The test rig, test rig drive, and pressurized water supply.

#### Test Rig

The heart of the test rig is the seal suspension assembly, shown in Fig. 2, with the housing, shaft seals and water passages removed for clarity. The cylindrical damping seal carrier has flanges at both ends which are captured between water-lubricated hydrostatic thrust bearings that also act as seals. The recesses in the thrust bearings are supplied through orifice restrictors that maintain nearly constant film thickness in the presence of supply pressure variations. The upstream thrust bearing is supplied from the inlet pressure, with connecting passages leading through the chamber wall to the downstream bearing, thus ensuring thrust balance over a range of inlet pressures. The downstream bearing

carries a greater thrust load, due to the unbalanced area of the damping seal. Bearing film thicknesses are of the order of one half mil.

The hydrostatic thrust bearings constrain the seal carrier to radial displacements in a plane normal to the shaft axis. To restrain rotation of the seal, the seal carrier is connected by two parallel links with spherical bearings to two short cantilever lugs on a torque bar which is mounted in bearings on the test rig housing. The kinematics of this mechanism allow free radial movement of the seal in any direction, through a combination of rotation of the torque bar about its axis, and inclination of the links. However, the fluid torque applies a couple to the links which is resisted by the torsional stiffness of the torque bar.

The same mechanism is used to pull the seal off center and release it, so as to initiate the oscillations mentioned above. A cam follower mounted on an arm at the end of the torque bar is engaged by a cam, driven by a small electric motor through a high gear reduction (not shown). Rotation of the cam is stopped by a limit switch the follower of which rides on a second cam shaped to allow one revolution only. A third cam cocks a release mechanism which does not permit the seal to move until the first cam follower is free of its cam surface; this prevents the seal from being slowed in its rapid return motion by the inertia of the mechanism.

The links are strain-gauged to allow measurement of the decentering force, as well as the torque due to fluid friction. The proximity probes and accelerometers mentioned above are mounted on a split circumferential band that supports the seal carrier; the padeyes for the links are welded to this band. This method of supporting the seal, in place of direct attachment to the seal carrier, is required to ensure complete axial symmetry in the seal carrier. Lack of symmetry in the seal carrier cross section is apt to lead to distortion of the flanges under thrust loading,

which must be avoided owing to the very small film thicknesses of the thrust bearings.

The hollow, stepped test shaft runs in preloaded angular contact ball bearings having an internal diameter of 30 mm. Two opposed bearings are located at the downstream end. At the upstream end, a single upstream bearing is preloaded against a pair of downstream bearings to increase the thrust capacity which is required to resist the unbalanced pressure load on a narrow shaft shoulder just ahead of the test seal. The bearings are supplied by SKF.

In view of the high shaft rotating speed and the high water pressure, the shaft seals are among the most critical components of the test rig. A pair of air-pressurized, segmented carbon seals is used at each end of the shaft to isolate the shaft bearings and their lubricant from the water. The downstream bushing seal provides closure of the test chamber against presumably low pressure; it, too, makes use of carbon running on stainless steel. A leakage path out of the test rig housing is provided; however, the seal is designed to be capable of running dry without damage.

The greatest technical challenge is posed by the upstream seal which must contain the maximum pressure of about 2200 psi. This is a film-riding, balanced bushing seal that depends on leakage past the lip for lubrication. It makes use of bronze and stainless steel at the sliding interface.

Orifice compensated hydrostatic bearings are incorporated in the radially floating seal to center it on the surface-hardened shaft. The recesses are supplied from the pressurized water entering the test rig housing through three radial openings.

All seals and hydrostatic bearings were designed, and are being built by the Stein Seal Company of Philadelphia.

In order to minimize the downstream stagnation pressure, the water emerging from the test seal is led into a circumferential diffuser from which it leaves through six tangentially oriented openings. It is caught in large tubes and dumped in a pond.

Considerable leakage must be accepted for lubrication of the seals and hydrostatic bearings: about 10 gpm for the upstream seal, and 6 gpm for each of the bearings. Since only the entering flow can be measured, by means of a strain-gauged flowmeter venturi, the leakage flow must be collected in 55 gallon drums and measured after the test, to determine the net flow through test seal.

Since the test rig must be disassembled several times for installation of different damping seals, its wet interior will be exposed to the atmosphere. To preclude corrosion which may deposit particles in the very small seal and bearing gaps, all housing components are made from stainless steel.

#### Test Rig Drive

The prime mover for the test rig is a surplus AVCO Lycoming helicopter gas turbine with a maximum output speed of 37,000 rpm, rated at 500 HP. It was originally intended to modify the high-speed turbine shaft so as to drive the test shaft directly. However, this would have removed some of the internal balance due to gear thrust components, which would have shortened the bearing life. Thus, loading of the turbine output shaft, by such means as a hydraulic pump working against a relief valve, would be required, together with a heat exchanger.

The complexity, cost and time required for these two modifications were considered excessive. The chosen alternate approach is based on a single-stage speed increaser gear box with a 1:6.2 ratio, with the low speed input shaft connected by a splined shaft to the turbine output shaft, and the high speed output shaft driving the test shaft through another spline

connection. The gearbox, with shafts running in hydrodynamic bearings, is a modification of a standard unit built by Philadelphia Gear Corporation in King of Prussia, Pennsylvania.

#### Pressurized Water Supply

The required flow of over 300 gpm, at pressures up to 2200 psi, will be supplied by an existing blowdown system originally built to simulate accident conditions involving safety relief valves in nuclear power plants. Its main components are a 340 cu ft pressure vessel (Figs. 3 and 4), and a pair of gaseous nitrogen storage tanks rated at 6000 psi (Fig. 5). In order to extend the run time, these tanks will be supplemented by two trailers carrying additional nitrogen bottles, supplied by NASA/MSFC. At the maximum flow rate, the required inlet pressure can be maintained for nine minutes.

The system schematic is shown in Fig. 6. The test rig supply line branches off from the existing 10 inch, carbon steel line from the pressure vessel into a set of filters provided to remove corrosion products; all lines downstream of the filter are made of stainless steel. A remotely actuated flow control valve and a flow meter are provided to meter the water flow.

The water in the pressure vessel is brought up to the required temperature by passing steam through it from an existing boiler. Thermocouples at three levels measure the water temperature.

With the high shaft speeds and small clearances, a failure of the pressurized water supply could very quickly lead to serious damage in the seals and bearings of the test rig. To protect against this, an emergency water supply, consisting of a high flow, low pressure centrifugal pump and a reservoir, is provided; it is isolated from the high pressure supply line by a check valve. An additional safety feature is the rapid response of the helicopter

turbine which, in its usual configuration, can reach full speed in 3.5 seconds, and even faster when connected to the low inertia of the test rig. It can be stopped very rapidly by shutting off the fuel supply, which will be implemented by a solenoid-actuated valve controlled by an emergency button.

#### Control and Instrumentation

Test rig controls have been purposely kept simple. Variables controlled in preparation for a test run include nitrogen pressure, pressure vessel water level and temperature, and flow rate set point. When all conditions are fulfilled water is admitted to the test rig by opening the main shutoff valve, and the turbine engine is started. The turbine speed is controlled manually through a valve that regulates the fuel supply. A manual switch then overrides the cam limit switch and initiates the decentering and release of the damping seal. The dynamic stability of the damping seal is determined visually by monitoring, on a CRT, the seal displacement measured by the proximity sensors. The turbine is shut down when oscillation amplitudes are seen to grow. Preset speed limits are provided for safely approaching stability limits.

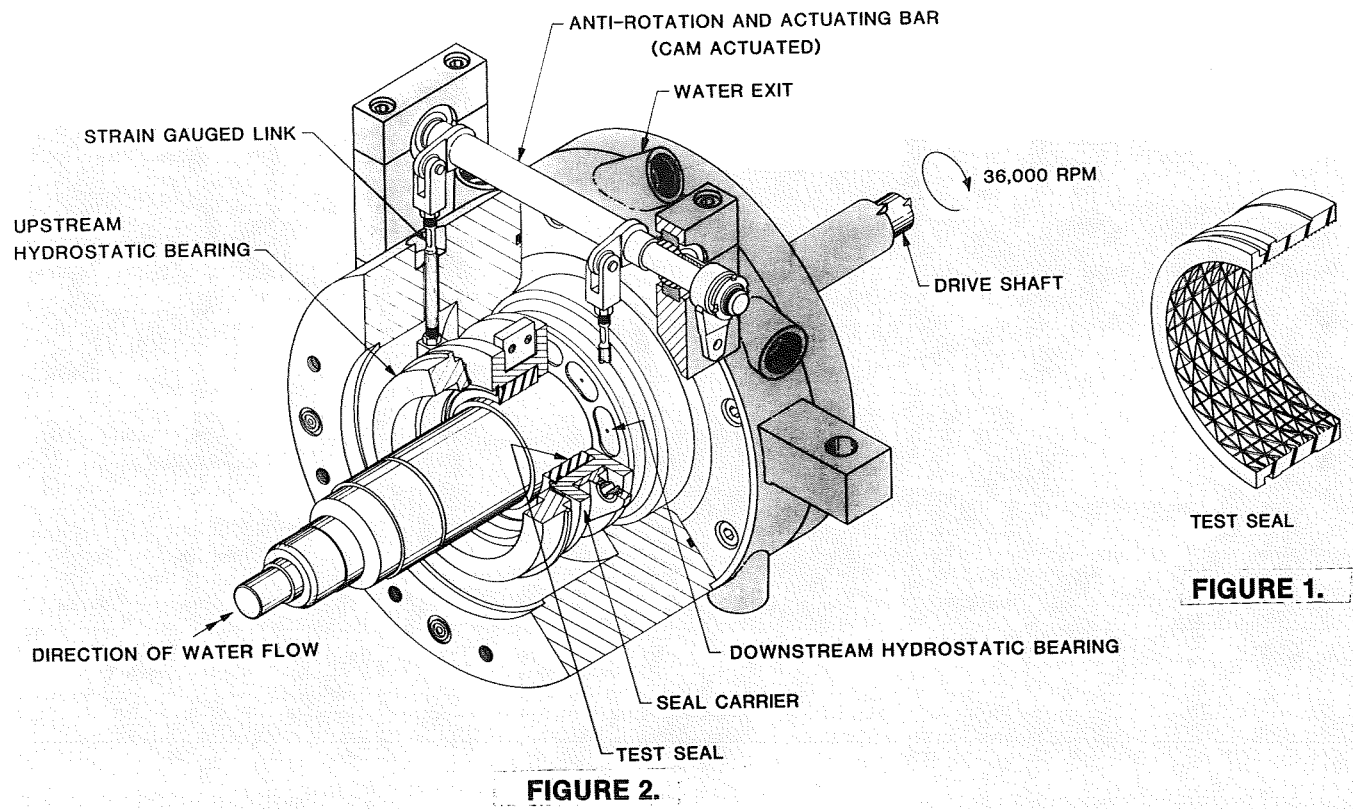
Data recorded on magnetic tape include turbine rpm, water temperature, flow rate, test rig inlet and discharge pressures, and the outputs of the proximity gauges and accelerometers on the damping seal carrier.

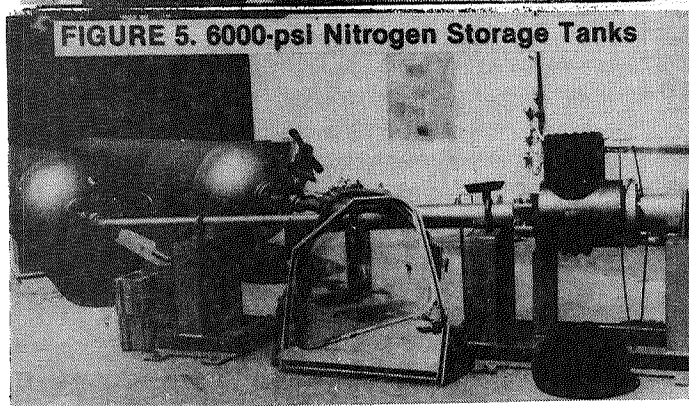
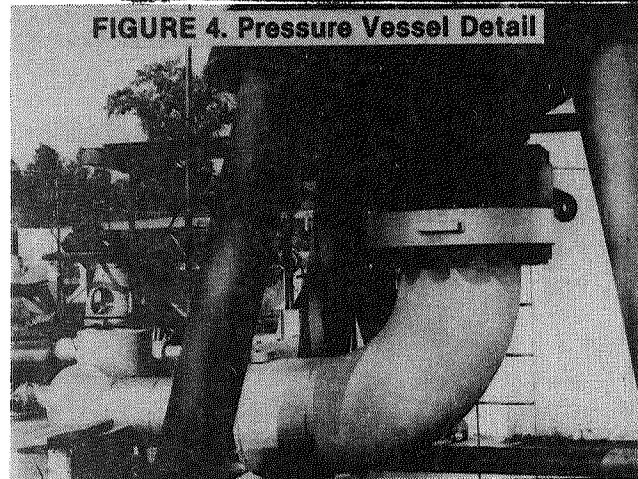
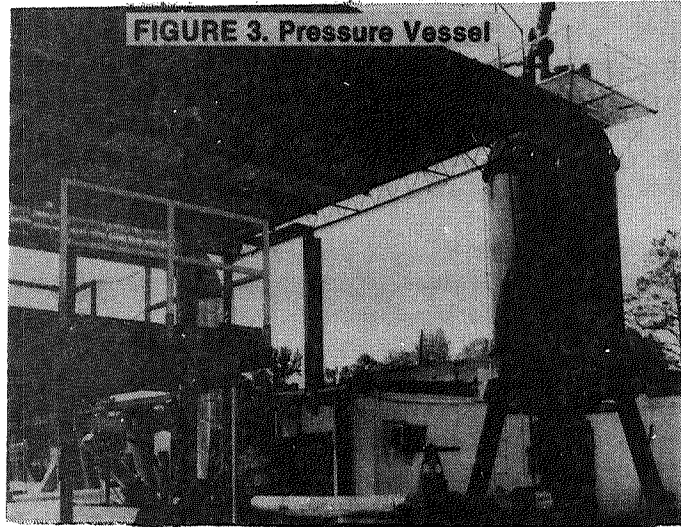
#### Current Status

Construction of the test rig is about to begin. The spline shafts connecting the gearbox to the test rig and turbine are in design, as is the modification of the standard gearbox. Modification of the blowdown test facility has begun.

### REFERENCES

1. Damping Seals for Turbomachinery, G. L. von Pragenau, NASA Technical Paper 1987 (1982).
2. A Discussion of the Theory of Sealing Devices, P. C. Stein, SAE Southern New England Section, 1961.
3. Heat Transmission, W. H. McAdams, McGraw-Hill, 1954 (data on water properties).





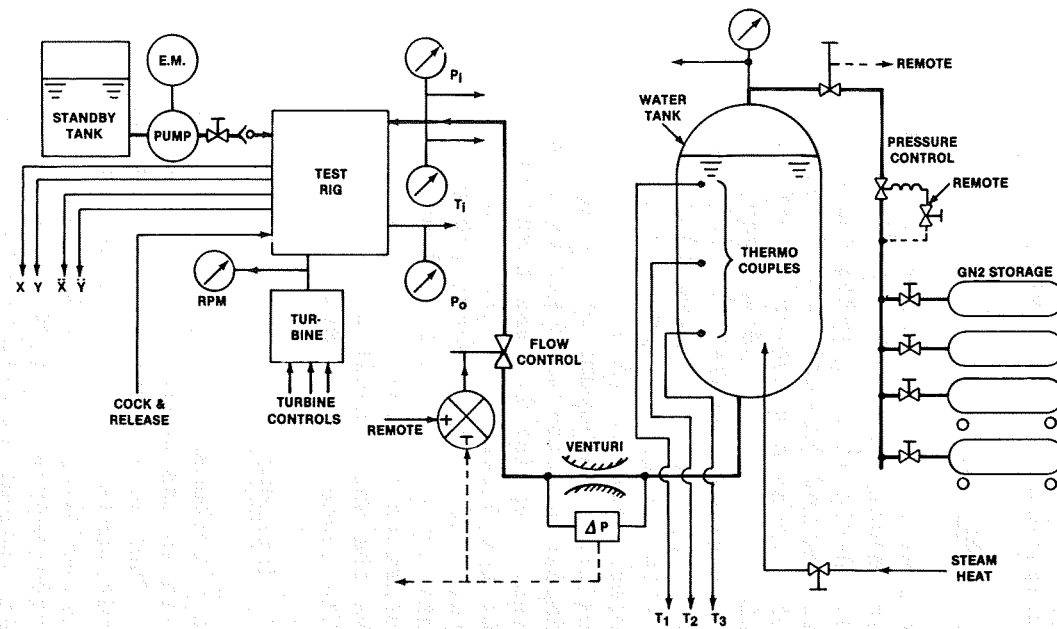


**FIGURE 6. Damping Seal Test Rig  
Instrumentation & Control  
(Preliminary)**

## DAMPING SEALS FOR TURBOMACHINERY

George L. von Pragenau  
Systems Dynamics Laboratory  
NASA Marshall Space Flight Center  
Huntsville, Alabama 35812 USA

### Abstract

The paper addresses rotor whirl stabilization of high performance turbomachinery which operates at supercritical speed. Basic whirl driving forces are reviewed. Stabilization and criteria are discussed. Damping seals are offered as a solution to whirl and high vibration problems. Concept, advantages, retrofitting, and limits of damping seals are explained. Dynamic and leakage properties are shown to require a rough stator surface for stability and efficiency. Typical seal characteristics are given for the case of the high pressure oxidizer turbopump of the Space Shuttle. Ways of implementation and bearing load effects are discussed. Feasibility was first proven analytically in a Center Director Discretionary Fund project in fiscal year 1981. The Rocketdyne Division of Rockwell International has since installed such seals in the high pressure oxidizer turbopump for development to raise the speed limit and thus achieve higher thrust for the Space Shuttle Main Engine.

### Introduction

High performance turbomachinery operates supercritically, i.e. with speeds above rotor resonances (critical speeds). Thus more power is being packed into lightweight units unless speed must be limited to prevent a rotor from whirling and causing damage. The speed limit challenged many as well as the writer to find a solution, not without earnest prayer (which God answered), and not without the foundation layed by others such as Dr. Henry Black from Scotland, who is well remembered.\*1-4

\* Deceased January 17, 1980.

### Constant Whirl Forces

Whirl is an orbital motion, superimposed upon the rotation of a rotor. Whirl forces are conceptually known, but accurate data are not readily available. Whirl forces (Fig. 1) are constant or increase with rotor motion.

Synchronous constant forces are caused by mass unbalance, runout rubbing, and seal runout. Subsynchronous constant forces are generated by rotating Coulomb friction forces in rotor joints.<sup>5</sup> The constant forces produce a forward whirl limit cycle response at synchronous or subsynchronous frequencies. Well balanced rotors with minute runout yield low vibrations, however, Coulomb friction in rotor joints can cause damaging rotor vibrations. Coulomb friction whirl can be reduced with lubricating the rotor joints and splines. The whirl can be avoided with tight but nonlubricated interference fits. Joint locking with a high rotor unbalance is not recommended.

### Proportional Whirl Forces

Increasing whirl forces can be most destructive. The simplest representation of the forces is a proportional relationship which couples rotor deflections by skewed-symmetric matrices to transverse whirl forces. Rotor hysteresis,<sup>6</sup> seal gaps,<sup>1</sup> journal bearings,<sup>7</sup> turbine blade bypass,<sup>8</sup> and impeller interactions drive usually subsynchronous forward whirls. External rotor rubbing drives a backward whirl that for hard rubbing can become supersynchronous (Fig. 1).

### Rotor Stabilization

The purpose of rotor stabilization is to negate the whirl regeneration of proportional forces while reducing the whirl limit cycle caused by constant forces. Rotor suspension damping, stiffness, and asymmetry are whirl stabilizers ordered after their efficiency. Natural damping is usually too low to prevent whirl in high pressure applications. Therefore, squeeze film dampers are used in turbomachinery



not only for vibration attenuation but also for whirl prevention.<sup>4</sup> However, such dampers are unsuitable for cryogenic applications. The difficulties prompted the development of damping seals.<sup>9</sup>

Damping seals are like annular seals, except for rough inner surfaces on stators (Fig. 2). Annular seals are a first step and were implemented to eliminate whirl from the high pressure turbopump (HPFTP) of the Space Shuttle Main Engine (SSME).<sup>2,3</sup> However, such seals can destabilize a rotor resonance below 1/2 the speed frequency. Damping seals improve this ratio to < 1/4, reduce leakage, and increase damping. Damping seals were recently installed in a high pressure oxidizer turbopump (HPOTP) for SSME development as shown in Figure 3.

### Stability Criterion

The stability condition of a single mass rotor (Fig. 4) suffices to examine the seal effect. Also, more complex models are represented, considering one resonant mode that is only negligibly detuned by the seal. Equation (1) describes the internal seal whirl effect with the whirl factor  $Q$  proportional to the seal damping  $C$ . The Couette factor  $c$  of equation (2) is the ratio of circumferential bulk flow velocity  $v$  to rotor surface velocity  $w$ .  $\Omega$  is the rotor speed in rad/s. Equation (3) is the characteristic equation of the model in Figure 4. Conformal mapping,<sup>10</sup> substituting with equation (1), and reordering produce the inequality (4) which sets the speed limit.  $K_y$  and  $K_z$  are the lateral suspension stiffnesses in  $y$  and  $z$ ,  $m_s$  is the rotor mass, and  $s$  is the Laplace operator.  $\Omega_1$  in equation (5) defines the first critical speed or resonance.

$$Q = c\Omega C \quad (1)$$

$$c = v/w \quad (2)$$

$$\begin{aligned} K_y K_z + Q^2 + sC(K_y + K_z) + s^2 [C^2 + m_s (K_y + K_z)] \\ + s^3 2Cm_s + s^4 m_s^2 = 0 \end{aligned} \quad (3)$$

9.1.0.1

442

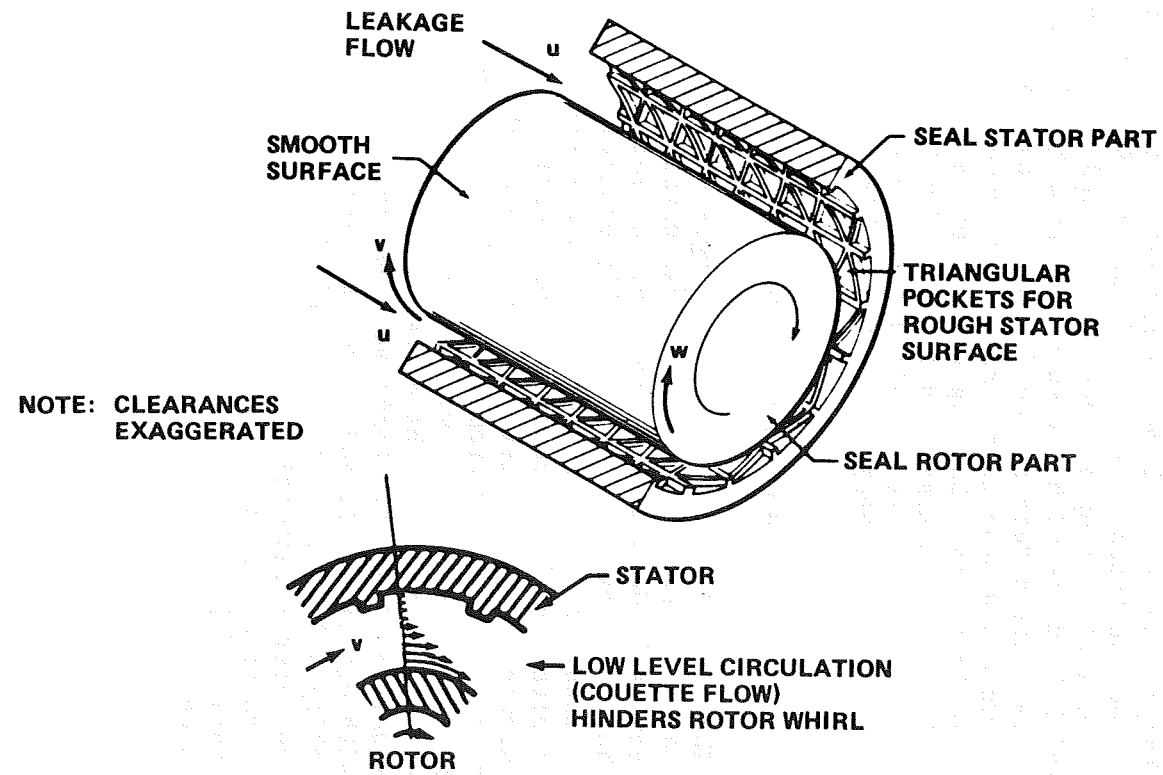


Figure 2. Damping Seal Concept.

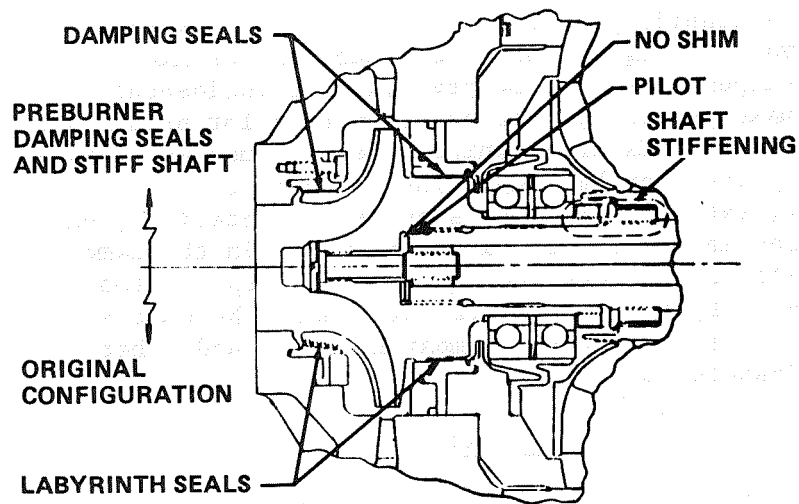


Figure 3. HPOTP Damping Seal Retrofit.

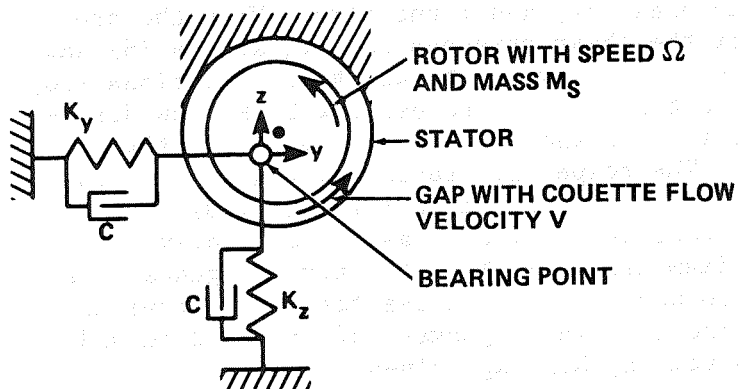


Figure 4. Simple Rotor Model.

$$\Omega < [(K_y + K_z)/2m_s + (K_y - K_z)^2/4C^2]^{1/2}/c \quad (4)$$

$$\Omega_1 = [(K_y + K_z)/2m_s]^{1/2} \quad (5)$$

The stability limit of inequality (4) is high for low  $c$  values, high rotor resonances, and asymmetric rotor suspensions. Asymmetry can be coincidental which makes symmetry a safer assumption for predicting speed limits. External whirl effects, such as turbine blade bypass, can be lumped into  $Q$  by raising  $c$ . Conversely, external damping, such as from bearings, can be lumped into  $C$  by reducing  $c$  to maintain the same  $Q$ . Thus external effects are equivalently represented internally by the Couette factor  $c$  which becomes a measure of stability for comparing seals and other rotor dynamic components.

#### Flow Friction

The flow velocities relative to the rotor and the stator differ because of rotation. The velocities describe bulk flow so turbulent flow can be treated similar to pipe flow. Equations (6) and (7) describe shear stresses  $\tau_r$  and  $\tau_s$  respective to the rotor and stator.  $f_r$  and  $f_s$  are respectively the rotor and stator surface frictions which generally differ.  $u$  is the axial bulk flow velocity and  $\rho$  is the fluid mass density. The seal gap pressure gradients are given in equations (8) and (9) for the axial and circumferential directions  $x$  and  $q$  respectively.  $h$  is the gap thickness,  $p$  the pressure, and  $t$  the time. Note the projections of the shear stresses from equations (6) and (7). The Reynolds numbers  $R_r$  and  $R_s$  in equations (10) and (11) are taken in the respective bulk flow directions of the rotor and the stator.  $\mu$  is the fluid viscosity. The respective rotor and stator friction factors  $f_r$  and  $f_s$  of equations (12) and (13) are Moody's approximation with  $2h$  as hydraulically equivalent pipe diameter  $D$ .<sup>11</sup> The effective roughnesses  $k_r$  and  $k_s$  reach pocket depth values for well circulating pockets. The triangular pockets of Figure 2 should be best for obtaining high  $k_s$  values.

$$\tau_R = \rho[u^2 + (v-w)^2]f_R/8 \quad (6)$$

$$\tau_S = \rho(u^2 + v^2)f_S/8 \quad (7)$$

$$-\partial p/\partial x = \rho[uf_R(u^2 + (v-w)^2)^{1/2} + uf_S(u^2 + v^2)^{1/2}]8h + \rho \, du/dt \quad (8)$$

$$-\partial p/\partial y = \rho[(v-w)f_R(u^2 + (v-w)^2)^{1/2} + vf_S(u^2 + v^2)^{1/2}]8h + \rho \, dv/dt \quad (9)$$

$$R_R = \rho 2h[u^2 + (v-w)^2]^{1/2}/\mu \quad (10)$$

$$R_S = \rho 2h(u^2 + v^2)^{1/2}/\mu \quad (11)$$

$$f_R = 0.0055 + 0.55(k_R/100h + 1/R_R)^{1/3} \quad (12)$$

$$f_S = 0.0055 + 0.55(k_S/100h + 1/R_S)^{1/3} \quad (13)$$

### Couette Flow

The rotor generates a Couette flow which is established downstream of the seal inlet according to equation (14) which follows from equation (9) for the case of negligible circumferential pressure gradients and flow accelerations. Equations (15) and (16) are the asymptotes for  $u = 0$  and  $u = \infty$  which enclose the Couette factor  $c$  for all surface friction ratios. Figure 5 shows  $c$  as a function of surface friction ratio and the axial velocity ratio  $u/w$ .  $c$  is low for high stator friction. The friction ratio is approximately the cubic root of the roughness ratio, as the equations (12) and (13) indicate. Therefore, large roughness ratios are required.

$$(v-w)f_R[u^2 + (v-w)^2]^{1/2} + vf_S(u^2 + v^2)^{1/2} = 0 \quad (14)$$

$$u = 0: c = 1/[1 + (f_S/f_R)^{1/2}] \quad (15)$$

$$u = : c = 1/(1+f_s/f_r) \quad (16)$$

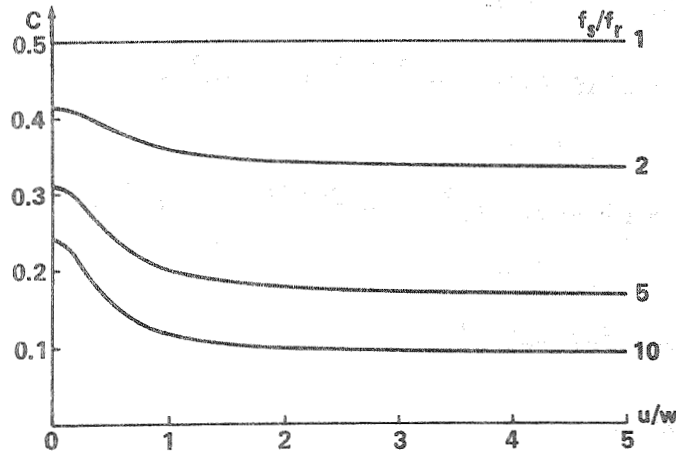


Figure 5. Couette factor  $c = v/w$  versus the friction and axial velocity ratios.

#### Dynamic Seal Parameters

The integral dynamic effect of a seal is described by stiffness  $K$ , damping  $C$ , mass  $m$ , whirl coupling  $c\Omega C'$ , and gyro coupling  $c\Omega m'$  as shown in vector equation (17).

$$\begin{bmatrix} F_y \\ F_z \end{bmatrix} = \begin{bmatrix} K+sC+s^2m & c\Omega(C'+sm') \\ -c\Omega(C'+sm') & K+sC+s^2m \end{bmatrix} \cdot \begin{bmatrix} y \\ z \end{bmatrix} \quad (17)$$

The detailed derivations are given in reference 9, except for minor differences in rearranging frequency square terms herein. Some parts of the derivation are repeated for continuity. Equations (18) through (22) define the dynamic parameters and their response to the whirl frequency  $\omega$ . The time constants are small. The basic stiffness  $K_0$ , damping  $C_0$ , and induced mass  $m_0$  are given in equations (23) through (25) for inlet loss  $f_1$ ; resistivities  $F$ ,  $G$ , and  $H$ ; dimensions  $h$ ,  $L$ , and  $r$  of seal gap, seal length, and seal radius; axial velocity  $u$ ; and mass density  $\rho$ . The resistivities are

given by the equations (26) through (32). The time constants are defined by the equations (33) through (36).

$$K = [K_o - (c\Omega)^2 m_o] / (1 + \omega^2 \tau^2) \quad (18)$$

$$C = [C_o (1 + \omega^2 \tau \tau_a) + m_o \omega^2 (\tau - \tau_b) - \tau K_o] / (1 + \omega^2 \tau^2) \quad (19)$$

$$m = [m_o (1 + \tau \tau_b (\omega^2 + (c\Omega)^2)) - C_o (\tau - \tau_a)] / (1 + \omega^2 \tau^2) \quad (20)$$

$$C' = [C_o (1 + \omega^2 \tau \tau_b) + 2m_o \omega^2 (\tau - \tau_b)] / (1 + \omega^2 \tau^2) \quad (21)$$

$$m' = [2m_o (1 + \omega^2 \tau \tau_b) - C_o (\tau - \tau_a)] / (1 + \omega^2 \tau^2) \quad (22)$$

$$K_o = (\pi r / h) u^2 (1 + f_1) \tau L (F + H) / 2 \quad (23)$$

$$C_o = (\pi r / h) (\tau / \tau_a) L^3 (F + G) / 12 \quad (24)$$

$$m_o = C_o \tau_o \tau_a / \tau_b \quad (25)$$

$$F = \rho [f_r (u^2 + (v-w)^2)^{1/2} + f_s (u^2 + v^2)^{1/2}] / 8h \quad (26)$$

$$G = \rho u^2 [(f_r - g_r) / (u^2 + (v-w)^2)^{1/2} + (f_s - g_s) / (u^2 + v^2)^{1/2}] / 8h \quad (27)$$

$$H = \rho [h_r (u^2 + (v-w)^2)^{1/2} + h_s (u^2 + v^2)^{1/2}] / 8h \quad (28)$$

$$g_r = h_r / (1 + R_r k_r / 100h) \quad (29)$$

$$g_s = h_s / (1 + R_s k_s / 100h) \quad (30)$$

$$h_r = (0.55/3) \cdot (k_r / 100h + 1/R_r)^{1/3} \quad (31)$$

$$h_s = (0.55/3) \cdot (k_s / 100h + 1/R_s)^{1/3} \quad (32)$$

$$\tau = \rho L / [\rho u(1+f_1) + L(F+G)] \quad (33)$$

$$\tau_a = \rho L / [\rho u(1+f_1) (4+6\rho u/L(F+G) + L(F+G))] \quad (34)$$

$$\tau_b = \rho L / [4\rho u(1+f_1) + L(F+G)] \quad (35)$$

$$\tau_o = \rho / (F+G) \quad (36)$$

The flow induced masses in equation (17) are dipol masses that are negligible against the rotor mass. The whirl coupling is indeed proportional to the Couette factor  $c$  as shown earlier in equation (1). Table 1 gives the dimensions of diverse inlet and outlet seals of the HPOTP preburner pump impeller (Fig. 3). Table 2 lists the analytical results for labyrinth, damping, and smooth annular seals. Table 2 shows that the leakage rates of labyrinth and damping seals are comparable, while the smooth annular seals leak 1.6 times more. Tests by Rocketdyne produced the same ratio. The whirl ratio of damping seals is  $< 1/4$  but 0.5 for the other seals. Damping seals have the highest damping while the smooth annular seals show the highest stiffness.

Table 1. HPOTP Preburner Pump Seal Dimensions for Inlet and Outlet at Full Power 30,367 RPM

PBP Seals Dimension	Gap mils 1	Diam. inch	Leng. inch	Pocket mils 2	Press psi 3
Inlet Laby.	6	2.85	0.63	230	2006
Inlet Damp.	6	2.898	0.66	10(20)	2006
Inlet Smooth	6	2.898	0.66	0.032	2006
Outlet Laby.	4	3.345	0.87	80	6505
Outlet Damp.	4	3.3371	0.88	10(20)	6505
Outlet Smooth	4	3.3371	0.88	0.032	6505

NOTE: 1 = radial gap, 2 - effective pocket depth (actual depth), 3 = pressure difference.

Table 2. HPOTP Preburner Pump Seals' Dynamic for Inlet and Outlet at Full Power 30,367 RPM

PBP Seals Dimension	Stif. Klb/in	Whirl Klb/in	Damp. Lbs/in	Ratio c %	Leak Lb/s
Inlet Laby.	2	2	1	50	4.94
Inlet Damp.	106	46	57	23	5.18
Inlet Smooth	151	105	53	50	7.90
Outlet Laby.	20	36	23	50	5.13
Outlet Damp.	447	281	388	22	5.09
Outlet Smooth	935	544	302	50	8.51

NOTE: % ratio times maximum speed must be below 1st critical speed. Analysis is for 0.25 inlet loss,  $2.59E-8$  psi-s lox viscosity, and  $1.05E-4$  psi(s/in.)<sup>2</sup> lox density.

#### Seal Installation

Figure 3 illustrates a retrofitting case where inlet and outlet labyrinth seals were replaced by damping seals to inhibit a 450 Hz whirl at 30,000 RPM. Damping seals fit always into the space of labyrinth seals. Leakages are comparable, but stiffness and damping are much higher as seen in Table 2. Both changes inhibit whirl, lower vibrations, and increase critical speed. Damping seals seem to be more effective than squeeze film dampers, simpler, and smaller. Damping seals are suggested instead of smooth annular seals to reduce leaks and to suppress whirl.

The high stiffness of damping seals must be, however, considered when replacing labyrinth seals. Eccentricities between bearings and seals can cause unexpected side loads.

#### Soft Seals

The side loads can be reduced with small eccentricities, if tight tolerance costs are not prohibitive. Soft seals are another concept worth

considering. Damping seals become softer as roughness is increased. Axial flow is thus reduced and the fluid compressibility much enhanced. Another way is the insertion of a labyrinth seal downstream to shorten a damping seal without changing leakage.

### Hard Seals

The hard seal approach takes advantage of high seal stiffness and uses the seals for supporting the rotor. Critical speeds are so increased and loads of pump and turbine discharges are shared by the seals. Tight tolerances (eccentricities) can be circumvented by loose fittings for the bearings' outer races. The bearings support the rotor at startup and cutoff when the seals are unpressurized or soft. At operation speed the seals are stiff and can take over. Good bearing life is expected because the bearings float mostly during their operation in a loadless condition. Outer race spinning due to floating can be prevented with antirotation devices.

### Conclusion

Damping seals are new technology for improving turbomachinery operations. The shown properties encourage many applications from retrofitting machines that are beset by whirl problems to new and more efficient designs. We are grateful and do not take this progress for granted - be blessed the same way.

### References

1. Black, H. F.: Effects of Hydraulic Forces in Annular Pressure Seals on the Vibrations of Centrifugal Pump Rotors. Journal M.E.Sc. vol. 11, no. 2, p. 206, 1969.
2. Childs, D. W.: The Space Shuttle Main Engine High-Pressure Fuel Turbopump Rotor-Dynamic Instability Problem. Trans. ASME, Journal of Engineering for Power, vol. 100, p. 48, January 1978.

3. Ek, M. C.: Solving Subsynchronous Whirl in the High-Pressure Hydrogen Turbomachinery of the SSME. AIAA Journal of Spacecraft and Rockets, vol. 17, no. 3, p. 208, May-June 1980.
4. Ehrich, F. F. and Childs, D. W.: Self-Excited Vibration in High-Performance Turbomachinery. Mechanical Engineering vol. 106, no. 5, p. 66, May 1984.
5. Kimball, A. L.: Internal Friction Theory of Shaft Whirling. General Electric Review, vol. 27, no. 4, p. 244, April 1924.
6. Bucciarelli, L. L.: On the Instability of Rotating Shafts due to Internal Damping. Journal of Applied Mechanics, vol. 49, p. 425, June 1982.
7. Newkirk, B. L., and Taylor, H. D.: Shaft Whipping due to Oil Action in Journal Bearing. General Electric Review, vol. 28, p. 559, 1925.
8. Alford, J.: Protecting Turbomachinery from Self-Excited Rotor Whirl. ASME Transactions, Journal of Engineering for Power, p. 333, October 1965.
9. von Pragenau, G. L.: Damping Seals for Turbomachinery. NASA Technical Paper no. 1987, March 1982.
10. Nyquist, H.: Regeneration Theory. Bell Systems Technical Journal, vol. 11, p. 126, January 1932.
11. Moody, L. F.: Friction Factors for Pipe Flow. Trans. ASME, New York, p. 671, November 1944.

VIBRATION CHARACTERISTICS OF THE HPOTP  
(High Pressure Oxygen Turbopump)  
OF THE SSME  
(Space Shuttle Main Engine)<sup>1</sup>

Dara W. Childs, Professor  
David S. Moyer, Graduate Research Assistant  
Mechanical Engineering Department  
Texas A&M University  
College Station, Texas 77843

Abstract

A review is presented of various rotordynamic problems which have been encountered and eliminated in developing the current flight engines, and continuing subsynchronous problems which are being encountered in developing a 109% power level engine. The basic model for the HPOTP including the structural dynamic model for the rotor and housing and component models for the liquid and gas seals, turbine-clearance excitation forces, and impeller-diffuser forces are discussed. Results from a linear model are used to examine the synchronous response and stability characteristics of the HPOTP, examining bearing load and stability problems associated with the second critical speed. Various seal modifications are examined and shown to have favorable consequences with respect to bearing reactions and stability. Difference between linear and nonlinear model results are discussed and explained in terms of simple models.

The transient nonlinear model is used to demonstrate forced subsynchronous motion similar to that observed in test data for models which are lightly damped but stable. The subsynchronous motion

---

<sup>1</sup>The work reported herein was supported in part by NASA Contract NAS8-34505 from the George C. Marshall Space Flight Center; Thomas Fox, Technical Monitor.

results from bearing clearance nonlinearities. Simulation results indicate that synchronous bearing loads can be reduced but that subsynchronous motion is not eliminated by seal modifications alone.

## INTRODUCTION

The SSME (Space Shuttle Main Engine) has been under development by Rocketdyne Division of Rockwell International since the early 1970's. The George C. Marshall Space Flight Center has administered the program development for NASA. The SSME is designed to operate at the following three conditions:

MPL (Minimum Power Level);  $\omega = 20,900$  cpm

RPL (Rated Power Level);  $\omega = 28,200$  cpm

FPL (Full Power Level);  $\omega = 30,380$  cpm

At RPL the turbines develop approximately  $1.71 \times 10^7$  watts (22,900 Hp). FPL is 109% of RPL. RPL performance is adequate for the equatorial orbits which have been flown to date; however, polar orbits require FPL performance. This paper concerns various rotordynamics problems related to the HPOTP (High Pressure Oxygen Turbopump) which were eliminated in developing a reliable RPL engine and new problems which are being encountered in developing FPL performance.

As compared to more conventional turbomachinery, liquid-rocket-engine turbopumps present the following distinctive rotordynamics development problems:

- (a) The units operate in ball bearings which are lubricated with the cryogenic fluid being pumped. The bearings themselves provide virtually no damping.
- (b) Because of the extraordinarily low viscosity of liquid oxygen and liquid hydrogen, neither fluid can be effectively used in a squeeze-film damper. Moreover, the presence of these cryogenic fluids precludes the use

of other fluids in conventional dampers or elastomeric dampers.

- (c) Oxygen-compatible motion transducers are under development; however, they are not currently available. Moreover, a typical turbopump design presents severe difficulty in access to the rotating assembly for relative motion measurements; particularly, when access for motion measurements was not a consideration in the initial design. Vibration data for the SSME turbopumps has largely been confined to the output of accelerometers mounted on the housing. For most of the development period of the HPOTP, there has been no speed probe pickup and no once-per-revolution phase mark from the shaft to use in data analysis.

The calculated linear critical speeds for the current nominal HPOTP are at approximately 12,500 cpm (208 Hz) and 32,500 cpm (540 Hz). These calculated values are for complete housing-rotor models including seals, clearance-excitation forces, gyroscopic coupling, etc. The arrangement of the high pressure turbopumps in the powerhead are illustrated in figure 1. The HPOTP rotating assembly is illustrated in figure 2. The undamped, zero-running-speed, rotor-housing modes associated with the first and second critical speeds are illustrated in figure 3. The modeshape associated with the first critical speed primarily involves overhung motion of the turbine with relatively small amplitudes at the bearings and main impeller. The modeshape associated with the second critical speed involves large amplitudes at the main impeller and bearings with small amplitudes at the turbine.

Initial vibration problems with the HPOTP involved motion associated with the first critical speed. Synchronous and subsynchronous (at approximately 200 Hz) motion was excessive. This problem was remedied by changing the turbine

interstage seal from a stepped-labyrinth configuration to a convergent taper seal with a honeycomb stator and a smooth rotor. This change was implemented based on the beneficial consequences of a similar change in the pump interstage seals of the HPFTP (High Pressure Fuel Turbopump) [1].

The second problem associated with the HPTOP involved subsynchronous vibrations at approximately 400-420 Hz. This motion tended to initiate when the running speed reached approximately 400 Hz, and persisted as subsynchronous motion when the running speed was increased. A failure and explosion of the HPOTP occurred in a test run when the running speed first traversed the maximum-amplitude frequency range and then was reduced to and remained at the now synchronous frequency. The failure was attributed to an inadequate bearing-carrier design which caused unequal load sharing of the bearings. Subsequently, redesigned bearing carriers eliminated the "400 Hz" subsynchronous motion. The general feeling was that the new bearing carrier designs caused a more equal load sharing and maintained the correct axial bearing preloads, thus realizing the "expected" radial stiffness of the bearings and elevated the rotor second critical speed.

The bearing-carrier redesign was sufficient to yield a reliable pump for RPL operations; however, demonstration of FPL capability has been impeded by repeated occurrence of subsynchronous motion in the 450-500 Hz frequency range. The incidence of this motion rarely occurs during initial operation at higher power levels, but tends to develop after an accumulation of time and develops more rapidly with higher synchronous vibration levels. However, once a unit begins to "whirl", it will repeatedly whirl, generally with progressively increasing severity. The frequency of the subsynchronous motion is sometimes at a fixed fraction of running speed ranging from 88 to 95%. This "tracking" characteristic is in marked contrast to the earlier "400 Hz" phenomenon where the whirl-frequency of the

subsynchronous motion remained constant, relatively independent of running speed.

Post-run inspection of turbopumps has revealed that, although the balls in some bearings, primarily bearing 2, appear to be unblemished, their diameters have in fact, been reduced by as much as 0.17 mm in some cases. The cause of this dimensional attrition is unknown, but has been ascribed to either excessive radial loads or the absence of radial loads which leads to skidding.

The analysis results which have been completed to date and are reported herein do not provide a complete or comprehensive explanation for the measured dynamic characteristics of the HPOTP; however, they do provide answers for the following questions:

- (a) What are the linear dynamic characteristics of the nominal turbopump model with respect to critical-speed locations, bearing reactions, predicted housing accelerometer levels, and predicted onset speeds of instability?
- (b) How can the linear dynamic characteristics be improved by feasible, physical modification of the HPOTP seals?
- (c) What causes the subsynchronous motion?
- (d) From a rotodynamics viewpoint, what are the principal problems experienced by the HPOTP?
- (e) What improvements are possible with the HPOTP?

The following section briefly describes the structure and components of the rotordynamic model, with the succeeding section describing the results of linear and nonlinear analysis.

#### THE ROTORDYNAMICS MODEL

Structural Dynamics Model. The structural-dynamics model of the rotor and the housing form the

basic framework of the turbopump model. Both the housing and rotor structural dynamics models used here were developed by Rocketdyne. A general three-dimensional finite-element approach was used to model the HPOTP housing without the rotor. A lumped parameter model was developed for the rotor using beam structural elements and lumped masses and inertias. The rotordynamics model uses modes from the housing model (without the rotor) and free-free rotor modes.

Bearings. The bearings are the structural elements which tie the rotors and housing together. As illustrated in figure 2, there are two sets of bearings. The net load from each set is transmitted through a plate-cylinder structure to the housing. The bearings in a bearing set are axially preloaded against each other, but are not designed to accept axial thrust loads from the turbopumps. A balance-piston arrangement at the discharge of the main impeller absorbs axial thrust, and radial clearances are provided at the bearing outer faces to allow the bearings to slip axially without developing excessive axial loads.

Experience and limited test data [2] for the SSME bearings indicate a nominal stiffness of approximately  $8.76 \times 10^7$  N/m. This is approximately one half of the values predicted by A. B. Jones-based analysis [3].

The radial clearances provided at the bearings to permit axial motion provides an essential "dead-band" nonlinearity. The clearance values used in this study are

$$\delta_P = 0.0127 \text{ mm}, \delta_T = 0.0127 \text{ mm} \quad (1)$$

where P and T denote pump and turbine bearings.

Liquid Seals. Liquid wear-ring seals are provided at the inlet and discharge of the boost impeller. The current inlet seal is a stepped labyrinth design with four cavities. The current

discharge seal is a three segment, stepped seal. Each constant-radius seal segment has a series of circumferential grooves.

Experience and limited test data [3] have shown that labyrinth or serrated seals of the type currently employed on the impeller inlet and discharge yield stiffness and damping coefficients which are substantially smaller than corresponding values for smooth constant clearance seals. Replacing the current grooved boost-impeller wear-ring seals with plain annular seals has the potential for a beneficial increase in stiffness and damping in the HPOTP. In fact, as the following discussion explains, various additional possibilities exist for optimizing seals.

The force-motion model for liquid seals has the form

$$- \begin{Bmatrix} F_X \\ F_Y \end{Bmatrix} = \begin{bmatrix} K & k \\ -k & K \end{bmatrix} \begin{Bmatrix} X \\ Y \end{Bmatrix} + \begin{bmatrix} C & c \\ -c & C \end{bmatrix} \begin{Bmatrix} \dot{X} \\ \dot{Y} \end{Bmatrix} + \begin{bmatrix} M & m \\ -m & M \end{bmatrix} \begin{Bmatrix} \ddot{X} \\ \ddot{Y} \end{Bmatrix}$$

In this model (X, Y) are the components of the relative motion between the rotor and housing. Black, et al. [5, 6] were responsible for most of the analytical developments related to the analysis of seals leading to the definition of stiffness, damping, and added-mass coefficients. His analysis demonstrates that the "cross-coupled" stiffness coefficient, k, arises solely due to fluid rotation within the seal. As a fluid element proceeds axially along an annular seal, shear forces at the rotor accelerate or decelerate the fluid tangentially until an asymptotic value is reached. For a seal with the same directionally-homogeneous surface-roughness treatment on the rotor and the housing, the average asymptotic tangential velocity is  $R\omega/2$  where R is the seal radius and  $\omega$  is the rotor running speed.

The cross-coupled stiffness coefficient k acts in opposition to the direct damping coefficient C to destabilize rotors. Hence, steps which can be taken

to reduce the net fluid rotation within a seal will improve stability by reducing  $k$ . The following two steps are currently under consideration for providing more net damping to the HPOTP rotating assembly:

- (a) If the inlet tangential velocity can be reduced, the high axial velocities in a cryogenic seal are such that the fluid may proceed through a seal without substantially increasing its tangential velocity. An antivortex web has been proposed at the inlet to the boost-impeller inlet seal to reduce the inlet tangential velocity and yield a reduced  $k$ . This practice has been followed previously for the labyrinth seals of high pressure compressors.
- (b) Von Pragenau [7] has recently demonstrated that the asymptotic tangential velocity can be modified if a different surface roughness is used for the rotor and stator elements. Rough rotor/smooth stator and smooth rotor/rough stator combinations yield higher and lower asymptotic values, respectively. Von Pragenau calls the rough stator/smooth rotor configuration a "damper seal" because of its enhanced stability characteristics. The roughness has the additional potential benefit of reducing leakage. Damper seal configurations are presently under consideration for both the inlet and discharge seals of the boost impeller.

Liquid seal coefficients for the boost impeller seals were calculated based on analysis by Childs and Kim [8]. Current analyses yield finite-length solutions for constant-clearance or convergent-tapered seals with different but directionally-homogeneous surface roughness treatments on the rotor and stator.

Gas Seals. The HPOTP turbines are shrouded, and single-cavity tip seals are provided to reduce

leakage between the turbine shroud and the stator. The interstage seal between the turbines uses a honeycomb stator element with a smooth rotor and inlet anti-vortex ribs to reduce the inlet tangential velocity component. A floating-ring shaft seal is provided at the turbine discharge to restrict leakage of the hot turbine gases towards the lox within the pump. The flow across this seal is choked.

Seal coefficients calculations used in the study are based on the analyses of Nelson [9]. The analyses apply to constant-clearance or convergent taper geometries, account for the development of tangential velocity within the seals, and different but directionally-homogeneous surface roughness on the rotor and stator.

Turbine Clearance Excitation Forces. Clearance excitation forces are developed by turbines due to the dependency of local efficiency on local clearances. The destabilizing force is modeled by

$$\begin{Bmatrix} F_X \\ F_Y \end{Bmatrix} = \begin{bmatrix} 0 & k_T \\ -k_T & 0 \end{bmatrix} \begin{Bmatrix} X \\ Y \end{Bmatrix} ; k_T = \frac{\beta T}{D_p H} \quad (3)$$

where T is the turbine torque, D<sub>p</sub> is the average pitch diameter of the turbine blades, H is the average height, and β defines the change in turbine efficiency due to uniform changes in clearance. Again, the components (X, Y) of Eq. (3) define the displacement of the turbine relative to the housing. Thomas initially identified this destabilizing phenomenon [10], while Alford [11] subsequently and independently developed the same model. Test results for shrouded turbines have yielded values for β on the order of 0.6 [12].

Impeller-Diffuser Forces. A test program has been under way at the California Institute of Technology for some time to measure the static and dynamic forces experienced by a pump impeller in either a volute or a vaned diffuser. Chamieh et al.

[13] have defined the following model on the basis of static measurements of an impeller within a vaned diffuser:

$$-\frac{1}{\rho A_2 V_2^2} \begin{Bmatrix} F_X \\ F_Y \end{Bmatrix} = \begin{bmatrix} K^* & k^* \\ -k^* & K^* \end{bmatrix} \begin{Bmatrix} X/R_2 \\ Y/R_2 \end{Bmatrix} = \begin{bmatrix} -2.0 & 0.7 \\ -0.7 & -2.0 \end{bmatrix} \begin{Bmatrix} X/R_2 \\ Y/R_2 \end{Bmatrix} \quad (4)$$

where  $R_2$  is the impeller radius,  $\rho$  is the fluid density,  $V_2 = R_2\omega$  is the impeller tip velocity, and  $A_2 = 2\pi R_2 b_2$  is the exit flow area. Note that the direct-stiffness coefficient in Eq. (4) is negative, i.e., the impeller-diffuser force causes a reduction in rotor stiffness. From Eq. (4), the dimensional impeller-diffuser coefficients are defined by

$$\bar{K} = K^* \frac{\rho A_2 V_2^2}{2R_2} = K^* (\pi \rho b_2 R_2^2) \omega^2 \quad (5)$$

$$\bar{k} = k^* (\pi \rho b_2 R_2^2) \omega^2$$

## ANALYSIS PROCEDURES AND RESULTS

### Introduction

The radial clearances which are provided at the outer races of the bearings to permit axial slipping and prevent the bearings from absorbing axial loads provide the essential nonlinearity in a rotordynamics model for the HPOTP. If these "dead band" clearances are eliminated, the resultant model is basically linear. As the following sections demonstrates, the results of linear and nonlinear analysis differ substantially, but linear analysis remains an efficient procedure for general characterization of the turbopump's rotordynamics.

### Linear Analysis Procedure and Results

#### **Rotordynamic Characteristics of the Nominal Model**

The analysis procedure used here is basically the same as that outlined in reference [1]. Modal

coordinates based on the zero-running-speed coupled rotor-housing mode are used. Gyroscopic coupling and forces due to seals, turbine clearance-excitation, the interaction of impellers and diffusers, damping, etc., couple the modal coordinates via modal stiffness, damping, and inertial matrices. The onset speed of instability for a turbopump configuration is defined by calculating the complex eigenvalues of the system dynamic matrix at various speeds. Synchronous-response amplitudes of bearing reactions and acceleration levels of accelerometers mounted on the turbopump housing due to imbalance are calculated.

For the purposes of the present discussion, the nominal linear model is defined as having bearing stiffness on the order of  $8.76 \times 10^7$  N/m ( $.5 \times 10^6$  lbs/in). Calculated seal coefficients are based on the dimensions of seals currently used in the turbopump. The clearance-excitation force coefficient at the turbines use a  $\beta$  of 0.4.

An inspection of the modeshapes of figure 3 indicates that the clearance-excitation force at the turbine represents the dominant destabilizing excitation force for motion associated with the first critical speed. Following the initial "400 Hz" subsynchronous vibration problem, the suggestion was made [15] that impeller-diffuser-interaction forces provided the principal destabilizing mechanism for motion associated with the second critical speed. The published cross-coupling coefficients of Eq. (4) certainly supported this view. If the nominal model includes the stiffness coefficients of Eq. (4), the OSI (Onset Speed of Instability) is only 17,200 cpm. However, the stability is very sensitive to damping; and the additional 875 Ns/m (5.0 lb sec/in) at the main impeller with no bearing damping elevates the OSI to 30,480 cpm. The whirl frequency at OSI is 536 Hz. This concentrated damping coefficient acts to restrain relative motion between the rotor and housing, and is used in the nominal linear model.

Figure 4 illustrates the bearing reaction for running speeds from 5,000 to 40,000 cpm. The first

and second critical speeds are evident, with the second critical speed clearly having little or no damping. Figure 5(a) illustrates the same results for speeds from 5,000 cpm to FPL. Figures 5(b) and (c) illustrate predicted acceleration levels for accelerometers mounted on the housing at the pump and turbine ends of the turbopump. Clearly, FPL is quite near the predicted second critical speed. Also, while the bearing reactions are responsive to the "rotor" critical speeds, the housing accelerometer levels may respond more sharply to rotor-housing combined modes. This is particularly true for the first critical speed at approximately 12,500 rpm. However, the predicted accelerometer levels are quite responsive to motion associated with the "rotor" second critical speed at approximately 32,500 cpm.

- (a) Response. The proximity of the second critical speed to FPL is a continuing cause for concern with respect to excessive bearing loads. Even modest losses of bearing stiffnesses are sufficient to drop the second critical speed into the operating range.
- (b) Stability. Based on the prior "400 Hz" experience with this turbopump, the second critical speed appears to be lightly damped and subject to instability.

#### **Seal Modifications to Improve Rotordynamic Response and Stability**

The preceding material demonstrated the relevant dynamic characteristics of the HPOTP with respect to response and stability. The present section deals with predicted improvements in rotordynamic response due to the following seal modifications:

- (a) Replace the current inlet and discharge seals of the boost impeller with "damper" seals using a rough stator and smooth rotor. Test results at Texas A&M University of proposed damper seal and smooth seals flight candidates show a substantial reduction in

leakage due to roughness and slight increases in direct stiffnesses and net damping [8].

- (b) Replace the current unshrouded impeller with shrouded impellers and use the outer surfaces of the shrouded impeller to develop seal forces.

Figure 6 illustrates the bearing reactions which result for choice (a), and a comparison of this result with the nominal-model results of figure 5 (a) indicates a sharp reduction in bearing reactions. Moreover, the OSI is increased moderately. Table 1 provides a summary of the results for both the nominal configuration and the seal modifications cited above and demonstrates that the damper seals yield a predicted reduction in bearing loads on the order of 37% and an increase of the predicted OSI to 36,350 rpm.

CONFIGURATION	OSI (cpm)	WHIRL FREQ. (Hz)	BEARING REACTIONS at FPL (lbs)			
			1	2	3	4
Nominal	30,480	536	553	635	667	548
Nominal with With Boost- Impeller Seals	36,350	576	251	349	513	411
Nominal with Shrouded- Inducer Seal	59,950	315	80	85	57	58

**Table 1. Linear OSI, whirl frequency, and predicted bearing reactions at FPL.**

Figure 7 illustrates the results for the shrouded inducer configuration. Stated briefly, the second critical speed is simply eliminated for this configuration, and OSI is much greater than FPL.

An assessment of the results presented in figures 6, 7, and table 1 supports the following general conclusions:

- (a) Modification of the boost impeller seals has the potential for significantly reducing bearing reactions at FPL as compared to the nominal model. However, the second critical speed remains only slightly above FPL and any loss of bearing stiffness will drop it into the operating range.
- (b) The damper-seal modification yields a predicted increase of the OSI by 19%.
- (c) The shrouded-inducer design eliminates both the second critical speed and the stability problem.

#### Nonlinear Analysis Procedures and Results

As noted previously, the bearing "dead-band" clearances provide the essential nonlinearity in the HPOTP model. The bearing clearances interact with the effects of side loads and rotor imbalance to yield significantly different results for a nonlinear model than those predicted by linear models.

Figure 8 illustrates the analytical model used by Yamamoto [14] to investigate the influence of bearing clearances on rotordynamic response in the absence of side loads. For zero bearing clearances, the model of figure 8 reduces to a simple Jeffcott model with viscous external damping. Figure 9 illustrates the response characteristics for a progressive increase in the ratio of bearing clearance to imbalance eccentricity  $\hat{e} = e/a$ . The results are for a damping ratio of 2.5%, and indicate the speed location of maximum bearing reactions is reduced by increasing  $\hat{e}$ . Moreover, the drop in amplitude for speeds above the maximum bearing-load can be precipitous. The response characteristics of figure 9 can give rise to "jump" phenomena with the synchronous vibration level jumping either up or down for very small changes in running speed. Flight data for the HPOTP have demonstrated sudden step increases in accelerometer levels.

From these results, one would anticipate that bearing clearances could easily drop the peak-bearing-load running speed location associated

with the second critical speed into the operating range. In fact, parametric studies of the bearing clearances clearly confirm this result [15]. They also confirm that peak-bearing-load speeds can be reduced below FPL for sufficiently large clearances. Hence for a given running speed, a nonlinear model with bearing clearances can yield either substantially larger or smaller bearing reactions than the linear model.

The nonlinear model was verified by comparison to results from the linear model, e.g., the second-critical-speed location at 32,500 cpm was obtained for zero bearing clearances. Figure 10 illustrates the bearing 2 reaction magnitude and turbine acceleration signals at FPL for the nominal model with the bearing clearances of Eq. (1). Observe the "clipping" of the bearing reaction magnitudes in figure 10 (a), which results from motion through the bearing deadband. Motion in and out of the deadband results as a combination of static displacement due to the impeller and turbine side loads and elliptical orbits due to imbalance. Bearing clipping generates a nearly periodic impulsive loading at the bearing that excites the beating motion which is evident in the accelerometer signal prediction of figure 10 (b). Spectrum analysis results of the accelerometer signals at FPL and two higher speeds are provided in figure 11 and reveal a subsynchronous signal at 26,500 cpm (443 Hz). Both the synchronous and subsynchronous signals are observed to decrease as the running speed increases. Observe that the frequency of the subsynchronous motion is consistent with frequencies observed in test data as opposed to the linear predictions of 520 Hz. The linear model corresponding to the result of figure 10 is lightly damped but stable. The nonlinear model remains in a limit cycle motion with subsynchronous components until the destabilizing force components at the main impeller are increased to 250% of their nominal values, but then diverge exponentially. Based on these observations, the subsynchronous component of figure 11 is deemed to be the result of bearing

nonlinearities and not the result of an instability. However, the nonlinear subharmonic motion can only be developed for light rotor damping.

The subsynchronous motion of figures 10 and 11 arises at speeds above the maximum synchronous response speed predicted by Yamamoto's model in figure 9. This statement is supported by the results in figure 12 which shows the bearing 2 reaction magnitude predictions at 29,450 cpm.

A second nonlinear model configuration which yielded a substantial subsynchronous vibration component was obtained by doubling both the imbalance magnitudes and the destabilizing force coefficients at the main impeller, adding damping at the bearing (350 Ns/m or 2 lb s/in), and increasing the damping at the main impeller to 2625 Ns/m (15 lb s/in). This configuration is predicted to be linearly stable at FPL. Spectral analysis results for this configuration at FPL and two higher speeds are presented figure 12. In this case, the subsynchronous component increases with running speed, while the synchronous component decreases.

The response characteristics of a nonlinear model including bearing clearances is sensitive to many parameters including bearing clearances, imbalance magnitudes, side load magnitudes, damping coefficients, destabilizing force magnitudes, etc., and a study including a systematic variation of all these parameter would be helpful. However, the simulation results of figures 10 through 12 are sufficient to support the following conclusions:

- (a) The subsynchronous motion which is evident in these results can be obtained due to bearing-clearance nonlinearities for a linearly-stable but lightly damped model.
- (b) A whirl frequency of subsynchronous motion at 440 Hz is predicted by the nonlinear model as compared to 520 Hz for the linear model. This whirl frequency reduction results solely from the bearing clearances, and does not require any stiffness reduction in the model at the bearings or elsewhere.

- (c) As predicted by Yamamoto [16] and earlier simulations [15], bearing clearances can drop the peak-vibration running speed into the operating range, and these synchronous vibration loads would appear to pose a more serious threat to bearing lifetime than the subsynchronous motion.

The following options are being pursued to improve the dynamic characteristics of the HPOTP:

- (a) Units are being prepared for tests which include a stiffened rotor, damper seals at the boost impeller, and a modified turbine interstage seal.
- (b) Although attractive from a dynamics viewpoint, the shrouded inducer design poses serious manufacturing problems and also raises concerns with respect to cavitation performance. Pending resolution of these problems, no test of this configuration are presently scheduled.

Figure 13 illustrates simulation results for the nominal nonlinear model with damper seals at 29,500 cpm. Observe the sharp reduction in synchronous bearing loads. This reduction is due to (a) load sharing by the seals and (b) increases in damping which, according to Yamamoto's predictions, lower the peak bearing reaction amplitudes. Figure 14 illustrates the bearing reaction above FPL. Observe that clipping of the bearing loads due to motion in and out of the deadband has actually increased. The corresponding accelerometer spectrum is given in figure 15, and demonstrates a rich spectrum of subsynchronous components. The damper seals increase bearing-reaction clipping by opposing the side load and moving the rotor towards the center of the bearing clearances. The model is setup with the seal and bearing centers coincident radially. In an actual engine, some lack of concentricity can be expected which might counteract the seals centering action.

An inspection of figures 13 through 15 support the following conclusions with respect to implementation of the damper seals:

- (a) In accordance with the linear predictions of figure 6, a marked reduction in synchronous bearing loads is predicted.
- (b) Motion in and out of the bearing clearances is increased with a consequent increase in bearing-reaction-magnitude clipping and an increase in subsynchronous motion.

If current bearing distress is the result of excessive synchronous loads, seal modification should be very beneficial. However, if the bearing problems are associated with unloading and ball skidding, seal modifications will be counter-productive.

#### CONCLUSIONS

Linear and nonlinear analyses of the HPOTP support the following conclusions:

- (a) By linear predictions, the second critical speed is only slightly above the FPL running speed and is lightly damped. Even a modest loss of bearing stiffness is sufficient to drop the second critical speed into the operating range and yield a prediction of excessive bearing loads.
- (b) Based on prior test experience, the HPTOP appears to be lightly damped.
- (c) The subsynchronous motion which is evident in test results can be obtained in a nonlinear model due to bearing clearances. Motion in and out of the deadband clearances excites subharmonic motion for a stable but lightly damped model.
- (d) A whirl frequency of subsynchronous motion at 440 Hz is predicted by the nonlinear model which is consistent with test results but at odds with a linear prediction of 520 Hz.

This whirl frequency reduction results solely from the bearing clearances, and does not require any stiffness reduction in the model at the bearings or elsewhere.

- (e) Bearing clearances can drop the peak-vibration running speed into the operating range yielding a prediction of excessive bearing loads.
- (f) Incorporation of damper seals into the boost impeller seals markedly reduces predicted synchronous bearing loads, but increases bearing-reaction clipping an subsynchronous motion at FPL.

#### ACKNOWLEDGMENT

Discussions with Robert Beatty concerning a parallel investigation at Rocketdyne were very helpful to the authors.

## REFERENCES

1. Childs, D. W., "The Space Shuttle Main Engine High-Pressure Fuel Turbopump Rotordynamic Instability Problem," ASME Trans. J. of Engineering for Power, Vol. 100, January, 1978, pp. 48-57.
2. Beatty, R. F. and Rowan, B. F., "Determination of Ball Bearing Dynamic Stiffness," Proceedings, Second Workshop on Rotordynamic Instability Problems in High Performance Turbomachinery, NASA CP 2250.
3. Jones, A. B., "A General Theory for Elastically Constrained Ball and Radial Roller Bearings Under Arbitrary Load and Speed Conditions," ASME J. of Basic Engineering, Vol. 82, No. 2, June 1960, pp. 309-320.
4. Black, H. F., and Cochrane, E. A., "Leakage and Hybrid Bearing properties of Serrated Seals in Centrifugal Pumps," Paper G5, 6th International Conference in Fluid Sealing, Munich, German Federal Republic, 27 February - 2 March 1973.
5. Black, H. F., and Jensen, D. N., "Effects of High-Pressure Ring Seals on Pump Rotor Vibrations," ASME Paper No. 71-WA/FE-38, Winter Annual Meeting, Washington, D. C., 1971.
6. Black, H. F., Allaire, P. E., and Barrett, L. E., "The Effect of Inlet Flow Swirl on the Dynamic Coefficients of High-Pressure Annular Clearance Seals," Ninth International Conference on Fluid Sealing, BHRA Fluid Sealing Conference, Leeuwenhorst, The Netherlands, April 1981.
7. von Pragenau, G. L., "Damping Seals for Turbomachinery," NASA TP-1987, March 1983.
8. Childs, D. W. and Kim C-H., "Analysis and Testing for Rotordynamic Coefficients of Turbulent Annular Seals with Different, Directionally-Homogeneous Surface-Roughness Treatment for Rotor and Stator Elements," presented at the Third Rotordynamics Instability Workshop at Texas A&M University, College Station, TX, May 28-30, 84.

9. Nelson, C. D., "The Rotordynamic Coefficients of High-Pressure Annular Gas seals," accepted for presentation at the 1984 ASME Gas Turbine Conference.
10. Thomas, J. J., "Instabilie Eigenschwingungen von Turbine Laufern, angefacht durch die Spaltströmungen Stopfbushsen un Beschau felungen, AEG-Soderdruck, 1958.
11. Alford, J., "Protecting Turbomachinery From Self-Excited Rotor Whirl," ASME Trans. J. of Engineering for Power, October 1965, pp. 333-345.
12. Hauck, L., "Measurement and Evaluation of Swirl-Type Flow in Labyrinth Seals," NASA CP 2250 Rotordynamic Instability Problems in High-Performance Turbomachinery, Proceedings of a workshop held at Texas A&M University, 10-12 May 1982.
13. Chamieh, D. S., Acosta, A. J., Brennen, C. E., Caughey, T. K.; and Franz, R.; "Experimental Measurement of Hydrodynamic Stiffness Matrices for a Centrifugal Pump Impeller," NASA CP 2250 Rotordynamic Instability Problems in High Performance Turbomachinery, Proceedings of a workshop held at Texas A&M University, 10-12 May 1982.
14. Yamamoto, T., "On the Critical Speeds of a Shaft," Memoirs of the Faculty of Engineering, Nagoga University, Vol. 6, No. 2, 1954.
15. Childs, D. W., Rotordynamics Analysis for the HPOTP (High Pressure Oxygen Turbopump) of the SSME (Space Shuttle Main Engine), an Interim Progress Report for NASA Contract NAS8-31233, Dept. of Mechanical Engineering, The University of Louisville, 1979.

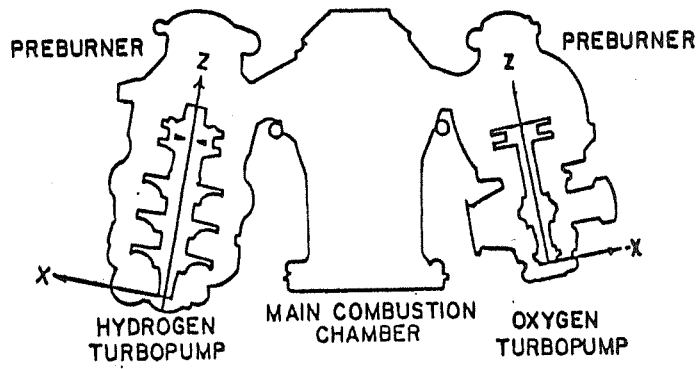


Figure 1. SSME powerhead component arrangement and local coordinate systems.

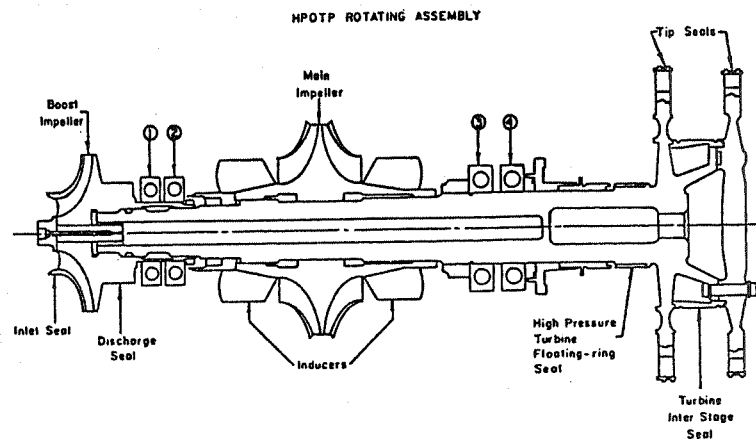


Figure 2. HPOTP rotating assembly.

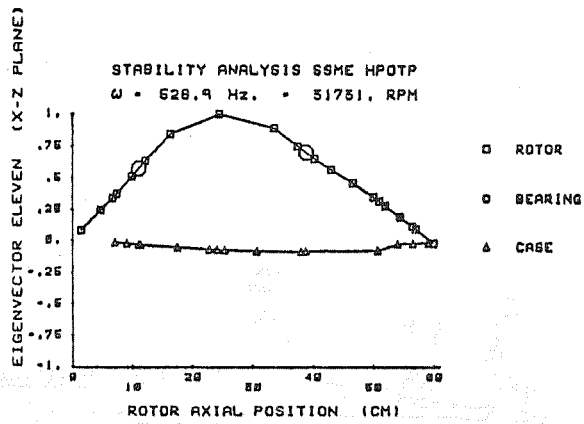
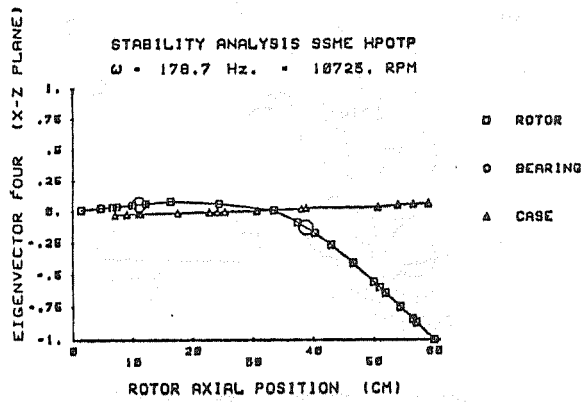


Figure 3. Undamped, zero-running-speed rotor-housing modes associated with the first and second critical speeds.

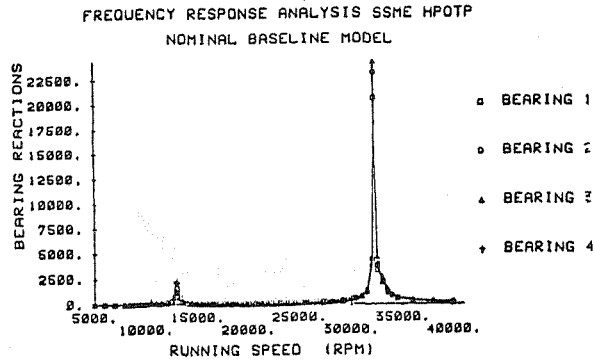


Figure 4. Bearing reactions for the nominal linear model with speeds out of 40,000 cpm.

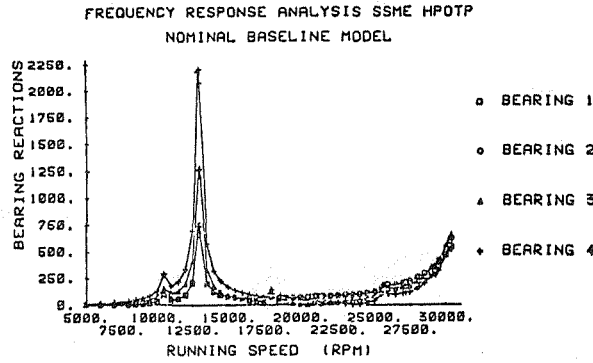


Figure 5 (a). Bearing reactions for the nominal linear model for speeds from 5,000 cpm to FPL.

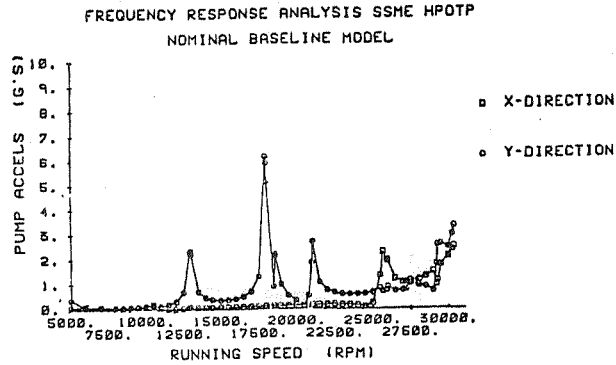


Figure 5 (b). Pump accelerometer levels in the X-Z and Y-Z planes.

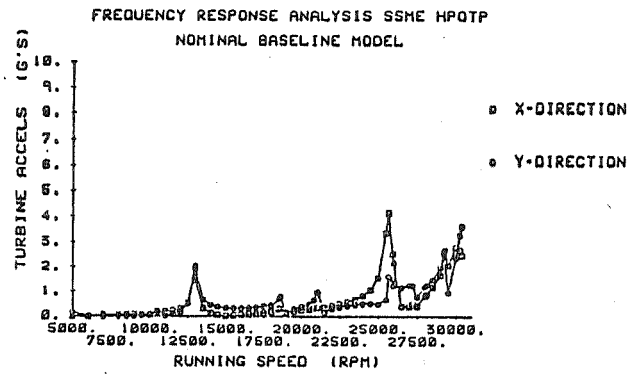


Figure 5 (c). Turbine accelerometer levels in the X-Z and Y-Z planes.

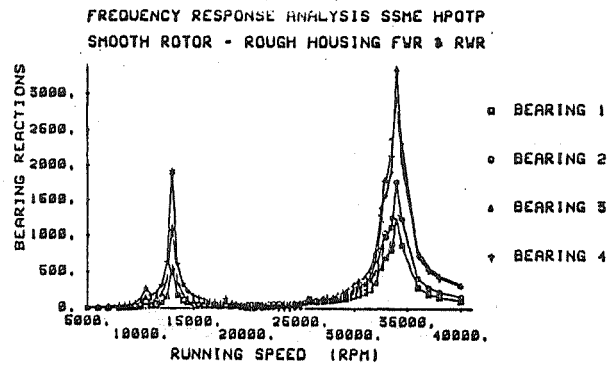


Figure 6. Bearing reactions for the nominal model with "damper" seal coefficients for the boost-impeller inlet and discharge seals.

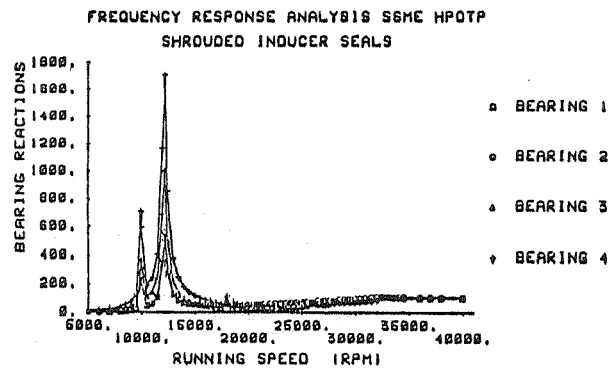


Figure 7. Bearing reactions for the model with seal coefficients for a shrouded impeller.

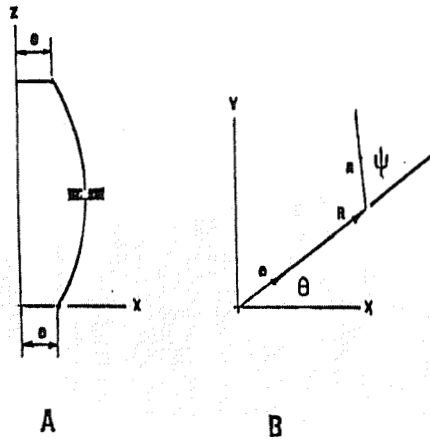


Figure 8. Yamamoto's model for synchronous response with bearing clearance.

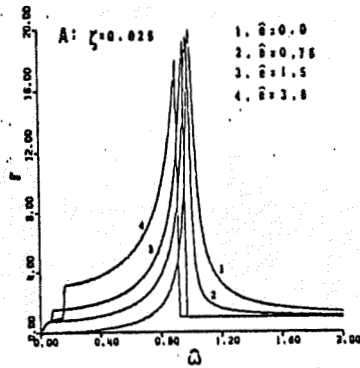


Figure 9. Synchronous-response characteristics for Yamamoto's model with increasing bearing clearances.

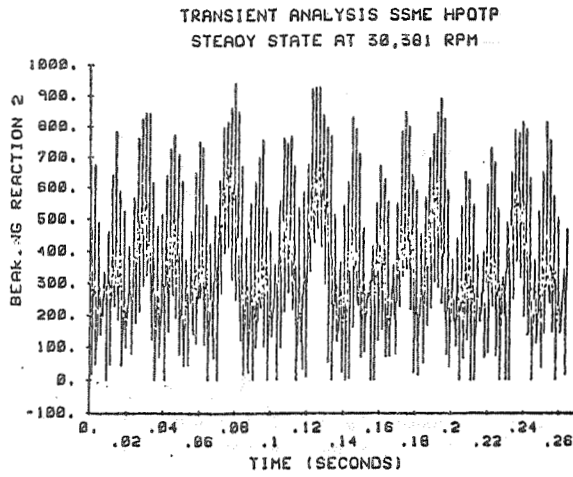


Figure 10 (a). Bearing 2 reaction magnitude versus time at FPL for the nominal nonlinear model.

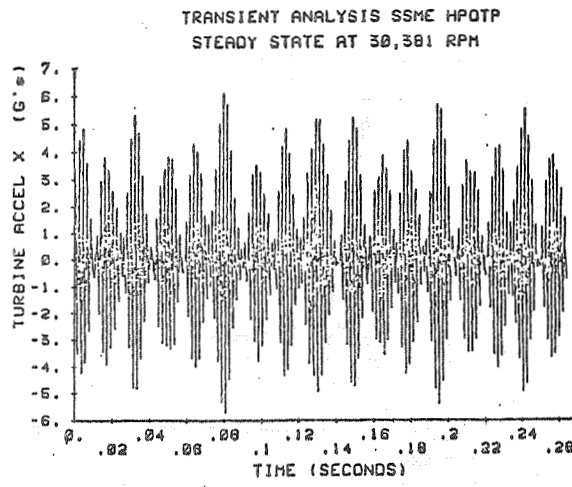


Figure 10 (b). Turbine X-Z plane acceleration magnitude versus time for the nominal nonlinear model.

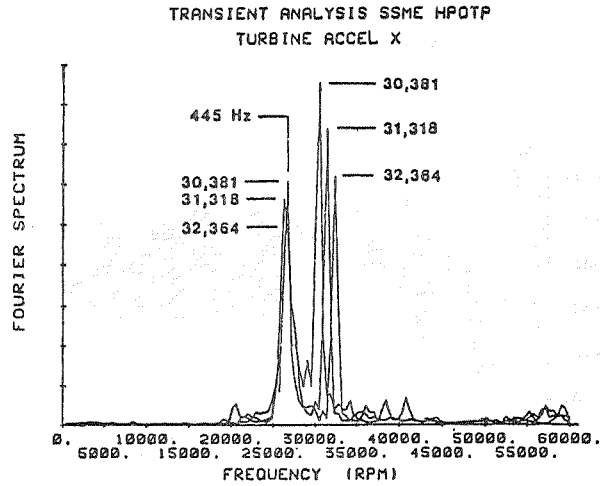


Figure 11. Turbine X-Z plane acceleration spectra at FPL and higher speeds for the nominal nonlinear model.

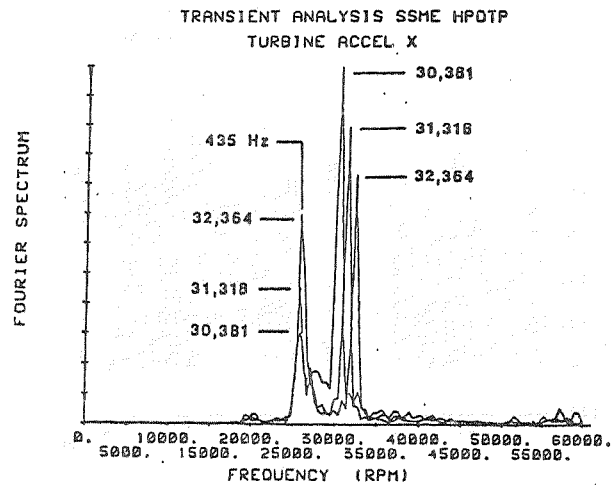


Figure 12. Turbine X-Z plane acceleration spectra at FPL and higher speeds for nonlinear model number 2.

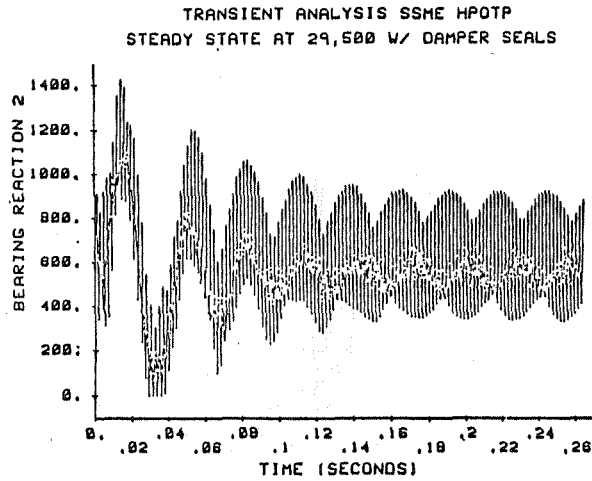


Figure 13. Bearing 2 reaction magnitude at 29,500 cpm for the nominal nonlinear model with damper seals at the boost impeller.

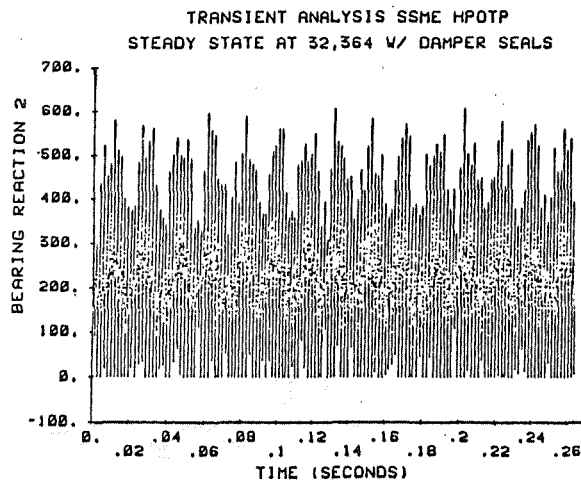


Figure 14. Bearing 2 reaction magnitude at above FPL for the nominal nonlinear model with damper seals at the boost impeller.

STEADY STATE AT 32,364 W/ DAMPER SEALS  
PREBURNER ACCEL X

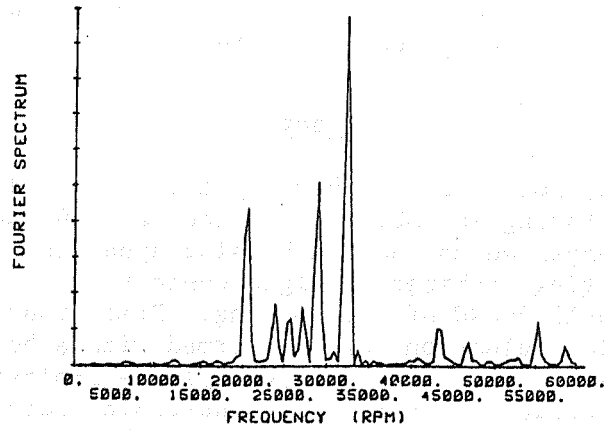


Figure 15. Preburner X-Z accelerometer spectrum at FPL for the nominal nonlinear model with damper seals at the boost impeller.

## HOUSING FLEXIBILITY EFFECTS ON ROTOR STABILITY

L. B. Davis, E. A. Wolfe,  
and R. F. Beatty

Rockwell International/Rocketdyne Division  
Canoga Park, California

### Abstract

Rotordynamic analyses have typically considered only the rotating assembly and in the last 10 years have been expanded to include housing dynamics. Advanced rotating machinery designs conceptually define the rotor well ahead of the housing. Preliminary rotordynamic evaluations are performed with a housing stiffness assumption that is typically determined only after the hardware is built. In addressing rotor stability, a rigid housing assumption has shown to predict an instability at a lower spin speed than a comparable flexible housing analysis. This rigid housing assumption therefore provides a conservative estimate of the stability threshold speed. A flexible housing appears to act as an energy absorber and dissipates some of the destabilizing force. The fact that a flexible housing is usually asymmetric and considerably heavier than the rotor has been related to this apparent increase in rotor stability. Rigid housing analysis is proposed as a valuable screening criteria and may save a significant amount of time and money in construction of elaborate housing finite element models for linear stability analyses.

### Introduction

A primary consideration for high-pressure turbomachinery such as used in liquid rocket engines is minimum weight. To achieve this while delivering the pressures and flows required by the system, the design trend is toward small diameters and very high speeds. The results of this trend are rather spectacular as shown in Fig. 1. As an example, the Space Shuttle

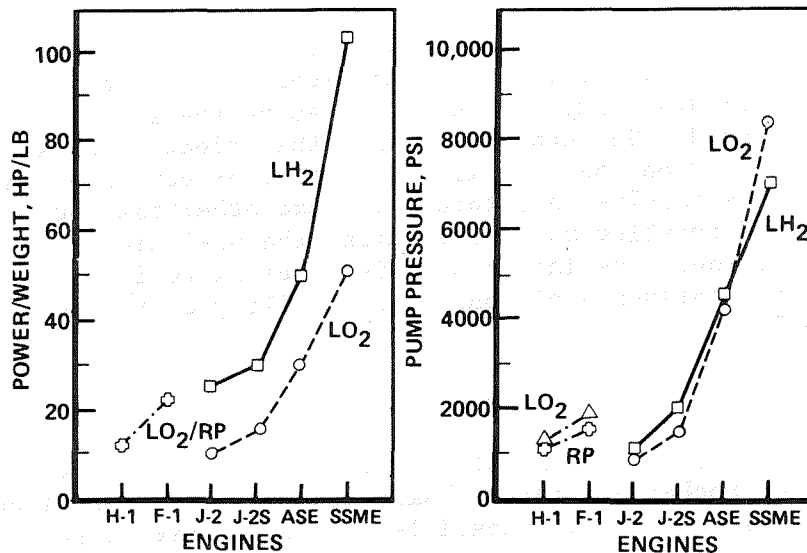


Fig. 1. Turbopump Power Growth

Main Engine High-Pressure Fuel Turbopump (SSME HPFTP) is one of the most advanced machines in the world with a power density of 100 horsepower/pound. While there is a substantial weight savings in the rotor with its small diameter, much of the savings is associated with the lightweight housing. A lightweight housing is designed primarily as a pressure shell with a minimum of additional structure added to support the rotor. At high speeds, housing motion becomes a significant feature affecting rotor critical speeds, stability, and bearing loads.

Housing designs are dictated by pressure, flow, hydrodynamic efficiency, structural loads, and assembly requirements. While low speed pumps with massive and stiff housings are generally used to discuss rotating machinery problems, advanced lightweight housings are not as simply treated. The flexibility of the housing, coupled through bearings and seals, results in a considerably more complex problem, which is not as amenable to simple rules of design as in the past. Rotor stability is much more difficult to accurately predict today due to the added variable of housing

dynamics and the interaction with the coupling mechanisms. These elements affect critical speeds and thus the rotor stability for operation above the rotor critical speed. The concern is with the effect of housing flexibility on the stability analysis, or can more conservative results be obtained in some other fashion for advanced rotating machinery during the preliminary study phase. The intent of this paper is to investigate the influence of housing flexibility on the rotor stability.

#### Approach

Initially, the housing dynamics influence on several of Rocketdyne rotordynamic analyses was determined. To accomplish this, compatible stability cases were repeated with a rigid or ground housing assumption to quantify the change in threshold speed with elimination of housing flexibility and dynamics. A total of six different turbopump designs were included in this survey including four SSME designs and two advanced rocket engine designs. The specific turbopumps included were:

1. High-pressure oxygen turbopump (HPOTP) of the SSME
2. Uprated high-pressure oxygen turbopump of the SSME for full power operation, referred to as the HPOTP Phase II
3. High-pressure fuel (liquid hydrogen) turbopump (HPFTP) of the SSME
4. MK38-0 redesign configuration that never materialized for a modified SSME
5. MK48-F high pressure fuel (liquid hydrogen) turbopump for the Orbital Transfer Vehicle (OTV)
6. MK49-F high pressure fuel (liquid hydrogen) turbopump for the Advanced Space Engine (ASE)

These six turbopump analyses were chosen because each has a detailed finite element model of its housing. The

following is a brief description of each of the turbopumps included in the survey.

The HPOTP is shown in Fig. 2 and a summary of its performance characteristics is provided in Table 1. Basically, the HPOTP consists of a double-entry centrifugal impeller supplying liquid oxygen to the main chamber. A portion of this discharge flow is diverted to a smaller centrifugal impeller mounted on the same shaft that supplies liquid oxygen to the preburners. A two-stage impulse turbine, which overhangs the bearings, drives the pump to a maximum operating speed of 27,900 rpm. Two pairs of duplex angular contact ball bearings support the rotor. Preload springs between the bearing outer races in each pair maintain the axial load independent of rotor axial position. The turbine hot gases are isolated from the pump by a series of floating ring seals. Axial thrust on the rotor is reacted by a double-balance piston built into the main impeller.

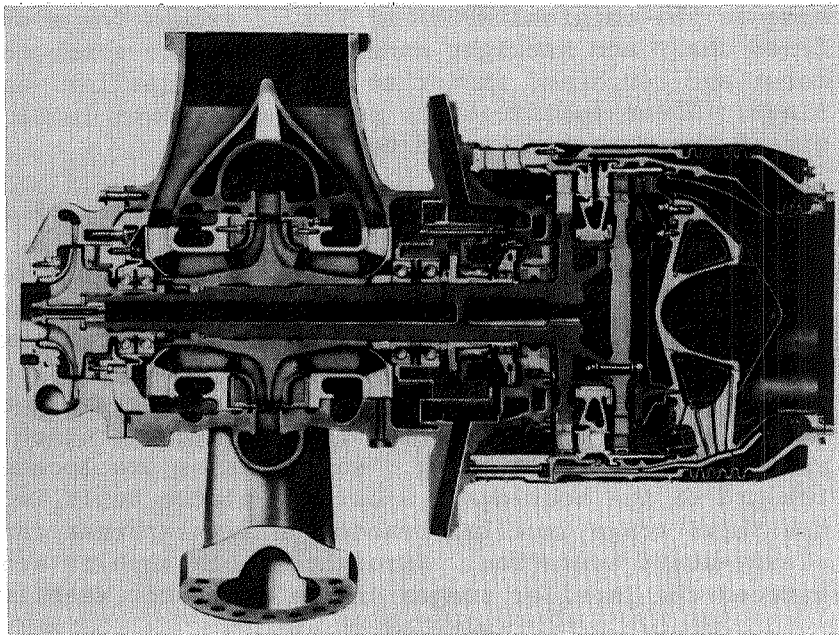


Fig. 2. High-Pressure Oxygen Turbopump

Table 1. SSME HPOTP PERFORMANCE DATA

KEY PERFORMANCE PARAMETERS BASELINE DATA JAN. 1984				
	RPL		FPL	
	MAIN	BOOST	MAIN	BOOST
PUMP INLET FLOWRATE, LB/SEC	1070.6	111.6	1157.8	129.4
PUMP INLET PRESS, PSIA	379.3	3985.9	392.4	4403.6
PUMP DISCHARGE PRESSURE, PSIA	4108.7	7106.7	4556.0	7861.2
PUMP EFFICIENCY	0.684	0.809	0.650	0.800
TURBINE FLOWRATE, LB/SEC	61.8		69.0	
TURBINE INLET PRESSURE, PSIA	5015.3		5660.8	
TURBINE INLET TEMP, R	1407.2		1596.3	
TURBINE PRESS RATIO	1.506		1.550	
TURBINE EFFICIENCY	0.749		0.755	
TURBINE SPEED, RPM	27102		29675	
TURBINE HORSEPOWER	22902		29174	

The uprated HPOTP Phase II design is basically the same as the original HPOTP of Fig. 2 except for a stiffened shaft and straight annular seals with a smooth rotor and roughened stator at the small impeller wear rings. These modifications permit full power level and extend the operating speed to 30,000 rpm.

The HPFTP is shown in Fig. 3 and a summary of its performance characteristics is provided in Table 2. The HPFTP consists of a three-stage centrifugal (liquid hydrogen) pump driven by a two-stage turbine to deliver the engine coolant. The turbopump operates at a maximum speed of approximately 37,000 rpm. Two pairs of duplex angular contact ball bearings support the rotor radially and a thrust bearing is provided for start and shutdown axial positioning. Rotor masses are located inboard of the bearings. A balance piston built into the third stage impeller reacts the axial thrust during steady-state operation. Straight smooth annular seals between the impeller stages ensure the rotor stability.

The MK38-0 redesign configuration included was a proposed concept for upgrading of the SSME to increase its thrust rating. Basically, this design has a direct

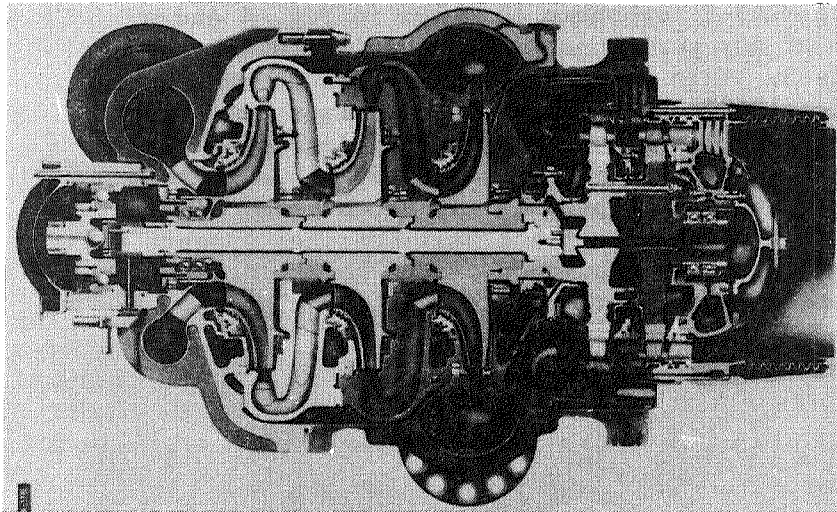


Fig. 3. SSME High-Pressure Fuel Turbopump

Table 2. SSME HPFTP Performance Data

KEY PERFORMANCE PARAMETERS	RPL	FPL
PUMP INLET FLOWRATE, LB/SEC	148.4	161.7
PUMP INLET PRESSURE, PSIA	204.1	214.0
PUMP DISCHARGE PRESSURE, PSIA	6254.8	7036.8
PUMP EFFICIENCY	0.758	0.757
TURBINE FLOWRATE, LB/SEC	147.5	164.0
TURBINE INLET TEMPERATURE, R	1898.4	1989.2
TURBINE PRESSURE RATIO	1.522	1.558
TURBINE EFFICIENCY	0.770	0.780
TURBINE SPEED, RPM	34,931	37,076
TURBINE HORSEPOWER	63,288	77,142

drive, two-stage turbine and two centrifugal impellers mounted on a shaft supported by angular contact ball bearings. The maximum operating speed is approximately 26,000 rpm.

The MK48-F turbopump is shown in Fig. 4 and a summary of its performance characteristics is provided in Table 3. This turbopump consists of a three-stage centrifugal (liquid hydrogen) pump driven by a two-stage overhung turbine. The pump design is similar to the HPFTP on a much smaller scale and has a maximum operating speed of approximately 95,000 rpm. Again, two pairs of angular contact ball bearings support the rotor radially and a balance piston built into the third stage impeller reacts the axial thrust.

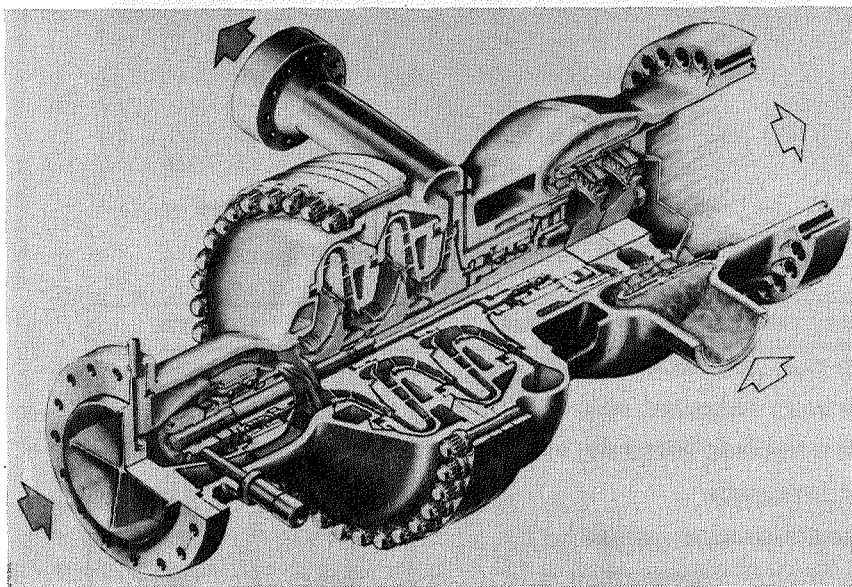


Fig. 4. MK48-F Liquid Hydrogen Turbopump

Table 3. MK48-F Performance Data

KEY PERFORMANCE CHARACTERISTICS	
FLOWRATE, GPM	628
DISCHARGE PRESSURE, PSI	4,560
DESIGN SPEED, RPM	95,000
TURBINE POWER, HP	2,543
WEIGHT, POUNDS	105

The MK49-F turbopump is shown in Fig. 5 with a performance characteristic summary given. This turbopump is very similar to the MK48-F but on a slightly smaller scale. The MK49-F has a maximum operating speed of 110,000 rpm and relies on straight smooth interstage seals to ensure the rotor stability.

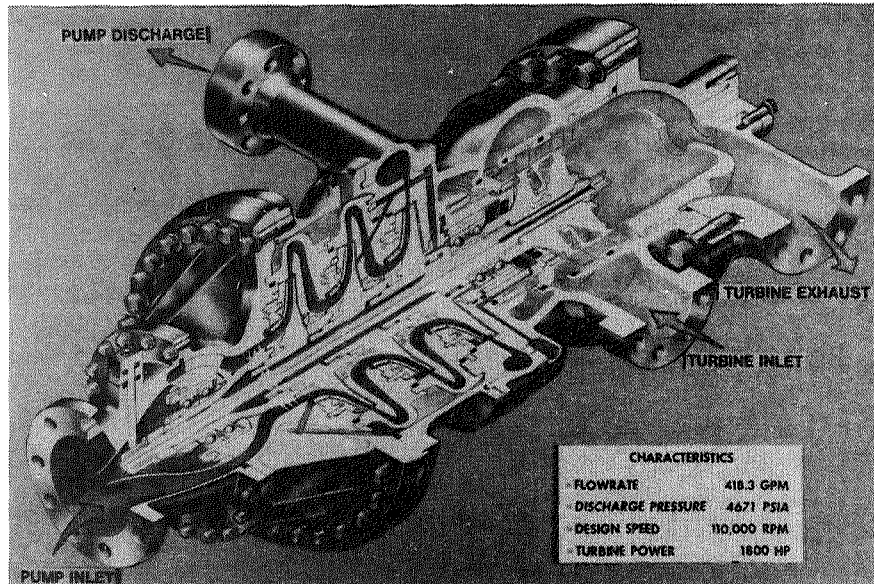


Fig. 5. MK49-F Liquid Hydrogen Turbopump

#### Mathematical Models Description

Existing finite element models of the rotor and housing for each of the six turbopumps included in the survey were used. The rotors are constructed of beam finite elements and the housings are typically composed of plate elements to include shell motion. Typical rotor and housing finite element models are shown in Fig. 6 and 7, respectively, for the SSME HPOTP. The coupled system was analyzed using modal synthesis techniques that combine substructures of the rotor and housing-to-engine support structure connected through linear bearings, seals, and hydrodynamic interactions. This approach has been described by Childs (Ref. 1) for rotor-dynamics applications. Generally, the housing-to-engine

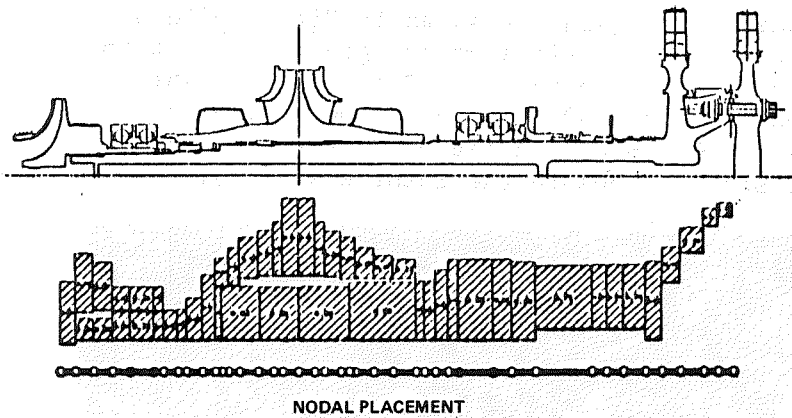


Fig. 6. SSME HPOTP Rotating Assembly  
Finite Element Model

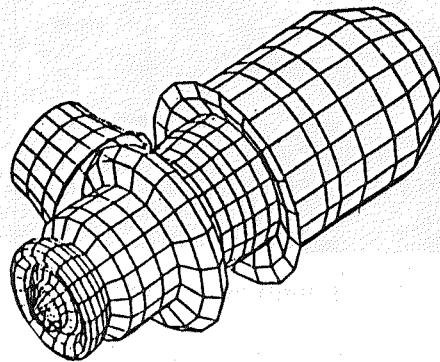


Fig. 7. SSME HPOTP Housing Finite  
Element Model

support structure is unsymmetric and is lightly damped. These linear models not only include bearing and seal coupling but also, impeller diffuser interaction, turbine aerodynamic cross coupling, bearing damping, and rotor and housing structural damping. Output capability includes damped critical speeds and stability.

#### Stability Calculations

The Rocketdyne internal stability criterion is similar to that of Lund (Ref. 2) and Bansal (Ref. 3), which considers a mechanical system at steady-state

which undergoes a perturbation. The motion takes one of three forms. When the deviation from the original motion decreases with time, the system is stable. If the deviation increases with time, the system is said to be unstable. Neutral stability occurs when the motion of the system after a perturbation is oscillatory with no change in amplitude with time.

The equation of motion for a typical mechanical system takes the following form:

$$m \ddot{y} = -ky - c\dot{y} + F(t) \quad (1)$$

Assume the solution to the homogeneous differential equation is as follows:

$$y = \tilde{Q}e^{\lambda t} \quad (2)$$

substituting into the equation of motion:

$$m \lambda^2 + c\lambda + k = 0 \quad (3)$$

where the eigenvalue is:

$$\lambda = \frac{-c \pm \sqrt{c^2 - 4km}}{2m} \quad (4)$$

$$\lambda = -a \pm bi \quad (5)$$

where:

$$a = \frac{c}{2m} \quad b = \frac{\sqrt{4km - c^2}}{2m}$$

Writing the general solution to the homogeneous equation of motion:

$$y = Q_1 e^{(-a + bi)t} + Q_2 e^{(-a - bi)t} \quad (6)$$

$$y = e^{-at} (Q_1 e^{bit} + Q_2 e^{-bit}) \quad (7)$$

Using Euler's formula, equation (7) can be rewritten in the general solution form:

$$y = e^{-at} [A\cos(bt) + B\sin(bt)] \quad (8)$$

Plotting the solution:

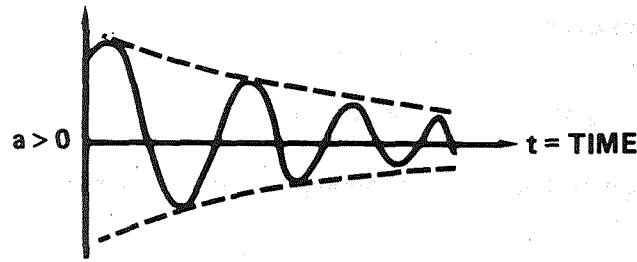


Fig. 8. Rate of Amplitude Change ( $a > 0$ )

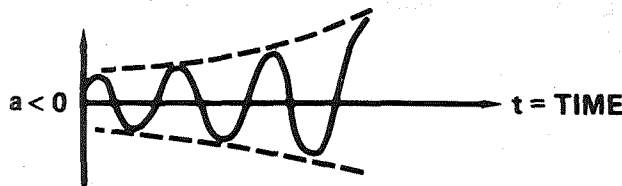


Fig. 9. Rate of Amplitude Change ( $a < 0$ )

Figure 8 displays decreasing amplitude with time, and therefore a stable system for  $a > 0$ . However, when the real part of  $\lambda$  is greater than zero, the system is unstable. This unstable motion is represented in Fig. 9. Lastly, if  $a = 0$ , the  $e^{-at}$  term becomes unity and the amplitude remains constant with time, as shown in Fig. 10. Therefore, the sign of the real part of the eigenvalue determines the stability of the system.



Fig. 10. Rate of Amplitude Change ( $a = 0$ )

### Stability Results of Survey

As previously mentioned, the stability results of a rigid versus a flexible housing assumption were compared. Figures 11 through 17 present rotor stability

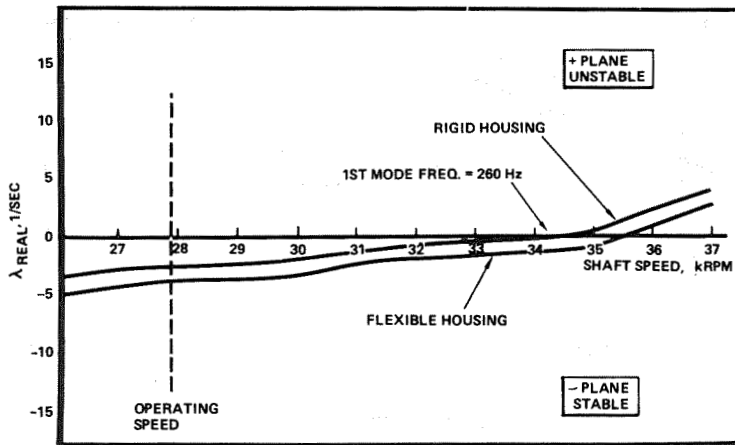


Fig. 11. HPOTP Stability Map of Turbine Overhang Mode (Hot Gas Seals Free to Float)

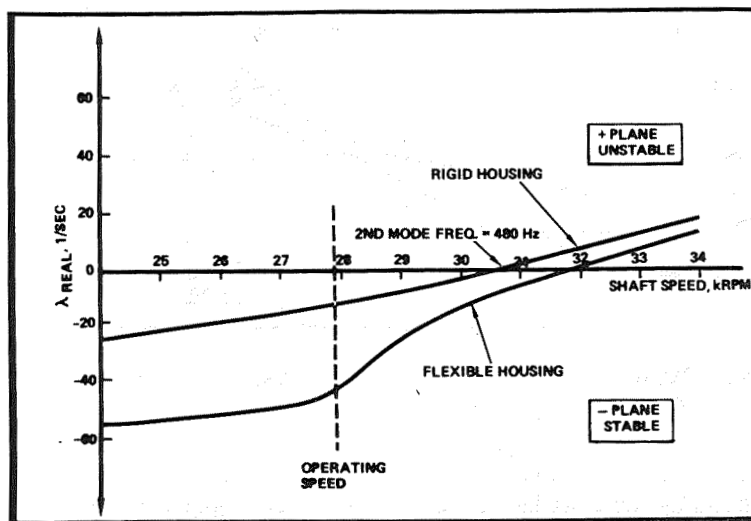


Fig. 12. HPOTP (104%) Rotor Stability Map (Second Rotor Mode)

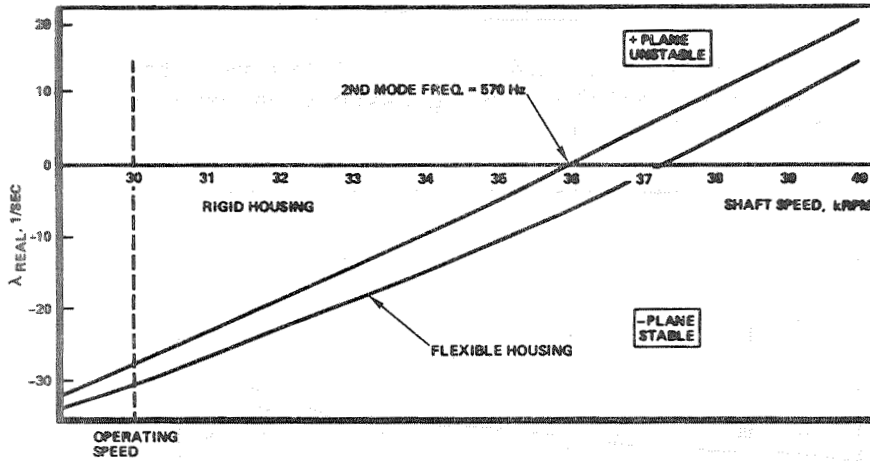


Fig. 13. HPOTP (109%) Rotor Stability Map  
(Second Rotor Mode)

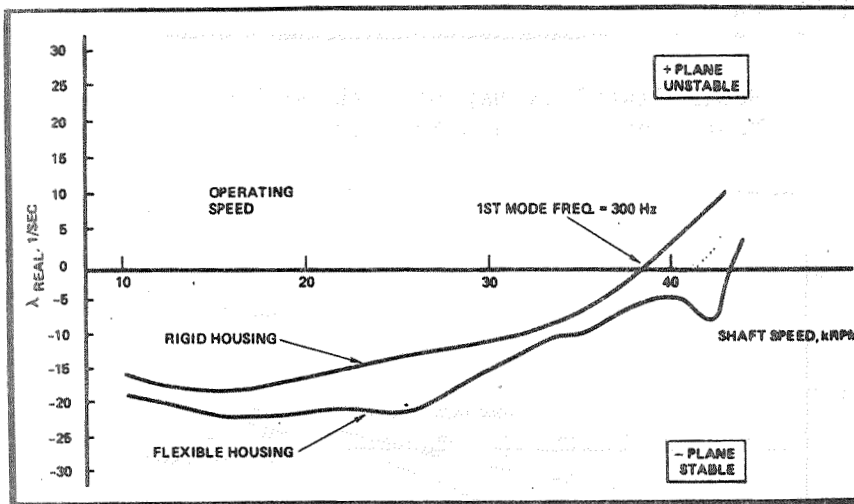


Fig. 14. MK38-0 (Redesign) Rotor Stability Map  
(1st Rotor Mode)

maps for each of the six turbopumps described for only the potentially unstable modes. The real part of the complex eigenvalue is plotted as a function of the rotor spin speed where a positive real part eigenvalue indicates the potential for unstable rotor motion to occur.

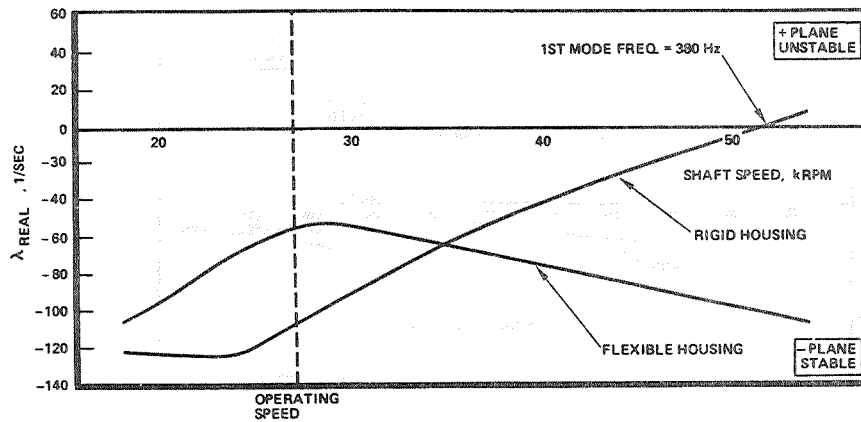


Fig. 15. HPFTP Rotor Stability Map  
(First Rotor Mode)

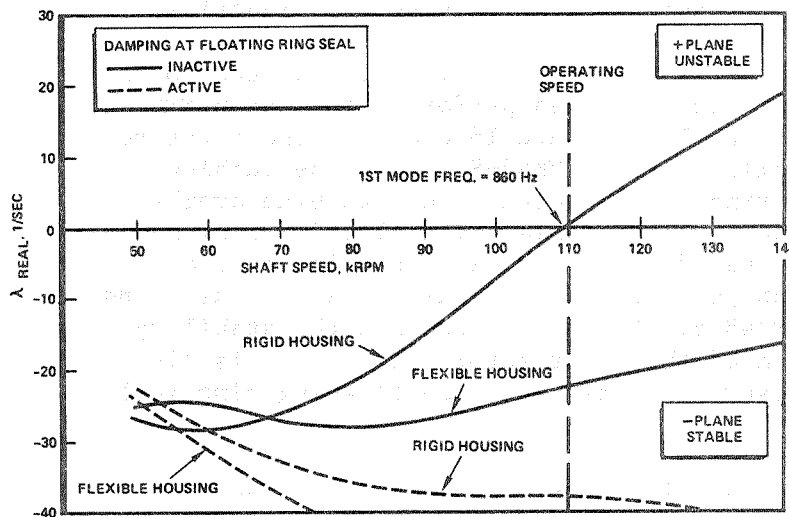


Fig. 16. MK49-F Rotor Stability Map  
(First Rotor Mode)

Figure 11 compares the lowest rotor mode stability of the HPOTP, which is the turbine overhang mode. With the hot gas seals free to float, the operating speed is far removed from the stability threshold speed for both a rigid and a flexible housing. A comparison of the second rotor mode stability of the HPOTP is shown in Fig. 12 and 13, which is the main impeller mode. Figure 14 compares the turbine overhang mode for the MK38-0

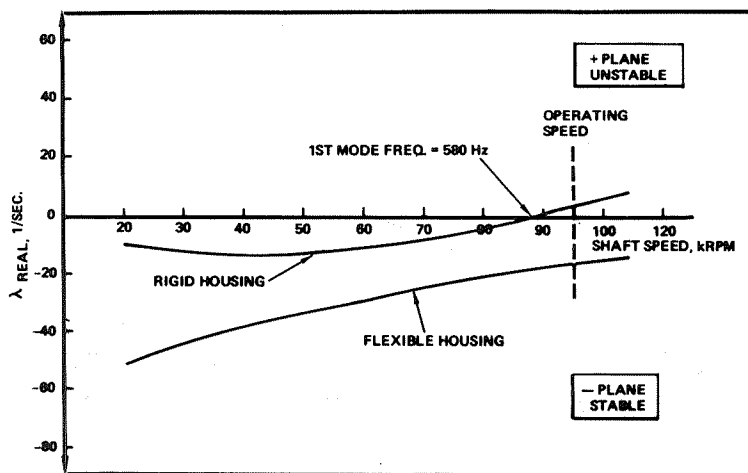


Fig. 17. MK48-F Rotor Stability Map (1st Rotor Mode - Floating Ring Seal Inactive)

redesign configuration. A comparison of the lowest rotor mode stability was performed for the HPFTP as shown in Fig. 15. Figure 16 compares the first rotor mode stability of the MK49-F. With the turbine floating ring seals present, this turbine overhang rotor mode remains stable. The floating ring seal was deactivated to produce an unstable rotor mode for comparison purposes. A similar situation was found for the MK48-F. Figure 17 presents the stability comparison of the first rotor mode, which is also a turbine overhang mode, with the floating ring seal inactive.

The stability maps described above indicate that as the rotor spin speed increases, the rotor in a flexible housing tends to approach an unstable condition at a higher speed than the rotor in a rigid housing. This observation is true for all six turbopumps. Thus, results of the survey to determine the effect of housing flexibility on rotor stability indicate that a rigid housing assumption is more conservative since it consistently predicts lower threshold speeds. It appears as though the housing acts as an energy absorber. This can be seen when it is considered that the housing adds relative motion terms.

Consider the following:

$$q_R = A \cos \omega t + B \sin \omega t$$

$$q_S = C \cos \omega t + D \sin \omega t$$

The elastic coupling force between the rotor and support is:

$$F = -(kq + c\dot{q}) = -[k(q_R - q_S) + C(\dot{q}_R - \dot{q}_S)]$$

The work, or energy, generated per cycle is:

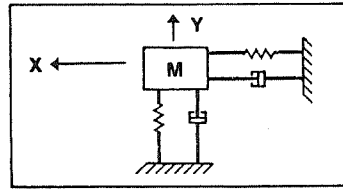
$$W = \int_0^{2\pi} \left\{ -[k(q_R - q_S) + c(\dot{q}_R - \dot{q}_S)] \cdot \dot{q}_R \right\} \frac{d(\omega t)}{\omega}$$

Rearranging the above equation as follows:

$$W = \int_0^{2\pi} [-kq_R + c\dot{q}_R] \cdot \dot{q}_R \frac{d(\omega t)}{\omega} - \int_0^{2\pi} [-kq_S + c\dot{q}_S] \cdot \dot{q}_R \frac{d(\omega t)}{\omega} .$$

Therefore it follows that if the housing support was rigid or ground, then  $q_S$  and  $\dot{q}_S$  are zero. All the constant available energy in a conservative system is then transmitted to the rotor and none dissipated in the housing. It follows then that a flexible housing absorbs some of the energy that would normally be present in the rotor.

Another aspect of housing construction that aids stability is its typical asymmetry. Several technical papers discuss bearing support asymmetry related to stability gain. Most turbopumps are unsymmetrically supported by manifolds, ducts, and brackets. This can be illustrated simply (Fig. 18) by representing a



**UNSYMMETRIC MODES**

$$K_{xx} \neq K_{yy}$$

$$C_{xx} \neq C_{yy}$$

Fig. 18. Simple Housing Model

housing as a mass attached to ground with two radial degrees of freedom relative to the centerline as shown below. The equations of motion for Fig. 18 are:

$$\begin{bmatrix} M & 0 \\ 0 & M \end{bmatrix} \begin{Bmatrix} \ddot{x} \\ \ddot{y} \end{Bmatrix} + \begin{bmatrix} c_{xx} & c_{xy} \\ c_{yx} & c_{yy} \end{bmatrix} \begin{Bmatrix} \dot{x} \\ \dot{y} \end{Bmatrix} + \begin{bmatrix} k_{xx} & k_{xy} \\ k_{yx} & k_{yy} \end{bmatrix} \begin{Bmatrix} x \\ y \end{Bmatrix} = \begin{Bmatrix} 0 \\ 0 \end{Bmatrix}$$

Assuming harmonic motion solution and appropriate derivations of:

$$\begin{Bmatrix} x \\ y \end{Bmatrix} = \begin{Bmatrix} X \\ Y \end{Bmatrix} e^{\lambda t}$$

give the following solution:

$$\begin{Bmatrix} X \\ Y \end{Bmatrix} \left\{ \begin{bmatrix} M & 0 \\ 0 & M \end{bmatrix} \lambda^2 + \begin{bmatrix} c_{xx} & c_{xy} \\ c_{yx} & c_{yy} \end{bmatrix} \lambda + \begin{bmatrix} k_{xx} & k_{xy} \\ k_{yx} & k_{yy} \end{bmatrix} \right\} = \begin{Bmatrix} 0 \\ 0 \end{Bmatrix}$$

Reformatting the solution yields:

$$\begin{vmatrix} (M\lambda^2 + c_{xx}\lambda + k_{xx}) & (c_{xy}\lambda + k_{xy}) \\ (c_{yx}\lambda + k_{yx}) & (M\lambda^2 + c_{yy}\lambda + k_{yy}) \end{vmatrix} = 0$$

The stability can be investigated by the Routh-Hurwitz criterion (Ref. 4) as follows. The characteristic equation is:

$$a_0\lambda^4 + a_1\lambda^3 + a_2\lambda^2 + a_3\lambda + a_4 = 0$$

where assuming  $c_{xy} = c_{yx} = 0$ , the coefficients for the above equation are:

$$a_0 = M^2$$

$$a_1 = M(c_{xx} + c_{yy})$$

$$a_2 = (k_{yy}M + k_{xx}M + c_{xx}c_{yy})$$

$$a_3 = (c_{xx}k_{yy} + c_{yy}k_{xx})$$

$$a_4 = (k_{xx}k_{yy} - k_{xy}k_{yx})$$

The system is stable if the following quantities are greater than zero:

$$D_1 = a_1$$

$$D_2 = \begin{vmatrix} a_1 & a_0 \\ a_3 & a_2 \end{vmatrix}$$

$$D_3 = \begin{vmatrix} a_1 & a_0 & 0 \\ a_3 & a_2 & a_1 \\ 0 & a_4 & a_3 \end{vmatrix}$$

$$D_4 = a_4 D_3$$

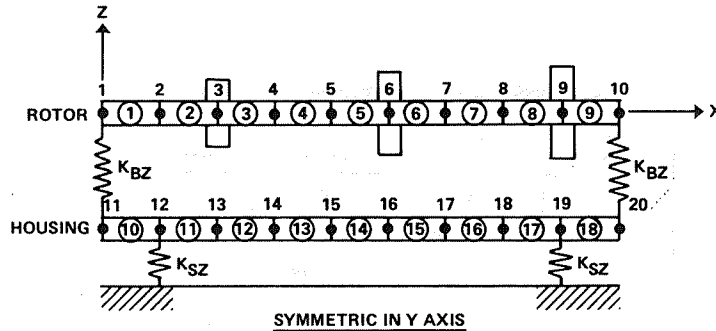
Substituting the above equations and expanding yields

$$\begin{aligned}
 D_1 &= M(c_{xx} + c_{yy}) \\
 D_2 &= M^2(c_{xx} k_{xx} + c_{yy} k_{yy}) + M(c_{xx}^2 c_{yy} + c_{xx} c_{yy}^2) \\
 D_3 &= c_{xx} c_{yy} M^2 (k_{xx} - k_{yy})^2 + k_{xy} k_{yx} M^2 (c_{xx} + c_{yy})^2 \\
 &\quad + M c_{xx} c_{yy} (c_{xx}^2 k_{yy} + c_{xx} c_{yy} k_{yy} + c_{xx} c_{yy} k_{xx} \\
 &\quad + c_{yy}^2 k_{xx}) \\
 D_4 &= (k_{xx} k_{yy} - k_{xy} k_{yx}) D_3
 \end{aligned}$$

Note that, since  $k_{xx}$ ,  $k_{yy}$ ,  $c_{xx}$ , and  $c_{yy}$  are usually greater than zero, the possibility for a system instability generally is controlled by the  $D_3$  quantity. Therefore, in a symmetric case if  $k_{xy} = -k_{yx}$ , the system stability tends to decrease. However, if asymmetry exists then  $k_{xx} \neq k_{yy}$  and the first term on the righthand side of the equation is positive and the trend is for stability to increase. Since the rotor response is relative to the housing and the housing stability is increased, then the rotor/housing system must follow. This stability criterion cannot predict the magnitude of the gain because in reality there are several coupling mechanisms that vary in some fashion with shaft speed. It was therefore necessary to construct a simple generic turbopump model where some of these ideas can be more easily evaluated.

#### Generic Turbopump Model

A model was constructed to simulate a typical turbopump with attention given to significant dynamic features. The finite element model consists of 10 lumped mass and inertia locations for both the rotor and housing. Three large masses reside at appropriate locations in the rotor model to analytically represent two impellers and a turbine disk. A description of the model is provided in Fig. 19.



MODEL: ROTOR SHAFT DIAMETER: OD = 3.0 INCHES, ID = 0.0 INCHES  
 MATERIAL STEEL, E =  $30 \times 10^6$  PSI  
 SIMULATED LUMPED MASSES: POUNDS J13 = 10  
 J16 = 15  
 J19 = 20

JOINT LENGTH = 3.0 INCHES  
 ROTOR LENGTH = 27.0 INCHES

HOUSING

DIAMETER. OD = 15 INCHES, ID = 14 INCHES  
 WEIGHT: 6/1 CASING/ROTOR WEIGHT RATIO

$K_{BZ} = K_{BY} = 500,000$  LB/IN.

$K_{SZ} = 1.0 \times 10^7$ ,  $1/3 = K_{SY}/K_{SZ}$

Fig. 19. 20 Lumped Mass Turbopump Model

Inputs to the analysis included mass and stiffness properties that were selected to be a generic representation of a turbopump. In addition, rotor/housing coupling coefficients for the HPOTP were arbitrarily selected as typical. These coefficients included the wear ring seal coupling on the first disk, the impeller-diffuser interaction on the second disk, and the turbine interstage seal coupling coefficients on the third disk. These coefficients are provided in Table 4.

To further study rotor stability with a flexible housing, several dynamically important parameters were varied. The weight of the housing was varied from one to seven times the weight of the rotor. A housing/rotor weight ratio of approximately 6:1 is typical of many existing turbopumps as shown in the data of

Table 4. Generic Turbopump Model Rotor/Housing  
Coupling Coefficients

**WEAR RING SEAL COUPLING ON FIRST DISK**

SPEED, RPM	$K_{xx}$ , LB/IN.	$K_{xy}$ , LB/IN.	$C_{xx}$ , LB-SEC/IN.
1,000	0.	0.	0.
10,000	$1.0 \times 10^5$	$1.5 \times 10^4$	$6.3 \times 10^1$
20,000	$4.2 \times 10^5$	$5.8 \times 10^4$	—
25,000	$6.5 \times 10^5$	$8.6 \times 10^4$	—
30,000	$9.3 \times 10^5$	$1.2 \times 10^5$	$2.1 \times 10^2$
35,000	$1.2 \times 10^6$	$1.6 \times 10^5$	—
40,000	$1.6 \times 10^6$	$2.0 \times 10^5$	—
45,000	$2.1 \times 10^6$	$2.7 \times 10^5$	$3.2 \times 10^2$

**IMPELLER - DIFFUSER INTERACTION  
ON SECOND DISK**

SPEED, RPM	$K_{xx}$ , LB/IN.	$K_{xy}$ , LB/IN.	$C_{xx}$ , LB-SEC/IN.
1,000	$-8.9 \times 10^1$	$-4.0 \times 10^1$	0.1
10,000	$-8.9 \times 10^3$	$-4.0 \times 10^3$	1.0
20,000	$-3.5 \times 10^4$	$-1.6 \times 10^4$	2.0
25,000	$-5.5 \times 10^4$	$-2.5 \times 10^4$	2.5
30,000	$-8.0 \times 10^4$	$-3.6 \times 10^4$	3.0
35,000	$-1.1 \times 10^5$	$-4.9 \times 10^4$	3.5
40,000	$-1.4 \times 10^5$	$-6.4 \times 10^4$	4.0
45,000	$-1.8 \times 10^5$	$-8.1 \times 10^4$	4.5

**TURBINE INTERSTAGE SEAL COUPLING  
ON THIRD DISK**

SPEED, RPM	$K_{xx}$ , LB/IN.	$K_{xy}$ , LB/IN.	$C_{xx}$ , LB-SEC/IN.
1,000	0.	0.	0.
10,000	$8.7 \times 10^3$	$1.9 \times 10^3$	2.3
20,000	$3.5 \times 10^4$	$7.9 \times 10^3$	6.1
25,000	$4.7 \times 10^4$	$1.3 \times 10^4$	8.8
30,000	$6.8 \times 10^4$	$2.1 \times 10^4$	12.8
35,000	$9.5 \times 10^4$	$3.1 \times 10^4$	17.3
40,000	$1.3 \times 10^5$	$4.6 \times 10^4$	23.0
45,000	$1.8 \times 10^5$	$6.4 \times 10^4$	29.6

Table 5. Since the significant dynamic difference between a rigid and flexible housing is asymmetric modes and with insight provided by Ref. 5, the effects of support asymmetry was determined by varying the support

Table 5. Housing/Rotor Weight Ratio of Existing Turbopumps

MODEL	ROTOR WEIGHT, POUNDS	HOUSING WEIGHT, POUNDS	HOUSING/ROTOR WEIGHT RATIO
MK38-O (104%)	81.	480.	6/1
MK38-O (109%)	81.	480.	6/1
MK38-F	128.5	649.	5/1
MK48-F	8.25	87.75	10/1
MK49-F	6.1	48.	8/1

stiffness ratio in orthogonal directions. Figure 20 shows the stability threshold speed plotted as a function of the support asymmetry ratio for a family of housing/rotor weight ratios. Results show that there is an optimum value of asymmetry that produces the

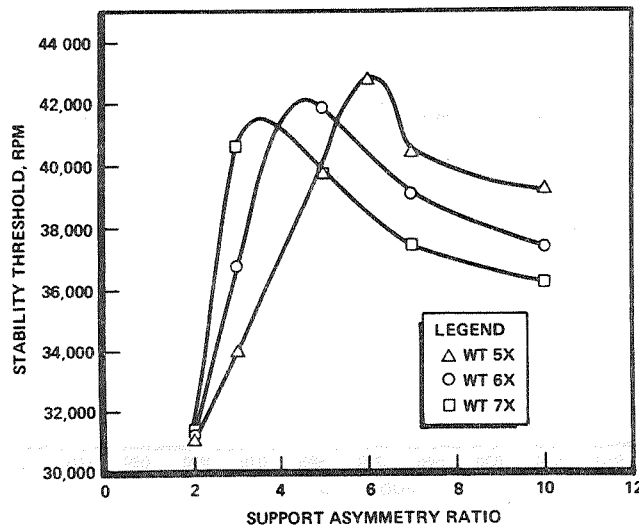


Fig. 20. 20 Lumped Mass Model (Stability Threshold vs Support Asymmetry Ratio)

maximum stability threshold speed for a given housing/rotor weight ratio. This optimum asymmetry ratio varies as the housing/rotor weight ratio is increased. The larger the housing/rotor weight ratio, the smaller the optimum asymmetry ratio to produce a maximum threshold speed. For example, an asymmetry ratio of 3:1 produces the highest threshold speed for a large housing/rotor weight ratio, whereas an asymmetry ratio of 10:1 requires a low weight ratio to produce the highest threshold speed.

Finally, housing modal damping was varied to determine its effect on rotor stability. The modal damping (percentage of critical damping) supplied by the housing structure was varied with increasing asymmetric support ratios. Figure 21 shows that as the housing modal damping is increased, the stability threshold speed remains nearly constant. This result does not change with the housing/rotor weight ratio.

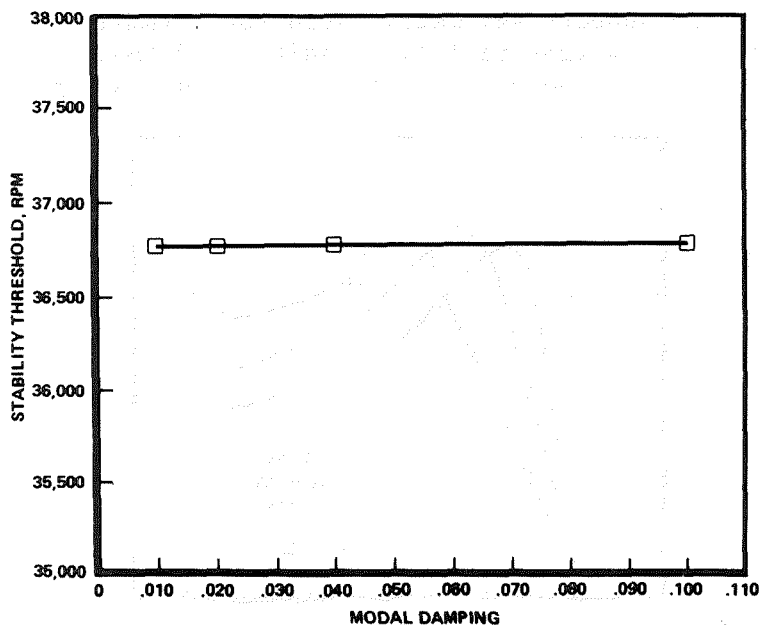


Fig. 21. Modal Damping vs Stability Threshold (20 Lumped Mass Model)

In an effort to compare the previously observed trends of the six turbopumps to this generic model, stability analyses using both a rigid and flexible housing assumption were performed. Figure 22 shows a stability map for the simple model. The flexible housing approaches an unstable condition at a higher speed than the rotor in a rigid housing. This result emulates the turbopump survey performed earlier. The analysis was performed with the typical 6:1 housing/rotor weight ratio and a support asymmetry ratio of 3:1.

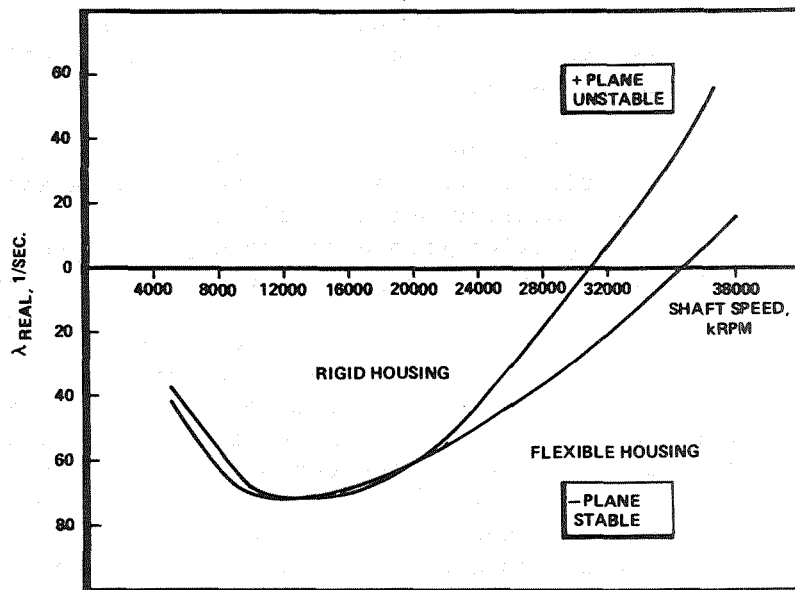


Fig. 22. Generic Turbopump Model Stability Map

Conclusions and Recommended Design Practice

A rotor stability analysis with a rigid housing assumption predicts an instability at a lower speed compared to a similar flexible housing case. Consequently, a rigid housing assumption is more conservative for design than the flexible model. Simple analysis approaches indicate that a flexible housing acts as an inefficient energy absorber and dissipates only a small portion of the destabilizing

forces in the rotor/housing system. The significant stability improvement associated with a housing is attributed to asymmetric supports. In a simple generic turbopump model, it was determined that the asymmetric support stiffness ratio grounding the housing should be greater than a value of 2:1. This simple model also indicated the optimum housing asymmetric support ratio is dependent on the housing/rotor weight ratio. Review of the weight data for the stable turbopumps included in the survey and the weight parametric study indicate most well behaved pumps have or should have at least a 5:1 housing to rotor weight ratio. Housing structural damping variations indicate no significant effect on the rotor stability.

For future designs, these results indicate some general rules to act as guidelines. These include: asymmetric housing supports of greater than a 2:1 ratio and heavier than a 5:1 housing to rotor ratio. Also, preliminary analyses should predict conservative stability results assuming a rigid housing depending on the accuracy of the coefficients that couple the rotor to the housing. Based on analytic results, in many cases complex housing models are not necessary for stability analyses. As a result, time and money are saved in the development of rotordynamic models.

Housing models would be required if detailed response analyses are necessary, however, the variation in response with unknown rotor unbalance distributions many times makes preliminary response work unreliable. In practice, a high-speed rotor balance in the housing is recommended to obtain minimal response.

#### Nomenclature

A,B = constants, determined by initial conditions  
c = damping, lb-sec/in.  
F = excitation force, pounds  
k = stiffness, lb/in.  
m,M = mass, lb-sec<sup>2</sup>/in.

$Q, Q_{1,2}$	=	arbitrary constants
$q_R$	=	rotor displacement, inches
$\dot{q}_R$	=	rotor velocity, in./sec
$q_S$	=	housing displacement, inches
$\dot{q}_S$	=	housing velocity, in./sec
$t$	=	time, seconds
$W$	=	work per cycle, lb-in./cycle
$\omega$	=	spin speed, rad/sec
$y$	=	displacement, inches
$\dot{y}$	=	velocity, in./sec
$\ddot{y}$	=	acceleration, in./sec <sup>2</sup>

#### References

1. Childs, Dara, "Simulation Models for Flexible Spinning Bodies," Transactions of the ASME, November 1975.
2. Lund, J. W., "Stability and Damped Critical Speeds of a Flexible Rotor in Fluid Film Bearings," Journal of Engineering for Industry, May 1975.
3. Bansal, P. N., "Stability and Damped Critical Speeds of Rotor-Bearing Systems," Journal of Engineering for Industry, November 1975.
4. Wylie, Advanced Engineering Mathematics, McGraw-Hill, p. 613, 1960.
5. Gunter and Trumble, "The Influence of Internal Friction on the Stability of High Speed Rotors With Anisotropic Supports," Journal of Engineering for Industry, p. 1105, November 1969.

## SESSION VII. FLUID AND GAS DYNAMICS

SESSION CHAIRMEN:       L. Povinelli (LeRC/NASA)  
                          H. Struck       (MSFC/NASA)

### OVERVIEW

The objective of the Fluid and Gas Dynamic Working Group is to obtain a clearer understanding of the interactions of the hot gas flow with the structure in the duct system, the flow passages of the rotating machinery, and the thrust chamber nozzle for the purpose of finding ways and means to increase the life and performance of the systems.

The working group plan contains some tasks which have been with us for a long time. Due to the urgency of finding an improved hot gas transfer system, the Duct Flow Non-uniformity Study (H2) was started in 1981. The Aerothermal Loads Definition Study (H5) was introduced by Lewis Research Center. It contains numerous subtasks which are mainly dealing with turbine and pump improvements. The five presentations of this session are selected from these two tasks.

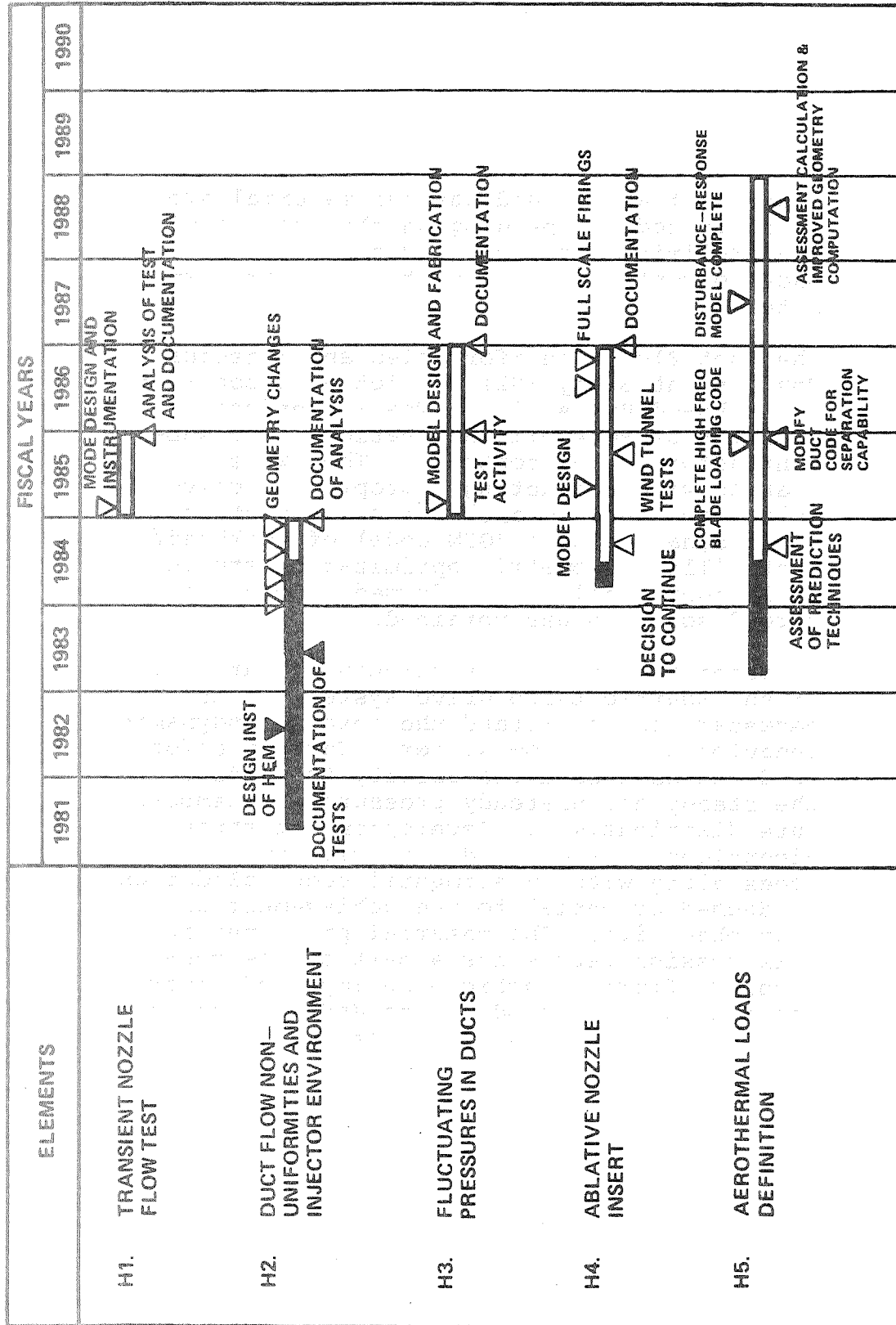
Let me describe briefly the rest of the tasks shown in the plan. The Transient Nozzle Flow Test (H1) is an inhouse task. The objective is to understand the shock-boundary layer interactions during transient flow and the resulting large side forces acting on the nozzle skirt. The Fluctuating Pressures in Ducts (H3) deals mainly with the fluid-structural interactions of the lox post tube banks in the injector. The Ablative Nozzle Insert Study (H4) has as its goal the performance improvement of the SSME.

Inserts of active and passive material are investigated. Depending on the results of the preliminary study a decision will be made to continue the investigation or terminate it.

The Duct Flow Nonuniformities and Injector Environment Study (H2) was let as a contract to Lockheed/Huntsville. The Rocketdyne Division of Rockwell International was subcontractor to the contract. They were charged with conducting appropriate scaled cold flow tests to anchor the computational fluid dynamics code (GYM code) of Lockheed/Huntsville. Geometric optimization studies could then easily be performed once a converged solution was obtained.

In order to improve the structural durability of the Shuttle turbo drive system, it is necessary to understand the aerothermodynamic behavior of the flow system. Current effort is directed toward the ability to predict the steady and unsteady pressure and temperature distributions. Development of three-dimensional viscous and inviscid computer codes along with experimental code validation is deemed essential to the achievement of that objective. The material presented in this session represents a part of the continuing effort to achieve an improved understanding of the aerodynamics and heat transfer through modeling and experimentation.

FLUID AND GAS DYNAMICS  
 WORKING GROUP PLAN  
 - KEY EVENTS -



COMPUTATIONS TO IDENTIFY REGIONS OF  
FLOW SEPARATIONS IN THE SSME TURNAROUND DUCT

L. A. Povinelli and K. L. McLallin  
National Aeronautics and Space Administration  
Lewis Research Center, Ohio 44135

Abstract not available.

The flow field in the SSME turnaround duct is analyzed using a three-dimensional, finite-difference, Navier-Stokes flow solver. The duct geometry is defined by a series of curved surfaces. The flow is assumed to be steady, laminar, and incompressible. The boundary conditions are specified at the inlet, outlet, and walls of the duct. The results of the computations are presented in the form of velocity profiles and streamlines. The flow is shown to separate from the walls of the duct in certain regions, which are identified and discussed. The location and extent of the separated regions are shown to depend on the duct geometry and the flow conditions. The results of the computations are compared with experimental data, and the agreement is found to be good.

The flow field in the SSME turnaround duct is analyzed using a three-dimensional, finite-difference, Navier-Stokes flow solver. The duct geometry is defined by a series of curved surfaces. The flow is assumed to be steady, laminar, and incompressible. The boundary conditions are specified at the inlet, outlet, and walls of the duct. The results of the computations are presented in the form of velocity profiles and streamlines. The flow is shown to separate from the walls of the duct in certain regions, which are identified and discussed. The location and extent of the separated regions are shown to depend on the duct geometry and the flow conditions. The results of the computations are compared with experimental data, and the agreement is found to be good.

EXPERIMENTAL EVALUATION OF AN ADVANCED SPACE  
SHUTTLE MAIN ENGINE HOT-GAS MANIFOLD  
DESIGN CONCEPT

D. G. Pelaccio, F. F. Lepore, G. M. O'Connor,  
G. V. R. Rao, G. H. Ratekin, and S. T. Vogt

Rockwell International/Rocketdyne Division  
Canoga Park, California

Abstract

The requirements of higher performance for the Space Shuttle Main Engine (SSME) and future space transportation earth-to-orbit propulsion systems dictate the use of efficient liquid rocket engines with engine cycles that invariably require lightweight, high-pressure, hot-gas ducts and manifolds that exhibit uniform flow, low turbulence levels, and minimal pressure drop characteristics. This study, using an extensively modified, full-scale SSME hot-gas manifold (HGM), established a detailed aerodynamic data base to support development of an advanced, three-dimensional, fluid-dynamic analysis computer model. In addition, the advanced SSME hot-gas manifold design used in this study demonstrated improved flow environment (uniformity) in the fuel side turbine exit and transfer duct exit regions.

Major modifications were incorporated in the full-scale HGM flow test article model using two large transfer ducts on the fuel turbine side of the HGM in place of the three small transfer ducts in the present design. Other model features included an increase in the flow areas downstream of the 180-degree turn and in the fishbowl regions. Tests were conducted at a Rockwell International blowdown facility using ambient temperature, high-pressure air that simulated a range of Reynolds numbers from 20 to 60 percent of the SSME rated power level. Detailed steady-state pressure measurement surveys of the flow field on the fuel side of the hot-gas manifold were conducted. Some high-frequency pressure measurements were included to quantify the turbulent nature of the flow in a qualitative

fashion. Data were scaled to engine conditions and were compared to similar data for the current SSME three-duct hot-gas manifold design.

The hot-gas manifold flow field data were found to be essentially independent of Reynolds number over the range examined. Major flow improvements were observed in the turbine exit/turnaround duct region, where the turbine exit circumferential pressure gradients were reduced by approximately 66 percent. Total and static pressure distributions in the regions downstream of the 180-degree turn were decreased by 75 percent from that exhibited by the present three-duct designs. Separation phenomena in the transfer duct exit planes were also substantially reduced. The maximum engine scaled Mach number exhibited for the two-duct HGM configuration in the transfer duct exit regions was lower by 38 percent from that observed on the current design.

### Introduction

The requirements for higher performance in current and future space transportation earth-to-orbit propulsion systems dictate the use of efficient liquid rocket engines with engine cycles that invariably require lightweight, high pressure, temperature and mass flow, hot-gas duct, and manifolds. In addition, it is also necessary that such propulsion systems be designed with an emphasis on long life, high reliability, and minimum maintenance requirements. Experience obtained during the development and certification of the Space Shuttle Main Engine (SSME), the first large rocket engine designed specifically for reuse, has underscored the importance of optimal design of manifold ducting systems subject to high-pressure, hot-gas streams.

The current SSME hot-gas manifold (HGM) is a double-walled, hydrogen-gas-cooled structural support and fluid manifold, which is shown in Fig. 1. It is the structural backbone of the engine and interconnects and supports the preburners, high-pressure

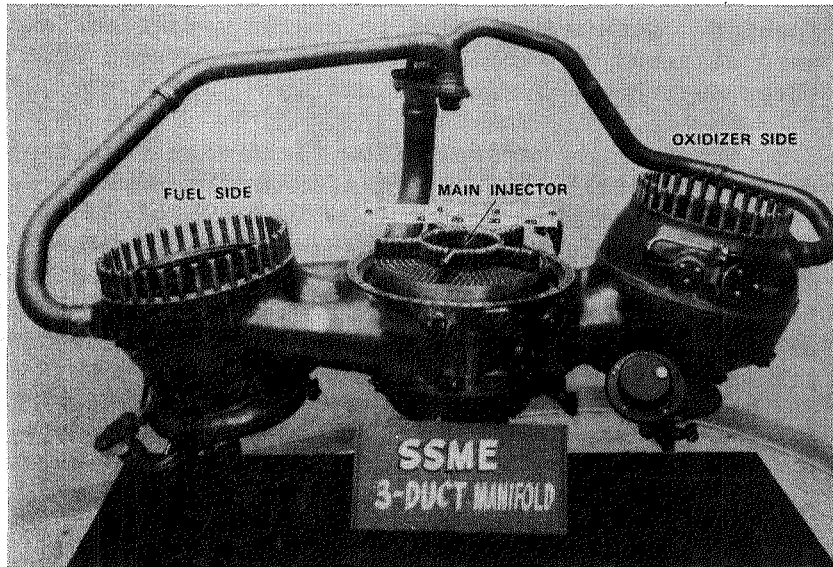


Fig. 1. Current SSME Hot-Gas Manifold

turbopumps, main combustion chamber, main injector, and heat exchanger as shown in Fig. 2. The high-pressure, high-flowrate, high-temperature, hydrogen-rich gas exits the fuel and oxidizer turbopumps and enters the hot-gas manifold. The annular shaped flow channel turns the flow 180 degrees, which then diffuses into large bowl (fishbowl) shaped volumes. The gas is then routed through five hot-gas transfer ducts, three on fuel side and two on the oxidizer pump side, into the main injector torus (racetrack) manifold where it is radially directed into the hot-gas cavity of the main injector. During steady-state operation of the engine, approximately 70 percent of the hot-gas flow is routed through the fuel side while the remaining 30 percent is passed through the oxidizer pump side (Table 1). This condition produces higher dynamic pressures and hence greater aerodynamic loading on the hot-gas manifold fuel side because the mass flow per flow path cross-sectional area is greater than that which is characteristic of the HGM oxidizer pump side.

During the development of the SSME, the flow distribution at the exit of the HGM fuel side ducts was

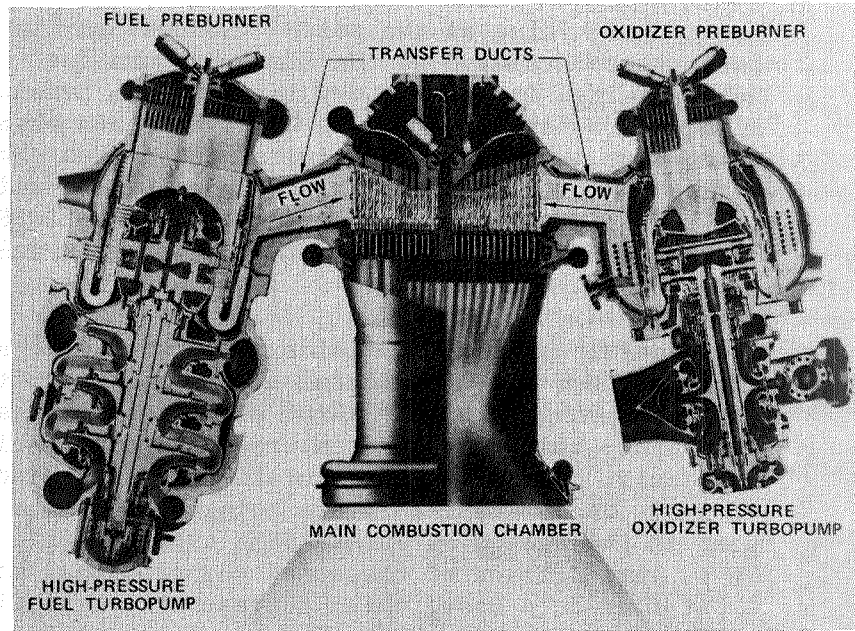


Fig. 2. SSME Powerhead

Table 1. SSME HGM Operating Conditions  
(Full Power Level, 109%)

HGM Region	Mass Flow, lbm/sec	Pressure, psia	Temperature, R
Fuel Pump Side	173.1	3589.5	1680.6
Oxidizer Pump Side	68.1	3589.1	1454.5

identified as being nonuniform and exhibiting large-scale separated flow regions. Typically, a large separation region is situated in the lower portion of the center transfer duct while smaller separation regions exist at the inner duct wall position of the outer transfer ducts. These flow nonuniformities at the exit of the fuel side transfer ducts in the current SSME hot-gas manifold design produce local high velocity flow regions that impinge on the main injector liquid oxygen (LOX) posts producing a high

aerodynamic force on the posts. Nonuniformities in the back pressure sensed by the high-pressure fuel turbine have resulted in oscillatory loads on the turbine blades. Highly turbulent flow levels have also been observed throughout the HGM flow circuit. These flow characteristics degrade lifetimes associated with the main injector LOX posts, high-pressure fuel turbopump (HPFT) blades, and duct cooling liners that have on occasion experienced cracking.

Additionally, flow fields associated with such manifold systems are complicated by the fact that they typically exhibit highly three-dimensional, separated, turbulent, swirling-flow features that make analysis difficult. At present, computational fluid dynamic analysis tools (Ref. 1-3) are being established to support in the design of future SSME type manifold systems. Thus, verification of these new computational models to a detailed data base, which represents a typical HGM flow type system, is essential to ensure confidence in their predictive accuracy.

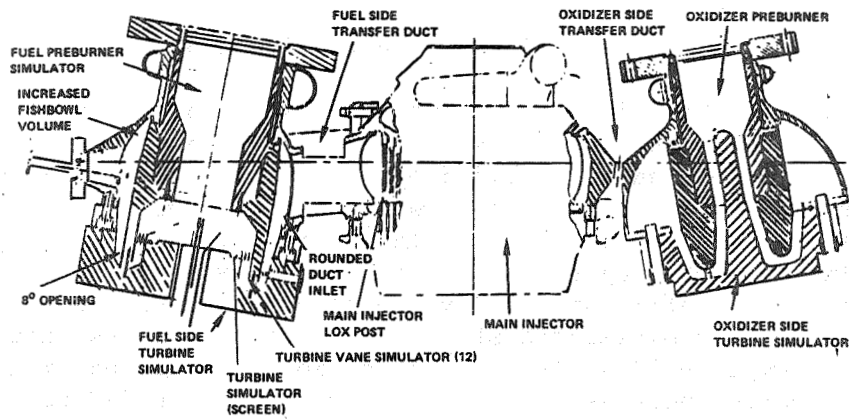
In this study, a full-scale, modified, fuel-side SSME was evaluated using a high-pressure ambient-temperature, air blowdown system, which was directed toward improving the overall flow distribution and decreasing turbulence levels in the turbine exit, turn-around duct, and transfer duct regions compared to the present SSME HGM design. Detailed steady-state pressure measurement surveys, using wall static ports, total pressure Kiel probes, directional probes, and total pressure rakes, of the HGM fuel-side flow field were performed. Some high frequency pressure measurements were also included to quantify the turbulent nature of the flow.

Data were scaled to engine conditions and were compared to similar data for the current SSME three-duct HGM design. From these comparisons, flow system improvement trends associated with the advanced SSME hot-gas manifold design were then established.

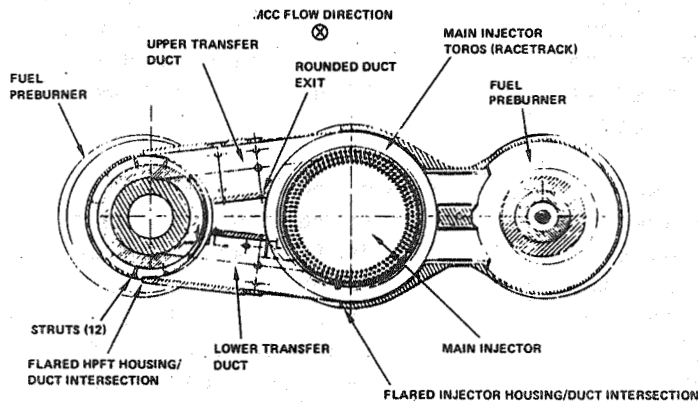
### Hot-Gas Manifold Concept Definition

A number of advanced HGM fuel-side design concepts were conceived and evaluated (Ref. 4). The concept options generated were guided by two major goals: (1) to produce a more favorable flow environment for the SSME main combustion chamber LOX injector posts and HPFT turbine by improving transfer duct flow distribution, velocity profile uniformity, decreasing turbulence levels, and minimizing streamline pressure losses; and (2) compatibility with flow conditions associated with projected increased SSME power levels. These HGM concepts were evaluated in terms of their flow aerodynamic, thermodynamic, structural, system integration, and fabrication characteristics. From this design option task, an enlarged area, fuel-side, two-transfer duct concept was selected as the HGM configuration that was fabricated, tested, and analyzed in this study.

The selected design has the following key features incorporated on the fuel turbine side of the manifold: (1) two 6.50-inch diameter ducts that increase flow area approximately 30 percent over the current configuration decreasing the flow dynamic head proportionally, (2) increase in turnaround duct area, 8-degree outer wall flaring after the 180-degree turn to decrease the flow dynamic head, (3) slightly rounded duct inlets to assist in turning the flow into the transfer ducts, (4) slightly rounded duct outlets to assist in distributing the flow around the main injector LOX post bundle, (5) flaired transfer ducts into the fuel preburner housing to assist in directing flow into transfer ducts and decreasing the HPFT exit pressure gradient, (6) faired transfer ducts into the main injector housing to assist in distributing flow around the main injector LOX post bundle, (7) increasing the HGM fishbowl volume by eliminating the present liner element to decrease the flow dynamic head in this region, and (8) compatibility to incorporate contoured turning vanes to assist in distributing flow into the transfer ducts and decreasing the HPFT exit pressure gradient. A schematic layout of this advanced HGM design identifying its key features is shown in Fig. 3.



A. SIDE VIEW



B. TOP VIEW

Fig. 3. Two-Duct HGM Air Flow Test Powerhead Configuration

A comparison of the two-duct HGM to the current SSME HGM design is displayed in Table 2. The major area increase in the turnaround duct exit area, fish-bowl cross-sectional area, and duct cross-sectional area associated with the two-duct HGM design tends to decrease the flow dynamic pressure for a given operational setting, which assists in gradual turning of the flow. These HGM design features also improve duct flow distribution, uniformity, and decrease flow turbulence, as well as assist in producing uniform flow conditions at the HPFT exit.

Table 2. HGM Design Comparisons

Feature	SSME HGM Current Design	Flow Study Design Model, 2 Ducts	Percentage Difference 2-Duct Design SSME Design
Turnaround Duct	FPL**	RPL (FMOF)***	--
Turnaround Duct Exit Area	29.5 in. <sup>2</sup>	49.68 in. <sup>2</sup>	68.5
Fishbowl Cross-Sectional Area	6.05 in. <sup>2</sup>	10.6 in. <sup>2</sup>	75.3
Duct Cross-Sectional Area	51 in. <sup>2</sup>	66.3 in. <sup>2</sup>	30.0
Faired Duct Inlets*	Yes	Yes	--
Faired Duct Outlets	No	Yes	--
*Slightly Rounded **Full Power Level Configuration ***Rated Power Level, First Manned Orbital Flight Configuration			

Hot-Gas Manifold Test Article Design/  
Fabrication/Instrumentation

A low-cost philosophy guided the design and fabrication of the hot-gas manifold test article. An existing surplus SSME hot-gas manifold was modified to produce the advanced, two-duct HGM test article. Additionally, where applicable, internal flow simulation components and instrumentation techniques that were successfully demonstrated in past HGM flow studies for the present SSME engine design (Ref. 5) were used. Numerous steady-state and high-frequency pressure instrumentation ports were incorporated in the fuel side of the model to define the flow field in detail from the model inlet to the transfer ducts exit. The test model was designed for a working pressure of 300 psia.

The oxidizer flow was modeled with a preburner/turbine simulator and turnaround duct. Flow enters the oxidizer preburner, which then transitions into an annulus passage that has six long, equally spaced blades to impart a swirl velocity component to the flow. The swirling flow is typical of turbine exit

flow conditions. The flow then enters the oxidizer turbine exit simulator where the flow direction is changed 180 degrees and exits into the large oxidizer side HGM fishbowl region (Fig. 3). In the SSME (Fig. 2), the oxidizer side HGM fishbowl region contains the heat exchanger component. Flow then exits through the two oxidizer transfer ducts into the main injector. Aluminum and Cres were the materials used in oxidizer side simulator hardware designs. This design simulates the gross features of the SSME oxidizer flow field but lacks proper simulation of flow field details. The degree of simulation designed into the test model was considered adequate because the oxidizer flow field does not influence the fuel side transfer duct flow field to a great extent. This is considered a good assumption because only approximately 30 percent of the total HGM gas flow goes through the oxidizer side of the HGM, while the remaining 70 percent is passed through the fuel side during hot-fire engine operation, as previously mentioned.

In contrast to the oxidizer side simulator design, the fuel preburner/turbine simulation hardware (Fig. 4 and 5) was designed to simulate an SSME fuel side flow field in detail. Like the oxidizer side simulator, the fuel side simulator was based on a design that was successfully demonstrated in past HGM flow studies. Past flow study test data showed that this simulator design produced an HGM fuel side flow that correlated well with that measured in an SSME engine. In this design, the flow enters the fuel preburner simulator where it is manifolded into an annular passage. At the annular passage entrance, a turbine simulator screen is placed to produce flow effects that are characteristic of those associated with a 15-degree swirl angle clockwise if viewed in the direction of the flow downstream of the screen, which is typical of SSME HPFT exit flow conditions at rated power level. Constant velocity conditions are produced by varying the orifice diameter as a function of radial position. The screen was designed for a pressure loss coefficient ( $\Delta P/q$ ) of

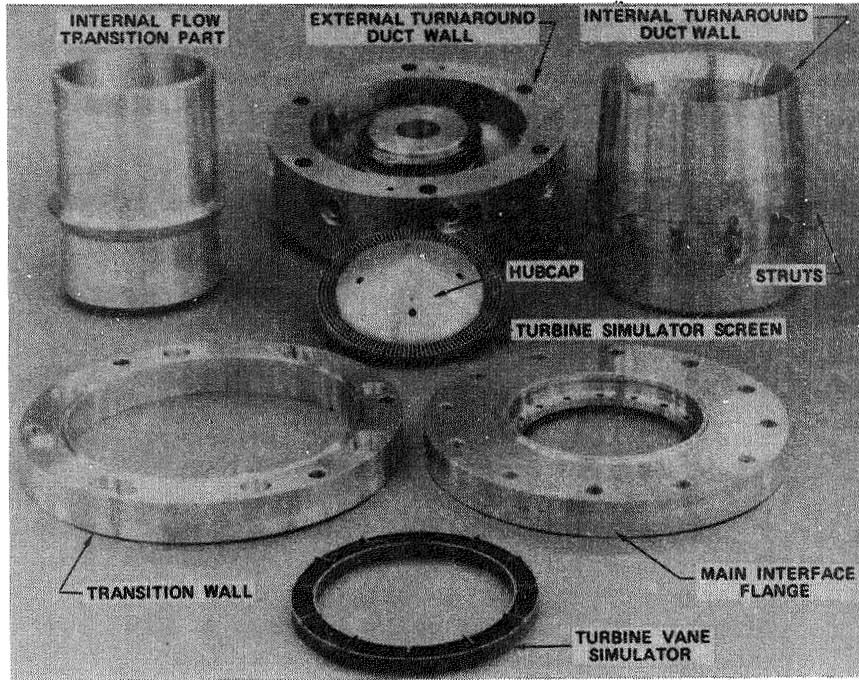


Fig. 4. Fuel-Side Simulator Components

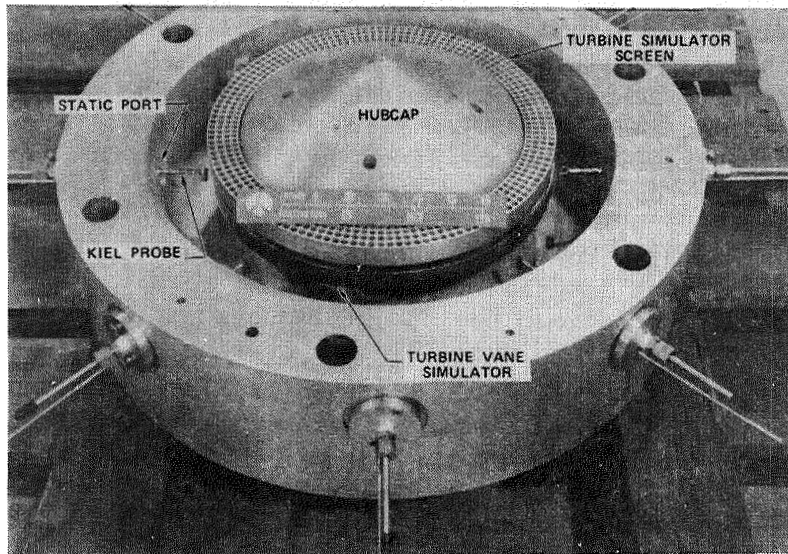


Fig. 5. Fuel-Side Turbine Simulator Assembly

5.6 psid, which is approximately 25 percent of that exhibited by the HPFT while still having enough resistance to stabilize flow exit conditions. Twelve thin fins, which span the width of the annular channel, are positioned just downstream of the screen exit in an equally spaced circumferential fashion. These fins simulate flow interference blockage associated with the turbine exit coolant liner supports. They are set on an angle of attack to the flow because of the swirl angular velocity component, and therefore add eddy vortex (vorticity) structure to the flow. The flow then changes direction, 180 degrees, in the turnaround duct region. The turnaround duct geometry simulates that used on the Space Shuttle Columbia's first set of flight engines known as the First Man Orbital Flight (FMOF) configuration. Downstream of the 180-degree turn, the outer wall of the annular flow channel is designed with an outward 8-degree taper. Twelve large support struts are then equally spaced circumferentially in the annular passage at the fishbowl entrance and simulate major structural components associated with the engine in this region. In the design of the HGM fuel-side fishbowl, the coolant liner was removed to increase the fishbowl volume. Two 6.5-inch constant ID ducts (Fig. 6) were integrated into the fishbowl and main injector housing, completing the fuel-side gas flow path to the main injector assembly. The coolant liner on the fuel side of the main injector was removed to accommodate the large transfer ducts. The two-duct HGM design also incorporates slightly rounded entrance and exit duct geometries and flush internal surfaces at the outer intersection points between the transfer ducts and the HGM fuel preburner and main injector housing (Fig. 3). Like the oxidizer simulator hardware, the fuel-side simulation hardware was designed to be made of aluminum and Cres material.

The SSME powerhead main injector was designed to be removable for ease in instrumentation and configuration changes. A modified SSME main combustion chamber (MCC), which incorporates the addition of a long throat ASME flow metering type nozzle is bolted

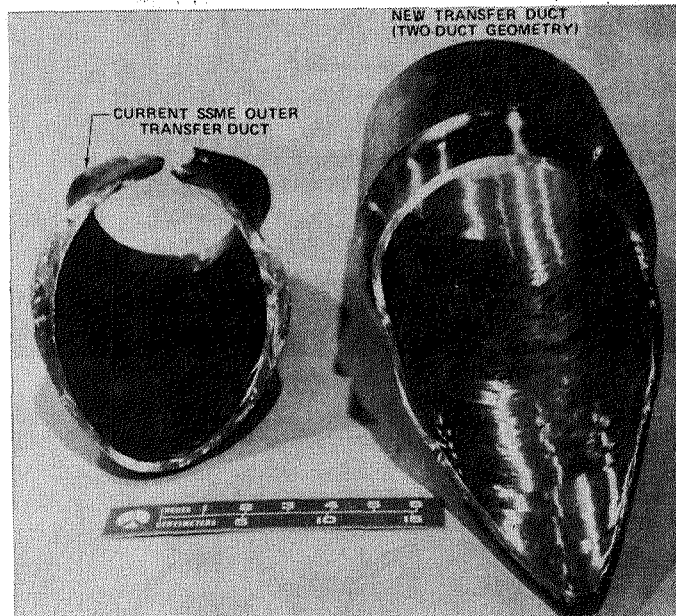


Fig. 6. Comparison of Current SSME Outer and New Transfer Duct

to the HGM main injector exit face. The flow metering nozzle chokes the flow maintaining high pressure within the flow model and also functions as a model total flow metering device.

Integration of an extensive amount of pressure instrumentation was incorporated into the fuel side test model. The model instrumentation measurement locations were placed to give detailed steady-state flow field definition at the model inlet, turnaround region, fishbowl entrance, transfer duct entrance, and exit planes. High frequency instrumentation is included in the model to give a qualitative assessment of the turbulent nature of the flow. A layout of instrumentation (location and type) is shown in Fig. 7 and listed in the legend given in Table 3, respectively. The upper transfer duct was designed to accept a pressure survey at the entrance. The entrance pressure rake layout configuration is shown in Fig. 8. Flow conditions are defined at both transfer duct

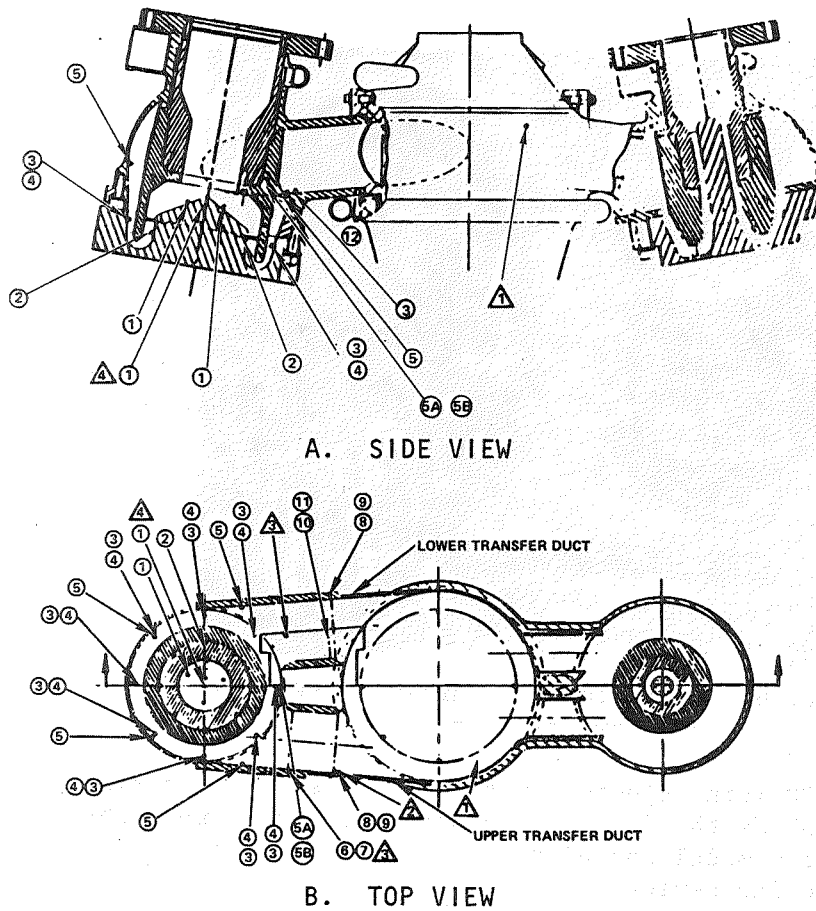


Fig. 7. Instrumentation Layout

exits (Symbols 8 and 9, Fig. 7) by placement of exit total pressure survey rakes shown in Fig. 9. In the lower duct, a pressure rake element (Fig. 7) was placed to measure the inner wall region flow field at a position 1.25 inches upstream of the exit rake plane. These total pressure rake elements were designed to be easily removable, have rotational capability, and be interchangeable with all rake locations. The three basic rake element types used are displayed in Fig. 10. When assembled the cross-sectional area blockage of the rakes was no greater than 9 percent of the total transfer duct cross-sectional area.

Table 3. Test Article Instrumentation Legend

Symbol	Location/Type
<u>Steady-State Pressure Measurements</u>	
①	Model Inlet/3 Static - 1 Total
②	Screen Exit - Upstream 180-Deg Turnaround/Static
③	Downstream 180-Deg Turnaround/Static
④	Downstream 180-Deg Turnaround/Total
⑤	Fishbowl - Entrance Upstream of Transfer Duct (3-D Probes)
⑤A	Fishbowl Entrance/Static
⑤B	Fishbowl Entrance/Total
⑥	Transfer Duct Entrance/Static
⑦	Transfer Duct Entrance/Total
⑧	Transfer Duct Exit Plane/Total
⑨	Transfer Duct Exit Plane/Static
⑩	Transfer Duct Exit Inner Wall/Static
⑪	Transfer Duct Exit Inner Wall/Total
⑫	Main Combustion Chamber/Total
<u>High-Frequency Measurements</u>	
△	CGIP - Racetrack Flow
△	Upper Transfer Duct - Exit
△	Upper Transfer Duct - Entrance
△	Fuel Side Model Inlet

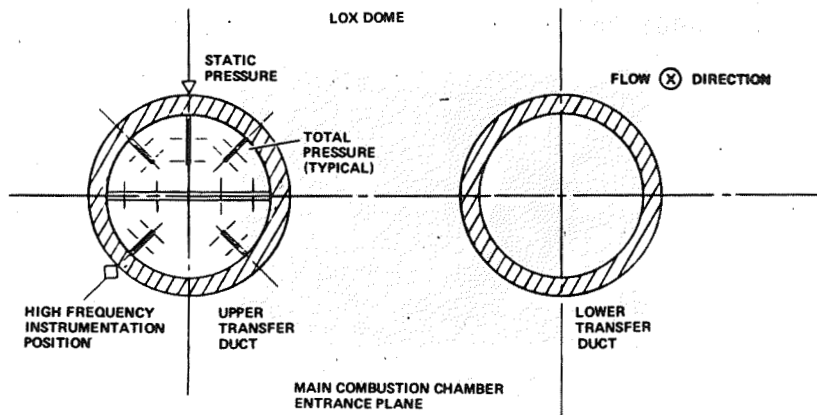


Fig. 8. Upper Transfer Ducts Entrance Rake Configuration

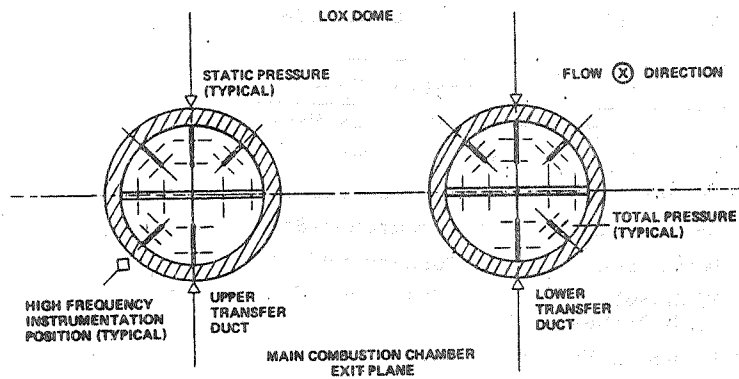
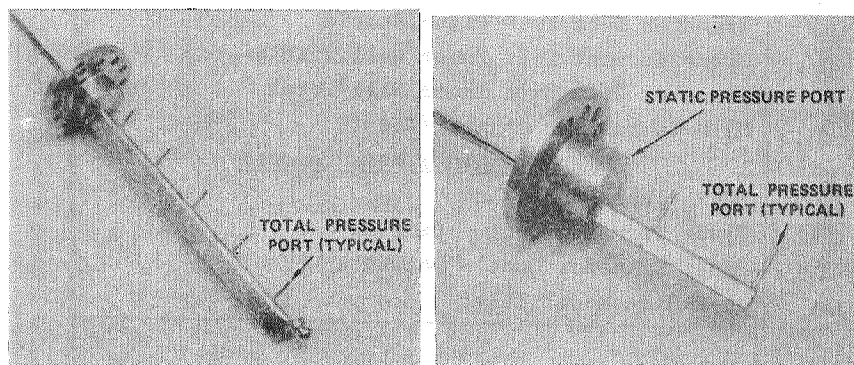
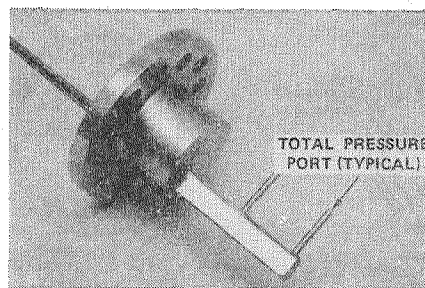


Fig. 9. Transfer Ducts Exit Rake Configuration



A. LARGE RAKE

B. MEDIUM RAKE



C. SMALL RAKE

Fig. 10. Total Pressure Rakes (Typical)

Total pressure Kiel probes were used downstream of the 180-degree turnaround region (Fig. 11) and three-dimensional directional probes were used to map flow at the fishbowl entrance plane (Fig. 12).

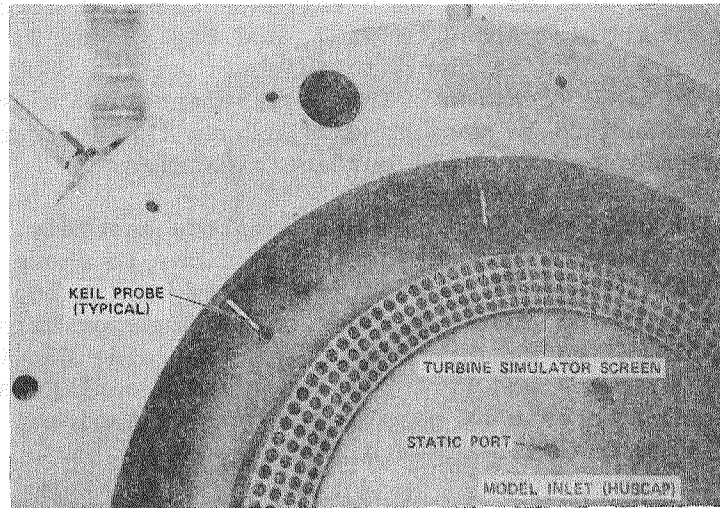


Fig. 11. Fuel Side Turbine Simulator (Closeup)



Fig. 12. Directional Probe Installation (Typical)

High-frequency pressure instrumentation was incorporated in the model at four positions. These locations are at the model inlet position on the pre-burner centerline upstream of the turbine simulator screen (Symbol 4, Fig. 7), at the upper transfer duct outer wall position at both entrance and exit locations (Symbols 2 and 3, Fig. 7, and Fig. 8 and 9, respectively), and in the main injector at the SSME manifold CGIP location. This instrumentation element was designed to be positioned flush in the surface to measure fluctuating wall surface pressures.

The advanced two duct HGM complete assembly, including installation of instrumentation, is shown in Fig. 13. Figure 14 is a detailed view of the top enlarged transfer ducts and fuel side simulator hardware. Detailed measurement of the fuel side HGM internal surfaces was performed to support configuration definition for use by complementary computational model flow analysis efforts (Ref. 2 and 3).

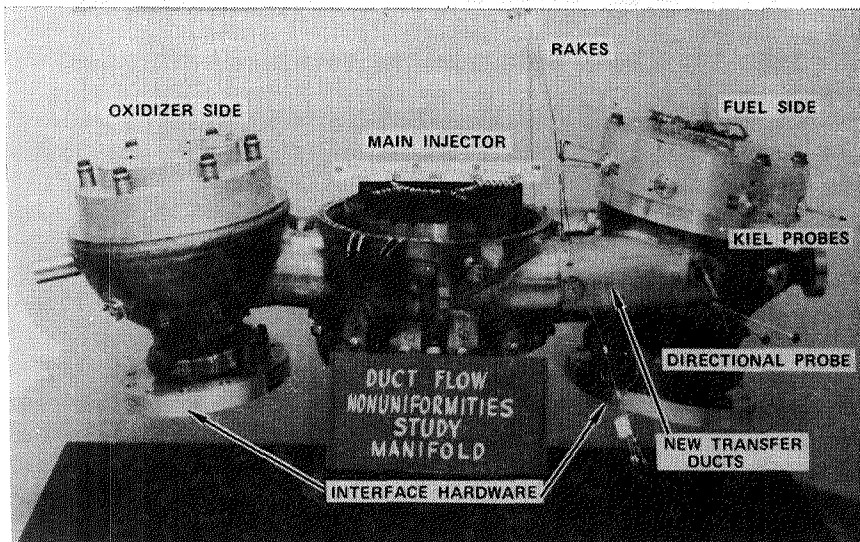


Fig. 13. Advanced Hot-Gas Manifold

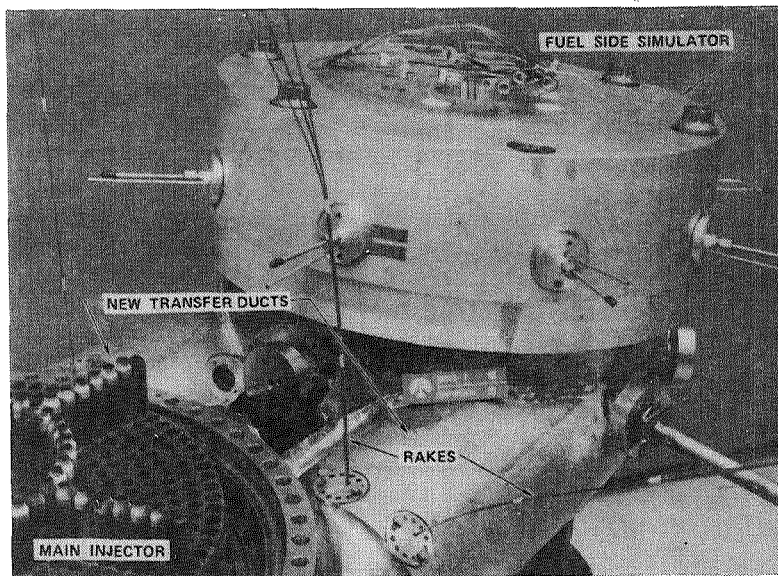


Fig. 14. Advanced HGM - Fuel Side

#### Test Facility/Operations

A high-pressure, air-blowdown test facility at Rockwell's North American Operations Aerospace Laboratory in El Segundo, California, was used. The blowdown facility was used to simulate up to 69 percent of the SSME rated power level Reynolds number at steady-state conditions for approximately 6 to 10 seconds, while transfer duct average Mach number ( $M$ ) is essentially matched. A comparison of facility conditions to the SSME for key test simulation parameters is shown in Table 4. With these key simulation parameters in the general range of engine conditions, accurate scalability of the air flow test data to engine system conditions is ensured.

A schematic layout displaying the main elements of the test facility is presented in Fig. 15. These main elements include the high-pressure air supply tank, main 18-inch valve, downstream plenum flow leg tee, 10-inch fuel and 6-inch oxidizer side flow legs with metering orifices, test model installed in the

Table 4. Engine/Facility Comparison

Parameter	Engine*	Two-Duct HGM Test Facility, Air
Pressure, psi	3000	300
Flowrate, lbm/sec	152	84
Mach Number	0.1	0.16
Reynolds Number, 1/ft	$1.90 \times 10^7$	$1.30 \times 10^7$
Percent, Reynolds Number	100	69

\*Rated Power Level Conditions

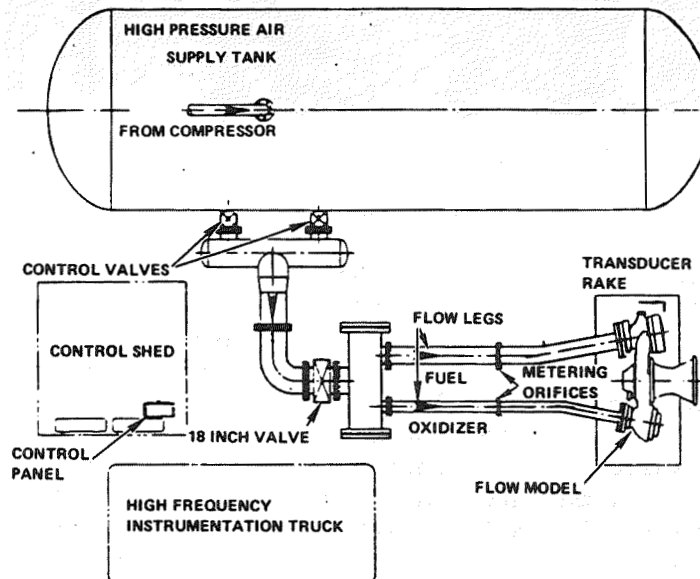


Fig. 15. NAAO Powerhead Blowdown Facility

support stand and the high frequency instrumentation recording room (truck). A detailed view of the flow model installed at the test facility is shown in Fig. 16.

The high pressure supply air tank is supplied by Cooper Bessemer, 11-stage, centrifugal, 4500-horsepower compressor up to a maximum pressure of 300 psia. The facility is controlled manually by

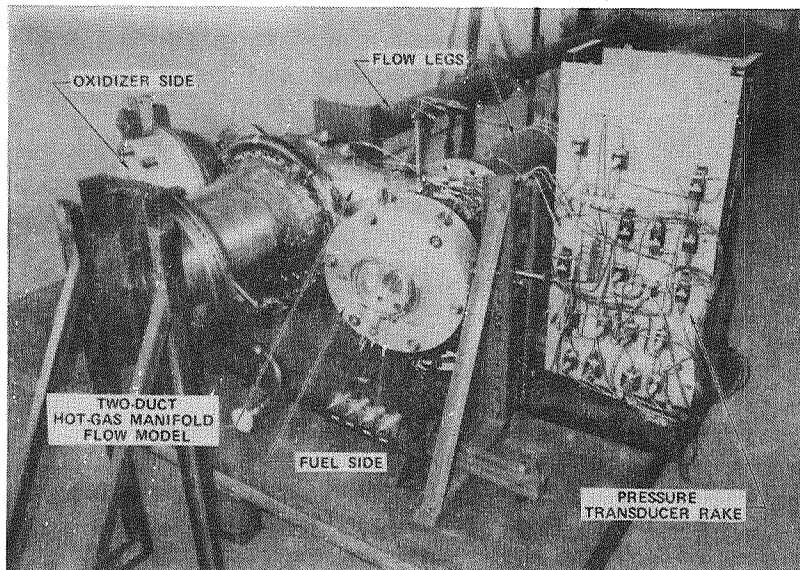


Fig. 16. Flow Model Installed

three pneumatically operated ball valves upstream of the test flow model. The upstream fuel and oxidizer feed leg flow metering orifices were sized in such a manner to properly simulate the mass flow split typical of SSME powerhead operation (70 percent fuel, 30 percent oxidizer).

Standard gauge and differential pressure transducers were used for steady-state pressure measurements. Up to 95 channels of steady-state instrumentation were recorded at 1 millisecond sampling intervals on the laboratory's data acquisition system. After testing, these data were then transferred by tape to Rockwell's IBM main frame computer where detailed reduction and analysis of the data were conducted. High-frequency pressure instrumentation was recorded on a tape recorder. These tapes were then analyzed on Rocketdyne's Analog Analysis System.

Due to the large number of steady-state pressure measurements required (number of transducers required) to properly define the three-dimensional flow field, three instrumentation configurations were required to fully characterize the flow field for a

given Reynolds number flow condition. Facility metering orifices, model inlet, and upper and lower transfer duct static pressure measurements were recorded in all tests to ensure repeatability between individual tests that were run at identical test conditions. Tests were run at three  $Re_D$  (Reynolds number based on transfer duct diameter) flow conditions ( $2.1 \times 10^6$ ,  $5.0 \times 10^5$ , and  $7.0 \times 10^6$ ) to determine the influence of Reynolds number on the fuel-side flow field.

### Results

The advanced, two-duct HGM data were scaled to engine conditions and compared to data associated with the present SSME three-duct HGM design. Discussion of the scaling techniques used in converting full-scale, cold-flow model data to simulated hot-fire conditions are presented in the Appendix. Detailed discussions of data concerning major hot-gas manifold flow field features are presented in Ref. 4, while data pertaining to engine operation and improvements associated with the advanced, two-duct HGM design concept are examined below.

It should be noted when examining the data that a 16-degree swirl was induced in the fuel-side flow at the turbine simulator screen in the clockwise direction (upper to lower transfer duct direction) when viewed from the top (LOX dome) of the flow model. In the fuel-side simulator region, the circumferential location was defined as 0 degree between the two transfer ducts, which then increase in location position angle in the counterclockwise direction when viewed from the top of the model (Fig. 17). The upper transfer duct (UTD) intersects the fuel-side simulator in a circumferential position sector between 15 and 85 degrees while the corresponding lower transfer duct (LTD) position intersects the fuel side between 275 to 345 degrees. The 180-degree position was defined opposite the region between the transfer ducts.

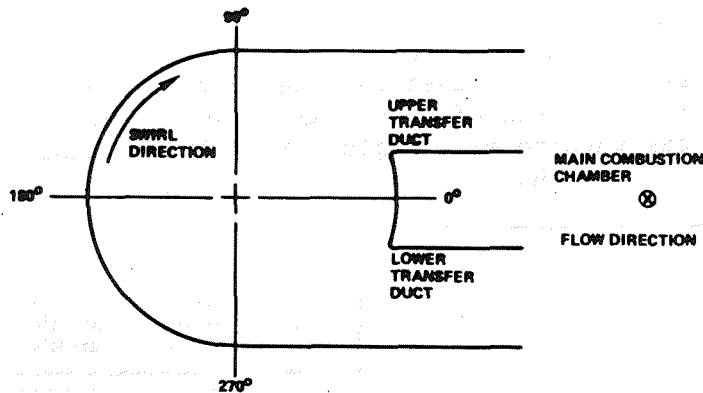


Fig. 17. Two-Duct HGM Fuel-Side Circumferential Location Legend

Test repeatability was considered quite good between individual tests at the approximate same operating conditions. In general, little or no Reynolds number effect was observed throughout the HGM fuel-side flow system except at the fishbowl entrance plane where the local dynamic pressure circumferential variations increased by approximately one dynamic pressure head at the low Reynolds number test condition ( $Re_D = 2.6 \times 10^6$ ). These results give confidence that at the high Reynolds number test conditions (69 percent of SSME rated power level Reynolds number), the critical Reynolds number conditions have been exceeded as is characteristic of engine operation. This implies that major separation and turbulent flow structure features present in a hot-gas manifold operated at engine conditions should also be present in the hot-gas manifold cold-flow model when operated at high Reynolds number test conditions.

The SSME HGM at the exit of the high pressure fuel turbopump imposes on the turbine considerable circumferential variations in static and total pressure. This effect is due to the compactness of the manifold and to its one-sided discharge through the transfer tubes. The predictions have been confirmed on SSME hot-firing tests, as well as by past HGM air-flow test studies (Ref. 5). The two-duct HGM

greatly reduced the pressure (flow) nonuniformities in the turbine exit/turnaround duct region compared to the present three-duct SSME design. A reduction of about two-thirds of the total pressure variation around the turbine exit region (Fig. 18) is achieved by the two-duct HGM design.

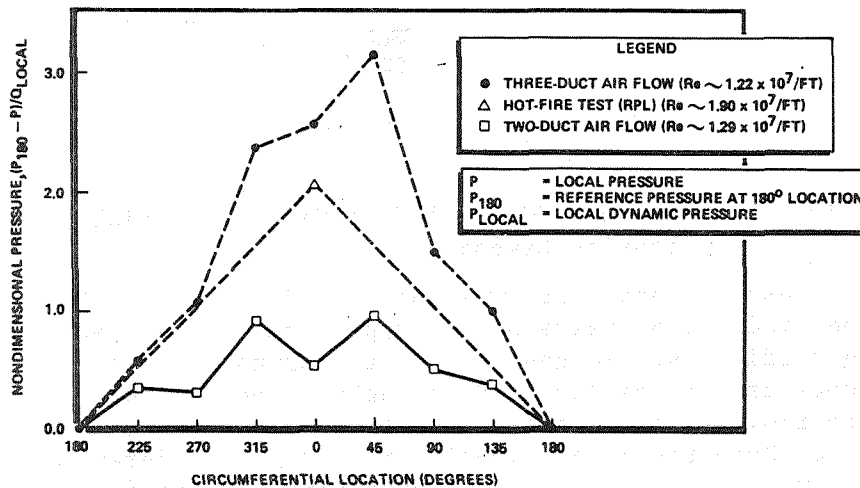


Fig. 18. Circumferential Static Pressure Variation at Turbine Exit

The turbine simulator screen in the flow model enforces constant velocity conditions implying that the static pressure distribution measured is characteristic of the total pressure distribution. The increased uniformity in the pressure distribution should result in the following improvements: (1) increased turbine life, (2) decreased radial loads and shaft movements, which tend to produce increased clearances and/or rubbing, (3) reduction or avoidance of maldistributions of coolant flow, (4) reduction in deformation and cracking of sheet metal, and (5) decreased HPFT turbine temperatures for a given power level.

Both the static and total circumferential pressure variation downstream of the 180-degree turnaround duct (Fig. 19 and 20, respectively) were greatly reduced for the two-duct HGM configuration.

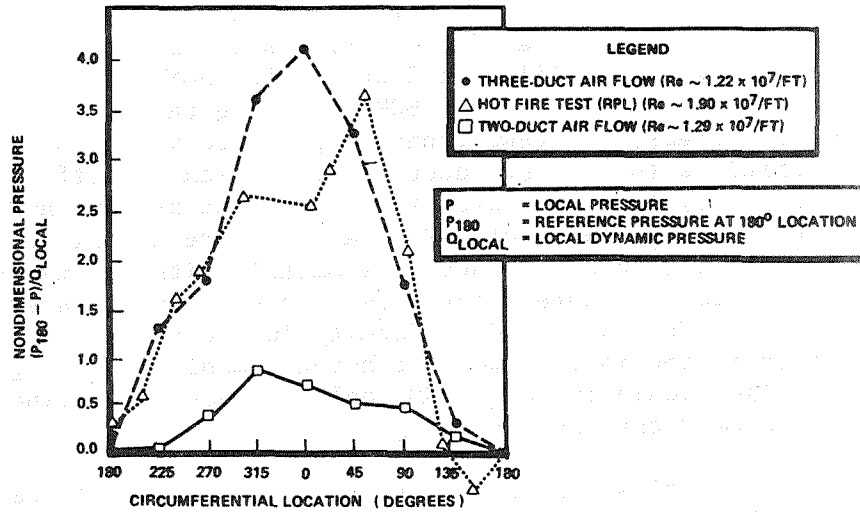


Fig. 19. Static Pressure Variation Downstream of 180-Degree Turn

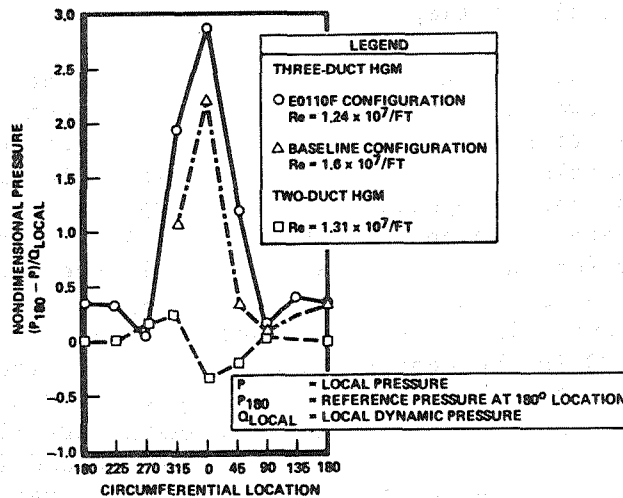


Fig. 20. Total Pressure Variation Downstream of Turnaround Duct 180-Degree Turn

Examination of Fig. 19 indicates the static pressure difference, referenced at the maximum pressure position at the 180-degree location, is approximately 25 percent of that exhibited in the present SSME HGM design. The minimum static pressure was recorded at

the 315-degree location for the two-duct configuration while the three-duct configuration minimum static was identified at 0 degree for HGM air-flow tests and 45 degrees for SSME hot-fire tests. The total pressure circumferential pressure variation exhibited for the two-duct HGM is radically different (Fig. 20) from that associated with the present HGM design. The two-duct HGM total pressure distribution varies little and is nearly symmetric with the maximum total pressure located between the two transfer ducts. The increased uniformity in the turnaround duct region in the two-duct hot-gas manifold configuration would increase HGM coolant sheet metal liner life over the present design.

The flow through the transfer duct exit planes of the two-duct manifold was more uniform than that present in the current three-duct manifold design. The improvement in flow uniformity should decrease main injector LOX posts loading and increase their operational lifetime.

The percentage of the flow area stagnant is less for the two-duct configuration. A rough comparison of stagnation areas for the two- and three-duct hot-gas manifold configurations is displayed in Fig. 21 for comparable Reynolds numbers. Typical mass flow splits are 52 percent in the UTD and 48 percent in the LTD for the two-duct system, while the three-duct configuration exhibits typical mass splits of UTD: 52 percent, CTD: 9 percent, and LTD: 39 percent, where CTD is the center transfer duct. Typical Mach number profiles for the two- and three-duct hot-gas manifold configuration scaled to engine RPL (100 percent) conditions are shown in Fig. 22 and 23, respectively. The maximum Mach number observed in the two-duct configuration is 0.16 while the three-duct HGM exhibited a maximum Mach number of 0.26.

Flow uniformity improvements for the two-duct HGM configuration are shown by examination of Fig. 24 and 25, where scaled air flow Mach number profiles along major transfer duct axes are plotted for

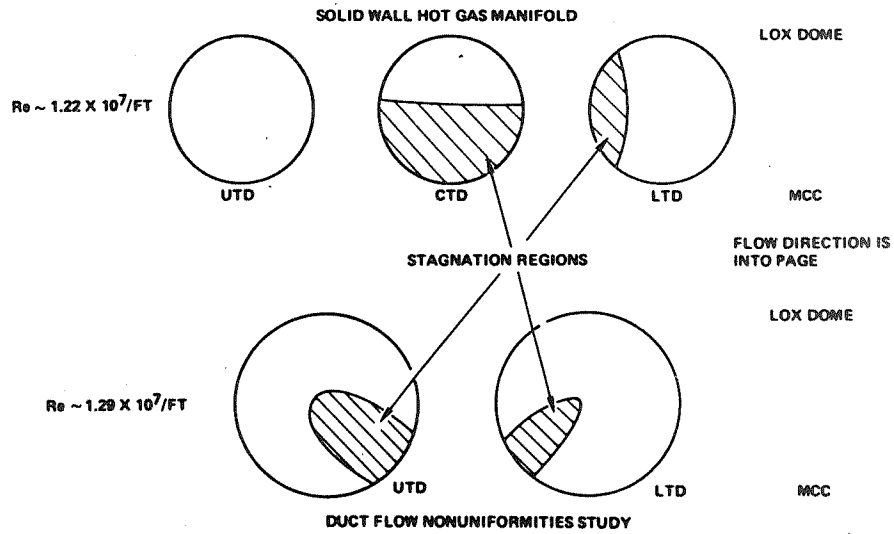


Fig. 21. Stagnation Region Comparison Between Two- and Three-Duct Configurations

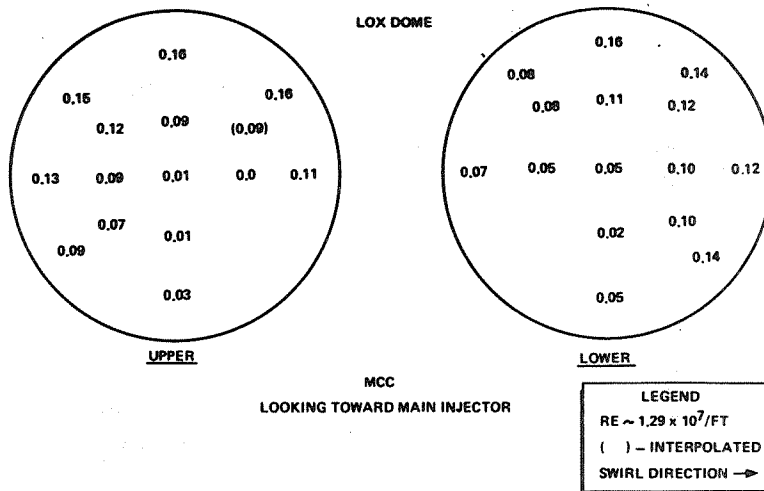


Fig. 22. Engine-Scaled Transfer-Duct Mach Number Profiles - Two-Duct HGM

both the three- and two-duct HGM configurations, respectively, for corresponding Reynolds number conditions.

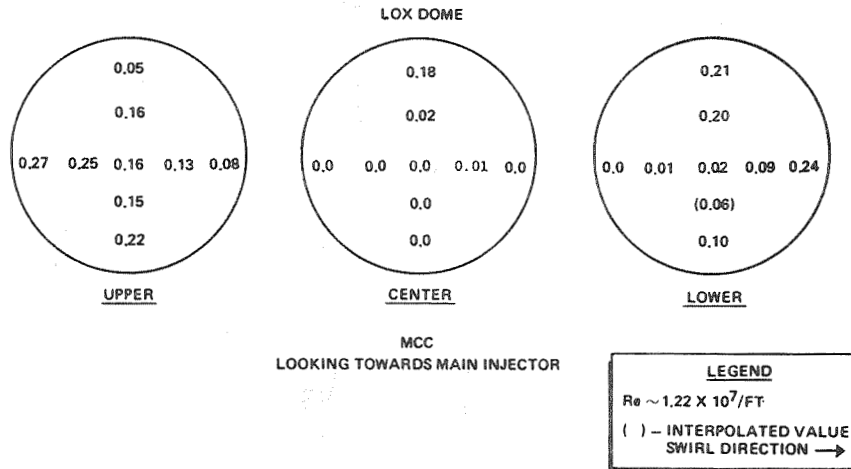


Fig. 23. Engine-Scaled Transfer-Duct Mach Number Profiles - Present Three-Duct SSME Design

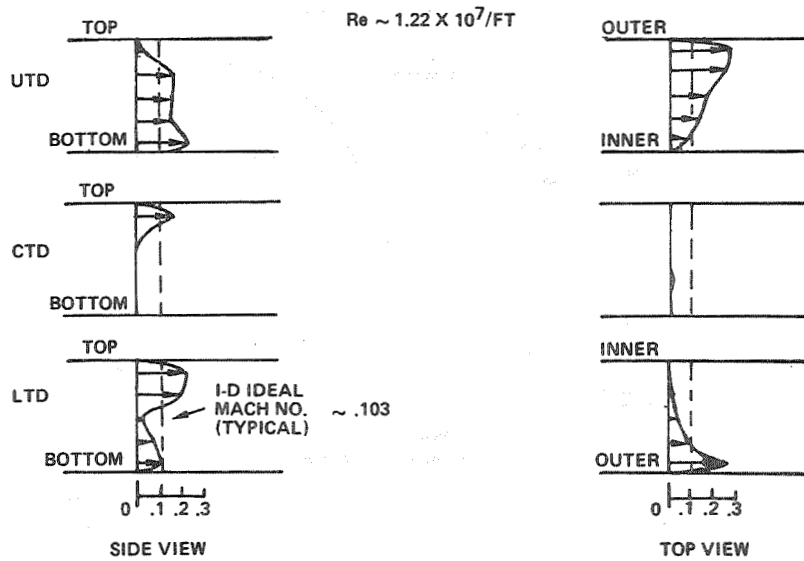


Fig. 24. Engine-Scaled Three-Duct Manifold Mach Number Profiles Along Duct Major Axes (100 Percent Power Level Condition)

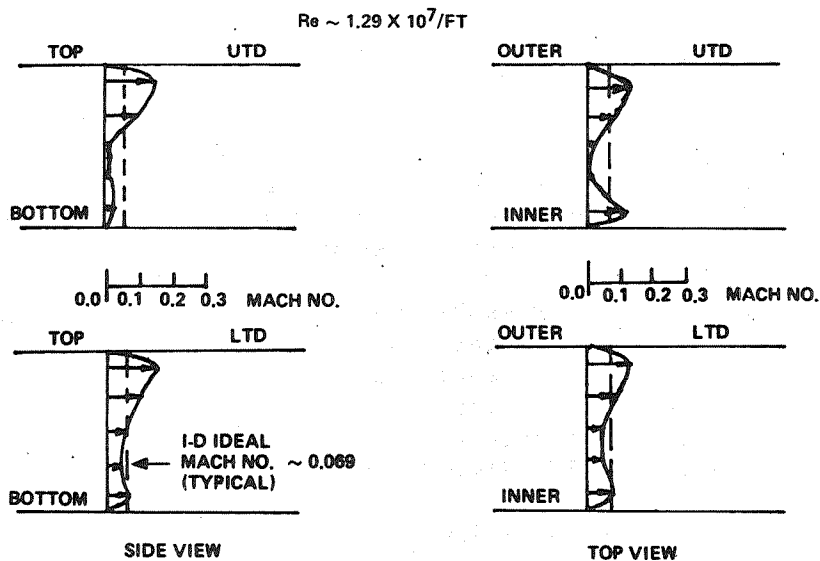


Fig. 25. Engine-Scaled Two-Duct Manifold Mach Number Profiles Along Duct Major Axes (100 Percent Power Level Condition)

It can be observed from the side view profiles (Fig. 25) that there is more flow in the upper portion of the ducts as expected because the flow has an upward bias after coming around the 180-degree turn. The contours of these vertical profiles are basically the same in both ducts. The top view shows that there is more flow on the outside of each duct. This is due to the fact that flow travels circumferentially in both directions around the fishbowl where most of the flow enters the transfer ducts at the outside regions. Examination of the corresponding Mach number profiles associated with three-duct manifold displays that little appreciable flow passes through the center transfer duct. In addition, the flow is nonuniform within each duct and from one duct to another. This observation is true for both the vertical and horizontal axis. The two-duct HGM configuration Mach number profiles for both ducts approach the one-dimensional ideal Mach number condition (0.069). This ideal Mach number uniformity condition was only approached in the upper transfer duct in the present

three-duct design. It should be noted that the one-dimensional constant Mach number profile across the transfer duct exit plane is the best flow condition achievable for a given mass flow and transfer duct cross-sectional area. The flow through the transfer duct exit plane, in the two-duct HGM configuration, is clearly more symmetrical and uniform than that associated with the current three-duct HGM design.

Fluctuating pressures were measured, as previously mentioned, at four locations within the model. These miniature, high-frequency transducers were installed just upstream of the model inlet (hubcap), at the transfer duct entrance and exit and at the main injector racetrack CGIP (Fig. 7).

Results at cold-flow conditions for two flow conditions are displayed in Table 5. Values shown are composite RMS values in the frequency range of 0 to 2000 Hz. Note that the fluctuating pressure at the transfer duct entrance is the highest measured for both tests. This may be due to flow separation from turbulence generated in the 180-degree turn in addition to separation effects resulting from flow entering the transfer ducts (Ref. 4). No predominant fluctuation frequency was found at any of the measurement locations. The trend indicated from these data suggest that the highest fluctuating pressures are experienced at the entrance to the transfer ducts and decay downstream. This is based on only these four measurements.

Table 5. Fluctuating Pressure ( $P'$ ) Results

Position	Reynolds Number ( $Re_D$ )	
	$5.08 \times 10^6$	$7.07 \times 10^6$
Hubcap	0.517*	0.514
Transfer Duct Entrance	0.942	1.27
Transfer Duct Exit	0.867	1.12
CGIP - Main Injector Racetrack	0.607	0.907
*(in psi)		
Note: $P'$ (RMS), Frequency Range (0-2 kHz)		

## Conclusions

An advanced SSME hot-gas manifold design was successfully demonstrated that improved flow uniformity in the HGM turnaround duct and transfer duct exit regions over that exhibited in the present fuel-side three-duct HGM design. This advanced HGM design shows promise in leading to longer life, higher power level SSME designs, as well as having application to future liquid rocket engine systems.

In this study, tests were successfully conducted on the advanced two-duct HGM design over a Reynolds number range from 22 to 69 percent of 100 percent SSME power level conditions with transfer duct average Mach number held essentially constant (0.15 to 0.16). For all tests conducted, little Reynolds number effect was observed on the data except in the fishbowl region where local dynamic pressure increase was observed in the low Reynolds number range. The HGM flow field exhibited little gross unsteadiness except in the transfer duct separation regions over the Reynolds number range investigated.

Major flow improvements, observed in the two-duct HGM design in the turbine exit/turnaround duct region, were accomplished by increasing the annular path cross-sectional area downstream of the 180-degree turn, the fishbowl volume, and by contouring the two large transfer ducts with the outer fishbowl housing. These features, in general, decreased the local dynamic pressure and allowed for adequate flow streamline relief required to gradually turn the flow into the transfer ducts in a more gentle manner than that exhibited by the present design. It was observed that the two-duct HGM turbine exit circumferentially pressure gradient was reduced by approximately 66 percent, while the total and static pressure distributions in the region downstream of the 180-degree turn were decreased by approximately 75 percent. These flow characteristics should improve turbine coolant distribution and increase liner life.

Flow uniformity was improved in the transfer duct exit planes. However, separation phenomena accounted for approximately 25 percent of the total cross-sectional area, and improved contouring of the inlets of these ducts could yield still greater reduction in peak flow velocities. The maximum engine scale Mach number exhibited for the two-duct HGM configuration was reduced by 38 percent from that observed on the current design. The increased total cross-sectional area associated with the two enlarged transfer ducts is believed to be the major contributing factor in duct exit flow improvement because of the corresponding decrease in average dynamic pressure. These two-duct HGM traits should substantially increase SSME main injector LOX post life.

#### Acknowledgements

This study was performed under NASA Contract NAS8-34507 under subcontract to Lockheed Missiles and Space Company, Inc., Huntsville, Alabama, Subcontract No. SM80C6620M. The exceptional support given by the personnel associated with this study is greatly appreciated. In particular, appreciation is expressed to Mr. Heinz Struck of NASA Marshall Space Flight Center; Mr. Alan Ratliff and Dr. Jurgen Thoenes of Lockheed Missiles and Space Company, Inc. Huntsville, AL; and Mr. F. M. Kirby, Mr. W. R. Wagner, and Mr. R. Kassner of Rocketdyne for their guidance. Support given by Mr. J. Rietdyk, Mr. T. Adams, and Mr. D. Peterson of Rocketdyne's Combustion Devices Group and Mr. J. Lindquist in the design and fabrication phases was instrumental in the success of this program. Commendation is also expressed to Mr. A. McKinstry, Mr. T. Hughes, and the NAAO Thermodynamic Laboratory test crew for their dedicated support associated with conducting the test program. Support given by Mr. J. Romero, Mr. J. Kingsley, and Ms. K. Gorham associated with the study data reduction task is appreciated. The exceptional support given by Mrs. C. Greminger in formal documentation tasks associated with the program was also greatly appreciated.

### References

1. Liang, P. Y., "An Inviscid Three-Dimensional Analysis of the Space Shuttle Main Engine Hot Gas Manifold," presented at the 18th Thermophysics Conference, Montreal, Canada, 1-3 June 1983.
2. Thoenes, J., "Duct Flow Nonuniformities Study," presented at Computational Fluid Mechanics Workshop, NASA MSFC, Huntsville, AL, 14 March 1984.
3. Rosen, R., Liang, P. Y., Quan, Y. H., Rao, G. V. R. and Yang, T. T., "Investigation of a Complex Rocket Engine Manifold Flow to Determine Its Major Characteristics," presented at AIAA/SAE/ASME 20th Joint Propulsion Conference, Cincinnati, Ohio, Paper No. 84-1462, June 1984.
4. Pelaccio, D. G., Duct Flow Nonuniformities Study - Final Report, Rocketdyne Report No. RI/RD83-160, Canoga Park, CA, 30 June 1983.
5. Lepore, F. F. and Vogt, S., Solid Wall Hot-Gas Manifold Testing Series IV Test Results, Rocketdyne Briefing No. AUT-83-006, Canoga Park, CA 13 January 1983.
6. Cheremisinoff, N. P., Fluid Flow Pumps, Pipes, and Channels, Ann Arbor Science Publications, Ann Arbor, Michigan, p. 125, 1981.

### Appendix A: Scaling Techniques

Though geometric and dynamic similarity may exist between the cold-flow model and hot-fire engine operation, these conditions are not sufficient for the direct application of raw test data to an actual hot-fire operation. Due to the difference in operating pressures, temperatures, and flowrates, a few conversion factors or scaling parameters must be utilized in order to convert raw cold-flow data to simulated hot-fire operations. Once the necessary scaling parameters have been calculated, the data base obtained from experiments can then be easily transformed into useful information directly applicable to hot-fire engine operation. With reference to the type of

experiments treated in this report, there are basic quantities for which scaling parameters may be obtained (Ref. 4): (1) steady-state pressure and (2) Mach number. In results discussed previously, scaling of steady-state pressure and Mach number was performed and will be addressed here. The methods described have proven to be very effective in the prediction of flow field definition in a hot-fire engine situation (Ref. 5).

When Reynolds number (Re) similarity exists between model and engine operation, it can be inferred that Euler number (Eu) similarity also exists between air flow test conditions and hot-fire engine operation. The Eu is defined (Ref. 6) as:

$$Eu = \frac{P}{\rho U^2} \quad (A-1)$$

where P = pressure,  $\rho$  = fluid density, and U = one-dimensional velocity.

In comparing an SSME powerhead (three-duct system) with the two-duct test model, it is more convenient to compare the Reynolds number per unit length rather than the nondimensional quantity, since there are major differences in the geometry, specifically: (1) SSME three-duct powerhead HGM with 4.9-inch exit diameter transfer ducts, while (2) the two-duct HGM has 6.5-inch constant diameter transfer ducts.

The Reynolds number per unit length is defined as:

$$\frac{Re_D}{D} = \frac{U}{\nu} = Re \quad (A-2)$$

where D is the transfer duct diameter, U the one-dimensional gas velocity, and  $\nu$  the kinetic viscosity. Table A-1 shows a Reynolds number comparison between various hot- and cold-flow conditions.

As Table A-1 suggests, the cold-flow Reynolds number per unit length achieved for full throttle is

Table A-1. Two-Duct/SSME HGM Reynolds Number Comparison

	COLD FLOW, 2-DUCT			SSME*, HOT-FIRE		
	LOW FLOW	MEDIUM FLOW	MAXIMUM FLOW	65% THROTTLE	100% THROTTLE	109% THROTTLE
FUEL MASS FLOW (LBM/S)	26.9	52.3	73.5	90.6	151.8	173
Re x 10 <sup>6</sup>	2.59	5.08	7.07	4.57	7.68	8.14
Re/D x 10 <sup>7</sup> (1/FT)	0.48	0.94	1.30	1.11	1.86	1.98
*BASED ON COLUMBIA SSME CONFIGURATION						

well within the same order of magnitude as that exhibited by the SSME. In light of this trend, reference will be made exclusively to the full throttle (maximum flow) air-flow conditions when cold-flow tests data are compared to hot-fire tests.

Differential pressure data are easily scaled by use of the Euler number analogy between hot fire and cold flow, which has previously been discussed, as:

$$Eu|_{\text{cold}} = Eu|_{\text{hot}} \quad (\text{A-3})$$

If a scaling factor is to be obtained for the difference in pressure between any two corresponding stations along a streamline designated as Station 1 and 2, then Eq. A-3 can be rewritten as:

$$\frac{P_1 - P_2}{\frac{1}{2} \rho U^2} \Big|_{\text{cold}} = \frac{P_1 - P_2}{\frac{1}{2} \rho U^2} \Big|_{\text{hot}} \quad (\text{A-4})$$

where both sides of the equation have been multiplied by 1/2 for convenience. The above equation can be rewritten in more general terms as:

$$\frac{\Delta P}{q} \Big|_{\text{cold}} = \frac{\Delta P}{q} \Big|_{\text{hot}} \quad (\text{A-5})$$

where  $q$  is the dynamic head to convert a measured cold flow pressure differential  $\Delta P|_{\text{cold}}$  to an equivalent

hot-fire value, Eq. (A-5) is solved for  $\Delta P|_{\text{hot}}$ :

$$\Delta P|_{\text{hot}} = \left( \frac{q|_{\text{hot}}}{q|_{\text{cold}}} \right) \Delta P|_{\text{cold}} = K \Delta P|_{\text{cold}} \quad (\text{A-6})$$

where K is the scaling factor and varies only as a function of the mass flowrate,  $\dot{m}$ .

Typical values of K for conversion to three-engine operating conditions of interest are given in Table A-2.

Table A-2. Typical Scaling Factors to Various Engine Power Levels (Transfer Duct Exit Location)

TEST NO.	TIME SLICE, SECONDS	$\dot{m}_{\text{FUEL}}$ LBM/SEC	$1/2 \rho u^2$ COLD, PSID	SCALING FACTORS		
				$K_{\text{MPU}}$ 65%	$K_{\text{RPU}}$ 100%	$K_{\text{FPU}}$ 109%
1.07	14.0 TO 14.7	61.63	2.169	5.52	10.08	11.80

The dynamic pressure  $q|_{\text{hot}}$  is computed from engine balance values of fuel flowrate,  $\dot{m}$ , gas temperature, T, and static pressure,  $P_s$ , and local cross-sectional area as defined in the relation below:

$$q|_{\text{hot}} = \frac{RT}{2g_c P_s} \left( \frac{\dot{m}}{A} \right)^2 \Bigg|_{\substack{\text{engine} \\ \text{balance}}} \quad (\text{A-7})$$

Similarly,  $q|_{\text{cold}}$  is obtained by use of Eq. (A-7) where the physical quantities are obtained from standard facility measurements.

Mach number values obtained from measured cold-flow tests can be scaled to engine conditions by the ratio of the one-dimensional value of M calculated for engine operation to those calculated for test model operations:

$$M_{\text{hot}}|_{\text{local}} = \left[ \frac{M_{\text{hot}}}{M_{\text{cold}}} \right]^{1-D} M_{\text{cold}}|_{\text{local}} \quad (\text{A-8})$$

The one-dimensional Mach number can be calculated either from the isentropic flow equations by use of the average total and static pressures measured in the test model, or from the law of conservation of mass by the formula given below:

$$M|_{1-D} = \frac{\dot{m}RT}{P_s A} \sqrt{g_c \gamma RT} \quad (\text{A-9})$$

Equation (A-9) can be applied to both cold-flow and hot-fire operation since test data and engine balance theoretical values are both available for direct use. In determining the two-duct transfer duct one-dimensional engine operational value, SSME HGM three-duct values must be adjusted to take into account the difference in transfer duct total cross-sectional area is:

$$A_{\text{two-duct}} = 1.30 A_{\text{three-duct}} \quad (\text{A-10})$$

A typical value of the one-dimensional M ratio, Eq. (A-8), for engine operation at rated power level conditions is approximately 0.62 for the two-duct HGM configuration. This number varies as a function of engine and test model operation conditions.

NUMERICAL ANALYSIS OF FLOW NON-UNIFORMITY  
IN THE HOT GAS MANIFOLD OF THE SPACE  
SHUTTLE MAIN ENGINE

J. Thoenes, S.J. Robertson, and A.W. Ratliff  
Lockheed-Missiles & Space Company, Inc.  
Huntsville, Alabama 35807

and

P.G. Anderson  
Continuum, Inc.  
Huntsville, Alabama 35808

Abstract

A numerical analysis was made of three-dimensional viscous flow in a conceptual hot gas manifold (HGM) for the Space Shuttle Main Engine High Pressure Fuel Turbopump (SSME HPFTP). A finite difference scheme was used to solve the Navier-Stokes equations including a mixing length turbulence model. The exact geometry of the SSME HGM was modeled using boundary fitted curvilinear coordinates and the General Interpolants Method (GIM) code. Slight compressibility of the subsonic flow was modeled using a linearized equation of state with artificial compressibility. Computations were performed on the CYBER 205 supercomputer. Experimental data were employed to provide boundary conditions for the computation. A time relaxation method was used to obtain a steady state solution.

Results are compared with experimental data and found to be in reasonably good agreement in terms of overall flow patterns, pressure distribution in the manifold, and total pressure loss along the flow path. In particular, flow separation regions in the transfer ducts as observed from the analysis are in good agreement with experimental data.

The results of this effort demonstrate the feasibility and potential usefulness of computational methods in assisting the design of SSME components whose function involves the flow of fluids within complex geometrical shapes.

## Introduction

Much of the U.S. activity in space over the coming years will be dependent upon the Space Shuttle and its derivative versions as a principal space transportation system. This dependence requires improved designs or techniques to extend the life, upgrade performance, reduce weight, lower operational costs, and generally improve the functional capability of the main propulsion system. The engines for this main propulsion system are advanced high pressure engines operating on oxygen and hydrogen. A need therefore exists to investigate, develop, and define basic concepts in support of the main propulsion system improvements. A basic problem which requires investigation and improvement is that of flow nonuniformities found to occur in the turbopump exhaust manifolds, their transfer ducts as well as in the main injector of the current engines.

Development and verification tests of the SSME have shown that the three transfer ducts connecting the high pressure fuel turbopump (HPFTP) to the main injector have an uneven flow distribution with large areas of separated flow. The outer transfer ducts each carry approximately twice the amount of gas flowing through the center duct. The attendant higher dynamic pressures in the duct exits impose severe gasdynamic forces on the main injector liquid oxygen (LOX) posts. In the past, this has led to the installation of support shields, thereby trading structural integrity for a reduction in gasdynamic efficiency. In subsonic flow, pressure nonuniformities will also propagate upstream, thereby causing oscillatory loads on the turbine blades of the HPFTP.

One way to conduct a design improvement effort is to replace deficient hardware with redesigned components and determine the results by testing. Unfortunately, this process is very expensive, and practically prohibitive if more than one alternative improvement is to be investigated. An alternate way to attack the problem is to use a combined analytical/experimental approach. The advent of large core, high speed scientific computers in conjunction with the development of powerful

numerical techniques has made the computational analysis of complex three-dimensional flow fields feasible. Realizing this opportunity, a joint analytical and experimental study was undertaken by Lockheed and Rocketdyne under the sponsorship of NASA. Based on a preliminary study of improvement alternatives, a conceptual two-duct HPFTP hot gas manifold was selected to be built and tested by Rocketdyne<sup>1</sup>. Test data obtained were then provided to Lockheed for comparison with computational results obtained from three-dimensional, viscous flow calculations. The methodology of the analysis and the results are briefly described in this paper.

### Numerical Analysis

#### Methodology

This study employed the General Interpolants Method (GIM)<sup>2</sup> for constructing numerical analogs of the partial differential equations governing fluid flow. The domain of interest is first described by appropriate subdivisions into an assemblage of interconnected finite elements. A boundary fitted computational grid is generated using an algebraic interpolation scheme based on three-dimensional general curvilinear coordinates. Shape functions based on a set of generalized interpolants are then used to describe the behavior of all variables over each element. The discretized equations are multiplied by a set of weight functions and integrated over the element volume. A choice of weight functions which are orthogonal to the shape functions leads to explicit nodal analogs. As a result of this spatial discretization, the partial differential equations are reduced to ordinary differential equations with time as the independent variable. The two-step MacCormick algorithm was used to integrate these ordinary differential equations to a steady state solution.

#### Geometric Treatment

The domain of interest is considered to be geometrically arbitrary in that any shape is represented as a bivariate blend of regular subdomains. Division into subdomains is made such that analytical functions can describe the shape of each edge (but it

can be made by point specification and piecewise linear edges). Attention is then focused on each region. Regions are blended at the junction to provide a continuous full domain geometry.

The geometrical definition of the HGM was obtained from drawings supplied by Rocketdyne. The model includes the "fishbowl" proper and the transfer ducts, but not the turnaround duct. Struts at the transition from the turnaround duct to the fishbowl were neglected. This simplification might influence the flow properties at the fishbowl entrance but should have negligible effect on the overall flow in the bowl and the transfer ducts. Flow contours of the manifold were modeled accurately including the slight round off of the transfer duct inlet edges.

Representing the initial step in a parametric investigation of changes in the geometrical configuration, a second manifold using a flared transfer duct inlet section was modeled also. This configuration is characterized by a greatly increased radius of curvature at the transfer duct inlet, mainly in the lower inner duct quadrant.

#### Flow Analysis

The full set of differential equations solved by the GIM code consists of the equations for the conservation of mass, momentum (Navier-Stokes) and energy, supplemented by one equation of state. The differential equations are solved in the strong conservation law form for the conserved variables. The relaxation procedure is started from initial conditions based on a reasonable estimate of the steady state flow field. Primitive variables, including the pressure, are evaluated after the completion of each time step in a decoding procedure.

Transport properties are specified in terms of dynamic viscosity and Prandtl number for turbulent flow. Effects of turbulence were modeled first in simple form by applying an appropriate multiplier to the laminar viscosity, and second, by using a Prandtl-Van Driest algebraic turbulence model which evaluates the turbulent viscosity as a function of a local mixing length and the three-dimensional vorticity.

The initial guess for the velocity field is obtained by performing a multiple stream tube analysis to obtain approximate values for the magnitude of the velocity and the flow direction at each point in the flow field. These data, in conjunction with an assumed total pressure, can be used to initialize the primitive variables using isentropic relationships. Properties at the fishbowl inlet were based on measured data and held fixed during the relaxation procedure. The calculations were performed on a CYBER 205 supercomputer using slightly less than 8000 nodal points to discretize the computed flow region.

### Results

A composite view of the computational (sparse) grid representing the fishbowl and the two transfer ducts is shown in Fig. 1. The geometric configuration is symmetric about a plane containing the pump axis. The inner flow surface, basically a circular cylinder, represents the turbine simulator, and the outer flow boundary is given by the spherical fishbowl wall. The exact position of the transfer ducts is more clearly seen as Fig. 2, representing an axial cut through the manifold and also showing the actual computational grid used in the calculations. The length and the exit face of the transfer ducts were determined by the location and orientation of pitot pressure probes installed in the experimental hardware.

Flowfield results obtained in the transfer ducts are shown in Figs. 3 and 4 in terms of a velocity vector map and a corresponding Mach number contour map, respectively. The region shown represents a longitudinal plane cut at an angle of approximately 45 deg to the fishbowl entrance plane (that is, a cut through the upper outer and lower inner quadrant of the transfer duct). Note the formation of a vortex, the location of which is in excellent agreement with experimental data which indicated a flow separation region in the same location. The separation region is more clearly delineated in the Mach number map of Fig. 4.

Measured and computed static and total pressures as functions of circumferential location in the

fishbowl at an axial location roughly corresponding to the lower edge of the transfer duct inlet are compared in Figs. 5 and 6. The computed results for the two turbulence models mentioned previously are seen to be in very good agreement with the measured data. The rather close agreement between the two turbulence models can be attributed to the fact that in this analysis it is the configuration geometry that represents the dominant cause for turbulence in the flow.

Having demonstrated that available numerical analysis is capable of producing results which agree with experimental data, a principal goal of the effort undertaken here was to use the analysis to explore changes in the configuration which would result in more favorable flow behavior. As an example, a computational grid incorporating a greatly enlarged radius of curvature of the transfer duct inlet fairing, especially in the region just upstream of the duct flow separation region found in the experimental configuration, is shown in Fig. 7. For clarity, only the outer flow boundary is shown. Neither the duct location, orientation nor size of the transfer ducts was affected by this modification. Flowfield calculations for the modified configuration were then performed using initial and boundary conditions identical to those previously used for the nominal configuration geometry. The results are shown in Figs. 8 and 9, again in terms of a velocity vector and a Mach number contour map. The most significant finding is the diminution of the flow separation region (see Figs. 3 and 4) as a result of increasing the transfer duct inlet fairing radius of curvature.

### Conclusions

Three-dimensional viscous flow in a conceptual twin-duct SSME hot gas manifold was numerically computed and the results were found to be in good agreement with measured data. The results of this study demonstrate the feasibility and potential usefulness of computational fluid dynamics methods in the design and improvement of multi-dimensional flow configurations as complex as those of certain SSME components.

### References

1. D.G. Pelaccio, F.F. Lepore, G.M. O'Connor, G.V.R. Rao, G.H. Ratekin, and S.T. Vogt, "Experimental Evaluation of an Advanced Space Shuttle Main Engine Hot-Gas Manifold Design Concept," AIAA/SAE/ASME 20th Joint Propulsion Conference, Paper AIAA-84-1463, June 1984.
2. L.W. Spradley, P.G. Anderson, and M.L. Pearson, "Computation of Three-Dimensional, Nozzle Exhaust Flow Fields with the GIM Code," NASA Contractor Report 3042, August 1978.

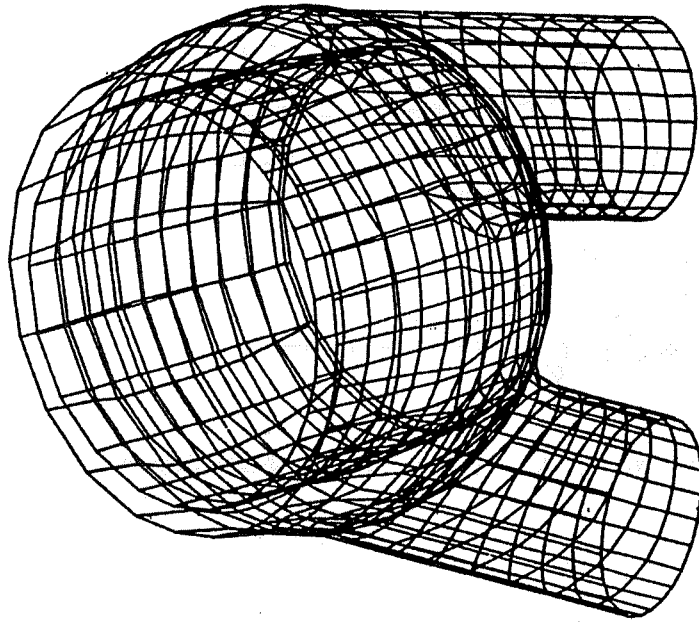


Fig. 1 SSME HGM Computational Grid, Sparse Representation, Viewed at 45 deg Angle to Bowl Axis

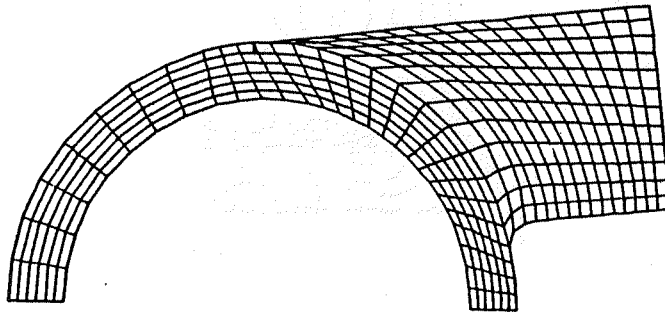


Fig. 2 SSME HGM Computational Grid, Viewed Along Bowl Axis

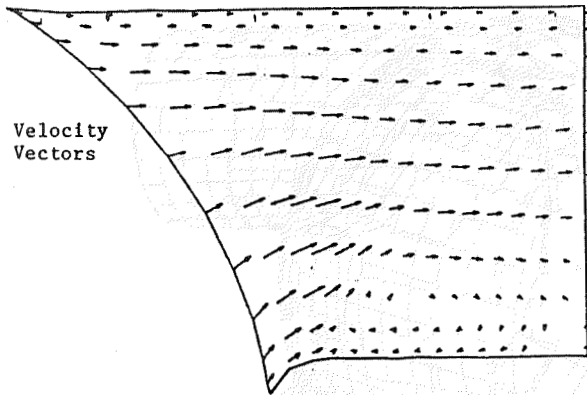


Fig. 3 SSME HGM Velocity Vector Map in Transfer Duct

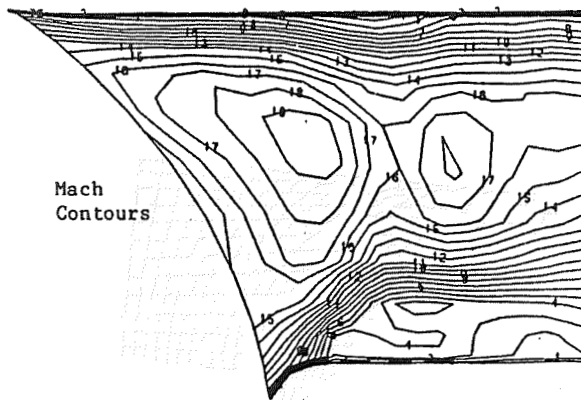


Fig. 4 SSME HGM Mach Contour Map in Transfer Duct

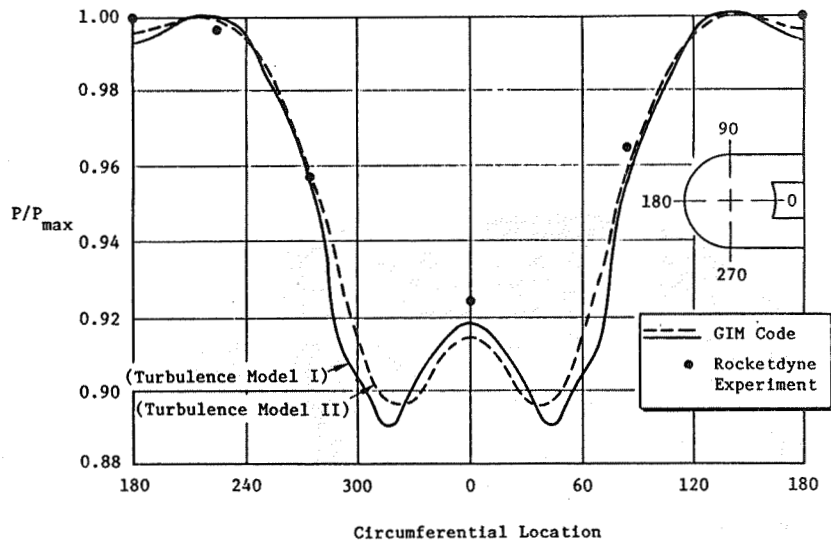


Fig. 5 Comparison of Computed Static Pressures to Measured Static Pressures in Bowl

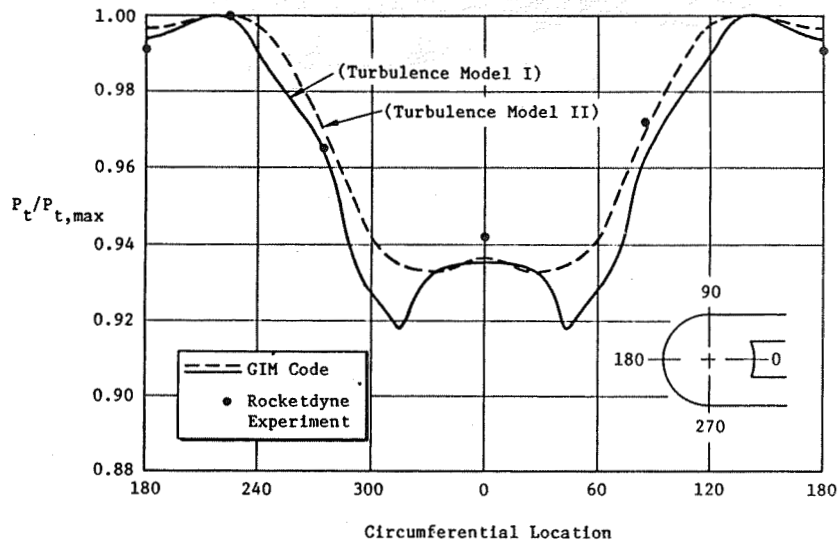


Fig. 6 Comparison of Total Pressures to Measured Data in Bowl

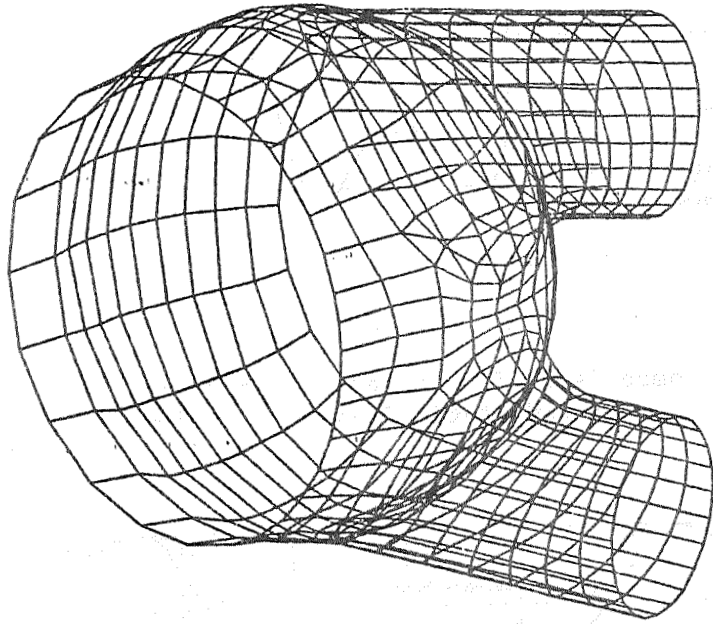


Fig. 7 SSME HGM Modified Grid

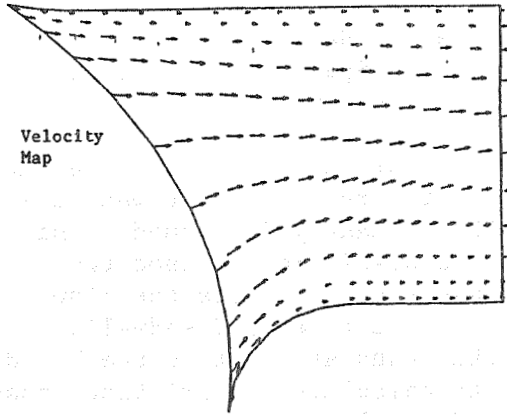


Fig. 8 Transfer Duct Velocity Vector Map in Modified Configuration

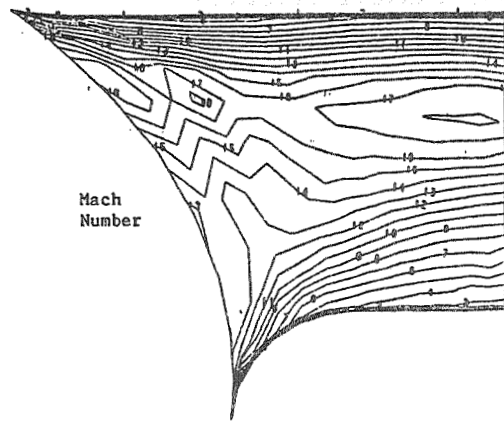


Fig. 9 Transfer Duct Mach Number Contour Map in Modified Configuration

## FUEL AND OXIDIZER TURBINE LOSS ANALYSIS

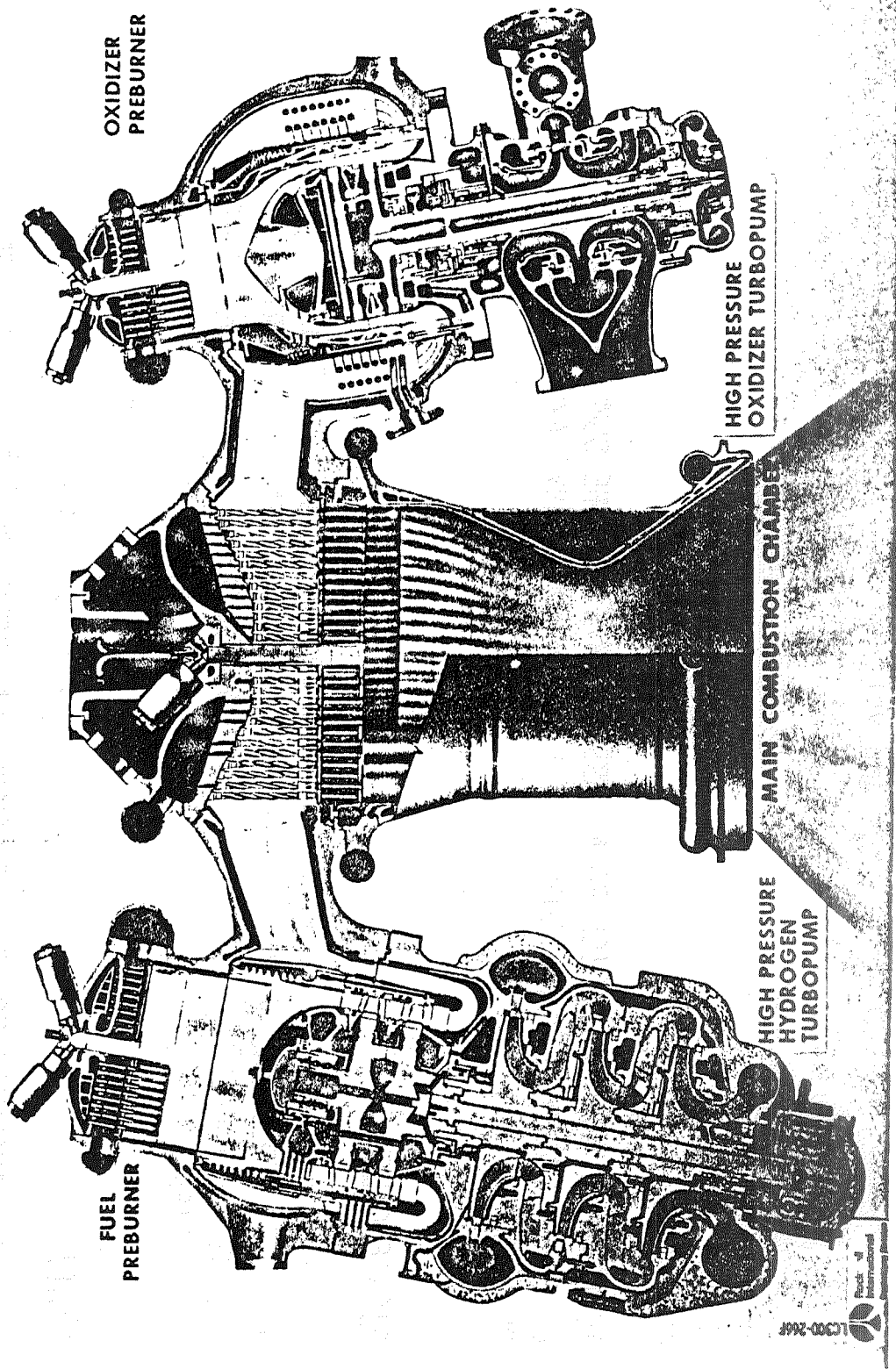
Jeffrey E. Haas  
National Aeronautics and Space Administration  
Lewis Research Center, Ohio 44135

An assessment of the turbine losses for the fuel and oxidizer turbines at the FPL condition was conducted using a quasi-3D loss analysis method. This recently developed loss analysis method uses two flow codes - MERIDL and TSONIC - to calculate the flow velocities along the blade surfaces and endwalls. These velocities are then used as input to the boundary layer code - BLAYER - to calculate the friction losses due to incidence, secondary flow, and tip clearance.

The results of the loss analysis for the fuel turbine indicated an overall two-stage efficiency of about 90 percent. The largest loss was due to rotor tip clearance. The loss analysis for the oxidizer turbine is nearly completed. Results for the first stage of the two-stage design indicated an efficiency of about 80 percent, with high losses due to rotor incidence and blade and endwall friction.

NASA  
C-82-0973

# SSME POWERHEAD COMPONENT ARRANGEMENT



## TURBINE LOSS ANALYSIS

- OBJECTIVE

TO CONDUCT TURBINE DESIGN POINT ASSESSMENTS FOR THE SSME FUEL AND OXIDIZER TURBINES USING QUASI-3-D FLOW AND BOUNDARY LAYER ANALYSIS METHODS.

- SIGNIFICANCE

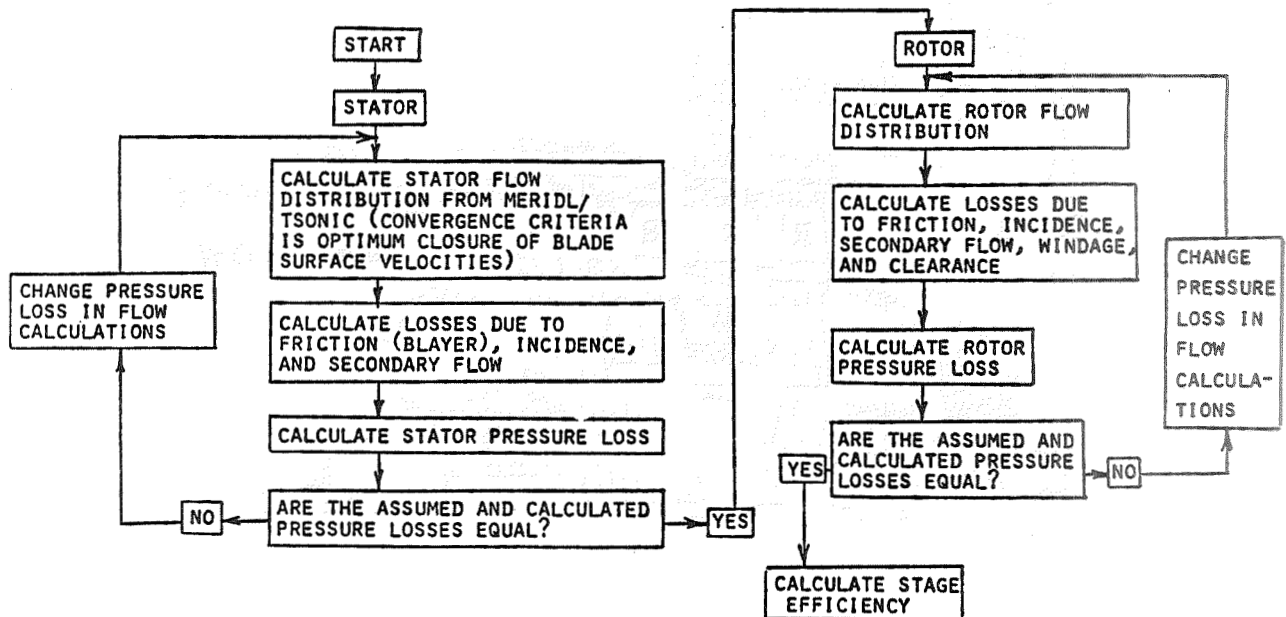
TO VERIFY THE DESIGN POINT EFFICIENCY GOALS FOR BOTH TURBINES, IDENTIFY POTENTIAL AREAS FOR EFFICIENCY IMPROVEMENT, AND FURTHER ASSESS THE ADEQUACY OF THE ANALYSIS PROCEDURE FOR FUTURE SSME DESIGN ACTIVITIES.

- STATUS

THE LOSS ANALYSIS FOR BOTH TURBINES HAS BEEN COMPLETED AT THE FPL CONDITION.

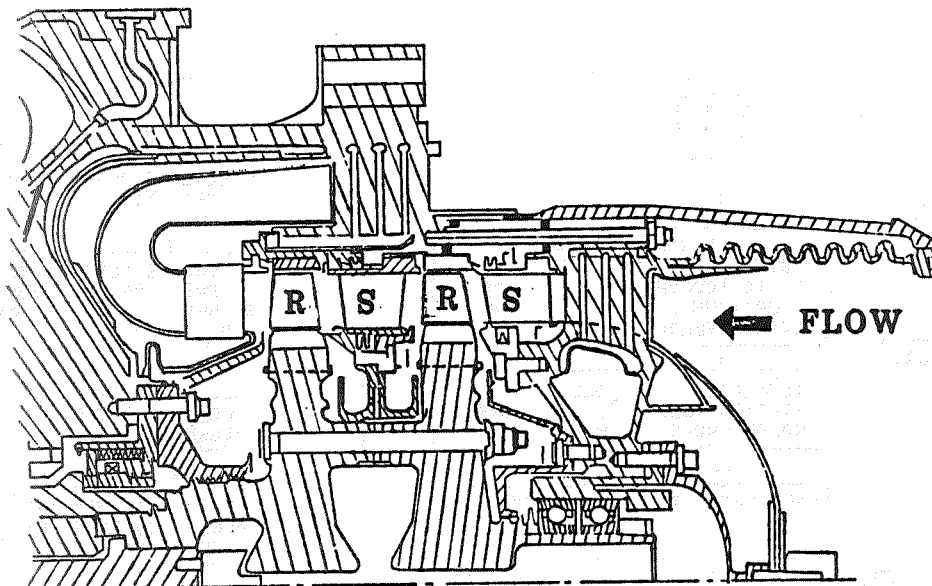
THE TURBINE LOSSES ARE COMPUTED ON A BLADE ROW BASIS. FOR EACH BLADE ROW TWO ITERATIVE LOOPS ARE EMPLOYED. THE INNER LOOP CONVERGES ON CLOSURE OF THE BLADE SURFACE VELOCITIES. THE OUTER LOOP CONVERGES ON THE TOTAL PRESSURE LOSS. COUPLING THE STATOR AND ROTOR LOSSES GIVES A STAGE EFFICIENCY. FOR THE SSME TURBINES, WHICH ARE TWO-STAGE DESIGNS, THE PROCEDURE SHOWN BY THE FLOW CHART IN THIS FIGURE MUST BE REPEATED TO CALCULATE AN OVERALL TWO-STAGE EFFICIENCY.

LOSS ANALYSIS FLOW CHART



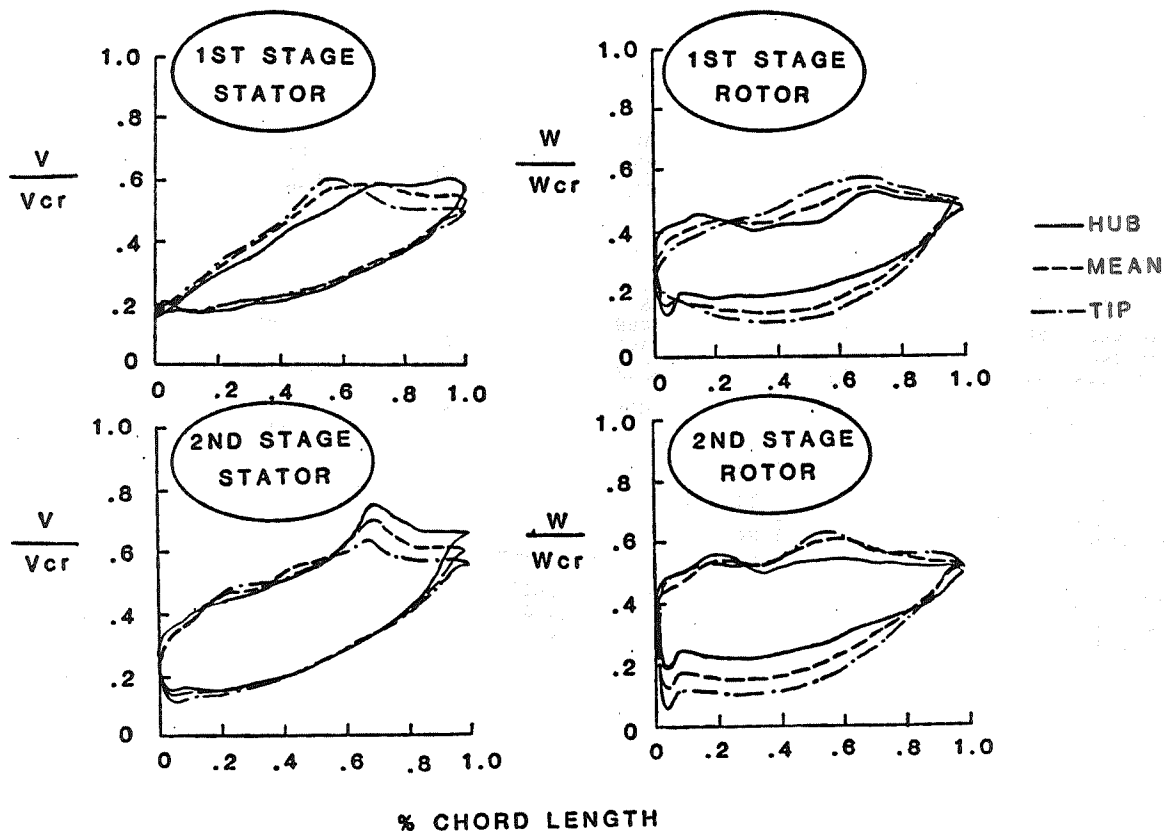
THE SSME FUEL TURBINE IS A TWO-STAGE DESIGN WITH A ROTOR MEAN DIAMETER OF 10 INCHES. THE BLADE HEIGHTS VARY FROM ABOUT 0.9 INCH FOR THE FIRST STAGE TO ABOUT 1.0 INCH FOR THE SECOND STAGE. THE HUB AND TIP ENDWALLS ARE CYLINDRICAL. THE ROTOR TIP CLEARANCES VARY FROM ABOUT 1.5 TO 2.0 PERCENT OF THE BLADE HEIGHT. THERE ARE ABOUT 40 BLADES IN EACH STATOR BLADE ROW AND ABOUT 60 BLADES IN EACH ROTOR BLADE ROW.

### SSME HIGH-PRESSURE FUEL TURBINE



THE BLADE SURFACE VELOCITIES FOR THE FUEL TURBINE AT THE FPL CONDITION ARE SHOWN IN THE NEXT FIGURE. THE FLOW IN ALL FOUR BLADE ROWS IS GENERALLY ACCELERATING, WITH SOME SMALL DIFFUSION INDICATED ON THE SUCTION SURFACES.

SSME FUEL TURBINE BLADE LOADINGS  
FPL CONDITION



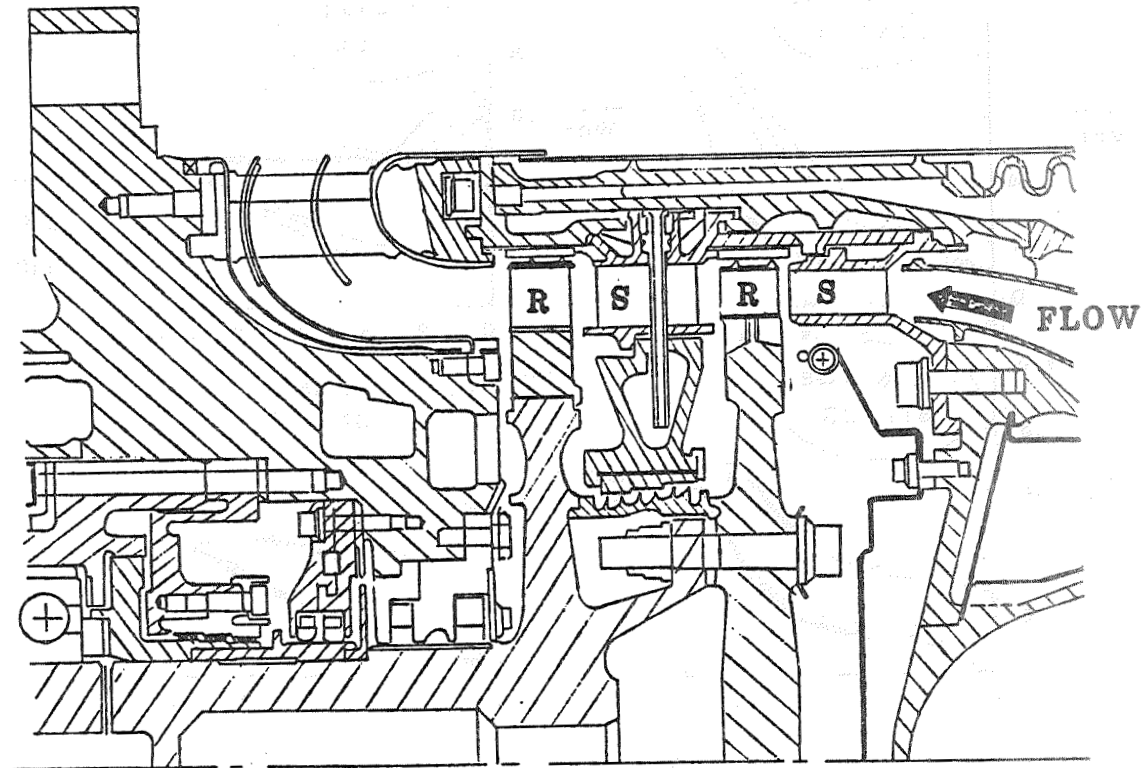
THE CALCULATED LOSSES FOR THE FUEL TURBINE AT THE FPL CONDITION ARE TABULATED IN THE NEXT FIGURE. AN OVERALL EFFICIENCY OF ABOUT 91 PERCENT WAS CALCULATED, WITH THE LARGEST LOSS (ABOUT 4 POINTS) DUE TO ROTOR TIP CLEARANCE.

SSME FUEL TURBINE LOSS ANALYSIS  
FPL CONDITION

	FIRST STAGE STATOR	FIRST STAGE ROTOR	SECOND STAGE STATOR	SECOND STAGE ROTOR
Profile + Mixing	.014	.016	.013	.017
Endwall Friction	.007	.002	.007	.002
Secondary Flow	.005	.009	.004	.009
Incidence	.001	.007	.001	.013
Tip Clearance	.000	.046	.000	.034
$\Delta \eta$ Blade Row	.027	.080	.025	.075
$P_r$ Blade Row	1.19	1.17	1.24	1.19
$\eta$ Stage	.893		.900	
$P_r$ Stage	1.292		1.327	
WF Stage	1.98		2.08	
$\eta$ Overall	.906			
$P_r$ Overall	1.715			
WF Overall	4.06			

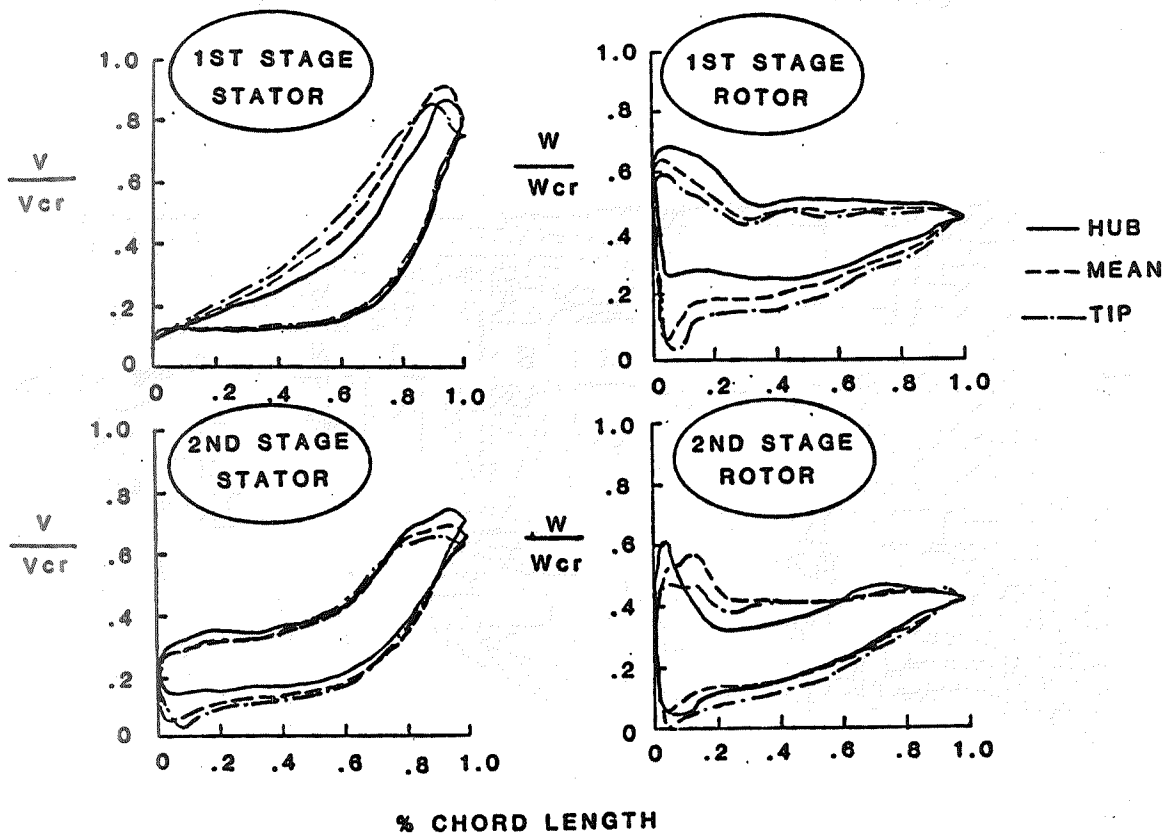
THE SSME OXIDIZER TURBINE IS A TWO-STAGE DESIGN WITH A ROTOR MEAN DIAMETER OF 10 INCHES. THE BLADE HEIGHTS VARY FROM ABOUT 0.5 INCH FOR THE FIRST STAGE TO ABOUT 0.7 INCH FOR THE SECOND STAGE. THERE ARE ABOUT 45 BLADES IN EACH STATOR ROW AND ABOUT 75 BLADES IN EACH ROTOR ROW. THE HUB AND TIP ENDWALLS ARE CYLINDRICAL AND THE ROTORS ARE SHROUDED.

### SSME HIGH-PRESSURE OXIDIZER TURBINE



THE BLADE SURFACE VELOCITIES FOR THE OXIDIZER TURBINE AT THE FPL CONDITION ARE SHOWN IN THE NEXT FIGURE. THE FLOW IS WELL ACCELERATED IN BOTH STATORS. HOWEVER, THE SUCTION SURFACE VELOCITIES FOR BOTH ROTORS, ESPECIALLY THE FIRST ROTOR, SHOW LARGE DIFFUSION, WHICH RESULTS IN HIGH FRICTION LOSSES.

SSME OXIDIZER TURBINE BLADE LOADINGS  
FPL CONDITION



THE CALCULATED LOSSES FOR THE OXIDIZER TURBINE AT THE FPL CONDITION ARE TABULATED IN THE NEXT FIGURE. AN OVERALL EFFICIENCY OF 80 PERCENT WAS CALCULATED. FOR THIS TURBINE THE LARGEST LOSS WAS DUE TO ROTOR INCIDENCE IN BOTH ROTOR BLADE ROWS, WITH LARGE FRICTION LOSS ALSO CALCULATED FOR THE FIRST ROTOR.

SSME OXIDIZER TURBINE LOSS ANALYSIS  
FPL CONDITION

	FIRST STAGE STATOR	FIRST STAGE ROTOR	SECOND STAGE STATOR	SECOND STAGE ROTOR
LOSSES ( $\Delta\eta'$ ):				
Profile + Mixing	.024	.049	.029	.024
Endwall Friction	.019	.011	.016	.004
Secondary Flow	.013	.028	.016	.016
Incidence	.000	.077	.000	.083
Tip Clearance	-----	-----	-----	-----
$\Delta\eta'$ Blade Row	.056	.165	.061	.127
$P_F$ Blade Row	1.48	1.20	1.32	1.15
$\eta'$ Stage	.779		.812	
$P_F$ Stage	1.446		1.346	
WF Stage	3.61		2.84	
$\eta'$ Overall	.801			
$P_F$ Overall	1.946			
WF Overall	6.45			

## CONCLUSIONS

- THE QUASI-3D ANALYSIS METHOD PROVED TO BE A USEFUL TOOL FOR ASSESSING THE LOSSES OF THE SSME TURBINES
- FOR THE FUEL TURBINE AN OVERALL EFFICIENCY OF 90.6% WAS PREDICTED WITH THE LARGEST LOSS DUE TO ROTOR TIP CLEARANCE
- FOR THE OXIDIZER TURBINE AN OVERALL EFFICIENCY OF 80.1% WAS PREDICTED WITH THE LARGEST LOSS DUE TO ROTOR INCIDENCE

# REDISTRIBUTION OF THE INLET TEMPERATURE PROFILE THROUGH THE SSME FUEL TURBINE

John R. Schwab  
Turbine Aerodynamics Section  
NASA - Lewis Research Center

## ABSTRACT

A three-dimensional Euler code was used to predict radial inlet temperature profile redistribution through the two-stage fuel turbo-pump turbine. The calculation was made at the FPL condition using a turbine inlet radial temperature profile supplied by Rocketdyne. This same calculation was made earlier on an inhouse-designed, single-stage turbine. In that case there was a redistribution of the temperature profile such that the hotter gas that originated at the midspan region at the turbine inlet was shifted to the hub and tip regions on the blade pressure surface at the rotor exit. However, for the SSME fuel turbine, there was no redistribution of the inlet temperature profile. No strong secondary flow patterns were identified. Preliminary assessment of the analytical results indicated that this trend was attributed to the high solidity SSME blading.

## INTRODUCTION

The life and durability of the SSME fuel turbine blading can be largely affected by redistribution of the inlet radial temperature profile due to secondary flow effects. This temperature redistribution can cause a convection of hot gas from the midspan region to the hub and tip endwalls, causing local hotspots and possible failure. To assess this redistribution effect for the SSME fuel turbine, a calculation was made using a three-dimensional Euler code (DENTON code) at the design operating condition for a prescribed inlet radial temperature profile.

## OBJECTIVE

ANALYZE POSSIBLE REDISTRIBUTION OF  
INLET RADIAL TEMPERATURE PROFILE DUE TO  
SECONDARY FLOW IN FUEL TURBINE

## RATIONALE

CONVECTION OF HOTTER GAS FROM THE MIDSPAN REGION  
TO THE HUB AND TIP ENDWALLS COULD INFLUENCE THE  
DEVELOPMENT OF HOTSPOTS

A three-dimensional Euler code (ref. 1) developed by J. D. Denton of Cambridge University was found to be useful in predicting redistribution of a nonuniform inlet radial temperature profile through an axial turbine stage (ref. 2). This code is an explicit time-marching solution of the Euler equations in finite-volume form for fixed or rotating turbomachinery blade rows. A two-level multigrid scheme was used to reduce computation time. For the 21 pitchwise x 21 spanwise x 75 streamwise grid used in these computations, the CPU time required was approximately 250 to 350 seconds on a CRAY-1. A uniform transverse grid was used to assure good resolution over the entire transverse flow plane. The blade and endwall surfaces were assumed to be adiabatic.

## METHOD

DENTON 3-D EULER CODE

EXPLICIT TIME-MARCHING SOLUTION

FINITE-VOLUME FORMULATION

2-LEVEL MULTIGRID SCHEME

UNIFORM GRID SPACING

21 PITCHWISE X 21 SPANWISE X 70 STREAMWISE

In order to circumvent the problems involved in calculating flow properties for the actual fuel mixture of superheated steam and hydrogen, the computations were performed for air at the same mean inlet temperature. The mean inlet pressure was calculated from equivalent conditions to match the mean radius Reynolds number at full power level (FPL) conditions.

#### METHOD

#### AIR CONDITIONS CALCULATED TO MATCH FPL INLET TEMPERATURE AND REYNOLDS NUMBER

REYNOLDS NUMBER (MEAN RADIUS)	21 830 000
MEAN INLET TEMPERATURE, DEG R	1 990
MEAN INLET PRESSURE, PSIA	3 234
MASS FLOW, LBM/SEC	274
SPEED, RPM	13 890

The inlet total pressure profile was calculated from a specified displacement thickness assuming a turbulent 1/7 power velocity profile in the boundary layer. Since the inviscid code could not accommodate no-slip conditions at the walls, a slip velocity of 50 percent of the free-stream velocity was used. Inlet radial profiles for each succeeding blade row were obtained by circumferentially averaging the outlet flow properties of the preceding blade row using mass flow averaging.

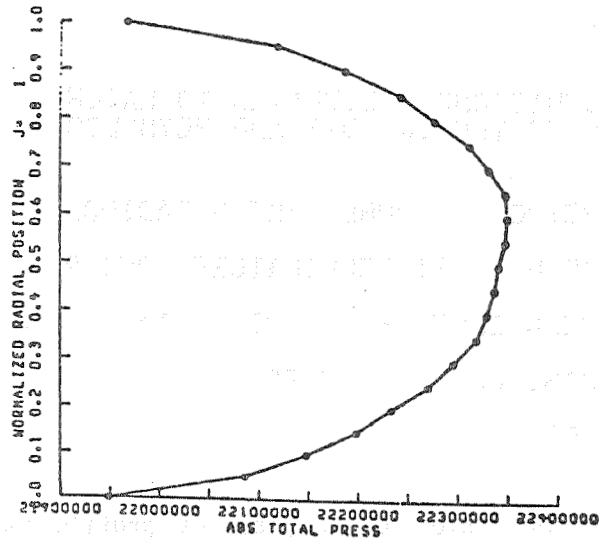
#### METHOD

INLET PRESSURE PROFILE CALCULATED FROM  
INLET DISPLACEMENT THICKNESS ASSUMING  
TURBULENT 1/7 POWER VELOCITY PROFILE

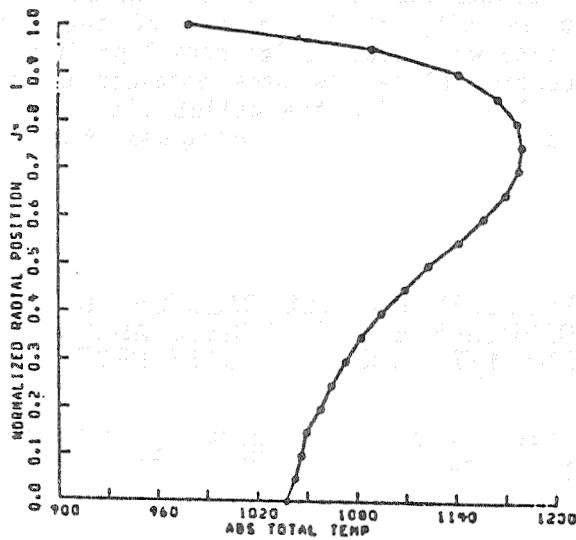
SLIP VELOCITY AT THE ENDWALLS SPECIFIED  
AS 50 % OF THE FREE-STREAM VELOCITY

INLET RADIAL PROFILES FOR SUCCEEDING BLADE ROWS  
OBTAINED BY CIRCUMFERENTIALLY AVERAGING THE  
OUTLET FLOW PROPERTIES OF THE PRECEDING BLADE ROW

Total pressure and total temperature radial profiles are shown for the first stage stator inlet. The normalized radial coordinate ranges from 0.0 for the hub to 1.0 for the tip. The total pressure is given in newtons per square meter, while the temperature is given in degrees kelvin. The temperature profile was obtained from Rocketdyne.

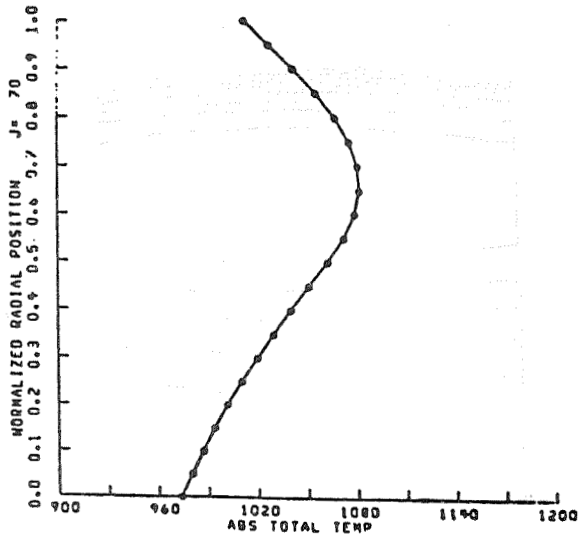


STATOR 1 INLET

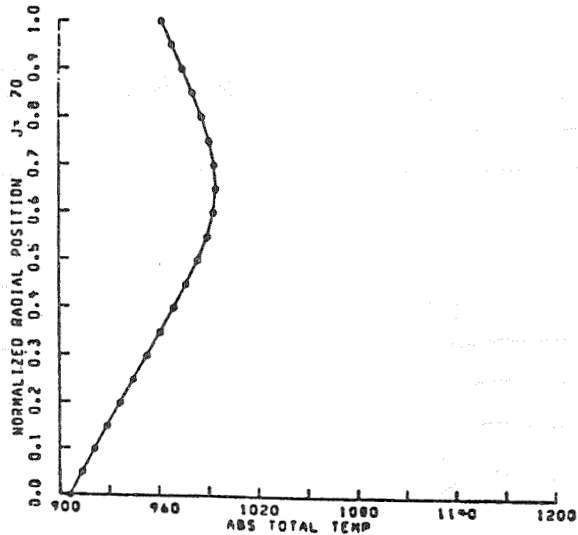


STATOR 1 INLET

Circumferentially averaged total temperature profiles are shown for the first and second stage rotor outlets. Some attenuation has occurred due to smoothing and numerical diffusion as well as the extraction of work across the rotors, but the profile persists through both stages.



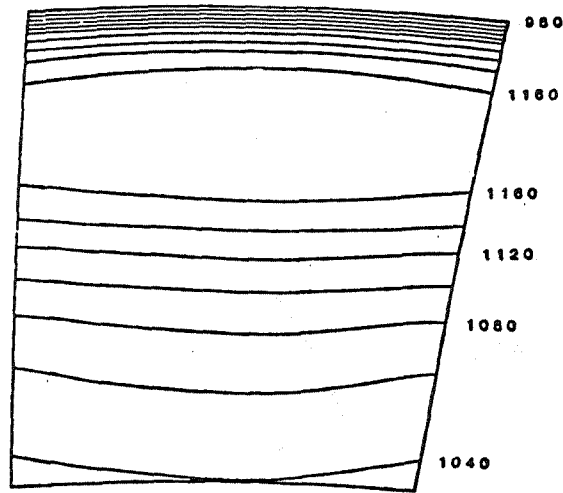
ROTOR 1 OUTLET



ROTOR 2 OUTLET

Contour plots of total temperature are shown in transverse planes at the first stage stator inlet and first and second stage rotor outlets. The absolute total temperature is shown for the stator, while the relative total temperature is shown for the rotors. The pressure surface is on the left side of the plot and the suction surface is on the right. There is no evidence of rotation of the temperature profiles due to secondary flow.

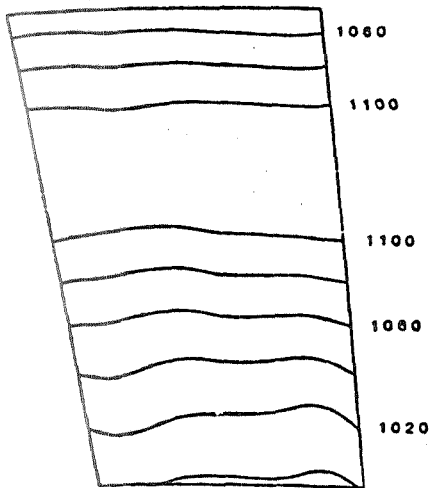
ABSOLUTE TOTAL TEMPERATURE, K



CROSS CHANNEL SURFACE J=1

STATOR 1 INLET

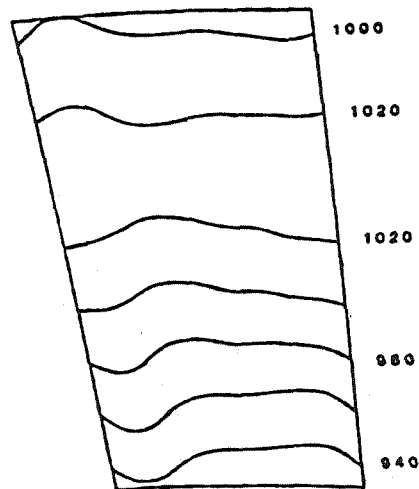
RELATIVE TOTAL TEMPERATURE, K



CROSS CHANNEL SURFACE J=70

ROTOR 1 OUTLET

RELATIVE TOTAL TEMPERATURE, K

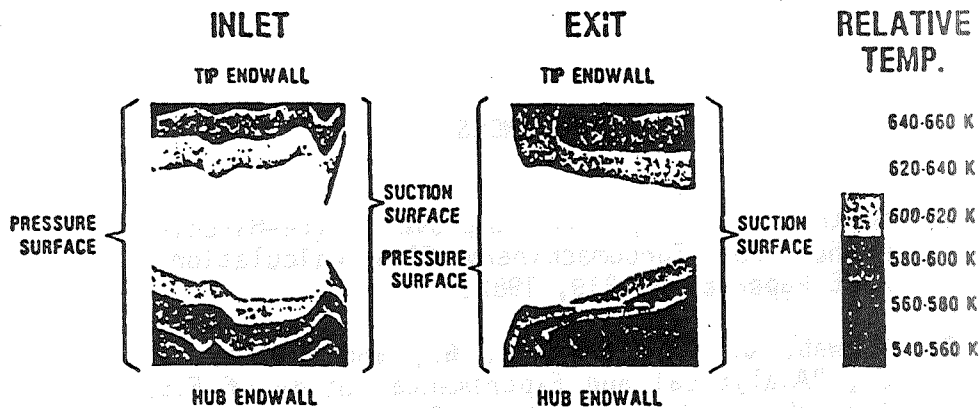


CROSS CHANNEL SURFACE J=78

ROTOR 2 OUTLET

Color contour plots of relative total temperature are shown at the inlet and exit of a core turbine rotor. Definite rotation of the profile can be discerned. Hotter gas from the midspan region has been convected by secondary flow into the hub and tip regions near the pressure surface. This rotor had solidity of 1.079 and turning of 112.7 degrees. The solidity and turning of the SSME fuel turbine rotors were 1.452 and 101.1 degrees for the first stage rotor and 1.412 and 96.1 degrees for the second stage rotor.

## REDISTRIBUTION OF INLET RADIAL TEMPERATURE PROFILE THROUGH AN AXIAL TURBINE ROTOR



- UNCOOLED 75° RESEARCH CORE TURBINE STAGE
- DENTON 3-D EULER CODE
- REALISTIC STATOR INLET RADIAL TEMPERATURE PROFILE
- MODERATE ROTATION OF RELATIVE TEMPERATURE PROFILE BY SECONDARY FLOW
- 60 K GAS TEMPERATURE RISE ON PRESSURE SURFACE AT HUB AND TIP FOR 670 K MEAN STATOR INLET TEMPERATURE

CG 1128

## CONCLUSIONS

CIRCUMFERENTIALLY AVERAGED RADIAL TEMPERATURE PROFILES SHOW MODERATE ATTENUATION DUE TO SMOOTHING AND NUMERICAL DIFFUSION AS WELL AS WORK EXTRACTION ACROSS THE ROTORS

NO EVIDENCE OF TEMPERATURE PROFILE ROTATION DUE TO SECONDARY FLOW

PRELIMINARY ASSESSMENT INDICATES THAT HIGHER SOLIDITY AND LOWER TURNING BLADE DESIGN PREVENTS TEMPERATURE PROFILE ROTATION

## REFERENCES

1. Denton, J. D., "An Improved Time-Marching Method for Turbomachinery Flow Calculation," ASME Paper 82-GT-239, 1982.
2. Schwab, J. R., Stabe, R. G., and Whitney, W. J., "Analytical and Experimental Study of Flow Through an Axial Turbine Stage with a Non-uniform Inlet Radial Temperature Profile," NASA TM 83431, 1983.

ANALYTICAL STUDY OF FLOW PHENOMENA IN SSME  
TURNAROUND DUCT GEOMETRIES

Kerry L. McLallin  
Turbine Aerodynamics Section  
NASA - Lewis Research Center

ABSTRACT

The SSME fuel turbopump hot gas manifold has been identified as a source of loss and flow distortion which significantly affects the performance and durability of both the drive turbine and the LOX injector area of the main combustion chamber. The turnaround duct is the axisymmetric part of the manifold at the exit of the turbine. The geometry is characterized by high wall curvature in the 180 degree turnaround region and the flow is essentially incompressible with a 9.37 degree swirl component out of the turbine. The fundamental flow phenomena in this duct have been investigated using the ADD code, an axisymmetric, viscous, marching code developed under contract by UTRC for LeRC.

Two current SSME geometries were studied, the Full Power Level (FPL) and the First Manned Orbital Flight (FMOF) configuration. Additional studies were conducted for the effects of turnaround duct geometry on flow losses and distortions, by varying wall curvature and flow area variation in the 180° turnaround region. The effects of the duct inlet flow phenomena such as the radial distortion of the inlet flow and inlet swirl level on turnaround duct performance were also investigated. Results show that of the two current geometries, the FMOF configuration had lower pressure losses and generated less flow distortion, but had a small flow separation bubble at the 180° turnaround exit. The study of the geometry effects has shown that by optimizing wall curvature and flow diffusion in the turnaround, improved duct performance can be achieved.

## INTRODUCTION

The SSME fuel turbopump hot gas manifold has been identified as a source of loss and flow distortion which significantly affects the performance and durability of both the drive turbine and the LOX injector area of the main combustion chamber. The turnaround duct is the axisymmetric part of the manifold at the exit of the turbine. The geometry is characterized by high wall curvature in the 180 degree turnaround region and the flow is essentially incompressible with a 9.37 degree swirl component out of the turbine. The fundamental flow phenomena in this duct are being investigated using the ADD code, an axisymmetric, viscous, marching code developed under contract by UTRC for LeRC.

Two current SSME geometries were studied, the Full Power Level (FPL) and the First Manned Orbital Flight (FMOF) configuration. Additional studies were conducted for the effects of turnaround duct geometry on flow losses and distortions, by varying wall curvature and flow area variation in the 180° turnaround region. The effects of the duct inlet flow phenomena such as the radial distortion of the inlet flow and inlet swirl level on turnaround duct performance were also investigated.

## ADD CODE DESCRIPTION

The viscous duct code used, A.D.D. code, handles turbulent swirling compressible flow in axisymmetric duct configurations. Flow separation can be predicted, but results cannot be computed past a point of separation if this separation is a significant part of the flow passage. At the high Reynold's numbers in air, consistent with SSME flow conditions, the solution is neutrally stable in the high curvature region of the TAD. The instability and numerical errors were localized to the inner wall of the turnaround where wall curvature is high and the boundary layer is grossly modified by the pressure gradients in the duct. The duct geometries were modeled from fuel turbine exit to the entrance of the middle transfer duct (i.e., the axisymmetric region of the exit duct). Two inlet flow profiles were used. The first is a uniform inlet with thin wall boundary layers, and the second is a radially distorted flow based on three-dimensional Euler code calculations through the fuel turbine.

## TURNAROUND DUCT GEOMETRIES

The A.D.D. code mesh setup was developed to provide acceptable stability and computation times while capturing the physics of the flow. The meshes shown were standardized to be 100 streamline and 90 potential lines for  $9 \times 10^4$  total grid points. The mesh distortion of model the wall boundary layers was chosen to yield the first mesh point off the wall at a  $Y^+$  of 1.0. Typical A.D.D. code runs on the CRAY-1S were 3 to 3.5 cpu minutes.

## TAD DESIGN INLET CONDITIONS

This study was done with air as the working fluid. The design inlet temperature and swirl were used and the flow and inlet pressure were adjusted to match design inlet Reynold's number and mach number.

## RESULTS FOR UNIFORM INLET

The results for the uniform inlet indicate that the majority of the duct loss is generated on the inner wall of the turnaround which has high surface curvature and higher mach numbers. Problems with numerical instability are also greatest in this region. The rapid flow acceleration on the inner wall causes the boundary layer to be reduced and shear stresses to become large.

The FPL TAD results are shown for the mach number profiles through the duct at each potential line. The figure shows the velocity peaking near the inner wall of the turnaround section and a resulting velocity deficit near that wall is shown at the duct exit indicating the high loss region. No flow separation or potential separation was indicated by the results for the FPL duct.

The FMOF TAD mach number profiles are also shown for uniform inlet flow. The FMOF geometry differs from the FPL in that the inner wall of the turn has a smaller radius resulting in higher inner wall curvature and a slight area increase from turnaround inlet to turnaround exit. Velocity peaks similar to those in the FPL are seen near the inner wall of the turnaround section and the velocity deficit region at TAD exit is also similar to the FPL duct. However, at the turnaround section exit on the inner wall the shear stress goes to zero indicating possible flow separation, although the calculated separation was only a small region of the flow for about 10 potential lines.

The calculated total pressure losses, based on the difference in mass averaged values of total pressure ratio to the inlet dynamic pressure, were significantly different for the two ducts. The losses were 0.096 and 0.069 for FPL and FMOF configurations, respectively. The larger FPL loss can be attributed to the higher wall shear stresses on both walls from 90 to 180° in the turnaround region. These high stresses are probably due to higher velocities in this region as there is an area contraction of 23 percent through the 180° turnaround for the FPL configuration.

#### TAD WALL SHEAR STRESSES

The variations in wall shear stresses are shown in the figure on hub and tip walls for FPL and FMOF ducts for the uniform inlet flow case. The turnaround region begins and ends at the  $X/LREF$  value of 0.225 for both ducts. This region on the tip wall shows the high wall shear stresses and numerical instabilities on the high curvature inner wall of the turnaround for both duct geometries. Comparison between FPL and FMOF results in this region show that the higher curvature of the FMOF yields higher shear stresses on the tip wall for the first 90 degrees of the turnaround, but diffusion of the flow by the FMOF geometry results in significantly lower shear stresses from 90° to turnaround exit where stresses go to zero. The hub wall shear stresses are also lower for FMOF from 90° through turnaround to the exit due to lower velocity level.

## RESULTS FOR DISTORTED INLET

The regions of high loss identified for the case of uniform inlet flow were not changed by the distorted inlet profiles for either the FPL or the FMOF duct. The comments above are still valid. The distorted inlet flow profiles are, however, somewhat mixed out passing through the TAD geometries.

The variation of Mach number profiles through the two TAD geometries is shown in the figure for the distorted inlet flow. The inlet distortions in mach number are mixed out and eliminated after entering the turnaround region for both ducts. Subsequent flow patterns downstream are similiar to those with uniform inlet conditions.

A comparison of total pressure losses between uniform inlet and distorted inlet indicates an increase in loss occurred for both TAD configurations. The losses were 0.105 and 0.086 for FPL and FMOF ducts, respectively. These increases in loss, based on percent of loss with uniform inlet were 9 and 25 percent for FPL and FMOF ducts, respectively. The FMOF geometry is apparently more sensitive to inlet flow distortion.

## TOTAL TEMPERATURE VARIATION FOR DISTORTED INLET

A significant gradient in total temperature exists at fuel turbine exit, based on Denton code results. The radial distribution in total temperature at each potential line through the duct is shown. Only the FMOF results are shown since they are very similar to the FPL results. While the maximum difference in total temperature across the duct passage has been reduced from inlet to exit of the ducts, significant radial distortion still exists.

## GEOMETRY STUDY RESULTS

The study of the two available SSME-TAD geometries has shown where the majority of losses are generated in the turnaround region. The results indicate a sensitivity to turnaround wall curvature and flow diffusion (streamwise area variation). Therefore, to check the sensitivity of loss to these parameters, a series of modified geometries were run on the ADD code using the uniform inlet flow profile. The basic premise was to minimize turnaround wall curvature within the radii envelope of the FPL and FMOF geometries and then to vary the area distribution through the turnaround so as to minimize the wall shear stresses in this region.

The overall results of this limited parametric study are shown. The parameter chosen to identify goodness was the TAD total pressure loss. The figure shows the variation of loss with the axial location of the center of the hub wall arc of the turnaround. For this series of cases the inlet area and exit area of the turnaround are equal, with the area being increased in the turnaround region by moving the hub arc center along the axis of rotation. Peak velocities are thereby lowered in the turnaround and wall shear stresses will be reduced in some areas. The trend shown in the figure indicates that loss is reduced as the center is moved out along the axis of rotation which increases the diffusion in the turnaround. No minimum loss is calculated, instead flow separation on the hub wall is encountered. Calculations could not proceed past this point due to code limitation of no gross flow separation. However, similar improvements can be obtained within a smaller envelope, i.e., reduced axial position of hub arc center, by introducing an overall area increase from turnaround inlet to exit. The tip wall radius in the turnaround was reduced incrementally but the inlet area was held constant,

thereby increasing the area at turnaround exit. The figure shows the trend in loss with tip arc radius. A minimum loss value of 0.067 obtained at an hub arc center axial position of 1.45 inches and a tip arc radius of 0.60 inches.

The mach number profiles through the modified TAD are shown in the next figure. While the peak velocity region on the tip arc and deficit in velocity at the exit are still present the overall distortion was reduced. It should be noted that the inlet section upstream of the turnaround accelerates the flow somewhat to allow a larger tip arc radius and therefore reduced wall curvature in the turnaround. The shear stresses are shown in the figure for hub and tip walls. Again the location of the tip arc center is about 0.225 while the hub arc center is about 0.261(X/LREF). The shear stresses in the turnaround are significantly reduced in comparison to the FPL geometry on both hub and tip walls. Comparison with the FMOF geometry is not quite as dramatic, but the flow separation bubble has been eliminated and peak shear stresses are less for the MOD TAD in the turnaround region.

#### TAD FLOW AREA DISTRIBUTIONS

The flow area distributions for three TAD geometries, (FPL, FMOF, and MOD) are shown in the figure. As can be seen, the area distributions in the 180° turnaround cover the range of possibility with area decrease (FPL), nearly constant area (FMOF) and area increase (MOD). Note that the inlet and exit flow areas are the same for the three ducts with an exit-to-inlet area ratio of 1.128 overall.

## REFERENCES

1. Anderson, O. L., and Edwards, D. E., "Extensions to an Analysis of Turbulent Swirling Compressible Flow in Axisymmetric Ducts," UTRC Report R81-914720-18, NASA Contract NAS3-21853, L. J. Bober, Project Manager.
2. Anderson, O. L., Hankins, G. B., and Edwards, D. E., "Extensions to an Analysis of Turbulent Swirling Compressible Flow for Application to Axisymmetric Small Gas Turbine Ducts," NASA CR-165597, 1982.
3. Anderson, O. L., Hankins, G. B., and Edwards, D. E., "Users Manual for Axisymmetric Diffuser Duct (ADD) Code. Vol. 1 - General ADD Code Description, Vol. 2 - Detailed ADD Code Description, and Vol. 3 - ADD Code Coordinate Generator," NASA CR-165598, 1982.
4. McLallin, K. L., Kofskey, M. G., and Civinskas, K. C., "Effects of Interstage Diffuser Flow Distortion on the Performance of a 15.41-Centimeter Tip Diameter Axial Power Turbine," NASA TM-83359 and AIAA 83-1179, 1983.

## TAD SWIRL STUDY

The sensitivity of the FPL and FMOF geometries to inlet swirl angle were studied. The inlet swirl angle was varied from 0 to 50° in 10° increments. The ADD code results are shown in the figure in terms of total pressure loss. Inlet values of total pressure, total temperature, and boundary layer displacement thickness, as well as axial mach number were held constant for this study (uniform inlet conditions). Therefore, the level of absolute inlet mach number increases with increasing swirl angle. This inlet mach number never exceeds 0.3.

The results indicate that losses decrease with increasing swirl levels until a minimum loss is reached. Continued increases in swirl angle then result in increasing losses. The minimum loss swirl angles were approximately 45° and 30° for FPL and FMOF ducts, respectively. While the FMOF configuration has lower losses over the entire swirl range investigated, the FPL configuration exhibited more sensitivity to inlet swirl. The reductions in loss from zero swirl to minimum loss swirl were 12.3 and 3.8 percent for FPL and FMOF ducts, respectively.

## ADD CODE DESCRIPTION

### TECHNIQUE

- COMPRESSIBLE VISCOUS SPACE MARCHING SOLUTION
- LAMINAR OR TURBULENT FLOW
- ORTHOGONAL COORDINATE SYSTEM WITH MESH PACKING IN BOUNDARY LAYERS

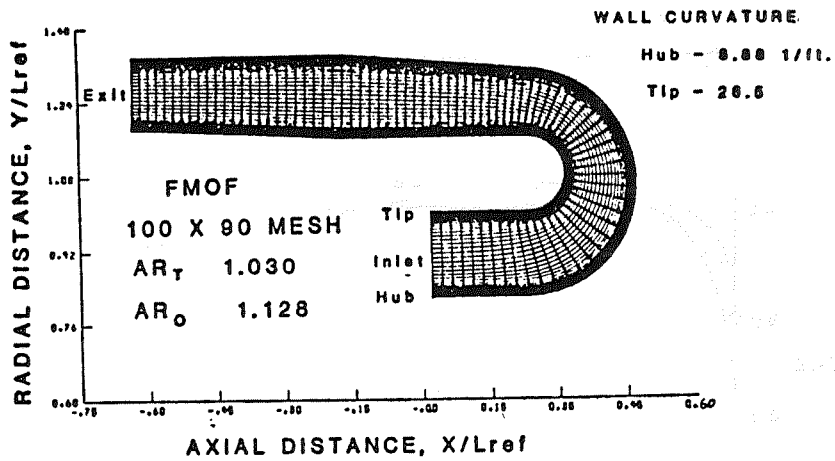
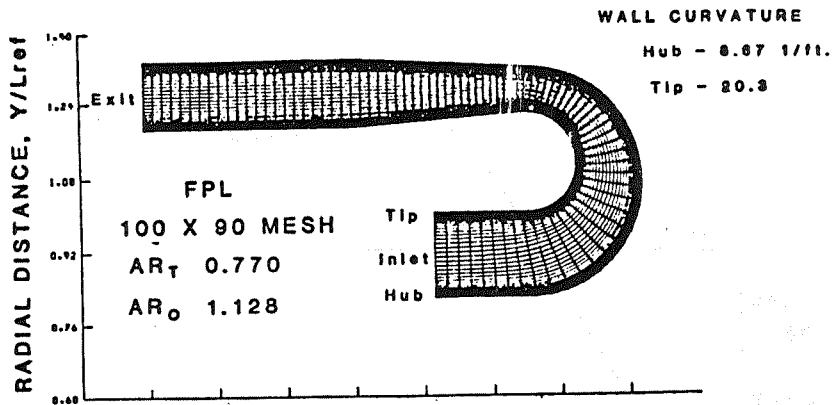
### APPLICATIONS

- AXISYMMETRIC DUCTS
- TURBULENT, SWIRLING, COMPRESSIBLE FLOW
- STRUTS AND GUIDE VANES USING CORRELATED AIRFOIL DATA
- COOLING SLOTS AND BLEED ON WALLS

### RESULTS

- GAS TURBINE INTERSTAGE DIFFUSER - AXIAL FLOW
- RADIAL TURBINE INLET DUCT AND EXHAUST DIFFUSER
- SSME TURNAROUND DUCT FUEL TURBINE EXIT

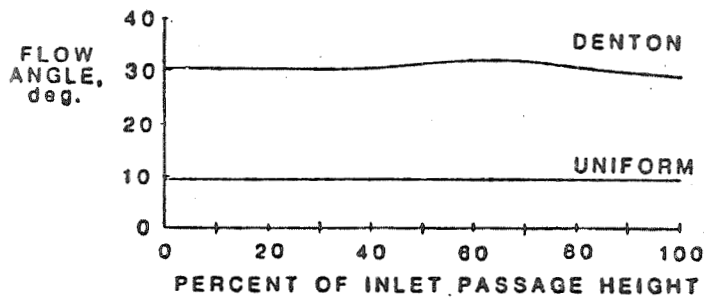
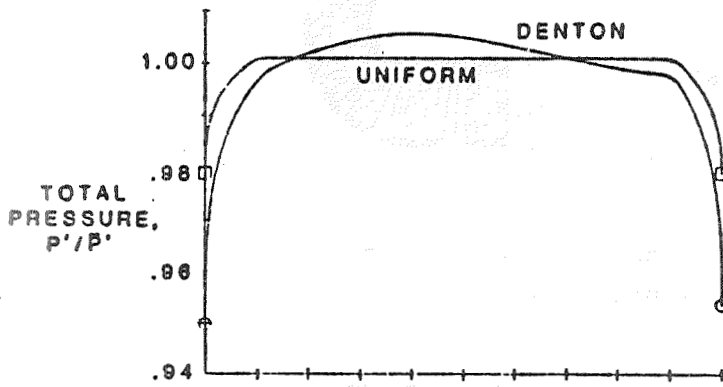
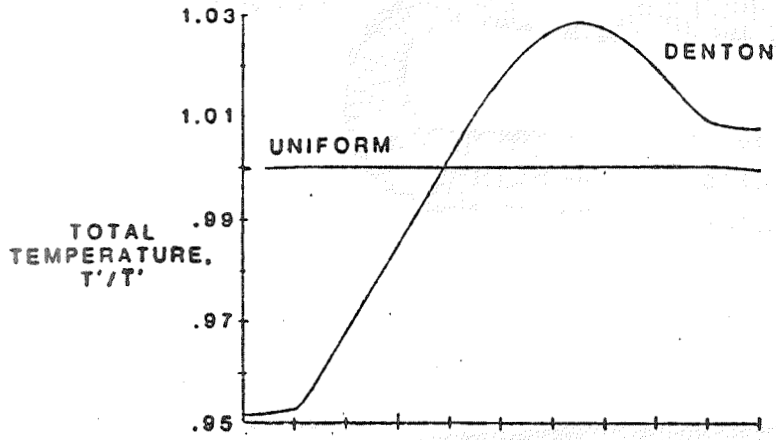
## TURNAROUND DUCT GEOMETRIES



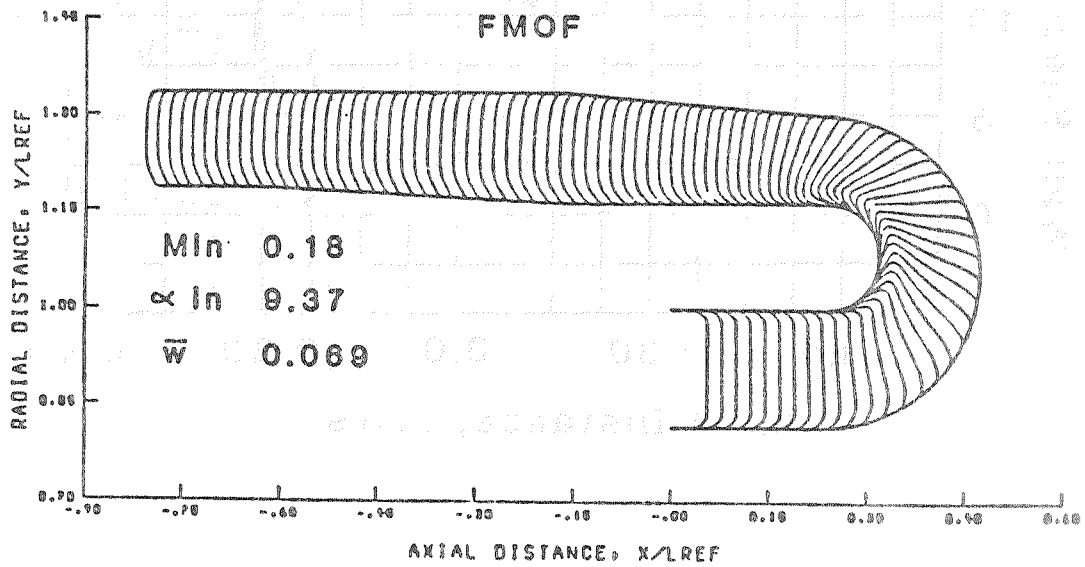
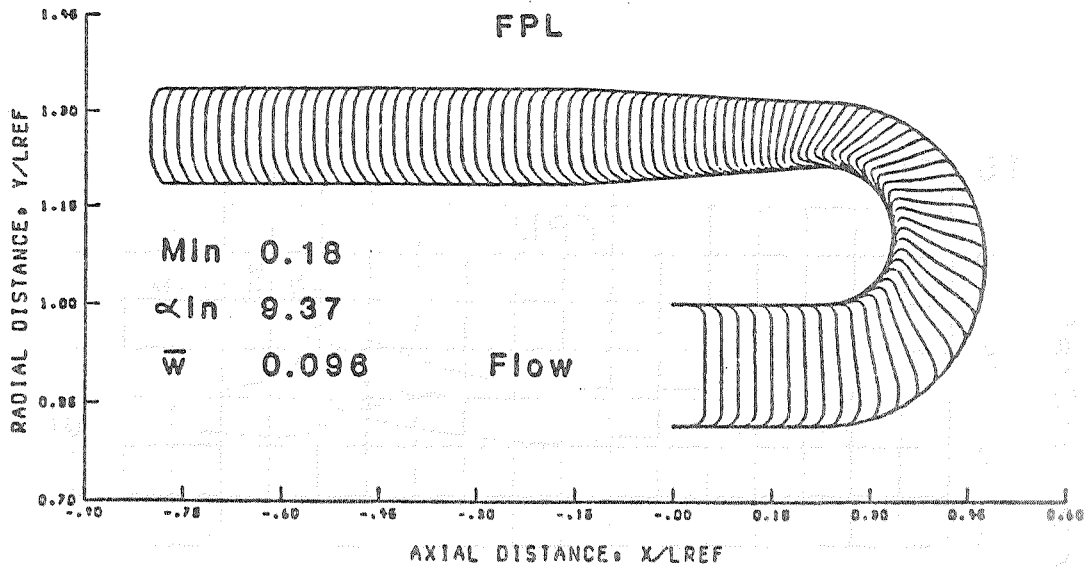
### TAD DESIGN INLET CONDITIONS

	SSME	STUDY
Fluid	Steam + H <sub>2</sub>	Air
Temperature, °R	1761.7	1761.7
Pressure, Atm	250	134.4
Reynolds Number	3.3 X 10 <sup>8</sup>	3.3 X 10 <sup>8</sup>
Mach Number	0.18	0.18
Swirl Angle, Deg.	9.37	9.37

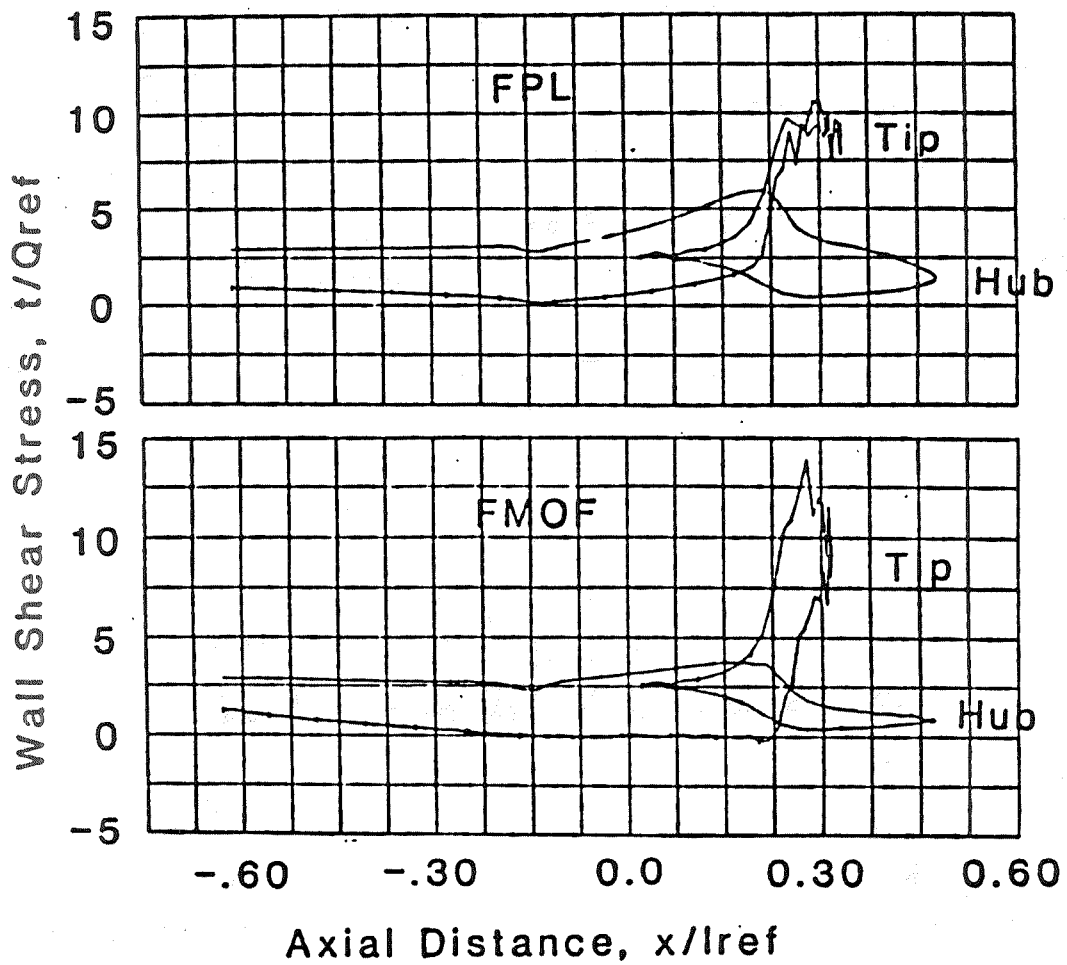
TAD INLET FLOW PROFILES



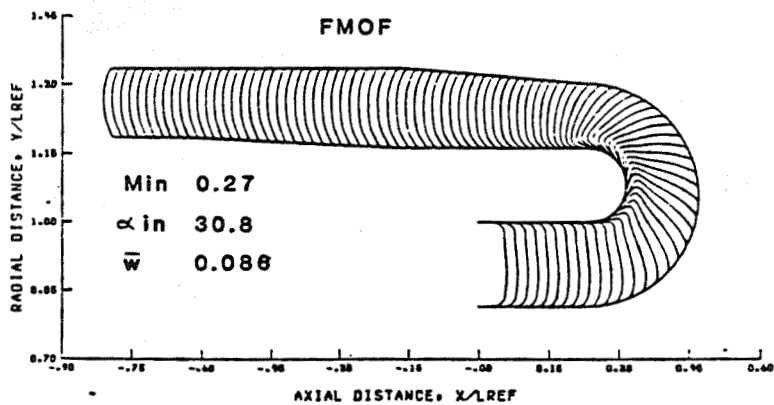
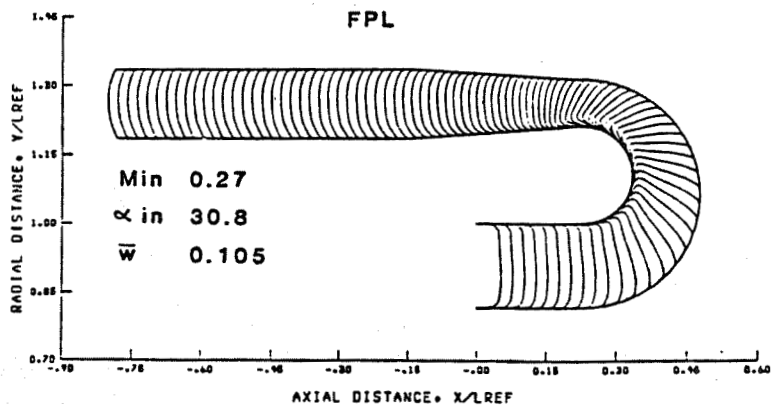
# RESULTS FOR UNIFORM INLET



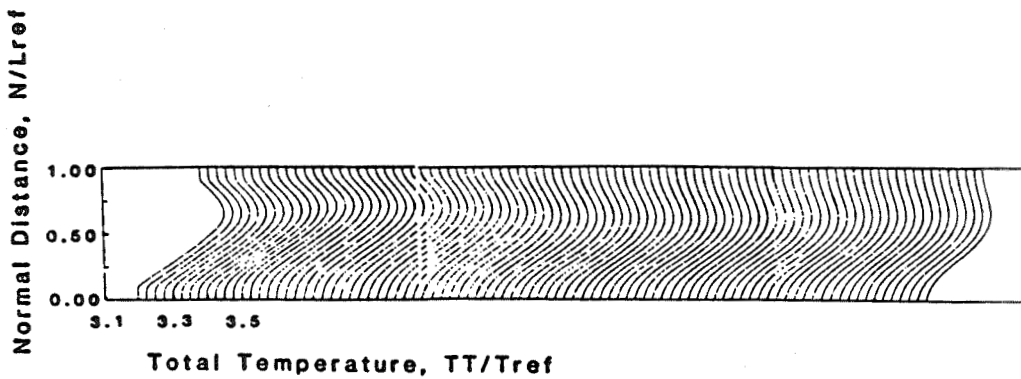
# TAD WALL SHEAR STRESSES



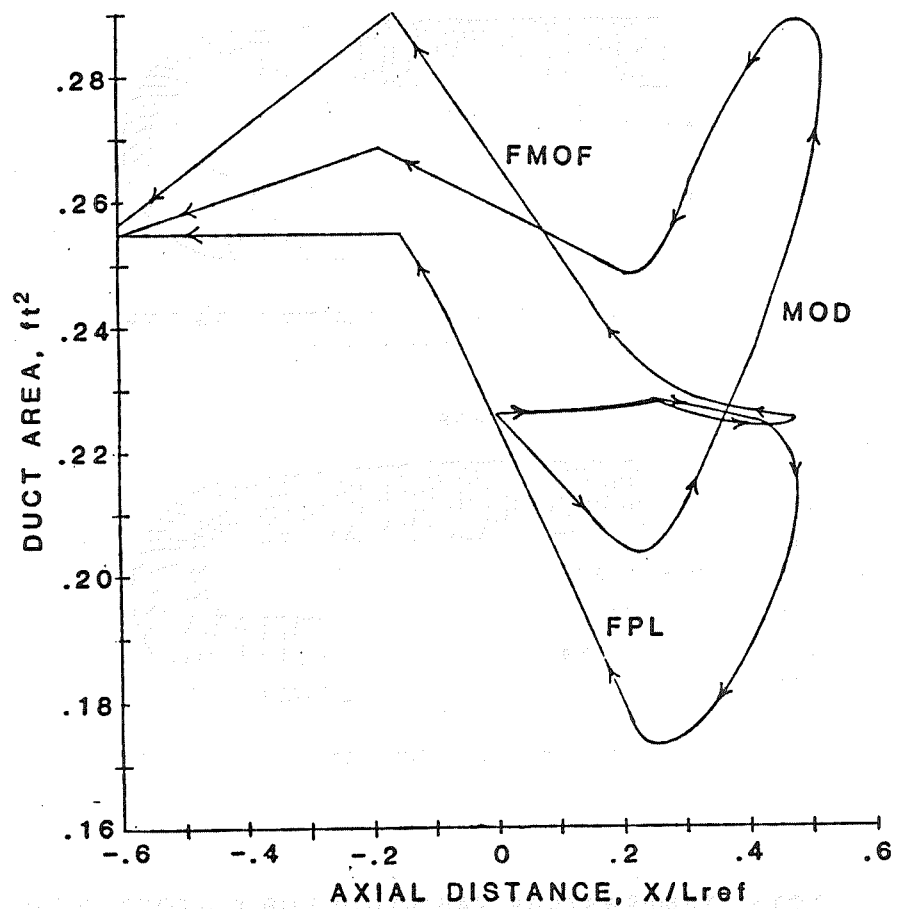
RESULTS FOR DISTORTED INLET



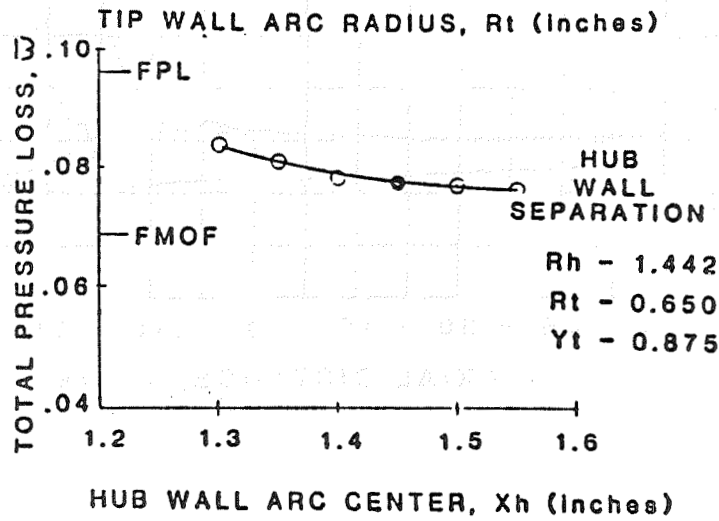
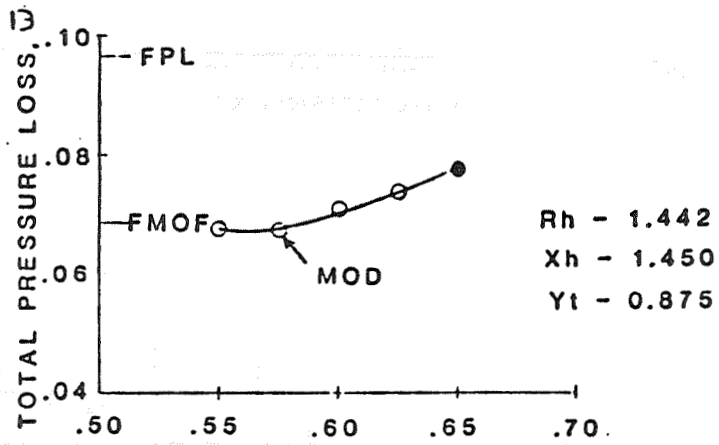
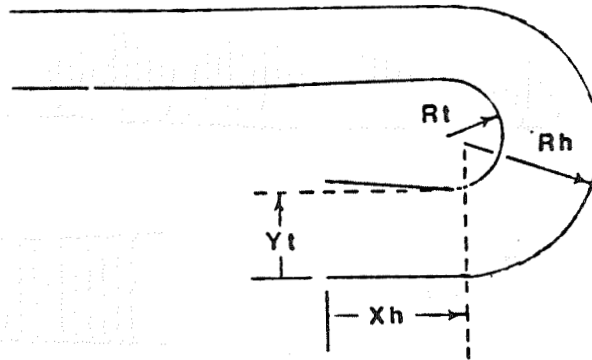
TOTAL TEMPERATURE VARIATION FOR DISTORTED INLET



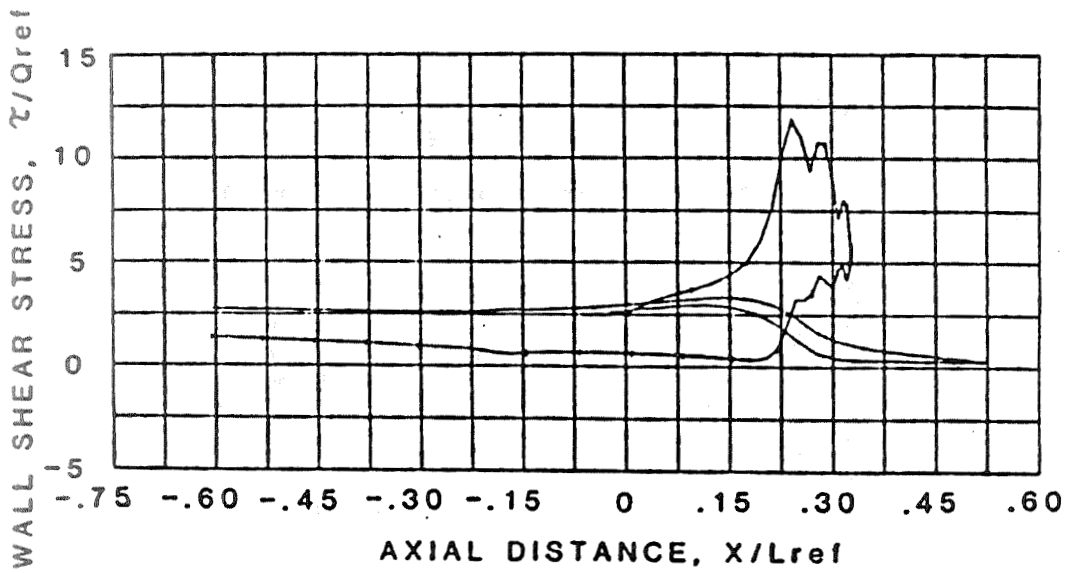
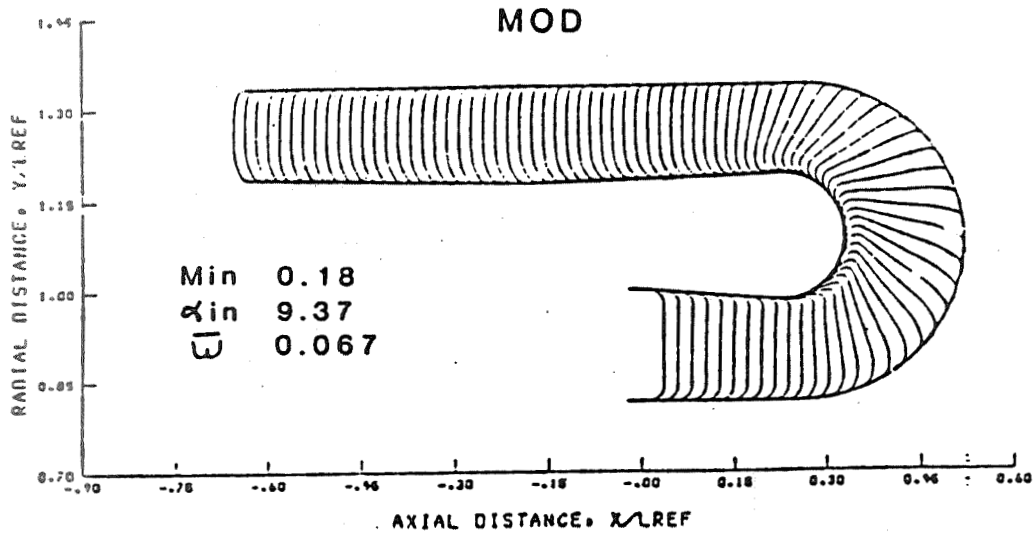
### TAD FLOW AREA DISTRIBUTIONS



# TAD GEOMETRY STUDY



# GEOMETRY STUDY RESULTS

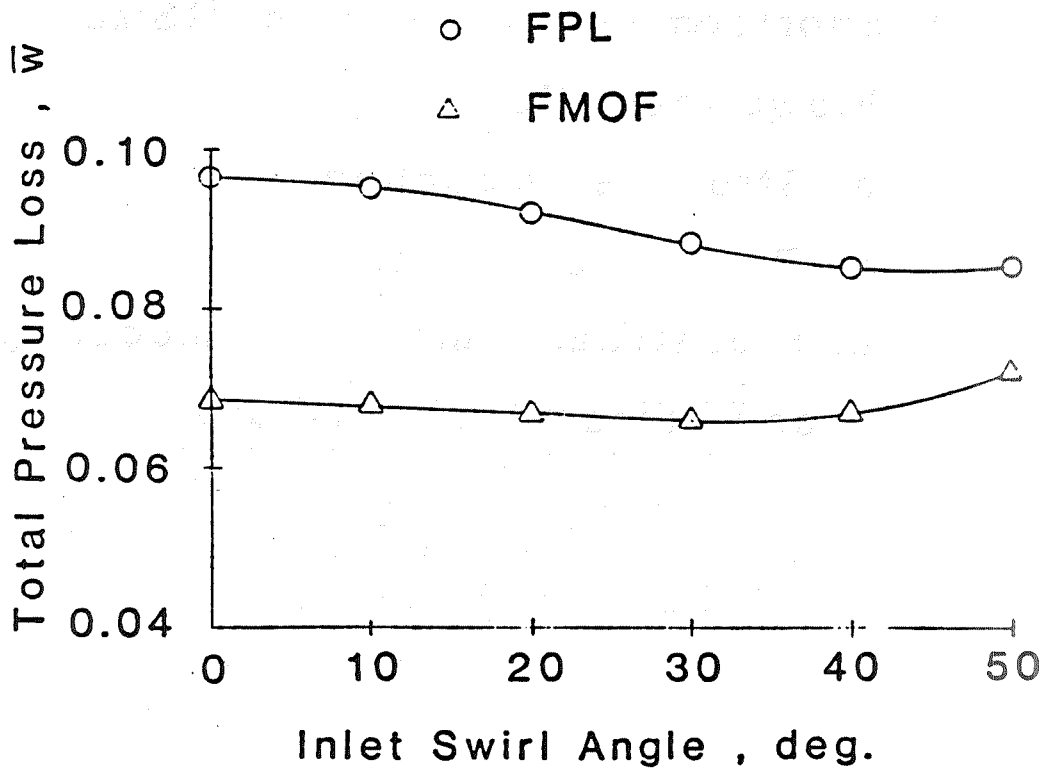


# TAD SWIRL STUDY

Uniform Inlet

$M_x$  0.18

$\delta^*$  0.0125  $H_{in}$



## CONCLUDING REMARKS

1. Useful Code for Design  
and Analysis of TAD Geometries
2. Results have Indicated Geometric  
and Flow Variables that Influence  
TAD losses
3. Shortcomings of Code for SSME  
Flows Identified
  - a. Strut loss modeling
  - b. Real fluid effects
  - c. Freestream Turbulence modeling  
and streamline curvature

SESSION VIII  
INSTRUMENTATION TECHNOLOGY  
OVERVIEW

W. C. Nieberding  
Instrumentation Research & Development Branch  
NASA/LeRC  
Cleveland, Ohio 44135 U. S. A.

The objective of the Instrumentation Technology program is to advance the state of the art of instrumentation associated with the SSME to improve service life and performance by providing increased measurement capability.

There are two broad categories of instrumentation technology being sought in this program. The first category includes sensors and systems destined to be used in and on the operational engine either during operation or between operations. The purpose of these measurements is to supply information necessary for engine control and/or diagnostics throughout the life of the engine. The second category includes measurement systems and techniques whose application will be to engine component test stands and possibly to the test bed engine but probably never to an operational engine. The primary purpose of these measurements is to provide the detailed information necessary to verify computer models of the performance of the various engine subsystems.

The accompanying charts show all of the elements of this program along with the schedules to the extent they are now known. Those elements for which progress is reported herein are denoted by an arrow on the right.

INSTRUMENTATION  
WORKING GROUP PLAN  
-KEY EVENTS-

ELEMENTS	FISCAL YEARS										
	1981	1982	1983	1984	1985	1986	1987	1988	1989	1990	
J1. REUSABLE ENGINE MAINTENANCE & INSTRUMENTATION		DESIGN START	DESIGN REVIEW		DESIGN COMPLETE						←
J3. CRYOGENIC MASS FLOWMETER RESEARCH		TECHNIQUE STUDY	FLOW STAND MOD.			SSME MODEL		SSME TESTING			←
J4. NON-INTRUSIVE SPEED MEASUREMENT FOR TURBOPUMPS			STUDY METHOD			LABORATORY TESTING		SSME TESTING			←
J5. RESEARCH & DEVELOPMENT OF BEARING INSTRUMENTATION	METHOD SELECTION		CRYO-SENSOR	PROTOTYPE							
J6. POSITION SENSOR RESEARCH							PROTOTYPE				
J7. RESEARCH OF PRESSURE INSTRUMENTATION		STUDY METHOD	BREADBOARD	BREADBOARD			SSME TESTING		SSME TESTING		←
J9. SPECTRAL SCANNER FOR EXHAUST PLUME ANALYSIS					STUDY METHOD		BREADBOARD		PROTOTYPE		
J11. PREBURNER GAS TEMPERATURE MEASUREMENT		STUDY		METHOD RESEARCH				PROTOTYPE			←

FOR PLANNING PURPOSES ONLY - SUBJECT TO CHANGE WITHOUT NOTICE.

7/1/84

INSTRUMENTATION  
WORKING GROUP PLAN  
-KEY EVENTS-

601

ELEMENT	FISCAL YEARS									
	1981	1982	1983	1984	1985	1986	1987	1988	1989	1990
J19. DISPLACEMENT INSTRUMENTATION INVESTIGATION							DESIGN & TEST	FAB		
J20. NON-INTRUSIVE TORQUE METER SENSOR TECHNOLOGY						FEASIBILITY STUDY		FAB		
J21. STATIC/DYNAMIC HIGH TEMPERATURE PRESSURE TRANSDUCER						FEASIBILITY STUDY	DESIGN	FAB	TEST	
J22. TRIBO ELECTRIC MASS FLOW SENSOR						FEASIBILITY STUDY	DESIGN	FAB	TEST	
J23. EXO ELECTRON FATIGUE TESTER						FEASIBILITY STUDY	DESIGN	FAB	TEST	
J24. INOBTRUSIVE DIAGNOSTIC SYSTEM				DEFINITION		LDV SYSTEM	CARS		VERIFICATION	

FOR PLANNING PURPOSES ONLY - SUBJECT TO CHANGE WITHOUT NOTICE

7/1/84

3  
3  
4

INSTRUMENTATION  
WORKING GROUP PLAN  
-KEY EVENTS-

ELEMENTS	FISCAL YEARS									
	1981	1982	1983	1984	1985	1986	1987	1988	1989	1990
J12. THIN FILM SENSORS FOR SPACE PROPULSION TECHNOLOGY				▽ SENSOR STUDY	△ EQUIPMENT ACQUISITION			SENSOR DEVELOPMENT		
J13. HEAT FLUX SENSORS CALIBRATOR				PROCUREMENT		▽ SYSTEM DELIVERY				
J14. OPTICAL FLOW MEASUREMENT						▽ EXPERIMENT VERIFICATION				
J15. OPTICAL STRAIN MEASUREMENT SYSTEM DEVELOPMENT						▽ ONE DIMENSIONAL SYSTEM		△ TWO DIMENSIONAL SYSTEM		△ APPLICATIONS
J16. HIGH TEMPERATURE HEAT FLUX SENSORS						SENSOR FAB		▽ SENSOR AVAILABLE		△ SENSOR TESTING
J17. HIGH TEMPERATURE/HIGH STRAIN GAGES						GAGE CONCEPT				▽ GAGE TESTING
J18. TRANSIENT GAS TEMPERATURE PROBE								▽ DEVELOPMENT		△ DEMONSTRATION

FOR PLANNING PURPOSES ONLY - SUBJECT TO CHANGE WITHOUT NOTICE

7/1/84

FIBER OPTIC RAMAN THERMOMETER FOR SPACE SHUTTLE  
MAIN ENGINE PREBURNER PROFILING\*

John A. Shirley  
United Technologies Research Center  
East Hartford, Connecticut 06108

Abstract

The feasibility of combustion gas temperature measurements in the SSME fuel preburner using non-intrusive optical diagnostics is being investigated. Temperature profiles are desired in the high pressure, hydrogen-rich preburner stream to evaluate designs to alleviate thermal stressing of the fuel pump turbine blades. Considering the preburner operating conditions and optical access restrictions, a spontaneous Raman backscattering system, implemented with optical fibers to couple to the combustion device, was selected as the most practical for gas temperature probing. A system is described which employs a remotely-located argon-ion laser to excite the molecular hydrogen Raman spectrum. The laser radiation is conveyed to the combustor through an optical fiber and focused through a window into the chamber by an optical head attached to the combustor. Backscattered Raman radiation from a localized region is collected by the head and transmitted through fiber optics to remotely-located spectrographic instrumentation for analysis. The gas temperature is determined from the distribution of rotational populations represented in the Raman spectrum.

Introduction

SSME Optical Temperature Diagnostics

Temperature nonuniformity is one hypothesis advanced to explain the cracking encountered in the

---

\* Work supported by NASA/Marshall Space Flight Center under Contract NAS8-34655.

SSME fuel pump turbine blades. The development of modifications leading to more uniform temperature profiles would be greatly facilitated by a diagnostic capable of spatially-precise gas temperature measurements in the combustor. A non-intrusive technique is desired to prevent flow and measurement disturbances and to insure survival of the apparatus. These considerations suggest the use of optical methods for remote diagnostics.

Since the advent of high power and tunable lasers a number of optical diagnostic techniques have been developed<sup>1-4</sup>. Typically, each of the techniques possesses advantages and disadvantages with respect to a particular application. The objective of the study reported herein is the development of an optical system for temperature profiling measurements in the SSME preburner and similar rocket combustors<sup>5</sup>. This report details interim progress that has been made on the construction and testing of breadboard hardware.

#### Environment Considerations

A large fraction of the hydrogen flow reacts with a smaller fraction of the oxygen flow in the preburner to provide a hot gas stream to drive the propellant turbopumps. The gas temperature in the preburners is approximately 970 K (1750 R) at the nominal power level. Equilibrium calculations indicate that molecular hydrogen represents 89.4 percent of the burnt gases and water vapor 10.6 percent. Atomic hydrogen and hydroxyl radical concentrations are calculated to be less than 1 ppb.

A cross sectional view of the fuel preburner, presented in Fig. 1, shows the limited optical access available. Fuel and oxidizer are injected into the combustion chamber through the face plate. Located within the chamber are three baffles, and a liner, both of which are cooled by a supply of hydrogen. Two transducer ports in the chamber walls afford optical access to the combustion medium. These ports are located in a plane at the end of the baffles, and are positioned at 165 and 360 degrees

with respect to the fuel inlet flange. Therefore optical access does not exist diametrically across the combustor. These restraints clearly favor single port optical techniques.

Other problems associated with measurements on a full scale operating rocket engine challenge the diagnostics designer. The engine may move in the test stand due to gimbaling and thrust loads. Prior to and during operation, a condensation cloud surrounds the engine and ice may form on engine parts near cryogenic propellant lines. Finally very high vibration and noise levels are experienced by any equipment near the engine.

As a final caveat, it should be pointed out that little is known about the optical properties of the flow in the combustor. Nonuniformities in the refractive index resulting from incomplete combustion and possible two-phase flow may be problematic. The magnitude of gas-phase density gradients due to turbulence or compressibility effects also are unknown.

#### Technique Selection

Several laser-optical techniques are available for remote pointwise temperature measurements<sup>1-4</sup> in combustion systems. Raman, fluorescence, and nonlinear optical techniques such as coherent anti-Stokes Raman spectroscopy (CARS) and stimulated Raman gain (SRG) have received the greatest attention, recently.

CARS and SRG<sup>4</sup> are very powerful techniques when used with high power lasers because a coherent, beam-like radiation is produced which can be captured with high efficiency. However these techniques require line-of-sight optical access, limiting their use when such is not available.

Fluorescence<sup>1,3,4</sup> is the emission of light from an atom or molecule promoted to an excited state. In laser-induced fluorescence, emission takes place following the absorption of a laser photon. The

hydroxyl radical is the only species in the preburner which is amenable to probing by existing laser sources. However its concentration is too low for practical measurements.

Raman scattering<sup>6,7</sup> is an inelastic scattering process in which an incident photon loses or gains a quantum of energy from the scatterer. Often Raman scattering is weak and easily overwhelmed by background luminosity or laser induced interferences in combustion systems because of the small scattering cross section ( $\sim 10^{-31}$  cm<sup>2</sup>/sR). Flame luminosity is small in O<sub>2</sub>/H<sub>2</sub> combustion and particulates are absent. The high gas density offsets the small cross section. The technique can be used with a single access port and furthermore, as will be shown, appears to be feasible with relatively low laser power so that optical fibers may be used to transport the probe radiation to the preburner.

#### Raman System Performance

The diagnostic capabilities of a system employing Raman scattering can be estimated based on the flow conditions in the preburner and known Raman properties of molecular hydrogen. The determination of the temperature from Raman scattering proceeds from an analysis of the spectral distribution, i.e. the Raman intensity variation with wavelength.

#### Signal level

The Raman scattered power of a particular rotational component with quantum number J is related to the incident optical power P<sub>L</sub> by

$$P_R = \left( \frac{2\pi\nu_J}{c} \right)^4 \frac{N_{vJ}}{2J+1} C_b S(J) f(J) P_L \quad (1)$$

where  $\nu_J$  is the Raman scattered frequency,  $N_{vJ}$  is the population of the sub-level,  $C_b$  is a factor which depends on the rigid rotator polarizability<sup>8</sup>,  $S(J)$  is the rotational line strength and  $f(J)$  is a correction for the centrifugal distortion caused by vibrational-

rotational interaction<sup>9</sup>. These factors are all known for hydrogen and are summarized in Ref. 5.

#### Temperature Measurements

The gas temperature is deduced from the distribution of intensity of the rotational sub-levels. The sensitivity of these rotational transitions to temperature is depicted in Fig. 2, which shows the intensity of transitions calculated for SSME preburner conditions. Two types of transitions or branches are shown as a function of Raman frequency shift. The lines grouped near zero frequency belong to pure rotational transitions, in which the rotational quantum number changes by 2 in the scattering process (+2 for the S-branch and -2 for the O-branch). Vibrational transitions representing the Q-branch ( $\Delta v = 1, \Delta J = 0$ ) are shown shifted by about  $4160 \text{ cm}^{-1}$ . Temperatures would be determined by comparing measured spectra to theoretical distributions. Any of the branches shown could be used, but the rotational S-branch is the strongest. The frequencies in hydrogen are well separated enough (except possibly in the Q-branch band head) to make analysis by spectral integration across the line straightforward.

#### Ortho-Para Modifications

Molecular hydrogen exists in two modifications depending on the orientation of the nuclear spins of the two atoms<sup>10</sup>. At room temperature and higher hydrogen is 75 percent ortho, in which the two spins are aligned anti-parallel, but at the normal boiling point (20.4 Kelvin) hydrogen is 99.79 percent para, in which the spins are both in the same direction. The conversion to the high temperature composition is slow<sup>11</sup> and may not be complete in preburner combustion. In practice this means that the even J transitions, which are para will be more intense than the odd transitions, depending on the amount of spin conversion. In the analysis of the spectral data, the even and odd manifolds will need to be analysed separately, but should yield the same temperature.

### Backscattering System Performance Estimate

The performance of diagnostics based on a Raman scattering system can be determined with respect to criteria established for a useful system. These specify a measurement with 1 cm spatial resolution, 10 millisecond temporal resolution, and a 6 Kelvin temperature accuracy. The existing optical access in the preburner determines the collection efficiency of the envisioned backscattering system in which the exciting laser and the collection of the Raman scattered radiation take place through the same window.

The results of calculations for the Raman spectral irradiance for realistic input conditions is shown in Fig. 3 for one of the lowest populated rotational levels. The laser intensity has been chosen to be typical of values which can be attained with current technology optical fibers. The Raman system is constrained to satisfy system spatial (0.5 - 1 cm) and temporal (10 millisecond) resolution design goals. Shown for comparison is a calculation of the thermal radiation from a solid with emissivity,  $\epsilon$ . This may represent a hot wall or particles in the flow. Note that an emissivity of 0.3 would typify a particle loading of 25 micrograms per cubic centimeter<sup>12</sup>, a high level. Therefore Raman signals should exceed the background by large margins.

### Raman System Design

The diagnostic system is conceived to consist of a high power laser, optical head mounted directly on the preburner, and a spectrograph/optical multichannel detector combination. The laser and the spectrograph/OMD would be located remotely, and would be joined to the head by optical fiber links. Figure 4 shows a schematic diagram of the apparatus. The design of the components is considered in this section. Currently these are being evaluated experimentally in a breadboard investigation.

### Optical Fiber Link

The use of optical fibers is growing in a wide variety of applications. The use of optical fibers in the present application affords location of the more delicate instrumentation away from the high noise rocket environment, while at the same time the integrity of the optical beam is insured. The low power requirements of Raman scattering for this high pressure application permit this benefit.

Naturally the fiber must be capable of transmitting the laser without serious attenuation. Optical fibers possess excellent transmission characteristics in the near infrared region of the spectrum, having attenuations as low as 0.5 dB/km. Raman scattering is stronger for short wavelengths however, so that operation is desired away from the best transmission windows for the fiber. Attenuation in the fiber generally follows an inverse fourth power relation with wavelength because the dominant loss mechanism is Rayleigh scattering. Applying this scaling, good fiber attenuation factors, in the operating range of argon ion lasers being considered for this application, would be on the order of 20 dB/km.

The transmission of several commercially available multimode fibers has been measured. The results for fibers with core diameters of 100 microns are presented in Fig. 5. Measurements have been made on smaller fibers as well. The lowest attenuation observed is 32 dB/km for the 488 nanometer line of an argon-ion laser. The required length of the fiber is about 40 meters so that the transmission is expected to be on the order of 45 percent including Fresnel reflection losses at the ends of the fiber.

The failure of several fibers has been experienced. Melting at either end of the fiber has been observed, although typically the failure occurs by melting at the output end of the fiber. One fiber exhibited nonlinear transmission characteristics, perhaps due to stimulated Brillouin scattering. <sup>13</sup>

## Optical Head

The function of the optical head is twofold. First is to take light from the laser and focus it at the measurement point in the preburner. Second is to collect Raman backscattered light and focus it into a fiber for transmission to the spectrometer/detector. The design of the optical head will define the measurement volume.

The design of the optical head is shown in Fig. 6. The beam from the laser is collimated and directed along the main optical axis of the head by a small prism. An intermediate lens brings the beam to a real focus and, finally, the focusing lens projects it into the measurement volume. The focusing lens collects the Raman backscattered light and focuses ultimately on an optical fiber. An absorptive glass filter can be used to block unshifted, scattered laser light. By moving either the intermediate lens or the focusing lens along the axis, the focal point of the laser can be changed so that this design can be used to probe points across the diameter of the combustor.

The optical head is forced by constraints of the preburner to operate at large f-numbers when viewing across the combustor. This increases the extent of the measurement volume along the axis, which determines the spatial resolution. It is desired to keep the resolution small, 0.5 to 1.0 cm. In a high f-number system, the on-axis rays contribute greatly to the sampling length. If the central rays are blocked the resolution can be improved.<sup>14</sup> The obscuration disk, shown in the figure, serves this purpose.

Measurements of the spatial resolution of an initial version of the head have been made by simulating Raman scattering in the measurement volume by a cell containing a dye that fluoresces in the incident laser light. The cell is thin (2 mm) in the direction of the axis and is translated along the axis to map out the spatial extent of the

optical response. The results of these tests are in accord with the simple relation derived in Ref. 14:

$$\Delta l = 2(A+B)f/D_0 \quad (2)$$

Here A is the collecting aperture (the fiber core diameter), B is the diameter of the laser focal volume, f is the distance of the focal point from the focusing lens, and  $D_0$  is the diameter of the obscuration disk. Restricting the focusing lens to operate at an f-number of 25, corresponding to viewing completely across the preburner through a 1 cm clear aperture window, it can be shown that the spatial resolution is given by  $19 Af/D_0$ . In order for the spatial resolution in this system to be less than 1 cm and the obscuration diameter no greater than 0.75 cm, the focal distance must be restricted to less than 4 cm. Although this may be acceptable for some measurements, other configurations using off-axis illumination and affording better resolution with less restriction will be sought.

#### Spectrograph

The spectrograph used to disperse the Raman signal for analysis must couple efficiently to the optical fiber. This requires fast (large aperture) optics in the instrument. Recently fast holographic gratings have been developed to couple to a fiber (f/3) dispersing the radiation onto a flat-field required by an optical multichannel detector. The spectrograph is designed with a dispersion of 2.5 nm/mm, so that the entire rotational branch will be spread over the central portion of the optical multichannel detector. Figure 7 shows a schematic of the spectrograph.

#### High Pressure Simulation Tests

The diagnostic capabilities of the Raman back-scattering system will be evaluated by testing with a high pressure hydrogen cell simulating conditions in the preburner. The electrically heated cell, shown in Fig. 8, can be heated to 1000 K and may be

pressurized to 6000 psia. The 1 cm diameter by 25 cm length duplicates the optical access of the preburner combustor. A metallic plug can be inserted into the cell to simulate the preburner liner.

#### Summary

The feasibility of remote optical diagnostics in the SSME fuel preburner has been investigated. The use of the laser Raman technique in a back-scattering configuration appears to have the best chance of meeting program objectives. The system would have radiation from a nominal 10 Watt argon ion laser, propagate through an optical fiber to an optical head attached to the combustor. The optical head will collect Raman scattered light and couple it into another fiber for transmission to analysis equipment. The optical head will require additional refinement to achieve 1 cm spatial resolution over distances greater than 5 cm.

It appears feasible to focus 4 to 5 Watts of optical power from the exit of the first fiber, and make temperature measurements in about 10 milliseconds. Additional development of the head optics will better determine any trade-offs which may be required in the program goals.

#### References

1. A. C. Eckbreth, P. A. Bonczyk and J. F. Verdick, Prog. Energy Comb. Science 5, 253 (1979)
2. B. T. Zinn, ed., Experimental Diagnostics in Gas Phase Systems, Progress in Astronautics and Aeronautics, Vol. 53, Amer. Inst. of Aeronautics and Astronautics, New York, 1977.
3. D. R. Crosley, Laser Probes for Combustion Chemistry, ACS Symposium Series 134, Amer. Chem. Society, Wash. D.C., 1980.

4. A. C. Eckbreth, "Recent Advances in Laser Diagnostics for Temperature and Species Concentrations in Combustion", 18th Symp. (Intl.) on Combustion, The Combustion Inst., 1981, p. 1471.
5. J. A. Shirley, Investigation of the Feasibility of Temperature Profiling Optical Diagnostics in the SSME Fuel Preburner, Final Report produced under contract NAS8-34774, 1983.
6. M. Lapp and C. M. Penney, eds, Laser Raman Gas Diagnostics, Plenum Press, New York, 1974.
7. M. C. Drake, C. Asawaroengchai, D. L. Drapcho, K. D. Veirs and G. M. Rosenblatt, "The Use of Rotational Raman Scattering for Measurements of Gas Temperature", in Temperature, J. F. Schooley ed., Amer. Inst. Physics, 1982, Vol.5, p. 621.
8. C. Asawaroengchai and G. M. Rosenblatt, J. Chem. Phys. 72, 2664 (1980).
9. T. C. James and W. Klemperer, J. Chem. Phys. 31, 130 (1959).
10. R. D. McCarty, Hydrogen: Its Technology and Implications, Vol. III Hydrogen Properties, CRC Press, Cleveland, OH, 1978.
11. M. Karplus, R. N. Porter and R. D. Sharma, J. Chem. Phys. 43, 3259 (1965).
12. H. C. Hottel and Sarofim, Radiative Transfer, McGraw-Hill, New York, 1967.
13. R. H. Stolen, "Nonlinear Properties of Optical Fibers", in Optical Fiber Telecommunications, S. E. Miller and A. G. Chynoweth, eds., Academic Press, New York, 1979.
14. A. C. Eckbreth and J. W. Davis, Appl. Optics 16, 804 (1977).

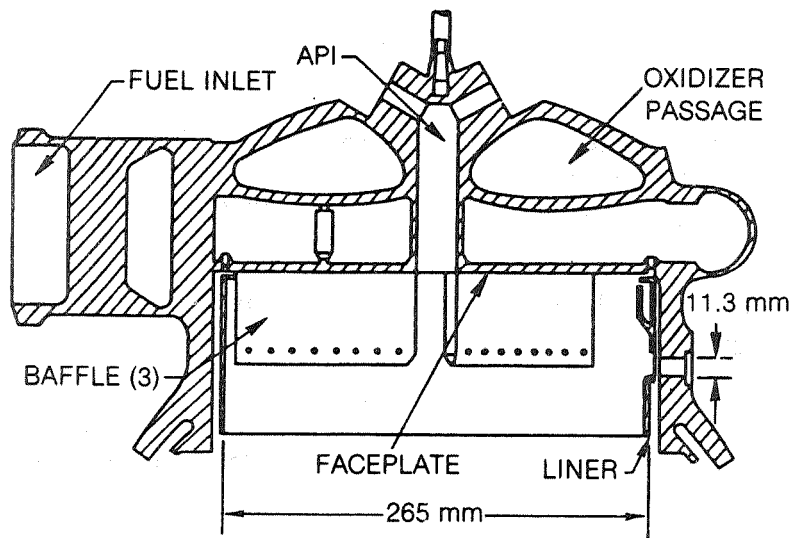


Figure 1 - Cross section view of SSME fuel preburner. The transducer are ports at 165° and 300°.

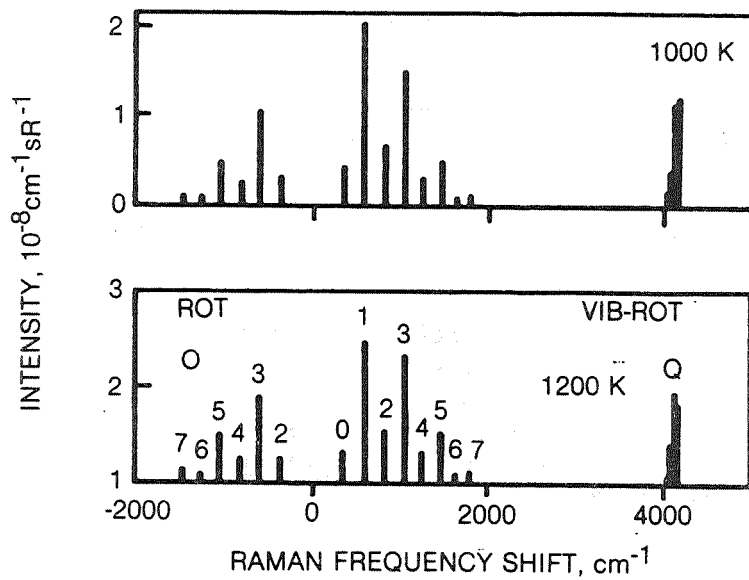


Figure 2 - Temperature dependence of calculated Raman spectra. Pressure = 5500 psia.

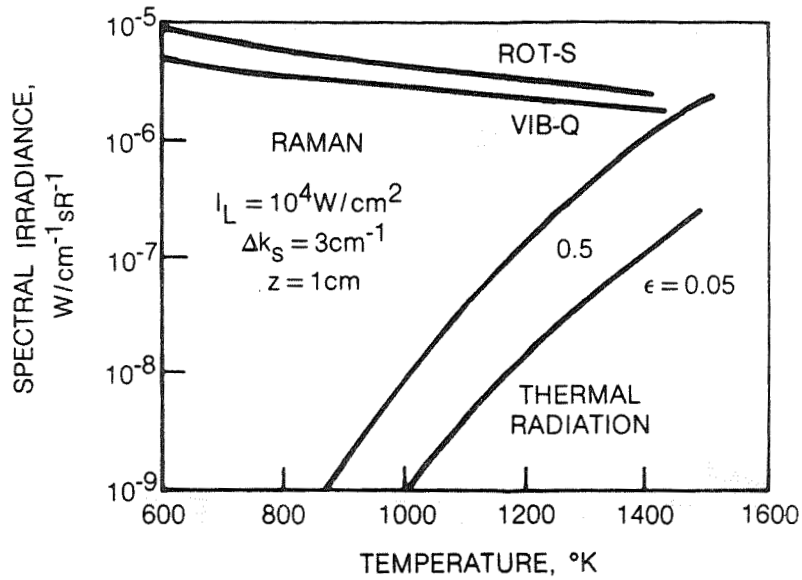


Figure 3 - Comparison of predicted Raman and thermal radiation irradiances.

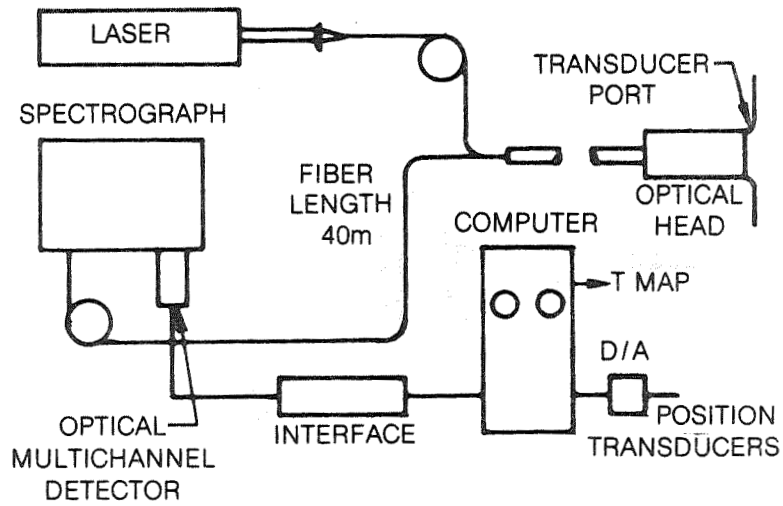


Figure 4 - Schematic diagram of the Raman back-scattering diagnostics system.

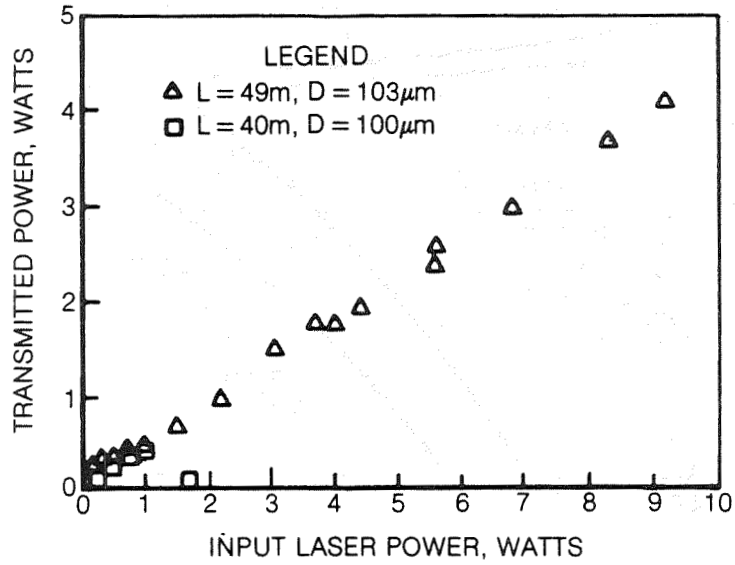


Figure 5 - Optical fiber transmission test results.  
Laser wavelength 488 nm line of Ar<sup>+</sup>.

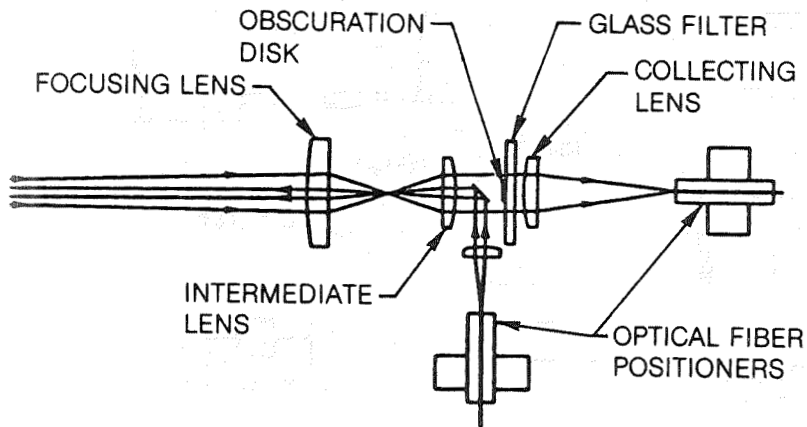


Figure 6 - Optical head design.

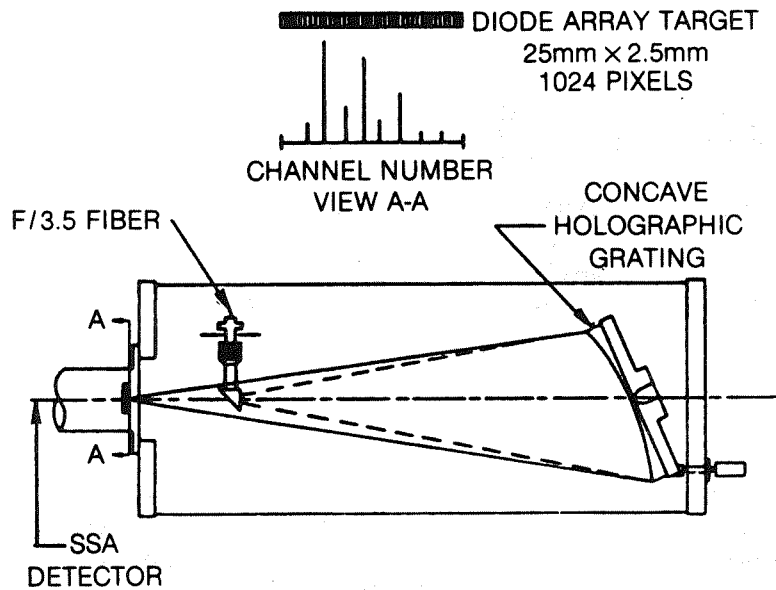


Figure 7 - Raman spectrograph designed for use with optical fiber.

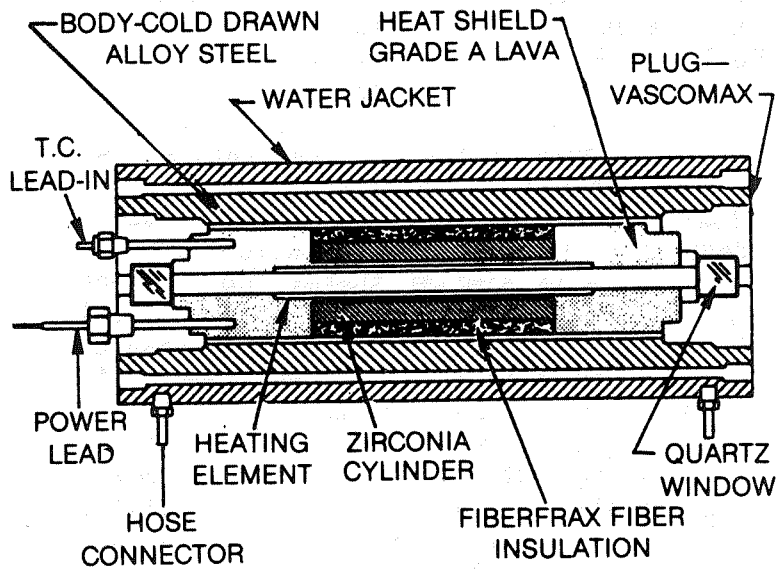


Figure 8 - Internally heated high pressure cell for Raman diagnostics testing. Operating conditions: 1300 K, 6000 psia.

AN ADVANCED SOLID STATE PRESSURE TRANSDUCER  
FOR HIGH RELIABILITY SSME APPLICATION

R. L. Johnson and D. B. Wamstad  
Solid State Electronic Division  
Honeywell, Incorporated  
Plymouth, Minnesota, 55441 U.S.A.

ABSTRACT

The objective of this research project is to define and demonstrate new methods to advance the state-of-the-art of pressure sensors for the Space Shuttle Main Engine. This includes improved reliability, accuracy, cryogenic temperature operation and ease of manufacture.

This paper presents the results of the "Feasibility and Breadboard Demonstration Phase" and the current status of the "Research Development Prototype Follow-on Phase." A technology breakthrough utilizing silicon piezoresistive technology was achieved in the first phase. Excellent silicon sensor performance, at liquid nitrogen temperature, was successfully demonstrated at NASA/MSFC.

The follow-on phase is in process. A transducer design concept for the SSME application utilizes packaging materials with similar thermal coefficients of expansion and maintains the transducer seals primarily in compression. The package mechanical integrity will be tested to the SSME requirements for temperature (-423°F to +250°F), pressure (9.5K psi), and vibration (400 g's). The silicon chip design will provide dual sensing outputs with laser trimmable integrated compensating electronics. The silicon resistor ion implant dose was customized for the SSME temperature requirement. A basic acoustic modeling software program was developed as a design tool to evaluate the frequency response characteristics for the package design. Successful completion of this research project will provide ten prototype SSME Solid State Pressure Transducers for NASA testing.

## INTRODUCTION

Previous research and development at Honeywell has demonstrated that silicon piezoresistive pressure-sensing diaphragms can be integrated with electronic components on a single chip to produce small, accurate, and rugged transducers. Also, the techniques used for precisely forming the pressure sensing diaphragm to a controlled thickness allow a common chip design to be used for a wide range of full scale pressures. The design can thus be used for a "family" of pressure sensors. A capsule summary of Honeywell's proposed concept of pressure instrumentation for the space shuttle main engine application is given below:

- Electrical conversion of sensor behavior integrated on the same chip as the solid state piezoresistive elements (single chip approach).
- Pressure ranges established simply by changing the silicon diaphragm thickness.
- Each transducer uniquely calibrated by laser trimming of on-chip thin film resistors.
- Temperature compensation achieved by on-chip signal conditioning circuitry.

The NASA Contract number of this research of pressure instrumentation study is NAS8-34769. Mr. Tom Marshall of the Marshall Space Flight Center, Huntsville, Alabama, is the technical monitor.

## FEASIBILITY STUDY AND BREADBOARD DEMONSTRATION PHASE

The objective of this phase was to develop breadboard type hardware capable of demonstrating the feasibility of the advanced solid state sensor concept and to provide a laboratory demonstration of MSFC of two SSME Breadboard Pressure Transducers.

## Circuit Development

The initial work of the feasibility study was a literature study of the behavior of silicon piezoresistors at cryogenic temperatures. The change in absolute resistance and the change in piezoresistance to pressure as a function of temperature both had to be determined in order to accurately condition the sensor's output signal. From the literature study, it was determined that peak doping levels of  $3 \times 10^{19}$  atoms/cm<sup>3</sup> to  $2 \times 10^{20}$  atoms/cm<sup>3</sup> for boron piezoresistors would yield compensatable performance and still provide adequate sensitivity to pressure.

After the behavior of existing experimental piezoresistors and other candidate circuit elements were characterized at cryogenic temperatures, a transducer circuit was designed to compensate and calibrate the sensors over the temperature range of -320°F to +165°F. A simplified schematic diagram of the SSME Breadboard Pressure Transducer circuit is given in Figure 1. Since only a portion of the available 10 volt excitation is required for the silicon sensor bridge to provide the required output level, the remainder of the excitation voltage is therefore available for signal conditioning of the sensor output.

In addition to the pressure sensing bridge and a reference non-pressure sensing bridge, the circuit mechanization consists of seven (7) laser trimmable thin film resistors and six (6) diodes (base-to-emitter pn junction of small signal transistor devices). The thin film resistor (TRF) networks are utilized to calibrate and compensate the sensor output over the full operating range at temperature and pressure. The following four functions are uniquely calibrated:

- 1) Null set at zero pressure
- 2) Span set at full scale pressure
- 3) Null change with temperature
- 4) Span change with temperature

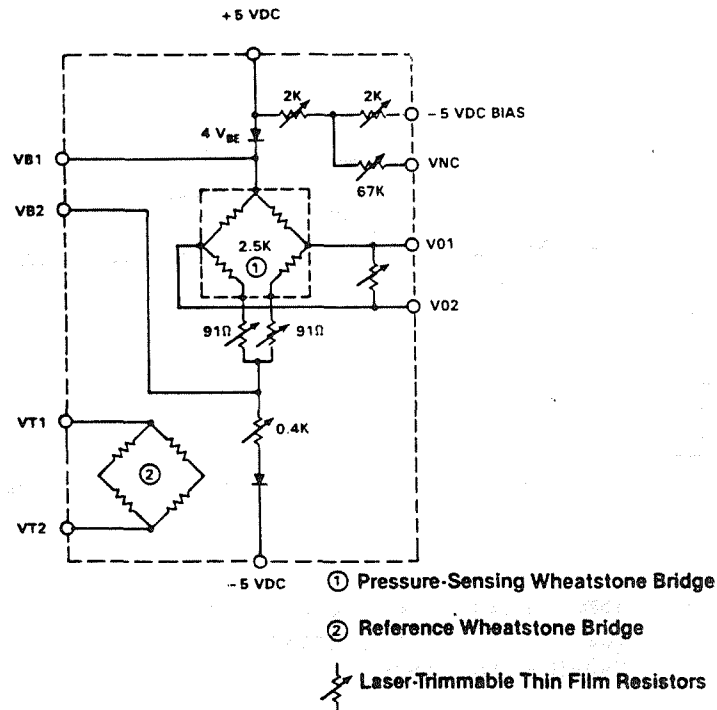


Figure 1: Simplified Schematic Diagram of SSME Breadboard Pressure Transducer

Span (pressure sensitivity) compensation of the silicon sensor bridge is accomplished by counteracting the change in pressure sensitivity to temperature by an opposite change in bridge excitation with temperature. For piezoresistance sensors, the sensitivity decreases with increasing temperature and increases proportionally with increasing bridge excitation. Therefore, properly controlling the bridge voltage as a function of temperature will cancel the effect of the sensor's strain sensitivity as a function of temperature. This span or sensitivity compensation technique is achieved in the circuit of Figure 1 by the interaction between the temperature coefficient of the sensor bridge itself and the circuit elements in series with the bridge.

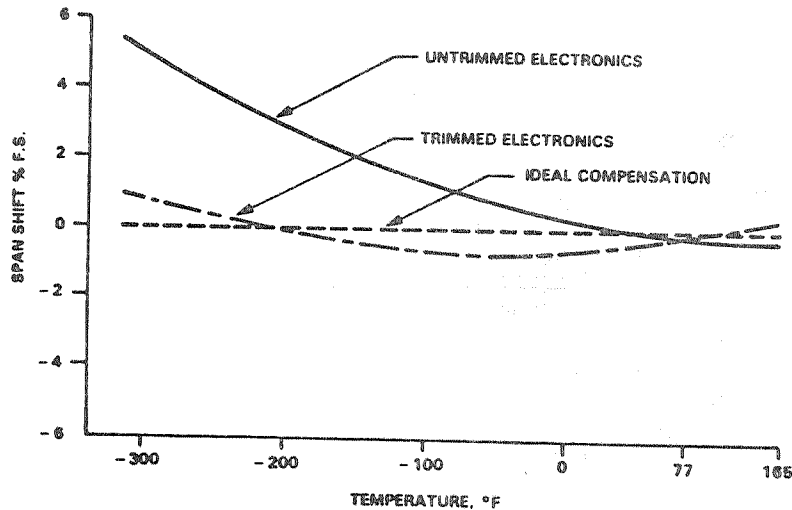


Figure 2: SSME Breadboard Pressure Transducer Span Shift Characteristics (-320°F to 165°F)

A typical pressure sensitivity compensation curve for the breadboard pressure transducer design is presented in Figure 2. By using laser trim calibration, span shifts of less than 1% over the temperature range of -320°F (LN<sub>2</sub>) to +165°F are attainable.

#### Breadboard Hardware Development

The design of the breadboard hardware for feasibility demonstration is presented in Figure 3. For the breadboard hardware, a hybrid mechanization of the electronics was designed using existing IC chips as shown in the top portion of Figure 3. For the prototype research pressure transducer, all the electronics, including the sensor bridge, will be integrated on a single chip. The ceramic circuit board is mounted into a stainless steel test vessel which houses the pressure sensor chip mounted on a pyrex tube as shown at the bottom of Figure 3.

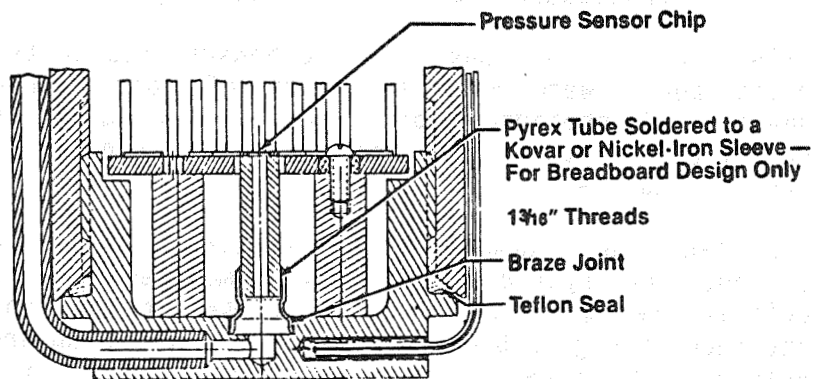
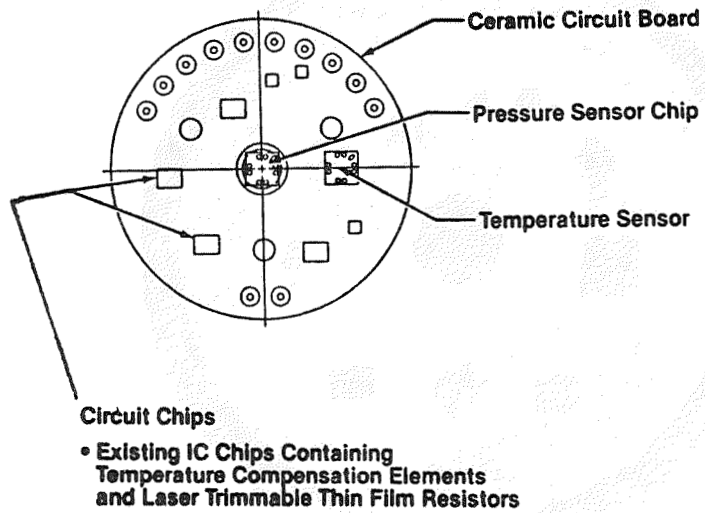


Figure 3: SSME Breadboard Pressure Transducer Test Vessel

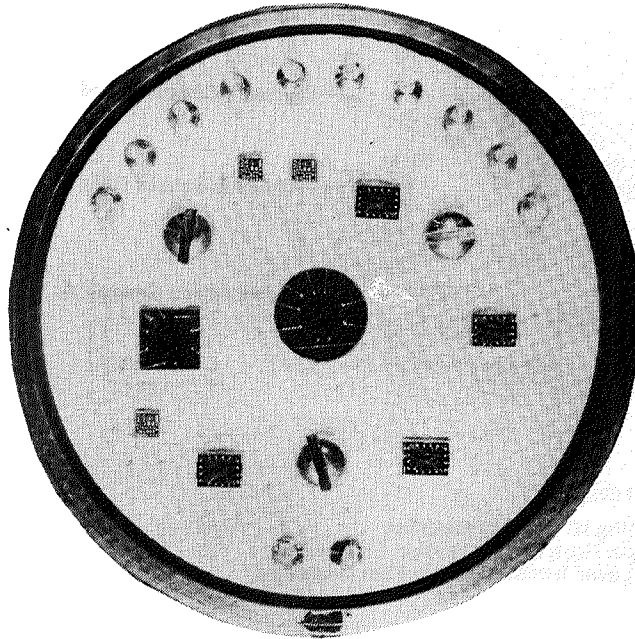


Figure 4: SSEM Breadboard Pressure Transducer  
Transducer - Electronics Assembly

Electrical connections from the Sensor Chip to the circuit board were made by means of gold interconnects. A photograph of a completed electronics assembly of the SSME breadboard pressure transducer is shown in Figure 4.

To facilitate demonstration testing in liquid nitrogen, the hybrid assembly was mounted into a specially designed housing as presented in the photograph of Figure 5 which shows the SSME Breadboard Pressure Transducer in its final form for demonstration testing. Pressure connection to the device was made via a copper tube soldered into the base of the test vessel. The leadwires from the transducer were brought out through a long metal tube and terminated with an appropriate connector for electrical interface.

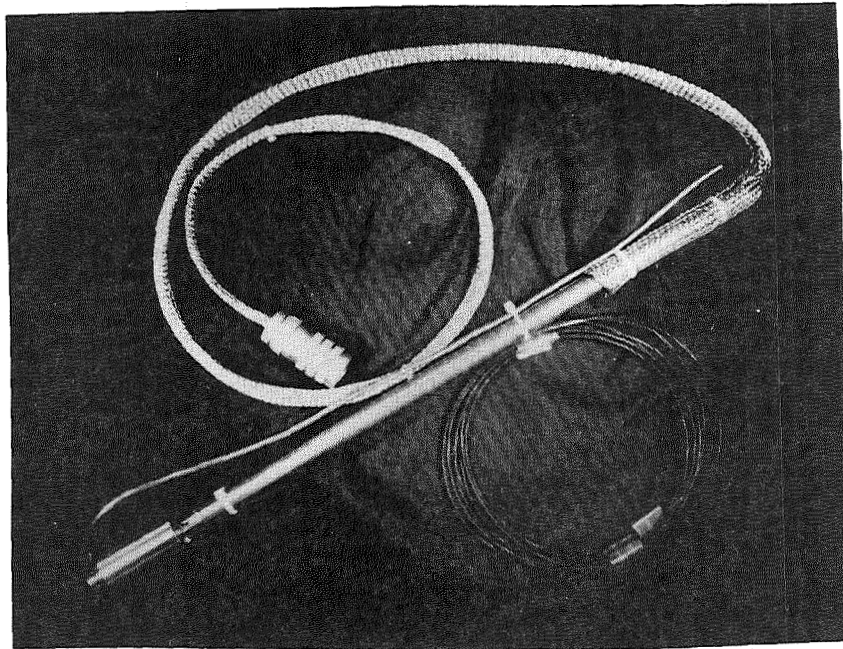


Figure 5: SSME Breadboard Pressure Transducer - Final Form

#### Breadboard Hardware Demonstration

Upon completion of the calibration and characterization of the SSME Breadboard Pressure Transducers, two units were delivered to and demonstration tested at the Marshall Space Flight Center in Huntsville, Alabama. Figure 6 shows the test setup used for the demonstration.

The demonstration consisted of performing a baseline room temperature pressure test, followed by a liquid nitrogen (LN<sub>2</sub>) test procedure, and concluding with post LN<sub>2</sub> room temperature pressure test. The baseline pressure test consisted of an upscale and downscale pressure profile using pressure increments of 20% full scale (the breadboard transducer used a 10 psi full scale sensor).

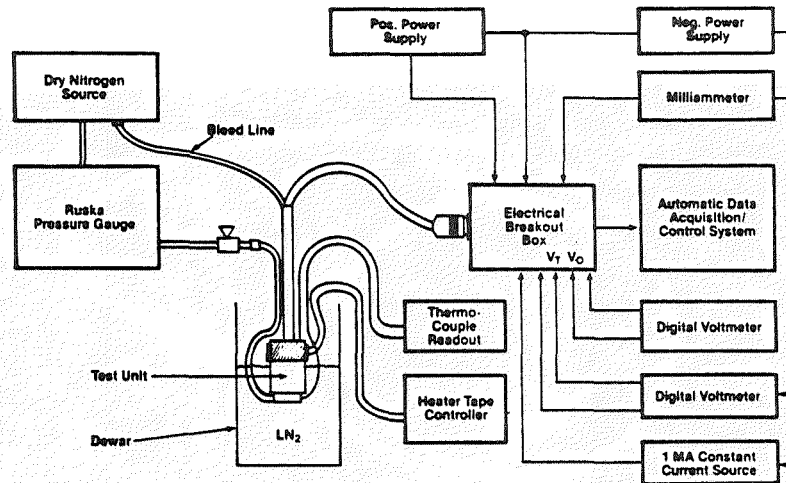


Figure 6: SSME Breadboard Pressure Transducer-Demonstration Test Setup.

The LN<sub>2</sub> test consisted of submerging the test unit in a LN<sub>2</sub> Dewar until the LN<sub>2</sub> was approximately one third the way up the large diameter portion of the device. A powered heater tape strapped to the top part of the test body was used to generate a 165°F thermal gradient across the body of the breadboard pressure transducer. Under this test condition, the sensor end of the transducer was at -320°F and the top part of the transducer was at -165°F. An up-down pressure profile was performed while maintaining the thermal gradient condition. In addition to the pressure profile, the null output was monitored during the temperature transition from room down to liquid nitrogen temperature. After the LN<sub>2</sub> test, the devices were allowed to restabilize and the baseline room temperature pressure test was repeated.

The results of the breadboard demonstration were very successful and the feasibility of the advanced solid state pressure sensing concept was clearly demonstrated.

A capsule summary of the significant accomplishments of the feasibility and breadboard demonstration phase is presented below.

- Accurate Calibration and Compensation of the Breadboard Pressure Sensor Using Laser Trim Technology
  - Null Voltage Set to Zero Within 1 Microvolt.
  - Full Scale Voltage Set to Within 10 Microvolts.
- Successful Breadboard Demonstration at NASA/MSFC.
- Key Results at Liquid Nitrogen (-320°F) Temperature
  - Null Shift: 0.1% FS
  - Sensitivity Shift: 1.9% FS
  - Pressure Hysteresis: 0.02% FS (0.01% FS at SSED)
  - Thermal Hysteresis: 0.03% FS (0.005% FS at SSED) (Non-Return to Zero)
  - Transient Null Shift: <1.0%FS Maximum (Measured During Temperature Excursion from Room Temperature to -320°F with a 165°F Thermal Gradient Across the Sensor Housing).

## DEVELOPMENT RESEARCH PROTOTYPE PHASE

The objective of the "Development Research Prototype Phase" is to design, develop and deliver ten prototype pressure transducers. These are targeted to meet the SSME transducer performance design goals. This phase consists of a study, experimental effort, prototype design and development phase. Three studies have been completed for this project and consist of the following:

1) Transducer Package Concept Study - Silicon chip mounting and packaging concepts were generated and analyzed to determine suitability for the SSME application. A concept which utilizes materials with similar thermal coefficients of expansion and maintains the transduced materials and seals primarily in compression was selected.

2) Materials and Process Study - A study was completed to select materials and determine processes for the selected transducer package concept. The materials and process selection was based on the temperature, pressure, vibration and pressure media requirements for the SSME application.

3) Acoustic Frequency Response Study - Based on this study an acoustic modeling software program was developed as a design tool to evaluate the frequency response characteristics for the transducer final package design.

The experimental phase of this project is partially complete and consists of the following:

1) Silicon Resistor Characterization at Cryogenic Temperature - Silicon resistor implant doses were experimentally varied to customize the silicon piezoresistors for the SSME temperature requirement ranging from -423°F to +250°F. The data from this task is presently being analyzed.

2) Pressure Sensor Chip Mounting Characterization  
- The mechanical integrity will be experimentally determined for the silicon chip mounting concept, selected in the study phase. Mechanical models will be tested to the SSME requirement for temperature (-423°F to +250°F), pressure (9.5K psi) and vibration (400 g's).

The performance and survivability of present solid state piezoresistive pressure transducers have been successfully demonstrated at cryogenic temperature (-320°F), based on the NASA Breadboard Demonstration, and at high pressure (10K psi), based on existing commercial sensors. The combined SSME requirements for temperature, pressure, vibration and pressure media have not been demonstrated and are extremely challenging. These will be demonstrated at the conclusion of the prototype phase. The following proposed Pressure Transducer Concept, dependent on the experimental results, will be designed, built and evaluated.

#### Transducer Design Goals and Approach

The SSME Pressure Transducer Design goals, based on the combined effects of cryogenic temperature, high pressure, vibration, absolute pressure sensing and package design are extremely challenging. The basic SSME design goals are summarized in Table 1.

The transducer design approach implements the NASA requirement for direct mounting of the pressure transducer to the SSME. This requires the pressure sensing element to be in direct contact with the high pressure cryogenic pressure media. It also requires, based on the state of the hydrogen/oxygen/nitrogen pressure media, that the silicon integrated circuits not be in direct contact with the pressure media. The design approaches incorporated in the selected pressure transducer concept are listed in Table 2.

Table 1. Summary of SSME Pressure Transducer Design Goals.

<u>CONDITION</u>	<u>DESIGN GOALS</u>
Transducer Configuration	- Same external configuration as RC7001
Pressure Ranges	- 0 to 600 psia - 0 to 3500 psia - 0 to 9500 psia
Pressure Rating	- 1.5x F.S. (No permanent null or calibration change) - 2.5x F.S. or 20K psi Maximum (No permanent damage)
Pressure Media	- Liquid/Gaseous Hydrogen - Liquid/Gaseous Oxygen - Helium - Nitrogen
Temperature Range	- -200°C to + 120°C (Goal of -253°C)
Vibration	- 0 to 2000 Hz; 400 g's (With superimposed random and steady-state vibration)
Acoustic Frequency Response	- Dynamic Design Goal of 300 Hz Minimum
Full Scale Output	- 30 ± 0.3mV at 10 VDC Excitation
Thermal Zero Shift	- ± 0.005% F.S./Degree
Electrical-To-Pressure Calibration	- +0.1% F.S. at 80% F.S. Correlation points at Ambient Temperature

Table 2. Design Approaches Incorporated in the NASA Pressure Transducer Concept.

<u>DESIGN PARAMETER</u>	<u>DESIGN APPROACH</u>
Sensing Element and Circuit	<ul style="list-style-type: none"> <li>- The sensing element, diaphragm, and circuit are contained on a single chip.</li> <li>- The circuit provides a fully compensated and calibrated linear output voltage proportional to pressure.</li> </ul>
Integrated Circuit Protection	<ul style="list-style-type: none"> <li>- The integrated circuit on the silicon is protected by the absolute transducer vacuum reference.</li> </ul>
Method of Calibration	<ul style="list-style-type: none"> <li>- Laser circuit trim capability is provided by thin film resistors on the silicon chip.</li> </ul>
Pressure Range Change	<ul style="list-style-type: none"> <li>- The operating pressure range is changed simply by changing the thickness of the silicon diaphragm.</li> </ul>
Pressure Media	<ul style="list-style-type: none"> <li>- To insure high reliability the circuit side of the silicon chip is protected from the pressure media.</li> <li>- The transducer package materials were selected for pressure media compatibility.</li> </ul>
Vibration	<ul style="list-style-type: none"> <li>- The attributes of silicon pressure transducers such as small size, low mass, integrated electronics and essentially no moving parts all contribute to high vibration capability.</li> <li>- The length of the electrical interconnects from the silicon chip to the terminal board will be controlled for high vibration capability.</li> </ul>
Cryogenic Temperature	<ul style="list-style-type: none"> <li>- Excellent silicon sensor performance, at liquid nitrogen temperature was successfully demonstrated at NASA/MSFC.</li> <li>- The implant dose of the ion implanted sensor elements will be customized for cryogenic temperature performance.</li> <li>- The transducer package materials were selected for cryogenic temperature compatibility.</li> </ul>
High Pressure	<ul style="list-style-type: none"> <li>- The transducer design concept maintains the transducer seals primarily in compression and utilizes high strength materials with similar coefficients of expansion.</li> </ul>
Acoustic Frequency Response	<ul style="list-style-type: none"> <li>- Acoustic modeling software was developed to analyze the frequency response characteristics and will be utilized in the final design to maximum frequency response.</li> <li>- Pressure port length will be minimized and Helmholtz Resonator Side Chambers added.</li> </ul>

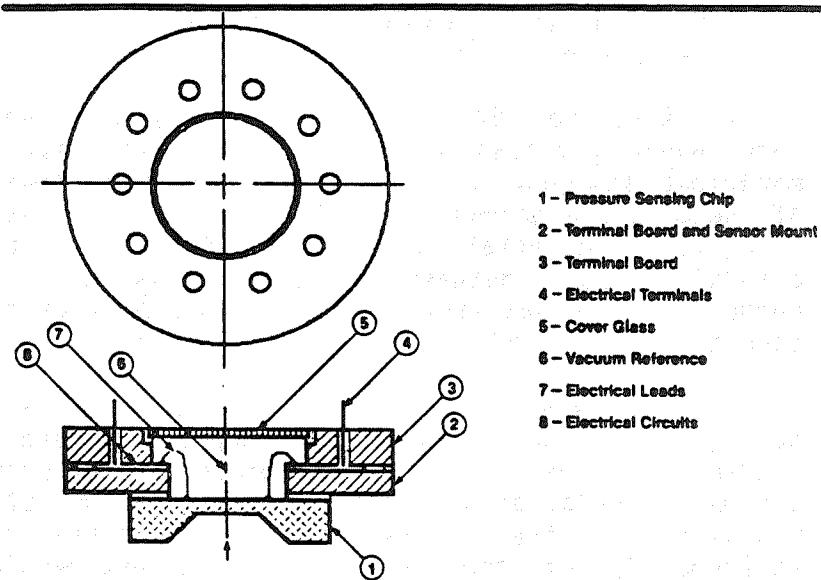
## Transducer Package Design

The SSME Transducer Package Design is documented in Figure 7 and Figure 8. This encompasses an absolute silicon pressure sensor chip with laser trimmable circuit electronics mounted to a silicon nitride backplate and terminal board. The chip mount vacuum reference of the absolute transducer is established through the hermetic seals of the silicon, silicon nitride and the pyrex cover glass. The sensor chip mount is housed in a common package with electrical interface and pressure port provision.

### Pressure Transducer Silicon Chip Mount

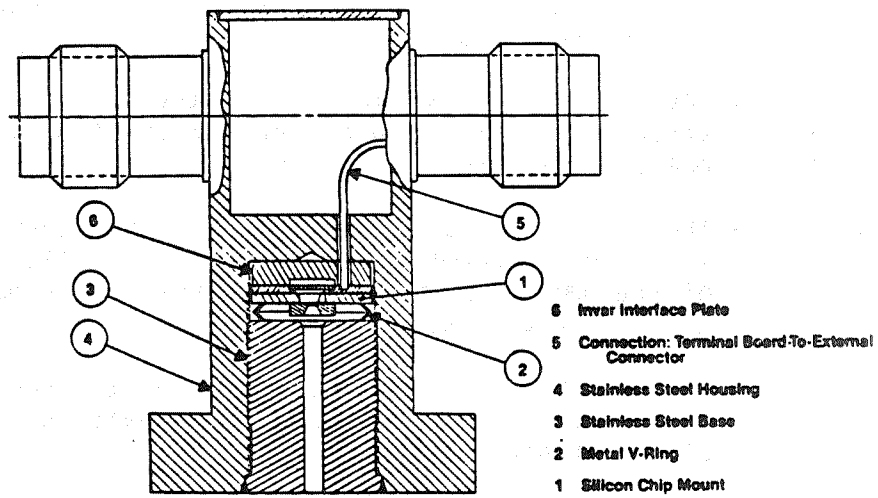
The pressure transducer silicon chip mount design is extremely important. Sensor performance, in terms of accuracy, repeatability and stability, is dependent on its interface with the transducer package and pressure media. There are four basic SSME requirements which dictate the pressure sensor chip mount design. These are:

1. Pressure Media Interface - The high pressure (9.5K psi), cryogenic temperature (-320°F) and pressure media (LOX, LH<sub>2</sub>, gaseous helium, nitrogen, oxygen, hydrogen, air and water vapor) require the active circuit side of the pressure sensor chip be separated from the pressure media. This is accomplished by applying the pressure to the backside of the pressure sensor chip.
2. High Pressure/Low Temperature - The combined high pressure and low cryogenic temperature requirements dictate that the pressure media be applied directly to the chip.
3. Active Laser Trimming - Active laser trimming of on-chip thin film resistor networks to calibrate sensor performance is normally completed after sensor packaging. This is done to eliminate the packaging and assembly process effects on transducer



- 1 - Pressure Sensing Chip
- 2 - Terminal Board and Sensor Mount
- 3 - Terminal Board
- 4 - Electrical Terminals
- 5 - Cover Glass
- 6 - Vacuum Reference
- 7 - Electrical Leads
- 8 - Electrical Circuits

Figure 7. Pressure Transducer Silicon Chip Mounting Design



- 6 Inner Interface Plate
- 5 Connection: Terminal Board To-External Connector
- 4 Stainless Steel Housing
- 3 Stainless Steel Base
- 2 Metal V-Ring
- 1 Silicon Chip Mount

Figure 8. Pressure Transducer Package Design

calibration. This dictates that the trimmable network be visible after packaging and further impacts the pressure sensor chip mounting.

4. Absolute Sensor - The absolute sensor requirement provides an additional challenge. The materials and processes utilized in the construction of the pressure transducer influence the sensor vacuum integrity. Materials were selected based on their diffusion and outgassing characteristics, high hermeticity capability and temperature pressure compatibility.

Testing was completed on a special sensor configuration to simulate the compressive pressure loading impact on transducer performance. The purpose of this testing was to determine the strain transmitted to the silicon chip (effect on transducer performance) by the impact of compressive loads applied to the outer edge of the silicon nitride. The key findings of this testing are:

- Comprehensive loading can result in substantial stress transmission to the sensor chip.
- The stresses transmitted to the sensor are strongly dependent on the method of clamping in the test fixture.
- The stress transmitted to the sensor is strongly dependent upon the condition (flatness) of the mating surfaces between the test samples and the test fixture.
- Changes in the piezoresistors ranged between 0-2% when close attention was paid to the aforementioned conditions.

Based on the results of this experimental testing, the original transducer package design concept was changed to minimize stress transmission to the sensor chip by either pressure or temperature. This design change involved adding an Invar interface, with

controlled surface flatness, between the silicon nitride and stainless steel, adding a surface flatness requirement to the silicon nitride parts and adding a metal compressive C-Ring between the silicon nitride and stainless steel (see Figure 2). This change will uniformly distribute the structural compressive load over the required transducer pressure and temperature range.

The pressure transducer silicon chip mount design utilizes materials with closely matched coefficients of expansion; silicon, silicon nitride, pyrex and invar. These will minimize the thermal stresses over the large temperature differential of 682°F required for the SSME application. To insure package survivability at high pressure and cryogenic temperatures the design maintains the transducer seals primarily in compression.

The acoustic response study determined methods of improving the frequency response characteristics. These primarily consist of minimizing the pressure port length and adding Helmholtz Resonator chambers in the housing wall. The influence of the pressure port length is detailed in Figures 9. As the length of the pressure port decreases the resonant frequency increases. Pressure port length of 2.245 inches has the first frequency response harmonic occurring at 2000 Hz. When the pressure port length is decreased to 1.000 inches, the frequency response harmonic increases to 3000 Hz. The use of Helmholtz Resonator chambers, as shown in Figure 10, decrease the peak pressure pulse. These features will be incorporated in the final design for the prototype SSME pressure transducers.

#### SUMMARY

The performance and survivability of present solid state piezoresistive pressure transducers have been successfully demonstrated at cryogenic temperature (-320°F), based on the NASA Breadboard Demonstration, and at high pressure (10K psi), based on existing commercial sensors. The combined SSME requirements for temperature, pressure, vibration and pressure

**Acoustic Pressure Frequency Response of the SSME Mounting Interface/Sensor Housing System**

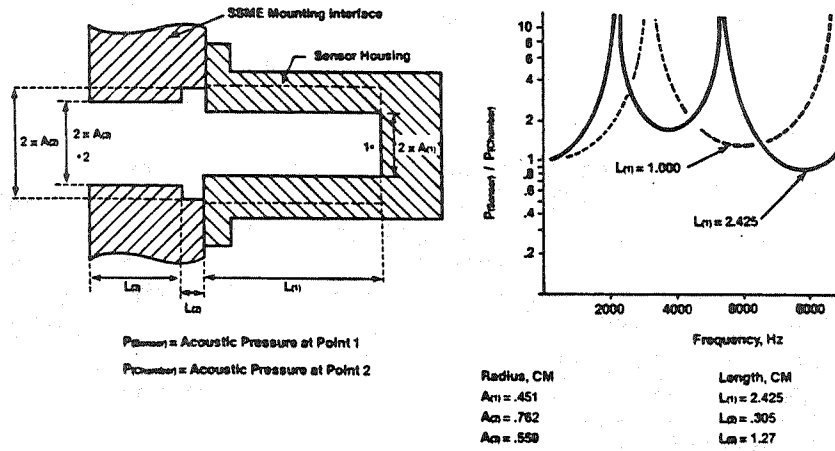


Figure 9. Influence of Pressure Port Length on Acoustic Frequency

**Acoustic Pressure Frequency Response of the SSME Mounting Interface/Sensor Housing with a Helmholtz Resonator Side Chamber**

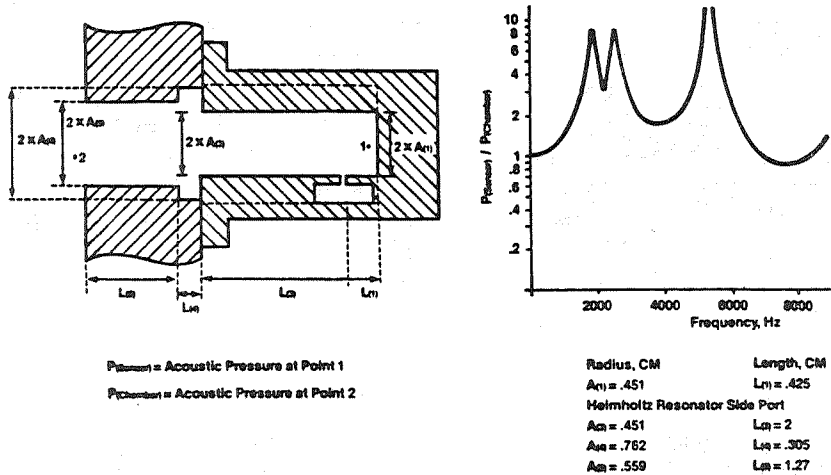


Figure 10. Influence of Pressure Port Side Chambers on Acoustic Frequency Response

media have not yet been demonstrated and are extremely challenging. These will be demonstrated at the conclusion of the prototype phase.

The intrinsic attributes of silicon pressure sensor technology, as summarized below, all contribute to the attainment of the research objectives.

- Solid State Reliability and Accuracy
- High Vibration and Pressure Capability
  - Small size
  - Low mass
- Integration of Sensor and Electronics on Single Chip
  - Reduces Package Complexity
  - Eliminates Errors Due to Thermal Gradients
- Extended Temperature Range Capability
  - Increased to -423°F and +250°F
  - Eliminates Need to Remote Mount Transducer
- Precision Laser Trim Calibration
- Enhancement of Frequency Response Increases Engine Performance Monitoring Capability
- Common Design for All Pressure Ranges
  - Enhances Ease of Manufacture
  - Cost Effective

#### CONCLUSIONS

The intrinsic attributes and innovativeness of Honeywell's Silicon Pressure Sensing Technology will significantly advance the state-of-the-art of pressure Transducers for the SSME application.

This in conjunction with successful completion of the NASA/MSFC Research Study, will provide the technology base for the development of Space Qualified Advanced Pressure Transducer Hardware for the current Operational Space Shuttle, as well as future "Smart Sensors" for the next generation of Space Vehicles.

## ACKNOWLEDGEMENTS

Successful accomplishments and completion of this research project require the efforts of many scientists and engineers at Honeywell. These include: W.T. Boord, E.B. Brynowsky, M.C. Glenn, G.E. Gustafson, R.F. McMullen, J.J. Shea and J.B. Starr.

## VORTEX SHEDDING FLOWMETERS FOR LIQUIDS AT HIGH FLOW VELOCITIES

J. D. Siegwarth  
National Bureau of Standards  
Chemical Engineering Science Division  
Boulder, Colorado 80303

### Abstract

A number of vortex shedding flowmeter designs for flow measurements in liquid oxygen ducts on the space shuttle main engines have been tested in a high head water flow test facility. The results have shown that a vortex shedding element or vane spanning the duct can give a linear response to an average flow velocity of 46 m/s (150 ft/s) in a 1½ inch nominal (41 mm actual) diameter duct while a vane partially spanning the duct can give a linear response to velocities exceeding 55 m/s (180 ft/s). The maximum pressure drops across the flow sensing elements extrapolate to less than 0.7 MPa (100 psi) at 56 m/s (184 ft/s) for liquid oxygen. The test results indicate that the vanes probably cannot be scaled up with pipe size, at least not linearly. The present successful designs of cantilevered vanes can be installed through the 11.2 mm (0.44 in) diameter pressure ports in the shuttle propellant ducts. The full vane shows some sensitivity to swirl and the cantilevered vane shows more.

### Introduction

The National Bureau of Standards (NBS) has been requested by NASA to determine whether vortex shedding flowmeters are suitable for measuring liquid oxygen (LOX) flow in ducts on the space shuttle main engine (SSME). The flowmeter will be subject to high levels of vibration, some swirl, and cryogenic temperatures. Also, in the main LOX duct, the maximum flow velocity is 50 m/s (164 ft/s) which is ten times higher than the maximum for which liquid flowmeters are commercially available.

The vortex shedding flowmeter consists of a vortex-shedding vane or strut spanning the pipe on a diameter<sup>1-4</sup> (see figures 4 and 6). The upstream face is generally flat with sharp corners along each edge. Vortices are alternately shed from these corners. The shed rate of these vortices is given by the Struhal equation

$$f = SV/d$$

where  $V$  is the velocity,  $d$  is the vane width and  $S$  is the Struhal number which is a constant nearly independent of any other fluid property for a properly designed meter. Thus, the flow rate is measured by counting vortices for a fixed time interval and multiplying by a conversion factor. The alternate shedding of vortices introduces a time varying pressure difference across the vane. This varying pressure can be measured with a pressure sensing device or can provide a time varying flow sensed by a thermal detector. This pressure provides a lift force that can be measured with a strain gauge. The vortices can also be counted downstream using ultrasonic techniques.

Whether the vortex shedding flowmeter could measure liquid flow at such high velocities can be determined at a much lower cost using water rather than LOX. Unfortunately, conventional water flow facilities are not capable of the high pressures required. The twenty-five diameter long section of straight pipe, recommended for proper meter installation, alone introduces an estimated 0.7 MPa (100 psi) pressure drop. The commercial flowmeter loaned to NBS as a starting point for the tests is estimated to introduce a 3.7 MPa (540 psi) pressure drop at 56 m/s flow.

Public Service Company of Colorado gave NBS permission to connect the test facility illustrated in Figure 1 to the penstocks at their Boulder Hydroelectric plant. The penstocks provide a 557 m (1828 ft) head and a maximum flow of 1.4 m<sup>3</sup>/s (22,000 gal/min). The 1½ in nominal diameter (41 mm actual) test section permitted testing of commercial meters of the smallest

size without using large quantities of water and introducing large pressure drops in the upstream portion of the flow test piping. The 4 in flowmeter served as a reference meter and was calibrated to 4.5 m/s flow velocity. It is assumed linear on up to 9 m/s.

### Flow Meter Test Results

The pressure drop across the only commercial meter tested varied as the velocity squared and extrapolated close to the manufacturers estimated 3.7 MPa at 56 m/s as shown in Figure 2. The vortex detector consisted of a magnetic disc oscillated near a pick up coil by the pressure fluctuations across the vane. The disc was demolished at high flow velocities and replaced by a 7 MPa (1000 psi) variable reluctance pressure transducer. As Figure 3 illustrates, the commercial meter was linear to about 30 m/s (100 ft/s).

The design specifications for a meter in the 4 in main LOX duct call for a maximum pressure drop not to exceed 0.7 MPa (100 psi) at 50 m/s flow. The next meter tested had a vane whose cross section was similar to the commercial meter vane but half the size. The vane was now 6.35 mm wide instead of 12.7 mm. As shown in Figure 2, the maximum pressure drop was now below 0.7 MPa. This vane was linear to about 45 m/s (150 ft/s) as shown in Figure 3. The shedding frequency of the narrower vane was slightly lower. This appears to contradict the Struhal equation. The 12.7 mm wide vane apparently blocked the pipe such that the velocity by the body is more than twice the velocity of the liquid past the 6.4 mm vane. The frequency does increase with decreasing width for vane widths below 6.4 mm.

The vortex detectors on these first vanes were pressure transducers referenced to ambient pressure and sensing the pipe pressure at a port in the side of the vane. The signal spectrum obtained with these vanes displayed on a spectrum analyzer had a high noise background and stray lines independent of flow.

The extra lines were probably resonances in the port and connecting line to the transducer.

The lift sensing vane shown in Figure 4 gave a greatly improved signal-to-noise ratio. Figure 5 shows some test data from models of this vane consisting of a 6.2 mm square vane section and a 6.4 mm wide triangular cross section.

The vane design shown in Figure 6 gave an even better signal-to-noise ratio. The vane portion of this meter was a beryllium copper link with a 5.1 mm wide by 4.2 mm deep rectangular cross section. The ferroelectric strain sensor (PZT) measured the strain in the mounting post. This link design eliminated vane failures from fatigue. The signal-to-noise ratio was 30 dB according to the spectrum analyzer. The filter band width in the signal-processing electronics could be set wide enough to include the flow range of interest without changing the count rate. Test results for this meter are shown in Figure 7 for swirl at various angles. This vane performed the best of any tested. A 3.8 mm wide trapezoidal cross-sectioned link vane tested had a vibration amplitude so extreme it was audible some distance from the pipe. The vane showed considerable wear after a very short period of testing and the sensitivity was not constant.

Since NASA would like to install a flow sensing device through a 11.2 mm pressure transducer port, partial vanes cantilevered from one wall of the pipe were tested. A preliminary test with the Figure 4 square vane cut off to 18 mm showed a vortex generated signal could be obtained. Similar vanes using the meter body and PZT sensor of Figure 6 with square, triangular and "T" shaped cross sections and spring sections of varying stiffness were tried. Many produced a vortex line in the signal spectrum but in general the signal-to-noise ratio was poor at best.

The spring mounted cantilevered vane evolved after testing a number of alternatives to the design

shown in Figure 8. Vanes with widths in the range of about 6 to 4.8 mm with depths around 80% of the width and sides at angles between  $90^\circ$  and  $93^\circ$  with the front face gave the best vortex signals and signal-to-noise ratios. The narrower vanes were better. Vanes 7.6 mm in width could use most of the 11.2 mm port diameter available but gave very poor results with the exception of one vane with a pressure sensor for vortices. The narrower vanes of Figure 8 design were giving sufficiently good signals to try a design that fit through a 11.2 mm port. Adding a 13 mm long by 11 mm cylindrical section between the vane and the mounting resulted in a poor signal-to-noise ratio again. A modification that placed the spring section in this cylindrical section with only a single PZT strain sensor produced a cantilevered vane with a signal-to-noise ratio exceeding 20 dB. This was the best cantilevered vane performance. Results of a flow test with this vane are shown in Figure 7 along with some swirl tests of the same width vane, with the Figure 6 mount. As Figure 7 shows, cantilevered vanes with the same widths as the link vane have a lower sensitivity. This probably results from some of the flow shifting to the side of the pipe opposite the vane.

Early swirl tests of a full vane showed a low sensitivity to swirl. Later tests of the link vane, Figure 7, showed that over  $15^\circ$  of swirl could be added 17 diameters upstream before the signal-to-noise ratio became poor. The sensitivity decreases somewhat, possibly from lost counts. The one cantilevered vane tested in swirl was more sensitive.

#### Tentative Conclusions

Some conclusions can be drawn from the tests thus far. Many of these are conditional in that other detector designs may give quite different results with the same vane. For instance, any cylinder with a cross section parallel to the flow and a flat upstream face with sharp corners must shed vortices. However, in these tests only vanes with a nearly rectangular cross section and with the width at least

equal to or greater than the depth gave strong signal spectrum lines. A trapezoidal cross sectioned vane with the wider side behind seems to be slightly better. The most successful vanes have had a flat back at least as wide as the front face. Probably, the above observations are the result of using the strain detection method. If an ultrasonic detection method were used, another vane shape may well be superior.

The mechanical design of the vane mounting and detection system seems to be important, judging from the results of tests of cantilevered vanes. As an example, the vane design shown in Figure 8 with a 5.1 mm wide vane gives a strong signal. When the 13 mm long cylindrical section was added between the base of the vane and the vane without any other change, a very poor signal was obtained. This result suggests that the vortex detection method works best when the spring section is close to the vane.

By reducing the width of a full vane to about 0.4 of the width of the commercial size vanes, a pressure drop less than 0.7 MPa (100 psi) at maximum flow is possible. The meter factor of such vanes are constant to about 46 m/s (150 ft/s) and repeatable to about 50 m/s (164 ft/s). The limit may be cavitation down stream of the vane. The tests of the link vane, however, show the break in the linearity occurs at nearly the same flow rate even when the pressure at the meter varies by more than 0.7 MPa (100 psi). This result suggests that the  $\Delta P$  may limit linearity more than the downstream pressure. This interpretation is not contradicted by the partial wave test results, which show a constant meter factor to much higher flow velocities for the same width vanes, since the pressure drop is lower.

Some commercial vanes above the 2 in nominal size are designed simply by scaling up all the dimensions. These 1½ in meter tests were done assuming that the same thing might be done with a 1½ in meter designed for high velocity. The cantilevered vane tests show that the vortex signal improved as the vane was narrowed from 7.6 mm width to 5 mm.

Larger vanes may not work any better in larger meters if flow separation from the vane sides is responsible for this result. This is ideal for the shuttle applications since this vane size fits easily through the 11.2 mm diameter pressure transducer ports. Tests of larger size meters should better define effects of vane width.

The 20% lower sensitivity of the cantilevered vane relative to a full vane of the same width probably results from the flow shifting away from the vane. This shifting of the flow to the opposite side of the pipe away from the vane probably contributes to the higher sensitivity of the cantilevered vane to swirl. Swirl generates higher transverse flow velocities at the cantilevered vane than at a full vane.

Some of the earlier testing suggested that reproducibility of a vane from one test to the next might be poor. Reproducibility was good from run to run and from vane to vane for vanes in the same body and with the same width and length if the depth and cross section are similar. Using orientation marks so a vane can be placed with the front face perpendicular to the flow direction is an important factor in reproducibility. The meters tested fit between pipe flanges. Gaskets protruding into the flow stream slightly can have a large effect on the meter factor, increasing it as much as 10 to 15%. Gasket intrusions, very likely caused at least some of the variations in meter factor noted in the earlier tests.

The vortex generated signal varies considerably in amplitude for all these vanes. The amplified signal amplitude goes from a few volts down to almost nothing for a cycle or two for almost every vane tested. This results in some amplifier gain sensitivity. The link vane signal, however, is sufficiently good that the gain of the first amplifier can be driven to saturation and output a signal of almost uniform amplitude. No instrumentation has yet been specifically designed for these flowmeters.

Testing to date suggests that the vortex shedding flowmeter can measure flow under the conditions prevailing in the space shuttle ducts. The testing is continuing in 51 mm (2 in) and 59 mm (2.3 in) diameter ducts.

#### Acknowledgements

The author wishes to thank Public Service Company of Colorado for permitting him to test flowmeters with water from their penstocks and George C. Marshall Space Flight Center who support this work through Government order # H-63458B.

#### References

1. White, D. F., Rodely, A. E., and McMurtrie, C. L., Flow, Its Measurement and Control in Science and Industry, Instrument Society of America, 1 (2) 967-974, (1974).
2. Lynworth, L. C., Physical Acoustics, Vol. XIV, Mason, W. P., and Thurston, R. M., editors; Academic Press, New York (1979).
3. Inkley, F. A., Walden, D. C., and Scott, D. J., Meas. and Control (GB) 13, 166 (1980).
4. Wiktorowicz, W. E., Proceedings, 57th School of Hydrocarbon Measurement, Norman, OK, 1982, 618. Available from K. E. Starling, 202 West Boyd, Norman, OK 73019.

Figure 1. The flowmeter test facility.

Figure 2. These curves show the pressure drop  $\Delta P$  across the meter as a function of flow with the pressure drop in an unobstructed pipe between pressure taps subtracted. The x data show  $\Delta P$  of the 12.7 mm wide commercial vane. The triangle data show  $\Delta P$  of a 6.2 mm square vane and the plus data that of a 6.35 mm wide vane with similar cross section to the commercial vane. The 5.1 mm wide link vane is shown by the circle data. This vane would be expected to have an even lower  $\Delta P$ . Different  $\Delta P$  instruments were used to measure the link vane  $\Delta P$  and the pipe correction which may account for the higher measured  $\Delta P$ . The curves show  $\Delta P$  as a function of velocity squared which the data should follow.

Figure 3. The counting rate of the 12.7 mm wide vane (circles) and the 6.35 mm wide vane (triangles) as a function of the average flow velocity in m/s.

Figure 4. Flowmeter with a lift-type sensor. The detector is a strain gauge on the upper end of the thin spring section. The lift forces caused by vortex shedding deflect this vane and generate the strain. The narrow annular gap allows, but limits, transverse movement of the upper end of the vane.

Figure 5. The triangles show the meter factor for a 6.2 mm vane of the Figure 4 design. This vane is more linear than a triangular cross sectioned vane with the same mount (circles). The pluses show data from a triangular vane of the same cross section with a pressure sensor which is more linear.

Figure 6. This approximately to scale drawing shows the link vane. A clamping ring and bolts for the plate to which the mounting post attaches has been excluded.

Figure 7. This figure shows the meter factors for the 5.1 mm wide link vane (upper data) and two 5.1 mm wide by 17.8 mm long partial vanes (lower data). The horizontal lines are drawn to demonstrate linearity and scatter. The circles and the diamonds show the link vane 22 and 5 diameters downstream respectively from a reducing section at zero swirl. The point-up triangles show the swirl generator set at  $11.5^\circ$ , the pluses at  $15.3^\circ$  and the x's at  $19.2^\circ$ . The point-down triangles show the Figure 6 design vane in zero swirl, the cross in square and the x minus points, the swirl generator set at  $5.1^\circ$  and at  $8.9^\circ$ , respectively. Beyond the maximum angles, the signal-to-noise ratio was too poor. The plus in a diamond points show the cantilevered vane inserted through a 11.2 mm diameter port.

Figure 8. Lift type cantilevered vane. The vortex sensing mechanism consists of two drive pins acting on PZT sensors connected so their output adds when the vane is moved transversely.

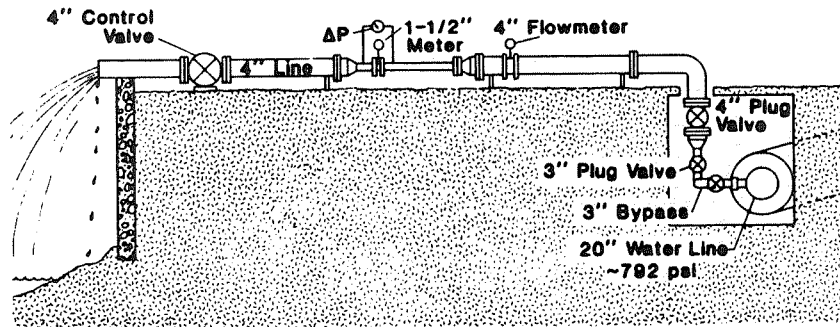


Figure 1.

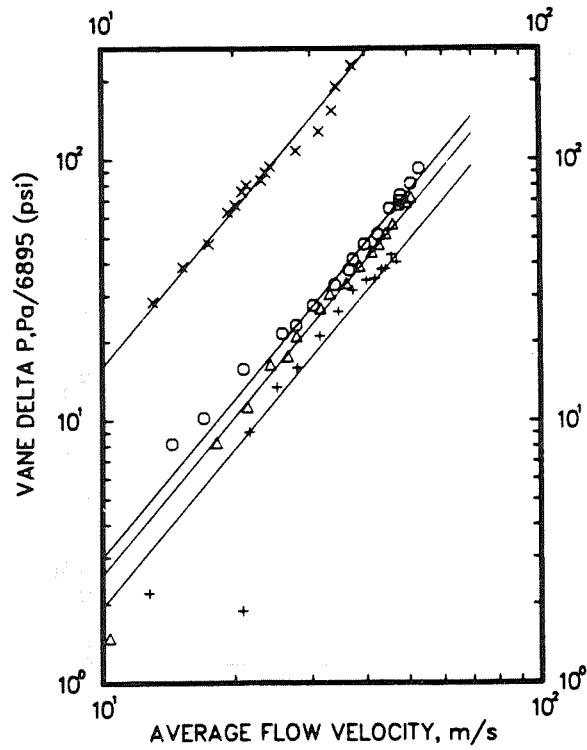


Figure 2.

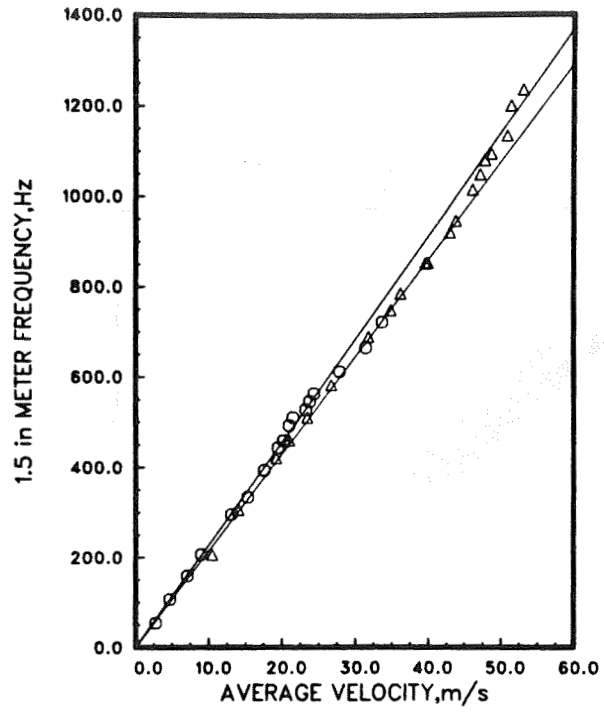


Figure 3.

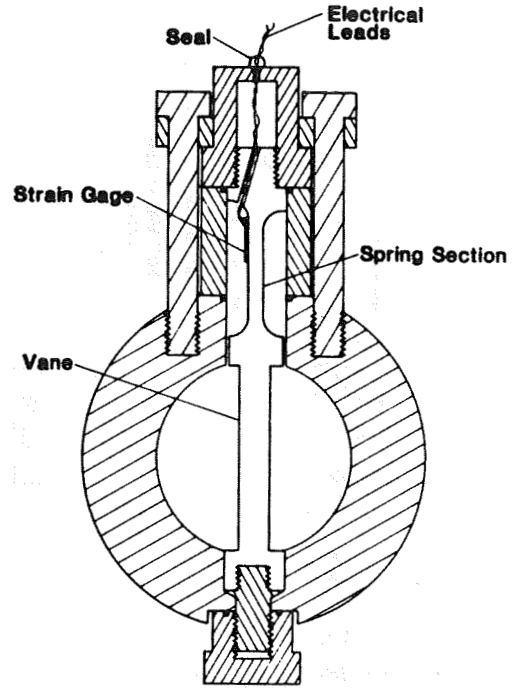


Figure 4.

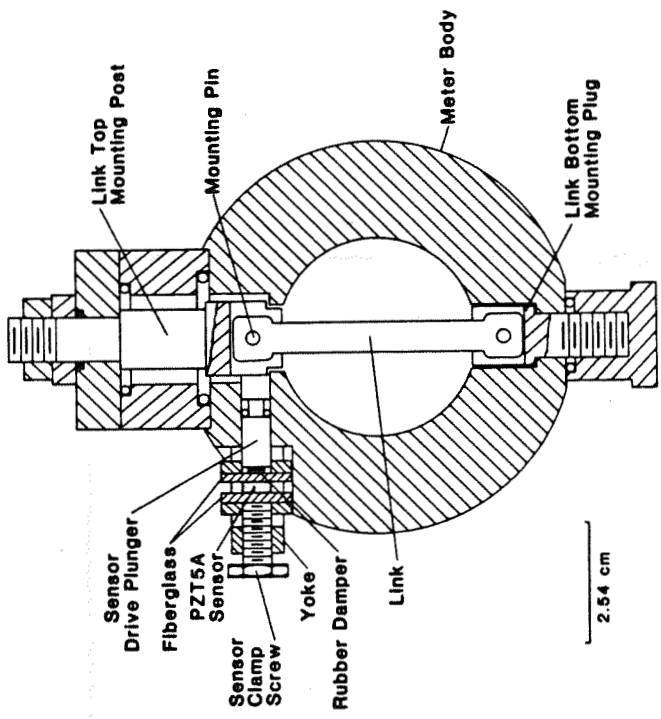


Figure 6.

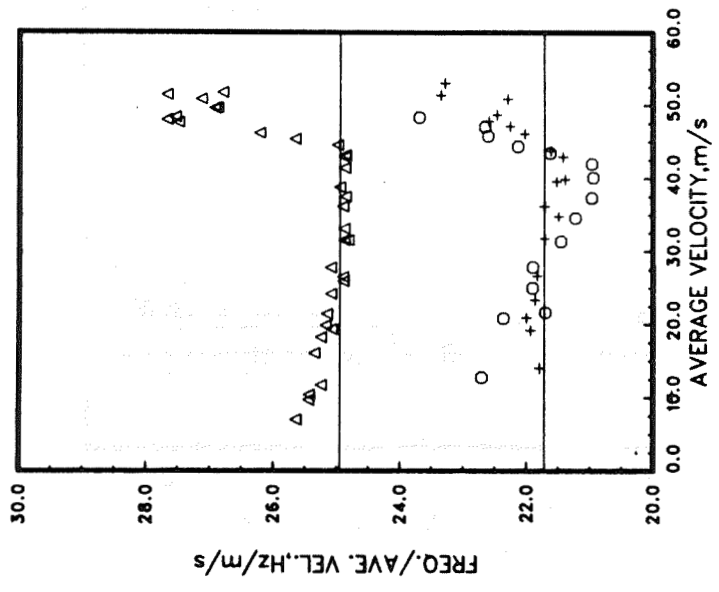


Figure 5.

# RESULTS OF 5.1mm WIDTH VANE TESTS

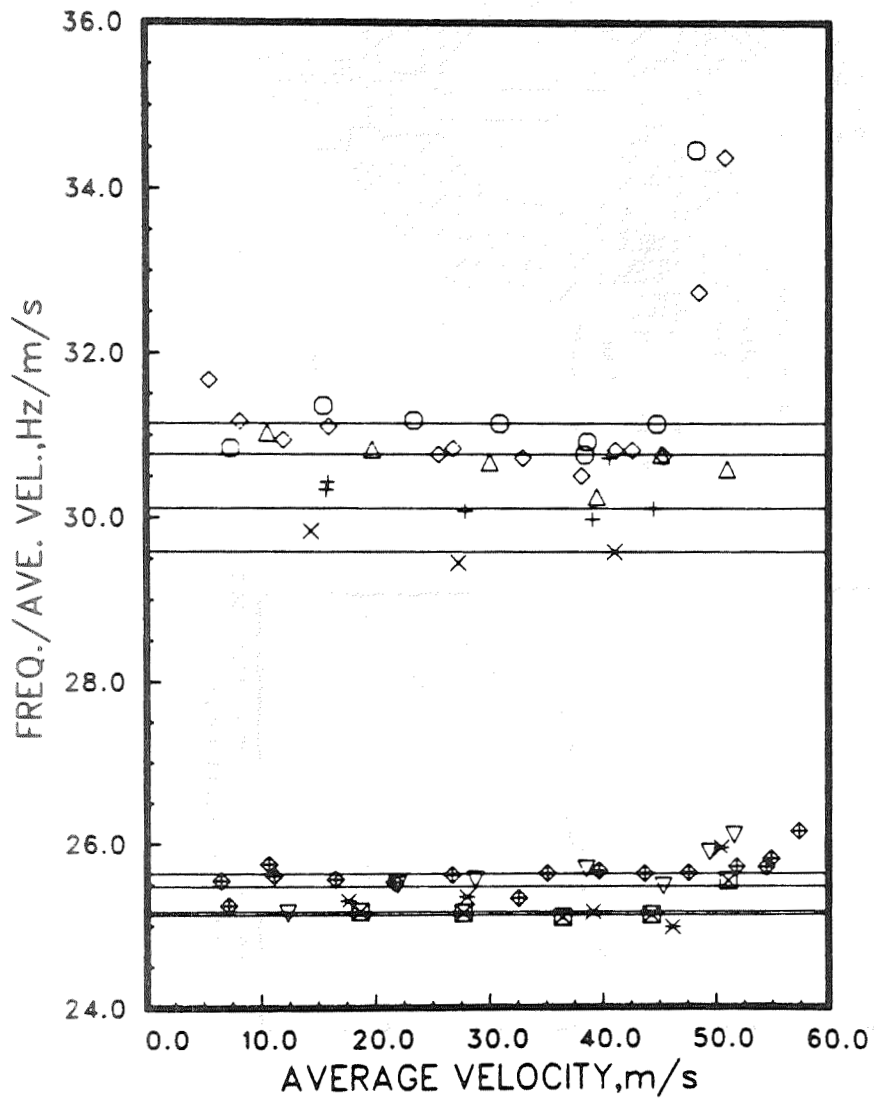


Figure 7.

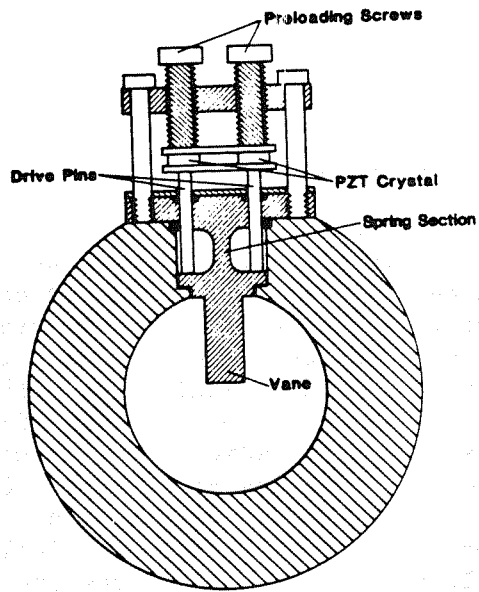


Figure 8.

REUSABLE ROCKET ENGINE TURBOPUMP  
CONDITION MONITORING

M. E. Hampson and S. Barkhoudarian

Rockwell International/Rocketdyne Division  
Canoga Park, California

Abstract

Significant improvements in engine readiness with attendant reductions in maintenance costs and turn-around times can be achieved with an engine condition monitoring system (CMS). The CMS provides real time health status of critical engine components, without disassembly, through component monitoring with advanced sensor technologies. Over 100,000 engine failure reports from the past 35 years were reviewed and categorized into 20 different modes of failure. Of the failure reports reviewed, rotor bearings and turbine blades were determined to be the most critical in limiting turbopump life. Over 200 in-flight and between-flight measurement technologies were then reviewed and matched to direct, noninferential detection of failure mode signatures. Three of these technologies were selected to monitor the rotor bearings and turbine blades: the isotope wear detector and fiberoptic deflectometer (bearings), and the fiberoptic pyrometer (blades). Signal processing algorithms were evaluated and ranked for their utility in providing useful component health data to unskilled maintenance personnel. Design modifications to current configuration Space Shuttle Main Engine (SSME) high pressure turbopumps and the MK48-F turbopump were developed to incorporate the sensors. Laboratory test fixtures have been designed for monitoring the rotor bearings and turbine blades in simulated operating environments.

---

Work performed under NASA-LeRC Contract No. NAS3-23349, under the direction of Robert Masters, Technical Manager.

## Introduction

Until the advent of the multiflight rocket engine of the Space Shuttle, the need for extensive engine condition monitoring was not seen as necessary or cost effective. However, the current life and performance requirements placed on the SSME and other high performance, reusable rocket engines now make a condition monitoring system (CMS) very attractive in these respects. Significant reductions in engine system, and therefore mission, costs, turnaround, and maintenance times can be achieved by implementing a CMS into the engine. These reductions are possible by knowing critical engine component health and expected remaining life from the information provided by the CMS. Other benefits include improved engine control and improved knowledge of the engine operating condition.

In September 1980, a program was initiated by the NASA Lewis Research Center with the objective of defining the requirements of a CMS and to perform tests of the system. The first phase of the program was a study in which engine failures from the past 35 years were reviewed and categorized into general failure categories. These categories were then matched to sensor technologies capable of monitoring them directly. The current phase further defined the CMS and determined design modifications necessary for incorporation into several high performance turbopumps. At the present, efforts are underway to design and fabricate turbopump simulation test fixtures in which laboratory testing of the CMS can be performed.

### Defining Turbopump Life Limiters

Documentation of rocket engine failures and/or discrepancies has been quite thorough over the past 35 years. Unsatisfactory Condition Reports (UCR) exist for every engine system made. This translates into over 100,000 individual pieces of information relating to engine failures or discrepancies. To successfully manage this volume of data for use on this program, a screening process was established that eventually reduced this number to 1771.

The first major screen was to consider only those engine systems still in production, and those designed for manned application in the Apollo program. The engine systems then remaining for consideration were the following:

1. SSME: Space Shuttle Orbiter
2. J-2: Saturn IB and V
3. H-1: Saturn IB
4. F-1: Saturn V
5. RS-27: Delta
6. Thor: Thor
7. Atlas: Atlas and Atlas-Centaur

The next screen eliminated from consideration those UCRs obtained from experimental engine systems. Following this, only those UCRs applying to engines during acceptance tests were allowed (an acceptance test contains hot-fire tests, mainstage simulations, and post-hot-fire tests). The next screen eliminated UCRs due to procedural problems, human error, low-frequency failures, obsolete hardware, and facility and vehicle discrepancies. Finally, since the bulk of the data was obtained from expendable rocket engine experience, only those remaining UCRs which had significance in a reusable rocket engine system were considered. Figure 1 shows the distribution of UCRs among the seven engine systems listed above.

Once the data base had been established, the next step was to search for common failure information. After a thorough review and grouping procedure, there emerged 16 general failure modes present in the data base:

1. Bolt Torque Relaxation
2. Coolant Passage Splits
3. Joint Leakage
4. Hot-Gas Manifold Transfer Tube Cracks
5. High Torque
6. Cracked Turbine Blades
7. Failure of Bellows
8. Loose Electrical Connectors
9. Bearing Damage

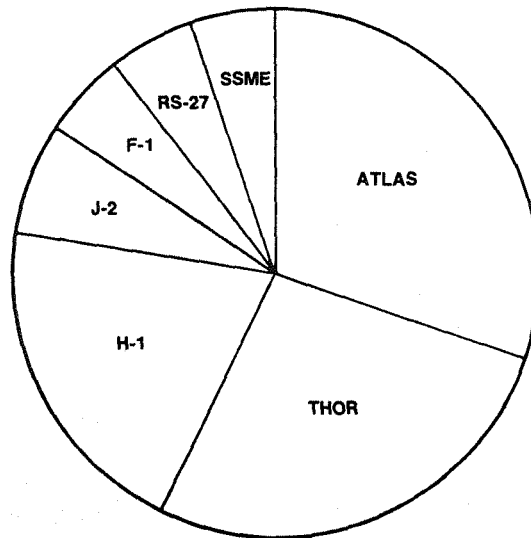


Fig. 1. Distribution of UCRs by Engine Systems After Screening

10. Tube Fracture
11. Turbopump Face Seal Leakage
12. Lube Pressure Anomalies
13. Valve Fails to Perform
14. Valve Internal Leakage
15. Regulator Discrepancies
16. Contaminated Hydraulic Control Assembly

As can be seen from the list above, several items apply directly to the reusable turbopump: high torque, cracked turbine blades, bearing damage, and face seal leakage. The second phase effort of the NASA Lewis program identified four other failure modes of the turbopump which were also considered significant: turbine blade erosion, turbine nozzle cracking, turbine sheet metal and housing cracking, and cavitation damage. The second phase effort has concentrated on developing the condition monitoring capability for the turbopump's turbine blades and bearings. This effort will be discussed in greater detail later in the paper.

### Correlating Sensors to Life Limiters

Attendant to each of the failure modes listed above is a characteristic failure mode signature. Each failure mode progresses along a failure propagation path, or one of several propagation paths, until engine shutdown or engine or engine component failure occurs. Figure 2 presents an example of a turbine blade failure propagation block diagram. At each major event along the path in Fig. 2 (e.g., blade cracking) there appears an attendant, detectable signature (e.g., vibration) that indicates the presence of that event. The next major step in the CMS study, then, was to develop failure propagation block diagrams for each of the failure modes, and correlate to the failure signatures advanced sensors capable of detecting their presence.

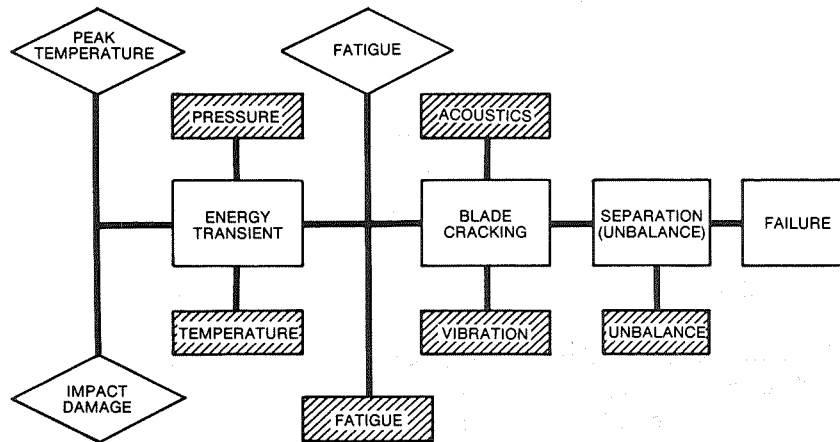


Fig. 2. Turbine Blade Failure

As a result of developing the failure propagation block diagrams, 23 distinct failure mode signatures, or measurands, were identified for in-flight and between-flight condition monitoring. For example, ball bearing damage exhibits such failure mode signatures as vibration, wear particles, excessive temperature, and rpm tailoff. Table 1 correlates each of the failure modes to the 23 signatures. Also indicated in Table 1

Table 1. Failure Modes Correlated to Signature

FAILURE MODE	FAILURE MODE SIGNATURE																										
	VIBRATION	ACOUSTICS	LEAKS	FRETTING	EXTENSION	METAL EMBRITTLEMENT	PRESSURE TRANSIENT	FLOW REDUCTION	M/S SHIFT	COMBUSTION TEMPERATURE RISE	TEMPERATURE TRANSIENT	TORQUE RIPPLES	WEAR PARTICLES	PM PARTICLES	CONTAMINANTS	BALANCE	TORQUE RELAXATION	SEPARATION	DEFORMATION	MOISTURE	EXCESSIVE TEMPERATURE	EXCESSIVE FRICTION	FOREIGN OBJECT	PHYSICAL INTERFERENCE	STUCK COMPONENTS	GALLING	
BOLT TORQUE RELAXATION	I																										
COOLANT PASSAGE LEAKAGE/RESTRICTION																											
JOINT LEAKAGE		IB																									
TRANSFER TUBE CRACK																											
HIGH TURBOPUMP TORQUE																											
CRACKED TURBINE BLADE																											
TURBINE BLADE EROSION																											
TURBINE NOZZLE CRACKING																											
TURBINE SHEET METAL AND HOUSING CRACKING																											
CRACKED CONVOLUTION, BELLOWS, SHIELDS																											
LOOSE ELECTRICAL CONNECTORS																											
BALL BEARING DAMAGE																											
SMALL TUBE FRACTURE																											
TURBOPUMP SEAL LEAKAGE																											
CAVITATION DAMAGE																											
LUBE PRESSURE ANOMALIES																											
VALVE FAILURE																											
VALVE INTERNAL LEAKAGE																											
REGULATOR DISCREPANCIES																											
CONTAMINATED HYDRAULICS																											

I = IN FLIGHT; B = BETWEEN FLIGHT

is whether the signature is used for in-flight condition monitoring (I), between-flight condition monitoring (B), or both (IB).

Four categories of sensing technologies exist that apply to rocket engine monitoring: conventional, such as temperature and pressure; rocket engine, i.e., sensors such as temperature and accelerometers with rocket engine operating experience; state of the art, such as the fiberoptic pyrometer and isotope wear detectors; and novel technologies, such as the exo-electron fatigue detector. The first step taken in identifying candidate sensors applicable to the CMS was to perform a literature search. A search of nearly six million citations on the subject yielded 289 abstracts and 78 articles, from which over 200 candidate sensors were selected. A screening procedure analogous to that used in reducing the UCR data base was established for final sensor selection. Based on the screening criteria, the list of 200 candidate sensors was reduced to 19: 11 novel, 6 state of the art, and 2 in the rocket engine category.

The 19 candidate sensors were then subjected to a grading and ranking procedure. Each of the sensors has liabilities and virtues in both technical and economic aspects. Many of the novel technologies require development time before being acceptable for use. The 19 candidates were evaluated in each of these areas and compared to the 20 failure modes listed in Table 1. The final sensor selection was made from this comparison. Detection of each failure mode was satisfied first, then only those sensors with the highest score were selected. Final sensor selection versus the failure modes is shown in Table 2. Note that several of the failure modes were not detectable with any viable condition monitoring technique. Also indicated in this table is whether the monitoring technology is an in-flight monitoring technology (I), between-flight monitoring technology (B), or both (IB).

Table 2. Sensors Correlated to Failure Modes

SENSORS	FAILURE MODES																			
	BOLT TORQUE RELAXATION	COOLANT PASSAGE LEAKS	JOINT LEAKAGE	TRANSFER TUBE CRACKS	HIGH TURBOPUMP TORQUE	CRACKED TURBINE TORQUE	TURBINE BLADE TORQUE	TURBINE BLADE EROSION	TURBINE NOZZLE CRACKING	CRACKED SHEET METAL AND HOUSING CRACKING	LOOSE CONVOLUTION, BELLAWS, SHIELDS	BALL BEARING DAMAGE	SMALL TUBE FRACTURE	TURBOPUMP SEAL LEAKAGE	CAVITATION DAMAGE	LUBE PRESSURE ANOMALIES	VALVE FAILURE	REGULATOR INTERNAL LEAKAGE	CONTAMINATED DISCREPANCIES	CONTAMINATED HYDRAULICS
FIBEROPTIC DEFLECTOMETER																				
PYROMETER																				
TUNABLE DIODE-LASER SPECTROMETER	IB																			
ISOTOPE WEAR DETECTOR				IB	B							IB	IB			IB	IB			
ULTRASONIC THERMOMETER		I																		
OPTICAL TACHOMETER																				
ULTRASONIC FLOWMETER		I																		
DIGITAL QUARTZ PRESSURE SENSOR		I																		
HALOGRAPHIC LEAK DETECTOR	B	B																		
THERMAL CONDUCTIVITY LEAK DETECTOR		B																		
EXO-ELECTRON FATIGUE DETECTOR					B															
CONNECTOR CONTINUITY CHECKING									B											
PARTICLE ANALYSIS				B						B			B			B	B	B	B	B

I = IN-FLIGHT MEASUREMENT; B = BETWEEN-FLIGHT MEASUREMENT

Selecting Useful Turbopump Condition-Monitoring Algorithms

Completion of the sensor selection process for the failure modes signaled the end of the first phase of the NASA Lewis program. It was decided at this point to develop a CMS for the most critical subsystem of pump-fed, liquid rocket engines: the reusable turbopump. The remainder of this paper, therefore, deals exclusively with the development of a CMS for the turbopump.

Failure mode detection does not stop upon receiving a signal from the sensor. Many of the signals received contain large amounts of information that reveal component health only upon processing and correlating to other sensor outputs. The signal processing selected for use must also be easily

used by nonskilled maintenance personnel, i.e., they must provide personnel with reliable go/no-go information. A block diagram illustrating the path followed by the failure mode signature is shown in Fig. 3. The most critical part of the CMS is in the signal processing and decision making processes.

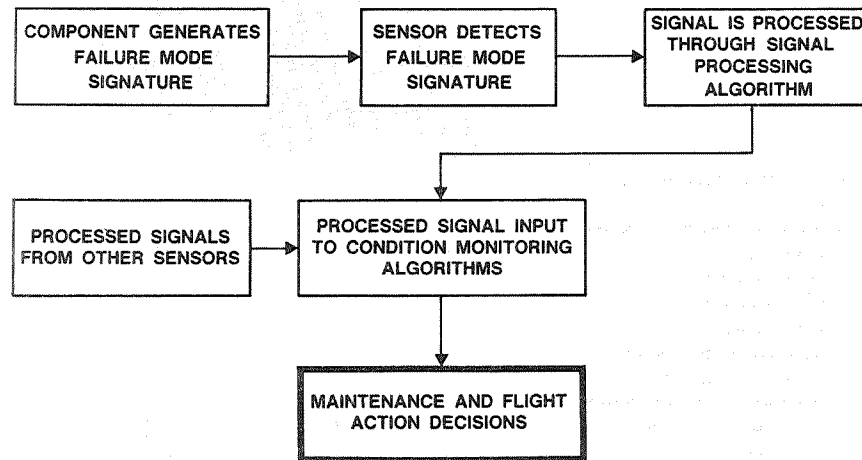


Fig. 3. Progression of Failure Mode Signatures

Each failure mode signature was reviewed and analyzed to determine what sensor output would occur during nominal and off-nominal component operation. Periods of steady-state operation were selected as the baseline engine operating condition for initial selection of the signal processing algorithms. Transient operating periods were incorporated later since they contain significant amounts of information relating to the remaining useful life of the component.

Fourteen signal processing algorithms were evaluated for their usefulness in providing component condition information. Listed in Table 3 are the algorithms along with the four criteria used in their evaluation: sensitivity, intelligence, isolation, and simplicity. Sensitivity is the ability of the algorithm to detect small or subtle changes in sensor output.

Table 3. Evaluation of Available Signal Processing Algorithms

ALGORITHMS	SENSITIVITY	INTELLIGENCE	ISOLATION	SIMPLICITY
AMPLITUDE HISTOGRAM	L	M	M	L
RMS HISTOGRAM	L	M	M	L
FILTERED HISTOGRAM	H	M	H	L
CROSS CORRELATION	H	M	M	L
TRANSFER FUNCTION	H	H	M	L
PRODUCTION HISTOGRAM	L	M	L	L
RATIO HISTOGRAM	M	M	M	L
DIFFERENTIATED HISTOGRAM	H	M	H	L
PHASE DIAGRAM HISTOGRAM	L	M	L	M
TIME PROFILE	L	L	L	L
POWER SPECTRUM DENSITY	L	H	M	M
INTEGRAL OVER THRESHOLD	L	L	L	H
RPM PROFILES	L	L	L	L
CAMPBELL DIAGRAM	L	L	L	L

GRADING LEGEND:  
L = LOW  
M = MID  
H = HIGH

Intelligence indicates the general utility of the information provided. Isolation refers to the algorithm's ability to discriminate between common signals generated by different sources. Simplicity is the ease at which the desired information can be retrieved. During the forthcoming system tests of the CMS, all 14 signal processing algorithms will be evaluated to determine their ability in producing the desired information.

Once the signal is processed, it is correlated with processed signals from other sensors, where appropriate, through a decision-making comparator. Routing the processed signals through a comparator increases confidence that the failure mode of interest is occurring. This is due to the fact that all failure modes generate more than one failure signature and can therefore be monitored by multiple sensors. All sensors capable of detecting a particular failure mode would have to register a change from nominal output before occurrence of the mode was confirmed.

### Testing the CMS in Turbopump Simulators

Evaluation of the CMS developed up to this point under controlled laboratory conditions is the next logical step toward full development of a CMS. Testing of the CMS in an operating turbopump would not only be expensive and hardware intensive, but may not provide a thorough understanding of the details involved in the signal processing and decision-making algorithms. It was at this point in the NASA Lewis program that the decision was made to perform condition monitoring tests on the two most critical turbopump failure modes identified: the rotor bearings and turbine blades.

A Turbopump Simulation Test Plan (TSTP) was developed that described the testing proposed to fully evaluate monitoring the condition of turbopump bearings and turbine blades. In developing the TSTP, environments and operating conditions to which these components are exposed during actual turbopump operation were identified. The baseline turbopumps to which the simulators were designed are the SSME High Pressure Fuel and High Pressure Oxidizer Turbopumps (HPFTP and HPOTP). Also defined in the TSTP are tests that evaluate the ability of the sensor to survive the environment in which it is installed.

Tests on the turbopump bearings simulate those conditions found in the SSME high pressure oxidizer turbopump turbine end bearings. The baseline conditions identified are the following:

1. Rotating radial loads up to 2000 lbf
2. Axial loads up to 6000 lbf (transient)
3. Speeds to 30,000 rpm
4. Liquid oxygen flowrates to 30 gpm

A bearing tester was designed and fabricated that emulated all of the above conditions except the liquid oxygen environment; liquid nitrogen is used as the coolant instead. As shown in Fig. 4, the tester incorporates two old configuration SSME high pressure oxidizer turbopump bearings, P/N RS007787, mounted

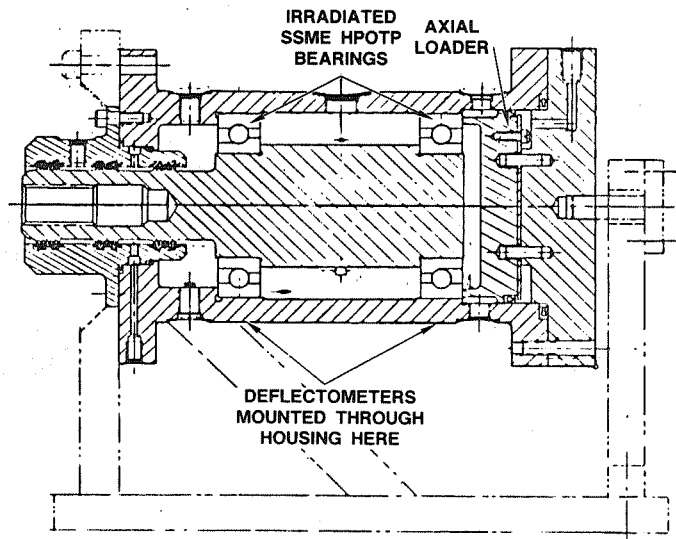


Fig. 4. Cryogenic Bearing Tester

to a shaft and installed in a housing that somewhat resembles a porcupine. Each bearing can be monitored with six fiberoptic deflectometers monitoring its outer surface. Either bearing can be monitored with the isotope wear detector by surface layer irradiation of part of the bearing, and then monitoring the wear *in situ* without disassembly. The drive-end bearing (shown to the left in the figure) is also monitored upstream and downstream by pressure and temperature probes. Accelerometers are mounted to the housing in three perpendicular planes to act as both real-time test monitors and known correlation to data received from the deflectometers. Axial loads are provided by a pneumatic piston to the right of the slave bearing and acting on the outer race of the same. Radial loads are provided by mounting weights in the form of set screws to the shaft. Liquid nitrogen can flow in any one of three directions: from drive-end to slave-end, vice-versa, or from midtester out to both bearings (parallel flow path).

Monitoring of bearing condition by the fiberoptic deflectometer is accomplished by utilizing reflected light from the bearing outer race surface.

Figure 5 illustrates this principle. Light is transmitted by a portion of the fibers in the probe to the race surface. Some of this light is reflected off the surface and is received by the remainder of the fibers. This light is then processed through a photodetector to provide an electrical signal proportional to bearing race surface deflection. Frequency and amplitude content analysis of the signal provides information on bearing condition.

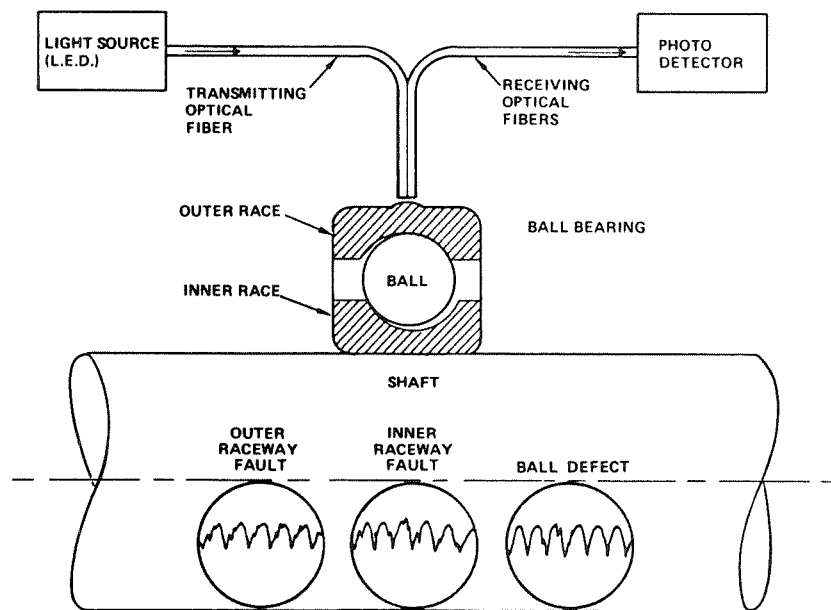


Fig. 5. Fiberoptic Deflectometer

The isotope wear detector monitors bearing health by directly measuring the amount of wear in a component that has been irradiated. For example, monitoring of bearing health by measuring outer race ball track wear depth is accomplished by irradiating the ball track to a certain depth and width (e.g., 0.032 x 0.025 inch), then monitoring the change in radioactive count rate of the isotope present in the race with a photomultiplier crystal. After accounting for half-life decay of the isotope, a direct determination of wear depth can be made from a calibration curve that

has correlated change in countrate to wear depth for the particular material in use. Measurements with the isotope wear detector are made *in situ*, since the radiation will penetrate the turbopump housing material. Activity levels of the isotope are quite low, usually below 10 microcuries, and therefore pose no health hazards to maintenance personnel. Note that the isotope wear detector is capable of monitoring any component that exhibits wear as a failure mode signature.

Tests on the turbine blades will simulate those conditions found in the SSME high pressure fuel turbopump first-stage turbine. The steady-state operating conditions found in the high pressure fuel turbopump are the following:

1. Speed to 38,000 rpm
2. Blade temperature to 1900 R
3. Active turbine disk cooling

An existing test fixture built on a previous NASA program proved to be sufficient in meeting the test goals. Shown in Fig. 6 is the rotating diagnostic device, more commonly known as the whirligig. The whirligig was originally built for evaluation of turbine blade dampers for both the SSME high pressure fuel and oxidizer turbopumps. It incorporates a 100-

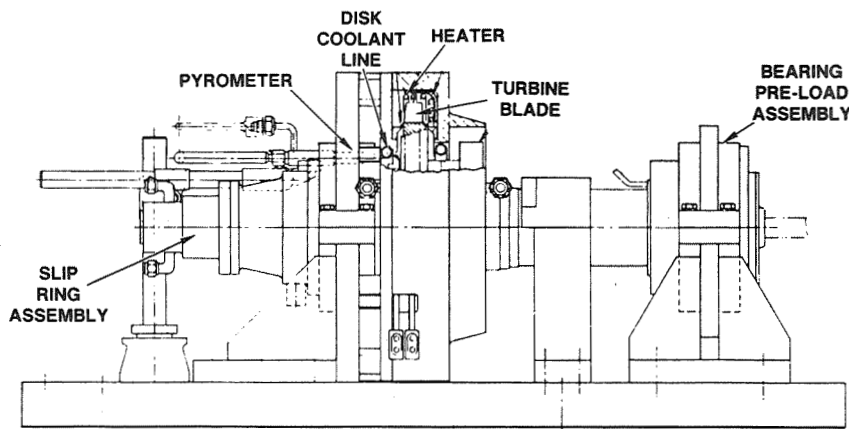


Fig. 6. Turbine Blade Monitoring With Pyrometer

channel slip ring assembly, soft bearing supports for excursion through critical speeds, and a bearing preload assembly, shown to the right in the figure. Modifications to the whirligig to meet the needs of this test program are incorporation of resistance heating elements in the turbine blade passage, and the addition of a coolant ring to maintain acceptable disk temperatures. The fiberoptic pyrometer monitors the blades through a window in the blade passage housing and is mounted to a support with 5 degrees of freedom: X, Y, Z, pitch, and yaw.

Monitoring turbine blade health is accomplished by monitoring thermal radiation emitted from the hot blade. Figure 7 illustrates operation of the pyrometer. Radiation emitted by the blades is focused by

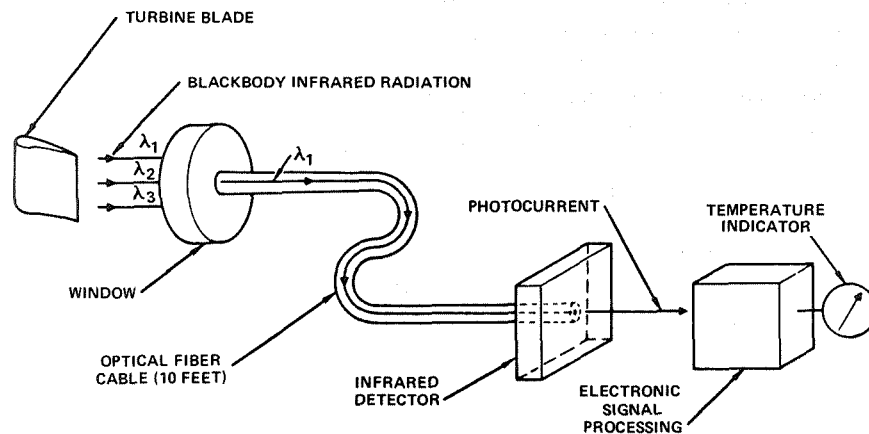


Fig. 7. Optical Pyrometer

the pyrometer's lens on fiberoptics, which transmit the radiation to a silicon photodetector. The photodetector provides an electrical signal proportional to turbine blade temperature, which is then processed to determine blade temperatures, blade temperature history, the presence of hot or cold blades, etc. Frequency reponse time of the associated electronics for the pyrometer must be high to accommodate the high blade passing frequency found in the turbopumps.

Environment compatibility is required only for the deflectometer and pyrometer. The isotope wear detector is a between-flight measurement and therefore will not be exposed to the operating turbopump environment. The test fixture shown in Fig. 8 evaluates the ability of the deflectometer to withstand the physical environment near the turbopump bearings. The test fixture is capable of pressures to 5000 psig and temperatures from cryogenic to 500 F, which simulate the extremes found in the bearing vicinity.

While the temperatures and pressure vary, the deflectometer is monitoring a stationary target mounted to its tip to register any changes in output that may occur during test. The test fixture shown in Fig. 9 evaluates the pyrometer's ability to withstand the environment found in the turbopump turbine. The test fixture is an exhaust duct to another tester that utilizes the combustion

products of hydrogen and oxygen. Temperatures in the flow passage reach 2000 F at pressures up to 3000 psig, which exceed current SSME high pressure fuel turbopump operating conditions. The pyrometer monitors a stationary, thermocoupled target on the opposite side of the flow channel from any one of three orientations: 20, 45, or 70 degrees. The actual surface that the pyrometer monitors is removable so that a variety of representative turbine blade materials can be viewed.

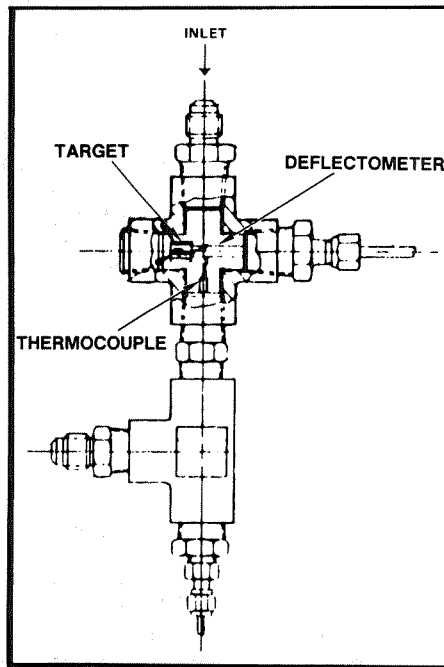


Fig. 8. Deflectometer Environment Tester

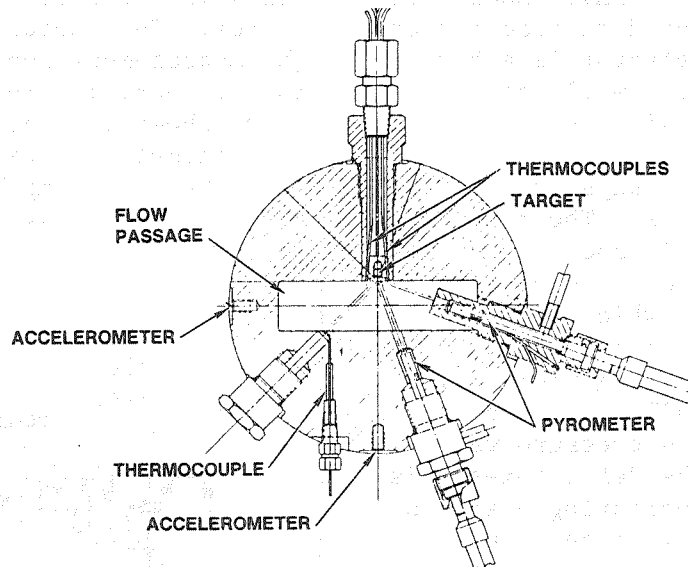


Fig. 9. Pyrometer Environment Tester

Cooling of the pyrometer, which has a maximum allowable face temperature, is achieved by a low level gaseous nitrogen purge.

#### Incorporating the CMS into Turbopumps

The optimum starting point in CMS design for a turbopump is, of course, at the beginning of the turbopump design itself. One program currently being directed by NASA Lewis is doing just that: Integrated Control and Health Monitoring for the Orbital Transfer Vehicle engine system. However, existing turbopump systems stand to gain significant savings in cost and turnaround time by retrofitting a CMS where possible. During the course of the current program, design layouts were developed for the SSME high pressure fuel and oxidizer and the MK48-F turbopumps, which incorporated the fiberoptic deflector, fiberoptic pyrometer, and isotope wear detector.

A representation of retrofitting a CMS in an existing turbopump design is shown in Fig. 10 and 11

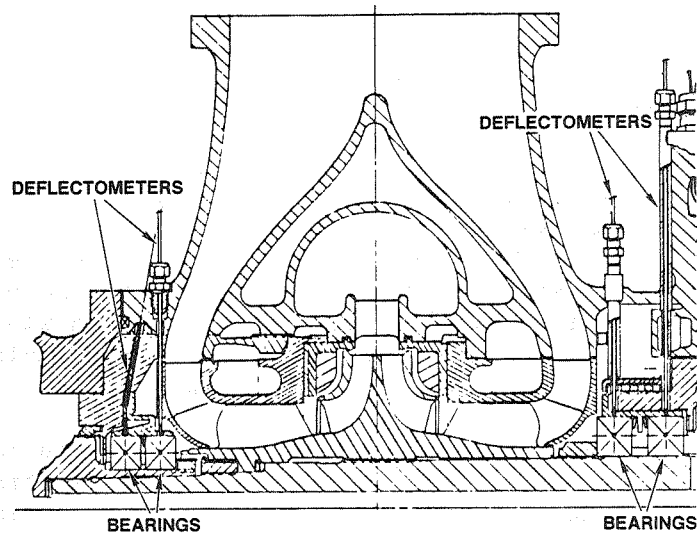


Fig. 10. Fiberoptic Deflectometers Monitoring SSME HPOTP Bearings

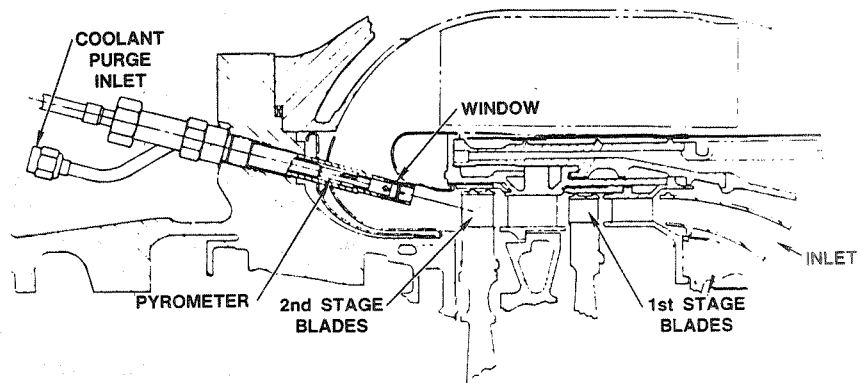


Fig. 11. Fiberoptic Pyrometer Monitoring SSME OPOTP Second-Stage Turbine Blades

for the SSME high pressure oxidizer turbopump. Shown in Fig. 10 is the design layout for installation of the fiberoptic deflectometer to monitor bearing condition. The fiberoptic probes penetrate the turbopump housing in the vicinity of the pump inlet

volute, continue through the housing, and penetrate the bearing isolators before obtaining an unobstructed view of the bearing race surface.

Figure 11 illustrates installation of the fiber-optic pyrometer for monitoring the second-stage turbine blades. The pyrometer is installed in the flange and penetrates the turbine discharge liner before being able to view the turbine blades via a window mounted in the sight tube. A coolant purge maintains acceptable temperatures in the pyrometer.

The isotope wear detector monitors radiation emitted by the irradiated bearing, which penetrates the turbopump housing in all directions. Readings with the sensor can be taken using a hand-held detector or by placing the detector in a simple, temporary mounting fixture in the vicinity of the bearings. Therefore, no design modifications are required to incorporate the isotope wear detector.

Conclusion: Saving Time and Money  
With a CMS

The ever-increasing demands placed on rocket engine performance and life expectancy establish the need to develop and incorporate a condition monitoring system into the engine system. The efforts put forth during this program to date have laid the groundwork and developed the data base from which all condition-monitoring systems can benefit. Common failure modes present in all rocket engine systems have been identified, screened, and categorized. Conventional to novel and state-of-the-art sensing technologies have been identified and correlated to the failure modes. Sensor signal and condition monitoring algorithms have been evaluated for their ability to directly determine the occurrence of the particular failure mode, and in predicting the component's remaining useful life. Testing is underway at this writing of the CMS in a laboratory setting.

Reductions in engine maintenance costs and turn-around time are easily recognized once the CMS is implemented. For instance, the estimated turnaround time savings alone for the SSME upon implementation of a CMS is better than 50 percent. This translates into a significant dollar savings over the useful life of the engine once launch delays, labor, and hardware requirements are considered.

Valuable knowledge of engine operating conditions can also be obtained through additional manipulation of the data provided by the CMS. Use of this knowledge can improve engine control capability, new component performance, and assessment of development engine performance. Knowledge of engine safety is a direct, significant output from the use of this information when used in conjunction with condition data provided by the algorithms. System safety information is perhaps the most important product of the CMS.

#### Bibliography

MacGregor, Charles, A., Reusable Rocket Engine Maintenance Study, Final Report, NASA CR-165569, January 1982.

## NONINTRUSIVE SHAFT SPEED SENSOR

S. Barkhoudarian, L. Wyett  
and J. Maram

Rockwell International/Rocketdyne Division  
Canoga Park, California

### Abstract

A computerized literature search on nonintrusive/noncontacting speed sensing technologies was performed, resulting in 550 abstracts and 42 articles. Fourteen techniques were identified and theoretically analyzed, resulting in the recommendation of the Microwave, Infrared, and Magnetic technologies for experimental evaluation.

Test results with a novel magnetic approach, consisting of a permanent magnet placed on the rotating shaft and a pickup coil placed on the housing, indicated detection of a strong signal (25 mV) from 3.5 inches at the lowest required speed (500 rpm).

### Introduction

Reusable rocket engines such as the Space Shuttle Main Engines (SSME), the Orbital Transfer Vehicles (OTV), etc., have throttling capabilities that require real-time, closed-loop control systems of engine propellant flows, combustion temperatures and pressures, and turbopump rotary speeds. In the case of the SSME, there are four turbopumps that require real-time measurement and control of their rotary speeds. Variable-reluctance magnetic speed sensors were designed, fabricated, and tested for all four turbopumps, resulting in the successful implementation and operation of three of these speed sensors during each of the 12 Shuttle flights. The fourth speed sensor, shown in Fig. 1, used in the High Pressure Oxidizer Turbopump (HPOTP), shown in Fig. 2, was removed due to structural weaknesses of its 3.5-inch long intrusive probe

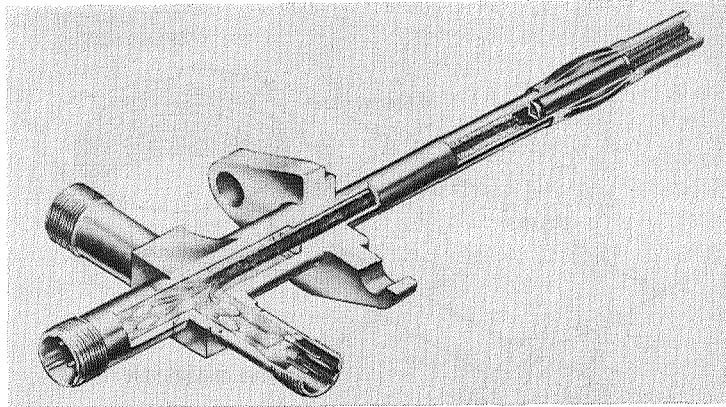


Fig. 1. High-Pressure Oxidizer Turbopump Speed Sensor

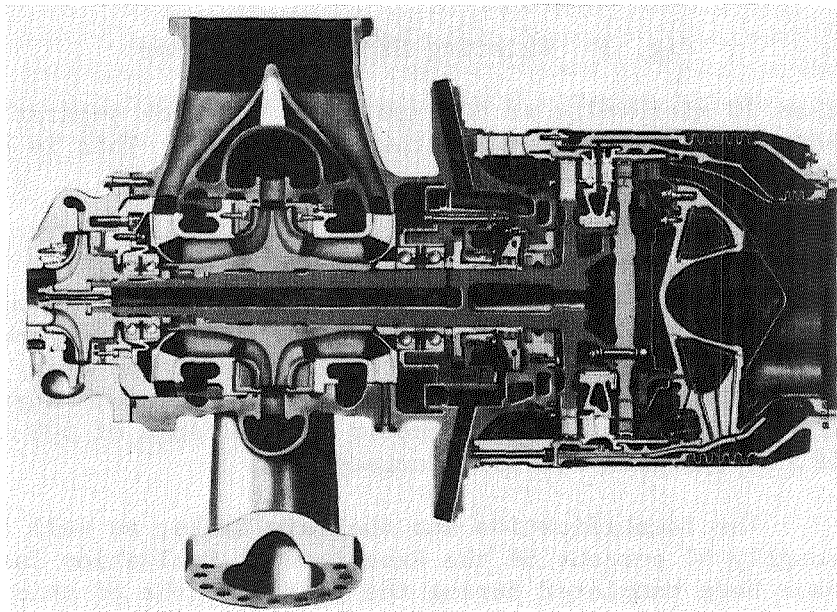


Fig. 2. High-Pressure Oxidizer Turbopump

tip, which had to withstand 200 ft/sec flow forces and 34.5 grms vibration in a liquid-oxygen environment, where loose-part collisions can ignite the propellant and have catastrophic consequences. The probe tip, shown in Fig. 3, could not have been shortened because the signal amplitude would have been reduced to less

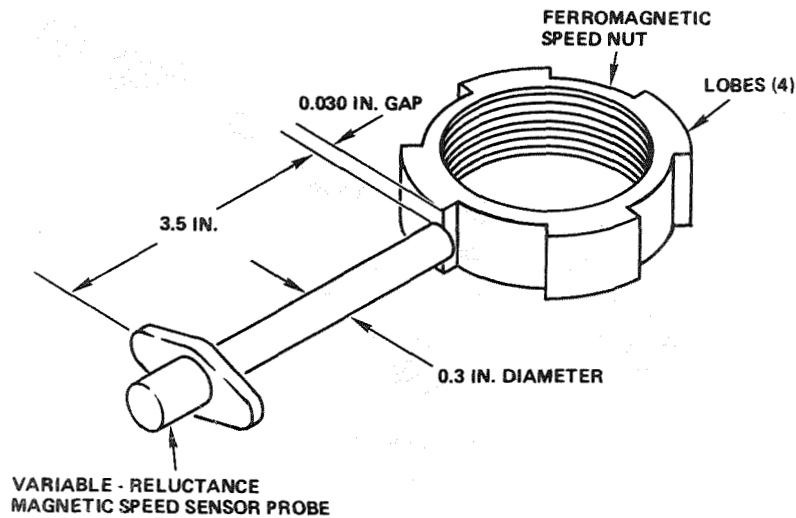


Fig. 3. Existing SSME Speed Sensor

than 20 microvolts at 500 rpm for a 3.5-inch separation between the speed nut and the pickup coil. This is an impractical signal value for SSME applications.

To overcome this problem, a technology program was initiated by MSFC resulting in a contract award to Rocketdyne. This program consists of identification, analysis, experimental evaluation of nonintrusive speed measurement techniques, and preliminary design of a selected nonintrusive speed sensor capable of measuring the speed of any SSME turbopump in the range of 500 to 50,000 rpm with  $\pm 25$  rpm accuracy.

The Identification and Analysis Tasks, as well as roughly 60 percent of the Experimental Evaluation Task, have been completed during the past 8 months of this 12-month program.

#### Identification and Description

To identify all nonintrusive speed sensing technologies, computerized literature searches were performed to identify published articles citing keywords such as "remote," "nonintrusive," "speed," "sensor," and "measurement." These searches yielded 550 abstracts

from which 42 articles were obtained for review, resulting in 6 new technologies in addition to 8 technologies already known to us, as shown in Fig. 4.

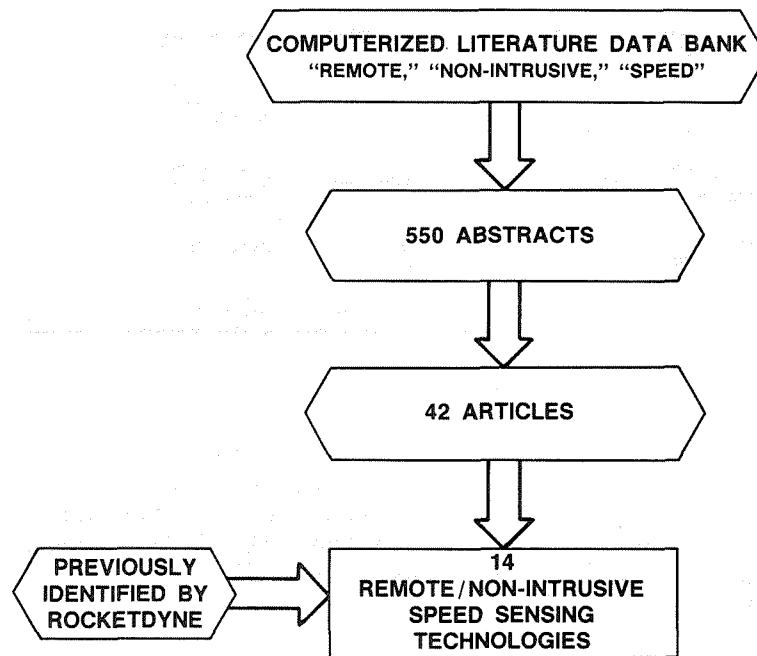


Fig. 4. Literature Search

These 14 candidate remote/nonintrusive speed sensing technologies, as shown in Table 1, were subjected to the subsequent theoretical and/or experimental evaluation. Each of the 14 technologies is briefly described below.

#### Capacitive Speed Sensor

A capacitive speed sensor consists of a conducting plate located at the pump housing wall and a conducting speed nut. It detects the varying capacitance due to variation in the separation between the plate and the rotating lobed speed nut and determines the shaft rotation speed from the repetition rate of these signals.

Table 1. Candidate Remote/Nonintrusive Speed (Sensing Technologies)

TECHNOLOGY	ANALYSIS APPROACH	CRITICAL PARAMETER
VARIABLE-SOURCE MAGNETIC HALL-EFFECT WIEGAND-EFFECT	MAGNETICS	LOW-RPM SIGNAL AMPLITUDE
INFRARED MICROWAVE AMPLITUDE MODULATION ELECTROMAGNETIC DOPPLER SHIFT	ELECTROMAGNETIC WAVE THEORY	CAVITATION/BUBBLE ATTENUATION
ACCELEROMETER FIBEROPTIC PROXIMETER PRESSURE PULSATION ACOUSTIC	FAST FOURIER TRANSFORMS	INTERMITTENCE, LOW-RPM SIGNAL AMPLITUDE
CAPACITANCE EDDY CURRENT ELECTROMAGNETOACOUSTIC	LUMPED ELECTRICAL CIRCUIT ELEMENTS	AMPLITUDE SENSITIVITY
ISOTOPE	ISOTOPES	HIGH-RPM ACCURACY

#### Eddy Current Speed Sensor

An eddy-current speed sensor consists of an energized coil at the port and a lobed conductive speed nut on the rotating shaft. The variation in their spacing generates a periodic signal in the coil. This signal could be processed to provide a measurement of shaft speed by measuring the repetition rate of these signals.

#### Electromagnetoacoustic Speed Sensor

An electromagnetoacoustic speed sensor consists of an array of closely spaced permanent magnets and an eddy-current induction coil. The coil, when excited with high-frequency a-c energy, induces eddy currents in the nearby metallic lobed speed nut. The permanent magnet array, combined with the induced current, generates in the speed nut an array of alternating force zones that creates an acoustic signal. Another similar transducer, acting as a receiver, generates a periodic electrical signal due to the varying separation between the detector and the speed nut. The repetition rate of the amplitude modulated signal can be processed to provide the measurement of the shaft speed.

#### Fiberoptic Proximeter Speed Sensor

A fiberoptic deflectometer consists of a fiberoptic proximity detection instrument that is inserted

through a bearing housing to detect the deflection of the external surface of the bearing's outer race due to rolling balls. The fiberoptic deflectometer output signal could be processed by a Fast Fourier Transform analyzer to provide frequency information for speed measurement purposes.

#### Accelerometer Speed Sensor

In this approach, piezoelectric accelerometers convert turbopump-housing structural vibrations into electrical signals. For speed measurement, the signals would be processed by a Fast Fourier Transform analyzer to extract frequency information for speed measurement purposes.

#### Pressure Pulsation Speed Sensor

In this approach, periodic fluctuations in turbopump pressure are measured by pressure transducers and processed by a Fast Fourier Transform analyzer to extract rotational shaft speed.

#### Acoustic Speed Sensor

An acoustic speed sensor consists of a piezoelectric transducer emitting ultrasonic energy to a lobed speed nut, another piezoelectric transducer receiving the reflected ultrasonic energy, and an electronic system capable of processing the periodic signal whose repetition rate is proportional to the shaft speed.

#### Isotope Speed Sensor

An isotope speed sensor consists of a radioisotope source mounted on the speed nut and a high-energy photon detector placed on the outside of the housing. The high-energy, gamma-ray photons are detected once each time the shaft rotates and the time between successive photon bursts is measured to determine the shaft rotation speed.

### Variable-Source Magnetic Speed Sensor

A variable-source magnetic speed sensor utilizes shaft-mounted, rare-earth magnets as flux generators and a nonintrusive, high-permeability pickup coil mounted at the speed sensor port at the outside of the housing. The periodic signal of such a sensor provides measurement of shaft speed.

### Hall-Effect Speed Sensor

A Hall-effect speed sensor is similar to the variable reluctance speed sensors used on the SSME, except that solid-state, Hall-effect detectors are used instead of a pickup coil for detection of magnetic field variations.

### Wiegand-Effect Speed Sensor

The Wiegand-effect speed sensor is similar to the variable reluctance speed sensor except that a Wiegand-effect core is used instead of a magnetically soft core for the pickup coil to generate a constant-amplitude signal. Such a speed sensor is presently used in commercial automotive applications.

### Infrared Speed Sensor

An infrared speed sensor consists of an infrared light-emitting diode or diode laser that directs its beam toward a speed nut encoder typically consisting of alternately polished and matted surfaces. A periodic infrared signal corresponding to the passage of the encoder surfaces is reflected back to a solid-state infrared detector. The output of the detector is processed to provide a shaft speed measurement.

### Microwave Speed Sensor

A microwave signal, generated by a Gunn diode, is transmitted through a hollow metal waveguide and a ceramic window to a lobed speed nut. The amplitude of

reflected microwave energy off the speed nut is collected and processed to produce a periodic signal whose repetition rate is a measure of shaft speed.

#### Electromagnetic Doppler Speed Sensor

The electromagnetic Doppler approach utilizes the change in frequency observed when a microwave signal is reflected from the moving speed nut. The speed of the nut is thus measured directly and continuously, unlike the microwave approach discussed above. Additionally, sharp encoder lobes are not required; the surface roughness of the existing turbopump shaft may reflect sufficient microwave energy for Doppler signal detection.

#### Analysis

Each of 14 technologies were theoretically analyzed to determine their compatibility with SSME turbopump hardware, performance, environment, and controller requirements. Those technologies that did not satisfy all the requirements were rejected. The remaining technologies were recommended for experimental evaluation. To facilitate the analysis, these 14 technologies are categorized according to the fundamental principles governing their performance. Thus, the capacitance, eddy-current, and electromagnetoacoustic speed-sensing technologies are grouped together because their performance can be evaluated by analyses of equivalent electrical lumped circuit components. The accelerometer, acoustic, pressure, and proximeter speed-sensing technologies are grouped together since their performance is dependent on the effectiveness of Fast Fourier Transform (FFT) analyses. The microwave, electromagnetic-Doppler, and infrared technologies are grouped together, the performance of each being affected by the propagation of electromagnetic waves through a cavitating liquid medium. The magnetic, Hall-effect and Wiegand-effect technologies are grouped together because their performance can be determined by analyses based on principles of magnetics.

#### Lumped-Electrical Circuit Group

This group was analyzed for sensitivity of detection using an effectively static lumped component

representing the housing, shaft, vanes, and sensor hole and an effective dynamic lumped component representing the changing gap of the speed nut periphery. All three technologies indicated a sensitivity of less than one part in ten thousand as determined from the following calculations.

The capacitance sensor configuration was simplified to represent a dynamic capacitance consisting of two port-size parallel plates separated by the distance from the port to the speed nut periphery ( $C_d = \epsilon A/g$ ), and by a static cylindrical capacitance [ $C_s = 2\pi EL / \ln(L/R\sqrt{3})$ ] generated by the sensor hole and the housing and shaft. The fractional change in total effective capacitance,  $\Delta C_d/C_s$ , was calculated to be less than  $1 \times 10^{-4}$ , which was considered to be too small for accurate measurements.

In a similar analysis, the eddy-current sensor configuration was broken down to dynamic and static mutual inductances resulting in a change in total mutual inductance of less than  $2 \times 10^{-5}$ , once again too small for accurate measurements.

The electromagnetoacoustic sensor, consisting of an eddy-current sensor superimposed with permanent magnets, was determined to be no more sensitive than the eddy-current sensor.

#### FFT Group Analysis

The feasibility of the fiberoptic proximeter, accelerometer, pressure pulsation, and acoustic speed sensing technologies was evaluated using data available from previous turbopump tests. The data were reprocessed to provide power spectral density (PSD) plots, time profiles, and isoplots, with the goal of identifying shaft speed related signals valid over the 500 to 50,000 rpm range of the turbopump. In all cases, the data indicated the presence of intermittent and unreliable signals below at least 3000 rpm rendering these approaches unacceptable to meet the SSME requirements.

The fiberoptic proximeter data revealed numerous bearing-related signals. The shaft rotation/inner race frequency, the cage frequency, the ball pass frequency, and their harmonics were identified in the bearing data. Although strong frequency trends do stand out in the data, there are many sampling periods when the signals are ambiguous and fade out completely, or are superimposed, thus making identification of the frequency component source for closed-loop measurements questionable. It was concluded that there were no readily identifiable amplitude or frequency relationships present that could be counted upon for continuous speed measurement over the duration of the tests.

The analyses of accelerometer data from previous SSME high pressure oxidizer turbopump tests has yielded readily identifiable synchronous frequencies and impeller blade-wake frequency harmonics (4x and 8x synchronous frequency) at steady-state high rpm speeds. However, the high pressure oxidizer turbopump data often contained High Pressure Fuel Turbopump (HPFTP) vibration signals, and all of the high pressure oxidizer turbopump related signals were found to have periods of intermittence during the tests. For example, no speed-related signals were found below 13,200 rpm and all synchronous frequencies below 3000 rpm were masked by noise.

Pressure pulses obtained from the SSME high pressure oxidizer turbopump high-frequency pressure sensors were responsive to changes in portions of turbopump speed ramp down (from 27,600 to 19,500 rpm) and ramp up (higher than 25,000 rpm) beyond 3 seconds after startup. The lack of reliable speed-linked pressure pulsations during all other turbopump operating conditions renders this technology unsuitable for closed-loop speed measurement over the required rpm range.

The ultrasonic vibration measurement system reported by Hamilton (cited in the Bibliography) presented test results of a small (1/4-inch diameter shaft) universal motor, but did not include any power spectral density curves of the output signal. It is our opinion that such an analysis would have produced power spectral

density plots similar to the ones obtained from fiberoptic deflectometer, accelerometer, and pressure pulsation measurements and followed, therefore, their destiny: the signal is intermittent, weak, and unreliable at low speeds. Therefore, this acoustic technology was also removed from consideration for experimental evaluation.

#### Isotope Speed Sensor Analysis

An analysis was performed to determine the total photon count at the isotope speed sensor detector and the relationship between the isotope source strength and the accuracy of speed measurement. For simplicity, it was assumed that the total photon count is proportional to source strength, solid angle of capture, absorption losses, detector efficiency, rotation period, multiplicity of isotope decay, and viewing angle. Specifically, it was assumed that the source had 5 millicurie strength, a decay multiplicity of 2, 1.1 MeV energy, a 1 percent solid angle capture, and is placed 2.7 inches away from an 80-percent efficient detector. With the above assumptions, a total photon count of only 2 was calculated at 30,000 rpm, which implies a 70-percent scatter (equivalent to one standard deviation) in measurement.

To approach a  $\pm 25$  rpm accuracy, 4 million counts are required, indicating that the isotope approach would require an extremely high strength source which would not be NRC-exempt, rendering it impractical.

#### Magnetic Group Analysis

An analysis was performed to determine the amplitude of the signal generated in a pickup coil by the rotating permanent magnet in the variable-source magnetic speed sensor, as shown in Fig. 5. It was assumed that if a peak magnetic induction of 6 Gauss can be generated by the four shaft-mounted magnets in a pickup coil at a distance of 2 inches, then the induction at the coil would vary from 0 to 6 Gauss over the time interval required for the shaft to rotate one quarter turn. The voltage generated at the

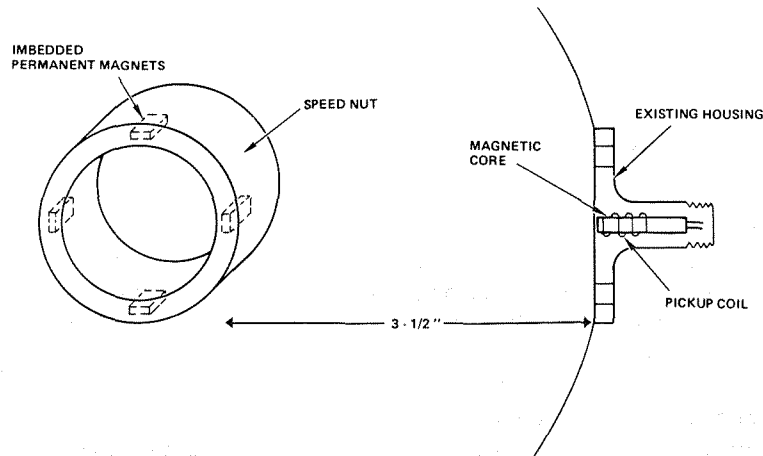


Fig. 5. Nonintrusive HPOTP Variable-Source Magnetic Speed Sensor

lowest usable SSME high pressure oxidizer turbopump speed (500 rpm) from a linear magnetic field distribution in an air-core pickup coil having 2400 turns (similar to the existing sensor coil) with a cross section equal to the existing port area was determined to be 4.7 mV, using an analysis based upon Faraday's Law. In practice, the magnetic field does not vary linearly. Rather, a much sharper flux density change over a distance approximately equal to the width of the magnet would be observed.

The analysis of Hall-effect or Weigand-effect magnetic speed sensors follows the analysis of the variable-source magnetic speed sensor except that in these approaches, the detector is not a pickup coil but is either a Hall-effect or Wiegand-effect detector. Hall-effect detectors require external excitation and so were rejected due to the possible hazard they could pose in a liquid oxygen environment. The Wiegand-effect detector generates a constant-amplitude signal due to triggering of a magnetically soft core, but requires impractically high magnetization levels for triggering and was not recommended for experimentation due to the anticipated low levels of magnetization

that would be generated in a Wiegand device by permanent magnets 3.5 inches away.

### Electromagnetic Group Analysis

Both the microwave and the infrared approach to nonintrusive speed sensing must demonstrate sufficient immunity to propellant cavitation to be considered as viable technologies. An analysis was therefore performed to determine the impact of cavitation on the effectiveness of these techniques.

From the Mie theory, the transmittance, T, through a medium with nonabsorbing spherical scatters takes the form:

$$T = \exp(-N\pi R^2 QL) = \exp(-3CQL/4R)$$

where

N = bubble concentration ( $\text{cm}^{-3}$ ) =  $3C/4\pi R^3$

C = cavitation fraction (by volume)

R = bubble radius (cm)

L = path length (= 20 cm roundtrip)

Q = scattering coefficient =  $2 - (4 \sin P)/P + 4(1 - \cos P)/P^2$

P =  $4\pi R(1-M)/\lambda$

M = ratio of refractive indices ( $n_1/n_2 = 0.8$ )

$\lambda$  = wavelength (cm)

Transmittances were calculated for assumed levels of cavitation (0.1 and 1 percent) for visible, infrared, and microwave wavelengths for bubble radii on the order of the wavelength utilized. The results of the calculations are presented in Table 2. The transmittances for both 0.1 and 1.0 cm wavelength microwaves indicate that acceptable signal levels will be detected even under conditions of severe cavitation, making the

Table 2. Mie Scattering Transmittance

ENERGY FORM	WAVELENGTH	TRANSMITTANCE	
		0.001 CAVITATION	0.01 CAVITATION
MICROWAVE	1 CM	>0.85	>0.20
	0.1 CM	>0.20	>10 <sup>-7</sup>
INFRARED	30 MICRON	<10 <sup>-4</sup>	0
	5 MICRON	<10 <sup>-10</sup>	0
	1.3 MICRON	0	0
VISIBLE	0.5 MICRON	0	0

microwave approach very promising. The shorter wavelengths, however, suffer considerably from the scattering effects of oxygen bubbles in liquid oxygen. The visible wavelength (0.5 micrometer) and the shorter infrared wavelengths (1.3 and 5 micrometers) undergo several signal loss by scattering and are rendered unusable. The 30-micrometer infrared radiation offers acceptable transmittance over most of the range of bubble radii for a cavitation level of 0.1 percent, but is unacceptable for 1 percent cavitation.

Mie scattering calculations performed at the same cavitation levels, but for bubble radii in the range of 0.01 to 1.0 centimeter demonstrate sufficient transmittance (5 to 97 percent) for both the infrared and microwave approach to be usable for remote speed sensing applications.

It is prudent to understand the assumptions inherent in the scattering derivation. It is assumed that all scattered light, including that scattered at small angles, is considered to be removed from the beam. This is equivalent to saying that the detector is assumed to be a very large distance from the scatterer, thus subtending an infinitesimally small solid angle. However, a practical application of microwave and infrared speed-sensing technologies will employ detectors at finite distances, thus subtending finite solid angles. Studies of the angular distribution of scattering indicate that a large portion of the scattering occurs in the forward direction (i.e., toward the detector), suggesting that the effective throughput will be much greater than that indicated by the tabulated

Mie scattering results. This may be sufficient to bring the infrared transmission up to acceptable signal levels, making it suitable for speed-sensing applications.

### Recommendations

The analysis of the 14 candidate technologies has screened from consideration (1) those approaches that fail to provide acceptable output signal level or accuracy, (2) those with intermittent or otherwise unreliable signals, and (3) those whose performance is masked by the extreme environments present in the SSME. The magnetic, microwave, and infrared technologies demonstrated promise for use in nonintrusive shaft speed sensing and were recommended for experimental evaluation. Specifically, the quantification of signal amplitude of the variable-source magnetic speed sensor at low rpm and the attenuation of microwave and infrared energy through a cavitating medium were recommended for experimental evaluation to verify the feasibility of these technologies.

### Experimental Evaluation

#### Variable-Source Magnetic Speed Sensor Experimentation

The variable-source magnetic speed sensor was tested in the laboratory to determine the detectability of the signal at low speeds and large separations. Four 0.5-inch diameter, disk-shaped ferrite magnets with measured pole strengths ranging from 400 to 500 Gauss were epoxied to a nonmagnetic wheel having an outside diameter equal to the SSME speed nut diameter (see Fig. 3). The wheel was rotated with an electric motor at speeds of 240, 480, and 720 rpm and magnetic pulses were observed at various distances from the wheel with an SSME high pressure oxidizer turbopump speed sensor coil. The results of these tests are graphed in Fig. 6, indicating the generation of a useful signal of 0.6 mV at the lowest required speed of (480 rpm) with a 3-inch separation.

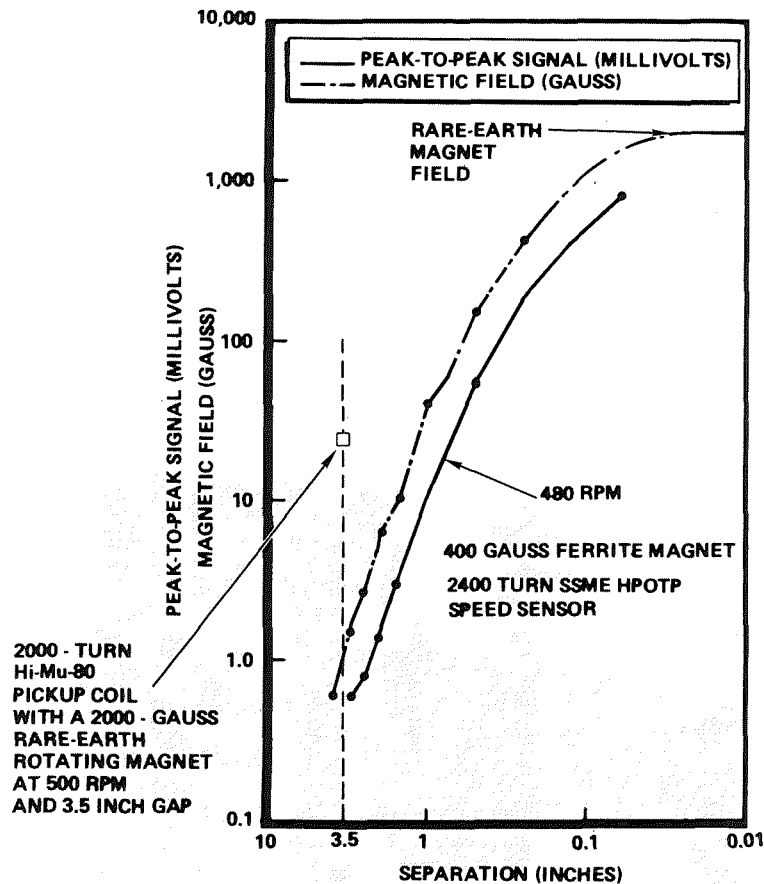


Fig. 6. Variable-Source Magnetic Speed Sensor  
(Electrical Signal and Field Strengths  
vs Separation of Magnet From Coil)

A similar test with a samarium-cobalt magnet produced a signal of 2.4 mV with the existing SSME speed sensor at a distance of 2 inches and a speed of 240 rpm. This was a threefold improvement over the signal derived from the ferrite magnet (0.8 mV at 2-inch separation). Further signal enhancement was obtained by using a hand-made 1000-turn pickup coil with a larger cross-sectional area (7/8 x 7/8 inch). At 240 rpm and 2 inches away, a signal of 25 mV<sub>p-p</sub> was obtained from the rare-earth magnet. The signal would be approximately 27 mV<sub>p-p</sub> at the minimum specified

speed of 500 rpm and 3-inch separation, representing a very strong signal for speed measurement.

Additional tests were performed at higher rpm's to determine the high-frequency shielding effect of turbine vanes and housing placed between the coil and magnets, as shown in Fig. 7. Four Ferrite magnets were next molded into an epoxy ring on a 2-inch diameter aluminum tube, which was spun over a speed range of 2000 to 6000 rpm with an existing test rig. Output pulses from a 2000-turn (7/8 x 7/8 inch) air core pickup coil were measured at a distance of 3.5 inches from the magnets, as shown in Fig. 8. Various metal plates

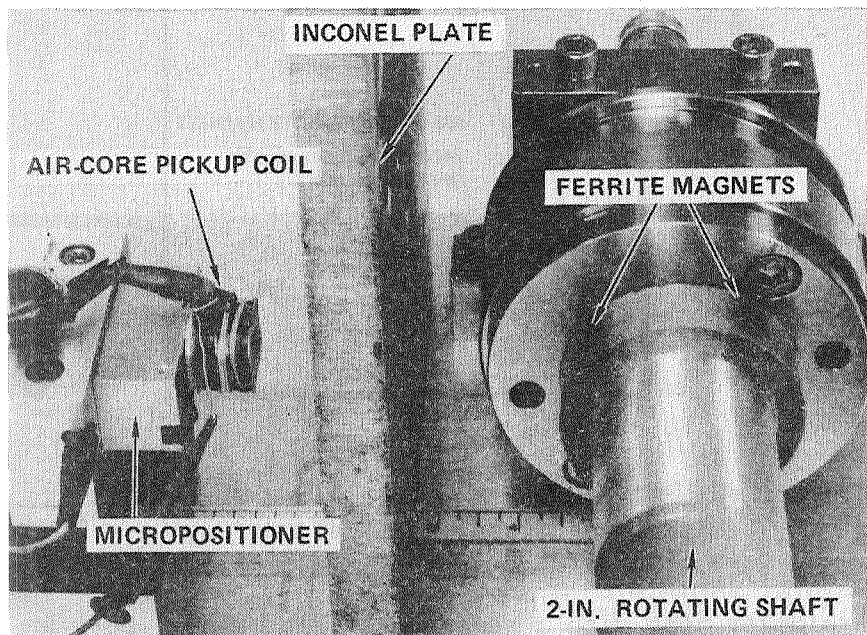


Fig. 7. Variable-Source Magnetic Speed Sensor Experimental Setup

were held tightly against the nylon spool of the pickup coil, simulating a housing-mounted coil as shown in Fig. 5. The results of the shielding of these plates are shown in Fig. 8, where a 1.2 x 12 x 18 inch Inconel 718 plate and 1.75 x 12 x 12 inch Inconel 625 plate did not attenuate the signal at all, yet a 0.75 x 7 x 16 inch aluminum plate significantly reduced the signal.

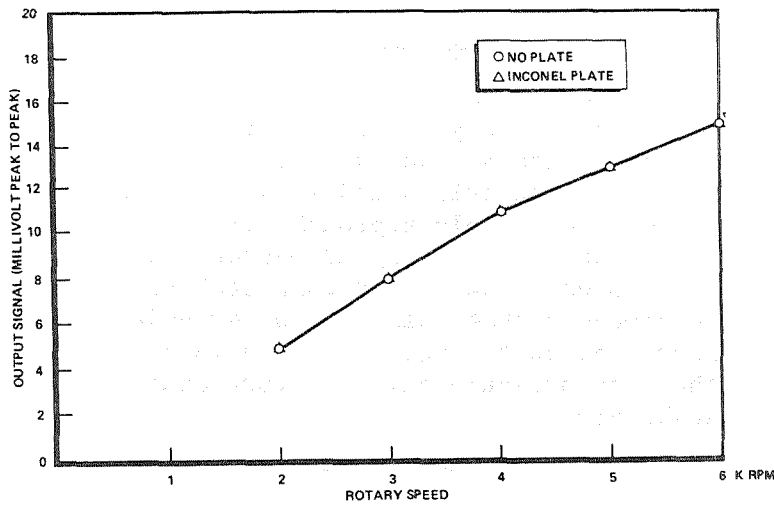


Fig. 8. Variable-Source Magnetic Speed Sensor  
(Signal Amplitude vs Rotating Speed)

The cause of this difference in signal reduction between aluminum and Inconel is due to the difference in electrical resistivity of the two metals. Aluminum is a very good conductor whose resistivity ranges from 1 to 3 microhm inches depending on the temperature, heat treatment, and alloy composition. The resistivity of Inconel is substantially greater than that of aluminum and ranges from 39 to 48 microhm inches even at cryogenic temperatures. Thus, eddy currents are not readily set up in Inconel, and the original magnetic field is not cancelled by its passage through Inconel.

In summary, the variable-source magnetic speed sensor, even at low speeds, can generate strong signals at a 3.5-inch distance from the speed nut, and does not lose any signal due to eddy currents in the existing intervening turbopump housing or vane materials. Thus, this sensor can be mounted completely external the turbopump housing. In view of this nonintrusiveness, and of the sensor's use of space-proven technology and its inherent immunity to bubbles and cavitation, we conclude that it is a highly viable and desirable sensor for the SSME.

### Conclusions

Based upon the results of the computerized literature search, technology identification, theoretical analysis, and experimental evaluation, we conclude that the variable-source magnetic speed-sensing technology is both a viable and a desirable approach for accurate and non-intrusive turbopump shaft speed measurement. In view of its space-proven hardware and complete nonintrusiveness, it is recommended that this technology undergo immediate preliminary design for incorporation into the SSME to restore the high pressure oxidizer turbopump speed measurement capability.

### Acknowledgements

This work was sponsored by NASA-MSFC under Contract NAS8-34658 with Mr. T. Marshall and H. Burke as Project Monitors. We gratefully acknowledge the support of George Kuhr and Don Hunter of Rocketdyne in the theoretical analysis and experimental verification of the variable-source speed sensor. We would also like to thank Dr. Ira Goldberg and Dr. Jim Rode of Rockwell International/Science Center for their consultation on the experimental evaluation of the microwave and infrared speed sensors.

### Bibliography

The following list of articles and reports generated as a result of the literature survey and utilized in the Theoretical Analysis, serves as a useful bibliography on the state of the art in nonintrusive speed sensors.

Anon, "Wiegand Effect: A New Pulse-Generating Option," *Automotive Engineering*, 86(2), February 2, 1978, pp. 44-48.

Bhartia, P. and M. A. K. Hamid, "Dropler Radar Determination of the Rotation Speed of Shafts," *IEEE Trans. Ind. Electronics and Control Instrumentation*, V. IECI-24, No. 1 (1977) p. 141.

Bucurenciu, S., "Dynamic Behavior of the Induction Tachometer," *Rev. Roum Sci Tech Electrotech Energ* 25(2) (1980) p. 149.

Gadrault, R., "Shaft Rotation Speed Measurement Device, Its Checking and Variations Checking," (U.S. Patent) February 25, 1976.

Hamilton, D. B. et al., Noncontact Devices for Measuring Vibrations and Deflections of Parts in Operating Turbopumps, Final Report, NASA CR124208.

Handlykken, M. B., "A Brushless D.C. Tachometer," (U.S. Patent) February 19, 1982.

Knoll, G. F., Radiation Detection and Measurement, Wiley, New York (1979), p. 504.

Macek, W., Electromagnetic Angular Rotation Sensing, Sperry Gyroscope Company Report, August 1964.

Noble, G. T., "Sensing Shaft Rotation With Proximity Switches," Power Transmission Des., 25(10), August 10, 1981, pp. 62-63.

Parmenov, V. I., Angular Velocity and Acceleration Pick Up, Foreign Tech. Div. Air Force Systems Command, Wright-Patterson AFB, May 26, 1964.

Transandote, A. et al., "A New Slip Monitor for Traction Equipment," Trans. of the ASAE (1977), p. 851.

Verdrunes, M. and W. E. Mace, "The Measurement of Engine Rotational Speed," AGARD Flight Test Instrumentation Series, V. 4 (1973).

Wilcox, G. and J. L. Mason, "Temperature Stabilized Tachometer for the Fuel Efficient Automobile," IEEE Trans. Consum. Electron, CE-26(3), August 3, 1980, pp. 664-669

A more detailed bibliography on nonintrusive/remote speed-sensor technologies was presented in the Nonintrusive Speed Sensor Monthly Report to NASA/MSFC for February 1984 (NASA Contract NAS8-34658).

SESSION IX IGNITION/COMBUSTION PROCESSES

D. E. Pryor

Structures & Propulsion Laboratory

NASA/MSFC

Marshall Space Flight Center, Alabama 35812 U. S. A.

The objective of the work elements within this session is to extend the state-of-the-art for main chamber and turbine drive combustion components with emphasis on operational and service life problem areas exposed during SSME development.

The approach is a combination of contracted and in-house NASA analytical/experimental research tasks under the two major combustion component headings mentioned above. Efforts thus far have been limited to the turbine drive technology area and the two papers presented herein address activity from that contracted work element. The overall objectives for this initial technology are to generate an advanced, comprehensive combustion analytical code, and to verify the combustion flow dynamic predictions from this model with hot test experimental data. The first paper, "Liquid Rocket Combustion Computer Code Development" by Mr. P. Liang, discusses the code development while the gathering of code anchoring data is the subject of "LASER Schlieren and Ultraviolet Diagnostics of Rocket Combustion" by Mr. S. Fisher.

Research in the main combustor area is scheduled to begin in the winter of 1984/1985. This contract will eventually compliment the ongoing turbine drive technology effort with a set of advanced main combustor hardware providing a scale model staged combustion system. Specific tasks on main chamber thermal/structural life and stability rating will be conducted leading to the selection of this advanced model main combustor.

The thermal/structural life assessment process for SSME configuration hardware has been modeled by a separate contracted task completed in early 1983, and

the forthcoming main chamber technology is intended to build on this analytical base.

The advanced version hardware from both the turbine drive and main combustor contracts is intended for government test at MSFC. Common scaling between the two combustors will allow them to be assembled into an advanced staged combustion model for high pressure test evaluation with results feeding into the full scale SSME Test Bed effort.

Long range technology from this working group includes an evaluation of derivative SSME concepts as they might appear within the dual throat engine concept.

LIQUID ROCKET COMBUSTOR COMPUTER CODE  
DEVELOPMENT\*

P. Y. Liang

Rockwell International/Rocketdyne Division  
Canoga Park, California

Abstract

This paper highlights the Advanced Rocket Injector/Combustor Code (ARICC) that has been developed at Rocketdyne to model the complete chemical/fluid/thermal processes occurring inside rocket combustion chambers. The code, derived from the CONCHAS-SPRAY code originally developed at Los Alamos National Laboratory (Ref. 1) incorporates powerful features such as the ability to model complex injector combustion chamber geometries, Lagrangian tracking of droplets, full chemical equilibrium and kinetic reactions for multiple species, a fractional volume of fluid (VOF) description of liquid jet injection in addition to the gaseous phase fluid dynamics, and turbulent mass, energy, and momentum transport. Atomization and droplet dynamic models from earlier generation codes are transplanted into the present code. Currently, ARICC is specialized for liquid oxygen/hydrogen propellants, although other fuel/oxidizer pairs can be easily substituted. ARICC is a two-dimensional/axisymmetric real-time transient code, and effort on developing a three-dimensional counterpart is underway.

Introduction

Combustion processes occurring in a fluid medium are probably among the most complex of all flow phenomena. The complexity stems from two primary reasons. Firstly, the so-called "combustion" process actually encompasses many physical processes of different types,

---

\*Sponsored by NASA under Contract NAS8-34928.

different natures, different temporal and spatial scales, and different degrees of being describable by deterministic models. Secondly, all of these processes are usually strongly coupled together, making it difficult to reduce the problem down to its individual component processes. Any attempt to numerically model such complex combustion phenomena would need to make careful distinction between those processes that can be considered as the primary driving ones, and hence, should be modeled as vigorously as possible, and those that can be considered secondary and are included only for their usefulness in "interpreting" the situation into the desired results. Such decisions are often as important as the quality of the mathematical models themselves.

Inside a liquid rocket engine, the process usually starts with the injection of fuel and oxidizer into the combustion chamber in both liquid and gaseous states under high pressure and at greatly different velocities so as to encourage rapid atomization of the liquid component. The flow created by such injection is highly turbulent and rotational. Furthermore, in the case of liquid oxygen/hydrogen engines, the propellants are at temperature extremes ranging from cryogenic (70 K) to superhot (3000+ K). Thus, even in the precombustion state the flow is fully elliptic and composed of multiple species with real gas/liquid properties. The inception of combustion magnifies the local temperature, pressure, and species concentration gradients, and adds one more time scale to those of the bulk flow transience and of the turbulence. In light of these circumstances, a list of requirements deemed necessary for the numerical modeling of the combustion process has been generated and are listed in Table 1.

The ARICC code represents an attempt to build a modular model to describe the complete combustion process inside a liquid rocket engine using state-of-the-art finite difference techniques. It is an advancement over earlier-generation performance codes, many of which are used as industrial standards, that frequently describe one aspect of the combustion

Table 1. Code Features Required for  
Liquid Rocket Engine Modeling

NECESSARY FEATURES	FEATURES INCORPORATED INTO ARICC
<ul style="list-style-type: none"> <li>• VISCOUS ELLIPTIC FLOW</li> <li>• FULL CHEMISTRY</li> <li>• LIQUID JET INJECTION/ 2 PHASE FLOW</li> <li>• DROPLET DYNAMICS</li> <li>• ATOMIZATION</li> <li>• FINE RESOLUTION IN CRITICAL AREAS</li> </ul>	<ul style="list-style-type: none"> <li>• FULL NAVIER-STOKES EQN. + SGS TURBULENCE MODEL, ALL FLOW SPEEDS.</li> <li>• MULTIPLE SPECIES KINETIC AND EQUILIBRIUM REACTIONS</li> <li>• VOF TWO-PHASE, FREE SURFACE DESCRIPTION</li> <li>• MONTE CARLO SCHEME/LAGRANGIAN DROPLET TRACKING, DROPLET HEATUP AND VAPORIZATION</li> <li>• CICM ATOMIZATION MODEL</li> <li>• ARBITRARY GRID WITH CLUSTERING.</li> </ul>

process in great detail (e.g., chemistry) but make gross assumptions about the other aspects (e.g., neglecting flow recirculation by using the stream tube method). These codes (Ref. 2-6) with their primary limitations are listed in Table 2. However, they all contain valuable experience and empirical models that have and will continue to be assimilated into the ARICC code.

Table 2. Earlier-Generation Rocket  
Combustion Codes

CODE NAME	PRIMARY FUNCTIONS	MAJOR LIMITATIONS
CICM <sup>2</sup>	STEADY-STATE ROCKET COMBUSTION OF H <sub>2</sub> /LOX FOR COAXIAL INJECTION	STREAM TUBE FLUID DYNAMICS. ATOMIZATION CORRELATIONS FROM J-2 ENGINE
TRANS78 <sup>3</sup>	MULTIPURPOSE CHEMISTRY CODE FOR ROCKET PERFORMANCE, DETONATION, CONSTANT P OR CONSTANT V COMBUSTION ETC.	1D EQUILIBRIUM ISENTROPIC. NO SPATIAL RESOLUTION OR FLOW DYNAMICS
SDER <sup>4</sup>	STEADY-STATE 1D FLUID DYNAMICS WITH 3D DROPLET DYNAMICS FOR IMPINGING TYPE ELEMENTS. LIQUID/GAS, SUB. AND SUPER-CRITICAL VAPORIZATION OF DROPLETS	DROPLET CORRELATIONS DEVELOPED FROM COLD FLOW. STREAM TUBE FLUID DYNAMICS
TPP <sup>5</sup>	TIME-DEPENDENT PROGRAM FOR SMALL PULSED TYPE ENGINES WITH HYPERGOLIC PROPELLANTS. 3D DROPLET DYNAMICS.	1D FLUID DYNAMICS. IMPINGING LIQUID-LIQUID ELEMENTS ONLY. SUBCRITICAL DROPLETS
GKAP <sup>6</sup>	STEADY-STATE CHEMICALLY REACTING GAS MIXTURES OF UP TO 150 SPECIES AND 70 NONEQUILIBRIUM REACTIONS.	1D FLOW. ADIABATIC COMBUSTION CHAMBER. NO DROPLETS.

### Process of Code Development

The process of code development consists of four steps: (1) identify the critical processes; (2) determine which of these processes can be described vigorously and which should be modeled empirically, and devise mathematical expressions for each category; (3) translate these expressions into numerical formulations and assemble a logical algorithm for evaluating them and displaying the results; and (4) design steps for verification of the model components and for "anchoring" or fine-tuning of the empirical model constants.

The above process is depicted in Fig. 1. As a result of the initial scrutiny in step one, several assertions can be made concerning liquid rocket combustion. First, of the two primary transport processes of diffusion and convection (radiation is not important at these temperatures), the former controls the transfer of species with respect to each other while the latter controls the bulk transfer of mass, momentum, and energy. As the liquid oxygen/hydrogen reactions are relatively fast, the steady-state flame is thus diffusion controlled and can be described sufficiently with equilibrium reactions. Viscosity (diffusive transfer

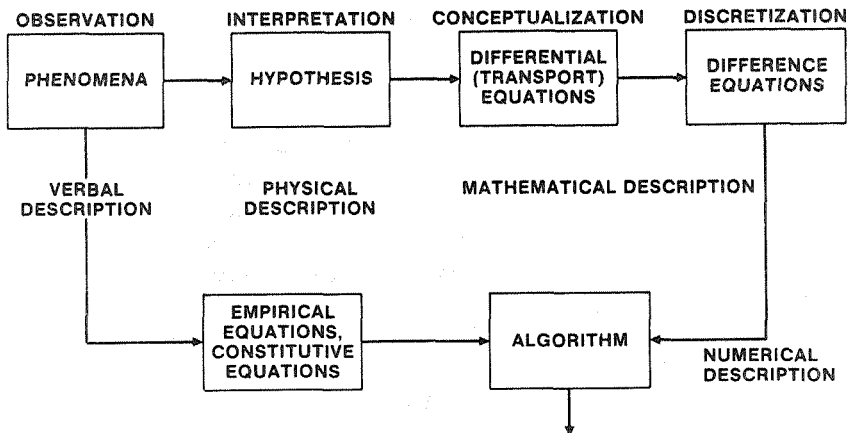


Fig. 1. Steps in Formulation of a Computer Model

of momentum) is important only in stagnant zones of the combustion chamber where recirculation controls wall heat transfer, and indirectly through the turbulence scale which affects the species diffusion and atomization processes. Second, the overall performance of the rocket engine is strongly dependent on the effectiveness of the atomization process. Unvaporized and hence uncombusted droplets are the greatest cause of loss of engine efficiency. Third, while the steady-state flame is adequately described by a diffusion-controlled equilibrium flame model, the ignition and flame holding mechanisms and wall-streaking phenomenon of concern can only be understood with detailed consideration to the local geometry and flow patterns and transient heat transfer processes. The life and durability of the engine depends largely on these last mechanisms.

In other words, an adequate numerical model must have the capability to fully describe the following types of phenomena: viscous flow as described by the full Navier-Stokes equations with turbulence modeling; multiple species chemical kinetics, liquid jet injection, atomization, and subsequent vaporization and transport of the droplets; and fine grid resolution near boundaries and corners of particular interest. All of these capabilities have been built into ARICC. The type of mathematical model used for each phenomena is listed in Table 3.

Before a more detailed description is given of the code, a comment about the code's verification is in order. The basic fluid dynamics, which forms the basis of the solution scheme, will and is being checked out with experimental laser velocimetry measurements done on a low pressure cold flow test chamber under the current contract, and the final results will be reported in a future writeup. Optical Schlieren and infrared data obtained in the same tests also provide a qualitative means of verifying the overall temperature profiles. Far more critical however are the verification needs pertaining to the empirical models, where the greatest uncertainty lies and where the greatest variation from problem to problem still exists in the form

Table 3. Mathematical Formulation Used for Various Physical Processes

I. FLUID THERMODYNAMICS MASS CONSERVATION (CONTINUITY) MOMENTUM CONSERVATION (NAVIER-STOKES) ENERGY CONSERVATION	PD PD PD
II. PHYSICAL MODELS EQN. OF STATE (CONSTITUTIVE) TURBULENCE CHEMISTRY RATE EQUATIONS EQUILIBRIUM EQUATIONS RADIATION	AL/TA AL/PD AL AL/TA PD
III. DROPLET DYNAMICS DISCRETE FORMULATION CONTINUUM FORMULATION	OD OD PD
<u>TYPE OF GOVERNING EQN.</u>	
PD = PARTIAL DIFFERENTIAL AL = ALGEBRAIC TA = TABULAR OD = ORDINARY DIFFERENTIAL	

of arbitrary coefficients. Replacing these coefficients with universal constants or expressions is a task of utmost concern. This applies to the turbulence model, supercritical droplet properties, the atomization model, as well as the droplet heatup and vaporization models. Few correlations are available and measurements are difficult to make and hard to come by, especially in the area of droplet dynamics. Finally, the choice of chemical equations, species, and rate or equilibrium constants to describe the chemical processes also represents a major area of uncertainty. In the case of oxygen/hydrogen kinetics, the role of the third body reactions is largely undetermined. An initial one-dimensional test case using the ARICC code however does indicate that the resulting temperature profile inside a premixed combustor tube is strongly influenced by the omission of certain third-body reactions. Much study is still required before any conclusion can be made.

## Code Description

### Code Organization

Figure 2 shows the organization of ARICC, which is typical of a full-fledged combustion code. As previously stated solution of the fluid dynamic governing equations of mass, momentum, and energy with attending boundary conditions form the core of the numerical algorithm. On top of that, the empirical models describing the gas or liquid properties (enthalpy tables, vapor pressure curve fits, etc.), the chemical reactions, the atomization and droplet heatup and evaporation processes, and the turbulence model are called

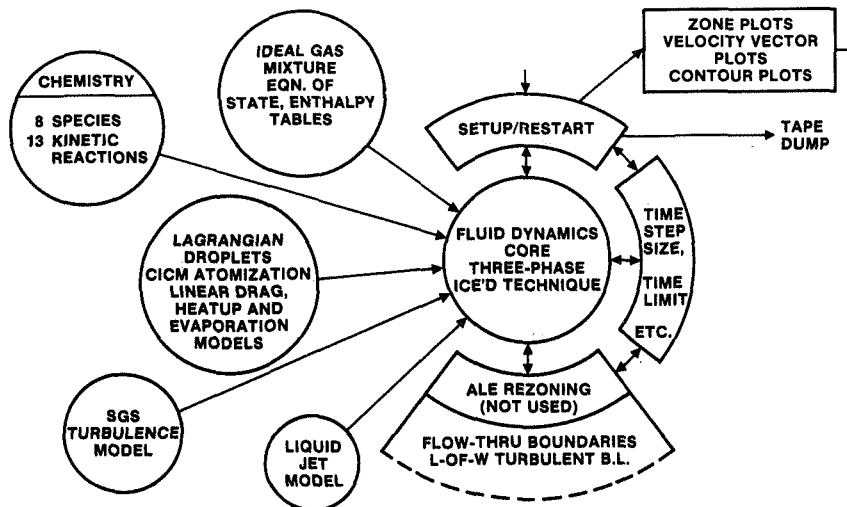


Fig. 2. Current ARICC Code Organization

as subroutines as and when they are required. To make an operationally useful code, however, the code must be given a flexible input/output capability for grid generation, field initialization, and graphical and tabular display of outputs. All these functions are in turn controlled by a master main program which also takes the responsibility of ensuring stability through time-step size control and various artificial numerical smoothing schemes. Figure 3 is a simplified flow chart of ARICC.

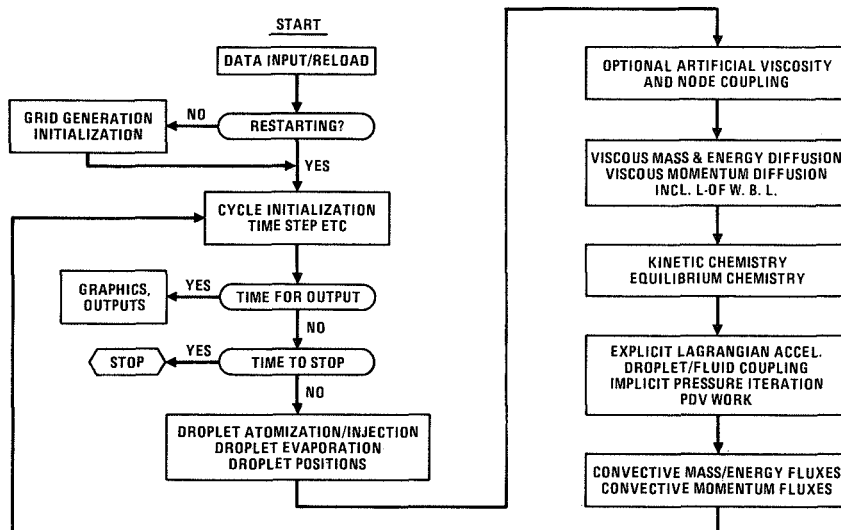
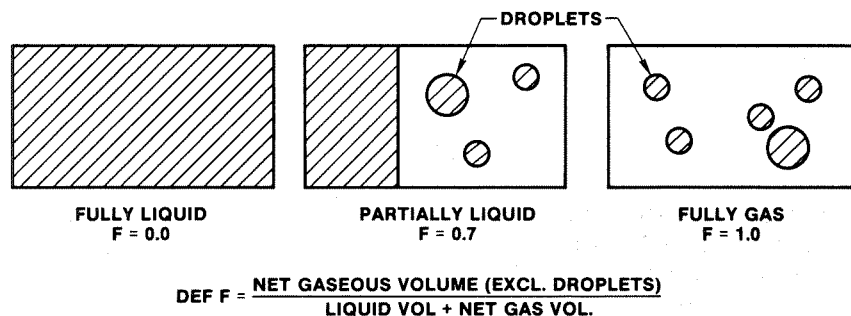


Fig. 3. Simplified Flow Chart ARICC Code

#### Basic Solution Algorithm

The basic Implicit Continuous Eulerian with Arbitrary Lagrangian-Eulerian (ICE'd-ALE) mesh treatment solution technique used in ARICC has been described in detail in Ref. 1 and will not be repeated here. The major complication involved in the ARICC code is the need to handle both compressible gases and incompressible liquid within the numerical framework. To do this, cells that contain liquid must first of all be distinguished from cells that do not. To this end, the Fractional Volume of Fluid method of description has been adopted from the free surface flow SOLA-VOF program (Ref. 7). A cell flag variable ( $F$ ) is used to represent the fraction of the volume of a cell that is occupied by compressible gases. Thus, three different kinds of active cells are possible (Fig. 4). Cells that are totally or partially gaseous (with  $F$  values greater than 0 and less than or equal to 1) will be treated as a "normal" cell using the standard ICE'd pressure iteration scheme. However, the cell volume used in the calculation will be that of the effective gaseous volume equal to  $F$  times the total active cell volume. Cells with flag value equal to

• ACTIVE CELLS DISTINGUISHED BY THEIR FLAG VALUES:



- DROPLETS MAY EXIST IN CELLS WITH  $F > 0.0$
- SINGLE-VALUED THERMODYNAMIC PROPERTIES FOR ALL CELLS
- PRESSURE IN FULLY LIQUID CELLS DETERMINED BY PRESSURE ITERATION SCHEME FOR INCOMPRESSIBLE FLUID

Fig. 4. Different Types of Active Cells in Two-Phase ARICC

0 are fully liquid cells, and while they are treated the same way in the rest of the program, in the pressure iteration step these cells are given a "pseudo-incompressible" treatment by using a pressure iteration scheme that tries to enforce a conservation of the fluid volume, and hence density (Ref. 8). No equation of state relation is applied to the liquid portions and a constant density (as well as temperature) is simply assumed. Chemical reactions are permitted only inside the gaseous phase and no direct mass or heat transfer takes place across the gas/liquid interface. Thus, other than for the fluid dynamical interactions, the only path by which the liquid affects the gaseous mixture is by first turning into droplets and evaporating. The atomization model is described below.

Since the main reason for inclusion of the liquid phase description is for modeling of the liquid jet column coming in through the coaxial injector of a rocket engine, the bulk of the liquid is currently assumed to be always around the central axis of the model. This simplifies the determination of the orientation of the liquid-gas interface necessary for the

calculation of the flux of liquid from one partially liquid cell to the next, and also simplifies the graphics scheme for plotting the interface. A generalization to accommodate the most arbitrary liquid-gas combination can be readily made.

### Atomization Model

At designated intervals, numerical droplet groups representing a number of particles of the same properties are created from the cells that contain a liquid-gas boundary. The atomization model consists of calculation of the stripping rate and the mean drop size (and possibly a statistical distribution function of the drop sizes) from the local fluid dynamic properties. Currently, the model used in ARICC is that taken from the CICM program (Ref. 2). The expressions are as follows:

$$\text{Mean Stripping Rate} \quad M_A = C_A \left[ \frac{\mu_j (\rho_g U_r)^2}{\sigma_j / \rho_j} \right]^{1/3} \pi D_j (\Delta Z)$$

$$\text{Mean Drop Size} \quad \bar{D}_j = B_A \left[ \frac{\mu_j (\sigma_j / \rho_j)^{1/2}}{\rho_g U_r^2} \right]^{2/3}$$

where

- $C_A, B_A$  = empirical constants
- $D_j$  = jet diameter
- $U_r$  = gas velocity relative to liquid jet
- $Z$  = axial location
- $\rho_g, \rho_j$  = gas, jet density
- $\mu_j$  = jet viscosity
- $\sigma_j$  = jet surface tension

At creation, the droplets are given a temperature and density equal to those of the liquid from which

they are created, and an appropriate amount of liquid is eliminated from the cell liquid volume. The reverse process of droplet "recondensation" into the liquid is also allowable, if the droplet velocity should lead it to head back toward a liquid surface. Also, the droplets are given an initial speed equal to that of the local liquid surface and a direction that randomly spans a 90-degree fan, ranging from being aligned with the liquid surface to being radially away. Obviously, these fine details of the model are somewhat arbitrary and can be changed as more experimental data becomes available.

Both because of the fact that the complete atomization process from liquid medium is being modeled and because of the substantial density and sizes of droplets dealt with in liquid rocket engines (up to 100 microns as compared with submicron droplets usually encountered in gas turbines), the droplets in ARICC are given a finite volume that would physically exclude gas and liquid from within the cell. Dynamically speaking, the "bouyancy" term is being included. Thus, the droplet volumes enter into the determination of the effective (gaseous) cell volume. This situation is also depicted in Fig. 4. However, a droplet can only be in one computational cell at any time, as its location is uniquely defined by a single set of coordinates. Currently, interaction among droplets (e.g., coagulation) and film formation along solid surfaces as the droplets hit the walls are not modeled.

This advanced description of the droplet spray plus the two-phase liquid jet description and the CICM atomization model make the ARICC code unique in its capability for modeling liquid rocket engines. The entire combustion process can now be analyzed, in whole rather than in parts. It combines the different branches of fluid dynamics, namely, two-phase flow, reactive flow, particulate flow, and compressible recirculating flow into a single transient finite difference model. The atomization process

that is so important to rocket engine performance can now be studied. Finally, the droplet finite volume displacement and recondensation features pave the way for simulation of droplet breakup and coagulation phenomena.

#### Oxygen/Hydrogen Chemistry Model

Although the primary reactions of the oxygen/hydrogen chemistry are well known, the secondary reactions, especially those involving third bodies, are much more difficult to pinpoint. Only equilibrium reactions are necessary for steady-state, strictly diffusion-control flames. But to simulate the transient processes of ignition and flame propagation, kinetic reactions must be used, otherwise it was found that the flame propagation speeds will be unrealistically large. In its present configuration, the chemistry model in ARICC consists of 13 kinetic reactions involving 8 chemical species, of which 9 are elementary reactions and 4 are third-body reactions. The elementary reactions are the same as those used by Westbrook (Ref. 9). These reactions are summarized in Table 4. The adequacy or redundancy of these reactions for various situations are still being investigated.

#### Boundary Conditions

To complete this brief description of ARICC, mention should also be made of the boundary conditions currently in effect. For the purpose of modeling coaxial injector combustion chambers, ARICC is run in its axisymmetric mode with specified inflow conditions. The exit plane, which in most cases is a sonic nozzle throat, is treated as a specified pressure boundary. Other outflow conditions such as a zero-velocity gradient or enforced sonic conditions can also be specified. On the solid walls or internal solid boundaries, the boundary layer is approximated with a law-of-the-wall treatment. Sometimes a simple no-slip boundary condition

Table 4. List of Hydrogen/Oxygen Kinetic Reactions Currently Used in ARICC

1. $H + O_2$	$\rightleftharpoons$	$O + OH$
2. $H_2 + O$	$\rightleftharpoons$	$H + OH$
3. $H_2O + O$	$\rightleftharpoons$	$OH + OH$
4. $H_2O + H$	$\rightleftharpoons$	$H_2 + OH$
5. $H_2O_2 + OH$	$\rightleftharpoons$	$H_2O + HO_2$
6. $HO_2 + H$	$\rightleftharpoons$	$2 OH$
7. $HO_2 + H$	$\rightleftharpoons$	$H_2 + O_2$
8. $H_2O_2 + O_2$	$\rightleftharpoons$	$2 HO_2$
9. $H_2O_2 + H$	$\rightleftharpoons$	$HO_2 + H_2$
<b>THIRD BODY REACTIONS:</b>		
10. $H + O_2 + H_2$	$\rightleftharpoons$	$HO_2 + H_2$
11. $H + 2O_2$	$\rightleftharpoons$	$HO_2 + O_2$
12. $H + O_2 + H_2O$	$\rightleftharpoons$	$HO_2 + H_2O$
13. $H_2O_2 + H_2O_2$	$\rightleftharpoons$	$2OH + H_2O_2$

is preferred in the case of complicated surface contours. Details of the law-of-the-wall treatment are also discussed in Ref. 1.

### Examples

Several cases of test runs are presented here to illustrate the qualitative features of the ARICC code.

#### Propagation of Flame Front

Figure 5 shows the model of a typical coaxial injector and combustion chamber. To check the one-dimensional flame propagation speed, the chamber is sealed off and filled with a premixed oxygen/hydrogen gas of 1:1 mixture ratio at 2000 psi and 298 K. At time 0, the entire upper row of cells is injected with a sufficient amount of energy to ignite the mixture, and the plane flame "sheet" propagates downward. It is interesting to note that a pressure wave travels at shock speed ahead of the flame front, which travels at the much lower speed of heat wave or concentration wave propagation. The flame front

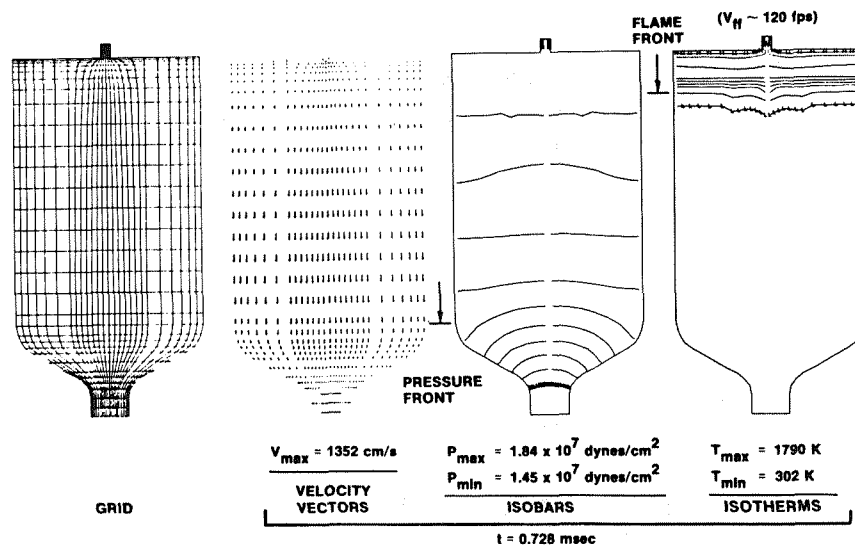
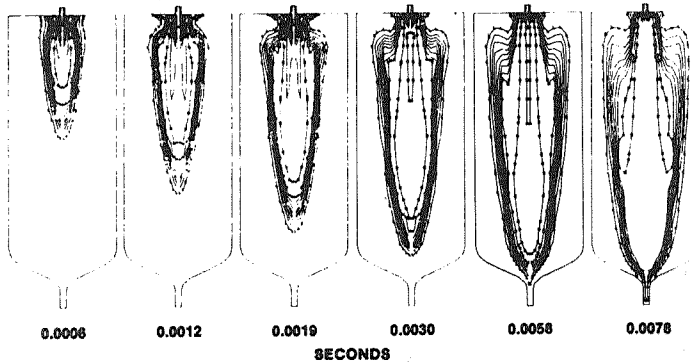


Fig. 5. Propagation of Plain Flame Front

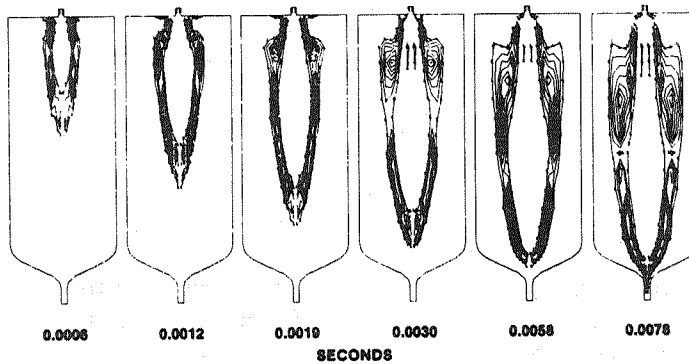
speed is estimated to be approximately 120 ft/sec, compared with the theoretical estimate (through SSME data correlation) of 114 ft/sec. Also at later times, it is noticeable that the planeness of flame front starts to deteriorate, partly because of the presence of the injector at the axis and partly because of the computational truncation errors toward the axis of symmetry.

#### Transient Ignition in Prefilled Chamber

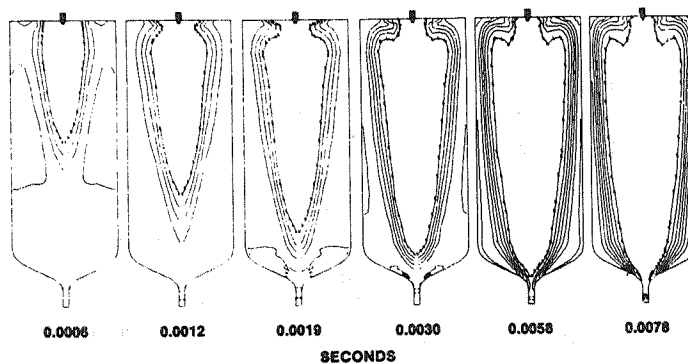
In the second example, a similar combustion chamber has been prefilled with pure oxygen gas at 15 psi at 298 K. At time zero, a coaxial stream of gaseous hydrogen and oxygen at a mixture ratio of 1 starts coming in through the injector. Near the injector entrance and slightly off the axis, a "spark" is ignited. The flow exits at the nozzle into atmospheric pressure. Figure 6 is a sequence of transient contour plots of water mass fractions, of hydrogen mass fractions, and of isotherms, and Fig. 7 is the velocity plot of the case early after startup showing the axisymmetric jet profile of the incoming hydrogen. The propagation of the major flame front, as diffused hydrogen reacts with the abundant oxygen, is evident. In this case, the



A. H<sub>2</sub>O Mass Fraction



B. OH Mass Fraction



C. Density

Fig. 6. Transient Ignition in an Oxygen-Prefilled Chamber

**VELOCITY VECTORS**  
**EARLY AFTER STARTUP**  
**T = 0.0006 SECONDS**  
**MR = 1.0**  
 **$V_{MAX} = 8.55 \times 10^4$  cm/sec**  
 **$V_{zh,H_2} = 7.55 \times 10^4$  cm/sec**  
 **$V_{zh,O_2} = 1.35 \times 10^4$  cm/sec**

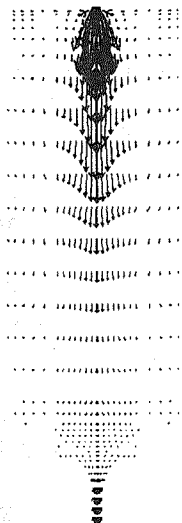


Fig. 7. Velocity Vector Plot of Incoming  $H_2/O_2$  Coaxial Jet Stream

flame front is clearly defined by the sharp temperature gradients and the presence of combusted products, such as water, with relatively uniform conditions in the combusted region behind. In addition to the major flame front, however, a smaller secondary and more permanent flame is being established right at injector entrance. This is the steady-state flame that is of more ultimate interest. At  $MR = 1$ , it is a fuel-rich flame, and both its size and intensity is dwarfed by the transient flame front propagating outward into the prefilled chamber. Yet as the transient flame propagates outward, its speed slows down, and it takes a long time (more than 20 msec) for it to consume all the prefill oxygen and burn itself out. For this reason, another case is run in an attempt to simulate the steady state in a reasonably short time.

#### Steady-State Hydrogen/Oxygen Flame

In the third example, the same combustion chamber is now prefilled with the combustion products of the incoming hydrogen/oxygen stream at the estimated steady-state chamber pressure of 98 psi and temperature of 797 K. The gaseous coaxial streams, this time

at the mixture ratio of 0.5, again comes in from the top. After approximately 3 msec, the "steady state" is well established. The isotherms, the H<sub>2</sub>O mass fraction contours, and the OH mass fraction contours are shown in Fig. 8. The presence of OH is probably the indicator of where the chemically active region is. In this case, however, difficulty has been experienced in maintaining the flame. As soon as the spark is turned off, the flame has a tendency to quench out. Indeed, in comparable experiments, sometimes, though not consistently, the same problem of flame ignition has been experienced. Thus, it appears that the problem is related to the details of the flame holding mechanism at the injector element tip, where the geometry is now only very coarsely modeled. A numerical model using

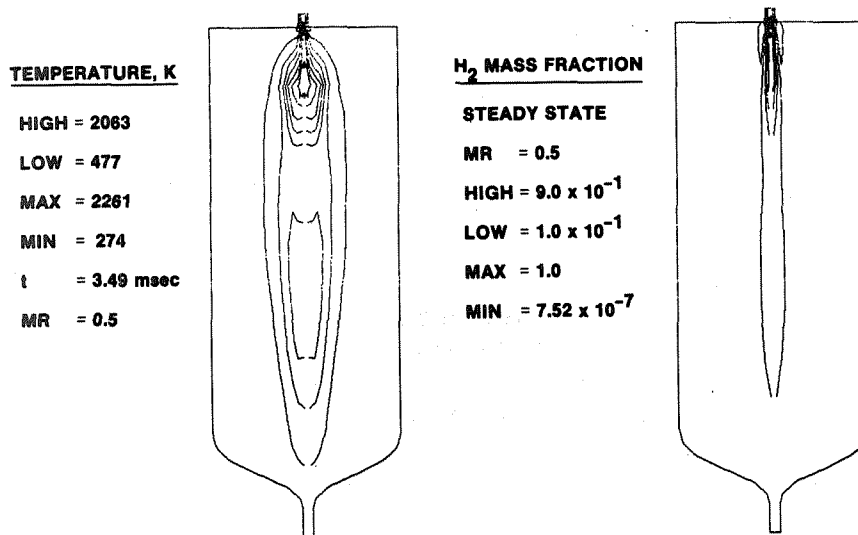


Fig. 8. Steady-State Combustion of Gaseous Oxygen/Hydrogen Flame

ARICC with very fine resolution around the injector should provide interesting insight into the exact nature of the flame holding mechanism there.

### Liquid Jet Injection and Atomization

In the final example, the unique capability of ARICC to handle two-phase flow and the creation of droplets from a liquid jet is demonstrated. Instead of gaseous oxygen, a stream of liquid oxygen (density = 69.97 lb/ft<sup>3</sup>, temperature = 94.4 K) comes in through the center of the injector element. Gaseous hydrogen at atmospheric temperature comes in through the outer annulus at the high speed of 278 ft/sec (compared with 4.4 ft/sec for the oxygen) to achieve a mixture ratio of one. The chamber is prefilled with hydrogen at 100 psi and atmospheric temperature. Figure 9 is a sequence of plots showing the atomization process, and

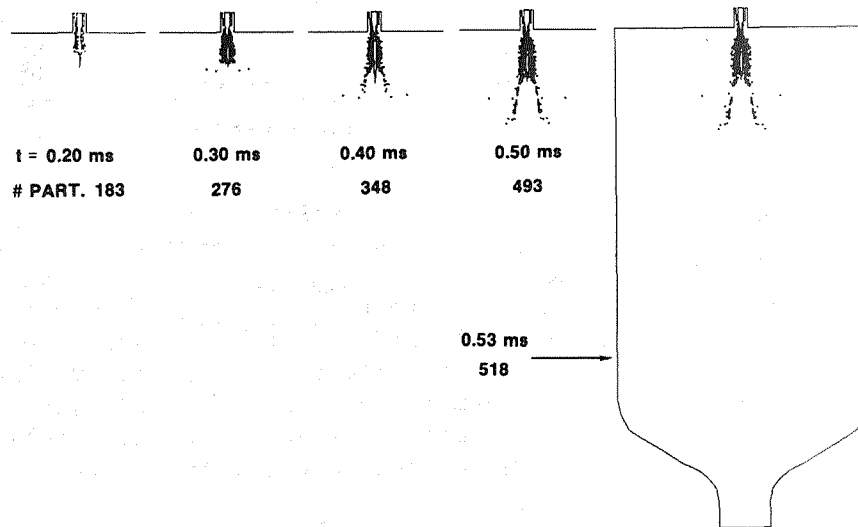


Fig. 9. Atomization Sequence of a Coaxial LOX Jet

Fig. 10 is a closeup view of the evolving shape of the liquid jet. At this range of relative velocities, droplets of the order of 10 microns are typically formed, mostly right in the recessed "cup" region shortly after injection. Note that the number of particles indicated in the figure are numerical droplet groups, with each group representing a certain number of actual physical particles depending on the local stripping rate at time of creation according to the

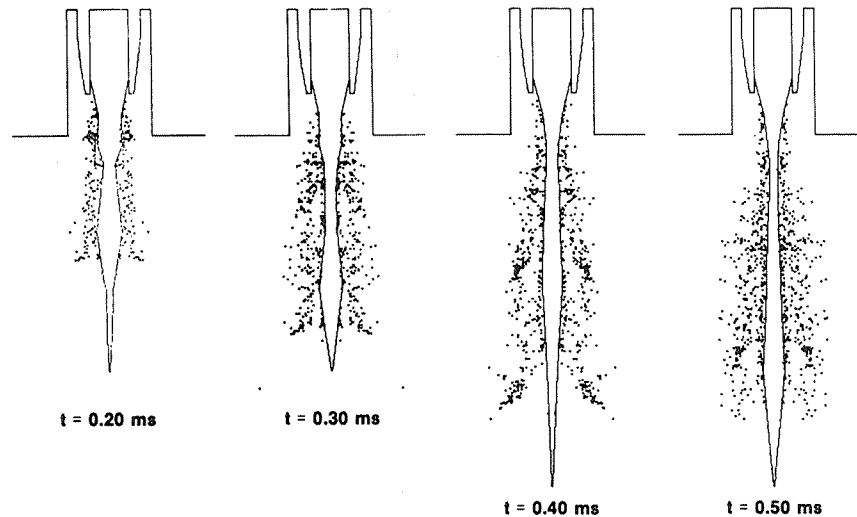


Fig. 10. Closeup Details of an Evolving Liquid (LOX) Jet

CICM atomization model. At the beginning of the run, the liquid jet column is given an arbitrary convenient shape (conforming to grid lines) with kinks on its surface. Toward the end of the run, at approximately 0.4 msec, it can be seen that the fluid dynamic forces have elongated the liquid column and smoothed out its surface. Though no experimental data are available now for a direct comparison, the simulated jet size and shape and the spray cone angle of the droplets (approximately 25 degrees) are all intuitively correct.

#### Conclusions and Recommendations

The ARICC code has shown that with present-day computers and numerical methodology, it is now possible to construct a complete model of the combustion process inside a liquid rocket engine. The development process points to many areas for further work, not the least of which is the need for experimental correlations to be fed into the many physical models that still need to be described empirically. Much specific measurements need to be done, using nonintrusive flow diagnostic techniques and spray measuring techniques, before the physical models can be confidently anchored and refined.

On the other hand, the availability of a tool like ARICC also opens up many potential applications. Already mentioned is the use of ARICC as a comprehensive simulator for injector/combustor hardware and other combustion devices. Secondly, ARICC can be used as an engine performance analyzer, especially when small but powerful dedicated computers are available. In this application, ARICC combines the diverse capability of and will eventually supercede the earlier generation codes stated previously (Ref. 2-6). The third and most promising area of application is ARICC as a research tool. While various physical models are now installed in ARICC, it can be turned around and used as a test bed for various upgraded models as new theories or data become available. Included in this category are areas for computational fluid dynamics research, such as turbulence models, algorithm efficiency improvements, and advanced graphics. Droplet dynamics research includes spray characteristics, droplet breakup/coagulation criteria, droplet deformation effects, atomization mechanism, and suspension flow or slurry flow. Thirdly, and most importantly, flame research using ARICC can be very fruitful in furthering understanding of diffusion flames, detonations, deflagrations, flame front propagation, ignition criteria, flame stability, and kinetic chemistry models. Finally, it should be remembered that ARICC is a two-dimensional/axisymmetric code. While already extremely valuable, most real-life hardware would require a fully three-dimensional model to study. Thus, the development of a three-dimensional counterpart to ARICC would be the logical next step to pursue.

#### Acknowledgement

The author wishes to acknowledge the following individuals at Rocketdyne for their continuing contributions to the development of ARICC: Mr. Steve Fisher, Dr. Mason Change, Dr. Robert Jensen, Mr. Raj Varma, and Mr. Paul Reiser for his programming expertise. Also acknowledged should be the authors of the CONCHAS-SPRAY code at Los Alamos National Laboratories.

## References

1. Cloutman, L. D., J. K. Dukowicz, J. D. Ramshaw, and A. A. Amsden, CONCHAS-SPRAY: A Computer Code for Reactive Flows With Fuel Sprays, Los Alamos National Laboratories Report LA-9294-MS (1982).
2. Sutton, R. D., M. D. Schuman, and W. D. Chadwick, Operating Manual for Injection Combustion Model, Final Report, NAS8-29664 (1974).
3. Svehla, R., FORTTRAN IV Computer Program Calculation of Thermodynamic and Transport Properties of Complex Chemical Systems (TRANS 78 Program), NASA TND-7056 (1973).
4. Schuman, M. D., Standardized Distributed Energy Release Computer Program, Final Report Vol. I and II, AFRPL-TR-78-7 (1978).
5. Weber, W. T., et al., Transient Performance Programs, Vol. I and II, AFRPL-TR-80-22 (1980).
6. Nicholson, G. R. and D. E. Coats, Computer Program for the ANALYSIS of Chemically Reacting Gas Mixtures, Ultra Systems, Inc. (formerly Dynamic Sci.) Irvine, California (1973).
7. Nichols, B. D., C. W. Hirt, and R. S. Hotchkiss, SOLA-VOF: A Solution Algorithm for Transient Fluid Flow With Multiple Free Boundaries, Los Alamos National Laboratories, LA-8355 (1980).
8. Amsden, A. A., H. M. Ruppel, and C. W. Hirt, SALE: A Simplified ALE Computer Program for Fluid Flow at All Speeds, Los Alamos National Laboratories, LA-8095, pp 10-12 (1980).
9. Westbrook, C. K., "Oxidation Kinetics in Detonations," Comb. Sci. Tech., Vol 29 (1982).

Laser Schlieren and Ultraviolet Diagnostics  
of Rocket Combustion

S. C. Fisher

Rockwell International/Rocketdyne Division  
Canoga Park, California

Abstract

A low pressure oxygen/hydrogen turbine drive combustor hot-fire test series was conducted on the Turbine Drive Combustor Technology Program (Contract NAS8-34728). The first objective of the test series was to gather data on an axisymmetric combustion system to support anchoring of a new combustion/fluid dynamics computer code under development on the same contract. The second objective was to gain insight into low mixture ratio combustion characteristics of coaxial injector elements.

This paper discusses the diagnostic test setup used in the hot-fire test program and the results obtained. Most of the data collected is in the form of high-speed laser Schlieren cinematography and ultraviolet cinematography of the actual ignition and combustion process inside a combustion chamber system. Details of the 9000 frames/sec laser Schlieren system and the ultraviolet cinematography system are described. The combustion model utilized in the program was designed to simulate the Space Shuttle Main Engine (SSME) oxidizer preburner ignition conditions.

Introduction and Background

The present start requirements on the SSME dictate that the oxidizer preburner ignite at overall mixture ratios as low as 0.3 (o/f), which is substantially below the well mixed flammability limit (Fig. 1). The preburner coaxial elements have regularly accomplished ignition under these conditions, however, repeatability is sensitive to small engine flow control variations and some delayed ignitions

have occurred. The physical mechanisms that allow coaxial element ignition at very low mixture ratios, and subsequently contribute to this sensitivity, are not well understood.

The basic coaxial element injector design is fundamentally a high durability and high performance injector concept. In general, this has been well substantiated on the

SSME preburners. However, there have been a number of instances where injector face, liquid oxygen (LOX) post, fuel sleeve, liner wall, and baffle erosions have occurred. These anomalies appear to be related to contamination in the injector elements, but this has not been positively established in all cases and the physical mechanisms whereby these erosions occur is also not well understood. As a corrective measure, additional hydrogen coolant has been selectively added at several locations of the injector. This is undesirable since it potentially reduces injector mixing efficiency and can potentially contribute to non-uniformities in the temperature profile within the hot gas delivered to the turbine.

Technology advancements are required that will increase the understanding of the physical mechanisms that influence low mixture ratio coaxial element operation, leading to analysis and design techniques that will improve the ignition, durability, and performance characteristics of turbine drive combustors for current and future liquid rocket engine systems.

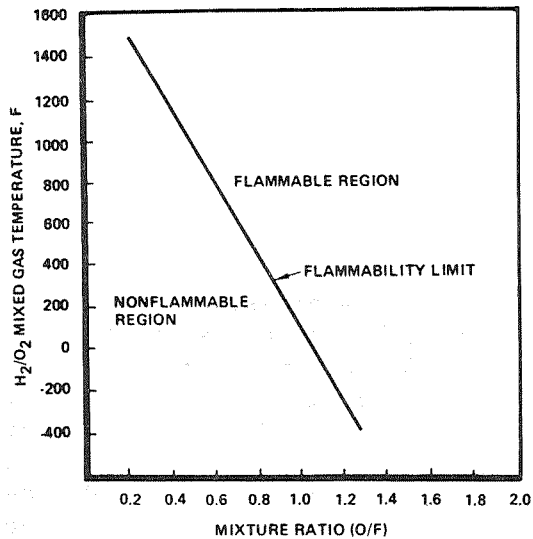


Fig. 1. Flammability Limits of Mixed Oxygen/Hydrogen

The Turbine Drive Combustor Ignition and Durability Technology Program includes a combination of computer modeling analysis and hot-fire testing that will lead to a better understanding of the physical mechanisms affecting turbine drive combustor ignition, durability, and performance. This paper discussed the high speed laser Schlieren and ultraviolet diagnostic setup and results of the first of two hot-fire test series to be performed on the Turbine Drive Technology Program. The low pressure ignition test series was conducted at the Thermodynamics Laboratory at the NAAO (North American Aircraft Operations) Division. All of the testing was done utilizing a 4-inch diameter solid wall combustor with 4-inch diameter fused silica windows on opposite sides of the combustion chamber. The ignition and combustion process was viewed through the windows and recorded on high-speed motion picture film utilizing both a laser Schlieren and an ultraviolet camera system.

A total of 115 ambient oxygen/ambient hydrogen ignition hot-fire tests were conducted. Ignition tests were run on both coaxial and micro-orifice type injector elements. The tests had chamber pressures ranging from 80 to 200 psia, flowrates ranging from 0.016 to 0.086 lb/sec, and mixture ratios ranging from 0.08 to 1.8 (oxygen/hydrogen).

#### Hardware Description

The combustor assembly used for the ignition test series is shown in Fig. 2 and 3. Three different injectors were hot-fire tested: a single SSME oxidizer preburner element injector, a four-inline SSME oxidizer preburner element injector, and a "micro-orifice" type injector. The coaxial design of the SSME oxidizer preburner element is shown in the cutaway view in Fig. 4. The micro-orifice injector was designed for a flowrate equivalent to three oxidizer preburner elements. The injector incorporates 27 elements that have a total of 163 individual orifices. The basic elements are a pentad type (four on one) with the center "showerhead" being an oxidizer hole. This pattern is shown in Fig. 5.

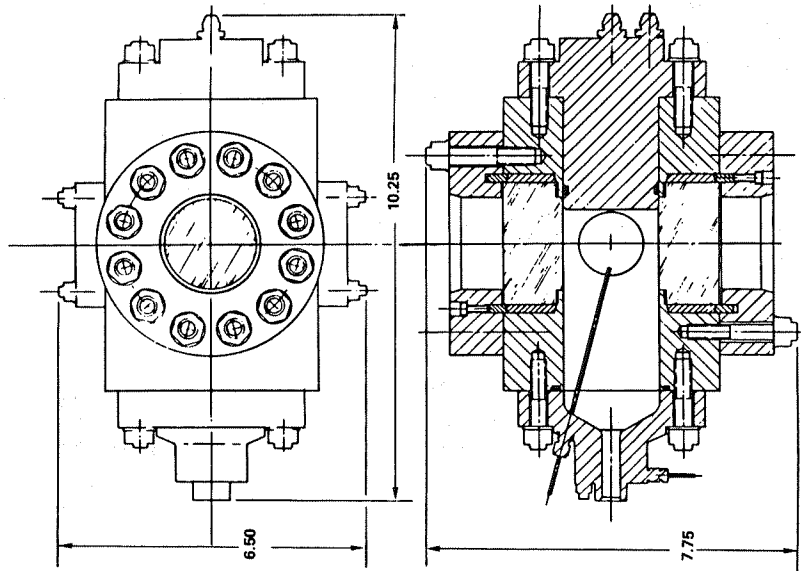


Fig. 2. Turbine Drive Combustor Technology Test Chamber

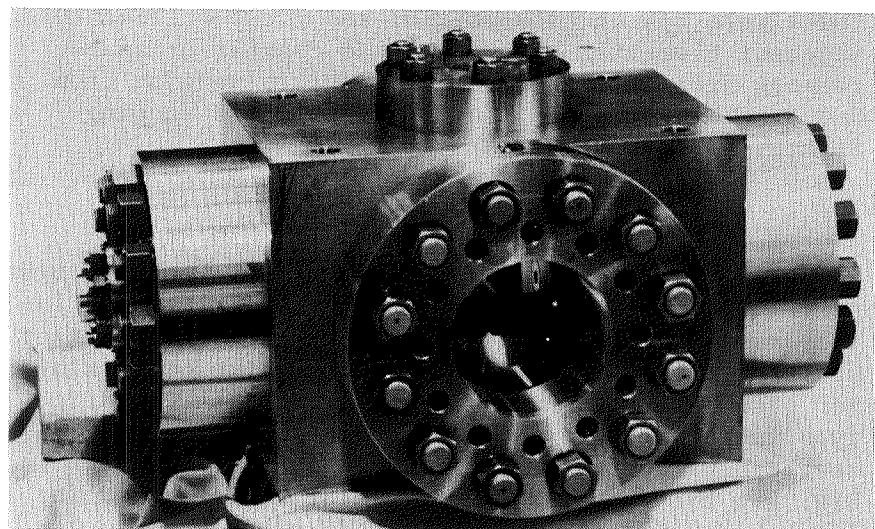


Fig. 3. Combustion Chamber Assembly

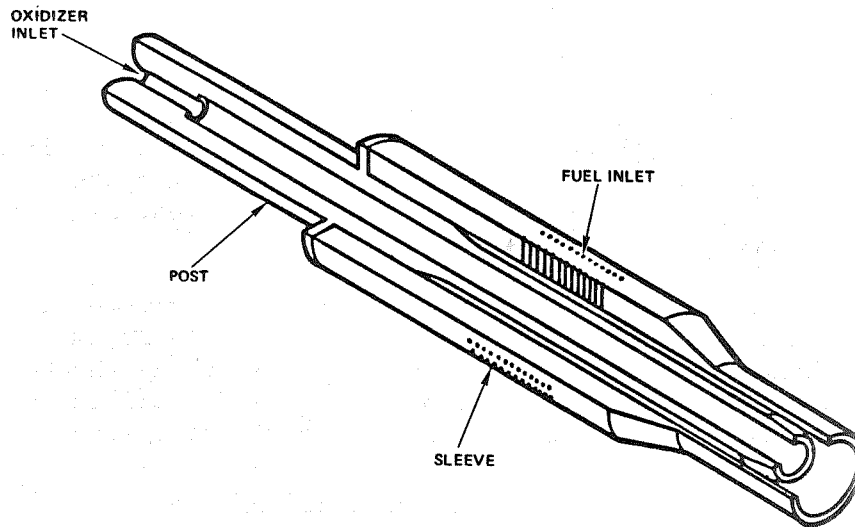


Fig. 4. Preburner Injector Element

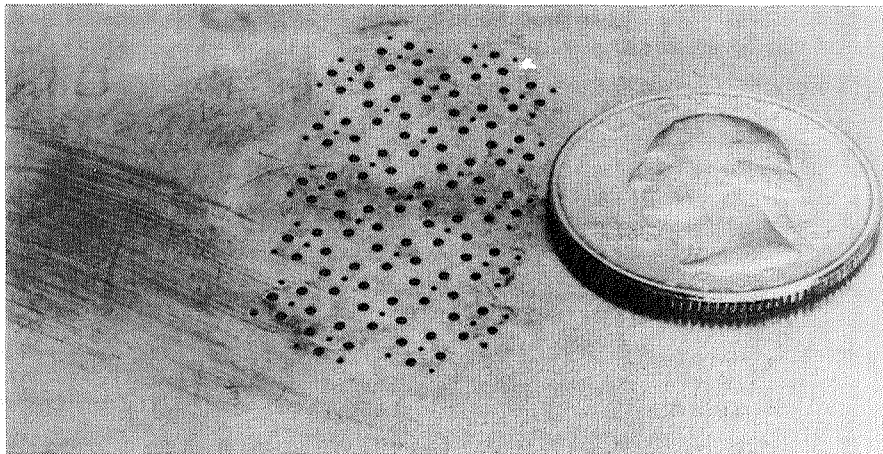


Fig. 5. Micro-orifice Injector

The chamber has two unique fused-silica window assemblies through which the combustion process can be viewed optically. Two instrumentation ports are located 90 degrees to both of the windows. These ports were used for special instrumentation requirements. Separate fittings were designed to accept pressure transducers, ignition probes, thermocouples, and thermocouple rake assemblies.

The chamber pressure was controlled by the back-pressure nozzle diameter. The nozzle is a nickel insert that is sealed to the exit housing by serrations machined into the housing and exit flange. Several nozzles of different diameters were fabricated for the various targeted mixture ratios and flowrates. All of the inlet flows were controlled externally by the facility utilizing calibrated critical venturis and regulated upstream pressures.

All of the combustor assembly details were designed to permit the test configuration to be easily changed. The facility mounting holes in the chamber body allow any detail to be removed and replaced without removing the assembly from the test stand.

### Diagnostic System Description

The high-speed cinematography diagnostic system is shown in Fig. 6. The diagnostic system was made up of four separate subsystems:

#### 1. High-Speed Ultraviolet Cinematography System

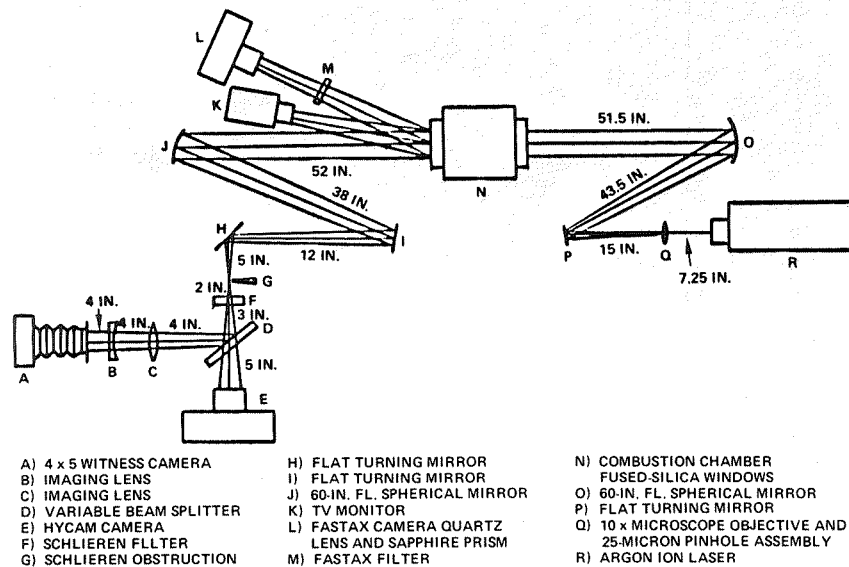


Fig. 6. Diagnostic Setup

2. High-Speed Laser Schlieren Cinematography System
3. Polaroid Laser Schlieren System
4. Vidicon TV Monitor System

#### High-Speed Ultraviolet Cinematography System

The High-Speed Ultraviolet Cinematography System was used to view the OH specie concentrations in the combustng flow. The ability to view only the OH concentrations is very useful in studying the oxygen/hydrogen combustion process. The OH radical is very short lived, kinetic (at the test conditions), and exists mainly as a part of the overall chain of reactions in the combustion process. Therefore, the OH concentrations are a direct indicator of the locations where the actual combustion reactions are taking place. At the low mixtute ratios (temperatures) typically run, OH concentrations are insignificant in the equilibrium exhaust products.

In a typical oxygen/hydrogen combustion process, the reactions are in part characterized by various species that emit radiation between 0.2 and 1.2 micron wavelengths. As can be seen in Fig. 7, OH is a pre-dominate contributor to the radiation emitted from the combustion process.

The OH species emits at a wavelength of approximately 0.31 micron, which is the ultraviolet range and can be detected with standard color film. However, standard "glass" type optics typically will not transmit below a wavelength of 0.38 to 0.4 micron. Because of this, all of the optical components in the ultraviolet diagnostic system were either quartz, fused silica, or sapphire.

On some of the tests, a special ultraviolet filter (0.25 to 0.35 micron) was used. On later tests, because of exposure problems and the fact that the filter only transmitted 60 to 70 percent of the light in its narrow band, the filter was not used. Since

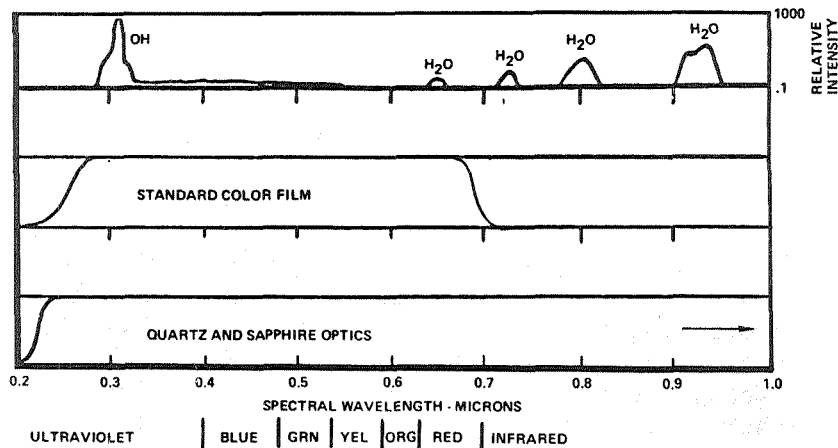


Fig. 7. Typical Spectral Transmission Response, and Optical Spectrum for Oxygen/Hydrogen Combustion System

the OH intensity is much higher than the  $H_2O_2$  intensities (Fig. 6), the high framing rates effectively filtered all but the OH radiation. This was verified by comparing films of identical conditions with and without the filter.

On the early tests in the program, a Faxtax camera with a sapphire prism, quartz lens, and 400 ASA color film was utilized. The speeds ranged from approximately 5000 frames/sec down to 2000 frames/sec. The film exposure at these speeds was very poor. A Milikan camera with a quartz lens was used to replace the Faxtax system. The Milikan camera with the 400 ASA film and a speed of approximately 400 frames/sec gave very good results even on the lower mixture ratio tests.

#### High-Speed Laser Schlieren Cinematography System

The high-speed laser Schlieren cinematography system proved to be a very useful diagnostic for the oxygen/hydrogen combustion system. Run at very high framing rates (9000 frames/sec), the system was able to record flow patterns, spark heated gas "puffs,"

spark ignition, propagation of the ignition process, flame outs, and steady-state combustion/flow patterns.

The Schlieren system utilized a 0.5 watt argon ion laser, standard Schlieren/laser optics, and a Hycam camera with 400 ASA film. Figures 8 and 9 show the actual diagnostic setup. The use of a laser light source for the Schlieren work is advantageous for two

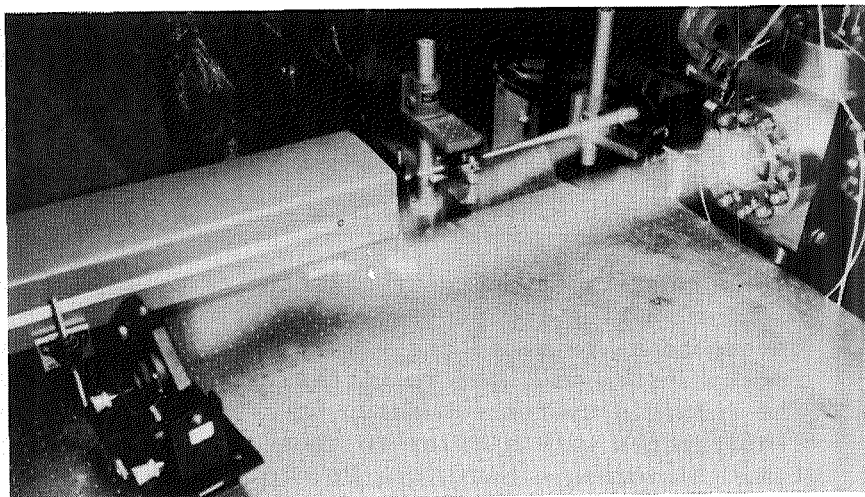


Fig. 8. Laser Schlieren Source

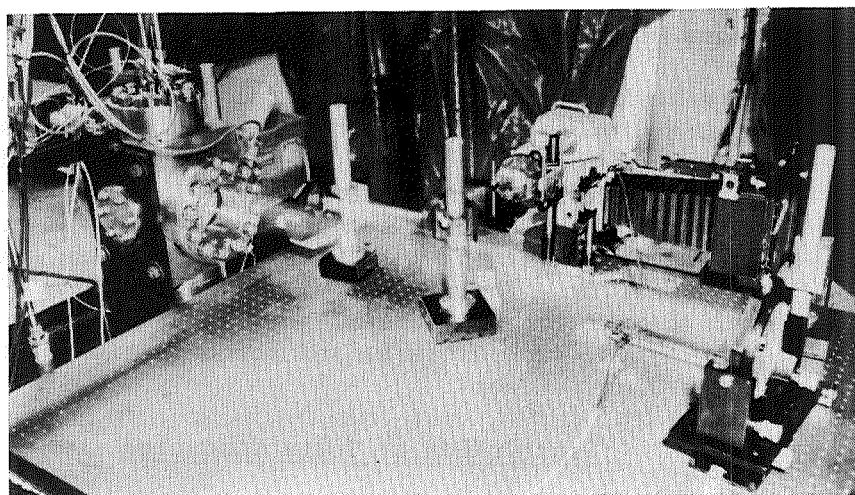


Fig. 9. Laser Schlieren Recording System

reasons. First, the intensity of the laser makes it possible to record Schlieren data at high framing rates on standard film. Second, it is a simple task to filter out the lumination created by the combustion process and view only the narrow band wavelengths of the laser/Schlieren system flow field data. An additional side benefit is that laser system is easier to work with optically.

Most of the tests were conducted with a camera speed of 9000 frames/sec and gave very good results. A few tests were conducted with framing rates of 11,000 frames/sec, but camera problems precluded running at these rates on a regular basis.

#### Polaroid Laser Schlieren System

To determine and correct setup or test problems without waiting for processed film from the Hycam camera to be returned and viewed, a parallel Polaroid camera system was used to witness the Schlieren tests. The Polaroid system was setup such that the exposure requirements were similar to those for the Hycam system. Following a test, the Polaroid film was reviewed to determine if the test should be rerun with different adjustments.

#### Vidicon Monitor System

A real-time TV monitor and recording system was set up to remotely monitor the hot-fire tests from the control room. No direct view of the test cell was available from the control room. The monitor was observed for real-time discrepancies during the tests. The tape was played back and studied following test stand securing. The monitor was very useful in discovering spark probe problems just prior to test, during tests, and posttest, and for detection of ignitions and flameouts.

#### Description of Tests Conducted

A total of 115 low-pressure ignition tests were conducted on three different injectors. The first

injector to be hot fired in the program was the single oxidizer preburner coaxial element injector. Following the single-element injector, the four-element coaxial injector was installed. The micro-orifice injector was the last injector to be hot fired in the ignition test series.

Seventy-seven single-element coaxial ignition tests were completed. Three different test sequences were used; fuel lead sequence, oxidizer lead sequence, and a sequence in which both propellants were flowing steady-state prior to initiation of the spark system.

All of the tests utilized a "point" ignition probe that was 1/8 inch in diameter and could be located anywhere within the chamber. This spark probe was placed in several different locations to determine ignition sensitivity of the coaxial elements to the spark location. Following completion of the "ignition" tests on the single-coaxial injector, the thermocouple rakes were installed to measure the temperature profile of the gas/gas combustion system.

Most of the tests were set up for a steady-state total flowrate of 0.02 lb/sec. However, a wide range of total flowrates (0.016 to 0.072 lb/sec) and mixture ratios (0.08 to 1.4 oxygen/hydrogen) were run.

Thirteen four-element coaxial low-pressure ignition tests were conducted. All of the tests utilized an oxidizer lead sequence. In addition to the ignition tests, thermocouple rake tests were also run. The total flowrates changed from 0.072 to 0.086 lb/sec with the mixture ratios varying from 0.10 to 0.62 oxygen/hydrogen.

Finally, the micro-orifice injector was subjected to a series of 25 low pressure tests. The 27 elements were sized for a flowrate equivalent to three SSME oxidizer preburner elements. Both oxidizer and fuel lead sequences were used. In addition to using the "normal" point ignition probe, the probe was modified to arc directly to the injector face on some tests.

The thermocouple rake assemblies were again used to map the temperature profile of the gas/gas combustion system.

The last tests to be conducted explored the ability of the micro-orifice injector to remain ignited as the mixture ratio was lowered. In all cases, the micro-orifice injector required a very high mixture ratio (compared with the coaxial injectors) for ignition and to remain ignited. The variable oxidizer flow was accomplished by opening a vent valve downstream of the sonic oxidizer venturi. The bypassed flow was regulated by an orifice and then vented to the atmosphere.

#### Diagnostic System Results and Conclusions

The review of the high speed laser Schlieren and ultraviolet films has yielded some new insights into the mechanisms of gas/gas coaxial element ignition which are listed below:

1. There appears to be a feature within the coaxial element flow stream that is acting as a flame holder near the injector face. This feature is able to flamehold even though the mean jet velocities are several times the theoretical flame propagation speed for a well mixed gas of similar mixture ratio.
2. Since the combustion process is unable to propagate upstream in the high velocity jet flow, another ignition mechanism is required to ignite the "flame holding feature" near the injector face. The observed mechanism appears to have two basic requirements. First, the gas/gas flow stream must be distributed, either slowed down, reversed, or blown sideways away from the element. Secondly, this disturbing action must take place while there is combustion (an ignition source) present in the recirculating gases surrounding the jet flow near the injector face. When the high velocity jet is disturbed, the flame holding feature becomes

exposed and can be ignited by the combustion in the surrounding gases.

3. Two forms of the required disturbance were observed:
  - a. The rapid flame propagation within the high mixture ratio recirculation gases present in the oxidizer lead tests provided the required disturbance. The rapid pressure increase from combustion in the recirculation gases actually reversed the element flow stream in some of the tests.
  - b. Ignition of a high mixture ratio flow stream, approximately 2 inches from the injector face, was also violent enough to disturb the element flow stream and allow ignition of the "flame holder" near the face. The phenomena was observed on fuel lead tests that had high enough mixture ratios in the recirculation zones to allow flame propagation within the slow moving recirculation gases that in turn ignited the element stream approximately 2 inches from the face. The ignition of this zone propagated rapidly and provided a pressure surge and the required disturbance of the element stream near the face. However, the flame did not propagate up the element stream. Only after the element stream was disturbed was the flame holding region able to be ignited.

In addition, the micro-orifice injector does not appear to have a flame holding mechanism at the conditions tested. The ultraviolet films show no indication of flame holding near the injector face. The recirculation gases appear to be the main source of combustion. Because of this, very high mixture ratios (1.4 or greater) are required to sustain combustion. A well mixed gas with this mixture ratio is ignitable, but the flame propagation speeds are much lower than

the injector velocities. Because of this, the bulk of the combustion is in the recirculating well mixed gases. This effect was seen in the thermocouple rake temperature profiles as well as the ultraviolet films.

Figure 10 is a collection of prints made from the high-speed laser Schlieren film from Test 10.1. Test 10.1 was a typical fuel lead test with a high mixture ratio (1.1 oxygen/hydrogen). This sequence of photos (only 15 frames out of a 400-foot roll) is presented to give a representation of the type of information available from the laser Schlieren films. Every fifth frame of the actual sequence was printed. The sequence goes from left to right. The actual framing rate was near 9000 frames/sec. The reproduction of the film for this paper unfortunately does not portray the quality and the information available from these films. To study any of the phenomena described, the actual test films must be reviewed. The author has all of the original test films (a total of 8 miles of film), which includes both the laser Schlieren and ultraviolet records.

Both the high-speed laser Schlieren and ultraviolet diagnostics have proven to be extremely useful tools in the study of the low-mixture ratio ignition and combustion of hydrogen and oxygen in a rocket combustion system. With the high speed laser Schlieren cinematography system flow patterns, the actual spark ignition process, combustion propagation, and "flame outs" can be visualized with great detail. The high-speed ultraviolet cinematography has allowed visualization of high OH concentrations and zones of the actual combustion process. Both of these very graphic visualization techniques go hand in hand and complement each other.

Because of the successful application of these techniques and the large amount of insight gained, additional refined studies into low mixture ratio oxygen/hydrogen ignition and combustion would be very productive in helping to further understand the mechanisms involved. The Turbine Drive Combustor

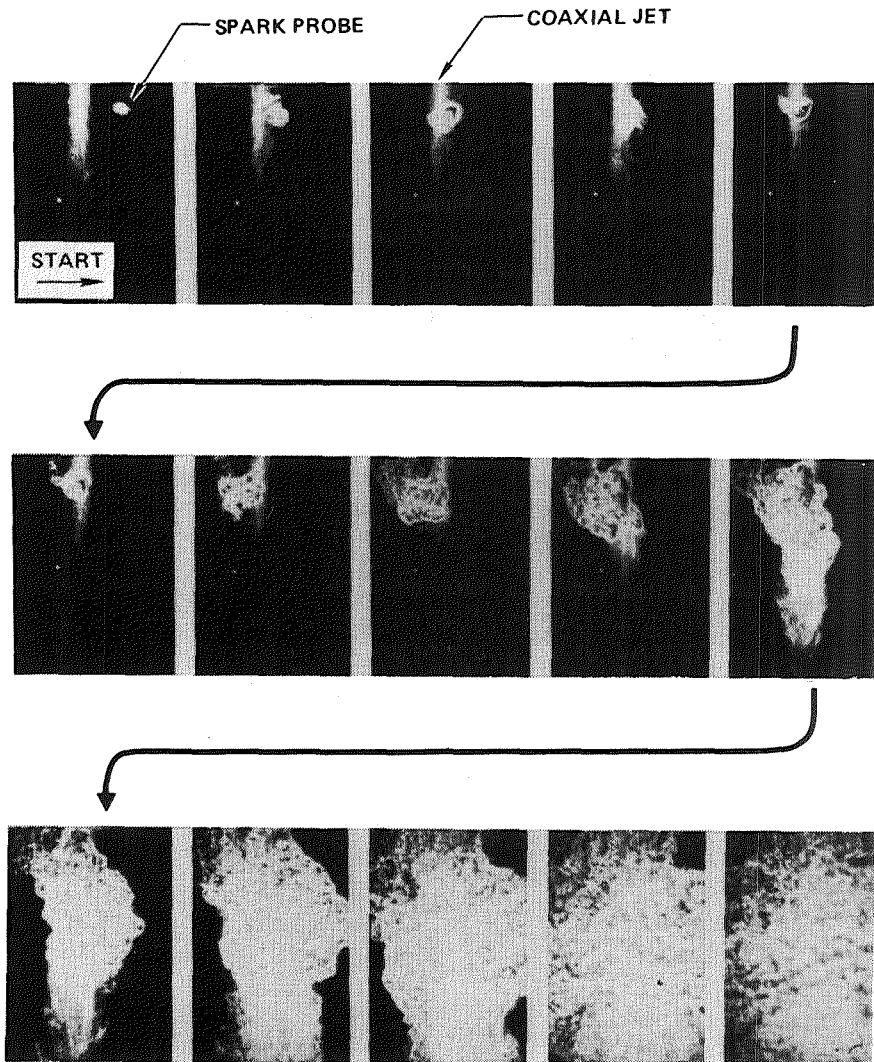


Fig. 10. Fuel Lead Ignition Sequence

Technology Program is currently making plans for additional tests that will study the flame holding aspects of the gas/gas coaxial element and study coaxial element oxygen/hydrogen combustion, using the same test hardware and diagnostics.

PARTICIPANTS LIST

W. S. Alter	David L. Christensen
Brenda Lindley-Anderson	Harry Cikanek
Charles Annis	Joseph C. Cody
C. Aukerman	Tom Coffin
Daniel Bales	Marcia Collins
S. Barkhoudarian	H. Coldwater
Donald A. Barnes	Donald R. Connel
R. F. Beatty	Richard Counts
Robert L. Bender	Brad A. Cowles
S. Bhattacharyya	Gorge B. Cox, Jr.
Carmelo J. Bianca, Jr.	Preston Craig
Dale Blount	T. A. Cruse
Donald Bolstad	Jeremy P. B. Cuffe
Rodney A. Boudreaux	Robert E. Cunningham
Lawrence Boulder	Dan David
Kim Bowen	Jack H. Davis
C. Bradford	William Day
Rodney Bradford	Fred J. Dolan
James W. Bransford	Tom Dollman
George F. Bremer	Robert Dominic
Steve Brolliar	Nathan S. Doughetry, Jr.
S. W. Brown	Robert E. Doyle
Venita Brown	Michael Drake
R. W. Buckman	Robert L. Dreshfield
Angie Bukley	Paul T. Falk
James Burka	Richard Farmer
H. D. Burke	Van S. Fehr
M. F. Butner	Geroge Fichtl
Dave F. Calhoon	Charles J. Finnegan
Warren Campbell	S. F. Fisher
Willie E. Campbell	David P. Fleming
James Cannon	Robert L. Fowler
K. L. Cappel	P. M. French
Harry W. Carpenter	Gerald Friedman
Edgar Carrasquillo	Joseph Fries
C. E. Cataldo	Donald Fulton
William V. Chambers	Frank Garcia
C. Chamis	Fred S. Garcia
W. T. Chandler	Henry Gawrylowicz
S. S. Chen	Anthony F. Giamei
Dara W. Childs	Harold M. Gibson

John Glasgow  
Otto Goetz  
Dennis Goode  
Sol Gorland  
Stanley Gray  
Terry Greenwood  
Donald Griffin  
Loren Gross  
Klaus Gross  
J. E. Haas  
Gary R. Halford  
David Hamilton  
M. E. Hampson  
James D. Hankins  
N. B. Hannum  
Harlan S. Harman  
Lt. Gregg Hawickhorst  
Arthur Henderson  
R. C. Hendricks  
Phil Hess  
R. Holmes  
Dale A. Hopkins  
Paul Howard  
James E. Jenkins  
John H. Johnson  
M. H. Johnson  
Russle L. Johnson  
Allen Johnston  
Larry Kiefling  
James P. Kiely  
Beverly Killman  
J. E. Kingsbury  
Ken G. Kirk  
William K. Knuth  
R. Douglas Kramer  
L. Krishnamurthy  
Carolyn Kurgan  
Walt E. Langhi  
J. R. Lewis  
Chester Lee  
Young Lee  
Pak-yan Liang  
Jerald L. Littles  
Sam Lowry

Carl H. Lund  
Charles A. Lundquist  
Wayne B. Lunn  
Werner P. Luscher  
John Moorehead  
S. J. Marsik  
John W. Martin  
Daniel E. Matejczyk  
Robert E. Maurer  
Stan McIntyre  
Gene McKannon  
K. L. McLallin  
Jim McLannan  
W. B. McPherson  
Jay Medley  
Edward E. Montgomery  
S. F. Morea  
Vito Moreno  
Paul Morris  
Harold E. Munson  
Neill C. Murphy  
Linda S. New  
William C. Nieberding  
Richard Norman  
William Norton  
Benny Nunnelle  
Robert O'Brien  
Robert A. Pallini  
Marcus L. Pearson  
Mark Pettitt  
Roy Pelmas  
Carlton D. Penn  
George Philyaw  
Chuck Pinson  
John E. Pond  
Jan S. Porowski  
William Powers  
Jerry Price  
D. Pryor  
Andrzej J. Prezekwas  
Richard J. Quentmeyer  
Gary Quill  
G. M. Reck

James C. Reese, Jr.  
Chris C. Rhemer  
Russel E. Rhodes  
Robert J. Richmond  
Jim Robertson  
Byron Rouse  
Robert Rowe  
Robert Rowe  
Richard Ryan  
Richard W. Salkeld  
James L. Sanders  
Doug Sandridge  
Charles Schafer  
Robert Schwinghamer  
Luck A. Schutzenhofer  
H. Scibbe  
Robert J. Scrip  
Max Sharpe  
Joyn A. Shirley  
J. D. Siegwarth  
Ashok K. Singhal  
Henry D. Snyder  
Jim Smith  
Tommy R. Smith  
Louis Spadiccini  
Larence Spadley  
James Spear  
Frank Stephensen  
M. Anthony Stone  
Heinz G. Struck  
Peter Sulyma  
C. V. Sundaram  
W. Swanson  
Shane Swint  
Jurgen Thoenes  
Robert Thom  
Jerrell M. Thomas  
Kevin Thomas  
R. G. Thompson  
Bruce K. Tiller  
George VonPragenau  
Jim Walton  
David B. Wamstad

J. P. Wanhainer  
Glen P. Westrich  
William B. White  
Warren Wiley  
Jimmy R. Williams  
James M. Yeager  
George Young  
Robert Zera  
E. S. Zori

1. REPORT NO. NASA CP-2372		2. GOVERNMENT ACCESSION NO.		3. RECIPIENT'S CATALOG NO.	
4. TITLE AND SUBTITLE Advanced High Pressure O <sub>2</sub> /H <sub>2</sub> Technology				5. REPORT DATE April 1985	
				6. PERFORMING ORGANIZATION CODE	
7. AUTHOR(S) S. F. Morea and S. T. Wu, Editors				8. PERFORMING ORGANIZATION REPORT #	
9. PERFORMING ORGANIZATION NAME AND ADDRESS George C. Marshall Space Flight Center Marshall Space Flight Center, Alabama 35812				10. WORK UNIT NO. M-481	
				11. CONTRACT OR GRANT NO.	
12. SPONSORING AGENCY NAME AND ADDRESS National Aeronautics and Space Administration Washington, DC 20546				13. TYPE OF REPORT & PERIOD COVERED Conference Publication	
				14. SPONSORING AGENCY CODE	
15. SUPPLEMENTARY NOTES S. F. Morea: George C. Marshall Space Flight Center, Huntsville, Alabama. S. T. Wu: The University of Alabama in Huntsville, Huntsville, Alabama. Administered by Department of Mechanical Engineering, The University of Alabama in Huntsville under the direction of the Research and Technology Office at the Marshall Space Flight Center.					
16. ABSTRACT <p>A conference on Advanced High Pressure O<sub>2</sub>/H<sub>2</sub> Technology was held on June 27-29, 1984, at the Marshall Space Flight Center. The purpose of the conference was to present to industry, government, and the university community the initial products that are beginning to emerge from the technology programs. The content of the conference was organized into nine sessions as follows:</p> <ol style="list-style-type: none"> <li>1. Fatigue/Fracture/Life and Ignition/Combustion Process Technology</li> <li>2. Manufacturing and Productivity Technology</li> <li>3. Material Technology</li> <li>4. Bearing Technology</li> <li>5. Structure Dynamics Technology</li> <li>6. Rotordynamics Technology</li> <li>7. Fluid and Gas Dynamics Technology</li> <li>8. Instrumentation Technology</li> <li>9. Ignition/Combustion Processes</li> </ol> <p>There was a total of forty-three papers presented and approximately 200 attendees from industry, government, and universities. The wide-spread interest in the technology programs demonstrates that the conference is an excellent forum for the exchange of information and ideas.</p>					
17. KEY WORDS O <sub>2</sub> /H <sub>2</sub> technology Industry Government University			18. DISTRIBUTION STATEMENT Unclassified - Unlimited  Subject Category 20		
19. SECURITY CLASSIF. (of this report) Unclassified		20. SECURITY CLASSIF. (of this page) Unclassified		21. NO. OF PAGES 752	22. PRICE A99

National Aeronautics and  
Space Administration

Washington, D.C.  
20546

Official Business  
Penalty for Private Use, \$300

SPECIAL FOURTH CLASS MAIL  
BOOK

Postage and Fees Paid  
National Aeronautics and  
Space Administration  
NASA-451



**NASA**

POSTMASTER: If Undeliverable (Section 158  
Postal Manual) Do Not Return

---

---

---